Ulrich Häussler-Combe

Computational Methods for Reinforced Concrete Structures

Ulrich Häussler-Combe
Computational Methods for
Reinforced Concrete Structures

Ernst & Sohn
A Wiley Brand

Ulrich Häussler-Combe

Computational Methods for Reinforced Concrete Structures

Ernst & Sohn
A Wiley Brand

Prof. Dr.-Ing. habil. Ulrich Häussler-Combe
Technische Universität Dresden
Institut für Massivbau
01069 Dresden
Germany

Cover: The photo shows a part of the façade of the Pinakothek der Moderne, Munich. The grid indicates the subdivision of a complex structure into small simple elements or finite elements, respectively.

Preface

This book grew out of lectures the author gives at the Technische Universität Dresden. These lectures are entitled "Computational Methods for Reinforced Concrete Structures" and "Design of Reinforced Concrete Structures." Reinforced concrete is a composite of concrete and reinforcement connected by bond. Bond is a key item for the behavior of the composite which utilizes compressive strength of concrete and tensile strength of reinforcement while leading to considerable multiple cracking. This makes reinforced concrete unique compared to other construction materials such as steel, wood, glass, masonry, plastic materials, fiber reinforced plastics, geomaterials, etc.

Numerical methods like the finite element method on the other hand disclose a way for a realistic computation of the behavior of structures. But the implementations generally present themselves as black boxes in the view of users. Input is fed in and the output has to be trusted. The assumptions and methods in between are not transparent. This book aims to establish transparency with special attention for the unique properties of reinforced concrete structures. Appropriate approaches will be discussed with their potentials and limitations while integrating them in the larger framework of computational mechancis and connecting aspects of numerical mathematics, mechanics, and reinforced concrete.

This is a wide field and the scope has to be limited. The focus will be on the behavior of whole structural elements and structures and not on local problems like tracking single cracks or mesoscale phenomena. Basics of multiaxial material laws for concrete will be treated but advanced theories for multiaxial concrete behavior are not a major subject of this book. Such theories are still a field of ongoing research which by far seems not to be exhausted up to date.

The book aims at advanced students of civil and mechanical engineering, academic teachers, designing and supervising engineers involved in complex problems of reinforced concrete, and researchers and software developers interested in the broad picture. Chapter 1 describes basics of modeling and discretization with finite element methods and solution methods for nonlinear problems insofar as is required for the particular methods applied to reinforced concrete structures. Chapter 2 treats uniaxial behavior of concrete and its combination with reinforcement while discussing mechanisms of bond and cracking. This leads to the model of the reinforced tension bar which provides the basic understanding of reinforced concrete mechanisms. Uniaxial behavior is also assumed for beams and frames under bending, normal forces and shear which is described in Chapter 3. Aspects of prestressing, dynamics and second-order effects are also treated in this chapter. Chapter 4 deals with strut-and-tie models whereby still a uniaxial material behavior is assumed. This chapter also refers to rigid plasticity and limit theorems.

Modeling of multiaxial material behavior within the framework of macroscopic continuum mechanics is treated in Chapter 5. The concepts of plasticity and damage are described with simple specifications for concrete. Multiaxial cracking is integrated within the model of continuous materials. Aspects of strain softening are treated leading to concepts of regularization to preserve the objectivity of discretizations. A bridge from microscopic behavior to macroscopic material modeling is given with a sketch of the microplane theory. Chapter 6 treats biaxial states of stress and strain as they arise with plates or deep beams. Reinforcement design is described based on linear elastic plate analysis and the lower bound limit

theorem. While the former neglects kinematic compatibility, this is involved again with biaxial specifications of multiaxial stress–strain relations including crack modeling.

Slabs are described as the other type of plane surface structures in Chapter 7. But in contrast to plates their behavior is predominantly characterized by internal forces like bending moments. Thus, an adaption of reinforcement design based on linear elastic analysis and the lower bound limit theorem is developed. Kinematic compatibility is again brought into play with nonlinear moment–curvature relations. Shell structures are treated in Chapter 8. A continuum-based approach with kinematic constraints is followed to derive internal forces from multiaxial stress–strain relations suitable for reinforced cracked concrete. The analysis of surface structures is closed in this chapter with the plastic analysis of simple slabs based on the upper bound limit theorem. Chapter 9 gives an overview about uncertainty and in particular about the determination of the failure probability of structures and safety factor concepts. Finally, the appendix adds more details about particular items completing the core of numerical methods for reinforced concrete structures.

Most of the described methods are complemented with examples computed with a software package developed by the author and coworkers using the PYTHON programming language.

- Programs and example data should be available under `www.concrete-fem.com`. More details are given in Appendix F.

These programs exclusively use the methods described in this book. Programs and methods are open for discussion with the disclosure of the source code and should give a stimulation for alternatives and further developments.

Ulrich Häussler-Combe   Dresden, in spring 2014

Contents

Notations

The same symbols may have different meanings in some cases. But the different meanings are used in different contexts and misunderstandings should not arise.

		firstly used
General		
$\bullet^T$	transpose of vector or matrix $\bullet$	Eq. (1.5)
$\bullet^{-1}$	inverse of quadratic matrix $\bullet$	Eq. (1.13)
$\delta\bullet$	virtual variation of $\bullet$, test function	Eq. (1.5)
$\delta\bullet$	solution increment of $\bullet$ within an iteration of nonlinear equation solving	Eq. (1.70)
$\tilde{\bullet}$	$\bullet$ transformed in (local) coordinate system	Eq. (5.15)
$\dot{\bullet}$	time derivative of $\bullet$	Eq. (1.4)
Normal lowercase italics		
a_s	reinforcement cross section per unit width	Eq. (7.70)
b	cross-section width	Section 3.1.2
b_w	crack-band width	Section 2.1
d	structural height	Section 7.6.2
e	element index	Section 1.3
f	strength condition	Eq. (5.42)
f_c	uniaxial compressive strength of concrete (unsigned)	Section 2.1
f_{ct}	uniaxial tensile strength of concrete	Section 2.1
f_t	uniaxial failure stress – reinforcement	Section 2.3
f_{yk}	uniaxial yield stress – reinforcement	Section 2.3
f_E	probability density function of random variable E	Eq. (9.2)
g_f	specific crack energy per volume	Section 2.1
h	cross-section height	Section 3.1.2
m_x, m_y, m_{xy}	moments per unit width	Eq. (7.8)
n	total number of degrees of freedom in a discretized system	Section 1.2
n_E	total number of elements	Section 3.3.1
n_i	order of Gauss integration	Section 1.6
n_N	total number of nodes	Section 3.3.1
n_x, n_y, n_{xy}	normal forces per unit width	Eq. (7.8)
p	pressure	Eq. (5.8)
p_F	failure probability	Eq. (9.18)
$\bar{p}_x, \bar{p}_z$	distributed beam loads	Eq. (3.58)
r	local coordinate	Section 1.3
s	local coordinate	Section 1.3

s_{bf}	slip at residual bond strength	Section 2.4
$s_{b\,\max}$	slip at bond strength	Section 2.4
t	local coordinate	Section 1.3
t	time	Section 1.2
t_x, t_y, t_{xy}	couple force resultants per unit width	Eq. (7.67)
u	specific internal energy	Eq. (5.12)
v_x, v_y	shear forces per unit width	Eq. (7.8)
w	deflection	Eq. (1.56)
w	fictitious crack width	Eq. (2.4)
w_{cr}	critical crack width	Section 5.7.1
z	internal lever arm	Section 3.5.4

Bold lowercase roman

$\mathbf{b}$	body forces	Section 1.2
$\mathbf{f}$	internal nodal forces	Section 1.2
$\mathbf{p}$	external nodal forces	Section 1.2
$\mathbf{n}$	normal vector	Eq. (5.5)
$\mathbf{t}$	surface traction	Section 1.2
$\mathbf{t}_c$	crack traction	Eq. (5.123)
$\mathbf{u}$	displacement field	Section 1.2
$\boldsymbol{v}$	nodal displacements	Section 1.2
$\mathbf{w}_c$	fictitious crack width vector	Eq. (5.122)

Normal uppercase italics

A	surface	Section 1.2, Eq. (1.5)
A	cross-sectional area of a bar or beam	Eq. (1.54)
A_s	cross-sectional area reinforcement	Example 2.4
A_t	surface with prescribed tractions	Section 1.2, Eq. (1.5)
A_u	surface with prescribed displacements	Eq. (1.53)
C	material stiffness coefficient	Eq. (2.32)
C_T	tangential material stiffness coefficient	Eq. (2.34)
D	scalar damage variable	Eq. (5.106)
D_T	tangential material compliance coefficient	Eq. (5.160)
D_{cT}	tangential compliance coefficient of cracked element	Eq. (5.132)
D_{cLT}	tangential compliance coefficient of crack band	Eq. (5.132)
E	Young's modulus	Eq. (1.43)
E_0	initial value of Young's modulus	Eq. (2.13)
E_c	initial value of Young's modulus of concrete	Section 2.1
E_s	initial Young's modulus of steel	Section 2.3
E_T	tangential modulus	Eq. (2.2)
F	yield function	Eq. (5.64)
F_E	distribution function of random variable E	Eq. (9.1)
G	shear modulus	Eq. (3.8)

G	flow function	Eq. (5.63)
G_f	specific crack energy per surface	Eq. (2.7)
I_1	first invariant of stress	Eq. (5.20)
J	determinant of Jacobian	Eq. (1.67)
J_2, J_3	second, third invariant of stress deviator	Eq. (5.20)
L_c	characteristic length of an element	Eq. (6.32)
L_e	length of bar or beam element	Section 1.3
M	bending moment	Section 3.1.2
N	normal force	Section 3.1.2
P	probability	Eq. (9.1)
T	natural period	Eq. (3.211)
V	shear force	Section 3.1.2
V	volume	Section 1.2, Eq. (1.5)

Bold uppercase roman

$\mathbf{B}$	matrix of spatial derivatives of shape functions	Section 1.2, Eq. (1.2)
$\mathbf{C}$	material stiffness matrix	Eq. (1.47)
$\mathbf{C}_T$	tangential material stiffness matrix	Eq. (1.50)
$\mathbf{D}$	material compliance matrix	Eq. (1.51)
$\mathbf{D}_T$	tangential material compliance matrix	Eq. (1.51)
$\mathbf{E}$	coordinate independent strain tensor	Eq. (8.15)
$\mathbf{G}_1, \mathbf{G}_2, \mathbf{G}_3$	unit vectors of covariant system	Eq. (8.16)
$\mathbf{G}^1, \mathbf{G}^2, \mathbf{G}^3$	unit vectors of contravariant system	Eq. (8.17)
$\mathbf{I}$	unit matrix	Eq. (1.85)
$\mathbf{J}$	Jacobian	Eq. (1.20)
$\mathbf{K}$	stiffness matrix	Eq. (1.11)
$\mathbf{K}_e$	element stiffness matrix	Eq. (1.61)
$\mathbf{K}_T$	tangential stiffness matrix	Eq. (1.66)
$\mathbf{K}_{Te}$	tangential element stiffness matrix	Eq. (1.65)
$\mathbf{M}$	mass matrix	Eq. (1.60)
$\mathbf{M}_e$	element mass matrix	Eq. (1.58)
$\mathbf{N}$	matrix of shape functions	Section 1.2, Eq. (1.1)
$\mathbf{Q}$	vector/tensor rotation matrix	Eq. (5.15)
$\mathbf{S}$	coordinate independent stress tensor	Eq. (8.24)
$\mathbf{T}$	element rotation matrix	Eq. (3.109)
$\mathbf{V}_n$	shell director	Section 8.1
$\mathbf{V}_\alpha, \mathbf{V}_\beta$	unit vectors of local shell system	Eq. (8.2)

Normal lowercase Greek

α	tie inclination	Eq. (3.157)
α_E, α_R	sensitivity parameters	Eq. (9.13)
α	coefficient for several other purposes	
β	shear retention factor	Eq. (5.137)
β	reliability index	Eq. (9.12)

β_t	tension stiffening coefficient	Section 2.7
ϵ	uniaxial strain	Section 1.4, Eq. (1.43)
ϵ	strain of a beam reference axis	Section 3.1.1, Eq. (3.4)
$\epsilon_1, \epsilon_2, \epsilon_3$	principal strains	Section 5.2.3
ϵ_{ct}	concrete strain at uniaxial tensile strength	Section 2.1
ϵ_{cu}	concrete failure strain at uniaxial tension	Eq. (5.152)
ϵ_{c1}	concrete strain at uniaxial compressive strength (signed)	Section 2.1
ϵ_{cu1}	concrete failure strain at uniaxial compression (signed)	Section 2.1
ϵ_I	imposed uniaxial strain	Section 2.2
ϵ_V	volumetric strain	Eq. (5.102)
ϕ	cross-section rotation	Eq. (3.1)
ϕ	angle of external friction	Eq. (5.91)
φ	angle of orientation	Section 6.1, Eq. (6.5)
φ	creep coefficient	Eq. (2.26)
φ_c	creep coefficient of concrete	Eq. (3.119)
γ	shear angle	Eq. (3.1)
γ_E, γ_R	partial safety factors	Eq. (9.44)
κ	curvature of a beam reference axis	Section 3.1.1, Eq. (3.4)
κ_p	state variable for plasticity	Section 5.5.1
κ_d	state variable for damage	Section 5.6
μ_E	mean of random variable E	Section 9.1
ν	Poisson's ratio	Eq. (1.44)
ν	coefficient of variation	Eq. (9.46)
θ	strut inclination	Eq. (3.148)
θ	deviatoric angle	Eq. (5.46)
ϑ	angle of internal friction	Eq. (5.89)
ρ	deviatoric length	Eq. (5.45)
ρ_s	reinforcement ratio	Eq. (6.8)
ϱ_s	specific mass	Eq. (1.52)
σ	uniaxial stress	Section 1.4, Eq. (1.43)
$\sigma_1, \sigma_2, \sigma_3$	principal stresses	Section 5.2.3
σ_E	standard deviation of random variable E	Section 9.1
τ	bond stress	Section 2.4, Eq. (2.44)
τ	time variable in time history	Section 2.2
τ_{bf}	residual bond strength	Section 2.4
$\tau_{b\,\max}$	bond strength	Section 2.4
ω	circular natural frequency	Eq. (3.211)
ξ	hydrostatic length	Eq. (5.44)

Bold lowercase Greek

$\boldsymbol{\epsilon}$	small strain	Section 1.2
$\boldsymbol{\epsilon}$	generalized strain	Eq. (1.33)
$\boldsymbol{\epsilon}_p$	plastic small strain	Eq. (5.61)

$\boldsymbol{\kappa}$	vector of internal state variables	Eq. (5.39)
$\boldsymbol{\sigma}$	Cauchy stress	Section 1.2
$\boldsymbol{\sigma}$	generalized stress	Eq. (1.34)
$\boldsymbol{\sigma}'$	deviatoric part of Cauchy stress	Section 5.2.2

Normal uppercase Greek

Φ	standardized normal distribution function	Eq. (9.19)

Bold uppercase Greek

$\boldsymbol{\Sigma}$	viscous stress surplus	Eq. (1.76)

Chapter 1

Finite Elements Overview

1.1 Modeling Basics

"There are no exact answers. Just bad ones, good ones and better ones. Engineering is the art of approximation." Approximation is performed with models. We consider a reality of interest, e.g., a concrete beam. In a first view, it has *properties* such as dimensions, color, surface texture. From a view of structural analysis the latter ones are irrelevant. A more detailed inspection reveals a lot of more properties: composition, weight, strength, stiffness, temperatures, conductivities, capacities, and so on. From a structural point of view some of them are essential. We combine those essential properties to form a *conceptual model*. Whether a property is essential is obvious for some, but the valuation of others might be doubtful. We have to choose. By choosing properties our model becomes approximate compared to reality. Approximations are more or less accurate.

On one hand, we should reduce the number of properties of a model. Any reduction of properties will make a model less accurate. Nevertheless, it might remain a good model. On the other hand, an over-reduction of properties will make a model inaccurate and therefore useless. Maybe also properties are introduced which have no counterparts in the reality of interest. Conceptual modeling is the art of choosing properties. As all other arts it cannot be performed guided by strict rules.

The chosen properties have to be related to each other in quantitative manner. This leads to a *mathematical model*. In many cases, we have systems of differential equations relating variable properties or simply *variables*. After prescribing appropriate boundary and initial conditions an exact, unique solution should exist for variables depending on spatial coordinates and time. Thus, a particular variable forms a field. Such fields of variables are infinite as space and time are infinite.

As analytical solutions are not available in many cases, a discretization is performed to obtain approximate numerical solutions. *Discretization* reduces underlying infinite space and time into a finite number of supporting points in space and time and maps differential equations into algebraic equations relating a finite number of variables. This leads to a *numerical model*.
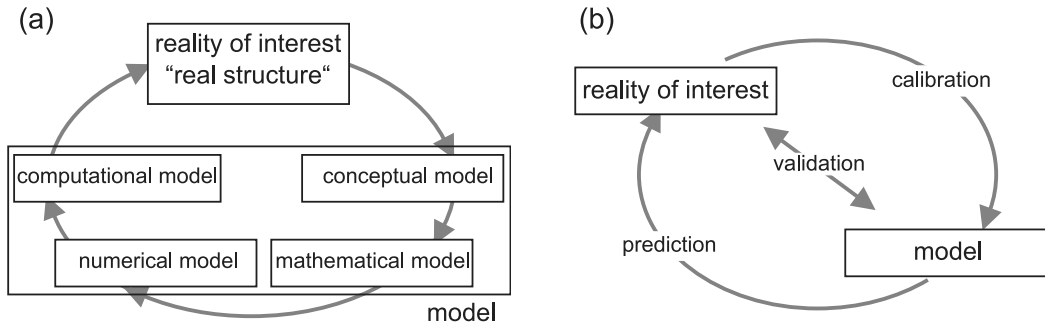
Figure 1.1: Modeling (a) Type of models following [83]. (b) Relations between model and reality.

A numerical model needs some completion as it has to be described by means of programming to form a *computational model*. Finally, programs yield solutions through processing by computers. The whole cycle is shown in Fig. 1.1. Sometimes it is appropriate to merge the sophisticated sequence of models into the *model*.

A final solution provided after computer processing is approximate compared to the exact solution of the underlying mathematical model. This is caused by discretization and round-off errors. Let us assume that we can minimize this mathematical approximation error in some sense and consider the final solution as a *model solution*. Nevertheless, the relation between the model solution and the underlying reality of interest is basically an issue. Both – model and reality of interest – share the same properties by definition or conceptual modeling, respectively. Let us also assume that the real data of properties can be objectively determined, e.g., by measurements.

Thus, real data of properties should be properly approximated by their computed model counterparts for a problem under consideration. The difference between model solution data and real data yields a *modeling error*. In order to distinguish between bad (inaccurate), good (accurate), and better model solutions, we have to choose a reference for the modeling error. This choice has to be done within a larger context, allows for discretion and again is not guided by strict rules like other arts. Furthermore, the reference may shift while getting better model solutions during testing.

A bad model solution may be caused by a bad model – bad choice of properties, poor relations of properties, insufficient discretization, programming errors – or by incorrect model parameters. *Parameters* are those properties which are assumed to be known in advance for a particular problem and are not object to a computation. Under the assumption of a good model, the model parameters can be corrected by a *calibration*. This is based upon appropriate problems from the reality of interest with the known real data. On one hand calibration minimizes the modeling error by adjusting of parameters. On the other hand, *validation* chooses other problems with known real data and assesses the modeling error without adjusting of parameters. Hopefully model solutions are still good.

Regarding reinforced concrete structures, calibrations usually involve the adaption of material parameters like strength and stiffness as part of *material models*. These parameters

are chosen such that the behavior of material specimen observed in experiments is reproduced. A validation is usually performed with structural elements such as bars, beams, plates, and slabs. Computational results of *structural models* are compared with the corresponding experimental data.

This leads to basic peculiarities. Reproducible experiments performed with structural elements are of a small simplified format compared with complex unique buildings. Furthermore, repeated experimental tests with the same nominal parameters exhibit scattering results. Standardized *benchmark tests* carving out different aspects of reinforced concrete behavior are required. Actually a common agreement about such benchmark tests exists only in the first attempts. Regarding a particular problem a corresponding model has to be validated on a case-by-case strategy using adequate experimental investigations. Their choice again has no strict rules as the preceding arts.

Complex proceedings have been sketched hitherto outlining a model of modeling. Some benefit is desirable finally. Thus, a model which passed validations is usable for *predictions*. Structures created along such predictions hopefully prove their worth in the reality of interest.

This textbook covers the range of conceptual models, mathematical models, and numerical models with special attention to reinforced concrete structures. Notes regarding the computational model including available programs and example data are given in Appendix F. A major aspect of the following is modeling of *ultimate limit states*: states with maximum bearable loading or acceptable deformations and displacements in relation to failure. Another aspect is given with *serviceability*: Deformations and in some cases oscillations of structures have to be limited to allow their proper usage and fulfillment of intended services. *Durability* is a third important aspect for building structures: deterioration of materials through, e.g., corrosion, has to be controlled. This is strongly connected to cracking and crack width in the case of reinforced concrete structures. Both topics are also treated in the following.

1.2 Discretization Outline

The finite element method (FEM) is a predominant method to derive numerical models from mathematical models. Its basic theory is described in the remaining sections of this chapter insofar as it is needed for its application to different types of structures with reinforced concrete in the following chapters.

The underlying mathematical model is defined in one-, two-, or three-dimensional fields of space related to a *body* and one-dimensional space of time. A body undergoes deformations during time due to loading. We consider a simple example with a plate defined in 2D space, see Fig. 1.2. Loading is generally defined depending on time whereby time may be replaced by a loading factor in the case of quasistatic problems. Field variables depending on spatial coordinates and time are, e.g., given by the displacements.

- Such fields are discretized by dividing space into *elements* which are connected by *nodes*, see Fig. 1.3a. Elements adjoin but do not overlap and fill out the space of the body under consideration.

- Discretization basically means *interpolation*,, i.e., displacements within an element are interpolated using the values at nodes belonging to the particular element.
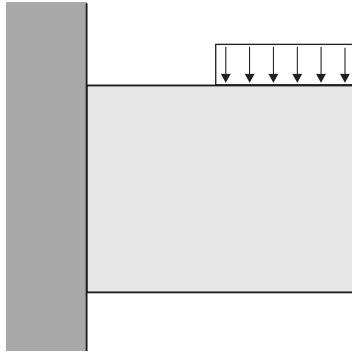
Figure 1.2: Model of a plate.

In the following this will be written as

$$\mathbf{u} = \mathbf{N} \cdot \boldsymbol{v} \tag{1.1}$$

with the displacements $\mathbf{u}$ depending on spatial coordinates and time, a matrix $\mathbf{N}$ of *shape functions* depending on spatial coordinates and a vector $\boldsymbol{v}$ depending on time and collecting all displacements at nodes. The number of components of $\boldsymbol{v}$ is n. It is two times the number of nodes in the case of the plate as the displacement $\mathbf{u}$ has components u_x, u_y. Generally some values of $\boldsymbol{v}$ may be chosen such that the *essential or displacement boundary conditions* of the problem under consideration is fulfilled by the displacements interpolated by Eq. (1.1). This is assumed for the following.
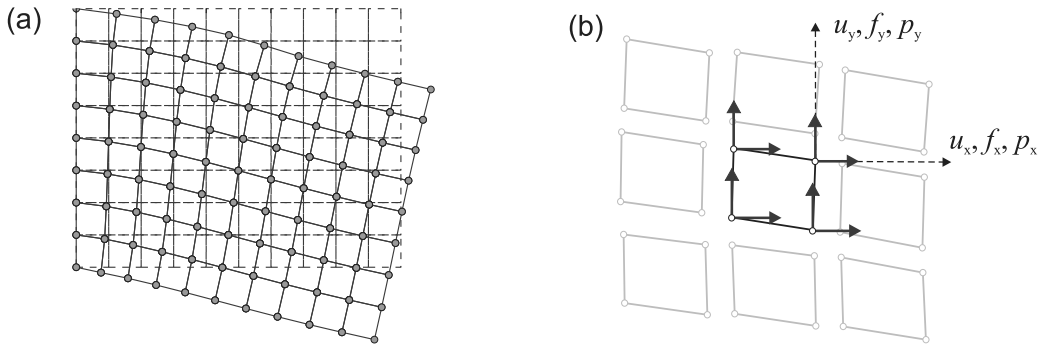
Figure 1.3: (a) Elements and nodes (deformed). (b) Nodal quantities.

Strains are derived from displacements by differentiation with respect to spatial coordinates. In the following, this will be written as

$$\boldsymbol{\epsilon} = \mathbf{B} \cdot \boldsymbol{v} \tag{1.2}$$

with the strains $\boldsymbol{\epsilon}$ depending on spatial coordinates and time, a matrix $\mathbf{B}$ of spatial derivatives of shape functions depending on spatial coordinates and the vector $\boldsymbol{v}$ as has been used in Eq. (1.1). The first examples for Eqs. (1.1, 1.2) will be given in Section 1.3.

- A field variable $\mathbf{u}$ is discretized with Eqs. (1.1, 1.2), i.e., the infinite field in space is reduced into a finite number n of variables in supporting spatial points or nodes which are collected in $\boldsymbol{v}$.

Thereby *kinematic compatibility* should be assured regarding interpolated displacements, i.e., generally spoken a coherence of displacements and deformations should be given.

Strains $\boldsymbol{\epsilon}$ lead to stresses $\boldsymbol{\sigma}$. A *material law* connects both. Material laws for solids are a science in itself. This textbook mainly covers their flavors for reinforced concrete structures. To begin with, such laws are abbreviated with

$$\boldsymbol{\sigma} = f(\boldsymbol{\epsilon}) \tag{1.3}$$

Beyond total values of stress and strain their small changes in time t have to be considered. They are measured with time derivatives

$$\dot{\boldsymbol{\epsilon}} = \frac{\partial \boldsymbol{\epsilon}}{\partial t}, \quad \dot{\boldsymbol{\sigma}} = \frac{\partial \boldsymbol{\sigma}}{\partial t} \tag{1.4}$$

Nonlinear material behavior is mainly formulated as a relation between $\dot{\boldsymbol{\epsilon}}$ and $\dot{\boldsymbol{\sigma}}$. The first concepts about material laws are given in Section 1.4.

An *equilibrium condition* is the third basic element of structural analysis beneath kinematic compatibility and material laws. It is advantageously formulated as principle of virtual work leading to

$$\int_V \delta\boldsymbol{\epsilon}^T \cdot \boldsymbol{\sigma} \, \mathrm{d}V = \int_V \delta\mathbf{u}^T \cdot \mathbf{b} \, \mathrm{d}V + \int_{A_t} \delta\mathbf{u}^T \cdot \mathbf{t} \, \mathrm{d}A \tag{1.5}$$

for quasistatic cases with the volume V of the solid body of interest, its body forces $\mathbf{b}$, its surface A, and its surface tractions $\mathbf{t}$ which are prescribed at a part A_t of the whole boundary A. Furthermore, virtual displacements $\delta\mathbf{u}$ and the corresponding virtual strains $\delta\boldsymbol{\epsilon}$ are introduced. They are arranged as vectors and $\delta\mathbf{u}^T, \delta\boldsymbol{\epsilon}^T$ indicate their transposition into row vectors to have a proper scalar product with $\boldsymbol{\sigma}, \mathbf{b}, \mathbf{t}$ which are also arranged as vectors. Fields of $\mathbf{b}$ and $\mathbf{t}$ are generally prescribed for a problem under consideration while the field of stresses $\boldsymbol{\sigma}$ remains to be determined. Surface tractions $\mathbf{t}$ constitute the *natural* or *force boundary conditions*.

- Stresses $\boldsymbol{\sigma}$ and loadings $\mathbf{b}, \mathbf{t}$ are in static equilibrium for the problem under consideration if Eq. (1.5) is fulfilled for arbitrary virtual displacements $\delta\mathbf{u}$ and the corresponding virtual strains $\delta\boldsymbol{\epsilon}$.

Thereby, $\delta\mathbf{u}$ is zero at the part A_u of the whole boundary A with prescribed displacement boundary conditions. Applying the displacement interpolation equation (1.1) to virtual displacements leads to

$$\delta\mathbf{u} = \mathbf{N} \cdot \delta\boldsymbol{v}, \qquad \delta\boldsymbol{\epsilon} = \mathbf{B} \cdot \delta\boldsymbol{v} \tag{1.6}$$

and using this with Eq. (1.5) to

$$\delta\boldsymbol{v}^T \cdot \left[\int_V \mathbf{B}^T \cdot \boldsymbol{\sigma} \, \mathrm{d}V \right] = \delta\boldsymbol{v}^T \cdot \left[\int_V \mathbf{N}^T \cdot \mathbf{b} \, \mathrm{d}V + \int_{A_t} \mathbf{N}^T \cdot \mathbf{t} \, \mathrm{d}A \right] \tag{1.7}$$

with transpositions $\delta\boldsymbol{v}^T, \mathbf{B}^T, \mathbf{N}^T$ of the vector $\delta\boldsymbol{v}$ and the matrices $\mathbf{B}, \mathbf{N}$. As $\delta\boldsymbol{v}$ is arbitrary a *discretized condition of static equilibrium* is derived in the form

$$\mathbf{f} = \mathbf{p} \tag{1.8}$$

with the vector $\mathbf{f}$ of *internal nodal forces* and the vector $\mathbf{p}$ of *external nodal forces*

$$
\begin{aligned}
\mathbf{f} &= \int_V \mathbf{B}^T \cdot \boldsymbol{\sigma}\, \mathrm{d}V \\
\mathbf{p} &= \int_V \mathbf{N}^T \cdot \mathbf{b}\, \mathrm{d}V + \int_{A_t} \mathbf{N}^T \cdot \mathbf{t}\, \mathrm{d}A
\end{aligned}
\tag{1.9}
$$

Corresponding to the length of the vector $\boldsymbol{v}$ the vectors $\mathbf{f}, \mathbf{p}$ have n components.

- By means of $\boldsymbol{\sigma} = \mathbf{f}(\boldsymbol{\epsilon})$ and $\boldsymbol{\epsilon} = \mathbf{B} \cdot \boldsymbol{v}$, Eq. (1.8) constitutes a system of n nonlinear algebraic equations whereby the nodal displacements $\boldsymbol{v}$ have to be determined such that – under the constraint of displacement boundary conditions – internal nodal forces $\mathbf{f}$ are equal to prescribed external nodal forces $\mathbf{p}$.

Nonlinear stress–strain relations, i.e., *physical nonlinearities*, are always an issue for reinforced concrete structures. It is a good practice in nonlinear simulation to start with a linearization to have a reference for the refinements of a conceptual model. *Physical linearity* is described with

$$\boldsymbol{\sigma} = \mathbf{C} \cdot \boldsymbol{\epsilon} \tag{1.10}$$

with a constant material matrix $\mathbf{C}$. Thus, using Eq. (1.2) internal forces $\mathbf{f}$ (Eq. (1.9)) can be formulated as

$$\mathbf{f} = \mathbf{K} \cdot \boldsymbol{v}, \qquad \mathbf{K} = \int_V \mathbf{B}^T \cdot \mathbf{C} \cdot \mathbf{B}\, \mathrm{d}V \tag{1.11}$$

with a constant stiffness matrix $\mathbf{K}$ leading to

$$\mathbf{K} \cdot \boldsymbol{v} = \mathbf{p} \tag{1.12}$$

This allows for a direct determination of nodal displacements which is symbolically written as

$$\boldsymbol{v} = \mathbf{K}^{-1} \cdot \mathbf{p} \tag{1.13}$$

Actually the solution is not determined with a matrix inversion but with more efficient techniques, e.g., Gauss triangularization. Stresses $\boldsymbol{\sigma}$ and strains $\boldsymbol{\epsilon}$ follow with a solution $\boldsymbol{v}$ given. A counterpart of physical linearity is *geometric linearity*:

- Small displacements and geometric linearity are assumed throughout the following if not otherwise stated.

This was a fast track for the finite element method. The rough outline will be filled out in the following. Comprehensive descriptions covering all aspects are given in, e.g., [98], [99], [9], [3]. The special aspects of reinforced concrete structures are treated in [16], [44], [81].

1.3 Elements

Interpolation performed with finite elements will be described with more details in the following. We consider the mechanical behavior of *material points* within a body. A material point is identified by its spatial coordinates. It is convenient to use a different coordinate system simultaneously. First of all, the global *Cartesian coordinate system*, see Appendix C, which is shared by all material points of a body. Thus, a material point is identified by global Cartesian coordinates

$$\mathbf{x} = (\ \ x \ \ \ y \ \ \ z \ \ )^T \tag{1.14}$$

in 3D space. In the following, we assume that the space occupied by the body has been divided into finite elements. Thus, a material point may alternatively be identified by the label I of the element it belongs to and its local coordinates

$$\mathbf{r} = (\ \ r \ \ \ s \ \ \ t \ \ )^T \tag{1.15}$$

related to a particular *local coordinate system* belonging to the element e. A material point undergoes *displacements*. In the case of translations they are measured in the global Cartesian system by

$$\mathbf{u} = (\ \ u \ \ \ v \ \ \ w \ \ )^T \tag{1.16}$$

Displacements in a general sense may also be measured by means of rotations

$$\boldsymbol{\varphi} = (\ \ \varphi_x \ \ \ \varphi_y \ \ \ \varphi_z \ \ )^T \tag{1.17}$$

if we consider a material point embedded in some neighborhood of surrounding points. The indices indicate the respective reference axes of rotation.

Isoparametric interpolation will be used in the following. The general interpolation form (Eq. (1.1)) is particularized as

$$\mathbf{u} = \mathbf{N}(\mathbf{r}) \cdot \boldsymbol{v}_e \tag{1.18}$$

whereby the global coordinates of the corresponding material point are given by

$$\mathbf{x} = \mathbf{N}(\mathbf{r}) \cdot \mathbf{x}_e \tag{1.19}$$

The vector $\boldsymbol{v}_e$ collects all nodal displacements of all nodes belonging to the element e and the vector $\mathbf{x}_e$ all global nodal coordinates of that element. Isoparametric interpolation is characterized by the same interpolation for geometry and displacements with the same shape functions $\mathbf{N}(\mathbf{r})$. Global and local coordinates are related by the *Jacobian*

$$\mathbf{J} = \frac{\partial \mathbf{x}}{\partial \mathbf{r}} \tag{1.20}$$

which may be up to a 3×3 matrix for 3D cases. Strains may be derived with displacements related to global coordinates through isoparametric interpolation. Their definition depends on the type of the structural problem. A general formulation

$$\boldsymbol{\epsilon} = \mathbf{B}(\mathbf{r}) \cdot \boldsymbol{v}_e \tag{1.21}$$

is used. Strains $\boldsymbol{\epsilon}$ finally lead to stresses $\boldsymbol{\sigma}$. Examples are given in the following.

– Two-node bar element along a line.

The line is measured by a coordinate x. Each coordinate has a cross section with a cross-sectional area. The *kinematic assumption* of a bar is that every material point in the cross section has the same displacement in the line direction.

A bar element e has nodes I, J with coordinates x_I, x_J. The nodes have the displacements u_I, u_J along the line. The origin of the local coordinate r is placed in the center between the two nodes. Regarding Eqs. (1.18, 1.19) we have

$$\mathbf{x} = \begin{pmatrix} x \end{pmatrix}, \quad \mathbf{u} = \begin{pmatrix} u \end{pmatrix}$$
$$\mathbf{N} = \begin{bmatrix} \frac{1}{2}(1-r) & \frac{1}{2}(1+r) \end{bmatrix}$$
$$\mathbf{x}_e = \begin{pmatrix} x_I \\ x_J \end{pmatrix}, \quad \boldsymbol{v}_e = \begin{pmatrix} u_I \\ u_J \end{pmatrix} \tag{1.22}$$

This leads to a scalar Jacobian

$$J = \frac{\partial x}{\partial r} = \frac{L_e}{2} \tag{1.23}$$

Strains are uniaxial and defined by

$$\epsilon = \frac{\partial u}{\partial x} = \frac{\partial u}{\partial r}\frac{\partial r}{\partial x} \tag{1.24}$$

leading to

$$\mathbf{B} = \frac{2}{L_e} \begin{bmatrix} -\frac{1}{2} & \frac{1}{2} \end{bmatrix} \tag{1.25}$$

with a bar length $L_e = x_J - x_I$ and finally, regarding Eq. (1.3), to uniaxial strains and stresses

$$\boldsymbol{\epsilon} = \begin{pmatrix} \epsilon \end{pmatrix}, \quad \boldsymbol{\sigma} = \begin{pmatrix} \sigma \end{pmatrix} \tag{1.26}$$

which are constant along the element.

– Two-node bar element in a plane

The plane is measured by coordinates x, y. The center axis of a bar is a line in this plane. Each point of the center axis again has a cross-sectional area and again the *kinematic assumption* of this bar is that every material point in the cross section has the same displacement in the direction of the center axis.

A bar element e has nodes I, J with coordinates x_I, y_I, x_J, y_J. The nodes have the displacements u_I, v_J, u_I, v_J in a plane. The origin of the local coordinate r is placed in the center between the two nodes. Regarding Eqs. (1.18) and (1.19) we have

$$\mathbf{x} = \begin{pmatrix} x \\ y \end{pmatrix}, \quad \mathbf{u} = \begin{pmatrix} u \\ v \end{pmatrix}$$
$$\mathbf{N} = \begin{bmatrix} \frac{1}{2}(1-r) & 0 & \frac{1}{2}(1+r) & 0 \\ 0 & \frac{1}{2}(1-r) & 0 & \frac{1}{2}(1+r) \end{bmatrix}$$
$$\mathbf{x}_e = \begin{pmatrix} x_I \\ y_I \\ x_J \\ y_J \end{pmatrix}, \quad \boldsymbol{v}_e = \begin{pmatrix} u_I \\ v_I \\ u_J \\ v_J \end{pmatrix} \tag{1.27}$$

Uniaxial strain is measured in the direction of the bar's center axis, i.e., in a rotated coordinate system x', y' with x' being aligned to the center axis. The rotation angle α (counterclockwise positive) and the transformation matrix $\mathbf{T}$ for global coordinates and displacements are given by

$$\mathbf{T} = \begin{bmatrix} \cos\alpha & \sin\alpha \\ -\sin\alpha & \cos\alpha \end{bmatrix}, \quad \cos\alpha = \frac{x_J - x_I}{L_e}, \quad \sin\alpha = \frac{y_J - y_I}{L_e} \tag{1.28}$$

with a bar length $L_e = \sqrt{(y_J - y_I)^2 + (x_J - x_I)^2}$. The scalar Jacobian is similar as before

$$J = \frac{\partial x'}{\partial r} = \frac{L_e}{2} \tag{1.29}$$

Strains are again uniaxial and defined by

$$\epsilon = \frac{\partial u'}{\partial x'} = \frac{\partial u'}{\partial r}\frac{\partial r}{\partial x'} \tag{1.30}$$

leading to

$$\mathbf{B} = \frac{2}{L_I}\begin{bmatrix} -\frac{1}{2} & \frac{1}{2} \end{bmatrix} \cdot \begin{bmatrix} \cos\alpha & \sin\alpha & 0 & 0 \\ 0 & 0 & \cos\alpha & \sin\alpha \end{bmatrix} \tag{1.31}$$

regarding Eqs. (1.22$_2$, 1.28). Uniaxial strains and stresses have a form as given by Eq. (1.26).

– Two-node spring element along a line.

The line is measured by a coordinate x. A spring element e has nodes I, J with coordinates x_I, x_J. The nodes may coincide and have the same coordinates. A *kinematic assumption* for springs may be stated as follows: only the displacement difference of two nodes is relevant irrespective of their original distance.

Springs are an abstract concept and do not occupy a space. They miss material points, local coordinates, and a Jacobian. Thus, regarding Eq. (1.21) it is

$$\boldsymbol{\epsilon} = \big(\Delta u\big), \quad \mathbf{B} = \begin{bmatrix} -1 & 1 \end{bmatrix}, \quad \boldsymbol{v}_e = \begin{pmatrix} u_I \\ u_J \end{pmatrix} \tag{1.32}$$

whereby this particular strain $\boldsymbol{\epsilon} = \big(\Delta u\big)$ corresponds to a difference in displacements of nodes and leads to a force $\boldsymbol{\sigma} = \big(F\big)$. The relation between Δu and F or spring characteristics may be linear or nonlinear.

– Two-node spring element in a plane.

The plane is measured with coordinates x, y. A spring element e has nodes I, J with coordinates x_I, y_I, x_J, y_J which may again coincide. In analogy to Eq. (1.32)

$$\boldsymbol{\epsilon} = \begin{pmatrix} \Delta u \\ \Delta v \end{pmatrix}, \quad \mathbf{B} = \begin{bmatrix} -1 & -1 & 0 & 0 \\ 0 & 0 & 1 & 1 \end{bmatrix}, \quad \boldsymbol{v}_e = \begin{pmatrix} u_I \\ v_I \\ u_J \\ v_J \end{pmatrix} \tag{1.33}$$

Generalized strain $\boldsymbol{\epsilon}$ leads to a generalized stress

$$\boldsymbol{\sigma} = \begin{pmatrix} F_x \\ F_y \end{pmatrix} \tag{1.34}$$

The relation between $\boldsymbol{\epsilon}$ and $\boldsymbol{\sigma}$ may again be linear or nonlinear. It may be appropriate to transform $\boldsymbol{\epsilon}$ to a rotated coordinate system before evaluating $\boldsymbol{\sigma}$ using a transformation matrix as given by $\mathbf{T}$ in Eq. (1.28). This requires back transformation of $\boldsymbol{\sigma}$ to the original coordinate system with the transposed $\mathbf{T}^T$.

– Four-node continuum element in a plane or *quad element*

The plane is measured with coordinates x, y. A continuum element has nodes I, J, K, L with coordinates $x_i, y_i, i = I, \dots, L$. They span a quad and are ordered counterclockwise. The following local coordinates are assigned: $I : r_I = -1, s_I = -1; J : r_J = 1, s_J = -1; K : r_K = 1, s_K = 1; L : r_L = -1, s_L = 1$. The *kinematic assumption* of a continuum is that displacements are continuous, i.e., no gaps or overlapping occur. Regarding Eqs. (1.18, 1.19), we have

$$\mathbf{x} = \begin{pmatrix} x \\ y \end{pmatrix}, \quad \mathbf{u} = \begin{pmatrix} u \\ v \end{pmatrix}$$
$$\mathbf{N}_i(r, s) = \frac{1}{4} \begin{bmatrix} (1 + r_i r)(1 + s_i s) & 0 \\ 0 & (1 + r_i r)(1 + s_i s) \end{bmatrix} \tag{1.35}$$
$$\mathbf{x}_{e,i} = \begin{pmatrix} x_i \\ y_i \end{pmatrix}, \quad \boldsymbol{v}_{e,i} = \begin{pmatrix} u_i \\ v_i \end{pmatrix}$$

with $i = I, \dots, L$ and

$$\mathbf{x}(r, s) = \sum_i \mathbf{N}_i(r, s) \cdot \mathbf{x}_{e,i}, \quad \mathbf{u}(r, s) = \sum_i \mathbf{N}_i(r, s) \cdot \boldsymbol{v}_{e,i} \tag{1.36}$$

This leads to a Jacobian matrix

$$\mathbf{J}(r, s) = \begin{bmatrix} \frac{\partial x}{\partial r} & \frac{\partial y}{\partial r} \\ \frac{\partial x}{\partial s} & \frac{\partial y}{\partial s} \end{bmatrix}, \quad J = \det \mathbf{J} \tag{1.37}$$

The Jacobian relates the partial derivatives of a function $\bullet$ with respect to local and global coordinates

$$\begin{pmatrix} \frac{\partial \bullet}{\partial r} \\ \frac{\partial \bullet}{\partial s} \end{pmatrix} = \mathbf{J} \cdot \begin{pmatrix} \frac{\partial \bullet}{\partial x} \\ \frac{\partial \bullet}{\partial y} \end{pmatrix} \quad \rightarrow \quad \begin{pmatrix} \frac{\partial \bullet}{\partial x} \\ \frac{\partial \bullet}{\partial y} \end{pmatrix} = \mathbf{J}^{-1} \cdot \begin{pmatrix} \frac{\partial \bullet}{\partial r} \\ \frac{\partial \bullet}{\partial s} \end{pmatrix} \tag{1.38}$$

with the inverse $\mathbf{J}^{-1}$ of $\mathbf{J}$. Small strains are defined by

$$\boldsymbol{\epsilon} = \begin{pmatrix} \epsilon_x \\ \epsilon_y \\ \gamma_{xy} \end{pmatrix} = \begin{pmatrix} \frac{\partial u}{\partial x} \\ \frac{\partial v}{\partial y} \\ \frac{\partial u}{\partial y} + \frac{\partial v}{\partial x} \end{pmatrix} = \begin{pmatrix} \frac{\partial u}{\partial r}\frac{\partial r}{\partial x} + \frac{\partial u}{\partial s}\frac{\partial s}{\partial x} \\ \frac{\partial v}{\partial r}\frac{\partial r}{\partial y} + \frac{\partial v}{\partial s}\frac{\partial s}{\partial y} \\ \frac{\partial u}{\partial r}\frac{\partial r}{\partial y} + \frac{\partial u}{\partial s}\frac{\partial s}{\partial y} + \frac{\partial v}{\partial r}\frac{\partial r}{\partial x} + \frac{\partial v}{\partial s}\frac{\partial s}{\partial x} \end{pmatrix} \tag{1.39}$$

leading to

$$\boldsymbol{\epsilon}(r, s) = \sum_i \mathbf{B}_i(r, s) \cdot \boldsymbol{v}_{e,i} \tag{1.40}$$

with $i = I \dots J$ and

$$\mathbf{B}_i(r,s) = \frac{1}{4}\begin{bmatrix} r_i(1+s_is)\frac{\partial r}{\partial x} + s_i(1+r_ir)\frac{\partial s}{\partial x} & 0 \\ 0 & r_i(1+s_is)\frac{\partial r}{\partial y} + s_i(1+r_ir)\frac{\partial s}{\partial y} \\ r_i(1+s_is)\frac{\partial r}{\partial y} + s_i(1+r_ir)\frac{\partial s}{\partial y} & r_i(1+s_is)\frac{\partial r}{\partial x} + s_i(1+r_ir)\frac{\partial s}{\partial x} \end{bmatrix} \quad (1.41)$$

The partial derivatives $\partial r/\partial x \dots$ are given the components of the inverse Jacobian $\mathbf{J}^{-1}$. Matrices $\mathbf{N}_i, \mathbf{B}_i$ related to single nodes are assembled in larger matrices to yield $\mathbf{N}, \mathbf{B}$. Finally, Cauchy stresses

$$\boldsymbol{\sigma} = \begin{pmatrix} \sigma_x \\ \sigma_y \\ \sigma_{xy} \end{pmatrix} \quad (1.42)$$

correspond to strains in a plane. Lateral strains ϵ_z or stresses σ_z come into play with the distinction of *plane stress*, that is $\sigma_z = 0$, which may lead to a lateral strain $\epsilon_z \neq 0$, or *plane strain*, that is $\epsilon_z = 0$ which may lead to a lateral stress $\sigma_z \neq 0$. The particular values in the z-direction have to be determined indirectly with a material law, see Section 1.4.

All mentioned stresses and the corresponding strains are conjugate with respect to energy, i.e., the product $\boldsymbol{\sigma} \cdot \dot{\boldsymbol{\epsilon}}$ corresponds to a rate of *internal energy* or a rate of specific internal energy. The concept of *stresses* may be *generalized*:

- Depending on the type of structural element $\boldsymbol{\sigma}$ may stand for components of Cauchy stresses or for components of forces or for components of internal forces in a beam cross section, see Section 3.1.1. *Strains* $\boldsymbol{\epsilon}$ are *generalized* correspondingly in order to lead to internal energy, e.g., including displacements in the case forces or curvature in the case of moments.

A basic property of the aforementioned elements is that they approximate coordinates and displacements by *interpolation*: nodal values and interpolated values are identical at nodes. For instance, for the four-node continuum element we have $\mathbf{u} = \boldsymbol{v}_{e,i}$ for $r = r_i, s = s_i \, i = I, \dots, L$. This property is shared by all types of finite elements.

Another issue concerns *continuity*: For the four-node continuum element the interpolation is continuous between adjacent elements along their common boundary. One sided first derivatives of interpolation exist for each element along the boundary but are different for each element. Thus, the four-node continuum element has C^0-continuity with these properties. Furthermore, the integrals for internal and external nodal forces (Eq. (1.9)) are evaluable. Other elements may require higher orders of continuity for nodal forces to be integrable.

Finally, the issue of *element locking* has to be mentioned. The four-node continuum element, e.g., does not allow us to model the behavior of incompressible solids. Constraining Eqs. (1.41) with the condition of incompressibility $\epsilon_x + \epsilon_y + \epsilon_z = 0$ makes the element much to stiff if internal nodal forces are exactly integrated [9, 8.4]. First basic hints to treat locking are given in Section 1.7. The locking problem is exemplary treated for shells in Section 8.6.

Only a few element types were touched up to now. Further elements often used are 3D-continuum elements, 2D- and 3D-beam elements, shell elements and slab elements as a special case of shell elements. Furthermore, elements imposing constraints like contact conditions

have become common in practice. For details see, e.g., [3]. Regarding the properties of reinforced concrete more details about 2D-beam elements including Bernoulli beams and Timoshenko beams are given in Section 3.3, about slabs in Section 7.4 and about shells in Chapter 8.

1.4   Material Behavior

From a mechanical point of view, material behavior is primarily focused on strains and stresses. The formal definitions of strains and stresses assume a homogeneous area of matter [64]. Regarding the virgin state of solids their behavior initially can be assumed as linear elastic in nearly all relevant cases. Furthermore, the behavior can be initially assumed as isotropic in many cases, i.e., the reaction of a material is the same in all directions. The concepts of *isotropy* and *anisotropy* are discussed in Section 5.3 with more details.

The following types of elasticity are listed exemplary:

– Uniaxial elasticity

$$\sigma = E\,\epsilon \tag{1.43}$$

with uniaxial stress σ, Young's modulus E, and uniaxial strain ϵ.

– Isotropic plane strain

$$\begin{pmatrix} \sigma_x \\ \sigma_y \\ \sigma_{xy} \end{pmatrix} = \frac{E(1-\nu)}{(1+\nu)(1-2\nu)} \begin{bmatrix} 1 & \frac{\nu}{1-\nu} & 0 \\ \frac{\nu}{1-\nu} & 1 & 0 \\ 0 & 0 & \frac{1-2\nu}{2(1-\nu)} \end{bmatrix} \cdot \begin{pmatrix} \epsilon_x \\ \epsilon_y \\ \gamma_{xy} \end{pmatrix} \tag{1.44}$$

with stress components $\sigma_x, \sigma_y, \sigma_{xy}$, Young's modulus E, Poisson's ratio ν, and strain components $\epsilon_x, \epsilon_y, \gamma_{xy}$. This is a subset of the triaxial isotropic linear elastic law as is described in Section 5.3.

– Isotropic plane stress

$$\begin{pmatrix} \sigma_x \\ \sigma_y \\ \sigma_{xy} \end{pmatrix} = \frac{E}{1-\nu^2} \begin{bmatrix} 1 & \nu & 0 \\ \nu & 1 & 0 \\ 0 & 0 & \frac{1-\nu}{2} \end{bmatrix} \cdot \begin{pmatrix} \epsilon_x \\ \epsilon_y \\ \gamma_{xy} \end{pmatrix} \tag{1.45}$$

ensuring $\sigma_z = 0$ for every combination $\epsilon_x, \epsilon_y, \gamma_{xy}$

– Plane bending

$$M = EJ\,\kappa \tag{1.46}$$

with the moment M, curvature κ, Young's modulus E, and cross-sectional moment of inertia J. This is covered by the concept of generalized stresses with $\boldsymbol{\sigma} = (M)$ and generalized strains $\boldsymbol{\epsilon} = (\kappa)$.

Equations (1.43)–(1.45) are a special case of

$$\boldsymbol{\sigma} = \mathbf{C} \cdot \boldsymbol{\epsilon} \tag{1.47}$$

with the constant material stiffness matrix $\mathbf{C}$ describing a linear material behavior. At the latest upon approaching material strength, the behavior becomes physically nonlinear. A simple case is given by the uniaxial elastoplastic law

$$\sigma = \begin{cases} E\left(\epsilon - \epsilon_p\right) & \text{for} \quad -\epsilon_p \le \epsilon \le \epsilon_p \\ \text{sign}\epsilon\, f_y & \text{otherwise} \end{cases} \tag{1.48}$$

and

$$\dot{\epsilon}_p = \dot{\epsilon} \quad \text{for} \quad |\sigma| = f_y \tag{1.49}$$

with a yield stress f_y (unsigned) and an internal state variable ϵ_p. The *internal state variable* indicates the actual remaining strain upon unloading, i.e., $\sigma = 0$ for $\epsilon = \epsilon_p$. An internal state variable captures the preceding load history. The approach covers elastic loading, yielding, elastic unloading and reloading, ongoing yielding in the opposite uniaxial range. This cycle may be repeated whereby yielding is without hardening. Equation (1.49) is a simple *evolution law* for internal state variables. More details about plasticity are given in Section 5.5.

In the case of nonlinear material equations at least an incremental form

$$\dot{\boldsymbol{\sigma}} = \mathbf{C}_T \cdot \dot{\boldsymbol{\epsilon}} \tag{1.50}$$

should exist with the *tangential material stiffness* $\mathbf{C}_T$, which is no longer constant anymore but might depend on stress, strain, and internal state variables. On occasion the *compliance* is needed, as a counterpart of stiffness, i.e.,

$$\boldsymbol{\epsilon} = \mathbf{D} \cdot \boldsymbol{\sigma} \quad \text{or} \quad \dot{\boldsymbol{\epsilon}} = \mathbf{D}_T \cdot \dot{\boldsymbol{\sigma}} \tag{1.51}$$

whereby compliance matrices are inverses of stiffness matrices: $\mathbf{D} = \mathbf{C}^{-1}$, $\mathbf{D}_T = \mathbf{C}_T^{-1}$.

1.5 Weak Equilibrium and Spatial Discretization

The preceding sections gave an introduction of (1) kinematic compatibility within the context of spatial discretization and of (2) material laws. The third cornerstone of structural mechanics is equilibrium which is formulated in a weak form as a principle of virtual work.

Boundary conditions have to be regarded in advance. Given a point on a boundary of a body, either a displacement boundary condition or a force boundary condition (zero force is also a condition) has to be prescribed for this point. Let us assume that displacements are prescribed with $\bar{\mathbf{u}}$ on surface part A_u, tractions are prescribed with $\bar{\mathbf{t}}$ on surface part A_t while A_u together with A_t contain the whole surface A but do not overlap. Thus, equilibrium is given by

$$\int_V \delta\boldsymbol{\epsilon}^T \cdot \boldsymbol{\sigma}\, dV + \int_V \delta\mathbf{u}^T \cdot \ddot{\mathbf{u}}\,\varrho dV = \int_V \delta\mathbf{u}^T \cdot \bar{\mathbf{p}}\, dV + \int_{A_t} \delta\mathbf{u}^T \cdot \bar{\mathbf{t}}\, dA \tag{1.52}$$

under the conditions

$$\mathbf{u} = \bar{\mathbf{u}} \ \text{on } A_u, \quad \delta\mathbf{u} = 0 \ \text{on } A_u \tag{1.53}$$

and $\delta\mathbf{u}$ arbitrary otherwise. The meaning of the symbols is summarized as follows:

$(\bullet)^T$	transpose of column vector $(\bullet)$ leading to row vector
$\mathbf{u}$	field of displacement vector
$\ddot{\mathbf{u}}$	field of acceleration vector
$\delta\mathbf{u}$	field of test functions or virtual displacement vector
$\delta\boldsymbol{\epsilon}$	field of virtual strain vector corresponding to $\delta\mathbf{u}$
$\boldsymbol{\sigma}$	field of stress vector
ϱ	specific mass
$\bar{\mathbf{p}}$	prescribed field of loads distributed in the body
$\bar{\mathbf{t}}$	prescribed field of tractions distributed over surface of the body
V	body volume
A	body surface
A_u	part of surface with prescribed displacements
A_t	part of surface with prescribed tractions

Formulation (1.52) covers structural dynamics and includes quasistatics as a special case. Concentrated loads are not explicitly included. For mathematically precise formulations also covering generalized variational principles see [96]. All listed parameters have to be considered as generalized. The following evaluations of are listed exemplary:

- In the case of a uniaxial bar, Eq. (1.52) becomes

$$\int_L \delta\epsilon\,\sigma\,A\mathrm{d}x + \int_L \delta u\,\ddot{u}\,\varrho A\mathrm{d}x = \int_L \delta u\,\bar{p}\,\mathrm{d}x + [\delta u\,\bar{t}]_0^L \tag{1.54}$$

  with $0 \le x \le L$ under the conditions

$$u_0 = \bar{u}_0,\ \delta u_0 = 0 \ \text{and/or}\ u_L = \bar{u}_L,\ \delta u_L = 0 \tag{1.55}$$

  with a cross-sectional area A and a load per length $\bar{p}$ in the bar direction whereby the formulation of the last term indicates the boundary term of a partial integration. Surface tractions degenerate to end forces $\bar{t}$ which are prescribed at either $x = 0$ or $x = L$ (or none, but not both at the same time).

- In the case of a plane Bernoulli beam equation (1.52) becomes

$$\int_L \delta w\,\ddot{w}\,\bar{m}\mathrm{d}x + \int_L \delta\kappa\,M\,\mathrm{d}x = \int_L \delta w\,\bar{p}\,\mathrm{d}x - [\delta\varphi\,\bar{M}]_0^L + [\delta w\,\bar{V}]_0^L \tag{1.56}$$

  with $0 \le x \le L$, the deflection w, the beam's slope φ, moment M, shear force V, a distributed mass $\bar{m}$ per length and a distributed lateral load $\bar{p}$ per length. Two boundary conditions can be given at each end $x = 0$ and $x = L$. There are corresponding pairs $(\varphi,\ M)$ and $(w,\ V)$. Only one quantity out of a pair can be prescribed at a boundary. Furthermore, at least two displacement boundary conditions should be given with at least one deflection $\bar{w}_0$ and/or $\bar{w}_L$.

The principle of virtual work or weak integral forms of equilibrium conditions treat a body as a whole. Strong differential forms consider forces applied to infinitesimally small sections or differentials of a body and lead to differential equations. Both are equivalent from a mechanical point of view. This is exemplary demonstrated for beams in Section 3.2. Weak forms are the starting point for *discretization* with finite elements. This has the following steps regarding Eq. (1.52):

1. Mesh generation

   The respective body has to be to filled with elements. No gaps between elements and no overlapping of elements are allowed in the body's interior. Elements may form facets or polygons on the exterior.

   Proportions and geometric distortions of single element may have a considerable influence on the mathematical approximation error.

2. Spatial interpolation of displacements with Eq. (1.18)

   An infinite number of degrees of freedom $\mathbf{u}$ is reduced to a finite number of nodal degrees of freedom $\boldsymbol{v}_e$ with *trial functions* according to Eq. (1.18). This leads to discretized strains $\boldsymbol{\epsilon}$ with Eq. (1.21).

3. Spatial interpolation of virtual displacements

   Interpolation of virtual displacements $\delta\mathbf{u}$ is performed with *test functions*. The method of Bubnov–Galerkin is generally used with the same functions as trial functions and test functions implying virtual nodal degrees of freedom $\delta\boldsymbol{v}_e$

$$\delta\mathbf{u} = \mathbf{N} \cdot \delta\boldsymbol{v}_e, \quad \delta\boldsymbol{\epsilon} = \mathbf{B} \cdot \delta\boldsymbol{v}_e \tag{1.57}$$

   and virtual $\delta\boldsymbol{\epsilon}$ strains are determined in the same way as strains.

4. Evaluation of stresses $\boldsymbol{\sigma}$ from stains $\boldsymbol{\epsilon}$ according to a prescribed material law

   This has to be performed by the integration of the incremental form (Eq. (1.50)). The details depend on the material and structural type and are a major issue in all what follows in this textbook.

5. The evaluation of integrals is performed element by element

$$
\begin{aligned}
\int_{V_e} \delta\boldsymbol{\epsilon}^T \cdot \boldsymbol{\sigma}\, \mathrm{d}V &= & \delta\boldsymbol{v}_e^T \cdot \mathbf{f}_e, \quad \mathbf{f}_e &= \int_{V_e} \mathbf{B}^T \cdot \boldsymbol{\sigma}\, \mathrm{d}V \\
\int_{V_e} \delta\mathbf{u}^T \cdot \ddot{\mathbf{u}}\, \varrho\mathrm{d}V &= & \delta\boldsymbol{v}_e^T \cdot \mathbf{M}_e \cdot \ddot{\boldsymbol{v}}_e, \quad \mathbf{M}_e &= \int_{V_e} \mathbf{N}^T \cdot \mathbf{N}\, \varrho\mathrm{d}V \\
\int_{V_e} \delta\mathbf{u}^T \cdot \bar{\mathbf{p}}\, \mathrm{d}x &= & \delta\boldsymbol{v}_e^T \cdot \bar{\mathbf{p}}_e, \quad \bar{\mathbf{p}}_e &= \int_{V_e} \mathbf{N}^T \cdot \bar{\mathbf{p}}\, dV \\
\int_{A_{e,t}} \delta\mathbf{u}^T \cdot \bar{\mathbf{t}}\, \mathrm{d}A &= & \delta\boldsymbol{v}_e^T \cdot \bar{\mathbf{t}}_e, \quad \bar{\mathbf{t}}_e &= \int_{A_{e,t}} \mathbf{N}^T \cdot \bar{\mathbf{t}}\, \mathrm{d}A
\end{aligned}
\tag{1.58}
$$

   with an element index e. This includes the element's *internal nodal forces* $\mathbf{f}_e$, its *mass matrix* $\mathbf{M}_e$ and its *external nodal forces* or loadings $\bar{\mathbf{p}}_e, \bar{\mathbf{t}}_e$ which are prescribed. For integration methods, see Section 1.6. Internal nodal forces in the end are functions of nodal displacements $\mathbf{f}_e = \mathbf{f}_e(\boldsymbol{v}_e)$.

6. Assembling of element contributions into a whole system

   Regarding, e.g., global internal nodal forces $\mathbf{f}$, the vector has entries for every degree of freedom of every global node. On the other hand, every meshing should have a table

which connects an element to the global nodes belonging to it. This table relates the position of the entries in $\mathbf{f}_e$ to a position in $\mathbf{f}$.

As a node generally gets contributions from more than one element, the value of an entry in $\mathbf{f}_e$ has to be *added* to the corresponding entry in $\mathbf{f}$. This is symbolically described by

$$\int_V \delta\boldsymbol{\epsilon}^T \cdot \boldsymbol{\sigma}\,\mathrm{d}V = \delta\boldsymbol{v}^T \cdot \mathbf{f} = \sum_e \delta\boldsymbol{v}_e^T \cdot \mathbf{f}_e \tag{1.59}$$

The same argumentation holds for $\delta\boldsymbol{v}_e \to \delta\boldsymbol{v}$, $\boldsymbol{v}_e \to \boldsymbol{v}$, $\mathbf{M}_e \to \mathbf{M}$, $\bar{\mathbf{p}}_e \to \bar{\mathbf{p}}$, $\bar{\mathbf{t}}_e \to \bar{\mathbf{t}}$. Global internal nodal forces in the end are a function of global nodal displacements $\mathbf{f} = \mathbf{f}(\boldsymbol{v})$.

7. Regarding arbitrary values of $\delta\boldsymbol{v}$ a spatially discretized system

$$\mathbf{M} \cdot \ddot{\boldsymbol{v}} + \mathbf{f}(\boldsymbol{v}) = \bar{\mathbf{p}} + \bar{\mathbf{t}} \tag{1.60}$$

finally results with the system's mass matrix $\mathbf{M}$, its internal nodal forces $\mathbf{f}$ and its loadings $\bar{\mathbf{p}}, \bar{\mathbf{t}}$. This is a set of ordinary differential equations of second order in time t for nodal displacements $\boldsymbol{v}$. It might be nonlinear due to the nonlinear dependence of internal nodal forces $\mathbf{f}$ on $\boldsymbol{v}$.

This procedure allows for physical nonlinearities. In the special case of *physical linearity* the linear material stiffness $\boldsymbol{\sigma} = \mathbf{C} \cdot \boldsymbol{\epsilon}$ leads to internal nodal forces

$$\mathbf{f}_e = \int_{V_e} \mathbf{B}^T \cdot \mathbf{C} \cdot \mathbf{B}\,\mathrm{d}V \cdot \boldsymbol{v}_e = \mathbf{K}_e \cdot \boldsymbol{v}_e \tag{1.61}$$

see Eqs. $(1.58)_1$ and (1.21), with a constant element stiffness matrix $\mathbf{K}_e$. Assembling leads to a system stiffness matrix $\mathbf{K}$

$$\mathbf{f}(\boldsymbol{v}) = \mathbf{K} \cdot \boldsymbol{v} \tag{1.62}$$

and regarding Eq. (1.60) to

$$\mathbf{M} \cdot \ddot{\boldsymbol{v}} + \mathbf{K} \cdot \boldsymbol{v} = \bar{\mathbf{p}} + \bar{\mathbf{t}} \tag{1.63}$$

which is a system of linear ordinary differential equations of second order in time t.

To treat physical nonlinearities the system's tangential stiffness is involved. The *tangential stiffness matrix* is needed for the solution of the nonlinear system and furthermore reveals characteristic properties, e.g., regarding stability properties. The tangential stiffness of an element is derived with

$$\mathrm{d}\mathbf{f}_e = \frac{\partial \mathbf{f}_e}{\partial \boldsymbol{v}_e} \cdot \mathrm{d}\boldsymbol{v}_e = \mathbf{K}_{Te} \cdot \mathrm{d}\boldsymbol{v}_e \qquad \text{or} \qquad \dot{\mathbf{f}}_e = \mathbf{K}_{Te} \cdot \dot{\boldsymbol{v}}_e \tag{1.64}$$

with

$$\mathbf{K}_{Te} = \int_{V_e} \mathbf{B}^T \cdot \frac{\partial \boldsymbol{\sigma}}{\partial \boldsymbol{\epsilon}} \cdot \frac{\partial \boldsymbol{\epsilon}}{\partial \boldsymbol{v}_e}\,\mathrm{d}V = \int_{V_e} \mathbf{B}^T \cdot \mathbf{C}_T \cdot \mathbf{B}\,\mathrm{d}V \tag{1.65}$$

see Eqs. $(1.58)_1$, (1.50), and (1.21), and a system tangential stiffness $\mathbf{K}_T$

$$\mathrm{d}\mathbf{f} = \mathbf{K}_T \cdot \mathrm{d}\boldsymbol{v} \qquad \text{or} \qquad \dot{\mathbf{f}} = \mathbf{K}_T \cdot \dot{\boldsymbol{v}} \tag{1.66}$$

Finally, the system (1.60) or (1.63) should be constrained with appropriate conditions regarding $\boldsymbol{v}$ to prevent rigid body displacements.

1.6 Numerical Integration and Solution Methods for Algebraic Systems

The integral formulation of equilibrium conditions requires the evaluation of integrals as given by Eq. (1.58). The evaluation is performed element by element. The integration of a quad element, see Section 1.3, is exemplary discussed in the following. A general function $f(x, y)$ indicates the integrand. The isoparametric quad element has a local coordinate system r, s with $-1 \leq r, s, \leq 1$, see Section 1.3. Thus, integration is performed by

$$\int_{V_I} f(x, y)\, \mathrm{d}V = \int_{-1}^{+1} \int_{-1}^{+1} f(r, s)\, J(r, s)\, b\, \mathrm{d}r \mathrm{d}s \tag{1.67}$$

with the determinant J of the Jacobian, see Eq. (1.37), and a thickness b. As closed analytical forms generally are not available for $f(r, s)$ a *numerical integration* has to be performed

$$\int_{-1}^{+1} \int_{-1}^{+1} f(r, s)\, J(r, s)\, b\, \mathrm{d}r \mathrm{d}s = b \sum_{i=0}^{n_i} \sum_{j=0}^{n_i} \eta_i \eta_j\, f(\xi_i, \xi_j)\, J(\xi_i, \xi_j) \tag{1.68}$$

with integration order n_i, sampling points ξ, and weighting factors η. An appropriate scheme is given by the Gauss integration. Its sampling points and weighting factors are listed in Table 1.1 up to an integration order $n_i = 3$. Weighting factors obey a rule $\sum_{i=0}^{n_i} \eta_i = 2$. Accuracy of integration is a key issue.

- Integration accuracy increases with increasing integration order. On the other hand, numerical integration leads to a major contribution to computational costs.

Gauss integration generally is most efficient compared to other numerical integration schemes: an integration order n_i gives exact results for polynoms of order $2n_i + 1$ disregarding round-off errors, e.g., a uniaxial integration of order 1 with two sampling points exactly integrates a polynomial of the order 3. Alternative numerical integration schemes are given by schemes of Simpson, Newton–Cotes, Lobatto.

Discretization and integration lead to a system of ordinary differential equations of second order in time for unknown nodal displacements $\boldsymbol{v}$, see Eq. (1.60). To begin with a

n_i	ξ_i	η_i
0	0.0	2.0
1	$\pm 0.57735\,02691\,89626$	1.0
2	$\pm 0.77459\,66692\,41483$	$0.55555\,55555\,55556$
	0.0	$0.88888\,88888\,88889$
3	$\pm 0.86113\,63115\,94053$	$0.34785\,48451\,37454$
	$\pm 0.33998\,10435\,84856$	$0.65214\,51548\,62546$
$\vdots$	$\vdots$	$\vdots$

Table 1.1: Sampling points and weights for Gauss integration (15 digits shown).

quasistatic analysis is considered with $\ddot{\boldsymbol{v}} = 0$ leading to

$$\mathbf{r}(\boldsymbol{v}) = \mathbf{p} - \mathbf{f}(\boldsymbol{v}) = \mathbf{0}, \qquad \mathbf{p} = \bar{\mathbf{p}} + \bar{\mathbf{t}} \tag{1.69}$$

with a *residual* $\mathbf{r}$, internal nodal forces $\mathbf{f}$ depending on displacements $\boldsymbol{v}$ and external nodal loads $\mathbf{p}$, which are assumed to be independent of $\boldsymbol{v}$. The general case is nonlinear dependence of $\mathbf{f}$ on $\boldsymbol{v}$. Thus, the solution of Eq. (1.69) has to be determined by an iteration with a sequence $\boldsymbol{v}^{(0)}, \ldots, \boldsymbol{v}^{(\nu)}$. Regarding an arbitrary iteration step (ν) we have $\mathbf{r}(\boldsymbol{v}^{(\nu)}) \neq 0$ and seek for a correction $\delta\boldsymbol{v}$. A linear Taylor expansion is used as a basic approach

$$\begin{aligned} \mathbf{r}(\boldsymbol{v}^{(\nu)} + \delta\boldsymbol{v}) \quad &\approx \mathbf{r}(\boldsymbol{v}^{(\nu)}) + \mathbf{K}_T^{(\nu)} \cdot \delta\boldsymbol{v} \\ &= 0 \end{aligned} \tag{1.70}$$

with a tangential stiffness matrix, see also Eq. (1.65)

$$\mathbf{K}_T^{(\nu)} = -\left.\frac{\partial\mathbf{r}}{\partial\boldsymbol{v}}\right|_{\boldsymbol{v}=\boldsymbol{v}^{(\nu)}} = \left.\frac{\partial\mathbf{f}}{\partial\boldsymbol{v}}\right|_{\boldsymbol{v}=\boldsymbol{v}^{(\nu)}} \tag{1.71}$$

leading to the *Newton–Raphson method*

$$\begin{aligned} \delta\boldsymbol{v} &= \left[\mathbf{K}_T^{(\nu)}\right]^{-1} \cdot \mathbf{r}(\boldsymbol{v}^{(\nu)}) \\ \boldsymbol{v}^{(\nu+1)} &= \boldsymbol{v}^{(\nu)} + \delta\boldsymbol{v} \end{aligned} \tag{1.72}$$

with (hopefully) an improved value $\boldsymbol{v}^{(\nu+1)}$. Iteration may stop if $\|\mathbf{r}(\boldsymbol{v}^{(\nu+1)})\| \ll 1$ and $\|\delta\boldsymbol{v}\| \ll 1$ with a suitable norm $\|\cdot\|$ transforming a vector into a scalar. The method generally has a fast convergence but is relatively costly. The tangential stiffness matrix has to be computed in every iteration step (ν) and a decomposition in order to solve (LU decomposition instead of inversion) has to be performed on it to determine $\delta\boldsymbol{v}$. Alternative iteration methods use variants of the iteration matrix like the modified Newton–Raphson method or the BFGS method or other quasi-Newton methods [3, 8.4], [9, 6.3],[99, 7]. For more details, see Appendix A.

Iterative methods like Newton–Raphson are embedded in an *incrementally iterative* scheme. Thus, loading is given as a history: $\mathbf{p} = \mathbf{p}(t)$. An appropriate choice is $0 \leq t \leq 1$ for the scaling of the load history time, which is different from real time in the case of a quasistatic analysis. The following steps are performed in the incrementally iterative scheme:

1. Discrete time values t_i are regarded with a time step $\Delta t = t_{i+1} - t_i$ and an initial time $t_0 = 0$. A loading $\mathbf{p}_i = \mathbf{p}(t_i)$ is prescribed for all time steps. The incremental material law (Eq. (1.50))

$$\dot{\boldsymbol{\sigma}}(t) = \mathbf{C}_T \cdot \dot{\boldsymbol{\epsilon}}(t) \tag{1.73}$$

is integrated by a numerical integration of stresses and strains using a trapezoidal rule

$$\begin{aligned} \boldsymbol{\sigma}_{i+1} &= \boldsymbol{\sigma}_i + \Delta t \left[\alpha\dot{\boldsymbol{\sigma}}_{i+1} + (1-\alpha)\dot{\boldsymbol{\sigma}}_i\right] \\ \boldsymbol{\epsilon}_{i+1} &= \boldsymbol{\epsilon}_i + \Delta t \left[\alpha\dot{\boldsymbol{\epsilon}}_{i+1} + (1-\alpha)\dot{\boldsymbol{\epsilon}}_i\right] \end{aligned} \tag{1.74}$$

with $\boldsymbol{\sigma}_i = \boldsymbol{\sigma}(t_i)$, $\boldsymbol{\epsilon}_i = \boldsymbol{\epsilon}(t_i)$ and an integration parameter α. The parameters α, Δt rule stability and accuracy of the numerical approach.

2. The implicit scheme with $\alpha = 1$ is used in the following to gain unconditional stability. Thus, Eqs. (1.73, 1.74) lead to

$$\boldsymbol{\sigma}_{i+1} = \boldsymbol{\sigma}_i + \mathbf{C}_{T,i+1} \cdot (\boldsymbol{\epsilon}_{i+1} - \boldsymbol{\epsilon}_i) \tag{1.75}$$

whereby $\mathbf{C}_{T,i+1}$ indicates dependence of the tangential material stiffness on $\boldsymbol{\sigma}_{i+1}$ and/or $\boldsymbol{\epsilon}_{i+1}$.

3. Unknowns are nodal displacements $\boldsymbol{v}_i = \boldsymbol{v}(t_i)$ leading to strains $\boldsymbol{\epsilon}_i$, stresses $\boldsymbol{\sigma}_i$ and internal nodal forces $\mathbf{f}_i$ except the initial state. This state described by $\boldsymbol{v}_0$, $\boldsymbol{\epsilon}_0$, $\boldsymbol{\sigma}_0$, $\mathbf{f}_0$ is assumed to be known and initial equilibrium is given by $\mathbf{r}_0 = \mathbf{p}_0 - \mathbf{f}_0 = \mathbf{0}$.

4. The solution starts with t_1 and $\boldsymbol{v}_1$ has to be determined. This is performed with an iteration $\boldsymbol{v}_1^{(0)}, \dots, \boldsymbol{v}_1^{(\nu)}$ with, e.g., the Newton–Raphson method using an initial $\boldsymbol{v}_1^{(0)} = \boldsymbol{v}_0$. The iteration involves $\boldsymbol{\epsilon}_1^{(\nu)}$, $\boldsymbol{\sigma}_1^{(\nu)}$, $\mathbf{C}_{T,1}^{(\nu)}$ according to Eq. (1.75).

5. A converged $\boldsymbol{v}_1$ and the corresponding strains $\boldsymbol{\epsilon}_1$ and stresses $\boldsymbol{\sigma}_1$ serve as a base for t_2 and so on until a target time is reached.

The procedure is illustrated in Fig. 1.4 and combined with integration according to Eq. (1.58) and assembling according to Eq. (1.59). The time t serves as a loading parameter in the quasistatic case. A scaling of time, i.e., multiplying time with a constant factor in each occurrence, does not have any influence upon the results.

This starts to become different with a *transient analysis*. A material behavior like creep, see Section 2.2, has to be regarded as transient. Such a behavior is modeled by incorporating viscosity [64, 6.4]. Thus, the incremental material law (Eq. (1.73)) is extended as

$$\dot{\boldsymbol{\sigma}} = \mathbf{C}_T \cdot \dot{\boldsymbol{\epsilon}} + \boldsymbol{\Sigma} \tag{1.76}$$
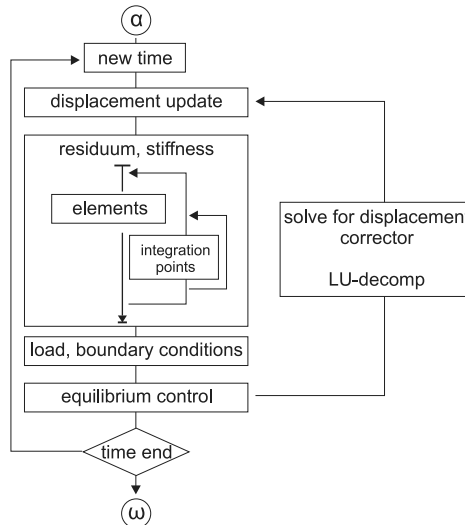
Figure 1.4: Flow of displacement-based nonlinear calculation.

with an additional term $\boldsymbol{\Sigma}$ depending on stress $\boldsymbol{\sigma}(t)$ and strain $\boldsymbol{\epsilon}(t)$. In a similar way as done with Eq. (1.73) leading to Eq. (1.75) this is integrated with

$$\boldsymbol{\sigma}_{i+1} = \boldsymbol{\sigma}_i + \mathbf{C}_{T,i+1} \cdot (\boldsymbol{\epsilon}_{i+1} - \boldsymbol{\epsilon}_i) + \Delta t\, \boldsymbol{\Sigma}_{i+1} \tag{1.77}$$

Internal nodal forces are determined according to Eq. $(1.58)_1$

$$\mathbf{f}_{i+1} = \int_V \mathbf{B}^T \cdot \boldsymbol{\sigma}_{i+1}\, \mathrm{d}V = \mathbf{f}_i + \mathbf{K}_{T,i+1} \cdot \Delta \boldsymbol{v} + \Delta t\, \bar{\mathbf{f}}_{i+1} \tag{1.78}$$

with element index e omitted and $\Delta \boldsymbol{v} = \boldsymbol{v}_{i+1} - \boldsymbol{v}_i$ and

$$
\begin{aligned}
\mathbf{f}_i &= \int_V \mathbf{B}^T \cdot \boldsymbol{\sigma}_i\, \mathrm{d}V \\
\mathbf{K}_{T,i+1} &= \int_V \mathbf{B}^T \cdot \mathbf{C}_{T,i+1} \cdot \mathbf{B}\, \mathrm{d}V \\
\bar{\mathbf{f}}_{i+1} &= \int_V \mathbf{B}^T \cdot \boldsymbol{\Sigma}_{i+1}\, \mathrm{d}V
\end{aligned}
\tag{1.79}
$$

The contributions $\mathbf{K}_{T,i+1}, \bar{\mathbf{f}}_{i+1}$ may involve nonlinearities due to the dependence of $\mathbf{C}_{T,i+1}, \boldsymbol{\Sigma}_{i+1}$ on strains and stresses. Equilibrium at a time t_{i+1} has the condition

$$
\begin{aligned}
\mathbf{r}_{i+1} &= \mathbf{p}_{i+1} - \mathbf{f}_{i+1} \\
&= \mathbf{p}_{i+1} - \mathbf{f}_i - \mathbf{K}_{T,i+1} \cdot \Delta \boldsymbol{v} - \Delta t\, \bar{\mathbf{f}}_{i+1} \\
&= \mathbf{0}
\end{aligned}
\tag{1.80}
$$

according to Eqs. (1.69, 1.78). We apply the Newton–Raphson method (Eq. (1.72)) to solve this system of algebraic equations within in incrementally iterative scheme, see Eq. (1.72). An extended tangential stiffness, see Eq. (1.71), is given by

$$\mathbf{A}_{T,i+1}^{(\nu)} = \mathbf{K}_{T,i+1}^{(\nu)} + \Delta t\, \left. \frac{\partial \bar{\mathbf{f}}}{\partial \boldsymbol{v}} \right|_{\boldsymbol{v} = \boldsymbol{v}_{i+1}^{(\nu)}} \tag{1.81}$$

with the iteration counter (ν) leading to an iteration scheme

$$\boldsymbol{v}_{i+1}^{(\nu+1)} = \boldsymbol{v}_{i+1}^{(\nu)} + \left[\mathbf{A}_{T,i+1}^{(\nu)} \right]^{-1} \cdot \mathbf{r}_{i+1}^{(\nu+1)} \tag{1.82}$$

The exact formulation of the extended tangential stiffness depends on the particular form of $\bar{\mathbf{f}}$ or $\boldsymbol{\Sigma}$, respectively. In the case of time steps Δt being small is $\mathbf{A}_T^{(\nu)} \approx \mathbf{K}_T^{(\nu)}$.

A particular case is given by the viscoelasticity of materials, see Section 2.2, leading to

$$\boldsymbol{\Sigma} = \mathbf{V} \cdot \boldsymbol{\epsilon} - \mathbf{W} \cdot \boldsymbol{\sigma} \tag{1.83}$$

with constant material terms $\mathbf{V}$, $\mathbf{W}$, see Eq. (2.27). Thus, $\boldsymbol{\Sigma}_{i+1} = \mathbf{V} \cdot \boldsymbol{\epsilon}_{i+1} - \mathbf{W} \cdot \boldsymbol{\sigma}_{i+1}$ and stress from Eq. (1.77) becomes

$$\boldsymbol{\sigma}_{i+1} = \boldsymbol{\sigma}_i + \mathbf{C}_{T,i+1} \cdot (\boldsymbol{\epsilon}_{i+1} - \boldsymbol{\epsilon}_i) + \Delta t\, \mathbf{V} \cdot \boldsymbol{\epsilon}_{i+1} - \Delta t\, \mathbf{W} \cdot \boldsymbol{\sigma}_{i+1} \tag{1.84}$$

leading to

$$\boldsymbol{\sigma}_{i+1} \quad = \quad [\mathbf{I} + \Delta t\, \mathbf{W}]^{-1} \cdot \Big([\mathbf{C}_{T,i+1} + \Delta t\, \mathbf{V}] \cdot (\boldsymbol{\epsilon}_{i+1} - \boldsymbol{\epsilon}_i) + \boldsymbol{\sigma}_i + \Delta t\, \mathbf{V} \cdot \boldsymbol{\epsilon}_i \Big) \tag{1.85}$$

with the unit matrix $\mathbf{I}$. Internal nodal forces according to Eq. $(1.58)_1$ are given by

$$\mathbf{f}_{i+1} = \int_V \mathbf{B}^T \cdot \boldsymbol{\sigma}_{i+1}\, \mathrm{d}V = \bar{\mathbf{f}}_i + \bar{\mathbf{K}}_{T,i+1} \cdot \Delta \boldsymbol{v} \tag{1.86}$$

with $\Delta \boldsymbol{v}$ as before and

$$
\begin{aligned}
\bar{\mathbf{f}}_i \quad &= \quad [\mathbf{I} + \Delta t\, \mathbf{W}]^{-1} \int_V \mathbf{B}^T \cdot (\boldsymbol{\sigma}_i + \Delta t\, \mathbf{V} \cdot \boldsymbol{\epsilon}_i)\, \mathrm{d}V \\
\bar{\mathbf{K}}_{T,i+1} \quad &= \quad [\mathbf{I} + \Delta t\, \mathbf{W}]^{-1} \int_V \mathbf{B}^T \cdot [\mathbf{C}_{T,i+1} + \Delta t\, \mathbf{V}] \cdot \mathbf{B}\, \mathrm{d}V
\end{aligned}
\tag{1.87}
$$

The residual, see Eq. (1.80), is given by

$$\mathbf{r}_{i+1} \quad = \quad \mathbf{p}_{i+1} - \bar{\mathbf{f}}_i - \bar{\mathbf{K}}_{T,i+1} \cdot \Delta \boldsymbol{v} \tag{1.88}$$

leading to an iteration scheme

$$\boldsymbol{v}_{i+1}^{(\nu+1)} = \boldsymbol{v}_{i+1}^{(\nu)} + \left[\bar{\mathbf{K}}_{T,i+1}^{(\nu)} \right]^{-1} \cdot \mathbf{r}_{i+1}^{(\nu+1)} \tag{1.89}$$

All quantities at time t_i can assumed to be known within a time stepping scheme. A potential source of nonlinearity is still given by $\mathbf{C}_{T,i+1}$. Formulation (1.87) is used as solution method for Examples 2.2 and 3.3.

Real time t is also a key factor for a *dynamic analysis* regarding inertia. Based on Eq. (1.60) we have in analogy to Eq. (1.69)

$$\mathbf{r} = \mathbf{p}(t) - \mathbf{M} \cdot \ddot{\boldsymbol{v}} - \mathbf{f} = 0, \qquad \mathbf{p}(t) = \bar{\mathbf{p}}(t) + \bar{\mathbf{t}}(t) \tag{1.90}$$

whereby the loading $\mathbf{p}$ is a prescribed function of the time t. The displacements $\boldsymbol{v}(t)$ and all derived values (velocities $\dot{\boldsymbol{v}}(t)$, accelerations $\ddot{\boldsymbol{v}}(t)$, internal nodal forces $\mathbf{f}$) are unknown before solution. Equation (1.90) is discretized in the spatial domain, but not yet in the time domain, i.e., it is system of ordinary differential equations of second order in time. Beneath displacement boundary conditions this problem needs initial conditions for the displacements $\boldsymbol{v}_0 = \boldsymbol{v}(0)$ and velocities $\dot{\boldsymbol{v}}_0 = \dot{\boldsymbol{v}}(0)$.

A widespread approach for the *temporal discretization* of acceleration together with velocities is given in the *Newmark method*

$$
\begin{aligned}
\dot{\boldsymbol{v}}_{i+1} \quad &= \quad \dot{\boldsymbol{v}}_i + \Delta t \Big[\gamma \ddot{\boldsymbol{v}}_{i+1} + (1 - \gamma) \ddot{\boldsymbol{v}}_i \Big] \\
\boldsymbol{v}_{i+1} \quad &= \quad \boldsymbol{v}_i + \Delta t\ \dot{\boldsymbol{v}}_i + \Delta t^2 \Big[\beta \ddot{\boldsymbol{v}}_{i+1} + (\tfrac{1}{2} - \beta) \ddot{\boldsymbol{v}}_i \Big]
\end{aligned}
\tag{1.91}
$$

with $\boldsymbol{v}_{i+1} = \boldsymbol{v}(t_{i+1})$, $\dot{\boldsymbol{v}}_{i+1} = \dot{\boldsymbol{v}}(t_{i+1})$, $\ddot{\boldsymbol{v}}_{i+1} = \ddot{\boldsymbol{v}}(t_{i+1})$ a time step length $\Delta t = t_{i+1} - t_i$ and integration parameters γ, β. Equations (1.91) are solved for the acceleration and velocity in time step $i + 1$. We get

$$\ddot{\boldsymbol{v}}_{i+1} = \frac{1}{\beta \Delta t^2} \left[\boldsymbol{v}_{i+1} - \tilde{\boldsymbol{v}}_{i+1} \right] \tag{1.92}$$

with an auxiliary quantity

$$\tilde{\boldsymbol{v}}_{i+1} = \boldsymbol{v}_i + \Delta t \ \dot{\boldsymbol{v}}_i + \frac{\Delta t^2}{2} (1 - 2\beta) \ddot{\boldsymbol{v}}_i \qquad (1.93)$$

and the velocity

$$\dot{\boldsymbol{v}}_{i+1} = \frac{\gamma}{\beta \Delta t} [\boldsymbol{v}_{i+1} - \boldsymbol{v}_i] + \left(1 - \frac{\gamma}{\beta}\right) \dot{\boldsymbol{v}}_i + \Delta t \left(1 - \frac{\gamma}{2\beta}\right) \ddot{\boldsymbol{v}}_i \qquad (1.94)$$

Finally, dynamic equilibrium equation (1.90) is applied for the time step $i + 1$ with the acceleration according to Eq. (1.92):

$$\mathbf{r}_{i+1} = \mathbf{p}_{i+1} - \frac{1}{\beta \Delta t^2} \mathbf{M} \cdot [\boldsymbol{v}_{i+1} - \tilde{\boldsymbol{v}}_{i+1}] - \mathbf{f}_{i+1} = 0 \qquad (1.95)$$

With the given parameters $\gamma, \beta, \Delta t$, a given previous state $\boldsymbol{v}_i, \dot{\boldsymbol{v}}_i, \ddot{\boldsymbol{v}}_i$, given mass matrix $\mathbf{M}$ and load $\mathbf{p}_{i+1}$, Eq. (1.95) has to be solved for $\boldsymbol{v}_{i+1}$ whereby the dependence of $\mathbf{f}_{i+1}$ on $\boldsymbol{v}_{i+1}$ is crucial and might be nonlinear.

We apply again the Newton–Raphson method (Eq. (1.72)). An extended tangential stiffness, see Eq. (1.71), is given by

$$\mathbf{A}_T^{(\nu)} = \frac{1}{\beta \Delta t^2} \mathbf{M} + \left. \frac{\partial \mathbf{f}}{\partial \boldsymbol{v}} \right|_{\boldsymbol{v}=\boldsymbol{v}_{i+1}^{(\nu)}} = \frac{1}{\beta \Delta t^2} \mathbf{M} + \mathbf{K}_T^{(\nu)} \qquad (1.96)$$

leading to an iteration scheme

$$\boldsymbol{v}_{i+1}^{(\nu+1)} = \boldsymbol{v}_{i+1}^{(\nu)} + \left[\mathbf{A}_T^{(\nu)}\right]^{-1} \cdot \left(\mathbf{p}_{i+1} - \frac{1}{\beta \Delta t^2} \mathbf{M} \cdot \left(\boldsymbol{v}_{i+1}^{(\nu)} - \tilde{\boldsymbol{v}}_{i+1}\right) - \mathbf{f}_{i+1}^{(\nu)}\right) \qquad (1.97)$$

This includes the linear case with

$$\mathbf{f}_{i+1}^{(\nu)} = \mathbf{K} \cdot \boldsymbol{v}_{i+1}^{(\nu)}, \qquad \mathbf{A}_T^{(\nu)} = \mathbf{A} = \frac{1}{\beta \Delta t^2} \mathbf{M} + \mathbf{K} \qquad (1.98)$$

and Eq. (1.97) simplifies to

$$\boldsymbol{v}_{i+1} = \mathbf{A}^{-1} \cdot \left(\mathbf{p}_{i+1} + \frac{1}{\beta \Delta t^2} \mathbf{M} \cdot \tilde{\boldsymbol{v}}_{i+1}\right) \qquad (1.99)$$

with no iteration necessary [2, 9.2.4]. Numerical integration parameters γ, β rule *consistency* and *numerical stability* of the method.

– Stability means that an amount of error introduced in a certain step due to a finite time step length Δt is not is not increased in the subsequent steps.

– Consistency means that the iteration scheme converges to the differential equation for $\Delta t \to 0$.

Stability and consistency are necessary to ensure that the error of the numerical method remains within some bounds for a finite time step length Δt. A choice $\beta = \frac{1}{4}, \gamma = \frac{1}{2}$ is reasonable for the Newmark method to reach consistency and stability [2, 9.4].

This section completes the basic discussion of procedures as they are directly used to solve problems of reinforced concrete structures. The following last section of this chapter touches some theoretical background regarding the finite element method.

1.7 Convergence

The major contribution to the mathematical approximation error, see Section 1.1, is the discretization error arising from the difference between mathematical and numerical model, see Fig. 1.1. This difference should become smaller with a mesh refinement, i.e., the numerical model should *converge* with respect to the underlying mathematical model. Under the assumption of geometrical and physical linearity the convergence behavior of the finite element method can be analyzed theoretically. Quasistatic problems are considered in the following.

The following mathematical symbols are used in this section:

$\forall$	for all
$\in$	element of
$\subset$	subset of
$\exists$	it exists
$\cap$	intersection
$\cup$	union

Given a linear material law

$$\boldsymbol{\sigma} = \mathbf{C} \cdot \boldsymbol{\epsilon} \tag{1.100}$$

the condition of weak, integral equilibrium equation (1.52), can be written as

$$\int_V \delta\boldsymbol{\epsilon}^T \cdot \mathbf{C} \cdot \boldsymbol{\epsilon} \, \mathrm{d}V = \int_V \delta\mathbf{u}^T \cdot \bar{\mathbf{p}} \, \mathrm{d}V + \int_{A_t} \delta\mathbf{u}^T \cdot \bar{\mathbf{t}} \, \mathrm{d}A \tag{1.101}$$

with a given body geometry V and given values for $\mathbf{C}$, $\bar{\mathbf{p}}$ and $\bar{\mathbf{t}}$. The boundary A of V is composed of A_u and A_t whereby $A = A_t \cup A_u$ and $A_t \cap A_u = 0$. Displacement boundary conditions or *Dirichlet conditions* are prescribed on A_u and force boundary conditions or *Neumann conditions* on A_t with $\bar{\mathbf{t}} = \mathbf{n} \cdot \boldsymbol{\sigma}$ with the boundary's normal $\mathbf{n}$. Displacement boundary conditions have to prevent rigid body motions.

Generalized strains $\boldsymbol{\epsilon}, \delta\boldsymbol{\epsilon}$ are derived from the generalized displacements $\mathbf{u}, \delta\mathbf{u}$ by a differential operator depending on the type of the structural problem under consideration. The trial functions according to Eq. (1.18) and test functions according to Eq. (1.57) are assumed to belong to a Sobolev function space H ($\rightarrow$ square integrable functions [2, 4.3.4]) defined over the body V and to fulfill the displacement boundary conditions.

Equation (1.101) can be written in a general form as

$$a(\mathbf{u}, \mathbf{v}) = (\mathbf{f}, \mathbf{v}) \quad \forall \mathbf{v} \in H \tag{1.102}$$

with a symmetric, bilinear operator $a(\cdot, \cdot)$, a further linear operator $(\mathbf{f}, \cdot)$, and $\mathbf{v}$ formally replacing $\delta\mathbf{u}$. This has the following properties:

– Symmetry

$$a(\mathbf{u}, \mathbf{v}) = a(\mathbf{v}, \mathbf{u}) \tag{1.103}$$

– Bilinearity

$$\begin{aligned} a(\gamma_1\mathbf{u}_1 + \gamma_2\mathbf{u}_2, \mathbf{v}) &= \gamma_1 a(\mathbf{u}_1, \mathbf{v}) + \gamma_2 a(\mathbf{u}_2, \mathbf{v}) \\ a(\mathbf{u}, \gamma_1\mathbf{v}_1 + \gamma_2\mathbf{v}_2) &= \gamma_1 a(\mathbf{u}, \mathbf{v}_1) + \gamma_2 a(\mathbf{u}, \mathbf{v}_2) \end{aligned} \tag{1.104}$$

– Linearity

$$(\mathbf{f}, \gamma_1 \mathbf{v}_1 + \gamma_2 \mathbf{v}_2) = \gamma_1 (\mathbf{f}, \mathbf{v}_1) + \gamma_2 (\mathbf{f}, \mathbf{v}_2) \tag{1.105}$$

A *norm* maps a function $\mathbf{v}$ into a nonnegative number. Sobolev norms $||\mathbf{v}||_i$ of order i are used in this context [2, 4.3.4,(4.76)]. Sobolev norms are built from integration of squares of functions and squares of their derivatives up to order i. It is assumed that $i = 1$ is appropriate for the following. It can then be shown that a has the properties

– Continuity

$$\exists\, M > 0: \quad |a(\mathbf{v}_1, \mathbf{v}_2)| \le M\, \|\mathbf{v}_1\|_1\, \|\mathbf{v}_2\|_1 \quad \forall \mathbf{v}_1, \mathbf{v}_2 \in H \tag{1.106}$$

– Ellipticity

$$\exists\, \alpha > 0: \quad a(\mathbf{v}, \mathbf{v}) \ge \alpha\, \|\mathbf{v}\|_1^2 \quad \forall \mathbf{v} \in H \tag{1.107}$$

whereby M, α depend on problem type and material values but not on $\mathbf{v}_1, \mathbf{v}_2, \mathbf{v}$.

Due to Eq. (1.107) $a(\mathbf{v}, \mathbf{v}) \ge 0$, i.e., a is a norm and may be physically interpreted as *energy*. It is twice the internal strain energy. It can be shown that the problem Eq. (1.102) – i.e., determine a function $\mathbf{u} \in H$ such that Eq. (1.102) is fulfilled for all $\mathbf{v} \in H$ – has a unique solution $\mathbf{u}$, see, e.g., [2, 4.3]. This is the *exact solution* of the mathematical model, see Fig. 1.1.

Discretization uses trial and test functions $\mathbf{u}_h, \mathbf{v}_h \in H_h$ of a subset $H_h \subset H$ based upon the concept of meshes and interpolation with elements and nodes, see Section 1.3. To simplify the derivations, a uniform mesh of elements is assumed with a mesh size parameter h, e.g., a diameter or length of a generic element. For nonuniform meshes see [2, 4.3.5]. The *approximate solution* $\mathbf{u}_h \in H_h$ of Eq. (1.102) is determined by

$$a(\mathbf{u}_h, \mathbf{v}_h) = (\mathbf{f}, \mathbf{v}_h) \quad \forall \mathbf{v}_h \in H_h \tag{1.108}$$

The difference between approximate and exact solution gives the *discretization error*

$$\mathbf{e}_h = \mathbf{u} - \mathbf{u}_h \tag{1.109}$$

The approximation $\mathbf{u}_h$ is known for H_h given, it can be determined according to the procedure described in Section 1.5. The error $\mathbf{e}_h$ has to be estimated. The approximate solution has the following properties:

– Orthogonality of error, see [2, (4.86)]

$$a(\mathbf{e}_h, \mathbf{v}_h) = 0 \quad \forall \mathbf{v}_h \in H_h \tag{1.110}$$

– Energy of approximation is smaller than exact energy, see [2, (4.89)]

$$a(\mathbf{u}_h, \mathbf{u}_h) \le a(\mathbf{u}, \mathbf{u}) \tag{1.111}$$

– Energy of error is minimized, see [2, (4.91)]

$$a(\mathbf{e}_h, \mathbf{e}_h) \le a(\mathbf{u} - \mathbf{v}_h, \mathbf{u} - \mathbf{v}_h) \quad \forall \mathbf{v}_h \in H_h \tag{1.112}$$

Combination of Eqs. (1.107), (1.112), and (1.106) leads to

$$
\begin{aligned}
\alpha \left\| \mathbf{e}_h \right\|_1^2 &= \alpha \left\| \mathbf{u} - \mathbf{u}_h \right\|_1^2 \le a(\mathbf{e}_h, \mathbf{e}_h) \\
&= \inf_{\mathbf{v}_h \in H_h} a(\mathbf{u} - \mathbf{v}_h, \mathbf{u} - \mathbf{v}_h) \le M \inf_{\mathbf{v}_h \in H_h} \left\| \mathbf{u} - \mathbf{v}_h \right\|_1^2
\end{aligned}
\tag{1.113}
$$

where inf is infimum, the largest lower bound[1]. This is rewritten as

$$
\left\| \mathbf{u} - \mathbf{u}_h \right\|_1 \le c \; d(\mathbf{u}, H_h)
\tag{1.114}
$$

with

$$
d(\mathbf{u}, H_h) = \inf_{\mathbf{v}_h \in H_h} \left\| \mathbf{u} - \mathbf{v}_h \right\|_1, \quad c = \sqrt{M/\alpha}
\tag{1.115}
$$

d is a "distance" of functions in H_h to the exact solution $\mathbf{u}$, c depends on the structural problem type and the values of its parameters, but *not* on H_h.

- *Convergence* means $\mathbf{u}_h \to \mathbf{u}$ or $\left\| \mathbf{u} - \mathbf{u}_h \right\|_1 \to 0$ with mesh size $h \to 0$.

Convergence can be reached with an appropriate selection of function spaces H_h whereby reducing the distance $d(\mathbf{u}, H_h)$.

A more precise statement is possible using interpolation theory. This introduces the interpolant[2] $\mathbf{u}_i \in H_h$ of the exact solution $\mathbf{u}$. Complete polynomials[3] of degree k are used for discretization and interpolation. Interpolation theory estimates the interpolation error with

$$
\left\| \mathbf{u} - \mathbf{u}_i \right\|_1 \le \hat{c} \, h^k \left\| \mathbf{u} \right\|_{k+1}
\tag{1.116}
$$

with the mesh size h and a constant $\hat{c}$ which is independent of h [2, (4.99)]. $\left\| \mathbf{u} \right\|_{k+1}$ is the $k+1$-order Sobolev norm of the exact solution. On the other hand a relation $\inf_{\mathbf{v}_h \in H_h} \left\| \mathbf{u} - \mathbf{v}_h \right\|_1 \le \left\| \mathbf{u} - \mathbf{u}_i \right\|_1$ must hold as $\mathbf{u}_i \in H_h$. Using this and Eqs. (1.114, 1.116) yields

$$
\left\| \mathbf{u} - \mathbf{u}_h \right\|_1 \le c \hat{c} \, h^k \left\| \mathbf{u} \right\|_{k+1}
\tag{1.117}
$$

The value $c\hat{c}$ can be merged to c, which depends on the structural problem type and the values of its parameters, but *not* on h. A further merging of c and $\left\| \mathbf{u} \right\|_{k+1}$ leads to the well-known formulation

$$
\left\| \mathbf{u} - \mathbf{u}_h \right\|_1 \le c \, h^k
\tag{1.118}
$$

whereby c depends on the structural problem type, the values of its parameters and the norm of the exact solution.

The following conditions for convergence can be derived [2, 4.3.2]:

- A prerequisite is theoretical integrability of all quantities. This leads to requirements for the integrands of the energy a and the arguments of the Sobolov norms, which are $\mathbf{u}_h, \mathbf{v}_h, \mathbf{u}$ or derivatives thereof.

  This corresponds to the requirement of *compatibility* or *continuity* – with a different meaning compared to Eq. (1.106) –, respectively, of finite element interpolation functions – generally displacement interpolations – along inter element boundaries.

---

[1] $\left\| \mathbf{u} - \mathbf{v}_h \right\|_1, \mathbf{v}_h \in H_h$ is a subset of real numbers. $\inf_{\mathbf{v}_h \in H_h} \left\| \mathbf{u} - \mathbf{v}_h \right\|_1$ is the largest number less or equal to the numbers in this subset.
[2] $\mathbf{u}$ and $\mathbf{u}_i$ coincide at nodes, but generally not apart from nodes. Generally is $\mathbf{u}_i \ne \mathbf{u}_h$.
[3] A polynomial in x, y is complete of order 1 if it includes x, y, complete of order 2 if of order 1 and including x^2, xy, y^2, complete of order 3 if complete of order 2 and including x^3, x^2y, xy^2, y^3 and so on.

– According to Eq. (1.118), a sequence of approximate solutions $\mathbf{u}_h$ with $h \to 0$ will converge[4] with respect to $\|\mathbf{u} - \mathbf{u}_h\|_1$ if $k \geq 1$.

  The case $k = 1$ is covered by the *patch test*, i.e., the ability to model fields with constant first derivatives of finite element interpolation functions in arbitrary element configurations [9, 8.3.2]).

– The convergence rate will be higher for larger values of k, i.e., if the finite element interpolation has a higher order of completeness.

Limitations of these arguments have to be mentioned. Under certain conditions the coefficient c may become so large that acceptable solutions, i.e., a sufficiently small value $\|\mathbf{u} - \mathbf{u}_h\|$, cannot be reached with realizable values h small enough. A particular occurrence is given by locking of approximate solutions with incompressible or nearly incompressible materials.

The locking problem motivates the inclusion of extended weak forms of equilibrium conditions. Equations (1.101, 1.102) are weak forms of *displacement based methods*, as a solution is given by a displacement field. Strains and stresses are derived from this solution. Extended weak forms allow us to involve fields for stresses and strains as independent solution variables. Most prominent are the *principles of Hu-Washizu* and *Hellinger-Reissner* [2, 4.4.2]. An abstract extended problem definition analogous to Eq. (1.108) is given by [3, (16)]

$$
\begin{aligned}
a(\mathbf{u}_h, \mathbf{v}_h) + b(\boldsymbol{\epsilon}_h, \mathbf{v}_h) &= (\mathbf{f}, \mathbf{v}_h) & \forall \mathbf{v}_h \in H_h \\
b(\mathbf{w}_h, \mathbf{u}_h) - c(\boldsymbol{\epsilon}_h, \mathbf{e}_h) &= 0 & \forall \mathbf{w}_h \in W_h
\end{aligned}
\tag{1.119}
$$

in which a, c are symmetric bilinear forms, b is a bilinear form, f is a linear form, H_h, W_h are appropriate functions spaces, $\mathbf{u}_h \in H_h, \boldsymbol{\epsilon}_h \in W_h$ are the approximate solutions. In most cases $\boldsymbol{\epsilon}_h$ stands for an independent field of strains or stresses. Such an approach requires an extension of the foregoing discussion related to displacement based methods including the widely referenced *inf-sup condition* [3]. The provided framework to include independent interpolations for displacements, strains, and stresses may avoid locking problems to a large degree. Cases of locking risks will be discussed individually if necessary in the following.

The foregoing discussion is related to linear problems. They cannot be strictly applied to nonlinear problems – physically nonlinear and/or geometrically nonlinear. But the conclusions to be drawn regarding element selection and discretization should also be considered for nonlinear and dynamic problems.

---

[4] Converge with respect to first order Sobolev norm $\|\mathbf{u} - \mathbf{u}_h\|_1$ may not be sufficient if generalized strains are derived from higher derivatives of displacements, e.g., with beams, slabs, shells. The theory has to be extended for this case.

Chapter 2

Uniaxial Structural Concrete Behavior

2.1 Scales and Short–Term Stress–Strain Behavior of Homogenized Concrete

Structural elements such as bars, beams, and columns are characterized by uniaxial states of stress and strain. Thus, it is sufficient to describe material behavior by uniaxial stress–strain relations for such elements. This simplifies stress–strain relations to a large extent.

On the other hand, different time scales have to be regarded for the behavior of concrete. This is related to the type and the duration of load application. We assume a *monotonic loading* which is uniformly applied from zero to a final value during a loading time and then holds its value constant after loading time. Another parameter to be considered is loading speed which is load magnitude related to loading time. Furthermore, material specimen with states of stress and strain constant or continuous in space, i.e homogeneous states of stress and strain are considered. Material behavior may be classified as follows with respect to time scales:

– *Short-term behavior* is observed as immediate response of a material specimen exposed to a loading whereby loading speed is slow. A slow loading speed does not have an influence on the stress–strain relation. It is only influenced by the magnitude of loading. In the case of concrete, the corresponding time horizon typically covers minutes up to days.

– *Long-term behavior* extends the time horizon beyond the application time of the loading. Material behavior is observed as delayed response of a material specimen after load application. Corresponding phenomena are creep and relaxation. The time horizon typically covers weeks up to years.

– *Highly dynamical behavior* is related to such as high loading speeds that loading speed influences stress–strain relations beneath the magnitude of loading itself. A corresponding phenomenon is the strain-rate effect where concrete strength is increased due to

high strain rates. The time horizon is restricted to milliseconds as very high loadings are reached within very short times due a high loading speed.

The strain-rate effect is still an open object of research. A first approach is given in [18].

Observation of uniaxial short-term behavior under monotonic loading is the first approach to characterize the behavior of materials. A typical stress–strain relation as is observed for concrete with a cylindrical or cubic specimen under compression is shown in Fig. 2.1a. The relation has the following parts:

– The initial linear part with the initial Young's modulus E_c.

– A nonlinear *hardening* part with decreasing tangential material stiffness but still increasing stress.

– A nonlinear *softening* part with negative tangential material stiffness and decreasing stress.
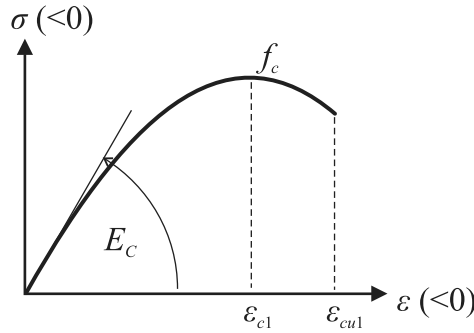
Figure 2.1: Uniaxial compressive stress–strain behavior of concrete.

Characteristic values are given by the maximum stress which corresponds to the compressive strength f_c (unsigned), the corresponding strain ϵ_{c1} (signed), and the ultimate failure strain ϵ_{cu1} (signed). A large variety of analytical forms are available for such a course. The approach of Saenz [21, 8.8.1] is chosen as an example. Stress σ depending on strain ϵ is given by

$$\sigma = \frac{E_c\,\epsilon}{1 + \left(\frac{E_c}{E_{c1}} - 2\right)\frac{\epsilon}{\epsilon_{c1}} + \left(\frac{\epsilon}{\epsilon_{c1}}\right)^2}, \quad 0 \geq \epsilon \geq \epsilon_{cu1} \tag{2.1}$$

with the secant modulus $E_{c1} = -f_c/\epsilon_{c1}$ at compressive strength f_c. Equation (2.1) yields $\sigma = -f_c$ for $\epsilon = \epsilon_{c1}$. Alternatives to the approach of Saenz are described by the Modelcode 2010 [18, 5.1.8.1] and the Eurocode 2 [26, 3.1.5].

The tangential material stiffness, see Eq. (1.50), is given by the tangential modulus

$$E_t = \frac{\partial \sigma}{\partial \epsilon} = \frac{E_c\left(1 - \frac{\epsilon^2}{\epsilon_{c1}^2}\right)}{\left(1 + \left(\frac{E_c}{E_{c1}} - 2\right)\frac{\epsilon}{\epsilon_{c1}} + \frac{\epsilon^2}{\epsilon_{c1}^2}\right)^2} \tag{2.2}$$

which leads to $E_t = E_c$ for $\epsilon = 0$; furthermore, $E_t = 0$ for $\epsilon = \epsilon_{c1}$ and $E_T < 0$ for $\epsilon < \epsilon_{c1}$, $|\epsilon| > |\epsilon_{c1}|$. Uniaxial tension in a simplified first approach is described by

$$\sigma = \left\{ \begin{array}{ll} E_c\, \epsilon, & \epsilon \leq f_{ct}/E_c \\ 0, & \text{else} \end{array} \right. \tag{2.3}$$

with the uniaxial tensile strength f_{ct}. The tangential stiffness corresponds to the initial stiffness $E_T = E_c$ for $\epsilon \leq f_{ct}/E_c$.

- These types of uniaxial stress–strain relations are the base for modeling and design of structural elements like bars and beams.

Spatial dimensions of bars and beams have a scale of meters (m) for spans or (m^{-1}) for cross sections. The latter is also the dimension of cylindrical or cubic specimen. This corresponds to the *macroscale*. A material description as given by Eqs. (2.1)–(2.3) is derived from macroscale specimen. Thus, it is only applicable to macroscale structures.

Other spatial scales are the *mesoscale* with spatial dimensions of millimeters (m^{-3}) and the *microscale* with spatial dimensions of micrometers (m^{-6}). A strict demarcation between spatial scales is not possible but depends on the particular problem under consideration. Further aspects regarding material models, scales, and the fundamental concept of *homogeneity* are discussed in Section 5.1.1.

Concrete obviously cannot be considered as homogeneous in the mesoscale. A spatial resolution of millimeters reveals its composition of aggregates and mortar leading to discontinuities in material properties. But the comprehension of the mesoscale is necessary to understand the failure of concrete. We consider *uniaxial tensile failure*. Its process is shown in Fig. 2.2a. The following successive phases can be distinguished:

- Development of *microcracks* with random distribution but progressing crack alignment normal to the stress direction.

- Coalescence of microcracks to larger cracks which form several branches and are still bridged by crack bridges.

- Fracturing of crack bridges and fusion of branched cracks into a *macrocrack*.
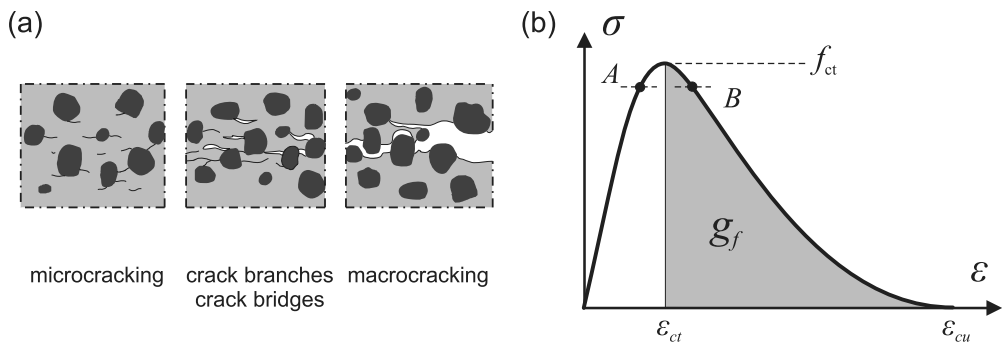
Figure 2.2: (a) Cracking in mesoscale. (b) Uniaxial tensile stress–strain behavior.

The notions of stresses and strains obviously become questionable in this view. But a change of view back to the macroscale and performing a homogenization, see Section 5.1.1, allows us to derive stress–strain relations. A characteristic course is shown in Fig. 2.2b. This is again characterized by an initial linear part, a hardening part with increasing strains and stresses and a *tension softening* part with increasing strains and decreasing stresses.

Uniaxial tension occurs with tension bars. The phenomenon of softening leads to a *localization* of strains within tension bars. Due to scatter the tensile strength measured over cross sections varies along a bar. Thus, tensile failure will start in the cross section with the smallest tensile strength. Due to tension softening the tensile force applied to the bar has to be reduced to avoid a sudden failure.

 – The failing cross section reaches a point B on the stress–strain curve, see Fig. 2.2b, while other cross sections, which were still in the hardening range, unload to point A.

 – Strains increase in the failing cross section while strains decrease in the other cross sections with ongoing unloading.

 – Softening spreads over a *process zone* with some thickness b_w as cracking involves microcracking, crack branches and crack bridges, see Fig. 2.2a. A synonym for process zone is the *crack band*.
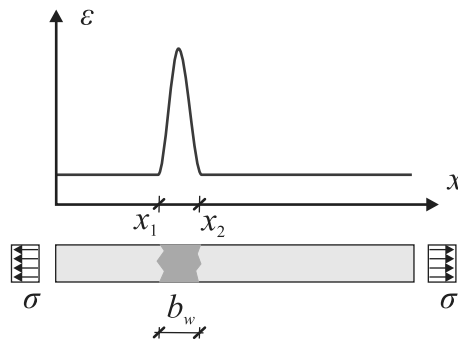
Figure 2.3: Scheme of localization in a tension bar.

 – Relatively high increasing strains develop in the process zone compared to decreasing strains in the rest of the bar, see Fig. 2.3.

 – The process ends with a macrocrack in the failing cross section while the rest of the bar has zero stresses and strains.

This qualitative description is illustrated with the following example.

Example 2.1 Concrete tensile bar with localization
A scheme of system and discretization is shown in Fig. 2.4. The following properties are chosen:

 – Uniaxial two-node bar elements are used for discretization, see Section 1.3. The length of the whole bar is chosen as $L = 0.5\,\mathrm{m}$, its cross section as $A_c = 0.1 \times 0.1\,\mathrm{m}^2$. The

element length has to be small compared to the length of the crack band to resolve the high strain gradient within it. Thus, the element length is determined with $L_e = 0.001\,$m leading to 500 elements.
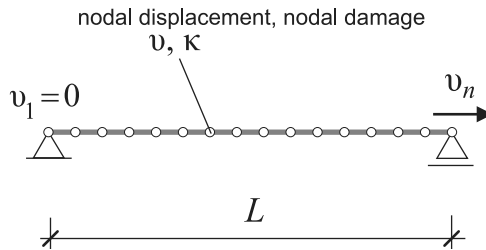
Figure 2.4: Example 2.1 scheme of system and discretization.

– The material properties are chosen according to a concrete grade C 40 as is described in [18, 5.1.5,5.1.7] with an initial Young's modulus $E_c = 36\,000\,\text{MN/m}^2$ and a tensile strength $f_{ct} = 3.5\,\text{MN/m}^2$. The damage formulation, see Section 5.6, is used to model material behavior. This formulation allows describing tension softening.

On the other hand, modeling of tension softening with finite elements needs a regularization, see Section 5.9. The gradient damage approach is used for the current example. This requires a characteristic length R as material parameter which corresponds to the length of the crack band and is chosen with $R = 0.03\,$m.

– Boundary conditions are prescribed with zero displacements on the left and with the prescribed displacement $u_N = 0.1333 \cdot 10^{-3}\,$m corresponding to a medium strain of $\epsilon = 0.2667 \cdot 10^{-3}$. An ideal clamping is assumed at both ends which prevents damage at the ends only.

– An incrementally iterative approach, see Section 1.6, is used for nonlinear problem solving. The size of loading increments is determined with arc length control: the prescribed displacement increment size is chosen such that a norm of the vector of local displacements has a prescribed fixed value, see Appendix A.

The computation leads to the following results:

– The load–displacement curve is shown in Fig. 2.5b. This starts with a linear behavior followed by nonlinear hardening while reaching the tensile strength. But in contrast to Fig. 2.2b, which exposes material behavior, this curve shows a *snap-back* after a short range of softening. Snap-back indicates nonhomogeneous structural behavior and is characterized by decreasing reaction forces and simultaneously decreasing displacements.

In the case of a relatively short length of the softening crack band, its elongation cannot compensate for elastic shortening of the elastic parts with the reduction of stress. The prescribed displacement of the right end has to be reduced in order to maintain equilibrium and kinematic compatibility. The resulting bar elongation nominally proceeds
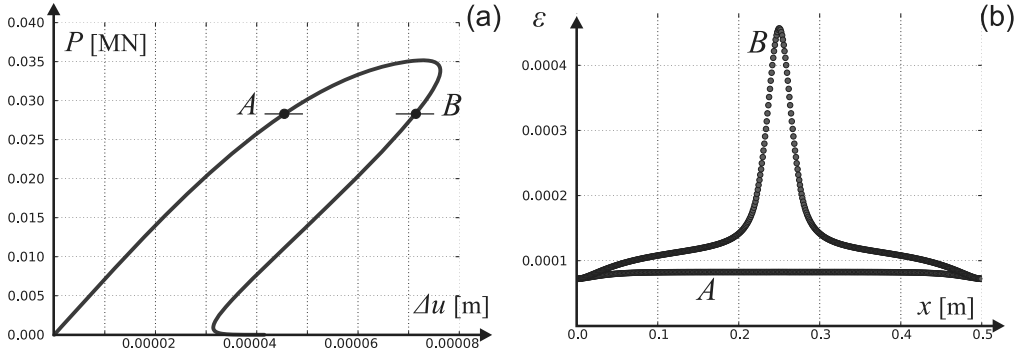
Figure 2.5: Example 2.1 (a) reaction force–displacement relation, (b) strains along bar.

when stress are reduced to zero. The snap-back characteristics depend on the ratio of the length of the crack band compared to the total length of the bar. With smaller ratios the snap-back behavior becomes more pronounced.

The whole process may be *un*stable under quasistatic conditions and it is difficult to realize experimentally as a displacement control of the softening area is required.

– Strain distributions along the bar for two loaded states are shown in Fig. 2.5b. Curve A shows the strain distribution before reaching the tensile strength in the hardening range, that is point A in Fig. 2.5a. Strain moderately increases in the mid-range of the bar due to prescribed zero nonlocal damage on both ends. Curve B in Fig. 2.5b shows the strain distribution in the softening range, that is point B in Fig. 2.5a. Strains strongly increase as a localization occurs within a short length and otherwise decrease due to the load decrease.

In a real specimen, the localization will not center exactly in the mid-point but in the weakest cross section. This cross section will arise due to the stochastic variation of material strength. Its cross-sectional strength and location cannot be determined exactly but only with their statistical parameters.

————————————————————————————— End Example 2.1

Computation of whole structural elements has to rely on the macroscale and homogenization of concrete behavior. A corresponding course[1] of strains $\epsilon_c(x)$ across the process zone with $x_1 \leq x \leq x_2$ and a crack band width $b_w = x_2 - x_1$ are shown in Fig. 2.3.

• The magnitude of the *crack band width* b_w is estimated from experimental observation with two to three times the largest aggregate size, see Fig. 2.2a.

This leads to the *fictitious crack* with a width

$$w = \int_{x_1}^{x_2} \epsilon_c(x)\,\mathrm{d}x \tag{2.4}$$

---

[1] Actually this is a calculational course under the assumption of a homogenized material.

as the difference between the displacements of the left- and right-hand cross sections bounding the process zone. A further homogenization leads to

$$w = b_w \, \epsilon_c \tag{2.5}$$

with the mean value ϵ_c of $\epsilon_c(x)$. The *crack strain* ϵ_c corresponds to the strain of the stress–strain relation shown in Fig. 2.2b. Thereby the softening range is bounded by the strain ϵ_{ct} corresponding to the tensile strength f_{ct} and the strain ϵ_{cr} where no stresses are transferred anymore: $\sigma_c = 0$ for $\epsilon_c \geq \epsilon_{cr}$. Equation (2.5) leads to a crack width for $\epsilon_c = \epsilon_{ct}$, but this is at first a calculational value.

- A stress transfer across a crack in progress related to a fictitious crack width is denoted as *cohesive crack*.

As cracking is an irreversible process leading to the creation of new surfaces energy is dissipated within the process zone. The volume-specific crack energy is given by

$$g_f = \int_{\epsilon_{ct}}^{\epsilon_{cr}} \sigma(\epsilon') \, \mathrm{d}\epsilon' \tag{2.6}$$

with $\sigma(\epsilon')$ according to Fig. 2.2a. Its integration along the thickness of the process zone leads to the surface-specific crack energy or simply *crack energy*

$$G_f = b_w \, g_f \tag{2.7}$$

The crack energy G_f indicates energy dissipation due to creation of new surfaces. Its value corresponds to the shaded area in Fig. 2.2a. Due to current state of knowledge it is assumed as a constant material parameter, so that Eq. (2.7) leads to a constraint for a $\sigma - \epsilon_c$ relation.

- Crack energy or energy dissipation due to cracking of concrete contributes to the *ductility* of concrete structures, i.e., the ability to deform while internal forces retain their level, and insofar is a significant property.

The extension of the uniaxial case to modeling of multiaxial cracking is described in Section 5.7, a biaxial application in Section 6.2 including aspects of unloading.

The failure mode is different under uniaxial compression but its understanding again requires the comprehension of the mesoscale. A model for the composition of aggregates and mortar within a concrete specimen is shown in Fig. 2.6. Furthermore, this figure schematically shows the mechanism of compressive force transfer which concentrates upon aggregates which are relatively stiff compared to the mortar. This is obviously connected with a redirection of forces leading to some lateral tensile forces which also have to be sustained by the mortar.

- As a consequence, concrete will fail due to internal lateral tension under homogeneous uniaxial compressive loading.

This is a diffuse failure – in contrast to local failure under tensile loading – as failure spreads throughout a whole specimen and is not localized. Actually, a bunch of cracks occur with
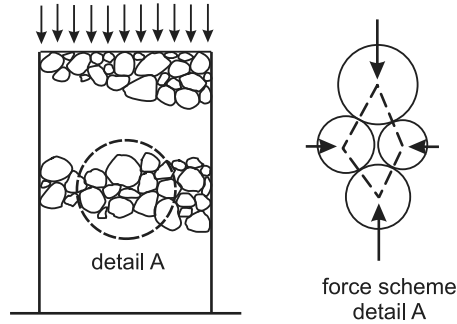
Figure 2.6: Simplified model for force transfer in composition of aggregates and mortar.

crack directions aligned to the load direction. But this requires an adequate experimental setup with minimized lateral constraints on the loaded faces of a plain concrete specimen.

While uniaxial material modeling of concrete is sufficient for structural elements like bars and beams a multiaxial approach is necessary for plates, slabs, and shells. Multiaxial material modeling of concrete is discussed in Section 5.1.1.

2.2   Long-Term Behavior – Creep and Imposed Strains

Creep occurs as a delayed response of a material specimen after load application. A concrete specimen exposed to a loading within minutes will have increasing strains within months while its loading is hold constant. The complementary phenomenon to creep is *relaxation*. Deformations imposed to a concrete specimen within minutes will lead to immediate stresses but these stresses will decrease within months while the imposed deformation is hold constant.

Mechanisms of creep and relaxation have to be treated in the microscale of materials and are connected to a relatively slow redistribution in the arrangement of microstructures and, in the case of mortar, water. All solids undergo creep and relaxation but its extent is different for different materials. Its extent is relatively large for, e.g., mortar and thus for concrete. A first approach to describe the development of uniaxial strain ϵ with time t for a constant uniaxial stress σ_0 is given by

$$\epsilon(t) = J(t)\ \sigma_0 \tag{2.8}$$

with a *creep function* $J(t)$. The creep function is specific for every material. Creep strain is proportional to the applied stress with this approach. Such a linear characteristic with respect to stress or *linear creep* is valid for moderate stress levels relative to strength. A qualitative course of a uniaxial creep strain derived from experimental data is shown in Fig. 2.7. Equation (2.8) is generalized as

$$\epsilon(t) = \int_0^t J(t,\tau)\ \dot{\sigma}(\tau)\,\mathrm{d}\tau, \quad 0 \leq \tau \leq t \tag{2.9}$$
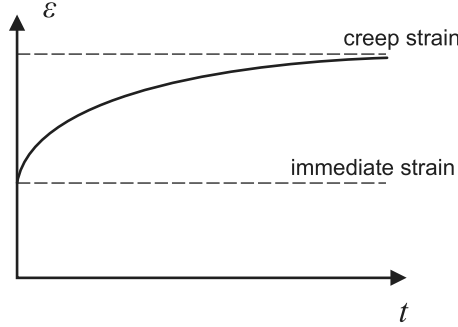
Figure 2.7: Uniaxial strain depending on time for a material with creep.

for stresses σ variable in time t with a stress time derivative $\dot{\sigma}(\tau)$ and an extended creep function $J(t, \tau)$. It describes the effect of a stress increment occurring in time τ on strain in the current time t. The following general approach is appropriate within this context:

$$J(t, \tau) = \sum_{\mu=0}^{N_\mu} J_\mu(t, \tau) \tag{2.10}$$

with

$$J_\mu(t, \tau) = \frac{1}{E_\mu} \left(1 - \mathrm{e}^{-[y_\mu(t) - y_\mu(\tau)]} \right), \quad y_\mu(\tau) = \left(\frac{\tau}{\tau_\mu} \right)^{q_\mu} \tag{2.11}$$

and material parameters τ_μ, q_μ, E_μ. For alternative approaches see, e.g., [4], [84, Sec. 28]. The parameter τ_μ has a dimension of time and the E_μ a dimension of stress. Equations (2.9-2.11) may be written as

$$\epsilon(t) = \sum_{\mu=0}^{N_\mu} \epsilon_\mu(t), \quad \epsilon_\mu(t) = \int_0^t J_\mu(t, \tau) \, \dot{\sigma}(\tau) \, \mathrm{d}\tau \tag{2.12}$$

A time parameter τ_μ approaching zero ($\tau_\mu \to 0$) yields a constant compliance $J_\mu = 1/E_\mu$ as a special case of creep. A choice $N_\mu = 0, \tau_0 = 0, E_0 = const.$ recovers linear elasticity

$$\epsilon(t) = \frac{1}{E_0} \ \sigma(t) \tag{2.13}$$

This has at least to be extended with $N_\mu = 1, \tau_\mu > 0$ to gain a qualitative course as is shown in Fig. 2.7.

We consider a sudden jump of stress at a time τ_0 from zero to a value σ_0. The *Dirac-Delta function* $\delta(\tau - \tau_0)$ is used to describe the time derivative of stress for this case. It is defined as

$$\delta(\tau - \tau_0) = \begin{cases} \infty & \tau = \tau_0 \\ 0 & \tau \neq \tau_0 \end{cases}, \qquad \int_{-\infty}^{\infty} \delta(\tau - \tau_0) \, \mathrm{d}\tau = 1 \tag{2.14}$$

Its integral is given by the *Heaviside function*

$$H(\tau - \tau_0) = \begin{cases} 0 & \tau < \tau_0 \\ 1 & \tau \geq \tau_0 \end{cases} \tag{2.15}$$

The Delta-Dirac function has the property

$$\int_{\tau_1}^{\tau_2} F(\tau)\,\delta(\tau - \tau_0)\,\mathrm{d}\tau = F(\tau_0), \qquad \tau_1 < \tau_0 < \tau_2 \tag{2.16}$$

We write $\sigma(\tau) = \sigma_0\,H(\tau - \tau_0)$, $\dot\sigma(\tau) = \sigma_0\,\delta(\tau - \tau_0)$ which yields from Eqs. (2.12, 2.16)

$$\epsilon_\mu(t) = \sigma_0 \int_0^t J_\mu(t,\tau)\,\delta(\tau - \tau_0)\,\mathrm{d}\tau = \sigma_0\,J_\mu(t,\tau_0) \tag{2.17}$$

Finally, regarding Eq. (2.11) with $\tau_0 = 0$

$$\epsilon_\mu(t) = \sigma_0\,J_\mu(t,0) = \sigma_0\,\frac{1}{E_\mu}\left(1 - \mathrm{e}^{-y_\mu(t)}\right), \quad y_\mu(t) = (t/\tau_\mu)^{q_\mu} \tag{2.18}$$

Thus, the creep strain ϵ_μ starts with zero for $t = 0$ and has an asymptotic value σ_0/E_μ. The approaching to the asymptotic value during time is ruled by the parameters τ_μ, q_μ. A variety of functions J_μ allow us to adopt to experimental creep data with any desired accuracy with a calibration of N_μ times a set E_μ, τ_μ, q_μ.

The assumption $q_\mu = 1$ allows for more simplifications. Regarding Eq. (2.11) all terms in Eq. (2.12) are trivially integrated leading to

$$\epsilon_\mu(t) \;=\; \frac{\sigma(t)}{E_\mu} - \frac{\mathrm{e}^{-\frac{t}{\tau_\mu}}}{E_\mu}\int_0^t \dot\sigma(\tau)\,\mathrm{e}^{\frac{\tau}{\tau_\mu}}\,\mathrm{d}\tau \tag{2.19}$$

The time derivative of this strain is given by

$$\dot\epsilon_\mu(t) \;=\; \frac{1}{\tau_\mu}\frac{\mathrm{e}^{-\frac{t}{\tau_\mu}}}{E_\mu}\int_0^t \dot\sigma(\tau)\,\mathrm{e}^{\frac{\tau}{\tau_\mu}}\,\mathrm{d}\tau \tag{2.20}$$

Thus, the strain $\epsilon_\mu(t)$ fulfills the differential equation

$$\eta_\mu\,\dot\epsilon_\mu(t) + E_\mu\,\epsilon_\mu(t) = \sigma(t), \qquad \eta_\mu = E_\mu\tau_\mu \tag{2.21}$$

Equation (2.21) describes a *Kelvin–Voigt element* with a spring and a viscous damper in parallel, see Fig. 2.8a. Equation $(2.12)_1$ yields a simple *Kelvin–Voigt chain*, i.e., a spring and a Kelvin–Voigt element in a row, see Fig. 2.8b. An alternative basic combination with spring and damper in a row is given by the *Maxwell element*, see Fig. 2.8a. The Maxwell element can be treated in analogy to the Kelvin–Voigt element by formally interchanging stress and strain and using a *relaxation function* $R(t,\tau)$ instead of a creep function $J(t,\tau)$. Creep and relaxation functions can be inverted into each other mathematically. A simple combination of a spring and a Maxwell element in parallel leads to a *Maxwell series*.

- Kelvin–Voigt elements and Maxwell elements are the basic blocks of *viscoelasticity*. Together with springs they may be combined in series and/or chains to form *rheological models* to describe linear creep and relaxation.
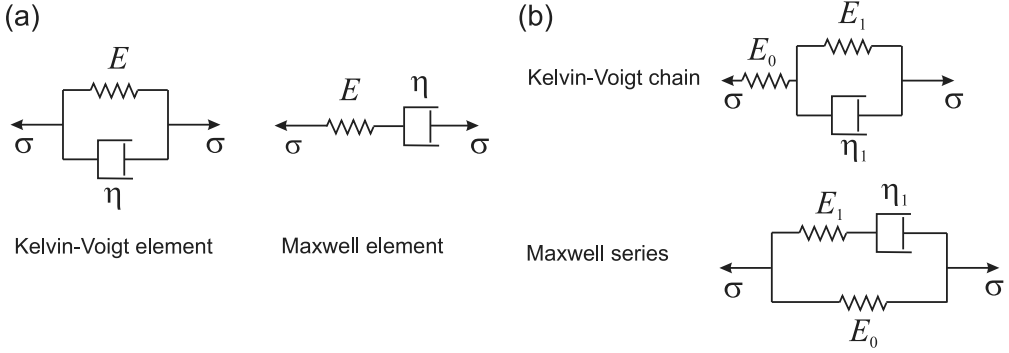
Figure 2.8: (a) Kelvin–Voigt and Maxwell element. (b) Chain and series.

The Kelvin–Voigt chain as shown in Fig. 2.8b is discussed in the following. The stress is the same in each member of the chain but the member's strains ϵ_0 and ϵ_1 add up to the total strain

$$\epsilon(t) = \epsilon_0(t) + \epsilon_1(t), \quad \dot{\epsilon}(t) = \dot{\epsilon}_0(t) + \dot{\epsilon}_1(t) \tag{2.22}$$

The relations for the partial strains are

$$E_0\,\epsilon_0(t) = \sigma(t), \quad \eta_1\,\dot{\epsilon}_1(t) + E_1\,\epsilon_1(t) = \sigma(t) \tag{2.23}$$

see Fig. 2.8b. The combination of Eqs. (2.22, 2.23) results in

$$\epsilon_1(t) = \epsilon(t) - \frac{\sigma(t)}{E_0}, \quad \dot{\epsilon}_1(t) = \dot{\epsilon}(t) - \frac{\dot{\sigma}(t)}{E_0} \tag{2.24}$$

This is inserted in Eq. $(2.23)_2$ to yield after a rearrangement

$$\dot{\sigma}(t) + \frac{E_0 + E_1}{\eta_1}\,\sigma(t) = E_0\,\dot{\epsilon}(t) + \frac{E_0 E_1}{\eta_1}\,\epsilon(t) \tag{2.25}$$

We introduce a final stiffness $1/E = 1/E_0 + 1/E_1$; consider E_0 as an initial stiffness and introduce a dimensionless *creep coefficient* φ defined by $\varphi = E_0/E - 1$. This leads to $E_1 = E_0/\varphi$ and Eq. (2.25) may be reformulated as

$$\dot{\sigma}(t) + \frac{1+\varphi}{\zeta}\,\sigma(t) = E_0\,\dot{\epsilon}(t) + \frac{E_0}{\zeta}\,\epsilon(t), \qquad \zeta = \frac{\varphi\,\eta_1}{E_0} \tag{2.26}$$

The parameter ζ has the dimension of time and is called *creep time* in the following. The differential equation (2.26) is a mathematical model for the conceptual model of the Kelvin–Voigt chain.

- The Kelvin–Voigt chain is a simple model for uniaxial linear creep and relaxation characterized by an initial Young's modulus E_0, a creep coefficient φ, and a creep time ζ. It can be used to model creep for bars and beams.

The mathematical model allows for variable stresses and strains. It is rewritten in a more general form as

$$\dot{\sigma}(t) = E_0 \, \dot{\epsilon}(t) + V \, \epsilon(t) - W \, \sigma(t) \tag{2.27}$$

for use in numerical solution methods, see Section 1.6, by

$$V = \frac{E_0}{\zeta}, \qquad W = \frac{1+\varphi}{\zeta} \tag{2.28}$$

according to Eqs. (1.76, 1.83). Its application is demonstrated with Examples 2.2 and 3.3.

To get a better insight of the meaning of φ and ζ Eq. (2.26) may be analytically solved for a constant stress $\sigma(t) = \sigma_0$, $\dot{\sigma} = 0$ with an initial strain $\epsilon(0) = \sigma_0/E_0$. The solution is

$$\epsilon(t) = \frac{\sigma_0}{E_0} \left[1 + \varphi \left(1 - e^{-\frac{t}{\zeta}} \right) \right] \tag{2.29}$$

The asymptotic strain is $\epsilon_{\text{asym}} = (1+\varphi)\sigma_0/E_0$ with a creep portion $\varphi \, \sigma_0/E_0$, i.e., φ-times the initial strain. The value of φ has to be determined from experimental data or see [26, 3.1.4], [18, 5.9.1.4]. Experimental data also provide a time $t^\star$ where a fraction α of the asymptotic creep part occurs with $0 \le \alpha < 1$. This leads to

$$1 - e^{-t^\star/\zeta} = \alpha \quad \rightarrow \quad \zeta = -\frac{t^\star}{\ln(1-\alpha)} \tag{2.30}$$

If, e.g., half of asymptotic creep occurs at time $t^\star$ with $\alpha = 0.5$ then $\zeta \approx 1.44 \, t^\star$. Thus, at least three points of an experimental uniaxial stress–strain relation are reproduced by the Kelvin–Voigt chain: the immediate strain after load application, the final asymptotic strain and an intermediate value at a time $t^\star$. A better approximation of experimental data requires extended Kelvin–Voigt chains or the combination of Maxwell elements.

Strains resulting from a mechanical loading have been discussed up to now. But strains are also imposed by a change of *temperature* or, in the case of concrete, *shrinkage*. Shrinkage results from enduring drying of concrete. Uniaxial temperature strains are given by

$$\epsilon_T = \alpha_T \, \Delta T \tag{2.31}$$

with the thermal expansion coefficient α_T and a temperature change ΔT (signed). Concrete shrinkage strains ϵ_{cs} mainly depend on time, humidity conditions, and ratio of surface to volume [26, 3.1.4], [18, 5.9.1.4]. The total *measurable strain* results from stresses and *imposed strains*. For the uniaxial case, it is given by

$$\epsilon = \frac{\sigma}{C} + \epsilon_I, \quad \epsilon_I = \epsilon_T + \epsilon_{cs} \tag{2.32}$$

with the uniaxial stress σ and a scalar material stiffness C, see Eq. (1.47). This leads to the basic form of a material law regarding imposed strains

$$\sigma = C \, (\epsilon - \epsilon_I), \quad \epsilon_I = \epsilon_T + \epsilon_{cs} \tag{2.33}$$

with an incremental formulation

$$\dot{\sigma} = C_T \, (\dot{\epsilon} - \dot{\epsilon}_I), \quad \dot{\epsilon}_I = \dot{\epsilon}_T + \dot{\epsilon}_{cs} \tag{2.34}$$

see Eq. (1.50). Stresses due to temperature or shrinkage are given by $\sigma_I = -C\,\epsilon_I$. A bar which is fully constrained, that is, $\epsilon = 0$ in Eq. (2.33), gets tensile stresses σ_I with an imposed contraction $\epsilon_I < 0$ and compressive stresses σ_I with an imposed elongation $\epsilon_I > 0$.

- *Constraint stresses* resulting from imposed strains are proportional to the stiffness of the material or the stiffness of the structure, respectively.

Aspects of temperature loading for beams are discussed in Section 3.5.2 and with Example 3.4.

Stresses from constraints may be reduced by creep or relaxation. To model this behavior Eq. (2.27) covering creep and relaxation is extended in analogy to Eq. (2.34) to include imposed strains:

$$\dot{\sigma}(t) = C_T \left[\dot{\epsilon}(t) - \dot{\epsilon}_I(t) \right] + V \left[\epsilon(t) - \epsilon_I(t) \right] - W\,\sigma(t) \qquad (2.35)$$

Appropriate solution methods for this type of material model leading to a transient problem have been described in Section 1.6. This is demonstrated with the following example.

Example 2.2 Concrete tensile bar with creep and imposed strains
The following properties are chosen:

- A homogeneous uniaxial state of stress and strain is assumed to expose pure material behavior. Thus, the absolute spatial dimensions and number of finite elements are basically irrelevant. Nevertheless, some data have to be chosen with a bar length of $L = 1.0\,\mathrm{m}$, a cross-sectional area $A_c = 1.0\,\mathrm{m}^2$ and a discretization with five uniaxial two-node bar elements, see Section 1.3.

- Material properties are the focus of the problem. Concrete is chosen with a Young's modulus $E_0 = 30\,000\,\mathrm{MN/m}^2$. Creep properties are assumed with a creep coefficient $\varphi = 2.0$ and a time $t^\star = 100$ [d] for $\alpha = 0.5$, i.e., half of total creep occurs after 100 days for a constant stress load. With Eq. (2.30), creep time is given by

$$\zeta = -\frac{100}{\ln 0.5} = 144\,\mathrm{d} \qquad (2.36)$$

Equation (2.28) leads to

$$V = 207.94\,\frac{\mathrm{MN}}{\mathrm{m}^2\mathrm{d}}, \quad W = 0.020794\,\frac{1}{\mathrm{d}} \qquad (2.37)$$

- Regarding boundary conditions the displacement of one bar end is prescribed with zero while a stress or a prescribed displacement is applied at the other bar end.

- An incrementally iterative approach according to Eq. (1.87) is chosen for problem solving. The time step is chosen with $\Delta t = 10\,\mathrm{days}$ while a period of 500 days is regarded.
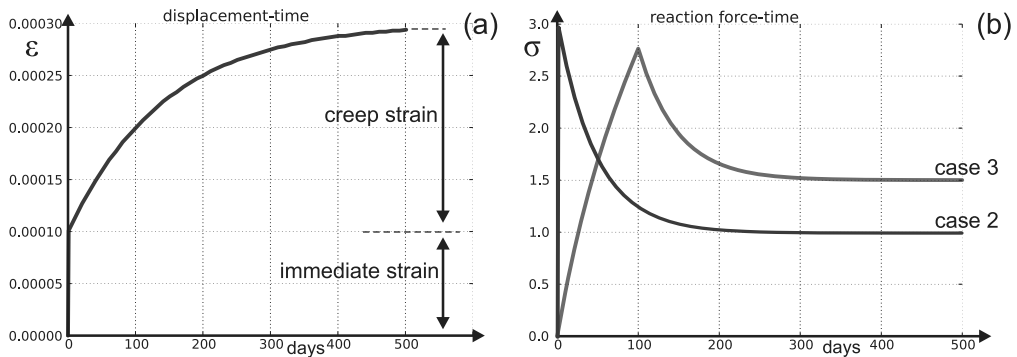
Figure 2.9: Example 2.2 time dependencies (a) Strain. (b) Stress.

The following cases are considered for the computation:

– A loading $\sigma_0 = 3.0\,\mathrm{MN/m^2}$ constant in time

   The computed *strain* depending on time is shown in Fig. 2.9a. An exact solution for this case is given by Eq. (2.29). Differences between exact solution and numerically computed solution are small and are not visible in the figure.

– An immediate right-end displacement corresponding to an immediate strain $\epsilon_0 = \sigma_0/E_0 = 0.1\text{‰}$ is applied and hold constant in time.

   The computed *stress* depending on time is shown in Fig. 2.9b, case 2. In contrast to the case before relaxation occurs with stress decreasing to an asymptotic value.

– A slow imposed contraction of 0.15‰ is linearly increased over a period of $t = 100$ days and then hold constant. The displacements of both ends are prescribed with zero. As total strain ϵ is prescribed with zero a tensile constraint stress is induced.

   The computed *stress* depending on time is shown in Fig. 2.9b, case 3. It becomes obvious that a constraint stress due to a slowly increasing imposed strain is strongly reduced already during its initiation.

End Example 2.2

While analytical, exact solutions are available for cases 1 and 2, the numerical approach is necessary for arbitrarily prescribed loads or displacements. Furthermore, more complex creep models, see e.g., [64, 6.4], [84, 28, 29], can only be solved with numerical models.

2.3 Reinforcing Steel Stress–Strain Behavior

Reinforcing steel has to be considered as a second basic component beneath plain concrete. Steel can be considered as homogeneous already in the mescoscale – with spatial dimensions of millimeters – in contrast to concrete. Furthermore, steel has the same behavior under compression and tension. Typical uniaxial stress–strain relations as are derived from
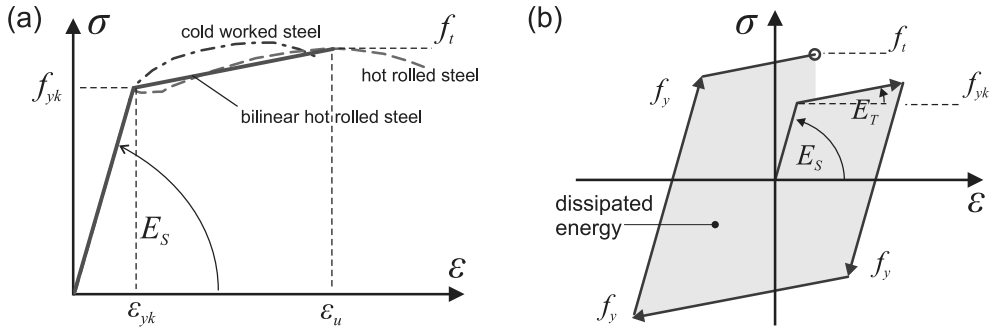
Figure 2.10: Reinforcing steel (a) Uniaxial stress–strain behavior. (b) Cyclic behavior with hardening.

experimental data are shown in Fig. 2.10a. The relation has the following major parts:

– The initial linear elastic part.

– The transition part with the initiation of yielding.

– The yielding part with high strains and slightly increasing stresses.

– A relatively short softening part closed by failure.

The characteristic of these parts varies with different types of steel. Relevant design properties of reinforcing steel are given in [26, 3.2],[18, 5.2]. A bilinear approximation of uniaxial stress–strain relations is generally used for the design and computation of reinforced concrete structures. It is characterized by the initial Young's modulus E_s, an initial yield stress f_{yk} (unsigned), a failure stress f_t (unsigned) and a corresponding failure strain ϵ_u (unsigned). As $f_t > f_{yk}$ a *hardening* occurs, i.e., the material gains strength. The yield strain and tangential material stiffness in the hardening range are given by

$$\epsilon_y = \frac{f_{yk}}{E_s}, \qquad E_T = \frac{f_t - f_{yk}}{\epsilon_u - \epsilon_y} \qquad (2.38)$$

Nonlinear steel behavior is characterized by *elastoplasticity*. Such nonlinear material behavior becomes obvious with unloading from the yielding part.

• *Plasticity* is characterized by approximately the same material stiffness for initial elastic loading and unloading. Thus, plastic strains remain as permanent strains while unloading from yielding to zero stresses.

This phenomenon results from sliding in the crystal microstructure. It is schematically illustrated in Fig. 2.10b with the cyclic behavior. Unloading from, e.g., a tensile regime may proceed to reloading into the compressive regime while crossing a zero stress. With the maximum stress f_y reached for tensile hardening the material behaves linear elastic during reloading until stress reaches $-f_y$ and plastic yielding continues with further hardening in

the compressive range. The cycle of loading–unloading–reloading–unloading with *isotropic hardening* is indicated in Fig. 2.10b. The uniaxial stress–strain relation for each branch is described by

$$\sigma = \begin{cases} E_s\,(\epsilon - \epsilon_p) & \text{if } \epsilon_p - \frac{f_y}{E_s} \le \epsilon \le \epsilon_p + \frac{f_y}{E_s} \\ \text{sign}\epsilon\, f_y & \text{else} \end{cases} \tag{2.39}$$

with the sign function, the current yield stress f_y and the actual plastic strain ϵ_p (signed) as an internal state parameter, see also Eq. (1.48). The evolution law for the internal state variable and the rule for hardening are given by

$$\left. \begin{aligned} \dot{\epsilon}_p &= \dot{\epsilon} \\ \dot{f}_y &= E_T\,|\dot{\epsilon}| \end{aligned} \right\} \quad \text{if} \quad \epsilon\,\dot{\epsilon} > 0 \text{ and } |\sigma| = f_y \tag{2.40}$$

with a tangential material stiffness or hardening modulus E_T, see Eq. $(2.38)_2$. Finally

$$\sigma = 0 \quad \text{if } |\epsilon| > \epsilon_u \text{ and for all strains following} \tag{2.41}$$

The hardening under consideration is *isotropic* as hardening in the tensile range also leads to a compressive strength increase and vice versa. Equations (2.39, 2.40) are an extension of Eqs. (1.48, 1.49) as the latter do not cover hardening. This yields a hardening modulus $E_T = 0$ which might lead to a singular tangential material stiffness $\mathbf{C}_T$, see also Eq. (1.50), and finally to a singular tangential stiffness matrix $\mathbf{K}_{Te}$, see also Eq. (1.65). The latter may prevent a solution determination, see Eq. (1.72). It is appropriate to assume some amount of hardening from a numerical point of view and the stress–strain relations (2.39, 2.40) are used for reinforcing steel in the following.

Elastoplasticity allows for closed cycles of stress–strain behavior, i.e., a particular point σ, ϵ in the hardening range can again be reached after a cycle with two times of unloading and reloading, see also Fig. 2.10b. The area within such a cycle amounts to the specific internal *dissipated energy*. On the other hand, energy dissipation in a structure contributes to its *ductility*, i.e., its ability to deform while its internal forces retain their level.

2.4   Bond between Concrete and Reinforcing Steel

Due to the limited tensile strength of concrete a reinforcement has to take over tensile forces. An experimental setup to expose transmission of forces between concrete and a rebar is shown in Fig. 2.11a: a single rebar is pulled out of a concrete block. The system is characterized by measures for the relative displacement of the rebar compared to the concrete block and the force system of rebar tension and concrete block retention. Transmission of forces relies on three mechanisms:

– Adhesion as a rigid connection of boundary layers of concrete and steel.

– Friction as slip between the boundary layers of concrete and steel combined with lateral pressure.

– Ordinary rebars have profiled surfaces with ribs or dents acting like consoles.
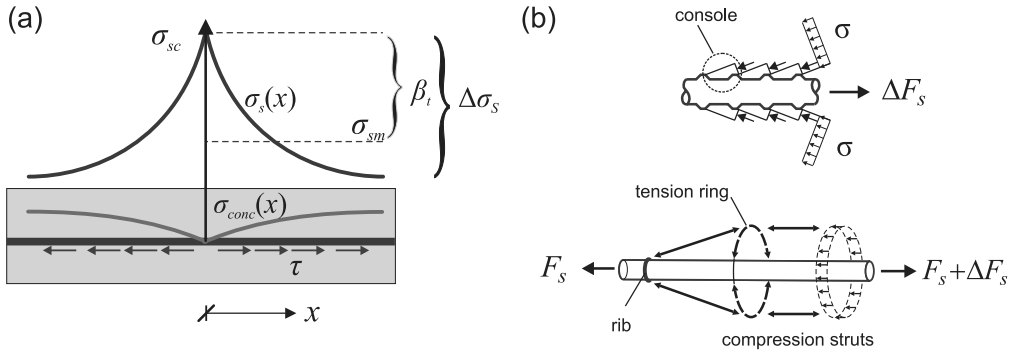
Figure 2.11: (a) Basic bond setup. (b) Main bond mechanism.

The last-mentioned console mechanism contributes the largest amount to the rebar force for a given relative rebar displacement. Such an interaction due to profiled surfaces leads to a triaxial state of stresses within the concrete body immediately surrounding the rebar. This is schematically illustrated in Fig. 2.11b. A system of skew concrete struts braces against rebar ribs in the view of a plane cross section. These concrete struts form a cone in the spatial view. A circumferential tensile ring is necessary to redirect the cone compression into a kind of a cylinder compression aligned to the rebar force.

The tensile cylinder around the rebar is activated through tensile stresses within the concrete body. A bond failure may occur with concrete splitting along a rebar in case that such tensile stresses exceed the limited tensile strength of concrete. This can be prevented by placing a lateral secondary reinforcement or through reducing tensile stresses by increasing the radial concrete cross section or by providing sufficient concrete cover, respectively.

Bond is a complex mechanical problem which requires the mesocale view for a thorough understanding and analysis whereby each rebar and concrete has to be considered as three-dimensional solids with nonlinear material behavior. A simplified model is necessary to make bond treatable from a macroscopic view. Such a model is shown in Fig. 2.12a. A cut in the
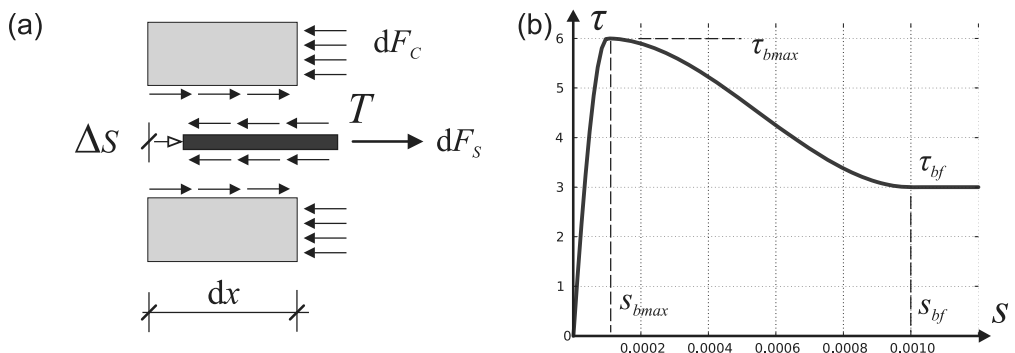
Figure 2.12: (a) Schematic bond equilibrium. (b) Typical bond law.

interface between a simplified cylindrical rebar and the concrete body exposes a *bond force flow T* which is a force related to length and obeys a relation

$$T = \frac{\mathrm{d}F_s}{\mathrm{d}x} = \frac{\mathrm{d}F_c}{\mathrm{d}x} \tag{2.42}$$

with the rebar force F_s and the resulting force F_c in the concrete body. The relative displacement between rebar and concrete is measured by a *slip s*. The notion of slip assumes the deformation of concrete in a cross section, see Fig. 2.12a, as approximately homogeneous beyond the immediate surroundings of the rebar and defines slip s as the difference between the longitudinal displacements of the outer concrete area and the center axis of the rebar. Thus, slip has a dimension of length.

The force variable T and kinematic variable s are connected by a *bond law* for the *flexible bond*

$$T = f_T(s) \tag{2.43}$$

An alternative formulation assumes a constant circumference U of a rebar and derives a bond stress $\tau = T/U$ with the dimension of stress leading to

$$\tau = f_\tau(s) \tag{2.44}$$

Such a formulation is generally used as it is independent from specific geometric properties and may be considered as a special case of a material law. A characteristic smoothed course of a bond law is shown in Fig. 2.12b. It has the following parts [18, 6.1.1]:

– A initial part with increasing nonlinear mechanisms due to nonlinear behavior of concrete and reinforcing steel.

– A point or range of maximum bond stress corresponding to bond strength τ_{max} which is related to the tensile strength of concrete, see the foregoing discussion of the console mechanism.

– A softening part with increasing slip and decreasing bond stress due to softening in the concrete's tensile range, see Fig. 2.2b.

– A final horizontal part with approximately constant bond stress τ_f and increasing slip due to the friction of sheared concrete consoles.

The particular curve of Fig. 2.12b is composed of a quadratic, cubic and linear polynomial with continuous derivatives at the connection points which improves convergence when applying, e.g., the Newton–Raphson method, see Eq. (1.71), for nonlinear problem solving. This course is ruled by the values of τ_{bmax}, τ_{bf} and the corresponding slip values s_{bmax}, s_{bf}. These characteristic values of a bond law have to be determined from experimental data. Some generalizing rules are given in [18, 6.1.1.1]. Analytical or numerical simulation models which cover the complex bond situation and yield reliable bond laws are not available due to current state of knowledge.

• Phenomenological bond laws are generally used in numerical macroscale models in case flexible bond has to be regarded.

Bond stress changes direction in the case of a reversed slip, i.e., the course of Fig. 2.12b can be mirrored for values $s, \tau < 0$. Monotonic loading with increasing slip was described up to now. Bond behavior in the case of unloading and reloading is discussed in [18, 6.1.1.4], [40].

A simpler, more convenient approach based on the concept of damage is as follows: begin with unloading from a point (s', τ') on a curve as given in Fig. 2.12b and the respective τ–s-relation goes through the origin on a straight line with reloading until a point $(-s', -\tau')$ is reached. The mirrored course is followed subsequently The application of the flexible bond is illustrated with the following Example 2.4. Basic ideas of damage are discussed in Section 5.6.

2.5 The Smeared Crack Model

Cracking, as has been discussed in Section 2.1, in its final stage of a macrocrack leads to a discontinuity of displacements regarding the crack surfaces. In the case of a uniaxial concrete tension bar the displacement field $u(x)$ has a jump at the place of a macrocrack. On the other hand, common finite elements as have been described in Section 1.3 do not allow for discontinuities in the displacement fields. The *smeared crack model* combines macrocracking and continuous displacement fields. This is discussed for the uniaxial two-node bar element, see Section 1.3 and includes not only the final macrocrack but also the foregoing tension softening process.

We consider the cracked element as a black box whose inner state cannot be inspected. The mean strain of such an element is assumed as

$$
\begin{aligned}
\epsilon &= \frac{1}{L_e} \left[(L_e - b_w) \, \epsilon_u + b_w \, \epsilon_c \right] \\
&= (1 - \xi) \, \epsilon_u + \xi \, \epsilon_c
\end{aligned}
\quad , \quad \xi = \frac{b_w}{L_e}
\tag{2.45}
$$

with the element length L_e and the strain ϵ_u of the uncracked material. For the crack band width b_w and the crack strain ϵ_c, see Section 2.1. The approach is illustrated in Fig. 2.13. The element length L_e results from a discretization while the crack band width b_w is assumed as the material constant. The ratio ξ is a constant for each element. A restriction $0 < \xi \leq 1$ is appropriate.
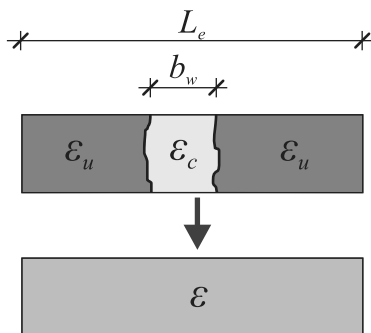
Figure 2.13: Smeared crack concept.

- A characteristic element length – corresponding to the element length L_e of uniaxial elements – should not be smaller than the crack band width for the smeared crack model.

$$b_w \le L_e \tag{2.46}$$

The strains ϵ_u, ϵ_c are still open. Thus, the smeared crack is connected with the concept of a cohesive crack, see Section 2.1. A typical relation for a uniaxial stress related to a crack strain is shown in Fig. 2.2b. A general form

$$\sigma = f_c(\epsilon_c) \tag{2.47}$$

is assumed. The key point is that this relation may be resolved for the crack strain

$$\epsilon_c = f_c^{-1}(\sigma) \tag{2.48}$$

On the other hand, a material law describes the relation between stress and strain in the uncracked material. A general form

$$\sigma = f_u(\epsilon_u) \tag{2.49}$$

is assumed. A corresponding compliance yields the material strain

$$\epsilon_u = f_u^{-1}(\sigma) \tag{2.50}$$

whereby the stress σ is the same for the uncracked material and within the crack band width due to equilibrium reasons. The combination of Eqs. (2.45, 2.48, 2.50) leads to

$$\epsilon = (1 - \xi) f_u^{-1}(\sigma) + \xi f_c^{-1}(\sigma) = d(\sigma) \tag{2.51}$$

with a compliance d for the smeared crack model. A further inversion leads to the stiffness

$$\sigma = d^{-1}(\epsilon) \tag{2.52}$$

of the crack band model.

Example 2.3 Simple uniaxial smeared crack model
A linear elastic law with the limited tensile strength is used for material behavior

$$\sigma = f_u(\epsilon_u) = E \, \epsilon_u \tag{2.53}$$

with Young's modulus E. Furthermore, a linear relation is used for the cohesive crack

$$\sigma = f_c(\epsilon_c) = \begin{cases} f_{ct} \left(1 - \dfrac{\epsilon_c - \epsilon_{ct}}{\epsilon_{cr} - \epsilon_{ct}} \right), & \epsilon_{ct} < \epsilon_c \le \epsilon_{cr} \\ 0, & \epsilon_{cr} < \epsilon_c \end{cases} \tag{2.54}$$

with $\epsilon_{ct} = f_{ct}/E$, the concrete tensile strength f_{ct} and the critical strain ϵ_{cr}. This critical strain is determined with $G_f = \frac{1}{2} b_w f_{ct}(\epsilon_{cr} - \epsilon_{ct})$ or $\epsilon_{cr} = 2 \, G_f/(b_w f_{ct}) + \epsilon_{ct}$ and recovers the

crack energy G_f, see Eq. (2.7). The strain range $\frac{f_{ct}}{E} < \epsilon \leq \epsilon_{cr}$ is regarded firstly. Resolving Eqs. (2.53, 2.54) for ϵ_u, ϵ_c leads to

$$\epsilon_u = \frac{\sigma}{E}, \qquad \epsilon_c = (\epsilon_{cr} - \epsilon_{ct})\left(1 - \frac{\sigma}{f_{ct}}\right) + \epsilon_{ct} \tag{2.55}$$

and using Eqs. (2.51, 2.52) to

$$\sigma = f_{ct}\,\frac{\xi\,\epsilon_{cr} - \epsilon}{\xi\,\epsilon_{cr} - \epsilon_{ct}}, \quad \epsilon_{ct} \leq \epsilon \leq \xi\,\epsilon_{cr} \tag{2.56}$$

This relation is limited in several ways.

  – $\xi = 1$: The crack fully occupies the element length and $\sigma = f_{ct}\,(\epsilon_{cr} - \epsilon)/(\epsilon_{cr} - \epsilon_{ct})$.

  – $\xi < 1$ and $\xi \to \epsilon_{ct}/\epsilon_{cr}$ makes σ infinite and gives a lower bound for ξ.

  – Neglecting crack energy with $G_f = 0$ leads to sudden stress drop to zero for $\epsilon > \epsilon_{ct}$.

Finally, $\sigma = 0$ for $\epsilon_c > \xi\,\epsilon_{cr}$.

————————————————————————————— End Example 2.3

A stress–strain relation like Eq. (2.56) blends or smears strains of uncracked parts and cracking strains into a unified continuous strain. Thus, common finite element interpolations, see Section 1.3, may still be used while regarding cracking of elements.

  • The smeared crack model leads to a modification of the material law of the uncracked material. Thus, it is applied to integration points within elements, which have a fixed position. But an exact crack position is not determined.

Furthermore, geometric characteristics of elements are introduced in the stress–strain relations. This particular feature makes the smeared crack model together with the cohesive crack suitable for regularization, see Section 5.9. The smeared crack model may be extended to two and three dimensions. This is demonstrated for the 2D case in Section 6.2.

2.6 The Reinforced Tension Bar

Basic components and mechanisms of reinforced concrete have been described up to now. Their interaction is demonstrated with the reinforced tension bar. The basic setup is shown in Fig.2.14a. A single reinforcement bar is embedded in a concrete bar. The left end of the rebar is fixed, while a displacement is prescribed for its right end. The conceptual model is also shown. It consists of a concrete part, a reinforcement part and a bond part. The basic scheme for a discretization is indicated together with the conceptual model.

The model is one-dimensional with a coordinate x and displacements u. The concrete part and the reinforcement part are discretized in the same way but each with its own nodes and elements. Concrete nodes and rebar nodes share the same x-position initially. They are connected by bond elements. The following properties are given for each part:
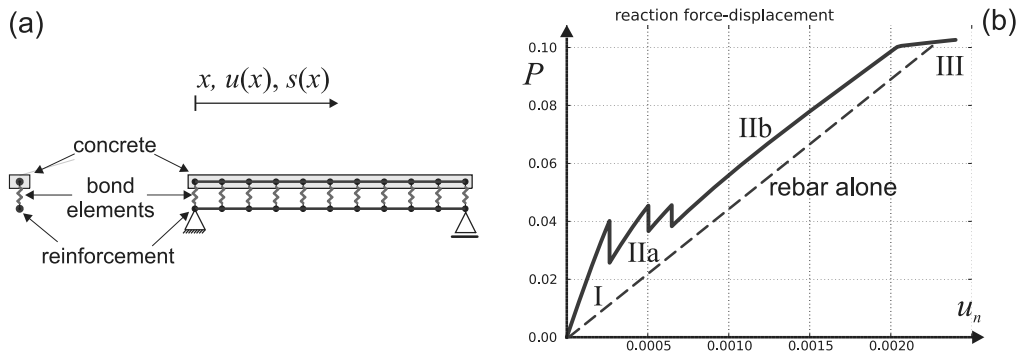
Figure 2.14: Example 2.4 (a) Geometry scheme of reinforced tension bar. (b) Force–displacement curve.

– A linear elastic behavior is assumed for the tensile behavior of concrete with a limited tensile strength f_{ct}

$$\sigma = \begin{cases} E_c\, \epsilon, & \epsilon \le \frac{f_{ct}}{E_c} \\ 0, & \text{else} \end{cases} \tag{2.57}$$

with a concrete Young's modulus E_c. The interpolation of displacements is performed with the two-node uniaxial bar element, see Section 1.3. This leads to a constant strain within an element.

– The rebar is modeled with the uniaxial elastoplastic material law with hardening, see Eqs. (2.39, 2.40). The interpolation of displacements is performed with the same elements as for the concrete part.

– The bond law is given by Fig. 2.12b and described in Section 2.4. It is characterized by the bond strength τ_{bmax}, the residual strength τ_{bf} and the corresponding slip values s_{bmax}, s_{bf}.

  The interpolation of the displacements is performed with the two-node spring element along a line, see Section 1.3. The variable Δu stands for the slip s and the variable F for the bond force flow T times element length L_e. Bond force flow is derived from the bond law by multiplying with a rebar circumference.

– The smeared crack model, see Section 2.4, is used for treating the cracking of concrete elements.

With determined element types – leading to forms for $\mathbf{N}$, $\mathbf{B}$, see Eqs. (1.18, 1.21) – and determined material behavior – leading to stresses $\boldsymbol{\sigma}$ and tangential material stiffness $\mathbf{C}_T$ – the numerical model may be built according to the procedure described in Section 1.5. Numerical integration is performed according to the one-dimensional variant of Eq. (1.68) with the integration order $n_i = 0$. The lowest order is sufficient due to constant strains and stresses within each element.

Most simple element types are used for the tension bar model to interpolate displacements and perform a discretization, respectively. A model complexity arises from the particular

material laws and the interaction of parts leading a nonlinear behavior. An incrementally iterative scheme has to be used for the solution, see Fig. 1.4. The application of the tension bar model is demonstrated with the following example.

Example 2.4 Reinforced concrete tension bar
The following geometric properties are chosen:

- Bar length $L = 1.0$ m, cross-sectional area of concrete $A_c = 0.1 \times 0.1\,\text{m}^2$, reinforcement $1 \oslash 16$ with cross-sectional area $A_s = 2.01\,\text{cm}^2$ and circumference $U_s = 5.02\,\text{cm}$.

- The concrete and the reinforcement part are each discretized with 100 bar elements with 101 nodes. This leads to 101 bond elements connecting concrete nodes and reinforcement nodes and 202 nodes totally and the same number of degrees of freedom.

- Bar element length is $L_e = 0.01$ m corresponding to a crack band width $b_w = 0.01$ m, see Eq. (2.46). This corresponds to a fine grained concrete and the crack energy G_f is neglected to simplify the calculation. As $b_w = L_e$ crack width of a cracked element is calculated by

$$w = L_e\,\epsilon \tag{2.58}$$

see Eq. (2.5) with $b_w = L_e$ and the crack strain ϵ_c corresponding to the element strain ϵ.

The chosen material properties are shown in Table 2.1. The corresponding equations for the material behavior are Eqs. (2.39, 2.40, 2.57). The bond law is derived from the characteristic values as a sequence of parabola, cubic polynomial, and horizontal line with the same slope in the connecting points. Bond strength is related to concrete tensile strength by the empirical relation $\tau_{\max} \approx 1.8\,f_{ct}$.

The loading of the tension bar is applied with prescribed displacement boundary conditions: Zero displacement for the left-hand reinforcement node, a prescribed displacement $u_N = 2.4$ mm for the reinforcement node on the right-hand incrementally applied in 100 steps during a loading time $0 \le t \le 1$. This leads to a final mean strain $\epsilon_{\text{mean}} = 2.4\text{‰}$.

Concrete		
Young's modulus E_c	MN/m^2	35 000
Tensile strength f_{ct}	MN/m^2	3.5
Reinforcing steel		
Young's modulus E_s	MN/m^2	200 000
Yield strength f_{sy}	MN/m^2	500
Bond		
Strength τ_{bmax}	MN/m^2	6.0
Slip at strength s_{bmax}	mm	0.1
Residual strength τ_{bf}	MN/m^2	3.0
Slip at residuum s_{bf}	mm	1.0

Table 2.1: Example 2.4 material parameters of RC tensile bar.

The *BFGS method*, see Appendix A, is used to determine a solution within a loading step, i.e., an increment of prescribed displacements, as the Newton–Raphson method fails due to discontinuities in the tangent stiffness.

The computed relation between reaction force and displacement is shown in Fig. 2.14b. The following states which are characteristic for reinforced concrete behavior can be seen:

– Uncracked state I with concrete stresses below tensile strength.

– Crack formation state IIa. Cracks develop in a sequence whereby each sudden reaction force decrease corresponds to a crack. The reaction force decrease results from a stiffness reduction of the bar due to cracking. A characteristic saw tooth pattern develops. This pattern is smoothed in case a crack energy is regarded for the smeared crack model, see Example 2.3.

– Stabilized cracking state IIb before rebar yielding. No new cracks occur while the bar's stiffness is significantly reduced compared to state I.

– Limit state III with rebar yielding. The slight increase in reaction forces results from rebar hardening. A numerical solution cannot be determined without the assumption of hardening as a singularity of the system's stiffness matrix would occur.

The stress distributions along the bar are shown in Figs. 2.15 and 2.16a for half-loading $t = 0.5$, $u_N = 1.2$ mm and for full loading $t = 1.0$, $u_N = 2.4$ mm.

– Concrete stresses are shown in Fig. 2.15a with zero stresses in a cracked element. Three cracks occur according to three peaks in the load–displacement curve, see Fig. 2.14b. Concrete tensile stresses for full loading are only slightly larger compared to full loading and remain below concrete tensile strength.

– Reinforcement stresses are shown in Fig. 2.15b with peak stresses at a crack and the characteristic garland pattern. Yielding of the reinforcement occurs in each cracked element for full loading with stresses slightly above the yield limit and high strains compared to all uncracked elements.
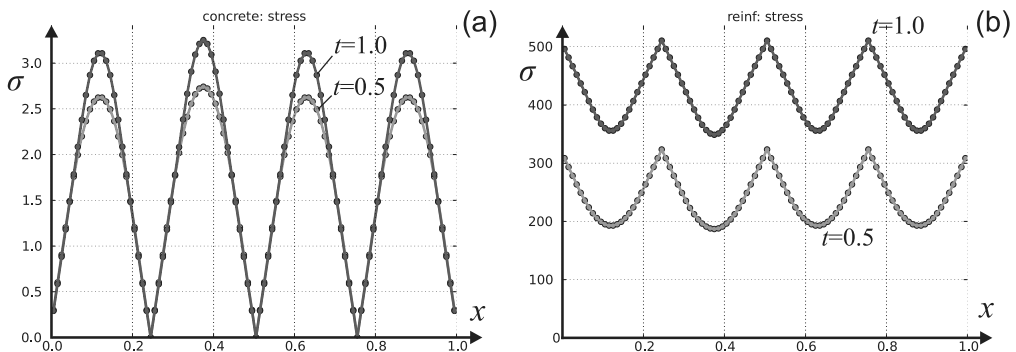
Figure 2.15: Example 2.4 (a) concrete stresses (b) rebar stresses.
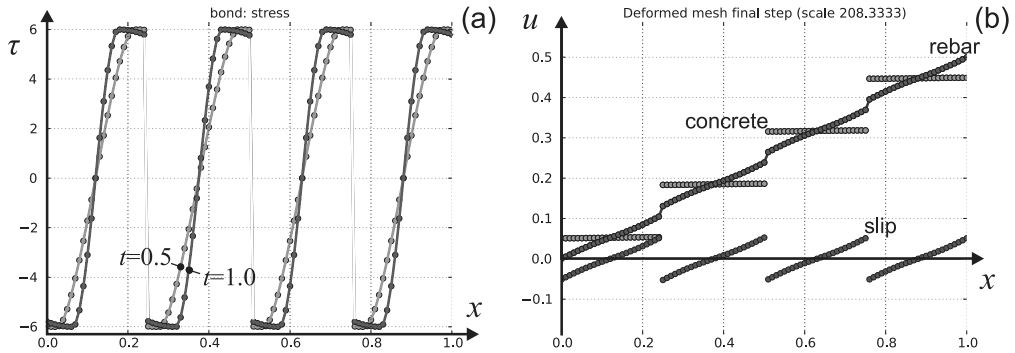
Figure 2.16: Example 2.4 (a) bond stresses (b) displacements.

– Bond stresses transfer forces among concrete and reinforcement between cracks, see Fig. 2.16a. Bond stresses have maximum absolute values near cracks and change sign across a crack. Bond strength is reached already after half loading. A more rectangular shape is given for full loading with a slight softening at cracks due to large slip and the prescribed bond law, see Fig. 2.12b.

Displacements u along the bar and the axis x are shown in Fig. 2.16b for all parts at full loading.

– Displacements of concrete elements and reinforcement elements are different due to the flexible bond. The difference of the values results in slip leading to bond stresses.

– Four nearly horizontal plateaus of concrete displacements arise with three cracks in between. The cracks jumps in concrete displacements correspond to the crack widths which are also given by the difference of the nodal displacements of a cracked element in accordance with Eq. (2.58). A typical value[2] is $w \approx 0.6\,\text{mm}$ for full loading with reinforcement yielding.

– Rebar displacements are given by an approximately straight line with small kinks at cracks. These kinks with increased displacement slope correspond to high strains for rebar elements corresponding to cracked concrete elements. These high rebar strains are related to the yielding of rebar elements.

End Example 2.4

The behavior of the model for reinforced concrete tension bar shows the typical characteristics of reinforced concrete behavior. It gives the base for the understanding of other structures like reinforced concrete beams and plates.

---

[2] y-value of Fig. 2.16b has to be divided by scale value. Dimension is [m].

2.7   Tension Stiffening of Reinforced Tension Bar

The tension bar has a lower limiting case with a rebar without concrete contributing to load bearing. The is indicated in Fig. 2.14b. The difference between the computed behavior and load bearing by the rebar alone indicates the tension stiffening effect.

- *Tension stiffening* results from the contribution of concrete between cracks to load bearing. This leads to a larger stiffness of a cracked reinforced concrete element compared to the corresponding rebar stiffness.

Tension stiffening will not increase the ultimate load of a reinforced tension bar, i.e., its ultimate load will be the same as for the corresponding rebar. An elaborated model has been derived in Section 2.6 to describe the contribution of concrete between cracks. This contribution leads to concrete tensile stresses below tensile strength and to reduced reinforcement stresses between cracks, see Fig. 2.15.

A simplified model to quantify tension stiffening can be derived based on the concept of mean stresses between cracks. It is assumed that the reinforcement has not yet reached its yield strength and that rebar strains have the same shape as rebar stresses. Thus, the *end* displacement of a tension bar can be determined from a mean rebar strain ϵ_{sm} multiplied by the bar length L. The bar force is ruled by the peak stresses σ_{sc} of the rebar at a crack – concrete does not contribute here by definition – multiplied by the rebar cross-sectional area A_s. Thus, the load–displacement behavior is determined by a relation deriving σ_{sc} from ϵ_{sm} independent from the particular geometric properties L, A_s. But some minimum length of a structural element is required to make such a relation applicable which is basically the crack distance or a small multiple of it, respectively.

A key to quantify a relation σ_{sc} and ϵ_{sm} is to consider the characteristics of stresses in crack situations. This is illustrated in Fig. 2.17a which gives a schematic cutout and aggregation of Fig. 2.15. The mean value of reinforcement strain between cracks may be estimated with

$$\epsilon_{sm} = \frac{1}{E_s} \left(\sigma_{sc} - \beta_t \, \Delta\sigma_s \right) \tag{2.59}$$

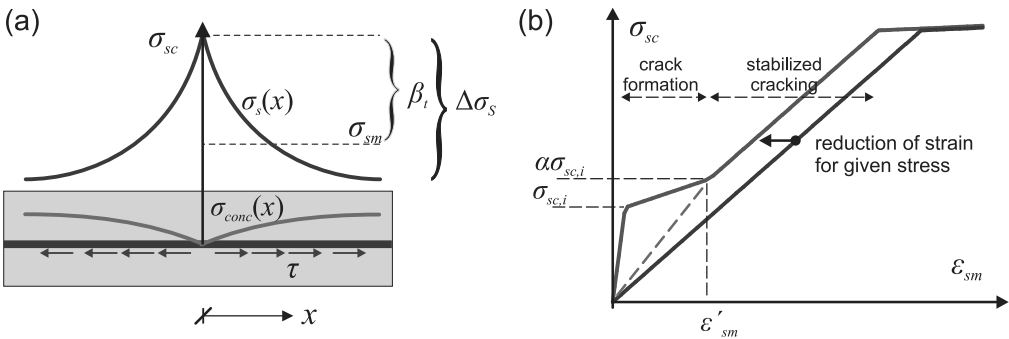Figure 2.17: (a) Cracks and stresses. (b) Tension stiffening model.

with reinforcement Young's modulus E_s, reinforcement stress decline $\Delta\sigma_s$ from crack to minimum value between cracks and a parameter $0 < \beta_t < 1$ for the shape of reinforcement stress distribution.

- The value of β_t characterizes the quality of bond. A value $\beta_t = 0$ indicates no stress transfer from rebar to concrete, i.e., no bond effective, a value $\beta_t = 1$ indicates immediate stress transfer from rebar to concrete, i.e., a *perfect bond* with no slip between concrete and rebar.

Values are assumed in the range $0.4 \leq \beta_t \leq 0.6$. The validity of such a range is determined by computations as shown in Example 2.4, even more sophisticated models and especially pure observation or phenomenology, respectively. Code provisions are also given for the choice of β_t, see for k_t in [26, 7.3.4] and for β in [18, 7.6.4.4]. This value will be assumed as given in the following.

A further parameter arises with the stress decline parameter $\Delta\sigma_s$. Two states of cracking have to be distinguished to derive an estimation for this parameter, *stabilized cracking* and the *crack formation*. Cracks occur one after the other during loading and not simultaneously. But all cracks generally occur within a relatively small band of deformations and an even smaller band of the corresponding forces or stresses, respectively. This is also indicated in Fig. 2.14b. The passage through these bands is connected with a formation of cracks and ends with stabilized cracking. Basically, no further cracks arise if cracking is stabilized.

The following relation is assumed for reinforcement stress decline in the case of *stabilized cracking*:

$$A_s \, \Delta\sigma_s = A_{c,\text{eff}} \, f_{ct} \tag{2.60}$$

with the effective concrete cross-sectional area $A_{c,\text{eff}}$. This value is smaller than a concrete cross-sectional area A_c as not all parts of a larger concrete cross section take part in the exchange of stresses with the reinforcement. Code provisions are given for the choice of $A_{c,\text{eff}}$ [26, 7.3.2]. Equation (2.60) leads to

$$\Delta\sigma_s = \frac{f_{ct}}{\varrho_{\text{eff}}} \tag{2.61}$$

with the effective reinforcement ratio $\varrho_{\text{eff}} = A_s / A_{c,\text{eff}}$. Combining Eqs. (2.59, 2.61) the relation for the reinforcement stress in cracks depending on the mean reinforcement strain is given by

$$\sigma_{sc} = E_s \, \epsilon_{sm} + \beta_t \, \frac{f_{ct}}{\varrho_{\text{eff}}} \tag{2.62}$$

for stabilized cracking. This corresponds to a shift of the pure rebar stiffness to the left, see Fig. 2.17b, i.e., a given mean strain has a higher stress with tension stiffening. This is limited by the yielding plateau of the reinforcement.

The corresponding relation for *crack formation* has two limiting points within a load–displacement relation or a rebar stress–mean strain relation, respectively. The first point is the point of the first crack, and the second point is the initial point of stabilized cracking, see Fig. 2.14b. The first point has a stress $f_{ct}/\varrho_{\text{eff}}$ and a strain f_{ct}/E_c with Young's modulus E_c of concrete. The following assumption is made for crack formation starting with the first limiting point:

$$\sigma_{sc} = k \left(\epsilon_{sm} - \frac{f_{ct}}{E_c} \right) + \frac{f_{ct}}{\varrho_{\text{eff}}}, \quad \epsilon_{sm} \geq \frac{f_{ct}}{E_c} \tag{2.63}$$

with a slope k which still has to be determined. This line should meet relation (2.62) at a stress $\alpha\sigma_{sc,i}$. leading to

$$k = E_c \frac{\alpha - 1}{\alpha - \beta_t - n\,\varrho_{\text{eff}}}, \quad n = \frac{E_s}{E_c} \tag{2.64}$$

The coefficient α marks the final stress point of crack formation or the initial stress point of stabilized cracking, i.e., the increase factor of the reinforcement stress during crack formation. Parameter studies and experimental data show that a value around $\alpha \approx 1.3$ is appropriate. The strain ϵ'_{sm} belonging to this stress value can be determined with Eq. (2.62) and $\sigma_{sc} = \alpha\,\sigma_{sc,i}$ leading to

$$\epsilon'_{sm} = \frac{1}{E_s}\frac{f_{ct}}{\varrho_{\text{eff}}}(\alpha - \beta_t) \tag{2.65}$$

A more simplified version might straighten the initial kink, see Fig. 2.17b, with

$$\sigma_{sc} = \frac{\alpha f_{ct}}{\varrho_{\text{eff}}\epsilon'_{sm}}\;\epsilon_{sm} \tag{2.66}$$

in the initial range up to the beginning of stabilized cracking. Further reference for tension stiffening and its comprehension into analysis are given in [7], [12], [18, 7.6.5.2, 7.6.7.2], [27]. In the following chapter, tension stiffening will be included as an option for reinforced concrete beams, see Section 3.5.3.

Chapter 3

Structural Beams and Frames

3.1 Cross-Sectional Behavior

3.1.1 Kinematics

Kinematic assumptions characterize the different types of models for structures thereby ensuring kinematic compatibility. Different types of such assumptions have already been discussed for bar, spring, and continuum elements in Section 1.3. Kinematic assumptions for beams need more elaboration but form the base for the powerful structural beam theory. Plane beams will be considered in the following which are straight in their undeformed configuration. Small displacements are assumed if not otherwise stated.

A *beam* first of all is characterized by a longitudinal direction with a *reference axis* and a longitudinal coordinate x. Every reference coordinate x has a cross section with a transverse height coordinate z, see Fig. 3.1. Every height coordinate z has a width which may be variable. Height and width form a *cross section* which is perpendicular to the reference axis in the undeformed configuration. It is *not* necessary to assume that the reference axis goes through the center of area of cross sections.
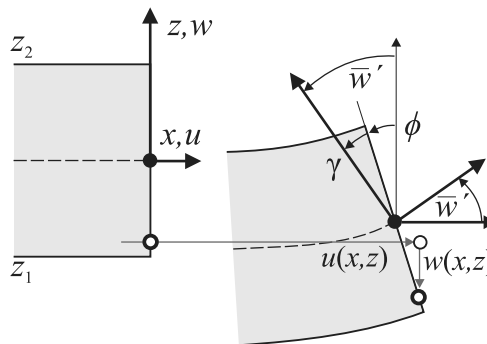
Figure 3.1: Kinematics of plane beam.

A *kinematic assumption* restrains the mathematical description of displacements:

- The *Bernoulli–Navier hypothesis* states that undeformed plane cross sections of a beam remain plane during a deformation.

Deformations are connected to displacements. The displacements of every material point of a beam with the coordinates x, z are given by the longitudinal displacement $u(x, z)$ in the x-direction and with the lateral displacement $w(x, z)$ in the z-direction. The Bernoulli hypothesis is included in the following formulation:

$$
\begin{aligned}
w(x, z) &= & w(x, 0) \\
&= & \bar{w}(x) \\
u(x, z) &= & \bar{u}(x) - z\,\phi(x) \\
&= \bar{u}(x) - z & \left[\frac{\partial \bar{w}(x)}{\partial x} - \gamma(x) \right]
\end{aligned}
\tag{3.1}
$$

with a *cross-sectional rotation angle* $\phi(x)$, a *shear angle* $\gamma(x)$, and a *longitudinal* $\bar{u}(x)$ and lateral displacement $\bar{w}(x)$ of the reference axis.

- Equation $(3.1)_1$ states that every material point in a cross section has the same lateral displacement but it may change with the longitudinal coordinate.

- Equation $(3.1)_3$ states that a cross section rotates by an angle ϕ during deformation.

- Equation $(3.1)_4$ decouples the rotation of the cross section ϕ and the slope of the reference axis $\partial \bar{w}/\partial x$ by the angle γ. The relation is

$$
\phi = \frac{\partial \bar{w}}{\partial x} - \gamma
\tag{3.2}
$$

The connection of γ with shear becomes evident with its relation to the shear strain, see Eq. $(3.3)_3$.

- The case $\gamma \ll \phi$ with the assumption $\gamma = 0$ leads to the *Bernoulli beam* where cross sections remain rectangular to the reference axis after deformation. The inclusion of shear deformation leads to the *Timoshenko beam*. Cross sections remain plane but are not rectangular to the reference axis after deformation for the Timoshenko beam.

The Timoshenko beam theory is more general. It will be treated in the following and the Bernoulli beam will be derived as a special case if appropriate.

Beam kinematics may be considered as restrained kinematics of plate kinematics, see Section 1.3. Thus, strains are defined according to Eq. (1.39) with y, v replaced by z, w. This leads to

$$
\begin{aligned}
\epsilon_x(x, z) &= & \frac{\partial u}{\partial x} &= \frac{\partial \bar{u}}{\partial x} - z \left[\frac{\partial^2 \bar{w}}{\partial x^2} - \frac{\partial \gamma}{\partial x} \right] \\
\epsilon_z(x, z) &= & 0 \\
\gamma_{xz}(x, z) &= & \frac{\partial u}{\partial z} + \frac{\partial w}{\partial x} &= -\frac{\partial \bar{w}}{\partial x} + \gamma + \frac{\partial \bar{w}}{\partial x} = \gamma
\end{aligned}
\tag{3.3}
$$

regarding Eq. (3.1). A notation $\partial \bullet /\partial x = \bullet'$, $\partial^2 \bullet /\partial x^2 = \bullet''$ is used in the following for abbreviation. Furthermore, the overbars on $\bar{u}, \bar{w}$ will be omitted in the following. To simplify the notation, u, w will be written instead. It is appropriate to introduce the variables

$$\epsilon(x) = u', \quad \kappa(x) = \phi' \tag{3.4}$$

and $\phi' = w'' - \gamma'$. The variable ϵ has the meaning of the strain of the reference axis in the context of beams while ϵ_x indicates the longitudinal strain in a cross section varying with z. With Eq. (3.3) this leads to longitudinal strains

$$\epsilon_x(x, z) = \epsilon(x) - z\,\kappa(x) \tag{3.5}$$

linearly varying along the beam height with extreme values on the top and bottom of the cross section.

- The variables ϵ, κ, γ are chosen as generalized strains for beams whereby ϵ indicates the longitudinal strain of the reference axis, κ the curvature of deformed cross sections and γ the shearing angle of deformed cross sections relative to the reference axis.

The curvature $\kappa = \phi'$ is different compared to the second derivative w'' of the lateral displacement w of the reference axis. Both are related by Eq. (3.4).

To describe material behavior, deformation variables have to be connected to force variables which are moment M, normal force N and shear force V in the case of plane beams. The following dependences are assumed

$$M = M(\epsilon, \kappa), \quad N = N(\epsilon, \kappa), \quad V = V(\gamma) \tag{3.6}$$

Basics of beam theory look conclusive but there are some inconsistencies:

- A shear strain γ_{xz}, which is constant over the cross section leads to nonvanishing shear stress at the lower and upper side of a beam. But this contradicts the local equilibrium conditions.

- On the other hand, a parabolic or other nonlinear course of shear stresses according to equilibrium conditions with linear normal stresses leads to a curved course of shear strains with vanishing values on top and bottom sides.

These contradictions can be resolved with the plate theory. Plane beam theory is its limiting case or a very useful approximation, respectively.

3.1.2 Linear Elastic Behavior

As longitudinal strains are given by Eq. (3.5) and shear strains by Eq. $(3.3)_3$ depending on generalized strains corresponding stresses may be determined with a material law. We start with linear elastic behavior; see Section 1.4 and refer to isotropic plane stress Eq. (1.45). The coordinate direction y has to be replaced by z according to beam conventions.

- In addition to the kinematic assumptions, Poisson's effect has to be neglected for beams with Poisson's ratio assumed as $\nu = 0$.

Thus, combining Eqs. (1.45, 3.3, 3.5) yields stresses

$$
\begin{aligned}
\sigma_x &= E\,\epsilon_x &&= E\,[\epsilon(x) - z\,\kappa(x)] \\
\sigma_z &= E\,\epsilon_z &&= 0 \\
\sigma_{xz} &= G\,\gamma_{xz} &&= G\,\gamma
\end{aligned}
\tag{3.7}
$$

with Young's modulus E and the *beam's shear modulus*

$$
G = \frac{1}{2}\,E
\tag{3.8}
$$

Internal forces of a beam are derived by the integration of stresses in a cross section leading to the normal force N, the bending moment M, and the shear force V

$$
\begin{aligned}
N &= \int_{z_1}^{z_2} \sigma_x\,b\mathrm{d}z &&= E \int_{z_1}^{z_2} b\mathrm{d}z\ \epsilon - E \int_{z_1}^{z_2} z\,b\mathrm{d}z\ \kappa \\
M &= -\int_{z_1}^{z_2} \sigma_x\,z\,b\mathrm{d}z &&= -E \int_{z_1}^{z_2} z\,b\mathrm{d}z\ \epsilon + E \int_{z_1}^{z_2} z^2\,b\mathrm{d}z\ \kappa \\
V &= \int_{z_1}^{z_2} \sigma_{xz}\,b\mathrm{d}z &&= G \int_{z_1}^{z_2} \gamma_{xz}\,b\mathrm{d}z = \alpha\,G \int_{z_1}^{z_2} b\mathrm{d}z\ \gamma
\end{aligned}
\tag{3.9}
$$

with the coordinate z_1 of the cross-section bottom line, the coordinate z_2 of the top line, the cross-section height

$$
h = z_2 - z_1
\tag{3.10}
$$

and the cross-section width b.

A shear correction factor α is introduced for the shear force V to compensate for the difference between mean shearing strain/stress over the cross section – see concluding remarks of Section 3.1.1 – and the shearing strain/stress γ, $G\gamma$ in the reference point $z = 0$ [36]. It is $\alpha = 5/6$ in the case of a rectangular cross-section shape with a reference axis through the center of area.

Evaluation of integrals in Eq. (3.9) leads to section properties with cross-sectional area A, sectional modulus S and second moment of area J

$$
A = \int_{z_1}^{z_2} b\mathrm{d}z, \quad S = \int_{z_1}^{z_2} z\,b\mathrm{d}z, \quad J = \int_{z_1}^{z_2} z^2\,b\mathrm{d}z
\tag{3.11}
$$

In case that the reference axis x coincides with the center of area

$$
S = \int_{z_1}^{z_2} z\,b\mathrm{d}z = 0
\tag{3.12}
$$

which formally simplifies the linear elastic case but is not mandatory. Finally, the linear elastic case with $S = 0$ yields the well-known relations

$$
N = EA\,\epsilon, \quad M = EJ\,\kappa, \quad V = \alpha\,GA\,\gamma
\tag{3.13}
$$

The sign of the moment is different compared to classical structural beam theory. The difference results from a different orientation of the z-axis, see Fig. 3.1. According to Eq. (1.47) these relations are collected in

$$
\boldsymbol{\sigma} = \mathbf{C} \cdot \boldsymbol{\epsilon}
\tag{3.14}
$$

with

$$\boldsymbol{\sigma} = \begin{pmatrix} N \\ M \\ V \end{pmatrix}, \qquad \mathbf{C} = \begin{bmatrix} EA & 0 & 0 \\ 0 & EJ & 0 \\ 0 & 0 & \alpha\,GA \end{bmatrix}, \qquad \boldsymbol{\epsilon} = \begin{pmatrix} \epsilon \\ \kappa \\ \gamma \end{pmatrix} \tag{3.15}$$

with the generalized stresses, generalized strains, and a material stiffness $\mathbf{C}$. Tangential material stiffness $\mathbf{C}_T$, see Eq. (1.50), is identical to $\mathbf{C}$ for linear materials. The subset

$$\boldsymbol{\sigma} = \begin{pmatrix} N \\ M \end{pmatrix}, \qquad \mathbf{C} = \begin{bmatrix} EA & 0 \\ 0 & EJ \end{bmatrix}, \qquad \boldsymbol{\epsilon} = \begin{pmatrix} \epsilon \\ \kappa \end{pmatrix} \tag{3.16}$$

is applied for the Bernoulli beam.

3.1.3 Cracked Reinforced Concrete Behavior

3.1.3.1 Compressive Zone and Internal Forces

Linear elasticity assumes unlimited strength of materials, both for compression and tension. This assumption is not valid for reinforced concrete (RC), in particular for the very limited tensile strength of concrete. Thus, cracked concrete cross sections have to be regarded in which longitudinal beam strains ϵ_x exceed the tensile limit strain ϵ_{ct} of concrete. Section properties as have been defined by Eq. (3.11) and also the notion of a center of area loose their immediate applicability. Nevertheless, the position of cross sections relative to the reference axis has to be defined.

- The reference axis is placed in the lateral center of a cross section irrespective of the shape of the cross section. The bottom side has the coordinate $z = z_1 = -h/2$ and the top side has the coordinate $z = z_2 = h/2$ with a cross-section height h.

The strain $\epsilon_x = \epsilon_1$ at the bottom side and that $\epsilon_x = \epsilon_2$ on the top side are given by

$$\epsilon_1 = \epsilon - z_1\,\kappa = \epsilon + \frac{h}{2}\,\kappa, \qquad \epsilon_2 = \epsilon - z_2\,\kappa = \epsilon - \frac{h}{2}\,\kappa \tag{3.17}$$

with Eq. (3.5). This leads to a relation for the curvature

$$\kappa = \frac{\epsilon_1 - \epsilon_2}{h}, \quad h = z_2 - z_1 \tag{3.18}$$

Correct signs for strains have to be considered, e.g., $\epsilon_1 > 0$, $\epsilon_2 < 0$ in bending with compression on the top side. The lateral coordinate of a line with a given strain $\epsilon_x = \epsilon'_x$ is also determined by Eq. (3.5)

$$z' = \frac{\epsilon - \epsilon'_x}{\kappa} \tag{3.19}$$

with the strain ϵ of the reference axis. The line with zero strains or *zero line* is determined as a special case with $\epsilon'_x = 0$ and

$$z_0 = \frac{\epsilon}{\kappa} \tag{3.20}$$

The vertical z-coordinates of the concrete's tensile limit strain ϵ_{ct} or compressive limit strain ϵ_{cu1} are be determined in a similar way. A value $\epsilon_{ct} = 0$ with an exclusion of concrete tensile stresses is assumed in the following. This assumption is not mandatory but simplifies the discussion.

- The contribution of concrete to cross-sectional behavior is determined through the *compression zone*. Its extent is determined by the position of the zero line.

Edge strains according to Eq. (3.17) and the position of the zero line according to Eq. (3.20) allow a classification

$z_0 < -h/2$ and $\epsilon_1 < 0$	cross section totally under compression
$z_0 < -h/2$ and $\epsilon_1 \geq 0$	totally under tension
$-h/2 \leq z_0 \leq h/2$ and $\epsilon_2 < 0$	upper bending compressive zone
$-h/2 \leq z_0 \leq h/2$ and $\epsilon_1 < 0$	lower bending compressive zone
$z_0 > h/2$ and $\epsilon_2 < 0$	totally under compression
$z_0 > h/2$ and $\epsilon_2 \geq 0$	totally under tension

A precise localization is given by the lower and upper compression zone coordinates z_{c1}, z_{c2}:

cross section totally under compression	$z_{c1} = z_1,\ z_{c2} = z_2$
totally under tension	no concrete contribution
upper bending compressive zone	$z_{c1} = z_0,\ z_{c2} = z_2$
lower bending compressive zone	$z_{c1} = z_1,\ z_{c2} = z_0$

with cross-section bottom and top coordinates z_1, z_2. This approach may be easily extended to consider a concrete's restricted compressive limit strain ϵ_{cu1} or an tensile limit strain ϵ_{ct} larger than zero through Eq. (3.19) with $\epsilon'_x = \epsilon_{ct}$ and/or $\epsilon'_x = \epsilon_{cu1}$.

Cross-section strain values $\epsilon_x > \epsilon_{ct}$ have to be considered regarding integrated cross-sectional behavior, e.g., for the inclusion of a reinforcement as shown in Fig. 3.2. A lower rebar has a coordinate $z_{s1} = -h/2 + d_1$ and a upper rebar has a coordinate $z_{s2} = h/2 - d_2$ where d_1, d_2 give the edge distances. Equation (3.5) leads to rebar strains

$$\epsilon_{s1} = \epsilon - \left(\frac{h}{2} - d_1\right)\kappa, \qquad \epsilon_{s2} = \epsilon + \left(\frac{h}{2} - d_2\right)\kappa \tag{3.21}$$

This approach is not restricted to an upper and a lower reinforcement but may be extended to an arbitrary number of rebar layers.
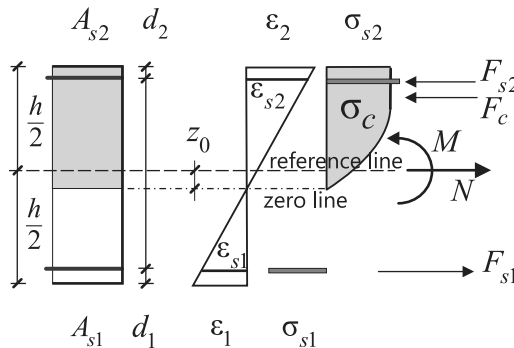
Figure 3.2: Reinforced-concrete cross section.

The strain of rebars with tension and the concrete strain within the compression zone share the same straight line according to the linear strain distribution following from Eq. (3.5). This implies perfect bond with disregarded slip between concrete and reinforcement in contrast to flexible bond, see also Sections 2.4 and 2.7.

- The extent of the compression zone, the concrete strains within it and the reinforcement strains are completely determined by the generalized beam strains ϵ and κ as has been shown in the preceding discussion.

With longitudinal strains given the concrete stresses are determined by, e.g., Eqs. (2.1, 2.3) and rebar stresses by Eq. (2.39). The corresponding internal forces are determined similar to Eq. (3.9) with a normal force

$$N = A_{s1}\,\sigma_{s1} + A_{s2}\,\sigma_{s2} + \int_{z_{c1}}^{z_{c2}} \sigma_c\,b\mathrm{d}z \qquad (3.22)$$

and a moment

$$M = -A_{s1}\sigma_{s1}\,z_{s1} - A_{s2}\sigma_{s2}\,z_{s2} - \int_{z_{c1}}^{z_{c2}} \sigma_c\,z\,b\mathrm{d}z \qquad (3.23)$$

The sign conventions follow the conventions of Fig. 3.2. Stresses in all cases have to be signed as positive for tension and negative for compression. The integration limits z_{c1}, z_{c2} may be variable due to the variable values of ϵ, κ.

- An analytical evaluation of integrals in Eqs. (3.22, 3.23) is generally not possible. A numerical integration has to be used instead.

As the course of concrete stresses is smooth, a simple integration scheme like the trapezoidal rule [54] with an interval number of the order of 10 is sufficient in most cases. A variable cross-section width $b(z)$ is easily regarded within a numerical integration scheme.

A relation between shear force V and shear angle γ cannot be derived within the isolated scope of a cracked cross section indicated by Fig. 3.2. An approach based on the truss model for shear is described in Section 3.5.4.

3.1.3.2 Linear Concrete Compressive Behavior with Reinforcement

Equations (3.22, 3.23) leading to internal forces are still open for various forms of uniaxial stress–strain relations. A linear relation may be assumed for concrete under compression

$$\sigma_c = E'_c\,\epsilon_x, \quad E'_c = \begin{cases} E_c & \epsilon_x \leq 0 \\ 0 & \text{else} \end{cases} \qquad (3.24)$$

while excluding tensile strength. Exclusion of tensile strength is a first distinctive feature compared to the linear elastic approach (Eq. (3.7)). The assumption of linear compressive is appropriate for moderate stress levels up to roughly 60% of the strength. Corresponding states of loading are investigated in the context of serviceability of structures, e.g., for the calculation of deformations.

A cross section with height h and width b is considered. The width may basically be variable along the cross section. With the given generalized beam strains ϵ, κ, a compressive

zone is determined, see Section 3.1.3.1. The compressive zone has an extension $z_{c1} \leq z \leq z_{c2}$ with a height $h_c = z_{c2} - z_{c1}$ and edge strains

$$\epsilon_{ce} = \mathbf{B}_\epsilon \cdot \boldsymbol{\epsilon} \tag{3.25}$$

with

$$\boldsymbol{\epsilon}_{ce} = \begin{pmatrix} \epsilon_{c1} \\ \epsilon_{c2} \end{pmatrix}, \quad \mathbf{B}_\epsilon = \begin{bmatrix} 1 & -z_{c1} \\ 1 & -z_{c2} \end{bmatrix}, \quad \boldsymbol{\epsilon} = \begin{pmatrix} \epsilon \\ \kappa \end{pmatrix} \tag{3.26}$$

This leads to edge stresses

$$\boldsymbol{\sigma}_{ce} = \begin{pmatrix} \sigma_{c1} \\ \sigma_{c2} \end{pmatrix} = E_c' \, \boldsymbol{\epsilon}_{ce} = E_c' \, \mathbf{B}_\epsilon \cdot \boldsymbol{\epsilon}, \tag{3.27}$$

In the range $z_{c1} \leq z \leq z_{c2}$ concrete stresses are linearly interpolated with

$$\sigma_c(z) = \frac{\sigma_{c1} z_{c2} - \sigma_{c2} z_{c1}}{z_{c2} - z_{c1}} + \frac{\sigma_{c2} - \sigma_{c1}}{z_{c2} - z_{c1}} \, z \tag{3.28}$$

Thus, concrete contributions to internal forces are given by

$$
\begin{aligned}
N_c &= \int_{z_{c1}}^{z_{c2}} \sigma_c(z)\, b\mathrm{d}z &&= \frac{\sigma_{c1} z_{c2} - \sigma_{c2} z_{c1}}{h_c} A_c - \frac{\sigma_{c1} - \sigma_{c2}}{h_c} S_c \\
M_c &= -\int_{z_{c1}}^{z_{c2}} \sigma_c(z) z \, b\mathrm{d}z &&= -\frac{\sigma_{c1} z_{c2} - \sigma_{c2} z_{c1}}{h_c} S_c + \frac{\sigma_{c1} - \sigma_{c2}}{h_c} J_c
\end{aligned}
\tag{3.29}
$$

see also Eq. (3.9), with cross-sectional values

$$A_c = \int_{z_{c1}}^{z_{c2}} b\mathrm{d}z, \qquad S_c = \int_{z_{c1}}^{z_{c2}} z \, b\mathrm{d}z, \qquad J_c = \int_{z_{c1}}^{z_{c2}} z^2 \, b\mathrm{d}z \tag{3.30}$$

A matrix notation of Eq. (3.29) is given by

$$\boldsymbol{\sigma}_c = \mathbf{A}_\sigma \cdot \boldsymbol{\sigma}_{ce} \tag{3.31}$$

with

$$\boldsymbol{\sigma}_c = \begin{pmatrix} N_c \\ M_c \end{pmatrix}, \quad \mathbf{A}_\sigma = \frac{1}{h_c} \begin{bmatrix} z_{c2} A_c - S_c & -z_{c1} A_c + S_c \\ -z_{c2} S_c + J_c & z_{c1} S_c - J_c \end{bmatrix}, \tag{3.32}$$

whereby $\boldsymbol{\sigma}_c$ and $\boldsymbol{\sigma}_{ce}$ have to be clearly distinguished: $\boldsymbol{\sigma}_c$ is the vector of internal forces and $\boldsymbol{\sigma}_{ce}$ the vector of edge stresses. The matrix $\mathbf{A}_\sigma$ is decomposed through

$$\mathbf{A}_\sigma = \mathbf{A} \cdot \mathbf{B}_\sigma, \quad \mathbf{A} = \begin{bmatrix} A_c & -S_c \\ -S_c & J_c \end{bmatrix}, \quad \mathbf{B}_\sigma = \frac{1}{h_c} \begin{bmatrix} z_{c2} & -z_{c1} \\ 1 & -1 \end{bmatrix} \tag{3.33}$$

The combination of Eqs. (3.27, 3.31) leads to

$$\boldsymbol{\sigma}_c = \mathbf{C}_c \cdot \boldsymbol{\epsilon} \tag{3.34}$$

with

$$
\begin{aligned}
\mathbf{C}_c &= E_c' \, \mathbf{A}_\sigma \cdot \mathbf{B}_\epsilon \\
&= E_c' \, \mathbf{A} \cdot \mathbf{B}_\sigma \cdot \mathbf{B}_\epsilon \\
&= E_c' \, \mathbf{A}
\end{aligned}
\tag{3.35}
$$

as $\mathbf{B}_\sigma \cdot \mathbf{B}_\epsilon = \mathbf{I}$ with the unit matrix $\mathbf{I}$. The matrix $\mathbf{C}_c$ is the material stiffness regarding the compression zone only. It is similar to to Eq. (3.16), but Eq. (3.34) couples normal force N_c as well as moment M_c each to both ϵ and κ.

- Beneath having a coupling effect the material stiffness of a cracked concrete cross section is nonlinear as the extent of the compression zone depends on the generalized beam strains ϵ, κ.

In the case of rectangular cross sections with the constant width b the cross-sectional values are evaluated to $A_c = b(z_{c2} - z_{c1})$, $S_c = \frac{b}{2}(z_{c2}^2 - z_{c1}^2)$, $J_c = \frac{b}{3}(z_{c2}^3 - z_{c1}^3)$, and in the case of $z_{c1} = -h/2$, $z_{c2} = h/2$ to $A_c = bh$, $S_c = 0$, $J_c = bh^3/12$.

The *incremental form* of Eq. (3.34) with a tangential stiffness $\mathbf{C}_{cT}$ is derived in the following. As $\boldsymbol{\sigma}_c$ is a function of edge stresses σ_{c1}, σ_{c2}, see Eq. (3.29), its rate may be written as

$$\begin{pmatrix} \dot{N}_c \\ \dot{M}_c \end{pmatrix} = \begin{bmatrix} \frac{\partial N_c}{\partial \sigma_{c1}} & \frac{\partial N_c}{\partial \sigma_{c2}} \\ \frac{\partial M_c}{\partial \sigma_{c1}} & \frac{\partial M_c}{\partial \sigma_{c2}} \end{bmatrix} \cdot \begin{pmatrix} \dot{\sigma}_{c1} \\ \dot{\sigma}_{c2} \end{pmatrix} + \begin{bmatrix} \frac{\partial N_c}{\partial z_{c1}} & \frac{\partial N_c}{\partial z_{c2}} \\ \frac{\partial M_c}{\partial z_{c1}} & \frac{\partial M_c}{\partial z_{c2}} \end{bmatrix} \cdot \begin{pmatrix} \dot{z}_{c1} \\ \dot{z}_{c2} \end{pmatrix} \tag{3.36}$$

or

$$\dot{\boldsymbol{\sigma}}_c = \mathbf{A}_\sigma \cdot \dot{\boldsymbol{\sigma}}_{ce} + \mathbf{A}_z \cdot \dot{\mathbf{z}}_c \tag{3.37}$$

with $\mathbf{A}_\sigma$ according to Eqs. (3.31, 3.32). The second term $\mathbf{A}_z \cdot \dot{\mathbf{z}}_c$ considers the change of integration borders. To simplify $\mathbf{A}_z$ a linear variation of width b is assumed with $b_1 = b(z_{c1}), b_2 = b(z_{c2})$. This yields

$$\mathbf{A}_z = \frac{1}{6} \begin{bmatrix} -\sigma_{c1}b_2 - 2\sigma_{c1}b_1 - 2\sigma_{c2}b_2 - \sigma_{c2}b_1 & \sigma_{c1}b_2 + 2\sigma_{c1}b_1 + 2\sigma_{c2}b_2 + \sigma_{c2}b_1 \\ (b_2z_{c1} + z_{c2}b_2 + z_{c1}b_1)\sigma_{c2}+ & (b_2z_{c1} - 3z_{c2}b_2 - z_{c2}b_1)\sigma_{c2}- \\ (b_2z_{c1} - z_{c2}b_1 + 3z_{c1}b_1)\sigma_{c1} & (z_{c1}b_1 + z_{c2}b_2 + z_{c2}b_1)\sigma_{c1} \end{bmatrix} \tag{3.38}$$

The variables z_{c1}, z_{c2} stand for lower or upper edges of the concrete compression zone. This may include the zero line determined by

$$z_0 = \frac{\epsilon}{\kappa}, \quad \dot{z}_0 = \frac{\dot{\epsilon}}{\kappa} - \frac{\epsilon}{\kappa^2}\dot{\kappa} \tag{3.39}$$

see Eq. (3.20). The following cases have to be considered:

1. Dominating bending with lower compression zone $z_{c1} = -h/2$, $z_{c2} = z_0 < h/2$ and $\dot{z}_{c1} = 0, \sigma_{c2} = 0, \dot{\sigma}_{c2} = 0$ and

$$\begin{pmatrix} z_{c1} \\ z_{c2} \end{pmatrix} = \begin{pmatrix} -\frac{h}{2} \\ \frac{\epsilon}{\kappa} \end{pmatrix}, \quad \begin{pmatrix} \dot{z}_{c1} \\ \dot{z}_{c2} \end{pmatrix} = \begin{bmatrix} 0 & 0 \\ \frac{1}{\kappa} & -\frac{\epsilon}{\kappa^2} \end{bmatrix} \cdot \begin{pmatrix} \dot{\epsilon} \\ \dot{\kappa} \end{pmatrix} \tag{3.40}$$

2. Dominating normal forces with fully compressed cross section $z_{c1} = -h/2, \dot{z}_{c1} = 0, z_{c2} = h/2, \dot{z}_{c2} = 0, h_c = h$ and

$$\begin{pmatrix} z_{c1} \\ z_{c2} \end{pmatrix} = \begin{pmatrix} -\frac{h}{2} \\ \frac{h}{2} \end{pmatrix}, \quad \begin{pmatrix} \dot{z}_{c1} \\ \dot{z}_{c2} \end{pmatrix} = \begin{bmatrix} 0 & 0 \\ 0 & 0 \end{bmatrix} \cdot \begin{pmatrix} \dot{\epsilon} \\ \dot{\kappa} \end{pmatrix} \tag{3.41}$$

3. Dominating bending with upper compression zone $z_{c1} = z_0 > -h/2$, $z_{c2} = h/2$ and $\dot{z}_{c2} = 0, \sigma_{c1} = 0, \dot{\sigma}_{c1} = 0$ and

$$\begin{pmatrix} z_{c1} \\ z_{c2} \end{pmatrix} = \begin{pmatrix} \frac{\epsilon}{\kappa} \\ \frac{h}{2} \end{pmatrix}, \quad \begin{pmatrix} \dot{z}_{c1} \\ \dot{z}_{c2} \end{pmatrix} = \begin{bmatrix} \frac{1}{\kappa} & -\frac{\epsilon}{\kappa^2} \\ 0 & 0 \end{bmatrix} \cdot \begin{pmatrix} \dot{\epsilon} \\ \dot{\kappa} \end{pmatrix} \tag{3.42}$$

Anyway, we set

$$\dot{\mathbf{z}}_c = \mathbf{B}_z \cdot \dot{\boldsymbol{\epsilon}} \tag{3.43}$$

with $\mathbf{B}_z$ according to one of the preceding cases. The rate of the edge stresses $\boldsymbol{\sigma}_{ce}$ in Eq. (3.37) is given by

$$\dot{\boldsymbol{\sigma}}_{ce} = E_c' \, \dot{\boldsymbol{\epsilon}}_{ce} \tag{3.44}$$

Equations (3.25, 3.43) lead to the rate of the edge strains

$$\begin{aligned} \dot{\boldsymbol{\epsilon}}_{ce} &= \mathbf{B}_\epsilon \cdot \dot{\boldsymbol{\epsilon}} - \kappa \, \dot{\mathbf{z}}_c \\ &= (\mathbf{B}_\epsilon - \kappa \mathbf{B}_z) \cdot \dot{\boldsymbol{\epsilon}} \end{aligned} \tag{3.45}$$

The combination of Eq. (3.45) with Eq. (3.37) yields the tangential material stiffness

$$\begin{aligned} \dot{\boldsymbol{\sigma}}_c &= E_c' \, \mathbf{A}_\sigma \cdot (\mathbf{B}_\epsilon - \kappa \mathbf{B}_z) \cdot \dot{\boldsymbol{\epsilon}} + \mathbf{A}_z \cdot \mathbf{B}_z \cdot \dot{\boldsymbol{\epsilon}} \\ &= \left[\mathbf{C}_c + (\mathbf{A}_z - \kappa E_c' \, \mathbf{A}_\sigma) \cdot \mathbf{B}_z \right] \cdot \dot{\boldsymbol{\epsilon}} \\ &= \mathbf{C}_{cT} \cdot \dot{\boldsymbol{\epsilon}} \end{aligned} \tag{3.46}$$

also considering the change of the extension of the concrete compressive zone beneath the material stiffness $\mathbf{C}_c$ itself.

The contribution of the reinforcement is derived from Eq. (3.22, 3.23) by

$$\boldsymbol{\sigma}_s = \mathbf{A}_s \cdot \boldsymbol{\sigma}_{se} \tag{3.47}$$

with

$$\boldsymbol{\sigma}_s = \begin{pmatrix} N_s \\ M_s \end{pmatrix}, \quad \mathbf{A}_s = \begin{bmatrix} A_{s1} & A_{s2} \\ -A_{s1}y_{s1} & -A_{s2}y_{s2} \end{bmatrix}, \quad \boldsymbol{\sigma}_{se} = \begin{pmatrix} \sigma_{s1} \\ \sigma_{s2} \end{pmatrix} \tag{3.48}$$

Reinforcement strains are given through Eq. (3.21)

$$\boldsymbol{\epsilon}_s = \mathbf{B}_s \cdot \boldsymbol{\epsilon} \tag{3.49}$$

with

$$\boldsymbol{\epsilon}_s = \begin{pmatrix} \epsilon_{s1} \\ \epsilon_{s2} \end{pmatrix}, \quad \mathbf{B}_s = \begin{bmatrix} 1 & -z_{s1} \\ 1 & -z_{s2} \end{bmatrix}, \quad \boldsymbol{\epsilon} = \begin{pmatrix} \epsilon \\ \kappa \end{pmatrix} \tag{3.50}$$

A linear elastic reinforcement behavior $\sigma_s = E_s \, \epsilon_s$ is assumed according to the assumption of the moderate loading level. Finally, this leads to

$$\begin{aligned} \boldsymbol{\sigma}_s &= E_s \, \mathbf{A}_s \cdot \mathbf{B}_s \cdot \boldsymbol{\epsilon} \\ &= \mathbf{C}_s \cdot \boldsymbol{\epsilon} \end{aligned} \tag{3.51}$$

which has to be superposed to the concrete part $\boldsymbol{\sigma}_c$. The tangential material stiffness equals the material stiffness $\mathbf{C}_{sT} = \mathbf{C}_s$ in the case of linear elastic behavior. The described approach may be easily extended for multiple reinforcement layers.

3.1.3.3   Nonlinear Behavior of Concrete and Reinforcement

Nonlinear stress–strain relations have to be regarded beneath a variable concrete compression zone to model limit states of structures. Such relations have already been introduced in Eq. (2.1) for the compression of concrete and in Eq. (2.39) for the reinforcement. Such relations can be used in Eqs. (3.22, 3.23) to determine internal forces for beams. Uniaxial strains serve as input. They are derived from the generalized beam strains by Eqs. (3.5, 3.21) whereby the extent of the compression zone is determined as has been described in Section 3.1.3.1. The evaluation of integrals in Eqs. (3.22, 3.23) generally has to be performed numerically and leads to nonlinear relations $M(\epsilon, \kappa)$ and $N(\epsilon, \kappa)$. In contrast to the linear elastic relations Eq. (3.16) moments M also depend on the strain ϵ of the reference axis beneath curvature κ and normal forces also depend on κ beneath ϵ.

Nonlinear material behavior leads to nonlinear system behavior which may be solved according to the approach described in Section 1.6. Thus, a tangential stiffness matrix together with a tangential material stiffness is required. The basic aspects regarding the general approaches (Eqs. (3.22, 3.23)) are discussed in the following. Uniaxial strain dependence on the generalized beam strains is given in Eq. (3.5) and leads to

$$\frac{\partial \epsilon_x}{\partial \epsilon} = 1, \qquad \frac{\partial \epsilon_x}{\partial \kappa} = -z \tag{3.52}$$

This is used for the derivatives of the normal forces (Eq. (3.22)) with respect to the generalized beam strains

$$
\begin{aligned}
\frac{\partial N}{\partial \epsilon} &= A_{s1} \frac{\partial \sigma_{s1}}{\partial \epsilon_x} \frac{\partial \epsilon_x}{\partial \epsilon} + A_{s2} \frac{\partial \sigma_{s2}}{\partial \epsilon_x} \frac{\partial \epsilon_x}{\partial \epsilon} + \int_{z_{c1}}^{z_{c2}} \frac{\partial \sigma_c}{\partial \epsilon_x} \frac{\partial \epsilon_x}{\partial \epsilon} \, b\mathrm{d}z \\
&= A_{s1} \frac{\partial \sigma_{s1}}{\partial \epsilon_x} + A_{s2} \frac{\partial \sigma_{s2}}{\partial \epsilon_x} + \int_{z_{c1}}^{z_{c2}} \frac{\partial \sigma_c}{\partial \epsilon_x} \, b\mathrm{d}z \\
\frac{\partial N}{\partial \kappa} &= A_{s1} \frac{\partial \sigma_{s1}}{\partial \epsilon_x} \frac{\partial \epsilon_x}{\partial \kappa} + A_{s2} \frac{\partial \sigma_{s2}}{\partial \epsilon_x} \frac{\partial \epsilon_x}{\partial \kappa} + \int_{z_{c1}}^{z_{c2}} \frac{\partial \sigma_c}{\partial \epsilon_x} \frac{\partial \epsilon_x}{\partial \kappa} \, b\mathrm{d}z \\
&= -A_{s1} \frac{\partial \sigma_{s1}}{\partial \epsilon_x} z_{s1} - A_{s2} \frac{\partial \sigma_{s2}}{\partial \epsilon_x} z_{s2} - \int_{z_{c1}}^{z_{c2}} \frac{\partial \sigma_c}{\partial \epsilon_x} z \, b\mathrm{d}z
\end{aligned} \tag{3.53}
$$

and for the derivatives of moments (Eq. (3.23))

$$
\begin{aligned}
\frac{\partial M}{\partial \epsilon} &= -A_{s1} \frac{\partial \sigma_{s1}}{\partial \epsilon_x} \frac{\partial \epsilon_x}{\partial \epsilon} z_{s1} - A_{s2} \frac{\partial \sigma_{s2}}{\partial \epsilon_x} \frac{\partial \epsilon_x}{\partial \epsilon} z_{s2} - \int_{z_{c1}}^{z_{c2}} \frac{\partial \sigma_c}{\partial \epsilon_x} \frac{\partial \epsilon_x}{\partial \epsilon} z \, b\mathrm{d}z \\
&= -A_{s1} \frac{\partial \sigma_{s1}}{\partial \epsilon_x} z_{s1} - A_{s2} \frac{\partial \sigma_{s2}}{\partial \epsilon_x} z_{s2} - \int_{z_{c1}}^{z_{c2}} \frac{\partial \sigma_c}{\partial \epsilon_x} z \, b\mathrm{d}z \\
&= \frac{\partial N}{\partial \kappa} \\
\frac{\partial M}{\partial \kappa} &= -A_{s1} \frac{\partial \sigma_{s1}}{\partial \epsilon_x} \frac{\partial \epsilon_x}{\partial \kappa} z_{s1} - A_{s2} \frac{\partial \sigma_{s2}}{\partial \epsilon_x} \frac{\partial \epsilon_x}{\partial \kappa} z_{s2} - \int_{z_{c1}}^{z_{c2}} \frac{\partial \sigma_c}{\partial \epsilon_x} \frac{\partial \epsilon_x}{\partial \kappa} z \, b\mathrm{d}z \\
&= A_{s1} \frac{\partial \sigma_{s1}}{\partial \epsilon_x} z_{s1}^2 + A_{s2} \frac{\partial \sigma_{s2}}{\partial \epsilon_x} z_{s2}^2 + \int_{z_{c1}}^{z_{c2}} \frac{\partial \sigma_c}{\partial \epsilon_x} z^2 \, b\mathrm{d}z
\end{aligned} \tag{3.54}
$$

The change of integration borders z_{c1}, z_{c2}, which has been considered in the previous approach, see Eq. (3.37), is disregarded in this approach to simplify the discussion and to avoid a blow-out of relations.

- Thus, the key for the derivatives of internal forces is given with the derivatives $\frac{\partial \sigma_{s1}}{\partial \epsilon_x}$, $\frac{\partial \sigma_{s2}}{\partial \epsilon_x}$, $\frac{\partial \sigma_c}{\partial \epsilon_x}$ of stresses with respect to strains. They are derived according to the discussion of uniaxial concrete behavior in Section 2.1 and reinforcing steel behavior in Section 2.3.

The terms are collected in a tangential material stiffness

$$\mathbf{C}_T = \begin{bmatrix} \dfrac{\partial N}{\partial \epsilon} & \dfrac{\partial N}{\partial \kappa} \\ \dfrac{\partial M}{\partial \epsilon} & \dfrac{\partial M}{\partial \kappa} \end{bmatrix} \tag{3.55}$$

The linear elastic, diagonal system is derived as a special case with $\frac{\partial \sigma_{s1}}{\partial \epsilon_x} = \frac{\partial \sigma_{s2}}{\partial \epsilon_x} = E_s$, $\frac{\partial \sigma_c}{\partial \epsilon_x} = E_c$ and $\int b\,\mathrm{d}z = A$, $\int z\, b\,\mathrm{d}z = 0$, $\int z^2\, b\,\mathrm{d}z = J$. To include shear forces, Eq. (3.55) has to be extended to

$$\mathbf{C}_T = \begin{bmatrix} \dfrac{\partial N}{\partial \epsilon} & \dfrac{\partial N}{\partial \kappa} & 0 \\ \dfrac{\partial M}{\partial \epsilon} & \dfrac{\partial M}{\partial \kappa} & 0 \\ 0 & 0 & \dfrac{\partial V}{\partial \gamma} \end{bmatrix} \tag{3.56}$$

whereby a coupling of shear with longitudinal actions has been neglected. The remaining coefficient $\frac{\partial V}{\partial \gamma}$ may be determined according to Section 3.5.4.

Regarding an isolated cross section the general nonlinear approach allows for several calculation types:

- Specification of strain ϵ, curvature κ and calculation of M, N.

  This is a standard procedure as has been described at the beginning of this subsection.

- Specification of curvature κ and normal force N and calculation of moment M. A result for ϵ occurs as side effect.

  This is a procedure to derive moment–curvature relations parametrized by a normal force. With N, κ given the nonlinear equation $f(\epsilon, \kappa) - N = 0$ has to be solved for ϵ. This may efficiently be done with a Newton–Raphson iteration, i.e.,

$$\epsilon^{(\nu+1)} = \epsilon^{(\nu)} - \frac{1}{\left.\dfrac{\partial f}{\partial \epsilon}\right|_{\epsilon=\epsilon^{(\nu)}}} \left(f(\epsilon^{(\nu)}, \kappa) - N \right) \tag{3.57}$$

  see Eq. (1.72). The starting value is $\epsilon^{(0)} = 0$. The derivative $\partial f/\partial \epsilon$ is given by Eq. (3.53)$_1$. With κ given and ϵ calculated, $M = f(\epsilon, \kappa)$ can be determined.

– Specification of moment M, normal force N and the calculation of κ and ϵ.

This is the inverse to the standard procedure to derive deformations from given internal forces. From Eqs. (3.22, 3.23), a nonlinear algebraic system arises for unknowns κ, ε after the evaluation of integrals of $\sigma_{s1}, \sigma_{s2}, \sigma_c$. This may also be solved with the Newton–Raphson method.

The second calculation type leads to moment–curvature relations which is demonstrated with the following example.

Example 3.1 Computation of moment–curvature relations for the given normal forces
An RC cross section of rectangular shape is given by the following properties:

– Cross-section height $h = 0.4\,\text{m}$ and width $b = 0.2\,\text{m}$.

– Concrete grade C 30/37 according to [26, Table 3.1] with a strength $f_c = 38\,\text{MN/m}^2$ and characteristic strains $\epsilon_{c1} = -2.2‰$, $\epsilon_{cu1} = -3.5‰$, see Fig. 2.1. The stress–strain curve is chosen as proposed by [26, 3.1.5]. The initial Young's modulus is $E_c = 33\,000\,\text{MN/m}^2$. A tensile strength is not considered.

– Reinforcement behavior is assumed according to Section 2.3 and [26, 3.2.7] with $f_{yk} = 500\,\text{MN/m}^2$, $f_t = 525\,\text{MN/m}^2$, $\epsilon_{y0} = 2.5‰$ and $\epsilon_u = 25‰$, see Fig. 2.10a.

– Upper and lower reinforcement each with a geometry 4 ⌀ 20, $A_{s2} = A_{s1} = 12.57\,\text{cm}^2$, $d_2 = d_1 = 5\,\text{cm}$.

All these values are *not* modified by safety factors. The moment–curvature relations are computed for $N = 0, -1, -2\,\text{MN}$. The curvature κ is increased starting from zero and N, κ serve as input values for nonlinear computation. The computed moments are of primary interest and lead to moment–curvature curves, see Fig. 3.3.

– The stiffness is ruled by the following factors: (1) height of the compression zone, (2) stiffness of concrete, (3) stiffness of steel. The cases with normal compression initially
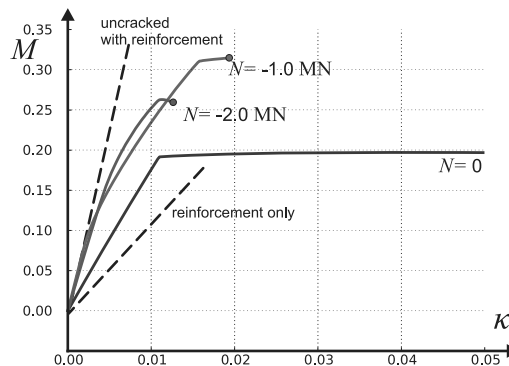

Figure 3.3: Example 3.1 moment–curvature relation.

have a higher compression zone leading to a higher stiffness with roughly the same material stiffness for all three cases.

– The contribution of stiffness reduces with increasing curvature due to the nonlinearity of the stress–strain curve, see Fig. 2.1. This is more pronounced in case with normal compression.

– The upper kinks result from the beginning of yielding of the reinforcement.

– The signed end points mark the state when ultimate concrete compressive stress of $\epsilon_{c1u} = -0.0035$ is reached. Ultimate moments increase with moderate normal compression due to the eccentricity of the resulting concrete force, see Fig. 3.2, but the ductility decreases.

The case of the uncracked, linear elastic cross section is shown as reference, furthermore the case with linear elastic reinforcement alone without concrete contribution. The initial bending stiffness of concrete alone is $EJ_c = 32.5\,\mathrm{MN/m^2}$, the initial bending stiffness of reinforcement alone is $EJ_s = 11.3\,\mathrm{MN/m^2}$ and the total initial stiffness is $EJ = 43.8\,\mathrm{MN/m^2}$.

———————————————————————————————————— *End Example 3.1*

A generalization of RC is given by *fiber models*. Every line along the beam axis cut by the cross section may be regarded as a *fiber*. Each fiber is strained according to beam kinematics which leads to a longitudinal stress. With the integration of stresses to result in internal forces any type of a uniaxial material law may be used for fibers. The quality of such fiber models is influenced by numerical integration methods. Simple methods like trapezoidal rule or Simpson rule may be used with a sufficient number of intervals. Gauss integration is not optimal, as the important upper and lower edges are not captured. Lobatto integration is an alternative.

3.2 Equilibrium of Beams

Kinematic compatibility and material laws for beams have been discussed in the preceding sections. Equilibrium remains to be added. We regard a loading $\bar{p}_x(x,t), \bar{p}_z(x,t)$ varying with place x and time t, see Fig. 3.4. Inertial effects will be considered. Therefore, the bar's (inertial) mass per length m and the second moment of inertia Θ have to be regarded.

The *strong differential formulation* of *dynamic equilibrium* for an infinitesimal section of a plane beam is given by differential equations

$$
\begin{aligned}
\bar{p}_x + N' &= m \cdot \ddot{u} \\
\bar{p}_z + V' &= m \cdot \ddot{w} \\
V + M' &= \Theta \cdot \ddot{\phi}
\end{aligned}
\tag{3.58}
$$

according to Newton's law – force = mass × acceleration – with the longitudinal acceleration $\ddot{u}$, the lateral acceleration $\ddot{w}$ and the acceleration of the cross-sectional rotation angle $\ddot{\phi}$.

To begin with, linear elastic case will be considered to connect these equations to well-known formulations. From Eq. (3.13)

$$
N = EA\,\epsilon = EA\,u', \quad M = EJ\,\kappa = EJ\,\phi', \quad Q = GA^\star \gamma
\tag{3.59}
$$
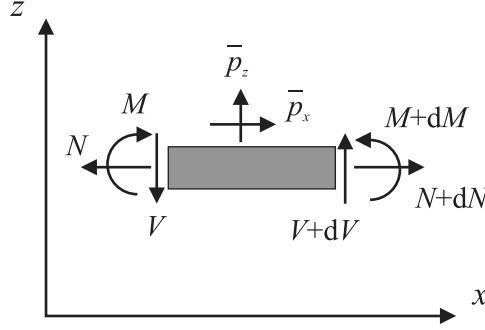
Figure 3.4: Equilibrium of infinitesimal beam element.

with $A^\star = \alpha A$. The combination of Eqs. (3.58, 3.59) leads to

$$
\begin{array}{rcl}
m\,\ddot{u} - EA\,u'' & = & \bar{p}_x \\
m\,\ddot{w} - GA^\star\,\gamma' & = & \bar{p}_z \\
\Theta\,(\ddot{w}' - \ddot{\gamma}) - EJ\,(w''' - \gamma'') & = & GA^\star\,\gamma
\end{array}
\tag{3.60}
$$

Equation $(3.60)_1$ represents the *one-dimensional wave equation*. We can set $m = \varrho\,A$ with the specific mass ϱ and $\bar{p}_x = 0$ to gain the familiar form. In the case of a normal, slender beam the shear rotation γ is small compared to the total rotation w'. The same holds true for the derivatives. Thus, we have $\phi'' \approx w'''$ and $\ddot{\phi} \approx \ddot{w}'$. Furthermore, the term $\Theta\,(\ddot{w}' - \ddot{\gamma})$ is neglected as $\Theta \ll 1$. Combining the derivative of Eqs. $(3.60)_3$ and $(3.60)_2$ finally leads to

$$
m\,\ddot{w} + EJ\,w'''' = \bar{p}_z
\tag{3.61}
$$

representing the differential *equation of dynamic beam bending* including the quasistatic case with $m = 0$.

Equilibrium has to be reformulated as *weak integral formulation* to have a base for discretization with finite elements. Such formulations utilize *test functions* or the so-called virtual displacements δu, δw, $\delta \gamma$, $\delta \phi = \delta w' - \delta \gamma$, see also Section 1.5, which are independent from each other. These test functions have to be kinematically compatible, i.e., they should be continuous and their first derivatives should exist.

Regarding a bar of finite length L with a longitudinal coordinate $0 \leq x \leq L$ and

- admitting all continuous functions of x as test functions

an equivalent to the strong form (Eq. (3.58)) is given by

$$
\int_0^L \delta u\,m\ddot{u}\ \mathrm{d}x - \int_0^L \delta u\,N'\ \mathrm{d}x + \int_0^L \delta w\,m\ddot{w}\,\mathrm{d}x - \int_0^L \delta w\,Q'\,\mathrm{d}x + \int_0^L \delta\phi\,\Theta\ddot{\phi}\,\mathrm{d}x - \int_0^L \delta\phi\,M'\,\mathrm{d}x
$$

$$
= \int_0^L \delta u\,\bar{p}_x\,\mathrm{d}x + \int_0^L \delta w\,\bar{p}_z\,\mathrm{d}x + \int_0^L (\delta w' - \delta\gamma)\,V\,\mathrm{d}x
\tag{3.62}
$$

The solutions of Eq. (3.62) also solve Eq. (3.58) and vice versa. Each differential equation is multiplied by its own test function, the product integrated over the beam length and finally all parts are added. Those terms with derivatives of internal forces are partially integrated in a further step:

$$
\begin{aligned}
\int_0^L \delta u\, N'\, \mathrm{d}x &= \big[\delta u(L)\, N(L) - \delta u(0)\, N(0)\big] - \int_0^L \delta\epsilon\, N\, \mathrm{d}x \\
\int_0^L \delta\phi\, M'\, \mathrm{d}x &= \big[\delta\phi(L)\, M(L) - \delta\phi(0)\, M(0)\big] - \int_0^L \delta\kappa\, M\, \mathrm{d}x \\
\int_0^L \delta w\, V'\, \mathrm{d}x &= \big[\delta w(L)\, V(L) - \delta w(0)\, V(0)\big] - \int_0^L \delta w'\, V\, \mathrm{d}x
\end{aligned}
\tag{3.63}
$$

with virtual deformations $\delta\epsilon = \delta u'$, $\delta\kappa = \delta\phi'$. Using this for Eq. (3.62) leads to

$$
\int_0^L \delta u\, m\ddot{u}\, \mathrm{d}x + \int_0^L \delta\phi\, \Theta\ddot{\phi}\, \mathrm{d}x + \int_0^L \delta w\, m\ddot{w}\, \mathrm{d}x + \int_0^L \delta\epsilon\, N\, \mathrm{d}x + \int_0^L \delta\kappa\, M\, \mathrm{d}x + \int_0^L \delta\gamma\, V\, \mathrm{d}x
$$
$$
= \int_0^L \delta u\, \bar{p}_x\, \mathrm{d}x + \int_0^L \delta w\, \bar{p}_z\, \mathrm{d}x + \big[\delta u\, N\big]_0^L + \big[\delta\phi\, M\big]_0^L + \big[\delta w\, V\big]_0^L
\tag{3.64}
$$

whereby the boundary terms in Eq. (3.63) have been abbreviated. The last equation may be interpreted as the *virtual work principle* and has the following parts:

- Inertial forces with the first three terms of the left-hand side.

- Internal forces with the last three terms of the left-hand side.

- Distributed loading with the first two terms of the right-hand side.

- Finally, the boundary terms with the forces at the beam's ends with the last three terms of the right-hand side.

A generalizing matrix notation of Eq. (3.64) is given by

$$
\int_0^L \delta\boldsymbol{\epsilon}^T \cdot \boldsymbol{\sigma}\, \mathrm{d}x + \int_0^L \delta\mathbf{u}^T \cdot \mathbf{m} \cdot \ddot{\mathbf{u}}\, \mathrm{d}x = \int_0^L \delta\mathbf{u}^T \cdot \bar{\mathbf{p}}\, \mathrm{d}x + \delta\mathbf{U}^T \cdot \bar{\mathbf{t}}
\tag{3.65}
$$

see also Eq. (1.52). In the case of beams the vector and matrix quantities have the components

$$
\boldsymbol{\epsilon} = \begin{pmatrix} \epsilon \\ \gamma \\ \kappa \end{pmatrix}, \qquad \boldsymbol{\sigma} = \begin{pmatrix} N \\ V \\ M \end{pmatrix}
$$

$$
\mathbf{u} = \begin{pmatrix} u \\ w \\ \phi \end{pmatrix}, \qquad \mathbf{m} = \begin{bmatrix} m & 0 & 0 \\ 0 & m & 0 \\ 0 & 0 & \Theta \end{bmatrix}, \qquad \bar{\mathbf{p}} = \begin{pmatrix} \bar{p}_x \\ \bar{p}_z \\ 0 \end{pmatrix}
$$

$$
\mathbf{U} = \begin{pmatrix} u_0 \\ w_0 \\ \phi_0 \\ u_L \\ w_L \\ \phi_L \end{pmatrix}, \qquad \bar{\mathbf{t}} = \begin{pmatrix} N_0 \\ V_0 \\ M_0 \\ N_L \\ V_L \\ M_L \end{pmatrix}
\tag{3.66}
$$

with $\bullet_L = \bullet(L)$, $\bullet_0 = \bullet(0)$ and $\phi = w' - \gamma$, $\kappa = \phi' = w'' - \gamma'$. The boundary force $\bar{\mathbf{t}}$ would need a sign convention $\bar{\mathbf{t}} = \begin{pmatrix} -N_0 & -V_0 & -M_0 & N_L & V_L & M_L \end{pmatrix}^T$ to be consistent with Eq. (3.63), but regarding a finite element discretization a global sign convention is more appropriate: internal forces on the left cross section are assumed as positive with the same directions as on the right cross section. Regarding the beam's ends, i.e., its boundary conditions, from each pair (u, N), (w, V), (ϕ, M) one quantity has to be prescribed for every end. In the case of prescribed forces they are marked with an overbar, i.e., $N \to \bar{N}, \dots$.

Shear deformations are still included up to now covering the *Timoshenko beam*. In the case of a normal, slender beam the shear rotation γ is small compared to the total rotation w'. The same holds true for the derivatives and

$$\phi = w', \quad \kappa = \phi' = w'' \tag{3.67}$$

is assumed. With $\gamma = 0$, the contribution $\delta\gamma V$ vanishes in Eq. (3.64). Thus, we set

$$\boldsymbol{\epsilon} = \begin{pmatrix} \epsilon \\ \kappa \end{pmatrix}, \qquad \boldsymbol{\sigma} = \begin{pmatrix} N \\ M \end{pmatrix} \tag{3.68}$$

and get the formulation for the *Bernoulli beam*. With N, M given the shear force V is determined by postprocessing using Eq. $(3.58)_3$ which still holds true for $\gamma = 0$. Apart from $\boldsymbol{\sigma}, \boldsymbol{\epsilon}$ all other quantities in Eqs. (3.66) remain unchanged for the Bernoulli beam.

Mass inertia is still included up to now and the formulations are applicable to *dynamics*. A simplification may be taken as the rotational inertia Θ generally is relatively small. Thus, the corresponding contributions may be neglected with $\Theta = 0$. This applies to the Timoshenko beam as well as for the Bernoulli beam. Finally, *quasistatics* is included for both beam types with mass inertia $m = 0$, $\Theta = 0$ leading to a mass matrix $\mathbf{m} = \mathbf{0}$ in Eq. (3.65).

The boundary terms $\mathbf{U}$, $\bar{\mathbf{t}}$ of Eq. (3.65) remain unchanged for all cases mentioned. The conditions (1.53) concerning the prescribed boundary displacements have to be applied also for the case of beams. It is easy to choose displacement trial functions such that they fulfill prescribed displacements on boundaries. Thus, test functions or virtual displacement may be set to zero along boundaries with kinematic boundary conditions. As a further consequence such end force components in $\bar{\mathbf{t}}$ belonging to prescribed displacement components in $\mathbf{U}$, see Eq. $(3.66)_6$ must not be specified. They come into play as reaction forces whereby corresponding to internal nodal forces, see Eq. $(1.58)_1$.

3.3 Finite Element Types for Plane Beams

3.3.1 Basics

A general form of displacement interpolation with finite elements is given by Eq. (1.18). This is specified for the interpolation of the beam displacement variables u, w, ϕ in the following whereby the considerations of Section 1.3 are applied to beams.

A beam with a coordinate range $0 \le x \le L$ is subdivided into a number n_E of elements. Each element has two nodes in a first approach leading to $n_N = n_E + 1$ nodes. An element e, $e = 1, \dots, n_E$, has the global nodal coordinates x_I, x_J, a length $L_e = x_J - x_I$ and a local

coordinate r. The relation between local and global coordinates is given by

$$x = \left[\begin{array}{cc} \frac{1}{2}(1-r) & \frac{1}{2}(1+r) \end{array}\right] \cdot \left(\begin{array}{c} x_I \\ x_J \end{array}\right) \tag{3.69}$$

with $x(-1) = x_I$, $x(1) = x_J$. This yields a Jacobian J

$$J = \frac{\partial x}{\partial r} = \frac{L_e}{2} \tag{3.70}$$

which is needed for the numerical integration, see Eq. (1.67). The inverse relation $r = (2x - x_J - x_I)/L_I$ leads to

$$\frac{\partial r}{\partial x} = \frac{2}{L_e} = J^{-1} \tag{3.71}$$

Polynomial forms

$$y(r,t) = \sum_{i=0}^{n} a_i(t) \cdot r^i \tag{3.72}$$

are chosen to interpolate displacement variables within an element. The coefficients a_i are functions of time t while y represents the displacement variables u, w, and ϕ. A particular formulation yields a *trial function*. According to the method of Bubnov–Galerkin *test functions* are chosen in the same way as the trial functions

$$\delta y(r,t) = \sum_{i=0}^{n} \delta a_i(t) \cdot r^i \tag{3.73}$$

Deformation variables ϵ, γ, κ and their variations are defined from displacement variables according to Section 3.1.1. With the given trial and test functions they are determined with the derivatives of Eqs. (3.72, 3.73).

Derivatives should be finite across elements to ensure the integrability of Eq. (3.65), see also Section 1.7. This leads to the following requirements for trial and test functions:

- In the case of Bernoulli kinematics $\phi = w'$ and $\kappa = w''$, i.e., deformation results from the second derivative of displacements. Thus, first derivatives of test functions have to be continuous across elements (C^1-continuity).

- In the case of Timoshenko kinematics $\kappa = \phi'$ and ϕ and w are decoupled by the shear deformation γ. Deformations result from the first derivatives of displacements and continuity of test functions across elements is sufficient (C^0-continuity).

Specifications of Eq. (3.72) are derived in the following based on these general remarks.

3.3.2   Finite Elements for the Bernoulli Beam

Nodal degrees of freedom of the two-node element for the Bernoulli beam are given by

$$\boldsymbol{v}_e = \left(\begin{array}{cccccc} u_I & w_I & \phi_I & u_J & w_J & \phi_J \end{array}\right)^T \tag{3.74}$$

The dependence on time t is not explicitly notified. A kinematic constraint relating lateral displacement w and cross-section rotation ϕ or curvature curvature κ, respectively, is given by Eq. (3.67)

$$\kappa = w'' \tag{3.75}$$

This formulation of $\mathbf{B}$ establishes that ϵ is constant within the element while κ is linear. This is no problem in the case of linear elastic material behavior according to Eq. (3.16) with N decoupled from κ and M decoupled from ϵ but may lead to artificial constraints in the case of coupled material behavior as is characteristic for the cracked RC, see Eq. (3.55).

This is discussed with a simple test. A single element is regarded with $u_I = w_I = \phi_I = 0$ and a material matrix

$$\mathbf{C} = \begin{bmatrix} C_{11} & C_{12} \\ C_{21} & C_{22} \end{bmatrix} \tag{3.83}$$

leading to

$$N = C_{11}\, u_J - \frac{6}{L_e} C_{12}\, r\, w_J + C_{12}\,(3r+1)\,\phi_J$$

$$M = C_{21}\, u_J - \frac{6}{L_e} C_{22}\, r\, w_J + C_{22}\,(3r+1)\,\phi_J \tag{3.84}$$

$$V = -M' = \frac{6}{L_e^2} C_{22}\,(2w_J - \phi_J\, L_e)$$

The conditions $N = 0$, $M = 0$, $V = \bar{V}$ are prescribed on the right-hand side $r = 1$. This results in displacements $u_J = 0$, $\phi_J = 1/(2C_{22})\,V L_e$, $w_J = 1/(3C_{22})\,V L_e^2$ and internal forces

$$N = \frac{C_{12}}{2C_{22}}\,(1-r)\,V\,L_e$$

$$M = \frac{1}{2}\,(1-r)\,V\,L_e \tag{3.85}$$

$$V = \bar{V}$$

While M, V are correctly computed an error in N arises due to the coupling material component C_{12}.

The artificial normal forces can be reduced with the introduction of an additional degree of freedom for the longitudinal displacement. The previous vector of nodal degrees of freedom according to Eq. (3.74) is extended with a component u_K as

$$\boldsymbol{v}_e = \begin{pmatrix} u_I & w_I & \phi_I & u_K & u_J & w_J & \phi_J \end{pmatrix}^T \tag{3.86}$$

Trial and test function of the Bernoulli beam element are *extended* as follows:

$$\mathbf{N}(r) = \begin{bmatrix} \frac{1}{2}r(r-1) & 0 & 0 & 1-r^2 & \cdots \\ 0 & \frac{r^3}{4} - \frac{3r}{4} + \frac{1}{2} & \frac{L_e r^3}{8} - \frac{L_e r^2}{8} - \frac{L_e r}{8} + \frac{L_e}{8} & 0 & \cdots \end{bmatrix} \tag{3.87}$$

This approach replaces the first row of the previous $\mathbf{N}$ with quadratic functions whereby the function corresponding to the additional degree of freedom corresponds to a bubble function [3]. This degree of freedom is not "visible" from the "outside" and not used for the interpolation of geometry and lateral displacements. The approach leads to

$$\mathbf{B}(r) = \frac{1}{L_e} \begin{bmatrix} 2r-1 & 0 & 0 & -4r & 2r+1 & 0 & 0 \\ 0 & \frac{6r}{L_e} & 3r-1 & 0 & 0 & -\frac{6r}{L_e} & 3r+1 \end{bmatrix} \tag{3.88}$$

and effects a linear longitudinal strain within an element corresponding to the linear curvature. The vectors $\mathbf{u}$, see Eq. (3.79), and $\boldsymbol{\epsilon}$, see Eq. (3.82), remain unchanged.

The simple test is also performed with the extended Bernoulli beam element. Internal forces are determined with

$$
\begin{aligned}
N &= -4C_{11}\,r\,u_K + C_{11}(2r+1)\,u_J - 6C_{12}\,r/L_e\,w_J + C_{12}(3r+1)\,\phi_J \\
M &= -4C_{21}\,r\,u_K + C_{21}(2r+1)\,u_J - 6C_{22}\,r/L_e\,w_J + C_{22}(3r+1)\,\phi_J \\
V &= 2(4C_{21}\,u_K\,L_e - 2C_{21}\,u_J\,L_e + 6C_{22}\,w_J - 3C_{22}\,\phi_J\,L_e)/L_e^2
\end{aligned}
\tag{3.89}
$$

An additional condition $N = 0$ is prescribed on the left-hand side. This results in displacements $u_K = 3C_{12}\,VL_e/8$, $u_J = C_{12}\,VL_e/2$, $w_J = -C_{11}VL_e^2/3$, $\phi_J = -C_{11}\,VL_e/2$ with $c = 1/(C_{12}C_{21} - C_{11}C_{22})$ and in internal forces

$$
\begin{aligned}
N &= 0 \\
M &= \tfrac{1}{2}(r-1)\,V\,L_e \\
V &= \bar{V}
\end{aligned}
\tag{3.90}
$$

All internal forces are correctly determined for the simple test.

The extended Bernoulli beam element will be predominantly for the following examples but generally it is not part of commercial finite element packages.

3.3.3 Finite Elements for the Timoshenko Beam

Nodal degrees of freedom of the two-node element for the Timoshenko beam are again given by

$$
\boldsymbol{v}_e = \begin{pmatrix} u_I & w_I & \phi_I & u_J & w_J & \phi_J \end{pmatrix}^T
\tag{3.91}
$$

but in contrast to the Bernoulli beam no kinematic constraints exist between lateral displacements and cross-section rotations. Regarding Eq. (3.72) a polynomial order $i = 1$ is sufficient for u, w, ϕ and

$$
\begin{aligned}
u &= \begin{bmatrix} \tfrac{1}{2}(1-r) & \tfrac{1}{2}(1+r) \end{bmatrix} \cdot \begin{pmatrix} u_I \\ u_J \end{pmatrix} \\
w &= \begin{bmatrix} \tfrac{1}{2}(1-r) & \tfrac{1}{2}(1+r) \end{bmatrix} \cdot \begin{pmatrix} w_I \\ w_J \end{pmatrix} \\
\phi &= \begin{bmatrix} \tfrac{1}{2}(1-r) & \tfrac{1}{2}(1+r) \end{bmatrix} \cdot \begin{pmatrix} \phi_I \\ \phi_J \end{pmatrix}
\end{aligned}
\tag{3.92}
$$

are assumed. This may again be abbreviated as

$$
\mathbf{u} = \mathbf{N}(r) \cdot \boldsymbol{v}_e
\tag{3.93}
$$

with $\boldsymbol{v}_e$ according to Eq. (3.91) and

$$
\mathbf{u} = \begin{pmatrix} u \\ w \\ \phi \end{pmatrix}, \quad
\mathbf{N}(r) = \begin{bmatrix}
\tfrac{1}{2}(1-r) & 0 & 0 & \tfrac{1}{2}(1+r) & 0 & 0 \\
0 & \tfrac{1}{2}(1-r) & 0 & 0 & \tfrac{1}{2}(1+r) & 0 \\
0 & 0 & \tfrac{1}{2}(1-r) & 0 & 0 & \tfrac{1}{2}(1+r)
\end{bmatrix}
\tag{3.94}
$$

Deformation variables are determined using Eqs. (3.4, 3.2, 3.70)

$$
\begin{aligned}
\epsilon &= \frac{\partial u}{\partial r}\frac{\partial r}{\partial x} &&= \frac{1}{L_e}\begin{bmatrix} -1 & 1 \end{bmatrix}\cdot\begin{pmatrix} u_I \\ u_J \end{pmatrix} \\[2mm]
\kappa &= \frac{\partial \phi}{\partial r}\frac{\partial r}{\partial x} &&= \frac{1}{L_e}\begin{bmatrix} -1 & 1 \end{bmatrix}\cdot\begin{pmatrix} \phi_I \\ \phi_J \end{pmatrix} \\[2mm]
\gamma &= \frac{\partial w}{\partial r}\frac{\partial r}{\partial x}-\phi &&= \frac{1}{L_e}\begin{bmatrix} -1 & -\frac{L_e}{2}(1-r) & 1 & -\frac{L_e}{2}(1+r) \end{bmatrix}\cdot\begin{pmatrix} w_I \\ \phi_I \\ w_J \\ \phi_J \end{pmatrix}
\end{aligned}
\tag{3.95}
$$

This is abbreviated with

$$
\boldsymbol{\epsilon} = \mathbf{B}(r)\cdot\boldsymbol{v}_e \tag{3.96}
$$

using

$$
\boldsymbol{\epsilon} = \begin{pmatrix} \epsilon \\ \kappa \\ \gamma \end{pmatrix}, \quad
\mathbf{B}(r) = \frac{1}{L_e}\begin{bmatrix}
-1 & 0 & 0 & 1 & 0 & 0 \\
0 & 0 & -1 & 0 & 0 & 1 \\
0 & -1 & -\frac{L_e}{2}(1-r) & 0 & 1 & -\frac{L_e}{2}(1+r)
\end{bmatrix}
\tag{3.97}
$$

The coupling effect arising with Bernoulli beam elements, see Section 3.3.2, is not an issue here. Both ϵ, κ are constant within the element and shear is decoupled with a material matrix (Eq. (3.56)).

But in the case of pure bending or slender beams with a low bending stiffness compared to shear stiffness the shear angle may be assumed as $\gamma \approx 0$. Thus, Eq. $(3.95)_3$ imposes a constraint on the nodal variables which is not justified by physics and leads to a severe artificial stiffening or *locking* effects. This will be analyzed as a special case of the behavior of elements for thin shells in Section 8.6.

The artificial locking can also be reduced with the introduction of additional degrees of freedom to relax stiffness. The previous vector of nodal degrees of freedom according to Eq. (3.91) is extended with components u_K, w_K as

$$
\boldsymbol{v}_e = \begin{pmatrix} u_I & w_I & \phi_I & u_K & w_K & u_J & w_J & \phi_J \end{pmatrix}^T \tag{3.98}
$$

Trial and test function of the Timoshenko beam element are *extended* with

$$
\mathbf{N}(r) = \begin{bmatrix}
\frac{r(r-1)}{2} & 0 & 0 & 1-r^2 & 0 & \frac{r(1+r)}{2} & 0 & 0 \\
0 & \frac{r(r-1)}{2} & 0 & 0 & 1-r^2 & 0 & \frac{r(1+r)}{2} & 0 \\
0 & 0 & \frac{(1-r)}{2} & 0 & 0 & 0 & 0 & \frac{(1+r)}{2}
\end{bmatrix}
\tag{3.99}
$$

leading to

$$
\mathbf{B}(r) = \frac{1}{L_e}\begin{bmatrix}
2r-1 & 0 & 0 & -4r & 0 & 2r+1 & 0 & 0 \\
0 & 0 & -1 & 0 & -4r & 0 & 0 & 1 \\
0 & 2r-1 & -\frac{L_e}{2}(1-r) & 0 & 0 & 0 & 2r+1 & -\frac{L_e}{2}(1+r)
\end{bmatrix}
\tag{3.100}
$$

The vectors $\mathbf{u}$, see Eq. (3.94), and $\boldsymbol{\epsilon}$, see Eq. (3.97), remain unchanged. The additional degrees of freedom again correspond to bubble functions [3]. Further discussion of locking problems is given in, e.g., [80].

3.4 System Building and Solution Methods

3.4.1 Elementwise Integration

The cornerstones of structural analysis for beams have been derived from the kinematic relation in Section 3.1.1, material behavior in Sections 3.1.2 and 3.1.3 and equilibrium in Section 3.2. The compilation in a numerical method is carried out with the evaluation of the weak integral equilibrium condition (Eq. (3.65)).

This is performed element by element, see Section 1.5 and Eq. (1.58). The evaluation of integrals is done numerically according to the one-dimensional variant of Eq. (1.67). In the case of structural beam elements the Jacobian is given by Eq. (3.70). Internal nodal forces, see Eq. $(1.9)_1$, are determined by

$$\mathbf{f}_e = \int_{L_e} \mathbf{B}^T(x) \cdot \boldsymbol{\sigma}(x) \, dx = \frac{L_e}{2} \int_{-1}^{1} \mathbf{B}^T(r) \cdot \boldsymbol{\sigma}(r) \, dr \tag{3.101}$$

where $\mathbf{B}$ is given according to the element type chosen and $\boldsymbol{\sigma}$ according to Eq. $(3.66)_1$ or Eq. (3.68). The internal force dimension has to match the row dimension of $\mathbf{B}$. According to Eq. (1.68) the numerical integration is performed through

$$\mathbf{f}_e = \frac{L_e}{2} \sum_{i=0}^{n_i} \eta_i \, \mathbf{B}^T(\xi_i) \cdot \boldsymbol{\sigma}(\xi_i) \tag{3.102}$$

The same procedure is applied to determine the tangential element stiffness matrix, see Eq. (1.65)

$$\mathbf{K}_{Te} = \frac{L_e}{2} \sum_{i=0}^{n_i} \eta_i \, \mathbf{B}^T(\xi_i) \cdot \mathbf{C}_T(\xi_i) \cdot \mathbf{B}(\xi_i) \tag{3.103}$$

with the tangential material stiffness according to Eqs. (3.55) or (3.16) in the case of Bernoulli beams, or (3.56), (3.15) in the case of Timoshenko beams. Furthermore, the element mass matrix, see Eq. $(1.58)_2$, is

$$\mathbf{M}_e = \frac{L_e}{2} \sum_{i=0}^{n_i} \eta_i \, \mathbf{N}^T(\xi_i) \cdot \mathbf{m} \cdot \mathbf{N}(\xi_i) \tag{3.104}$$

with $\mathbf{m}$ according to Eq. (3.66), and the element distributed loading, see Eq. $(1.58)_3$

$$\bar{\mathbf{p}}_e = \frac{L_e}{2} \sum_{i=0}^{n_i} \eta_i \, \mathbf{N}^T(\xi_i) \cdot \bar{\mathbf{p}}(\xi_i) \tag{3.105}$$

with $\bar{\mathbf{p}}$ according to Eq. (3.66). Boundaries of beams are embodied by nodes. Thus, the elements boundary loading can be directly taken from Eq. $(3.66)_7$

$$\bar{\mathbf{t}}_e = \begin{pmatrix} \bar{N}_I & \bar{V}_I & \bar{M}_I & \bar{N}_J & \bar{V}_J & \bar{M}_J \end{pmatrix}^T \tag{3.106}$$

in case that nodal loads are prescribed for a particular element.

The numerical integration has to be as precise as possible to minimize the discretization error. The integration error of the Gauss integration is determined by the integration order n_i, see Eq. (1.68). Disregarding round-off errors an integration order n_i gives exact results for polynomials of order $2n_i + 1$.

– The Bernoulli beam element with strains according to Eq. (3.82) yields a stiffness matrix $\mathbf{K}_{Te}$ with highest polynomial degree 2 in the case of constant material stiffness within an element. This requires $n_i = 1$ and two sampling points with Gauss integration.

– The same argument holds for the Timoshenko beam element, see Eq. (3.97), due to the shear deformation parts. Reduced integration $n_i = 1$ neglects the linear contribution of shear deformations but might solve the locking problem in the case of slender beams.

Finally, integration of an ordinary Bernoulli or Timoshenko beam two-node element ends up with, e.g., a vector of internal nodal forces

$$\mathbf{f}_e = \left(\begin{array}{cccccc} N_I & V_I & M_I & N_J & V_J & M_J \end{array} \right)^T \tag{3.107}$$

The number of components corresponds to the components of nodal displacements, see Eqs. (3.74, 3.91) with $N_i \leftrightarrow u_i$, $V_i \leftrightarrow w_i$, $M_i \leftrightarrow \phi_i$, $i = I, J$, and to number of columns in the matrix $\mathbf{B}$ or rows in $\mathbf{B}^T$. The number of rows in $\mathbf{B}$ has to be equal to the dimension of the material stiffness square matrices $\mathbf{C}$, $\mathbf{C}_T$, see Eqs. (3.15, 3.16, 3.55, 3.56). The same argument applies to the matrix $\mathbf{N}$, if necessary in connection with the mass matrix $\mathbf{m}$, see Eq. (3.66).

In a similar way as for internal nodal forces $\mathbf{f}_e$ Eq. (3.105) leads to

$$\bar{\mathbf{p}}_e = \left(\begin{array}{cccccc} \bar{N}_I^p & \bar{V}_I^p & \bar{M}_I^p & \bar{N}_J^p & \bar{V}_J^p & \bar{M}_J^p \end{array} \right)^T \tag{3.108}$$

where $\bar{N}_{I1}^p, \dots$ should not be confused with $\bar{N}_{I1}, \dots$ from $\bar{\mathbf{t}}_I$, see Eq. (3.106). According to these dimensions the element stiffness matrix $\mathbf{K}_{Te}$ according to Eq. (1.65) and the element mass matrix $\mathbf{M}_e$ according to Eq. (1.58) have a dimension 6×6 for the ordinary two-node beam elements.

Additional degrees of freedom arise with the extended elements, see Eqs. (3.86, 3.98). They may be condensed on the element level and then will not arise as additional unknowns on the system level. Alternatively they can be carried over the system level and are connected with the corresponding internal and external nodal force components.

3.4.2 Transformation and Assemblage

The longitudinal axis of a beam element and the global x-axis have the same direction up to now. But a 2D structural beam may have an orientation in 2D space. Thus, we have to consider a transformation of vectors in 2D Cartesian coordinate systems.

The direction of a straight element is assumed with the first element node as start and the last element node as end. A rotation angle α is assumed starting from global x-direction to the local $\tilde{x}$-direction of an element, see Fig. 3.5. Regarding Eq. (C.8) the following relations hold true for the transformation of nodal displacements, see e.g., Eq. (3.74), and nodal forces, see Eq. (3.107), of two-node elements from the global system into the local system

$$\tilde{\boldsymbol{v}}_e = \mathbf{T} \cdot \boldsymbol{v}_e, \quad \tilde{\mathbf{f}}_e = \mathbf{T} \cdot \mathbf{f}_e \tag{3.109}$$

and vice versa

$$\boldsymbol{v}_e = \mathbf{T}^T \cdot \tilde{\boldsymbol{v}}_e, \quad \mathbf{f}_e = \mathbf{T}^T \cdot \tilde{\mathbf{f}}_e \tag{3.110}$$
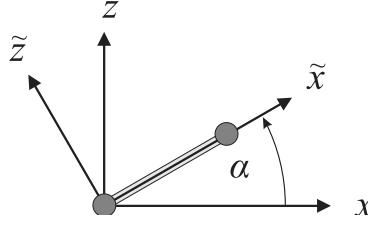
Figure 3.5: Beam orientation in 2D space.

with

$$\mathbf{T} = \begin{bmatrix} \cos\alpha & \sin\alpha & 0 & 0 & 0 & 0 \\ -\sin\alpha & \cos\alpha & 0 & 0 & 0 & 0 \\ 0 & 0 & 1 & 0 & 0 & 0 \\ 0 & 0 & 0 & \cos\alpha & \sin\alpha & 0 \\ 0 & 0 & 0 & -\sin\alpha & \cos\alpha & 0 \\ 0 & 0 & 0 & 0 & 0 & 1 \end{bmatrix} \tag{3.111}$$

whereby $\bullet^T$ denotes the transpose of $\bullet$. The rotation angles ϕ_I, ϕ_J and moments M_I, M_J remain unchanged with this transformation. Equations (3.109) are also valid for increments $\mathrm{d}\tilde{\boldsymbol{v}}_e$, $\mathrm{d}\boldsymbol{v}_e$, $\mathrm{d}\tilde{\mathbf{f}}_e$, $\mathrm{d}\mathbf{f}_e$ and for loadings $\tilde{\mathbf{p}}_e$, $\mathbf{p}_e$.

The tangential element stiffness matrix is at first defined in the local system of a beam by

$$\mathrm{d}\tilde{\mathbf{f}}_e = \tilde{\mathbf{K}}_{Te} \cdot \mathrm{d}\tilde{\boldsymbol{v}}_e \tag{3.112}$$

see Eq. (1.66). Using the transformation rules of Eq. (3.109) and considering $\mathbf{T}^{-1} = \mathbf{T}^T$ this yields

$$\mathbf{T} \cdot \mathrm{d}\mathbf{f}_e = \tilde{\mathbf{K}}_{Te} \cdot \mathbf{T} \cdot \mathrm{d}\boldsymbol{v}_e \quad \rightarrow \quad \mathrm{d}\mathbf{f}_e = \mathbf{T}^T \cdot \tilde{\mathbf{K}}_{Te} \cdot \mathbf{T} \cdot \mathrm{d}\boldsymbol{v}_e \tag{3.113}$$

and finally results in a transformation rule for the tangential element stiffness matrix

$$\mathbf{K}_{Te} = \mathbf{T}^T \cdot \tilde{\mathbf{K}}_{Te} \cdot \mathbf{T} \tag{3.114}$$

Similar arguments lead to the transformation rule for the element mass matrix

$$\mathbf{M}_e = \mathbf{T}^T \cdot \tilde{\mathbf{M}}_e \cdot \mathbf{T} \tag{3.115}$$

In the case of the extended two-node Bernoulli element, see Section 3.3.2, the transformation matrix $\mathbf{T}$ is given by

$$\mathbf{T} = \begin{bmatrix} \cos\alpha & \sin\alpha & 0 & 0 & 0 & 0 & 0 \\ -\sin\alpha & \cos\alpha & 0 & 0 & 0 & 0 & 0 \\ 0 & 0 & 1 & 0 & 0 & 0 & 0 \\ 0 & 0 & 0 & 1 & 0 & 0 & 0 \\ 0 & 0 & 0 & 0 & \cos\alpha & \sin\alpha & 0 \\ 0 & 0 & 0 & 0 & -\sin\alpha & \cos\alpha & 0 \\ 0 & 0 & 0 & 0 & 0 & 0 & 1 \end{bmatrix} \tag{3.116}$$

The central 1 belongs to the additional degree of freedom of the interior node. This value should not be rotated as it corresponds to a local longitudinal displacement without relating to the global system. Apart from the change in $\mathbf{T}$, all transformations remain unchanged.

Element contributions $\mathbf{f}_e, \mathbf{p}_e, \mathbf{K}_{Te}, \mathbf{M}_e$ must be assembled to system vectors and matrices, see Section 1.5. The procedure is basically the same for all element types. Regarding a particular node which is shared by several elements, the elements contributions to nodal forces and nodal loads have to sum up to zero with respect to equilibrium.

3.4.3   Kinematic Boundary Conditions and Solution

Displacements at boundaries or kinematic boundary conditions still have to be regarded. There must be enough boundary conditions to prevent rigid body motions. They are applied by prescribing nodal values of u_{Ii}, w_{Ii}, ϕ_{Ii}. To simplify the description the quasistatic linear case

$$\mathbf{K} \cdot \mathbf{u} = \mathbf{p} \qquad (3.117)$$

is considered, see Eqs. (1.69, 1.62). The lateral displacement w_I of an element e with a prescribed value $\bar{w}$ is treated exemplary.

If necessary, the value has to be transformed to the global system according to Eq. (3.109). Let the global index of this degree of freedom be k, see Section 1.5. Let n be the total number of degrees of freedom. To apply the particular boundary condition one may set

$$
\begin{array}{rcll}
p_i & = & p_i - K_{ik}\,\bar{w} & i = 1, \ldots, k-1, k+1, \ldots, n \\
p_k & = & \bar{w} & \\
K_{kk} & = & 1 & \\
K_{kj} & = & 0 & j = 1, \ldots, k-1, k+1, \ldots, n \\
K_{ik} & = & 0 & i = 1, \ldots, k-1, k+1, \ldots, n
\end{array}
\qquad (3.118)
$$

for the components of the right-hand side and the matrix in Eq. (3.117), i.e., the k-row and column of $\mathbf{K}$ are zeroed. With $p_k = \bar{w}$ and $K_{kk} = 1$ this must lead to $w_k = \bar{w}$ after solving the system of equations. The additional terms $K_{ik}\,\bar{w}$ on the right-hand side apply constraint forces in the case $\bar{w} \neq 0$.

The degree of freedom k has to be excluded from balancing equilibrium by summing up nodal force contributions from elements and loadings, see e.g., Eq. (1.69). The corresponding internal nodal forces result in a support reaction. The procedure as has been described for the linear case may also be applied for every iteration step within an incrementally iterative scheme, see Section 1.6. Thus, fulfillment of kinematic boundary conditions is reached in the same way for nonlinear and dynamic cases.

Nonlinear systems are given for beams with cracked RC cross sections due to the nonlinear relations between moment, normal force, curvature, and longitudinal strain. The incrementally iterative scheme is appropriate to solve such systems. A loading history is followed whereby a real time ($\rightarrow$ dynamic or transient case) or a pseudo time ($\rightarrow$ quasistatic case) is used to control the load. Solution increments correspond to time steps. The Newton–Raphson method, see Eq. (1.72), is generally appropriate for equilibrium iteration within each increment. Alternative methods like the BFGS method, see Appendix A, may be required in some cases.

A first application example is given in the following.

Example 3.2 Simple RC beam

Geometry, discretization, and boundary conditions are chosen as follows:

- Single span beam with $L = 5.0\,\text{m}$, square cross section with width $b = 0.2\,\text{m}$, and height $h = 0.4\,\text{m}$, see Fig. 3.6a.

- Discretization with $n_E = 10$ extended two-node Bernoulli beam elements, see Section 3.3.2.

- Hinge bearing of left-hand and right-hand node, i.e., lateral displacements are zero but rotations are not restricted. The longitudinal displacement of the left node is zero, the right-node displacement is not restricted in the longitudinal direction.
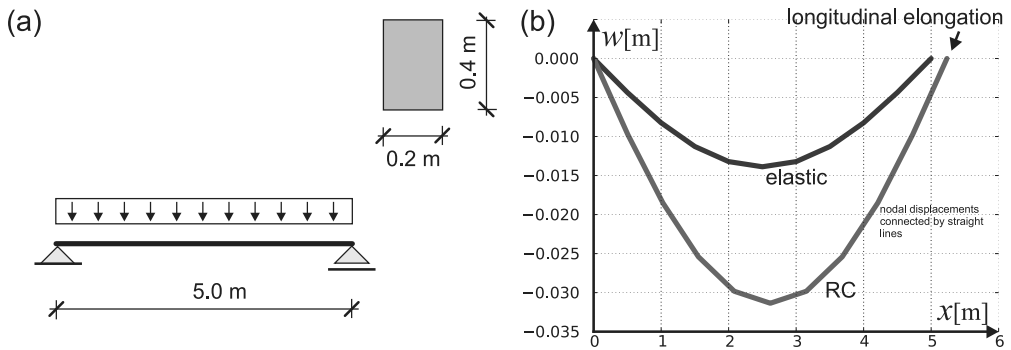
Figure 3.6: Example 3.2 (a) System. (b) Deflection curve at final loading.

The following material properties and loading are assumed:

- Concrete grade C30/37 according to [26, Table 3.1] with an initial Young's modulus $E_c = 33\,000\,\text{MN/m}^2$. Concrete compressive strength is assumed with $f_c = 38\,\text{MN/m}^2$ with $\epsilon_{c1} = -0.0023$, $\epsilon_{cu1} = -0.0035$, see Fig. 2.1. A tensile strength is disregarded. The uniaxial stress–strain curve is chosen according to [26, 3.1.5].

- Reinforcing steel according to [26, 3.2.7] with $f_{yk} = 500\,\text{MN/m}^2$, $f_t = 525\,\text{MN/m}^2$, $\epsilon_{y0} = 0.0025$, $\epsilon_u = 0.025$, see Fig. 2.10a. Reinforcement with $4 \oslash 20$, $A_{s1} = 12.57\,\text{cm}^2$, $d_1 = 5\,\text{cm}$. No compression reinforcement.

- In the same way as demonstrated in Example 3.1 an ultimate moment $M_u \approx 0.20\,\text{MNm}$ is determined with $N = 0$. This leads to uniform ultimate load of $q_u = 8M_u/L^2 = 64\,\text{kN/m}$. A load $q = 60\,\text{kN/m}$ is chosen for the computation.

An incrementally iterative scheme with Newton–Raphson iteration within each loading increment, as described in Section 1.6, is used as the solution method. A loading step $\Delta t = 0.1$ is chosen for time discretization with the final target 1.
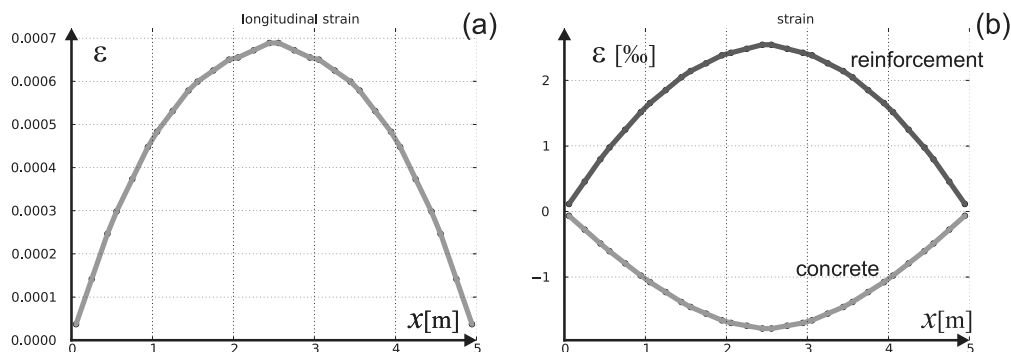
Figure 3.7: Example 3.2 final loading state (a) Strain of reference axis. (b) Upper concrete strain and lower reinforcement strain.

The computation leads to the following results:

– As a statically determined system is given the course of the bending moment can be computed with $M = \frac{q}{2}(l - x)x$ and a mid-span maximum value $M_{\max} = \frac{ql^2}{8} = 0.125\,\mathrm{MNm}$ in this particular case.

  Linear statics can only be approximately applied in the case of statically indeterminate systems as the bending stiffness is no longer constant but depends on internal forces.

– Deflections of cracked concrete beams – even for statically determinate systems – can no longer be determined with linear elastic statics and require methods as have been described before.

  Fig. 3.6b shows the computed deflection curve. The uncracked linear elastic case with a bending stiffness $EJ = 33\,000 \cdot 0.2 \cdot 0.4^3/12 = 35.2\,\mathrm{MNm}$ is shown as comparison. The difference roughly amounts to a factor of 2.4.

– A special property of cracked reinforced cross sections is given by the fact, that the reference axis changes its length even if there is no resulting normal force. In the case of this example, the reference axis and with it the beam becomes slightly longer after loading, see Fig. 3.6b.

  This is connected with longitudinal strains of the reference axis, see Fig. 3.7a. It is caused by a coupling of normal forces to curvature, i.e., $N = N(\kappa, \epsilon)$, see Section 3.1.3, which leads to $\epsilon \neq 0$ for $\kappa \neq 0$ even in the case $N = 0$.

– Finally, the computed strains of the upper compressed concrete edge and the strains of the reinforcement, as they can be determined on the basis of Eq. (3.5), are shown in Fig. 3.7b for the final loading.

  They have to be compared to the concrete strain corresponding to strength $\epsilon_{c1} = -0.0023$ and to steel strain corresponding to yield $\epsilon_y = f_y/E_s = 0.0025$.

_____ End Example 3.2

3.5 Further Aspects of Reinforced Concrete

3.5.1 Creep

Creep leads to increasing deformations of concrete structures regarding the long-term behavior. This concerns the serviceability of structures with moderate levels of loading. Thus, the assumption of linear concrete compressive behavior with the exclusion of concrete tensile strength, see Section 3.1.3.2, is appropriate. Furthermore, viscoelastic material laws according to Section 2.2 can be used to model the creep of cracked RC beams.

We start with collecting previous items. Equations (2.27, 2.28) are applied to concrete

$$\dot{\sigma}_c = E'_c\,\dot{\epsilon}_x + \frac{1}{\zeta_c}\,E'_c\,\epsilon_x - \psi_c\,\sigma_c, \quad \psi_c = \frac{1+\varphi_c}{\zeta_c} \tag{3.119}$$

with longitudinal strains ϵ_x and E'_c according to Eq. (3.24). Reinforcing steel is assumed as linear for moderate loading levels

$$\sigma_s = E_s\,\epsilon_x, \qquad \dot{\sigma}_s = E_s\,\dot{\epsilon}_x \tag{3.120}$$

Kinematics is ruled by Eq. (3.5)

$$\epsilon_x = \epsilon - z\,\kappa, \quad \dot{\epsilon}_x = \dot{\epsilon} - z\,\dot{\kappa} \tag{3.121}$$

Strain of reinforcement is considered with

$$\epsilon_{s1} = \epsilon - z_{s1}\,\kappa, \quad \dot{\epsilon}_{s1} = \dot{\epsilon} - z_{s1}\,\dot{\kappa}, \qquad \epsilon_{s2} = \epsilon - z_{s2}\,\kappa, \quad \dot{\epsilon}_{s2} = \dot{\epsilon} - z_{s2}\,\dot{\kappa} \tag{3.122}$$

according to Eq. (3.21). Finally, regarding Eqs. (3.22, 3.23) internal forces are

$$\begin{aligned}
N_c &= \int_{z_{c1}}^{z_{c2}} \sigma_c\,b\mathrm{d}z \\
N_s &= A_{s1}\,\sigma_{s1} + A_{s2}\,\sigma_{s2} \\
M_c &= -\int_{z_{c1}}^{z_{c2}} \sigma_c\,z\,b\mathrm{d}z \\
M_s &= -A_{s1}\sigma_{s1}\,z_{s1} - A_{s2}\sigma_{s2}\,z_{s2}
\end{aligned} \tag{3.123}$$

and $N = N_c + N_s$, $M = M_c + M_s$. The coordinates z_{c1}, z_{c2} indicate the range of the concrete's compression zone.

Internal forces of concrete $\boldsymbol{\sigma}_c = (\ N_c \quad M_c\ )^T$ will be connected to the concrete edge stresses, of the compression zone $\boldsymbol{\sigma}_{ce} = (\ \sigma_{c1} \quad \sigma_{c2}\ )^T$, see Section 3.1.3.2. A combination of Eqs. (3.44, 3.45, 3.119) yields rates of edge including visco-elasticity or creep of the compression zone:

$$\dot{\boldsymbol{\sigma}}_{ce} = E'_c\,(\mathbf{B}_\epsilon - \kappa\,\mathbf{B}_z)\cdot\dot{\boldsymbol{\epsilon}} + \frac{E'_c}{\zeta_c}\,\mathbf{B}_\epsilon\cdot\boldsymbol{\epsilon} - \psi_c\,\boldsymbol{\sigma}_{ce} \tag{3.124}$$

This is connected to rates of internal forces by Eq. (3.37)

$$\dot{\boldsymbol{\sigma}}_c = \mathbf{A}_\sigma\cdot\dot{\boldsymbol{\sigma}}_{ce} + \mathbf{A}_z\cdot\dot{\mathbf{z}}_c \tag{3.125}$$

with $\mathbf{z}_c = (\ z_{c1} \quad z_{c2} \ )^T$. Combining edge stresses, Eq. (3.124), internal forces (Eq. (3.125)), and regarding Eq. (3.43) connecting rates of $\mathbf{z}_c$ and the generalized beam strains $\boldsymbol{\epsilon}$ leads to

$$
\begin{aligned}
\dot{\boldsymbol{\sigma}}_c &= \mathbf{A}_\sigma \cdot \left[E_c'(\mathbf{B}_\epsilon - \kappa \mathbf{B}_z) \cdot \dot{\boldsymbol{\epsilon}} + \frac{E_c'}{\zeta_c} \mathbf{B}_\epsilon \cdot \boldsymbol{\epsilon} - \psi_c \boldsymbol{\sigma}_{ce} \right] + \mathbf{A}_z \cdot \mathbf{B}_z \cdot \dot{\boldsymbol{\epsilon}} \\
&= \left[E_c' \mathbf{A}_\sigma \cdot \mathbf{B}_\epsilon + (\mathbf{A}_z - \kappa E_c' \, \mathbf{A}_\sigma) \cdot \mathbf{B}_z \right] \cdot \dot{\boldsymbol{\epsilon}} + \frac{E_c'}{\zeta_c} \, \mathbf{A}_\sigma \cdot \mathbf{B}_\epsilon \cdot \boldsymbol{\epsilon} - \psi_c \mathbf{A}_\sigma \cdot \boldsymbol{\sigma}_{ce}
\end{aligned}
\tag{3.126}
$$

The term in the parenthesis in the second line corresponds to the tangential material stiffness $\mathbf{C}_{cT}$ for elastic behavior in the compression zone, see Eq. (3.46). Furthermore, with $\mathbf{A} = \mathbf{A}_\sigma \cdot \mathbf{B}_\epsilon$, $\mathbf{C}_c = E_c' \mathbf{A}$ and $\boldsymbol{\sigma}_{ce} = \mathbf{A}_\sigma^{-1} \cdot \boldsymbol{\sigma}_c$, see Eqs. (3.31, 3.32, 3.35), Eq. (3.126) is written as

$$
\dot{\boldsymbol{\sigma}}_c = \mathbf{C}_{cT} \cdot \dot{\boldsymbol{\epsilon}} + \frac{1}{\zeta_c} \, \mathbf{C}_c \cdot \boldsymbol{\epsilon} - \psi_c \, \boldsymbol{\sigma}_c
\tag{3.127}
$$

whereby $\mathbf{C}_{cT}$, $\mathbf{C}_c$, and $\boldsymbol{\sigma}_c$ in the end are functions of the generalized beam strains $\boldsymbol{\epsilon}$. The material properties are given by Young's modulus E_c' of the compression zone, which is in $\mathbf{C}_{cT}$, $\mathbf{C}_c$, and the creep parameters ζ_c, ψ_c.

The rate of the internal forces of the reinforcement $\boldsymbol{\sigma}_s = (\ N_s \quad M_s \ )^T$ is determined by a combination of Eqs. (3.120, 3.122, 3.123):

$$
\boldsymbol{\sigma}_s = \mathbf{C}_s \cdot \boldsymbol{\epsilon}, \qquad \dot{\boldsymbol{\sigma}}_s = \mathbf{C}_s \cdot \dot{\boldsymbol{\epsilon}}
\tag{3.128}
$$

with

$$
\mathbf{C}_s = E_s \left[\begin{array}{cc} A_{s1} + A_{s2} & -A_{s1} z_{s1} - A_{s2} z_{s2} \\ -A_{s1} z_{s1} - A_{s2} z_{s2} & A_{s1} z_{s1}^2 + A_{s2} z_{s2}^2 \end{array} \right]
\tag{3.129}
$$

Adding concrete and reinforcement contributions $\boldsymbol{\sigma} = \boldsymbol{\sigma}_c + \boldsymbol{\sigma}_s$, $\dot{\boldsymbol{\sigma}} = \dot{\boldsymbol{\sigma}}_c + \dot{\boldsymbol{\sigma}}_s$ yields

$$
\dot{\boldsymbol{\sigma}} = \left[\mathbf{C}_{cT} + \mathbf{C}_s \right] \cdot \dot{\boldsymbol{\epsilon}} + \left[\frac{1}{\zeta_c} \, \mathbf{C}_c + \psi_c \, \mathbf{C}_s \right] \cdot \boldsymbol{\epsilon} - \psi_c \, \boldsymbol{\sigma}
\tag{3.130}
$$

This forms a system of ordinary differential equations of first order for $\boldsymbol{\sigma}$ depending on time t driven by $\boldsymbol{\epsilon}(t), \dot{\boldsymbol{\epsilon}}(t)$. Strains generally come from a superordinated calculation. Equation (3.130) is a specification of Eqs. (1.76, 1.83)

$$
\dot{\boldsymbol{\sigma}} = \mathbf{C}_T \cdot \dot{\boldsymbol{\epsilon}} + \boldsymbol{\Sigma}, \qquad \boldsymbol{\Sigma} = \mathbf{V} \cdot \boldsymbol{\epsilon} - \mathbf{W} \cdot \boldsymbol{\sigma}
\tag{3.131}
$$

with

$$
\begin{gathered}
\boldsymbol{\sigma} = \begin{pmatrix} N \\ M \end{pmatrix}, \quad \boldsymbol{\epsilon} = \begin{pmatrix} \epsilon \\ \kappa \end{pmatrix} \\
\mathbf{C}_T = \mathbf{C}_{cT} + \mathbf{C}_s \\
\mathbf{V} = \frac{1}{\zeta_c} \, \mathbf{C}_c + \psi_c \, \mathbf{C}_s, \quad \mathbf{W} = \psi_c \, \mathbf{I}
\end{gathered}
\tag{3.132}
$$

with the unit matrix $\mathbf{I}$. This is embedded into the incrementally iterative solution method for transient analysis, see Section 1.6, using Eqs. (1.86–1.89). The application is demonstrated with the following example.

Example 3.3 Creep deformations of RC beam

Geometry, boundary conditions, and discretization are adopted from Example 3.2, see Fig. 3.6a. The following material properties are assumed:

– Concrete grade C 30/37 according to [26, Table 3.1] without tensile strength with a Young's modulus $E_c = 33\,000\,\mathrm{MN/m^2}$ in the compressive range. Creep properties with $\varphi = 2.0$ and $t^\star = 100$ [d] for $\alpha = 0.5$, i.e., half of total creep occurs after 100 days for a constant stress load. With Eq. (2.36) $\zeta = 144\,\mathrm{d}$ and with Eq. (3.119) $\psi = 0.020793\,\mathrm{1/d}$.

– Reinforcement with 4 $\oslash$ 20, $A_{s1} = 12.57\,\mathrm{cm^2}$, $d_1 = 5\,\mathrm{cm}$. Young's modulus is $E_s = 200\,000\,\mathrm{MN/m^2}$ for the reinforcing steel.

The loading and the resulting loading level are determined as follows:

– According to Example 3.2 the ultimate limit moment of the cross section is given by $M_u \approx 0.20\,\mathrm{MNm}$ corresponding to a uniform load of $60\,\mathrm{kN/m}$. Roughly a third of this is assumed to occur as a permanent load under service conditions, therefore $p = 20\,\mathrm{MN/m}$. This leads to a maximum bending moment of $M = 0.0625\,\mathrm{MNm}$.

– The absolute value of the corresponding concrete strain is estimated as a third of the maximum absolute concrete strain of Example 3.2, see Fig. 3.7b leading to $\epsilon_c \approx -0.6‰$. This has to be compared with the strain at strength $\epsilon_{c1} = -2.3‰$, see Fig. 2.1, for C 30/37. A linear concrete behavior can obviously be assumed in the compressive range and the loading level can be regarded as moderate.

Thus, the prerequisite of creep modeling as stated at the beginning of this section is fulfilled. A time step $\Delta t = 10\,\mathrm{days}$ is chosen for time discretization. An incrementally iterative with Newton–Raphson iteration within each time increment is used for solving as is described in Section 1.6. A period of 500 days is regarded. This leads to the following results:

– Fig. 3.8 shows the computed mid-span deflection in the course of time. The short-term uncracked linear elastic deflection value ($EJ = 31\,900 \cdot 0.2 \cdot 0.4^3/12 = 34.03\,\mathrm{MNm}$) is given for comparison to cracked short-term and long-term deflection values.
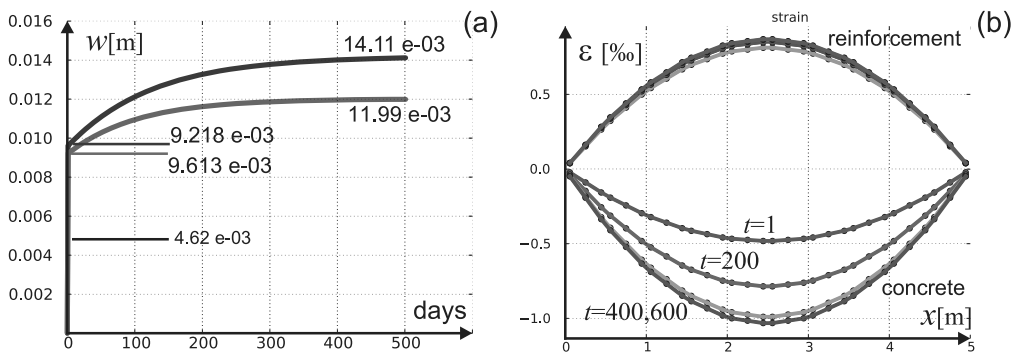
Figure 3.8: Example 3.3 (a) Mid-span deflection during time. (b) Concrete and reinforcement strains along beam for certain time steps.

– Influence of concrete creeping can be characterized as follows: concrete contraction becomes larger with a constant concrete stress, while reinforcement extension remains the same. This leads to an increasing curvature, see Eq. (3.18), and an increasing deflection. But the increase factor is less than $1 + \varphi$ due to bending and reinforcement. Small variations of stresses and reinforcement strain result from a small change of the internal lever arm.

– As a variation, the influence of a compressive reinforcement $2 \oslash 20, A_{s2} = 6.28 \, \text{cm}^2$, $d_2 = 5 \, \text{cm}$ is regarded. It can be seen, that a compressive reinforcement further reduces long-term creep deflections, as concrete deformations are constrained to some extent.

——————————————————————————————— *End Example 3.3*

For the treatment of creep problems, see also [84, Chapter 29]. The creep model may be combined with modeling of imposed strains, see Section 3.5.2, and prestressing, see Section 3.6.

3.5.2   Temperature and Shrinkage

Imposed deformations due to temperature or shrinkage may lead to constraint stresses. This has to be considered for ultimate limit states and serviceability. Uniaxial considerations for imposed deformations, see Section 2.2, can be directly transferred to strains and stresses of beams.

According to Eq. (2.32) rates of measurable longitudinal strains are given by

$$\dot{\epsilon}_x = \frac{1}{E_T} \, \dot{\sigma}_x + \dot{\epsilon}_{Ix}, \qquad \dot{\epsilon}_{Ix} = \dot{\epsilon}_{Tx} + \dot{\epsilon}_{cs,x} \tag{3.133}$$

with the longitudinal stress σ_x, the tangential modulus E_T, temperature strains ϵ_{Tx}, see Eq. (2.31), and shrinkage strains $\epsilon_{cs,x}$. leading to

$$\dot{\sigma}_x = C_T \, (\dot{\epsilon}_x - \dot{\epsilon}_{Ix}) \tag{3.134}$$

A linear variation of imposed longitudinal strains is assumed over the height of a beam cross section according to Eq. (3.5)

$$\epsilon_{Ix}(z) = \epsilon_I - z \, \kappa_I \tag{3.135}$$

The imposed strain of the reference axis ϵ_I and imposed curvature κ_I can be determined with the prescribed imposed strains $\epsilon_{I1}, \epsilon_{I2}$ of bottom and top edge of the cross section. The reference axis is placed in the midpoint of a cross-section height without loss of generality, see Section 3.1.3.1. Thus, the imposed strain of the reference axis is given by

$$\epsilon_I = \frac{\epsilon_{I1} + \epsilon_{I2}}{2} \tag{3.136}$$

With the cross-section height h the imposed curvature is given by

$$\kappa_I = \frac{\epsilon_{I1} - \epsilon_{I2}}{h} \tag{3.137}$$

in accordance to Eq. (3.18). Equation (3.135) yields $\epsilon_{Ix}(-h/2) = \epsilon_{I1}$, $\epsilon_{Ix}(h/2) = \epsilon_{I2}$ with these definitions.

The rate of the longitudinal stress (Eq. (3.134)) can be directly integrated in the linear elastic case $E_T = E_0 = const.$

$$\sigma_x = E_0 \left(\epsilon_x - \epsilon_{Ix} \right) \tag{3.138}$$

Using kinematics according to Eq. (3.5), internal forces relations (3.9) and cross-section properties (Eq. (3.11)) finally yields

$$\boldsymbol{\sigma} = \mathbf{C} \cdot (\boldsymbol{\epsilon} - \boldsymbol{\epsilon}_I) = \mathbf{C} \cdot \boldsymbol{\epsilon} - \boldsymbol{\sigma}_I \tag{3.139}$$

with

$$\boldsymbol{\sigma} = \left(\begin{array}{c} N \\ M \end{array} \right), \quad \mathbf{C} = E_0 \left[\begin{array}{cc} A & -S \\ -S & J \end{array} \right], \quad \boldsymbol{\epsilon} = \left(\begin{array}{c} \epsilon \\ \kappa \end{array} \right) \tag{3.140}$$

and the generalized imposed strains and *internal constraint forces*

$$\boldsymbol{\epsilon}_I = \left(\begin{array}{c} \epsilon_I \\ \kappa_I \end{array} \right), \qquad \boldsymbol{\sigma}_I = \mathbf{C} \cdot \boldsymbol{\epsilon}_I \tag{3.141}$$

As internal forces lead to internal nodal forces, see Eqs. (1.9, 3.101), internal constraint forces lead to constraint nodal forces

$$\mathbf{f}_{eI} = \int_{L_e} \mathbf{B}^T \cdot \boldsymbol{\sigma}_I \, \mathrm{d}x \tag{3.142}$$

Imposed strains $\boldsymbol{\epsilon}_I$ and therefore also constraint forces are prescribed as, e.g., function of time. Thus, constraint nodal forces are also prescribed.

- Constraint forces from imposed strains may be shifted from the internal left-hand side of the discretized equilibrium condition, see e.g., Eq. (1.8), to the right-external load side becoming part of the external nodal forces.

This approach can also be used for nonlinear material behavior. Rates of internal constraint forces are given by

$$\dot{\boldsymbol{\sigma}}_I = \mathbf{C}_T \cdot \dot{\boldsymbol{\epsilon}}_I \tag{3.143}$$

in the case of nonlinear material behavior corresponding to Eq. (1.50) and are regarded within the incrementally iterative scheme, see Section 1.6. The integration of $\dot{\boldsymbol{\sigma}}_I$ or Eq. (3.143) is performed in the way as is done with $\dot{\boldsymbol{\sigma}}$ or Eq. (1.73) using Eq. (1.75). The resulting constraint forces are larger for stiff materials or smaller for soft materials through the influence of $\mathbf{C}_T$.

The influence of imposed strains in form of temperature strains is demonstrated with the following example.

Example 3.4 Effect of temperature actions on an RC beam
We refer to Example 3.2 with the same system with the exception of boundary conditions. The original system is statically determinate and thus will have not imposed forces in the case of temperature actions. It will be changed into a statically indeterminate system through changed boundary conditions. Furthermore, the amount of upper reinforcement is increased. The following data are changed or added compared to Example 3.2:

– Left and right node are totally constrained, i.e., lateral and longitudinal displacements and rotations are set to zero.

– Upper and lower reinforcement with $A_{s1} = A_{s2} = 12.57\,\mathrm{cm}^2$, $d_1 = d_2 = 5\,\mathrm{cm}$.

– Thermal expansion coefficient is chosen with $\alpha_T = 1 \cdot 10^{-5}\,\mathrm{K}^{-1}$ both for concrete and reinforcement.

The same type of nonlinear material behavior is assumed for concrete and reinforcement as in Example 3.2 with concrete tensile strength neglected. A corresponding linear elastic case is regarded as a reference case with a Young's modulus $E = 33\,000\,\mathrm{MN/m^2}$ and a bending stiffness $EJ = 35.2\,\mathrm{MNm^2}$. Two load cases are investigated:

1. Dead and service load with $q = 20\,\mathrm{kN/m}$ as in Example 3.3.

2. Dead and service load together with temperature loading on the lower edge with $T_1 = -10\,\mathrm{K}$ and on the upper edge with $T_2 = 10\,\mathrm{K}$. Such a temperature gradient would cause an upward movement of a statically indeterminate system, i.e., a positive constraint has to be applied to reach compatibility with the zero rotation of boundaries.

   In the case of physical nonlinearities all loadings have to considered together as a superposition is not allowed.

The incrementally iterative scheme is chosen as solution method, see Section 1.6, with the BFGS method for equilibrium iteration in each load increment. This leads to the following computation results:

– Fig. 3.9a shows the bending moments for the linear elastic reference case whereby the reinforcement is neglected. Load case 1 has an end moment $M_e = -0.0402\,\mathrm{MNm}$ and a field moment $M_f = 0.0209$, which agrees with the analytic solution $-qL^2/12$ and $qL^2/24$, respectively. Small differences may arise as moments are determined in integration points of elements in finite element calculations.

   Load case 2 can be superposed due to linearity with a constant $M^{\mathrm{tem}} = -EJ\,\kappa^{\mathrm{tem}}$ with $\kappa^{\mathrm{tem}} = \alpha_T(T_1 - T_2)/h = -0.5 \cdot 10^{-3}$ leading to $M^{\mathrm{tem}} = 0.0176$.

– Fig. 3.9b shows the bending moments for the case of RC.

   First of all distribution of moments in a statically indeterminate system depend on stiffness relations. Those depend on loading in the case of RC. For RC the bending
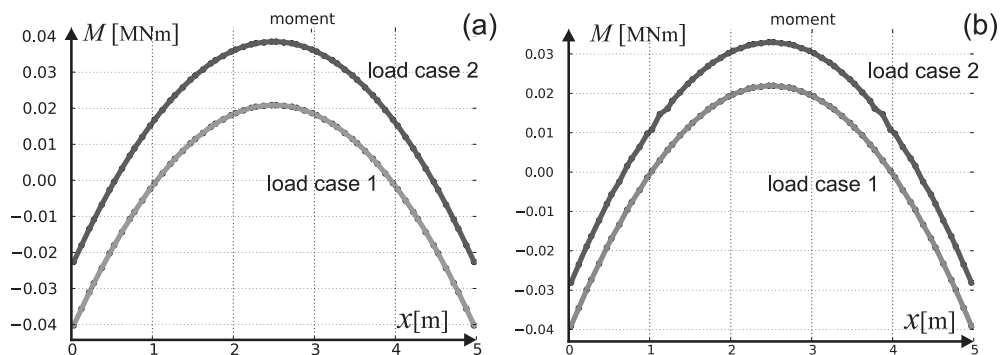
Figure 3.9: Example 3.4 bending moments. (a) Linear elastic. (b) RC (different scale!).
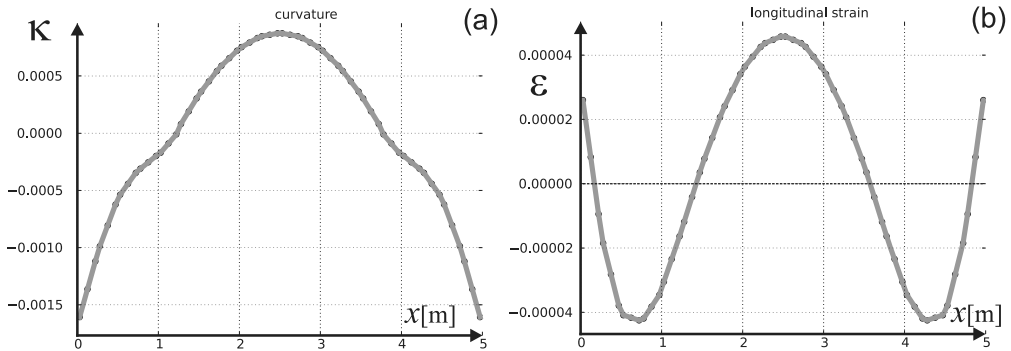
Figure 3.10: Example 3.4 RC. (a) Curvature (b) Strain of the reference axis.

stiffness is generally lower compared to the linear elastic case, but the stiffness relations do not differ very much. Thus, we get $M_e = -0.0391$, $M_f = 0.0220$ in load case 1 for RC, i.e., the field area is somehow stiffer and attracts bending moments.

The computed mid-span deflection is $w_{\max} = 1.23\,\text{cm}$ in load case 1 for RC and is higher compared to the linear elastic case with $w_{\max} = qL^4/384EJ = 0.92\,\text{cm}$ due to overall reduced stiffness.

Superposing is not allowed for load case 2 due to the physical nonlinearities of RC. Computed total moments are $M_e = -0.0281$, $M_f = 0.0330$ leading to imposed moments $M_e^{\text{tem}} = 0.0391 - 0.0281 = 0.0110$, $M_f^{\text{tem}} = -0.0220 + 0.0330 = 0.0114$. The additional temperature moment is lower compared to the linear elastic case. A computation with temperature loading alone without other loading would lead to a constant $M^{\text{tem}} = 0.0143$, i.e., a superposition would not be correct.

– Figure 3.10 shows the deformation state for RC for load case 2.

For the curvature along the beam, see Fig. 3.10a. The course is no longer analog to the bending moment course as it would be in the linear elastic case.

Figure 3.10b shows the strain of the reference and center axis, respectively. Such strains arise in contrast to the linear elastic case, as cracked RC beams tend to elongate without longitudinal displacement restrictions. An overall elongation is not allowed in the example due to boundary conditions, i.e., a normal compressive force is induced on one hand, and on the other hand strain values occur depending on M/N-ratio. But the integral of strains must sum up to zero.

End Example 3.4

As has already been shown in Example 2.2 constraint forces are reduced by creep regarding the long-term behavior. Regarding beams this may be modeled by a combination of methods of Examples 2.2 and 3.4. This requires the prescription of temperature and/or shrinkage histories.

3.5.3   Tension Stiffening

A model for the tension zone of a bending beam, see Fig. 3.2, is given by the reinforced tension bar which has been discussed in Section 2.6. Such a bar shows a cracking pattern whereby cracks arise with specific distances. Such a pattern will also arise in the tension zone of RC beams. A simple example is shown in Fig. 3.11 with a single span beam with a constant moment in its center area and stabilized cracking. Crack spacing in connection with bond, i.e., a transmission of forces between reinforcement and concrete, leads to the effect of tension stiffening. Due to bond concrete carries tensile stresses between cracks up to its tensile strength.
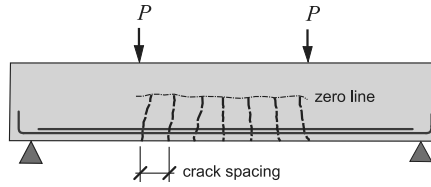
Figure 3.11: Crack pattern of RC beam with constant moment.

These mechanisms have already been discussed with the example of the reinforced tension bar in Section 2.7. The same mechanisms are active in the tensile zone of beams. A quantitative model works with the reduction of reinforcement strains between cracks, i.e., reinforcement strains in cracks are replaced by reinforcement mean strains while the peak values of reinforcement stresses in cracks are still used. This leads to the following modified stress–strain relations for the reinforcement, see Eqs. (2.62, 2.66), whereby σ_{sc} is replaced by σ_s and ϵ_{sm} is replaced by ϵ_s

$$
\sigma_s = \begin{cases}
\dfrac{\alpha f_{ct}}{\varrho_{\text{eff}} \epsilon_s'} \, \epsilon_s & \text{for} \qquad \epsilon_s \leq \epsilon_s' \\[2ex]
E_s \, \epsilon_s + \beta_t \, \dfrac{f_{ct}}{\varrho_{\text{eff}}} & \epsilon_s' < \epsilon_s \leq \epsilon_y \\[2ex]
f_y + E_T \left(\epsilon_s - \epsilon_y \right) & \epsilon_y < \epsilon_s
\end{cases}
\tag{3.144}
$$

with the reinforcement yield stress f_y and

$$
\epsilon_s' = \frac{1}{E_s} \frac{f_{ct}}{\varrho_{\text{eff}}} (\alpha - \beta_t), \qquad \epsilon_y = \frac{1}{E_s} \left(f_y + \beta_t \frac{f_{ct}}{\varrho_{\text{eff}}} \right)
\tag{3.145}
$$

and with k according to Eq. (2.64). The relation is shown in Fig. 2.17b and leads to a nominal stiffening of a rebar's stress–strain relation.

For the discussion of the parameters β_t, α, ϱ_{eff} see Section 2.7. A basic parameter is given by β_t, which controls the quality of bond. The value $\beta_t = 0$, e.g., indicates no stress transfer from rebar to concrete and no effective bond. This leads to $\epsilon_s' = \alpha f_{ct}/\varrho_{\text{eff}}$, $\epsilon_y = f_y/E_s$ and retains the relation $\sigma_s = E_s \, \epsilon_s$. A reasonable choice for this parameter is $\beta_t = 0.4$.

It has to be regarded that the tension zone of a beam cross section exposed to bending is not homogeneous as tension on one side gradually changes into compression on the other side. This is considered through the effective concrete cross-sectional area $A_{c,\text{eff}}$ and the

effective reinforcement ratio $\varrho_{\text{eff}} = A_s/A_{c,\text{eff}}$ with the reinforcement cross-sectional area A_s. The value of $A_{c,\text{eff}}$ is smaller than the area of the tensile zone as not all of its parts contribute to the exchange of stresses with the reinforcement but only some neighborhood around the main tensile reinforcement. Code provisions are given for the choice of $A_{c,\text{eff}}$, see [26, 7.3.2], which are based on more elaborated models, parameter studies and experimental data.

Finally, the parameter α covers the range of crack formation starting with the first crack and ending with stabilized cracking. The parameter indicates the increase factor of the reinforcement stress during crack formation and can be assumed with $\alpha \approx 1.3$ due to parameter studies and experimental data.

Equation (3.144) may replace $\sigma_s = E_s\,\epsilon_s$ in Eqs. (3.22, 3.23) and all which is derived from these equations. The tangential material stiffness has to be adjusted in a corresponding way to reach convergence in equilibrium iterations. The application is demonstrated with the following example.

Example 3.5 Effect of tension stiffening on an RC beam with external and temperature loading
We refer to *Example 3.2* with the same data. Additionally to the material values of Example 3.3 the following values are assumed to model tension stiffening

$$f_{ct} = 3.0\,\text{MN/m}^2, \quad \beta_t = 0.6, \quad \alpha = 1.3 \tag{3.146}$$

The effective cross-sectional area is determined with an effective height of $h_{c,ef} = 0.1\,\text{m}$ according to [26, 7.3.2] leading to $A_{c,\text{eff}} = b\,h_{c,ef} = 0.02\,\text{m}^2$ and further to

$$\varrho_{\text{eff}} = \frac{0.1257 \cdot 10^{-2}}{0.02} = 0.063, \quad \epsilon'_{sm} = 0.215 \cdot 10^{-3} \tag{3.147}$$

with ϵ'_{sm} according to Eq. (2.65). Three loading values are examined: $q = 60\,\text{kN/m}$, which is near to the ultimate limit load, furthermore $q = 40\,\text{MN/m}$ and finally $q = 20\,\text{MN/m}$ which roughly corresponds to dead load and service load. The mid-span deflections with and without tension stiffening are determined with

	$q = 20$	$q = 40$	$q = 60$
with tension stiffening	0.83	1.86	2.98
without tension stiffening	0.98	2.01	3.13

with a deflection unit of [cm]. The absolute deflection difference for the same loading is constant. Thus, the influence of tension stiffening is larger for lower loading levels. This corresponds to the constant horizontal offset of stress–strain relation for the reinforcement.

As beam stiffness is increased due to tension stiffening an influence on constraint forces may be supposed. To examine this effect, we refer to *Example 3.4*. All system and loading parameters are kept but with tension stiffening included. The tension-stiffening parameters of Eqs. (3.146, 3.147) are used. Load case 2 – dead/service load and temperature – is regarded. Figure 3.12a shows the computed bending moments for the cases with and without tension stiffening. The difference is quite small as the stiffness relations basically do not change even if the absolute values of stiffness change.
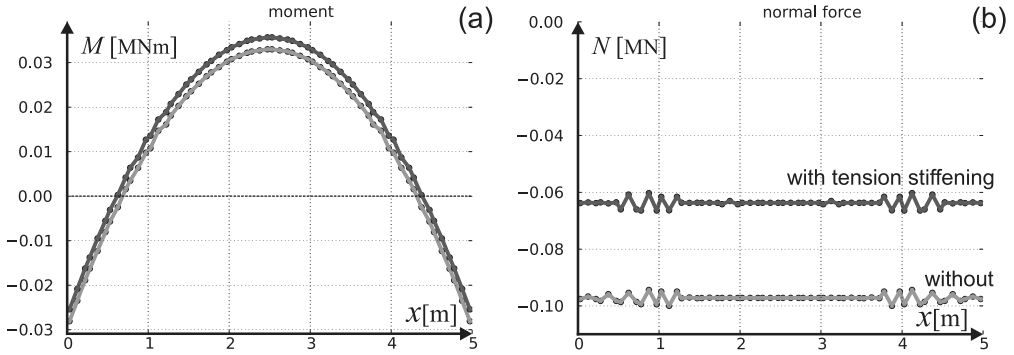
Figure 3.12: Influence tension stiffening Example 3.5. (a) Moment. (b) Normal force.

The induced compression normal force is shown as a further result in Fig. 3.12b. A compression is caused from the potential elongation of the reference axis of cracked RC section, see Fig. 3.6b, which is prevented by boundary conditions in this case. The potential elongation is smaller in case with tension stiffening as the same moment has a smaller mean rebar strain compared to the case without tension stiffening. This induces a smaller compression in case with tension stiffening.

Some scatter is seen in the normal forces especially in those areas with low moments. This scatter is caused by the coupling of both normal forces and moments to the strain of the reference axis ϵ and the curvature κ, see Eq. (3.55). This scatter effect is erroneous. It is compensated in the balance of nodal forces as the obvious peak values are computed in the integration points which compensate in the average of an element. This effect can be reduced with a finer discretization.

End Example 3.5

3.5.4 Shear Stiffness for Reinforced Cracked Concrete Sections

Up to now a shear stiffness has been derived for the linear elastic material behavior only, see Eq. (3.15) and the relation between the shear force V and the shear angle γ. This bases upon the linear elastic relation between shear stresses and shear strains derived from plane elasticity, see Eq. (3.7)$_3$. The shear behavior of cracked RC sections has to be derived from the truss model for shear instead [26, 6.2.3]. A square cross section is assumed with geometric height h and width b to simplify the discussion.

The model has *concrete struts* and *reinforcement ties*. The geometry of struts is shown in Fig. 3.13a. The strut geometry is characterized by a bunch of lines inclined with an angle θ against the reference axis within a part z of the cross-section height.

- The length z corresponds to the internal lever arm of bending as the distance of compression chord and tensile chord.

Regarding such a strut line its undeformed length is given by

$$l_u = \frac{z}{\sin \theta} \tag{3.148}$$
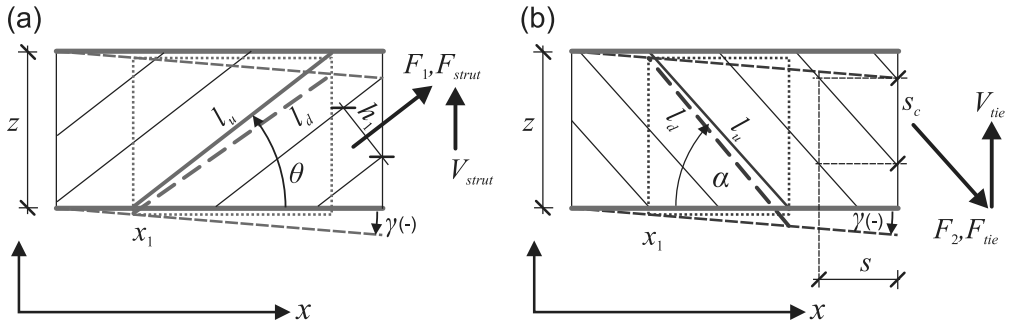
Figure 3.13: Shear stiffness (a) Struts. (b) Ties.

A rotation ϕ of the cross section is not regarded. Thus, the inclination of the reference axis corresponds to the shear angle γ, see Fig. 3.13a. With a reference to a longitudinal coordinate x_1 a cross section moves laterally over a length $z/\tan\theta$ by $\gamma \, z/\tan\theta$ and the deformed length of the respective strut is given by

$$l_d = \sqrt{\left(\frac{z}{\tan\theta}\right)^2 + \left(z + \frac{z}{\tan\theta}\gamma\right)^2} \tag{3.149}$$

whereby sign convention for γ has to be considered. With $\gamma \ll 1$ this may be written as

$$l_d = l_u \sqrt{1 + 2\gamma \sin\theta \cos\theta} \tag{3.150}$$

whereby γ^2 has been neglected. The strut strain is given by

$$\epsilon_1 = \frac{l_d - l_u}{l_u} = \sqrt{1 + 2\gamma \sin\theta \cos\theta} - 1 \tag{3.151}$$

The root term is expanded with a Taylor series. As $\gamma \ll 1$, this leads to

$$\epsilon_1 = \sin\theta \cos\theta \; \gamma \tag{3.152}$$

A corresponding strut force has to be determined next. A linear material behavior with Young's modulus E is assumed. Furthermore, a strut has a width b and a height h_1 in its own cross section and the strut force is given by

$$F_1 = b h_1 \, E \, \epsilon_1 = b h_1 \, E \, \sin\theta \cos\theta \; \gamma \tag{3.153}$$

whereby in case of $\gamma > 0$ forces F_1, F_2 are directed as shown in Figures 3.13. A cross section of the beam involves $n = \frac{z}{h_1/\cos\theta}$ struts, see Fig. 3.13b. Summing up all strut forces of a cross section leads to

$$F_{\text{strut}} = n \, F_1 = \frac{z}{h_1/\cos\theta} \, F_1 = b z \, E \, \sin\theta \cos^2\theta \; \gamma \tag{3.154}$$

To have equilibrium a shear force and a strut force are related by $V = F_1 \sin\theta$. Thus, shear forces from struts are given by

$$V_{\text{strut}} = bz\, E\, \sin^2\theta \cos^2\theta\ \ \gamma \tag{3.155}$$

and finally a shear stiffness from struts

$$\frac{\partial V_{\text{strut}}}{\partial \gamma} = E\, bz\, \sin^2\theta \cos^2\theta \tag{3.156}$$

is derived.

The contribution of shear reinforcement or ties to the shear stiffness can be derived in the same way. A tie with an inclination α is considered, see Fig. 3.13a. It has an undeformed length

$$l_u = \frac{z}{\sin\alpha} \tag{3.157}$$

a deformed length

$$l_d = \sqrt{\left(\frac{z}{\tan\alpha}\right)^2 + \left(z - \frac{z}{\tan\alpha}\gamma\right)^2} = l_u\,\sqrt{1 - 2\gamma\sin\alpha\cos\alpha} \tag{3.158}$$

whereby the sign convention for γ again has to be considered and a strain

$$\epsilon_2 = \frac{l_d - l_u}{l_u} = \sqrt{1 - 2\gamma\sin\alpha\cos\alpha} - 1 \approx -\sin\alpha\cos\alpha\ \ \gamma \tag{3.159}$$

A linear elastic behavior with a Young's modulus E_s is assumed. With a cross section A_s of the tie or rebar the force is given by

$$F_2 = A_s\, E_s\, \epsilon_2 = -A_s\, E_s\, \sin\alpha\cos\alpha\ \ \gamma \tag{3.160}$$

The spacing s_c of rebars in a beam cross section and their longitudinal spacing s are related by $s_c/s = \tan\alpha$. Thus, a cross section involves $n = z/s_c = z/(s\tan\alpha)$ rebars. Summing up all ties involved in a cross section leads to

$$F_{tie} = \frac{z}{s_c/\tan\alpha}\, F_2 = -z\, \frac{A_{s2}}{s}\, E_s\, \sin^2\alpha\cos\alpha\ \ \gamma \tag{3.161}$$

A shear force and a tie force are related by $V = -F_2 \sin\alpha$ for equilibrium. Thus, shear forces from ties are given by

$$V_{tie} = z\, a_{s2}\, E_s\, \sin^3\alpha\cos\alpha\ \ \gamma \tag{3.162}$$

with $a_s = A_s/s$ and finally a shear stiffness from ties is

$$\frac{\partial V_{tie}}{\partial \gamma} = z\, a_{s2}\, E_s\, \sin^3\alpha\cos\alpha \tag{3.163}$$

Finally, the total shear stiffness is given by

$$\frac{\partial V}{\partial \gamma} = \frac{\partial V_{\text{strut}}}{\partial \gamma} + \frac{\partial V_{tie}}{\partial \gamma} = z\,\left(b\, E_c\, \sin^2\theta \cos^2\theta + a_{s2}\, E_s\, \sin^3\alpha\cos\alpha\right) \tag{3.164}$$

As a special case we consider stirrups as ties with $\alpha = \pi/2$ and a strut inclination $\theta = \pi/4$. This leads to a shear stiffness

$$\frac{\partial V}{\partial \gamma} = \frac{1}{4}\, zb\, E_c = \frac{1}{2}\, zb\, G_c \tag{3.165}$$

with the shear modulus G_c according to Eq. (3.8). We compare this with the linear elastic case, Eq. $(3.13)_3$, with a geometry coefficient α. Here a relation $zb = \alpha_c A$, $\alpha_c = z/h$ is used with a similar geometry coefficient α_c. Thus, relations $(3.13)_3$ and (3.165) differ by a factor of 2. In the current argument, concrete tensile struts are disregarded due to the limited tensile strength of concrete and shear reinforcement was assumed as vertical stirrups, which do not directly contribute to V. Thus, the current setup and the linear elastic case coincide for $\theta = \pi/4$.

There is some margin to choose the concrete shear strut angle, see [26, 6.2.3], [18, 7.3.3.3]. The limits are roughly by a range $20° \leq \theta \leq 45°$. As a first estimation, the same strut angle should be used as for the design of the stirrups.

3.6 Prestressing

Prestressing applies lateral redirection forces and normal forces on a beam, see Fig. 3.14. While the redirection forces act against dead and variable loads a moderate normal force may increase the bearing capacity for moments, see Example 3.1. But these positive effects involve demands for prestressing tendons. A concrete beam and its untensionend reinforcement on one hand and the tendons with high strength steel on the other hand are regarded as separated structural elements in the following.

Originally, the generalized stress $\boldsymbol{\sigma}$ is formulated as a function of the generalized deformations $\boldsymbol{\epsilon}$, e.g.,

$$\boldsymbol{\sigma} = \mathbf{C} \cdot \boldsymbol{\epsilon} \tag{3.166}$$

For $\mathbf{C}$ see, e.g., Eq. (3.140). The linearity of $\mathbf{C}$ is not necessarily required. This concept is extended with respect to prestressing, i.e., an additional part is assigned to the generalized stresses resulting from *prestressing tendons*

$$\boldsymbol{\sigma} = \mathbf{C} \cdot \boldsymbol{\epsilon} + \boldsymbol{\sigma}^p \tag{3.167}$$
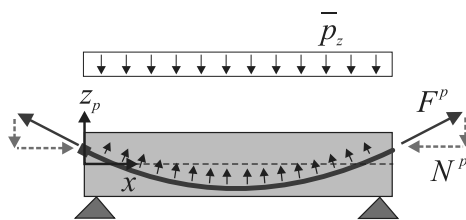
Figure 3.14: Redirection forces from prestressing.

This additional part depends on the tendon profile. In the case of the Bernoulli beam

$$\boldsymbol{\sigma}^p = \left(\begin{array}{c} N^p \\ M^p \end{array} \right) = -F^p \left(\begin{array}{c} \cos \alpha_p \\ -z_p \cos \alpha_p \end{array} \right) \tag{3.168}$$

compare Eq. (3.68), with the prestressing force F^p, the height coordinate or lever arm z_p of the tendon, and the inclination $\alpha_p = \mathrm{d}z_p/\mathrm{d}x$ of the tendon against the beam reference axis. This may be extended with respect to shear forces in combination with the Timoshenko beam. Using the extended generalized stresses (Eq. (3.167)) for the internal nodal forces (Eq. (3.101)) leads to a split

$$\mathbf{f}_e = \int_{L_e} \mathbf{B}^T \cdot \boldsymbol{\sigma} \, \mathrm{d}x = \int_{L_e} \mathbf{B}^T \cdot \mathbf{C} \cdot \boldsymbol{\epsilon} \, \mathrm{d}x + \int_{L_e} \mathbf{B}^T \cdot \boldsymbol{\sigma}^p \, \mathrm{d}x = \mathbf{f}_e^\epsilon + \mathbf{f}_e^p \tag{3.169}$$

The part $-\mathbf{f}_e^p$ may be regarded as a further contribution to the load vector, see Eq. (1.69). This approach integrates prestressing in the given framework whereby all procedures but for a part of load evaluation remain unchanged.

An alternative and conventional view of prestressing of beams is based on Eq. (3.58). We consider the quasistatic case, split internal forces into a part $\bullet^\epsilon$ from beam deformation, a part $\bullet^p$ from prestressing and eliminate shear forces

$$\begin{aligned} -N^{\epsilon\prime} - N^{p\prime} &= \bar{p}_x \\ -M^{\epsilon\prime\prime} - M^{p\prime\prime} &= \bar{p}_z \end{aligned} \tag{3.170}$$

Furthermore, Eq. (3.168) is used leading to

$$\begin{aligned} -N^{\epsilon\prime} &= \bar{p}_x - \left(F^p \cos \alpha_p \right)' \\ -M^{\epsilon\prime\prime} &= \bar{p}_z + \left(z_p F^p \cos \alpha_p \right)'' \end{aligned} \tag{3.171}$$

The weak form of these differential equations, see Section 3.2, conforms to Eqs. (3.167, 3.168).

A common approximation is $F^p \approx const.$, $\cos \alpha_p \approx 1$ resulting in

$$- M^{\epsilon\prime\prime} = \bar{p}_z + z_p'' F^p \tag{3.172}$$

wherein $z_p'' F^p$ is a lateral redirection force in the z-direction from the curvature z_p'' of the tendon geometry. This term may be seen as an additional lateral loading counteracting the other loadings, see Fig. 3.14 with negative $\bar{p}_z$.

Some characteristic properties of prestressing have to be regarded for the evaluation of $\boldsymbol{\sigma}_p$ or $\mathbf{f}^p$, respectively:

– Tendon profile parameters z_p, α_p may vary with the beam coordinate x according to prestressing design.

– The prestressing force may vary due to the loss of prestress from friction of the tendon in a conduit.

– Furthermore, a beam deformation may lead to a change in the tendon profile after application and fixing of prestressing. Two cases have to be considered:

1. *Prestressing without bond*: total length of the tendon changes. This leads to a global change of the prestressing force.

2. *Prestressing with bond*: length of the tendon changes locally to keep the geometric compatibility with the concrete. This leads to locally varying changes in the prestressing force.

Two subsequent stages have to be considered for prestressing:

– Application stage of prestressing with the prescribed prestressing force F_0^p

Prestressing is gradually applied at a beam's ends through anchors. The value of F_0^p may vary along the longitudinal beam coordinate x due to friction losses. Such losses have to determined from prescribed friction coefficients and the curvature of the tendon geometry. Tendons are grouted at the end of this stage in the case of prestressing with bond.

– Fixed stage of prestressing with locked anchors

The prestressing force F_0^p changes into F_p according to the enumeration above concerning with/without bond. Different approaches are necessary to describe the global or local change of the tendon geometry for the both cases in this stage.

The tendon geometry plays a key role within this context. It may be described for each finite beam element in analogy to the Bernoulli beam shape function (Eq. (3.76)) with

$$z_p = \left[\frac{r^3}{4} - \frac{3r}{4} + \frac{1}{2} \quad \frac{L_e r^3}{8} - \frac{L_e r^2}{8} - \frac{L_e r}{8} + \frac{L_e}{8} \quad -\frac{r^3}{4} + \frac{3r}{4} + \frac{1}{2} \quad \frac{L_e r^3}{8} + \frac{L_e r^2}{8} - \frac{L_e r}{8} - \frac{L_e}{8} \right]$$
$$\cdot \begin{pmatrix} cz_{pI} \\ \alpha_{pI} \\ z_{pJ} \\ \alpha_{pJ} \end{pmatrix} \quad (3.173)$$

with the element length L_e and the tendon inclination

$$\alpha_P = \frac{\partial z_p}{\partial x} = \frac{\partial z_p}{\partial r} \frac{\partial r}{\partial x} = z_p' \quad (3.174)$$

Lateral tendon position and inclination on the left- and right-element end are given by z_{pI}, α_{pI} and z_{pJ}, α_{pJ}. The local element coordinate is in the range $-1 \leq r \leq 1$. This approach reproduces $z_p(-1) = z_{pI}$, $z_p'(-1) = \alpha_{pI}$ and $z_p(1) = z_{pJ}$, $z_p'(1) = \alpha_{pJ}$. The geometric length of tendon in an element e is given by

$$L_e^P = \frac{L_e}{2} \int_{-1}^{1} \sqrt{(x_p')^2 + (z_p')^2} \ \mathrm{d}r \quad (3.175)$$

whereby the derivative of the tendon position x_p in the longitudinal direction has also to be regarded. Equation (3.175) has to be integrated numerically for each element, e.g., with a Gauss integration, see Section 1.6.

Equation (3.173) for tendon geometry is on one hand applied to the nominal undeformed tendon geometry according to design with

$$
\begin{pmatrix} x'_p \\ z_{pI} \\ \alpha_{pI} \\ z_{pJ} \\ \alpha_{pJ} \end{pmatrix} = \begin{pmatrix} 1 \\ z_{p0I} \\ \alpha_{p0I} \\ z_{p0J} \\ \alpha_{p0J} \end{pmatrix}
\tag{3.176}
$$

with the prescribed values $z_{p0I}, \alpha_{p0I}, z_{p0J}, \alpha_{p0J}$. On the other hand, Eq. (3.173) gives the tendon geometry considering beam deformation with

$$
\begin{pmatrix} x'_p \\ z_{pI} \\ \alpha_{pI} \\ z_{pJ} \\ \alpha_{pJ} \end{pmatrix} = \begin{pmatrix} 1 + \epsilon \\ z_{p0I} + w_I \\ \alpha_{p0I} + \phi_I \\ z_{p0J} + w_J \\ \alpha_{p0J} + \phi_J \end{pmatrix}
\tag{3.177}
$$

with the longitudinal strain ϵ of the beam's reference axis and the beams nodal displacements w_I, ϕ_I, w_J, ϕ_J. The total length L^P of a tendon is computed by adding all element contributions.

Regarding prestressing *without bond*, the tendon length can be determined separately for application stage, with a value L_0^P, and for the fixed stage with a value L^P. Equations (3.175, 3.177) can be used with the appropriate deformations or displacements, respectively. Regarding Eq. (3.168), this leads to a prestressing force

$$
F^p = \frac{L^P}{L_0^P} F_0^p
\tag{3.178}
$$

in the fixed stage of prestressing.

Regarding prestressing *with bond* a tendon gets a local elongation after fixing of prestressing due to bond. This local elongation is ruled by the beam's deformation kinematics equation (3.5), i.e., the additional strain of the tendon is given by

$$
\Delta\epsilon_p(x) = \Delta\epsilon(x) - z_p \, \Delta\kappa(x)
\tag{3.179}
$$

with the variable values $\Delta\epsilon$, $\Delta\kappa$ of the beam deformations during the fixed stage of prestressing. This leads to to a prestressing force

$$
F^p(x) = F_0^p + E_p A_p \, \Delta\epsilon_p(x)
\tag{3.180}
$$

with Young's modulus E_p of the prestressing steel, the cross section area A_p of prestressing tendons and $F^p(x)$ used in Eq. (3.168).

The particular procedures concerning prestressing can be summarized as follows:

– Define the tendon geometry and prestressing force

– Compute internal forces from prestressing

– Compute nodal loads from prestressing

– Compute system reaction

– Iterate if neccessary to capture changing in prestressing force

The application is demonstrated with the following example.

Example 3.6 Prestressed RC beam
We refer to Example 3.2 with basically the same system, but the span is doubled to $L = 10$ m. Thus, the structure's load bearing capacity is strongly reduced. Prestressing is used to increase the bearing capacity. The relevant system parameters are as follows:

– A concrete cross section $b = 0.2, h = 0.4$, a compressive strength $f_{cd} = 38 \, \mathrm{MN/m^2}$ and a lower and upper reinforcement $A_{s1} = A_{s2} = 12.57 \, \mathrm{cm^2}$, $d_1 = d_2 = 5 \, \mathrm{cm}$ yield an ultimate bending moment $M_u \approx 0.20 \, \mathrm{MNm}$ with $N = 0$, see Example 3.1. This corresponds to a uniform loading $q_u = 8 M_u/L^2 = 15.2 \, \mathrm{kN/m}$ which should be increased by prestressing.

– A nominal uniform concrete prestressing stress of $\sigma_{c0} = -10 \, \mathrm{MN/m^2}$ is chosen in a first approach leading to $F_0^p = 0.8 \, \mathrm{MN}$. The nominal tendon geometry of the whole beam is given by a parabola starting and ending in the center line with a downward camber h_p. This is described by

$$z_p = 4h_p \left(\frac{x^2}{L^2} - \frac{x}{L} \right) \tag{3.181}$$

A value $h_p = 0.15 \, \mathrm{m}$ is chosen in this example.

– Prestressing tendon and steel properties are chosen with a cross section area $A_p = 6 \, \mathrm{cm^2}$, elastic limit $f_{p0,1} = 1600 \, \mathrm{MN/m^2}$, strength $f_p = 1800 \, \mathrm{MN/m^2}$, and Young's modulus $E_p = 200\,000 \, \mathrm{MN/m^2}$. Nominal initial steel stress is $\sigma_0^p = 1\,333 \, \mathrm{MN/m^2}$ with a strain $\epsilon_0^p = 6.67 \, ‰$.

– A dead load is assumed with $q = 5 \, \mathrm{kN/m}$.

Loading is applied in two stages: (1) Application of prestressing and dead load, (2) fixing of prestressing and additional application of a service load $q_p = 25 \, \mathrm{kN/m}$. Frictional losses are neglected to simplify this example. Both cases – prestressing with and without bond – are alternatively regarded for the fixed stage of prestressing. The solution method is incrementally iterative with Newton–Raphson iteration within increments.

This leads to the following results for prestressing *without* bond:

– The computed increase in prestressing force after load step 2 according to Eq. (3.178) is minimal with $F^p/F_0^p = 1.002$. This results from the low ratio $h_p/L = 1/67$.

– For the computed mid-span displacements, see Fig. 3.15a. The deflection starts with an uplift during application of prestressing. The final mid-span deflection is quite large with 0.113 m ($\approx 1/90$ of the span), but the load-carrying capacity is not yet exhausted with an upper mid-span concrete compressive strain of $-2.2 \, ‰$ (limit strain is $-3.5 \, ‰$). Serviceability is presumably not given without further provisions due to high slenderness (1/25).
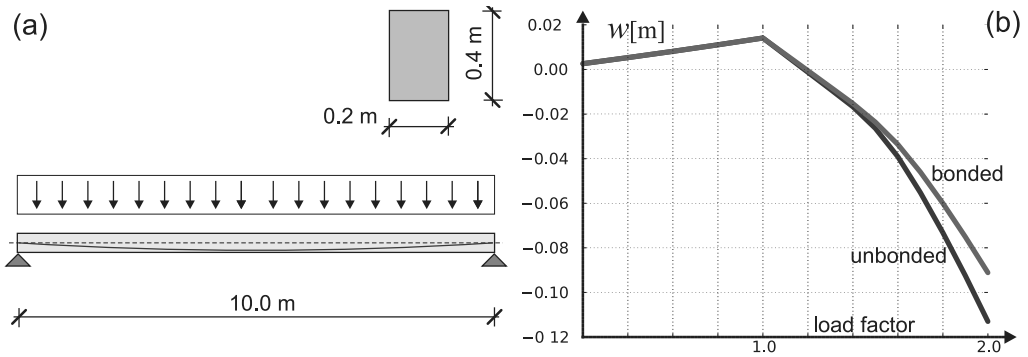
Figure 3.15: Example 3.6 (a) System (b) Mid-span load–deflection curve.

– For the bending moment and normal force in the RC cross section, see Fig. 3.16a. Total moment from the dead load weight and the service load is $M_q = 0.03 \times 10^2/8 = 0.375$ MNm. The computed RC mid-span contribution is $M_c = 0.255$ and the contribution from prestressing $M_p = 0.120$. The increased RC moment compared to the initial estimation results from the compressive normal force.

Furthermore, the results for prestressing *with* bond:

– In the case of bond, the tendon gets a local additional strain due to the locally varying deformation of the beam, see Eq. (3.179). This leads to an additional prestressing force, see Eq. (3.180) and Fig. 3.16b, and in the end to higher contribution of prestressing to load bearing capacity and a higher total load bearing capacity.

– Detail results are given by final mid-span deflection 0.12 m, see Fig. 3.15b, RC moment contribution $M_c = 0.220$, see Fig. 3.16a, contribution from prestressing $M_p = 0.155$.

Prestressing roughly leads to a doubling of ultimate limit loads in this example. Aspects of serviceability have to be treated separately.
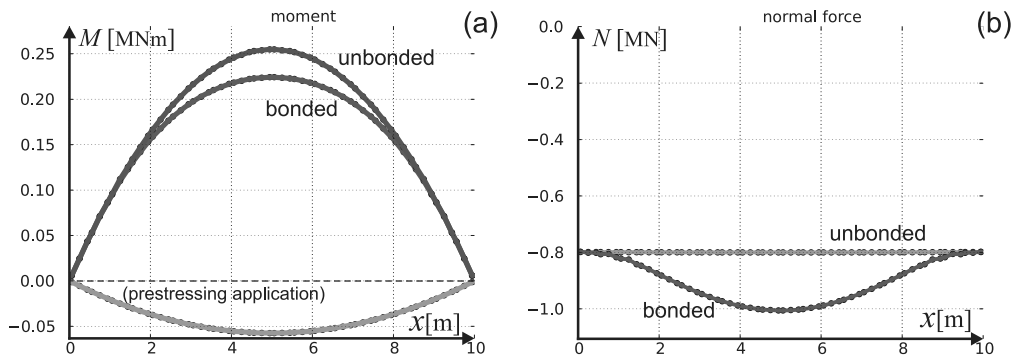
Figure 3.16: Final stage Example 3.6 (a) RC bending moment. (b) RC normal force.

The comparison between prestressing with and without bond in this example is somehow academic, as in practice prestressing with bond is exposed to more nonmechanical effects, which might lead to some restrictions to fully utilize the load carrying capacities of the prestressing steel. Details are ruled in codes.

<div align="right">*End Example 3.6*</div>

Some remarks concerning prestressing remain to be added. All methods and procedures may be also applied to material laws of a rate type, see Eq. (1.50), instead of Eq. (3.166) within an incrementally iterative scheme, see Section 1.6.

Prestressing may be superposed with creep of concrete (Section 3.5.1), temperature and shrinkage (Section 3.5.2), and tension stiffening (Section 3.5.3). All described approaches are compatible and may be used in any combination. The application has been demonstrated in Example 3.6 for a single-span beam which is statically determinate.

- Methods and procedures in same way may be applied to statically indeterminate systems as solution procedures always simultaneously regard equilibrium, material behavior, and kinematic compatibility.

High strength steel is used for prestressing with roughly three times the strength of ordinary rebar steel. Relaxation, see Section 2.2, occurs for such types of steel. The approach of, e.g., Eq. (2.27) can basically be used for the phenomena of creep and relaxation and in a first approach for steel as well as for concrete. It can be also applied to the prestressing force F^p, see Eq. (3.168), leading to a transient analysis as in a similar way has already been discussed in Section 3.5.1.

3.7 Large Deformations and Second-Order Analysis

Up to now, we considered the equilibrium of structures in their undeformed configuration. The displacements of a structure were neglected in the balance of external actions and internal forces and a *geometrically linear analysis* was performed. This is justified for RC beams which are exposed to predominant bending or tension. Structural deformations generally will not have an appreciable influence on internal forces in such cases. This might change for structural members exposed to compression. Depending on their slenderness internal forces may considerably increase due to structural deformations and deformations have to be considered regarding equilibrium. This leads to *geometrical nonlinearities*.

We consider a section of a plane beam in some deformed configuration, see Fig. 3.17. A quasistatic analysis shall be performed whereby equilibrium should be given in the deformed configuration. Thus, the integration of the equilibrium condition (Eq. (3.65)) of a section of length L

$$\int_0^L \delta\boldsymbol{\epsilon}^T \cdot \boldsymbol{\sigma} \, \mathrm{d}s = \int_0^L \delta\mathbf{u}^T \cdot \bar{\mathbf{p}} \, \mathrm{d}s + \delta\mathbf{U}^T \cdot \bar{\mathbf{t}} \tag{3.182}$$

has to be performed in the deformed configuration with the coordinate s along the beam axis. It is appropriate to relate the generalized stresses $\boldsymbol{\sigma}$ and the generalized strains $\boldsymbol{\epsilon}$, see Eqs. (3.66, 3.68), to a local *corotational coordinate system*. A single element is considered in the following which is straight in the undeformed configuration.
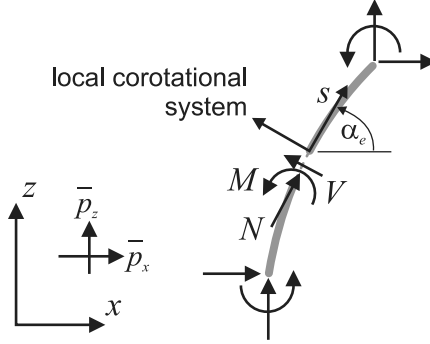
Figure 3.17: Equilibrium of beam section in the deformed configuration.

- It is assumed that the curvature of a single element is still small in the deformed configuration and that its deformed geometry can be approximated with a straight line connecting its end nodes.

This assumption is appropriate for RC structures failing with relatively small strains. Furthermore, the deformed geometry may be approximated with any desired accuracy by refining the discretization.

The corresponding element orientation is given by the angle α_e. Global nodal degrees of freedom $\boldsymbol{v}_e$ are transformed to the local system with Eq. (3.109)

$$\tilde{\boldsymbol{v}}_e = \mathbf{T}(\alpha_e) \cdot \boldsymbol{v}_e \tag{3.183}$$

Local displacements and strains are given according to Eqs. (3.78, 3.81)

$$\tilde{\mathbf{u}}(r) = \mathbf{N}(r) \cdot \tilde{\boldsymbol{v}}_e, \quad \boldsymbol{\epsilon}(r) = \mathbf{B}(r) \cdot \tilde{\boldsymbol{v}}_e \tag{3.184}$$

leading to virtual strains

$$\delta\boldsymbol{\epsilon}^T = \delta\boldsymbol{v}_e^T \cdot \mathbf{T}^T(\alpha_e) \cdot \mathbf{B}^T(r) \tag{3.185}$$

Internal nodal forces of a beam element are given by Eqs. (3.101, 3.110)

$$\mathbf{f}_e = \mathbf{T}^T(\alpha_e) \cdot \frac{L_e}{2} \int_{-1}^{1} \mathbf{B}^T(r) \cdot \boldsymbol{\sigma}(r) \, \mathrm{d}r \tag{3.186}$$

with the actual element length L_e whereby the orientation α_e depends – beneath the initial coordinates of the element's nodes – on the values of the nodal degrees of freedom or displacements, respectively.

- With the internal nodal forces depending on the deformation the problem becomes geometrically nonlinear. This is combined with physical nonlinearity in the case of RC beams due to the nonlinear behavior between the generalized strains and stresses.

The evaluation of the tangential stiffness is mandatory for such problems. The tangential element stiffness matrix is determined by

$$\mathbf{K}_{Te} = \frac{\partial \mathbf{f}_e}{\partial \boldsymbol{v}_e} \tag{3.187}$$

see Eq. (1.64). Regarding Eq. (3.186) this leads to

$$\mathbf{K}_{Te} = \mathbf{K}_{TMe} + \mathbf{K}_{TGe} \tag{3.188}$$

with the tangential stiffness contribution from material behavior

$$
\begin{aligned}
\mathbf{K}_{TMe} &= \mathbf{T}^T \cdot \frac{L_e}{2} \int_{-1}^{1} \mathbf{B}^T \cdot \frac{\partial \boldsymbol{\sigma}}{\partial \boldsymbol{\epsilon}} \cdot \frac{\partial \boldsymbol{\epsilon}}{\partial \tilde{\boldsymbol{v}}_e} \cdot \frac{\partial \tilde{\boldsymbol{v}}_e}{\partial \boldsymbol{v}_e} \, \mathrm{d}r \\
&= \mathbf{T}^T \cdot \frac{L_e}{2} \int_{-1}^{1} \mathbf{B}^T \cdot \mathbf{C}_T \cdot \mathbf{B} \, \mathrm{d}r \cdot \mathbf{T} \\
&= \mathbf{T}^T \cdot \widetilde{\mathbf{K}}_{Te} \cdot \mathbf{T}
\end{aligned}
\tag{3.189}
$$

according to Eqs. (1.65, 3.114) and furthermore with the tangential stiffness contribution from geometry

$$\mathbf{K}_{TGe} = \frac{\partial \mathbf{T}^T}{\partial \alpha_e} \cdot \tilde{\mathbf{f}}_e \cdot \frac{\partial \alpha_e}{\partial \boldsymbol{v}_e}^T \tag{3.190}$$

with the local internal nodal forces

$$\tilde{\mathbf{f}}_e = \frac{L_e}{2} \int_{-1}^{1} \mathbf{B}^T \cdot \boldsymbol{\sigma} \, \mathrm{d}r \tag{3.191}$$

Regarding the Bernoulli beam element, see Section 3.3.2 and Eq. (3.111), the factors of Eq. (3.190) are given by

$$
\frac{\partial \mathbf{T}^T}{\partial \alpha_e} =
\begin{bmatrix}
-\sin\alpha_e & -\cos\alpha_e & 0 & 0 & 0 & 0 \\
\cos\alpha_e & -\sin\alpha_e & 0 & 0 & 0 & 0 \\
0 & 0 & 0 & 0 & 0 & 0 \\
0 & 0 & 0 & -\sin\alpha_e & -\cos\alpha_e & 0 \\
0 & 0 & 0 & \cos\alpha_e & -\sin\alpha_e & 0 \\
0 & 0 & 0 & 0 & 0 & 0
\end{bmatrix}
\tag{3.192}
$$

and

$$
\tilde{\mathbf{f}}_e =
\begin{pmatrix}
N_I \\ V_I \\ M_I \\ N_J \\ V_J \\ M_J
\end{pmatrix}, \qquad
\frac{\partial \alpha_e}{\partial \boldsymbol{v}_e} = \frac{1}{L_e}
\begin{pmatrix}
\sin\alpha_e \\ -\cos\alpha_e \\ 0 \\ -\sin\alpha_e \\ \cos\alpha_e \\ 0
\end{pmatrix}
\tag{3.193}
$$

This leads to a geometric tangential element stiffness

$$
\mathbf{K}_{TGe} =
\begin{bmatrix}
-A_I \sin\alpha_e & A_I \cos\alpha_e & 0 & A_I \sin\alpha_e & -A_I \cos\alpha_e & 0 \\
B_I \sin\alpha_e & -B_I \cos\alpha_e & 0 & -B_I \sin\alpha_e & B_I \cos\alpha_e & 0 \\
0 & 0 & 0 & 0 & 0 & 0 \\
-A_J \sin\alpha_e & A_J \cos\alpha_e & 0 & A_J \sin\alpha_e & -A_J \cos\alpha_e & 0 \\
B_J \sin\alpha_e & -B_J \cos\alpha_e & 0 & -B_J \sin\alpha_e & B_J \cos\alpha_e & 0 \\
0 & 0 & 0 & 0 & 0 & 0
\end{bmatrix}
\tag{3.194}
$$

for the two-node Bernoulli beam element with

$$A_i = \sin\alpha_e N_i + \cos\alpha_e V_i, \quad B_i = \cos\alpha_e N_i - \sin\alpha_e V_i, \quad i = I, J \tag{3.195}$$

Internal nodal forces from Eq. (3.186) have to be in equilibrium with the external nodal forces. External nodal forces for distributed loading are determined in analogy to Eq. (3.105) leading to

$$\bar{\mathbf{p}}_e = \frac{L_e}{2} \int_{-1}^{1} \mathbf{T}^T(\alpha_e) \cdot \mathbf{N}^T(r) \cdot \mathbf{Q}(\alpha_e) \cdot \bar{\mathbf{p}}(r) \, dr \tag{3.196}$$

with the vector rotation matrix $\mathbf{Q}$, see Eq. (C.6), and for the boundary terms with Eq. (3.106)

$$\bar{\mathbf{t}}_e = \begin{pmatrix} \bar{N}_I & \bar{V}_I & \bar{M}_I & \bar{N}_J & \bar{V}_J & \bar{M}_J \end{pmatrix}^T \tag{3.197}$$

for the two-node Bernoulli beam element. The components of $\bar{\mathbf{t}}_e$ and $\bar{\mathbf{p}}$, see Eq. (3.66), are related to the global coordinate system. The extended Bernoulli beam element, see Section 3.3.2, and the Timoshenko beam elements, see Section 3.3.3, can be treated in the same way with the adaption of $\boldsymbol{v}_e$, $\boldsymbol{\epsilon}$, $\boldsymbol{\sigma}$ and $\mathbf{T}$.

The system equations are assembled from the element contributions, as is described in Section 1.5, leading to a condition for quasistatic equilibrium

$$\mathbf{f}(\boldsymbol{v}) = \mathbf{p} \tag{3.198}$$

with $\mathbf{p} = \bar{\mathbf{p}} + \bar{\mathbf{t}}$, compare Eq. (1.60). The solution is determined with an incrementally iterative scheme, see Section 1.6, whereby the tangential stiffness should include material stiffness and geometric stiffness as are given for single elements with Eqs. (3.189, 3.190).

The described approach corresponds to a *corotational updated Lagrangian* discretization [9, 4.4, 4.6]. It may be applied to cases with large deformations and small strains. *Second-order analysis* is included as a special case whereby displacements are linearized with respect to an initially undeformed configuration. A first validation is given by the following example.

Example 3.7 Stability limit of cantilever column

We consider a simple cantilever column with linear elastic behavior and a discretization with one two-node Bernoulli beam element, see Fig. 3.18. It has a vertical concentrated load at its top acting along the axis of gravity. A buckling from the initial configuration or instability will occur within a theory regarding equilibrium in deformed configurations. The buckling load shall be determined for this simple model.

The model has three degrees of freedom with u, w, ϕ at the top node. The initial configuration is given by $\alpha_e = \pi/2$. The material stiffness is determined by Eq. (3.189) with $\mathbf{B}$ from Eq. (3.82), $\mathbf{C}_T = \mathbf{C}$ from Eq. (3.16) and $\mathbf{T}$ from Eq. (3.111) with α_e replacing α. This yields

$$\mathbf{K}_{TM} = \begin{bmatrix} \frac{12EJ}{L^3} & 0 & \frac{6EJ}{L^2} \\ 0 & \frac{EA}{L} & 0 \\ \frac{6EJ}{L^2} & 0 & \frac{4EJ}{L} \end{bmatrix} \tag{3.199}$$

for the actual degrees of freedom. The geometric stiffness according to Eq. (3.194) is determined by

$$\mathbf{K}_{TG} = \bar{N}_J \, \mathbf{K}_{TG}^0, \qquad \mathbf{K}_{TG}^0 = \begin{bmatrix} \frac{1}{L} & 0 & 0 \\ 0 & 0 & 0 \\ 0 & 0 & 0 \end{bmatrix} \tag{3.200}$$
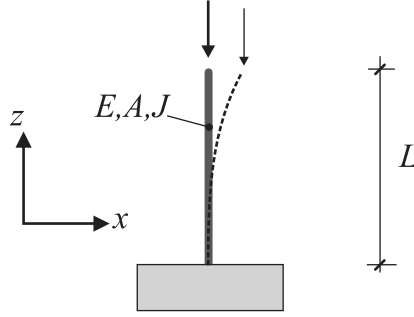
Figure 3.18: Cantilever column.

The matrix $\mathbf{K}_{TG}^0$ is independent from loading and covers the geometry of the initial undeformed configuration.

The incremental system behavior is described by Eq. (1.66)

$$(\mathbf{K}_{TM} + \mathbf{K}_{TG}) \cdot \mathrm{d}\boldsymbol{v} = \mathrm{d}\mathbf{f} \tag{3.201}$$

- An instability is given by *nonzero* increments of displacements $\mathrm{d}\boldsymbol{v}$ in connection with *zero* increments of nodal forces $\mathrm{d}\mathbf{f}$.

This leads to the generalized eigenvalue problem

$$\mathbf{K}_{TM} \cdot \mathrm{d}\boldsymbol{v} = -N_{Jb} \ \mathbf{K}_{TG}^0 \cdot \mathrm{d}\boldsymbol{v} \tag{3.202}$$

with the buckling load N_{Jb}. The solution for this model is

$$N_{Jb} = \frac{3\,EJ}{L^2} \tag{3.203}$$

whereby the relation between lateral displacement and rotation is determined with $9\tilde{w}_J + 6L\,\phi = 0$. The exact solution is given by $\pi^2\,EJ/4L^2 \approx 2.47\,EJ/L^2$ according to the well-known Euler cases for buckling. The error in N_{Jb} results from the discretization with one element which is a rough approximation of the exact cosine solution. A refinement of the discretization should improve the solution for N_{Jb}.

————————————————————————————— End Example 3.7

The method described for the stability analysis of a cantilever column is based on the generalized eigenvalue problem (3.202). It may be applied to all types of columns and frames with compressive members in the undeformed configuration. Furthermore, the approach may be generalized for the stability analysis of all types of structures [9, 6.5].

Up to now, we regarded linear elastic material behavior. The nonlinear behavior of cracked RC cross sections, see Section 3.1.3, has to be considered in the next step. This will be described for Bernoulli beams in the following.

A deformed configuration is given within an incremental iterative scheme, see Section 1.6, with an orientation angle α_e and an actual length L_e for each element. Generalized strains

ϵ and generalized stresses $\boldsymbol{\sigma}$ or internal forces, see Eq. (3.68), are determined in the local corotational system. With the generalized strains given the internal forces are determined from Eqs. (3.22, 3.23) and the tangential stiffness $\mathbf{C}_T$ from Eq. (3.55). This yields the basic quantities required for the internal nodal forces in the global system (Eq. (3.186)), the tangential material stiffness (Eq. (3.189)) and the tangential geometric stiffness (Eq. (3.194)). The external nodal forces in the global system are finally determined from Eqs. (3.196, 3.197) for a new loading target. Prescribed displacements are treated as described in Section 3.4.3. The nonlinear problem – including the continuing updating of α_e, L_e – is solved by, e.g., the Newton–Raphson method, see Eqs. (1.71, 1.72).

The application is demonstrated with the following example.

Example 3.8 Ultimate limit for RC cantilever column
The stability of the cantilever column has already been treated in Example 3.7 as a buckling or the generalized eigenvalue problem whereby resembling the classical Euler case. This assumes a centered load without eccentricity and a linear elastic material behavior and leads to an upper bound for the load carrying capacity. A load eccentricity and the nonlinear behavior of a cracked RC sections are considered while regarding large displacements or second order effects, respectively. Geometry, discretization, and boundary conditions are as follows:

- Cantilever column with a height $L = 5.0\,\mathrm{m}$, square cross section with width $h = 0.4\,\mathrm{m}$ and a depth $b = 0.2\,\mathrm{m}$, see Fig. 3.6a.

- Discretization with $n_E = 10$ extended two-node Bernoulli beam elements, see Section 3.3.2.

- The bottom node is clamped with zero displacements and zero rotations.

The column is assumed to be stabilized in the out-of-plane direction. The material properties and the reinforcement are chosen as with Example 3.1:

- Concrete grade C30/37 according to [26, Table 3.1] with an initial Young's modulus $E_c = 33\,000\,\mathrm{MN/m^2}$. Concrete compressive strength is assumed with $f_c = 38\,\mathrm{MN/m^2}$ with $\epsilon_{c1} = -0.0023$, $\epsilon_{cu1} = -0.0035$, see Fig. 2.1. A tensile strength is disregarded. The uniaxial stress–strain relation is chosen according to [26, 3.1.5].

- Reinforcement behavior is assumed according to Section 2.3 and [26, 3.2.7] with $f_{yk} = 500\,\mathrm{MN/m^2}$, $f_t = 525\,\mathrm{MN/m^2}$, $\epsilon_{y0} = 2.5\%_0$ and $\epsilon_u = 25\%_0$, see Fig. 2.10a.

- Left and right reinforcement each with a geometry $4 \oslash 20$, $A_{s2} = A_{s1} = 12.57\,\mathrm{cm^2}$, $d_2 = d_1 = 5\,\mathrm{cm}$.

The elastic in-plane stability limit or buckling load is determined as

$$P_b = \frac{\pi^2}{4}\frac{EJ}{L^2} = \frac{\pi^2}{4}\frac{33\,000 \cdot 0.001067}{5.0^2} = 3.47\,\mathrm{MN} \tag{3.204}$$

The vertical downward load target is chosen with $P = 2\,\mathrm{MN}$ with an eccentricity of $e = 0.032\,\mathrm{m}$, see Fig. 3.19a. The moment–curvature for this compressive force has been determined in Example 3.1 and is shown in Fig. 3.3.
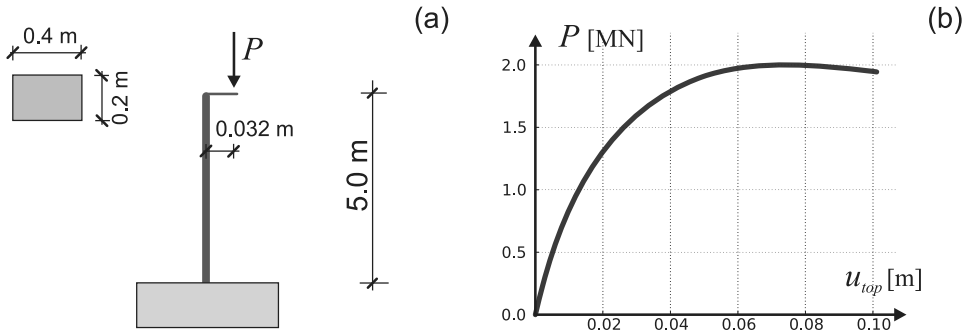
Figure 3.19: Example 3.8 (a) System (b) Vertical load–horizontal displacement relation.

An incrementally iterative scheme with arc length control to determine load increments, see Appendix A, and Newton–Raphson iteration within each loading increment, see Section 1.6, is used as the solution method. The computation leads to the following results:

– The computed relation between horizontal top displacement and vertical load is shown in Fig. 3.19b. It is nonlinear due to both geometrical and physical nonlinearities. The prescribed maximum is reached with a horizontal displacement of $u_u = 0.071$ m. The vertical load has to be reduced for larger horizontal displacements to maintain equilibrium in the deformed configuration. The arc length method is mandatory to model this structural softening behavior effect.

A load value of $P = 2$ MN cannot be reached with initial eccentricities $e > 0.032$ m as the structural softening behavior will start with lower loads.

– The computed moments along the column are shown in Fig. 3.20a for different loading factors. The computed top moment $M_{z=4.94} = 0.067$ MNm corresponds to the prescribed eccentricity moment of $eP \to 0.064$ MNm. In the same way the computed bottom moment $M_{z=0.06} = 0.206$ MNm corresponds to the prescribed plus
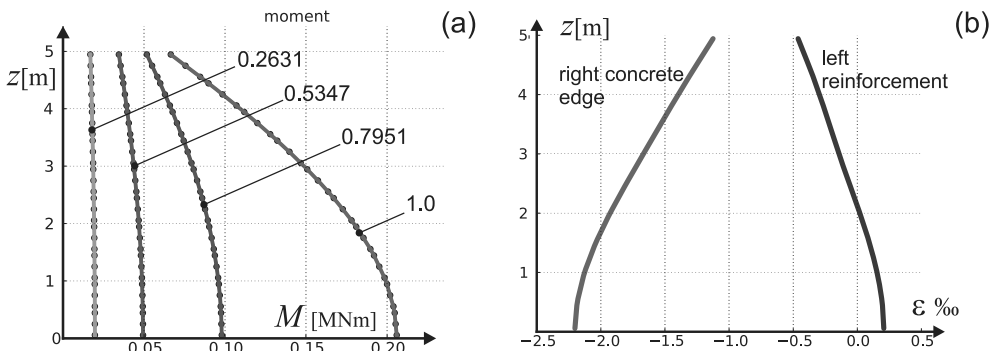
Figure 3.20: Example 3.8 (a) Moments along column. (b) Strains along column.

deformation eccentricity moment $(e + u_u) P \to 0.206\,\text{MNm}$. This exceeds the moment from first-order theory by the factor of 3.2. Using a linear elastic material behavior with $E = 33\,000\,\text{MN/m}^2$ would lead to a stiffer behavior with a moment $M_{x=0.06} = 0.172\,\text{MNm}$.

The maximum bottom bending moment connected to the ultimate structural load is considerably lower compared to the ultimate cross-sectional moment of $M_u = 0.261\,\text{MNm}$, see Example 3.1 with Fig. 3.3, indicating a structural instability.

– Strain distributions along the column for the left-reinforcement and the right-concrete edge are shown in Fig. 3.20b for the final loading state. The materials limit strains – e.g., $\epsilon_{cu1} = -0.0035$ for concrete – are not reached although the system has reached its limit load.

The cantilever column is the most important case for second order computations for RC structures. But the described approach may also be directly applied to other types of columns and to all kinds of plane multistory frames.

End Example 3.8

Considering certain effects like some amount of tensile strength or tension stiffening will increase the stiffness of the model. Tension stiffening may be regarded with a modification of the stress–strain relation for the reinforcement, see Section 3.5.3. A value for the tensile strength is considered with the lower and upper compression zone coordinates z_{c1}, z_{c2}, see Section 3.1.3.1, with an extended definition of the zero line z_0, see Eqs. (3.19, 3.20).

On the other hand, an effect like creep will increase the deformations and also the internal forces in the deformed configuration. But the load level should be lower as only a permanent or quasi-permanent loading will lead to creep. The approach for creep as is described in Section 3.5.1 can be combined with the method for large displacements to investigate creep effects.

3.8   Dynamics of Beams

Dynamic actions on structures may arise from walking pedestrians, vehicular traffic, rotating machines, wind, seismicity, impact, and explosions. Decisive is a structure's largest *natural period* compared to a characteristic time of an action. Such characteristic times may come from the step frequency of pedestrians, velocity of vehicles, rotational frequency of machines, frequency of gusts or ground motions, duration of impact and explosions. If the largest natural period of a structure is not considerably smaller than the characteristic action time a structure's inertia comes into play. The manifold aspects of dynamics of civil engineering structures are treated by, e.g., [10], [37], [53].

Basics of inertia for beams are given in Eqs. (3.58, 3.65), which introduce the inertial mass m per unit length of a beam and the inertial mass moment Θ. In the case the center line of area coincides with the beam's reference axis, see Section 3.1.1, they are given by

$$m = \varrho\,A, \quad \Theta = \varrho\,J \tag{3.205}$$

with the material's specific mass ϱ, the cross-sectional area A and the second moment of area J. If the center line of area does not coincide with the reference axis the definition of Θ has

to be modified. On the other hand, contributions connected with the inertial mass moment Θ are often neglected, as they are relatively small. Some care should be given to the units.

- Specific mass ϱ has to be distinguished from specific weight, i.e., a given specific weight has to be divided by earth acceleration.

Appropriate methods to solve dynamic problems have already been laid down. The basic approach for a discretized system is given by Eq. (1.90)

$$\mathbf{M} \cdot \ddot{\boldsymbol{v}}(t) + \mathbf{f}(t) = \mathbf{p}(t) \tag{3.206}$$

with the time t and element contributions from

- element mass matrices $\mathbf{M}_e$ according to Eq. (3.104),
- element nodal displacements $\boldsymbol{v}_e$ according to, e.g., Eq. (3.74) or (3.86),
- element internal nodal forces $\mathbf{f}_e$ according to Eq. (3.102),
- element nodal loads $\mathbf{p}_e = \bar{\mathbf{p}}_e + \bar{\mathbf{t}}_e$ according to Eqs. (3.105, 3.106).

in the case of beams. Nodal loads $\mathbf{p}(t)$ are generally defined as a function of t. Equation (3.206) forms a system of ordinary differential equations of the second order in time t. Thus, initial conditions have to be prescribed for the nodal displacements and velocities at a time $t = 0$. Internal nodal forces are given by

$$\mathbf{f}(t) = \mathbf{K} \cdot \boldsymbol{v}(t) \tag{3.207}$$

in the case of linear material behavior and small displacements with the element contributions to the stiffness matrix $\mathbf{K}_e$ in analogy to Eq. (3.103). This leads to

$$\mathbf{M} \cdot \ddot{\boldsymbol{v}}(t) + \mathbf{K} \cdot \boldsymbol{v}(t) = \mathbf{p}(t) \tag{3.208}$$

instead of Eq. (3.206). Two fundamental solution approaches are given:

- Modal decomposition
- Direct integration in time

Modal decomposition presupposes constant symmetric matrices $\mathbf{M}$, $\mathbf{K}$ and at first neglects loading $\mathbf{p}(t)$. An oscillation may occur with such a system due to initially prescribed displacements or velocities. The system

$$\mathbf{M} \cdot \ddot{\boldsymbol{v}}(t) + \mathbf{K} \cdot \boldsymbol{v}(t) = 0 \tag{3.209}$$

of ordinary differential equations of second order in time t is solved by

$$\boldsymbol{v} = \boldsymbol{\xi} \sin \omega t \tag{3.210}$$

with a constant vector $\boldsymbol{\xi}$ and a constant number ω. They will come out as eigenvector and *circular natural frequency*. Circular natural frequency and *natural period* are related by

$$T = \frac{2\pi}{\omega} \tag{3.211}$$

A generalized matrix eigenvalue problem is derived from Eqs. (3.209, 3.210) with

$$\mathbf{K} \cdot \boldsymbol{\xi} = \omega^2 \mathbf{M} \cdot \boldsymbol{\xi} \tag{3.212}$$

This has n solutions $\boldsymbol{\xi}_i$, ω_i, $i = 1, \ldots, n$ for a system with n nodal degrees of freedom whereby the length of a vector $\boldsymbol{\xi}_i$ remains undetermined. For the solution methods for the generalized matrix eigenvalue problem, see [3, 10., 11.].

The eigenvectors $\boldsymbol{\xi}_i$ constitute a matrix $\boldsymbol{\Xi}$ used for transformations into the modal space. Firstly, the transformation $\tilde{\boldsymbol{v}} = \boldsymbol{\Xi} \cdot \boldsymbol{v}$ is applied. Secondly, the transformations $\tilde{\mathbf{K}} = \boldsymbol{\Xi}^T \cdot \mathbf{K} \cdot \boldsymbol{\Xi}$ and $\tilde{\mathbf{M}} = \boldsymbol{\Xi}^T \cdot \mathbf{M} \cdot \boldsymbol{\Xi}$ each lead to a diagonal matrix. Thirdly, multiplying Eq. (3.208) from left with $\boldsymbol{\Xi}^T$ decouples this set of equations into n single degree of freedom systems of second differential order in time. This decoupling extremely facilitates the solution. This short description outlines *modal analysis*. Only some aspects of modal analysis, which is a powerful tool for all types of structures, can be given within this context. A comprehensive presentation is given by, e.g., [43].

A few basic items of linear structural dynamics remain to be added. The smallest circular natural frequency ω_1 is determined through the *Rayleigh quotient*

$$\omega_1 = \min \left(\sqrt{\frac{\bar{\boldsymbol{v}}^T \cdot \mathbf{K} \cdot \bar{\boldsymbol{v}}}{\bar{\boldsymbol{v}}^T \cdot \mathbf{M} \cdot \bar{\boldsymbol{v}}}} \right) = \frac{2\pi}{T_1} \tag{3.213}$$

with an appropriate displacement vector $\bar{\boldsymbol{v}}$. This also gives the largest natural period T_1 which is relevant for the estimation of dynamic situations. In the case of a single-degree of freedom system – a mass m connected with a base through a spring with stiffness k – this leads to the well-known relation

$$\omega = \sqrt{\frac{k}{m}}, \quad T = 2\pi \sqrt{\frac{m}{k}} \tag{3.214}$$

In the case of multidegree of freedom systems with $n > 1$, as is given within this framework, ω_1 and T_1 may be approximately determined with a $\bar{\boldsymbol{v}}$ resulting from a quasistatic analysis with dead loading.

Finally, the relation for the largest natural period of a simple single span hinged beam shall be derived. The base is given with the homogeneous differential equation of beam bending (Eq. (3.61))

$$m \ddot{w} + EJ w'''' = 0 \tag{3.215}$$

with a bending stiffness EJ. This is solved by

$$w(x, t) = \sin \frac{\pi x}{L} \sin \omega t \tag{3.216}$$

with a span L and leads to

$$\ddot{w} = \frac{\partial^2 w}{\partial t^2} = -\omega^2 \sin \frac{\pi x}{L} \sin \omega t, \quad w'''' = \frac{\partial^4 w}{\partial x^4} = \frac{\pi^4}{L^4} \sin \frac{\pi x}{L} \sin \omega t \tag{3.217}$$

Thus, boundary conditions $w(0, t) = w(L, t) = 0$ and $EJ w''(0, t) = EJ w''(L, t) = 0$ are fulfilled. Furthermore, combining Eqs. (3.215, 3.217) yields

$$\omega = \frac{\pi^2}{L^2} \sqrt{\frac{EJ}{m}} \tag{3.218}$$

and with Eq. (3.211) the longest natural period of a single span hinged beam

$$T = \frac{2L^2}{\pi} \sqrt{\frac{m}{EJ}} \tag{3.219}$$

This is a useful relation to derive reference values for the longest natural period of beams. The reciprocal $\nu = 1/T$ gives the largest natural frequency, i.e., the number of cycles of a structure's free oscillations per time unit.

The application of modal analysis is restricted to linear or linearized problems. Such a restriction does not apply if the basic Eq. (3.206) is directly integrated in time. A well-known method for numerical integration in time is given by the Newmark method, see Section 1.6 and Eq. (1.97). This may immediately be applied to Eq. (3.206) and is demonstrated with the following example.

Example 3.9 Beam under impact load
We refer to Example 3.2 with the same geometry and boundary conditions. A sudden concentrated single point load or *impact* is applied in mid span. A linear elastic behavior is assumed in a first approach to demonstrate basic characteristics of dynamic behavior under impact. Following data are chosen:

– Young's modulus is assumed with $E = 33\,000\,\text{MN/m}^2$ and the the specific *weight* with $25\,\text{kN/m}^3$. With an earth acceleration $g \approx 10\,\text{m/s}^2$ this leads to a specific *mass* $\varrho = 0.025/10 = 2.5 \times 10^{-3}\,\text{MNs}^2/\text{m}^4$ and with the cross-sectional area $A = 0.2 \cdot 0.4\,\text{m}^2$ to a beam mass per length $m = 0.2 \times 10^{-3}\,\text{MNs}^2/\text{m}^2$.

– With the given parameters the longest natural period is determined with $T = \frac{2L^2}{\pi} \sqrt{\frac{m}{EJ}} = 0.038\,\text{s}$ and a frequency $\nu = 26\,\text{Hz}$.

The point load is characterized by an amplitude P_0 and a time variation function

$$P(t) = P_0\, f(t) \tag{3.220}$$

The time function is chosen as a step function with limited duration

$$f(t) = \begin{cases} 1 & \text{for} & t \le t_d \\ 0 & & t > t_d \end{cases} \tag{3.221}$$

Thus, loading is characterized by the parameters P_0, t_d. Values $P_0 = -0.07\,\text{MN}$ and $t_d = 0.1\,\text{s}$ are used for the linear elastic reference case.

The spatial discretization is performed with $n_E = 20$ extended two-node Bernoulli beam elements, see Section 3.3.2. The Newmark method, see Section 1.6, is used for time integration with a time step $\Delta t = 0.001$s. The investigated time span is chosen with $0.06\,\text{s}$ which has to be related to the longest natural period, see above.
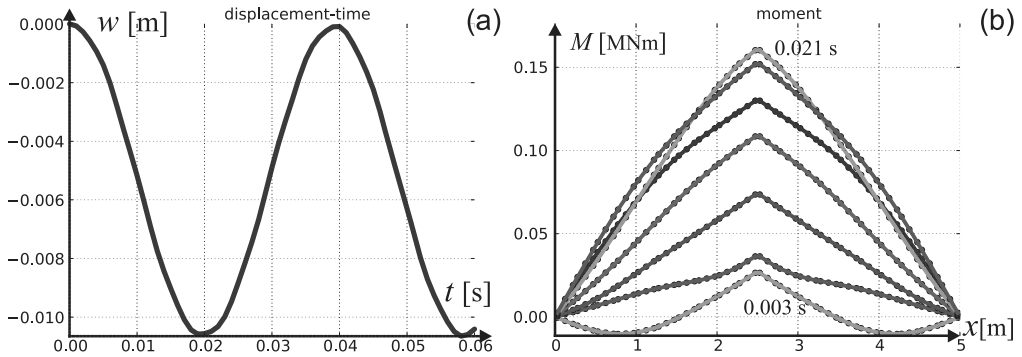
Figure 3.21: Example 3.9 linear elastic (a) Mid-span deflection with time. (b) Moments along beam until the first maximum deflection.

Figure 3.21a shows the computed mid-span deflection during time with the following characteristics:

– A cosine-shaped oscillation occurs.

– The maximum deflection doubles with an absolute value of 0.0106 m compared to the deflection value 0.0053 m caused by a quasistatic loading P_0.

In the same way maximum internal forces are doubled compared to the quasistatic case. Figure 3.21b shows the bending moments along the beam in certain time steps up to the time 0.02 s when the first mid-span maximum is reached. The following points are remarkable:

– Internal forces do not immediately follow the load due to inertial effects.

– There is no longer a triangular course due to a wave propagation effect of moments. In the beginning moments are initiated in the impact point, while the support areas are unaffected. In the following period moment waves travel along the beam and bring the whole beam into action.

Impact loads often have a short duration. Thus, a small parameter study is performed with varying load duration t_d and constant load amplitude $P_0 = -0.07$ MN. Figure 3.22a shows the computed maximum mid-span deflections related to the quasistatic deflection depending on t_d related to the longest natural period. If we consider a very short load duration time, e.g., $t_d = 0.001$ s, the beam gets only roughly 20% of the quasistatic moment. Or in other words, it may sustain five times the original load to have the same internal forces. This is generalized by the following conclusion:

• Very short loadings are compensated by inertia and only partially result in internal forces.
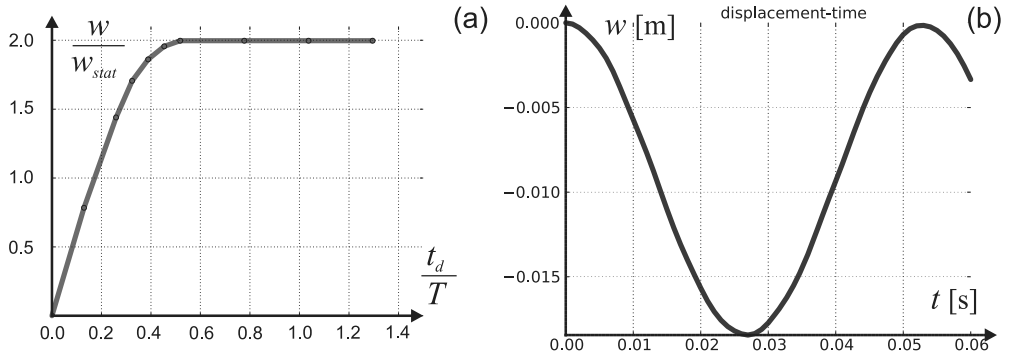
Figure 3.22: Example 3.9 (a) Related maximum deflection depending on related load duration time (b) RC deflection time curve.
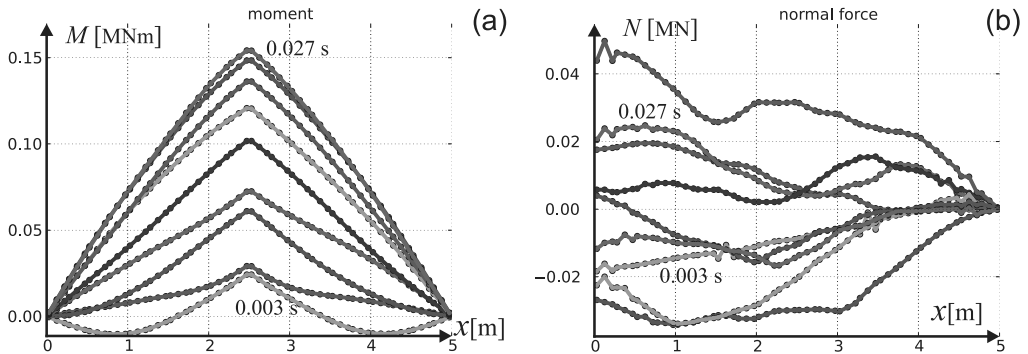
Figure 3.23: Example 3.9 RC (a) Moments along beam until first maximum displacement. (b) Normal forces along beam.

Finally, we consider the original reference case $P_0 = -0.07\,\text{MN}$ and $t_d = 0.1\,\text{s}$ but with a *nonlinear RC section* instead of linear elastic behavior. Material properties and reinforcement are chosen as in Example 3.2 with an additional reinforcement $A_{s2} = 12.57\,\text{cm}^2$, $d_2 = 5\,\text{cm}$ on the upper side. The computation leads to the following results:

- Figure 3.22b shows the mid-span displacement during time. Due to the reduced stiffness the period of the oscillation grows, compare Fig. 3.21a. Maximum mid-span displacement grows to 0.019 m, roughly a doubling occurs compared to the linear elastic case.

- Figure 3.23a shows the bending moments along the beam up to the time 0.027 s when first mid-span maximum is reached. The same moments occur with some time shift compared to the linear elastic case, see Fig. 3.21a.

- In the case of RC some normal forces arise without normal force loading, see Fig. 3.23b. This is caused by the beam's movement in the longitudinal direction due to cracking, which is constrained by the beam's inertia.

– The ultimate limit state is not reached for the given load with maximum absolute values of concrete strain $\epsilon_c \approx -1\text{‰}$ and $\epsilon_s \approx 2\text{‰}$.

The characteristics of the beam's response are to a large extent determined by the time variation function $f(t)$, see Eq. (3.220). The direct integration in time allows for arbitrary characteristics. A harmonic type would potentially lead to a *resonance* if the excitation frequency is near the natural periods. This effect may occur both for linear and nonlinear behavior.

End Example 3.9

Another aspect of dynamics is *damping*. Damping leads to a *dissipation of energy*. A first model of dissipation has already been given by viscosity, see Fig. 2.8. Dissipation may be treated on the material level and on the system level.

An example of dissipation on the material level has been given by the cyclic behavior of steel, see Fig. 2.10b. This is implicitly covered by the incremental material description (Eq. (1.50)) leading to different tangential stiffness in the case of loading and unloading and thus to energy dissipation within cycles of stress–strain histories.

Dissipation on the system level can be treated in analogy to Eq. (2.21) describing a Kelvin–Voigt element which is extended with a term for mass inertia. This extension is introduced in the generalized form (3.208)

$$\mathbf{M} \cdot \ddot{\boldsymbol{v}}(t) + \mathbf{C} \cdot \dot{\boldsymbol{v}}(t) + \mathbf{K} \cdot \boldsymbol{v}(t) = \mathbf{p}(t) \tag{3.222}$$

with a viscosity matrix $\mathbf{C}$. For aspects determining $\mathbf{C}$ in the case of structural systems and solution methods for Eq. (3.222) see, e.g., [3, 9.3].

Chapter 4

Strut-and-Tie Models

4.1 Elastic Plate Solutions

Beams are characterized insofar as height and width of their cross section are small compared to their span. This allows applying the Bernoulli–Navier hypothesis: undeformed plan cross sections remain plane during a deformation. This kinematic assumption is no longer valid for *plates* where height has the same dimension as span.

An example is given with the single-span deep beam with an opening, see Fig. 4.1a, as a special case of a plate. It is supported by a column on the lower left side and fixed in a larger shear wall on the right side. The loading is given by a distributed load and a concentrated load on the upper side.

Even if linear elastic material behavior is assumed an analytic solution is not available for such a system. A numerical method has to be used instead for solution and the finite element method is appropriate. The discretization may be performed with the plane four-node continuum element, see Section 1.3. The displacement field has two degrees of freedom u, v, see Eq. (1.35). Strains and stresses have components

$$\boldsymbol{\epsilon} = \begin{pmatrix} \epsilon_x \\ \epsilon_y \\ \gamma_{xy} \end{pmatrix}, \quad \boldsymbol{\sigma} = \begin{pmatrix} \sigma_x \\ \sigma_y \\ \sigma_{xy} \end{pmatrix} \tag{4.1}$$

see Eqs. (1.39, 1.42). The steps of the discretization follow the general outline as has been described in Section 1.5. The evaluation of integrals is performed with a Gauss integration according to Section 1.6 and Eq. (1.68). Integration order is 2×2 with $n_i = n_j = 2$.

Regarding the material a linear elastic behavior should be assumed in a first approach to assess such a problem. Plane strain or plane stress conditions, see Eqs. (1.44, 1.45), can be assumed for a plate beam depending on the width. With a thickness of $b = 0.6\,\text{m}$ for the given example plane stress conditions seem to be more appropriate, but the differences do not have a major effect. Both are subsumed as 2D states. After prescribing boundary conditions for u, v and loading a solution can be computed in one step according to Eq. (1.13) and an equilibrium iteration is not necessary.

Results for the problem formulated in Fig. 4.1a are shown in Fig. 4.1b. Results are given as principal stresses in each integration point of each element. A *principal stress state* is

(a)

4.0 m

5.0 MN

1.0 m

120 kN/m

4.0 m

$b = 0.6$ m

1.5m 1.0m

2.75 m

shear wall

1.5 m

0.5 m

11.0 m

(b)

principal compression
principal tension
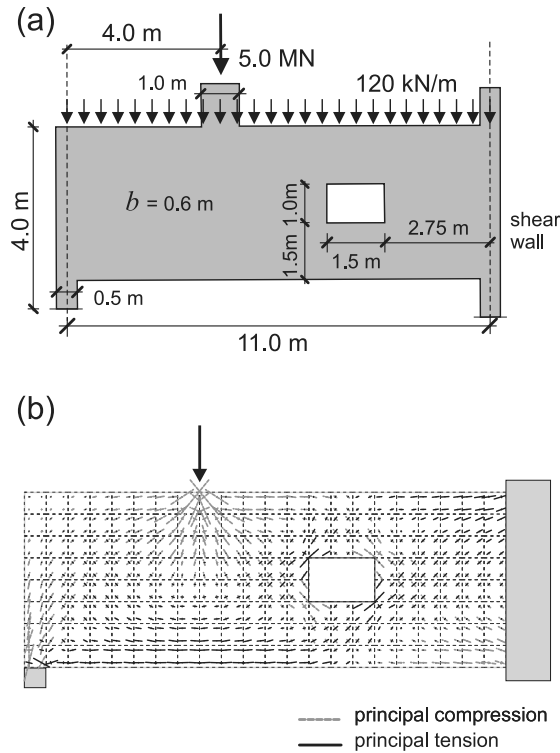
Figure 4.1: Deep beam (a) System (b) Principal stresses.

characterized by two principal stress values σ_1, σ_2 and an orientation angle φ which indicates the inclination of the stress component σ_1 against the global x-axis. The orientation of the stress component σ_2 is perpendicular. Due to their inclination principal stresses σ_1, σ_2 are locally in equilibrium to stresses $\sigma_x, \sigma_y, \sigma_{xy}$. More details regarding the principal values will be given in Sections 5.2.3 and 6.1.2.

The varying orientation of principal stresses leads to principal stress trajectories which are derived from the orientation of the principal stresses only.

- Plane *principal stress trajectories* indicate the flow of forces for 2D states.

As an example, Fig. 4.1b basically shows such a flow force. A compression arch arises from the point of the concentrated load to the lower left and right bearing. The lower left bearing which may displace horizontally is tied to the right end through a tension band. The upper right side of the deep beam has a tension band as it is fixed in the shear wall. Furthermore, the compression arch is disturbed by the opening which leads to a secondary system of compression and tension bands.

The rough outline of force flow from immediate inspection may be stated more precisely through a construction of trajectories. Let $y(x)$ be the function describing the course of a stress trajectory in the x, y-plane and x_1, y_1 with $y_1 = f(x_1)$ be a starting point.

Such a starting point should lie on a bounding edge. The fields of stress components $\sigma_x(x,y)$, $\sigma_y(x,y)$, $\sigma_{xy}(x,y)$ have to be known. As discrete values are practically given with results in integration points an interpolation has to be used to construct fields yielding results for every desired coordinate. Such a method is described in Example 6.1. With this prerequisite, the equation

$$\frac{\mathrm{d}y}{\mathrm{d}x} = \varphi = f(\sigma_x(x,y),\,\sigma_y(x,y),\,\sigma_{xy}(x,y)) \tag{4.2}$$

provides an ordinary differential equation whereby the orientation angle φ of principal stresses is determined through, e.g., Eq. (6.5). This problem at least can be solved numerically for $y(x)$. The inspection of a number starting points on the boundary finally leads to a pattern of trajectories.

Such a relatively elaborate procedure may be simplified for practical purposes.

- A manual sketch of curves along principal stress orientations underlayed by a diagram of principal stresses is generally sufficient to approximate trajectories in order to understand the force flow in a plate.

Some trajectories have to be chosen out of a more or less dense band such that they give a characteristic pattern of force flow or – more generally – a conceptual model, see Section 1.1. This task again has not a unique solution but is essential for strut-and-tie models.

4.2 Modeling

The survey of trajectories and a potential way of force flow is a base for the design of plates consisting of reinforced concrete. Such a design may have as premises:

– Trajectories under compression are assigned to *concrete struts*.

– Trajectories under tension are assigned to *reinforcement ties*.

Such assignments are approximate. First of all, trajectories or force flow itself may be derived by a (presumably) sound estimation. Furthermore, trajectories are curved but struts and ties should be straight by definition. Thus, the geometries of the chosen characteristic trajectories are approximated by straight-line segments. A rough approximation with only a few line segments is generally sufficient. This approach leads to a truss with

– compression members corresponding to struts,

– tensile members corresponding to ties,

– and nodes connecting struts and ties.

which altogether form a *strut-and-tie model*. A possible model for the example of Fig. 4.1a is shown in Fig. 4.2a [16, 8.8]. Determination of member layout obviously has a margin of discretion. An alternative for the same system is given in [17, 6].

The approach using trajectories as orientation or the *trajectory method* has the *load path method* as an alternative. A load path connects the points where loads are applied to a
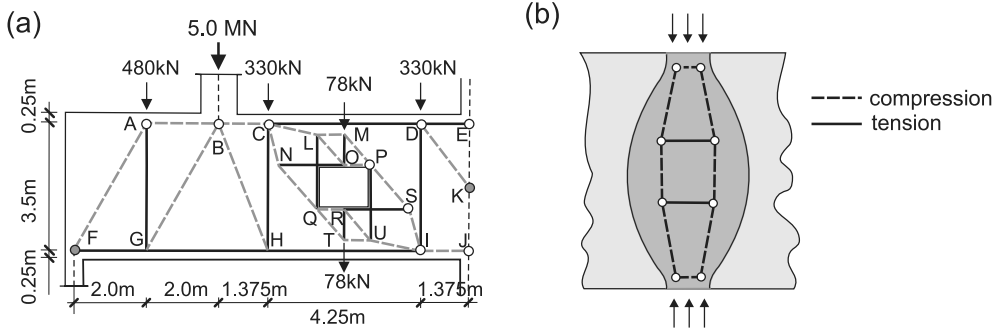
Figure 4.2: (a) Example truss system. (b) Compression field as strut-and-tie model.

structure to its support points by straight-line segments with minimized length. From a statical point of view these line segments correspond to compression members or struts in most cases. As a load path necessarily involves redirections, redirection forces are necessary from a statical point of view to ensure equilibrium. Such redirection forces may be compressive corresponding to struts or tensile corresponding to ties. Both the load path method and the trajectory method should lead to similar results for a given structural task. Both methods may be combined with criteria of total energy minimization to optimize member layout of a strut-and-tie modeling.

Such a result of strut-and-tie modeling is used for the reinforcement design of the given task. This leads to a new aspect in the model of modeling as has been discussed in Section 1.1.

- In contrast to the intention of conventional modeling the layout of strut-and-tie models to some extent influence the behavior of the corresponding plates or the reality of interest, respectively.

Plates as all structures of civil engineering initially behave linear elastic as has been sketched in Section 4.1. This changes during crack formation of reinforced concrete plates: the force flow changes according to the design of rebars and their interaction of compressive zones. The strut-and-tie model is "good" if some extent of agreement is given between *compression fields* of the reality of interest and the struts of the model.

Anyway, properties have to be assigned to a strut-and-tie model beneath its member layout. Struts and ties are uniaxial structural elements which must be given a cross section. While this is naturally given for ties through rebar cross-sectional areas the assignment of cross sections to struts is artificial to some extent. Struts may be regarded as models of compression fields as is exemplary shown in Fig. 4.2b with a characteristic oval shape and a fan-out and fan-in of stresses. A single strut obviously lends itself for a secondary strut-and-tie model. The strut's outer oval may be replaced by a rectangle of equal area leading to a width. A cross-sectional area is determined in combination with depth. This outlines one approach of alternatives for the cross section determination of struts.

Material properties have to be assigned beside geometric properties. They can be derived according to Section 2.1 for the uniaxial behavior of concrete and according to Section 2.3 regarding rebars. Tension-stiffening effects on rebars may be treated as is described in Sec-

tion 2.7. Connection of struts and ties in nodes is outlined in Section 4.5. Code provisions for strut-and-tie models are given in [26, 5.6.4,6.5], [18, 7.3.6]. Reductions of uniaxial concrete strength due to lateral tensile stresses – frequently occurring in biaxial stress fields but unseizable with a truss – have to be regarded in particular.

The foregoing reasoning should lead to a strut-and-tie model for a given structural problem together with boundary conditions and loading. A more detailed description of the method is given in [16, 8], with a comprehensive collection of examples in [17]. Methods to determine forces in struts and ties and the load-carrying capacity of structures remain to be described.

4.3 Solution Methods for Trusses

A strut-and-tie model has to be analyzed as truss. Thus, we consider a plane truss with n_E bars and n_N nodes. Every node has two degrees of freedom u, v. Some nodes must be supported and degrees of freedom constrained to keep the truss in position. This leads to a total number of n degrees of freedom. Structural behavior of trusses is again ruled by kinematic compatibility, equilibrium, and material behavior.

We start with considering kinematic compatibility or the *kinematic assumption* for a truss. A truss member e is given by the end nodes I, J. It has an orientation angle α from I to J and node displacements $\tilde{u}_J^e$, $\tilde{u}_I^e$ in the longitudinal member direction. The strain ς of member e is defined as

$$\varsigma^e = \tilde{u}_J^e - \tilde{u}_I^e \tag{4.3}$$

This differs from the conventional definition of strain, but is more convenient for the following argumentation. Displacements in the longitudinal bar direction have to be transformed into the global system. This leads to global displacements of nodes I, J

$$\boldsymbol{v}_I = \left(\begin{array}{c} u_I \\ v_I \end{array} \right) = \left(\begin{array}{c} \cos \alpha^e \\ \sin \alpha^e \end{array} \right) \tilde{u}_I^e, \quad \boldsymbol{v}_J = \left(\begin{array}{c} u_J \\ v_J \end{array} \right) = \left(\begin{array}{c} \cos \alpha^e \\ \sin \alpha^e \end{array} \right) \tilde{u}_J^e \tag{4.4}$$

see Fig. 4.3a, resulting in

$$\tilde{u}_I^e = \left(\begin{array}{cc} \cos \alpha^e & \sin \alpha^e \end{array} \right) \cdot \boldsymbol{v}_I, \quad \tilde{u}_J^e = \left(\begin{array}{cc} \cos \alpha^e & \sin \alpha^e \end{array} \right) \cdot \boldsymbol{v}_J \tag{4.5}$$
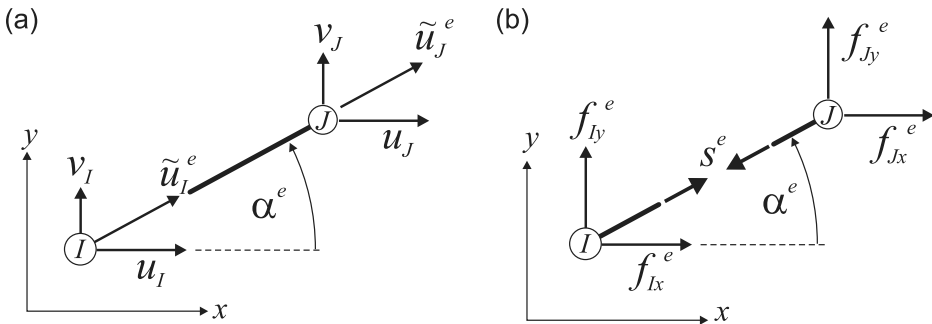
Figure 4.3: Truss (a) Member strain. (b) Member force and nodal forces.

Combining Eqs. (4.3, 4.5) leads to the strain of member e depending on global displacements

$$\varsigma^e = \left(\begin{array}{cc} -\cos\alpha^e & -\sin\alpha^e \end{array} \right) \cdot \boldsymbol{v}_I + \left(\begin{array}{cc} \cos\alpha^e & \sin\alpha^e \end{array} \right) \cdot \boldsymbol{v}_J \tag{4.6}$$

Collection of all bars in a vector gives a formulation

$$\left(\begin{array}{c} \vdots \\ \varsigma^e \\ \vdots \end{array} \right) = \left[\begin{array}{ccccc} & \vdots & \vdots & \vdots & \vdots \\ \cdots & -\cos\alpha^e & -\sin\alpha^e & \cdots & \cos\alpha^e & \sin\alpha^e & \cdots \\ & \vdots & \vdots & \vdots & \vdots \end{array} \right] \cdot \left(\begin{array}{c} \vdots \\ u_I \\ v_I \\ \vdots \\ u_J \\ v_J \\ \vdots \end{array} \right) \tag{4.7}$$

or in a matrix notation

$$\mathbf{e} = \mathbf{B} \cdot \boldsymbol{v}, \quad \mathbf{B} \in \mathbb{R}^{n_E \times n}, \, \boldsymbol{v} \in \mathbb{R}^n, \, \mathbf{e} \in \mathbb{R}^{n_E} \tag{4.8}$$

whereby d in $\mathbb{R}^d$ indicates the dimension of matrices and vectors. The vector $\mathbf{e}$ collects all n_E member strains and $\boldsymbol{v}$ all n nodal displacements. There is a similarity compared to Eq. (1.2) for strains within finite elements.

Equilibrium has to be considered in the next step. A member e has end nodes I, J and a member force s^e (tension positive, compression negative). Member e contributes forces both to the nodes I, J, see Fig. 4.3b, leading to global nodal forces

$$\mathbf{f}_I^e = \left(\begin{array}{c} f_{Ix}^e \\ f_{Iy}^e \end{array} \right) = s^e \left(\begin{array}{c} -\cos\alpha^e \\ -\sin\alpha^e \end{array} \right), \quad \mathbf{f}_J^e = \left(\begin{array}{c} f_{Jx}^e \\ f_{Jy}^e \end{array} \right) = s^e \left(\begin{array}{c} \cos\alpha^e \\ \sin\alpha^e \end{array} \right) \tag{4.9}$$

Local equilibrium condition for nodes I, J with external nodal loads $\mathbf{p}_I, \mathbf{p}_J$ requires

$$\sum_e \mathbf{f}_I^e = \mathbf{p}_I, \quad \sum_e \mathbf{f}_J^e = \mathbf{p}_J \tag{4.10}$$

The global equilibrium condition is given through assembling of all node contributions

$$\left[\begin{array}{ccc} & \vdots & \\ \cdots & -\cos\alpha^e & \cdots \\ \cdots & -\sin\alpha^e & \cdots \\ & \vdots & \\ \cdots & \cos\alpha^e & \cdots \\ \cdots & \sin\alpha^e & \cdots \\ & \vdots & \end{array} \right] \cdot \left(\begin{array}{c} \vdots \\ s^e \\ \vdots \end{array} \right) = \left(\begin{array}{c} \vdots \\ p_{Ix} \\ p_{Iy} \\ \vdots \\ p_{Jx} \\ p_{Jy} \\ \vdots \end{array} \right) \tag{4.11}$$

or in a matrix notation

$$\mathbf{f} = \mathbf{p}, \qquad \mathbf{f}, \mathbf{p} \in \mathbb{R}^n \tag{4.12}$$

with

$$\mathbf{f} = \mathbf{B}^T \cdot \mathbf{s}, \qquad \mathbf{B}^T \in \mathbb{R}^{n \times n_E}, \, \mathbf{s} \in \mathbb{R}^{n_E} \tag{4.13}$$

whereby the vector $\mathbf{s}$ collects all n_E member forces, $\mathbf{f}$ the nodal forces and $\mathbf{p}$ all n nodal loads. Here we see again the matrix $\mathbf{B}$ of Eq. (4.8), but it has been transposed. There is a similarity compared to Eq. $(1.58)_1$ for internal nodal forces of finite elements.
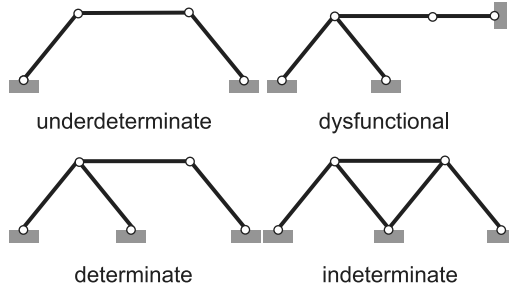
Figure 4.4: Truss system types.

A case $n_E < n$ indicates an *statically underdeterminate* system or kinematic chain, see Fig. 4.4, $n_E = n$ a *statically determinate* and $n_E > n$ a *statically indeterminate* system. Member forces for a statically determinate system may be determined directly from Eq. (4.13) by $\mathbf{s} = \mathbf{B}^{-1} \cdot \mathbf{p}$ in case $\mathbf{B}$ is not singular and the inverse $\mathbf{B}^{-1}$ exists. A singular $\mathbf{B}$ indicates an *dysfunctional* system. Statically underdeterminate systems are possible for strut-and-tie models of plates as stability is reached through the concrete body surrounding struts and ties. Member forces may be determined regarding equilibrium of one node after another in a sequence of neighbored nodes for such cases. The introduction of blind members should be considered to make an underdeterminate system determinate. Member forces calculation of indeterminate systems requires implication of stiffness and kinematic compatibility. This is resolved in the following.

Material behavior has to be considered in the last step. To begin with, a uniaxial linear elastic material behavior is assumed, see Eq. (1.43). A_e is used for the cross-sectional area of a member e, L_e as its length and E_e as its Young's modulus. With $s_e = A_e \, \sigma_e$ with the stress σ_e of member e and $\epsilon_e = \varsigma^e / L_e$, where ϵ_e is the physical strain of member e, member forces are given by

$$s_e = C_e \, \varsigma_e, \quad C_e = \frac{E_e A_e}{L_e}, \quad e = 1, \ldots, n_E \tag{4.14}$$

In a matrix notation this can be written as

$$\mathbf{s} = \mathbf{C} \cdot \mathbf{e}, \quad \mathbf{C} \in \mathbb{R}^{n_E \times n_E} \tag{4.15}$$

where the material matrix $\mathbf{C}$ is diagonal with coefficients C_e. Combination of Eqs. (4.13, 4.15, 4.8) leads to

$$\mathbf{K} \cdot \boldsymbol{v} = \mathbf{p}, \quad \mathbf{K} = \mathbf{B}^T \cdot \mathbf{C} \cdot \mathbf{B}, \quad \mathbf{K} \in \mathbb{R}^{n \times n} \tag{4.16}$$

with a constant symmetric stiffness matrix $\mathbf{K}$. There is a similarity of Eq. (4.16) compared to Eq. (1.61) for the linear stiffness matrix of finite elements. This completes the linear elastic framework for trusses. Obviously strong similarities to finite element approaches are given. In fact, a plane truss member corresponds to a two-node bar element in plane, see Section 1.3, with a one-point integration. An application is demonstrated with the following example.

Example 4.1 Deep beam with strut-and-tie model
We refer to the problem given in Fig. 4.1a and linear elastic principal stresses shown in Fig. 4.1b. This problem is also discussed in [16, 8.8]. The chosen strut-and-tie model is shown in Fig. 4.2a. Obviously there is some effort to circumvent the central rectangular hole. The resulting total load has been distributed to upper nodes according to the loading scheme of Fig. 4.1a.

The system has $n_E = 36$ bars and 21 nodes. Seven nodal degrees of freedom are restrained by boundary conditions leading to $n = 2 \cdot 21 - 7 = 35$. Thus, we have "nearly" a statically determinate system. Internal forces are influenced by the stiffness of the members to a small extent.
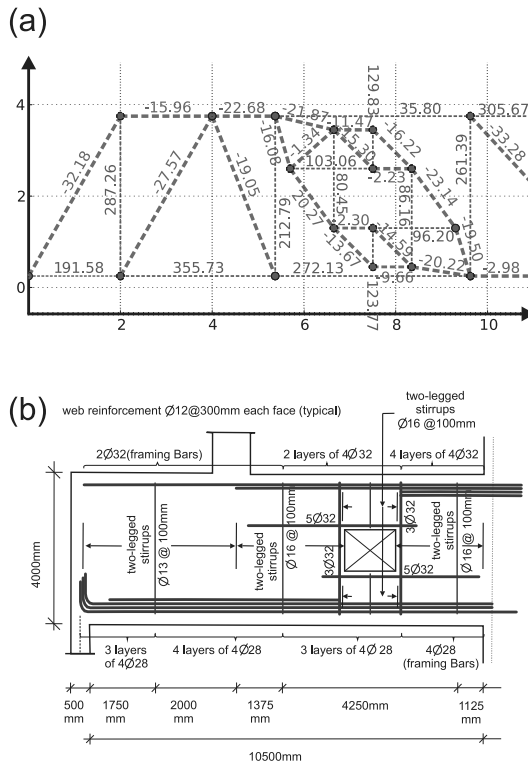

Figure 4.5: Example 4.1 (a) Member stresses. (b) Proposed reinforcement scheme.

A preliminary computation reveals a distinction between struts ($\rightarrow$ compressive) and ties ($\rightarrow$ tensile). The following reference values for Young's modulus and cross-sectional area are chosen for the ties: $E_s = 200\,000\,\mathrm{MN/m^2}$, $A_s = 10 \times 10^{-3}\,\mathrm{m^2}$, and for the struts: $E_c = 30\,000\,\mathrm{MN/m^2}$, $A_c = 0.12\,\mathrm{m^2}$. The last value corresponds to a deep beam thickness $b = 0.6\,\mathrm{m}$ and an assumed strut width of 0.2 m.

Computed stresses of struts and ties are shown in Fig. 4.5a. Negative values with small amount correspond to struts, and positive values with relatively large amount correspond to ties. According to each individual stress value the reference value of cross-sectional area may be increased or reduced for the corresponding member to gain some target stress. Target stress values may be derived from strength values in codes, see e.g., [26, 6.5].

A reinforcement scheme as proposed in [16, Fig. 8.49] is shown in Fig. 4.5b. Single vertical ties of the model are distributed as stirrups with a small spacing. The width of cracks occurring with ties may be estimated according to Appendix B.

——————————————————————————————— End Example 4.1

An iteration has to be considered in the case of statically indeterminate systems as revaluation of cross-sectional areas of rebars influences the stiffness of ties and insofar the results of a statically indeterminate calculation. On the other hand, assumptions about the stiffness of struts are basically uncertain. Thus, statically determinate systems are preferred for strut-and-tie models.

A nonlinear material behavior is considered for trusses in the following. Actually struts and ties have limited bearing capacities. This may in a first approach be described with an uniaxial elastoplastic material law, see Section 2.3 applied to both the reinforcement and the compressive concrete.

The linear elastic material law (Eq. (4.14)) changes into the incremental form

$$\dot{s}_e = C_{Te}\,\dot{\varsigma}_e, \quad e = 1, \ldots, n_E \tag{4.17}$$

or in the matrix notation

$$\dot{\mathbf{s}} = \mathbf{C}_T \cdot \dot{\mathbf{e}} \tag{4.18}$$

with a diagonal tangential material stiffness $\mathbf{C}_T$. The coefficients C_{Te} are determined according to Section 2.3 whereby the material model of elastoplasticity is also applied to uniaxial concrete behavior with adapted material parameters. The combination of Eqs. (4.8, 4.13, 4.17) leads to rates of nodal forces

$$\dot{\mathbf{f}} = \mathbf{K}_T \cdot \dot{\boldsymbol{v}} \tag{4.19}$$

with a tangential system stiffness in analogy to Eq. (4.16)

$$\mathbf{K}_T = \mathbf{B}^T \cdot \mathbf{C}_T \cdot \mathbf{B}, \qquad \mathbf{K}_T \in \mathbb{R}^{n \times n} \tag{4.20}$$

One has to distinguish upper T for transposed from lower T for tangential. Equilibrium has a condition

$$\mathbf{r}(\boldsymbol{v}) = \mathbf{p} - \mathbf{f}(\boldsymbol{v}) \tag{4.21}$$

in analogy to Eq. (1.69). The solution may be determined along the outline for the incrementally iterative scheme as has been described in Section 1.6.

The application of strut-and-tie models is not restricted to deep beams. Every plane structure which does not behave according to the Bernoulli–Navier hypothesis of plane deformed cross sections lends itself for strut-and-tie models. This is demonstrated with the following corbel example in connection with an elastoplastic analysis.

Example 4.2 Corbel with an elastoplastic strut-and-tie model
Corbel geometry, loading and strut-and-tie model are shown in Fig. 4.6. The model has $n_E = 14$ members and $n = 12$ degrees of freedom, i.e., the system is twofold statically indeterminate. A provisional first calculation has to be performed to distinguish between tensile and compressive members. Basing upon this calculation member properties are chosen as follows:

- Tensile members 1–7 are chosen as elastoplastic ties with a Young's modulus $E = 200\,000\,\mathrm{MN/m^2}$, an initial yield strength $f_{yk} = 500\,\mathrm{MN/m^2}$ and a reference cross-sectional area $A_{s,\mathrm{ref}} = 10\,\mathrm{cm^2} = 10 \times 10^{-4}\,\mathrm{m^2}$. The cross-sectional area of each particular member is modified by a factor which is also given in Fig. 4.6b.

- Compressive members 8–14 are chosen as struts with a Young's modulus $E = 30\,000\,\mathrm{MN/m^2}$. Concrete is assumed as elastoplastic in this context with an initial yield limit $f_{yk} = 40\,\mathrm{MN/m^2}$. The assumed value is relatively large. Code provisions restrict allowable concrete stresses to a large extent, see e.g., [26, 6.5]. The cross-sectional area of all struts is assumed with a width $h = 0.05\,\mathrm{m}$ and a corbel depth of $b = 0.5\,\mathrm{m}$ leading to $A_c = 0.025\,\mathrm{m^2}$.

- The entity of all struts in the model corresponds to a single oval strut, see Fig. 4.2b. The redirection forces of this larger oval strut are assigned to the intermediate horizontal and vertical ties or stirrups.

- Finally, a slight hardening, see Section 2.3, is assumed for the yielding of the reinforcing steel and the concrete to avoid singularities of the tangential stiffness.

An approach for system building and solution is given by Eqs. (4.19–4.21). The finite element method with 2D-bar elements in a plane according to Section 1.3, material law according to
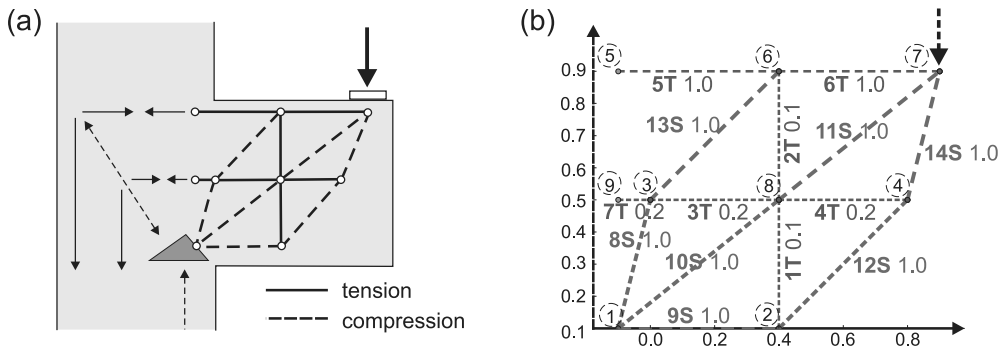
Figure 4.6:   Corbel example 4.2 (a) System. (b) Strut-and-tie model.
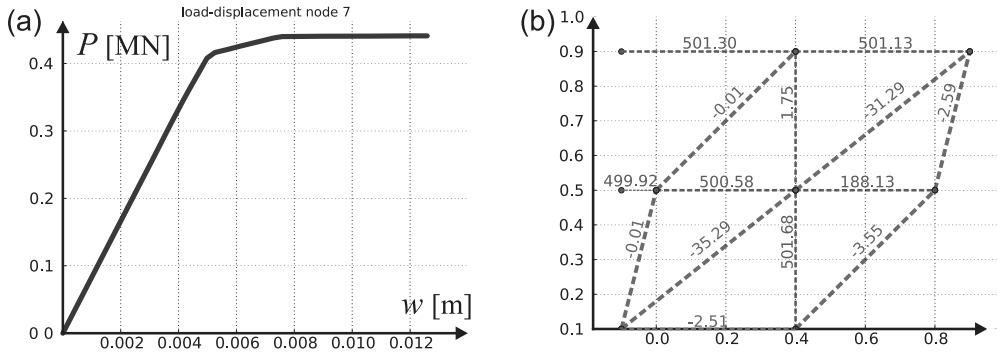
Figure 4.7: Example 4.2 (a) Load–displacement curve. (b) Member stresses.

Section 2.3, and system building according to Section 3.4 may be applied alternatively and leads to the same results.

Loading is applied with prescription of the vertical displacement of the load bearing node. The solution is determined incrementally iterative with the Newton–Raphson approach, see Section 1.6, and arc length control, see Appendix A. The computed load-displacement curve is shown in Fig. 4.7a. The deformation behavior can be described as follows:

– A linear elastic behavior is given initially up to reaching the first yielding of a tie.

– A strongly decreased stiffness occurs with the first tie yielding but some more loading can be applied.

– The ultimate limit state is reached with the yielding of other ties in the statically indeterminate system such that the system becomes "*nearly* kinematic." The system does not become "*really* kinematic" with the hardening assumption. Without hardening the tangential system stiffness would become singular and a unique solution could not be determined anymore.

The computed member stresses in the final state are shown in Fig. 4.7b. The yield limit is reached in most ties and slightly exceeded due to hardening. Struts are not critical in this particular case, but not far away from reaching the nominal yield limit.

End Example 4.2

Inclusion of limited strength, e.g., with elastoplasticity, allows for a direct determination of ultimate loads of strut-and-tie models. The computed deformation behavior has to be judged with some caution due to the limited ability of struts to model the behavior of compression fields.

4.4   Rigid-Plastic Truss Models

Strut-and-tie models offer a relatively simple way to determine the relation between loading on one hand and reinforcement stresses and estimated demands of concrete on the other hand

ending up with the ultimate limit loads. The ability of strut-and-tie models to determine the deformation behavior of real structures is limited as the material laws (Eqs. (4.14, 4.18)) are principally limited in their capability to capture in particular the deformation behavior of compressions fields.

There is no easy way to overcome this presumable drawback. Thus, we accept it as a characteristic property of strut-and-tie models. However, a way to simplify the description of material behavior is opened. We reformulate the problem of elastoplasticity for trusses. First of all, conditions for kinematic compatibility according to Eq. (4.8) (n_E equations) and equilibrium according to Eq. (4.13) (n equations) are kept. But the material behavior is described with

– a limit state or *strength condition*

$$|s_e| \leq s_{eu}, \quad s_{eu} = f_{ey}\, A_e, \ e = 1, \ldots, n_E \tag{4.22}$$

with signed forces s_e, unsigned bearing capacities s_{eu}, yield strength f_{ey} and cross section areas A_e of members,

– an assumption about strains or *flow rule*

$$|\varsigma_e| \begin{cases} = 0 & \text{for} \quad |s_e| < s_{eu} \\ > 0 & \quad |s_e| = s_{eu} \end{cases}, \quad e = 1, \ldots, n_E. \tag{4.23}$$

with the member strain according to Eq. (4.3),

– a dissipation condition or *Kuhn–Tucker conditions*

$$s_e\, \varsigma_e \geq 0, \quad \mathbf{s} \cdot \mathbf{e} \geq 0, \quad \mathbf{s}, \mathbf{e} \in \mathbb{R}^{n_E} \tag{4.24}$$

Elastic deformations are no longer considered in this *rigid-plastic* approach. This is convenient regarding the uncertain estimation of elastic stiffness properties of struts.

The balance of equations versus unknowns for a truss with m_E members and n nodal degrees of freedom shows the following: On one hand there are m_E member forces $\mathbf{s}$, n nodal displacements $\mathbf{u}$ and n_E bar strains $\mathbf{e}$ as unknowns, on the other hand there are $2 \times n_E + n$ equations (4.8, 4.13, 4.23) plus $2 \times n_E$ constraint equations (4.22, 4.24).

The solution of this problem is *not* straightforward. It is provided by methods of optimization and linear programming, see e.g., [63]. For the sake of simplicity, we restrict to a loading type

$$\mathbf{p} = \lambda\, \mathbf{p}_0, \quad \lambda > 0 \tag{4.25}$$

with a unit load $\mathbf{p}_0$ which is fixed and a loading factor λ. The basic solution idea is regarding a maximization problem

$$\lambda \to \max \tag{4.26}$$

while fulfilling equilibrium and the strength condition, i.e., constraints

$$\mathbf{B}^T \cdot \mathbf{s} = \lambda\, \mathbf{p}_0 \quad \text{and} \quad |s_e| \leq s_{eu}, \ e = 1, \ldots, n_E \tag{4.27}$$

The quantities $\mathbf{B}$, $\mathbf{s}_u$, $\mathbf{p}_0$ are known and $\mathbf{s}$, λ are unknown in this formulation. Equation (4.26) can be interpreted as maximization of loading.

Furthermore, linear programming theory states a so-called dual problem associated with the maximization problem. This is a minimization problem

$$\bar{\mathbf{s}}_u \cdot \bar{\mathbf{e}} \to \min \tag{4.28}$$

where $\bar{\mathbf{e}}$ collects all $|\varsigma_e|$ and $\bar{\mathbf{s}}_u$ all s_{eu}. The notation $\bar{\bullet}$ should be interpreted as operator on $\bullet$ in this context. The minimization has constraints

$$\mathbf{B} \cdot \mathbf{e} = \mathbf{u} \quad \text{and} \quad \mathbf{p}_0 \cdot \mathbf{u} = 1 \tag{4.29}$$

i.e., essentially kinematic compatibility. The quantities $\mathbf{B}$, $\mathbf{s}_u$, $\mathbf{p}_0$ are known and $\mathbf{e}$, $\mathbf{u}$ are unknown in this formulation. Equation (4.28) can be interpreted as minimization of energy.

Linear programming theory finally states that solutions $\mathbf{s}^\star$, $\lambda^\star$ exist for the maximization and $\mathbf{e}^\star$, $\mathbf{u}^\star$ for the minimization. The target functions (Eqs. (4.26, 4.28)) have the same optimal value

$$\lambda^\star = \bar{\mathbf{s}}_u^\star \cdot \bar{\mathbf{e}}^\star \tag{4.30}$$

with $\lambda^\star > 0$. It may be shown that the solutions fulfill the conditions

$$e_e^\star = 0 \text{ if } |s_e^\star| < s_{eu} \quad \text{and} \quad \mathbf{s}^\star \cdot \mathbf{e}^\star > 0 \tag{4.31}$$

The relations may be summarized as follows:

- The solutions $\mathbf{s}^\star$, $\lambda^\star$, $\mathbf{e}^\star$, $\mathbf{u}^\star$ of the associated optimization problems for load maximization and dissipated energy minimization are also the solutions of the rigid-plastic problem.

The rigid-plastic problem is also fulfilled by $\mathbf{s}^\star$, $\lambda^\star$, and $\beta\mathbf{e}^\star$, $\beta\mathbf{u}^\star$ with an arbitrary scalar $\beta > 0$. But this may violate the constraint $\mathbf{p}_0 \cdot \mathbf{u} = 1$ and the minimization problem is no longer solved. Regarding the rigid-plastic problem the absolute values of the deformations are *in*determinate. Only the relation between the deformation components is determined to some extent.

The rigid-plastic problem and the corresponding elastoplastic problem – with the same parameters but additional elasticity before yielding *without* hardening – share the solution. The vectors $\mathbf{s} = \mathbf{s}^\star$, $\mathbf{p} = \lambda^\star \mathbf{p}_0$ fulfill Eqs. (4.12, 4.13) and (4.19, 4.21) for arbitrary values of Young's modulus for members. Thus, the elastic stiffness does not influence the limit state for forces and loads. But elasticity influences the deformations of the elastoplastic problem due to elastic deformations prior to plastic deformations.

The solution method for the optimization problems still needs to be discussed. Primarily we are interested in loads $\lambda \mathbf{p}_0$ and member bar forces $\mathbf{s}$. Thus, we have to solve the maximization problem defined in Eqs. (4.26, 4.27). The solution is simple for statically determinate systems with $n = n_E$ and a square and nonsingular $\mathbf{B}$. The maximum value of λ can be easily found from $\mathbf{s} = \lambda \mathbf{B}^{-1} \cdot \mathbf{p}_0$, see Eq. (4.27), and the condition $|s_e| \le s_{eu}$, $e = 1, \dots, n_E$. For small statically indeterminate systems a solution may be found by inspection or trial and error as is demonstrated in Example 4.3.

Larger problems require systematic methods of linear programming, e.g., the *simplex method* or general methods of optimization. The simplex method is a standard method to solve linear constrained optimization problems whereby a formulation like Eqs. (4.26, 4.27)

describes problems in all disciplines of science, technology and economics. The detailed description has to be omitted here for the sake of brevity, but is given, e.g., in [63].

Correspondence of the optimization problems to the rigid-plastic structural problem leads to the *limit theorems of plasticity*:

1. Any equilibrium state which fulfills the limit state condition, see Eqs. (4.26, 4.27), gives a *lower* bound for the loading factor λ.

2. The work $\bar{\mathbf{s}}_u \cdot \bar{\mathbf{e}}$ of load-bearing capacities on kinematically admissible deformations with a constraint $\mathbf{p}_0 \cdot \mathbf{u} = 1$, see Eqs. (4.28, 4.29), yields an *upper* bound value for the loading factor λ. An unconstrained formulation of this theorem is given by $\bar{\mathbf{s}}_u \cdot \bar{\mathbf{e}} = \lambda\, \mathbf{p}_0 \cdot \mathbf{u}$ or

   • internal work = external work

   leading to the

   $$upper \text{ bound of loading factor} \lambda \quad \rightarrow \quad \frac{\bar{\mathbf{s}}_u \cdot \bar{\mathbf{e}}}{\mathbf{p}_0 \cdot \mathbf{u}} \tag{4.32}$$

   whereby magnitudes of $\bar{\mathbf{e}}$, $\mathbf{u}$ are arbitrary but proportional.

These theorems are generally stated as a kind of postulates. Actually, their exact formulation and proof corresponds to linear programming theory.

Finally, deformations are regarded to make the outline complete. The following approach is appropriate instead of solving the minimization problem. Kinematic compatibility equation (4.8) is considered and reformulated with a unit matrix $\mathbf{I}_{n_E} \in \mathbb{R}^{n_E \times n_E}$

$$\mathbf{B} \cdot \mathbf{u} = \mathbf{I}_{n_E} \cdot \mathbf{e}, \quad \mathbf{e} \in \mathbb{R}^{n_E}, \mathbf{u} \in \mathbb{R}^n, \mathbf{B} \in \mathbb{R}^{n_E \times n}, n_E \geq n \tag{4.33}$$

As $\mathbf{B}$ has n linear independent rows Eq. (4.33) can be transformed into

$$\begin{bmatrix} \mathbf{I}_n \\ \mathbf{0} \end{bmatrix} \cdot \mathbf{u} = \begin{bmatrix} \mathbf{P} \\ \mathbf{Q} \end{bmatrix} \cdot \mathbf{e}, \quad \mathbf{I}_n \in \mathbb{R}^{n \times n}, \mathbf{0} \in \mathbb{R}^{(n_E-n) \times n}, \mathbf{P} \in \mathbb{R}^{n \times n_E}, \mathbf{Q} \in \mathbb{R}^{(n_E-n) \times n_E} \tag{4.34}$$

by Gauss elimination, see [54], with a unit matrix $\mathbf{I}_n$, a zero matrix $\mathbf{0}$ and generally fully occupied matrices $\mathbf{P}$, $\mathbf{Q}$. Equation (4.34) leads to

$$\mathbf{u} = \mathbf{P} \cdot \mathbf{e}, \quad \mathbf{Q} \cdot \mathbf{e} = 0 \tag{4.35}$$

Equation $(4.35)_2$ describes the kinematic compatibility of indeterminate systems. In the case $n_E = n$ the matrix $\mathbf{P}$ is the inverse of $\mathbf{B}$ and $\mathbf{Q}$ vanishes. From an analysis of forces and Eq. (4.23) a set of members can be determined with strains $\varsigma_i \neq 0$, $i = 1, \ldots, n_Y$ and all other members with $\varsigma_j = 0$, $j = n_Y + 1, \ldots, n_E$. The parameter n_Y indicates the number of yielding members. Thus, a submatrix $\mathbf{Q}'$ of $\mathbf{Q}$ is given in case $n_E > n$ by

$$\mathbf{Q}' \cdot \mathbf{e}' = 0, \qquad \mathbf{e}' \in \mathbb{R}^{n_Y}, \mathbf{Q}' \in \mathbb{R}^{(n_E-n) \times n_Y} \tag{4.36}$$

where $\mathbf{e}'$ collects all yielding ς_i. Two cases have to be distinguished.

– $n_Y \leq n_E - n$: Eq. (4.36) can only be fulfilled with $\mathbf{e}' = 0$, i.e., no deformation occurs at all.

– $n_Y > n_E - n$: a number of $n_Y - (n_E - n)$ components of $\mathbf{e}'$ may be chosen arbitrarily under the condition Eq. (4.24) while the rest is determined by Eq. (4.36). This leaves the absolute deformations undetermined.

Only the relations of the deformation components are determined to some extent by this approach. This is a characteristic property of rigid-plastic systems.

Things simplify in the case of a statically determinate system $n_E = n$. Kinematic compatibility of indeterminate systems $(4.35)_2$ vanishes and strains of yielding bars may be given arbitrary values, while all other strains are zero. With given strains $\mathbf{e}$ displacements $\mathbf{u}$ can be determined directly by Eq. $(4.35)_1$.

Example 4.3 Corbel with rigid-plastic strut-and-tie model
We refer to Example 4.2. The same system is treated as rigid-plastic using the first limit theorem of plasticity. This requires the knowledge of the cross-sectional areas of members and their yield stress. The values are taken from Example 4.2. Young's modulus and hardening behavior after reaching the yield limit are not relevant. Basic parameters are: number of $n_E = 14$ bars, nine nodes, three boundary nodes, and $n = 12$ degrees of freedom.

The following bases upon a linear elastic precalculation distinguishing between compressive and tensile members. To start with the states fulfilling the first limit theorem of plasticity are determined. Equilibrium is described by Eq. (4.13)

$$\mathbf{B}^T \cdot \mathbf{s} = \lambda \, \mathbf{p}_0 \qquad (4.37)$$

with the vector of member forces $\mathbf{s}$, a loading factor λ, a unit load

$$\mathbf{p}_0 = \begin{pmatrix} 0 & 0 & 0 & 0 & 0 & 0 & 0 & 0 & 0 & -1 & 0 & 0 \end{pmatrix}^T \qquad (4.38)$$

applied vertically downward on node 7, see Fig. 4.7b, and

$$\mathbf{B}^T =$$

$$\begin{bmatrix}
0 & 0 & 0 & 0 & 0 & 0 & 0 & 0 & 1 & 0 & 0 & -0.707 & 0 & 0 \\
-1 & 0 & 0 & 0 & 0 & 0 & 0 & 0 & 0 & 0 & 0 & -0.707 & 0 & 0 \\
0 & 0 & -1 & 0 & 0 & 0 & 1 & 0.243 & 0 & 0 & 0 & 0 & -0.707 & 0 \\
0 & 0 & 0 & 0 & 0 & 0 & 0 & 0.971 & 0 & 0 & 0 & 0 & -0.707 & 0 \\
0 & 0 & 0 & 1 & 0 & 0 & 0 & 0 & 0 & 0 & 0 & 0.707 & 0 & -0.243 \\
0 & 0 & 0 & 0 & 0 & 0 & 0 & 0 & 0 & 0 & 0 & 0.707 & 0 & -0.971 \\
0 & 0 & 0 & 0 & 1 & -1 & 0 & 0 & 0 & 0 & 0 & 0 & 0.707 & 0 \\
0 & 1 & 0 & 0 & 0 & 0 & 0 & 0 & 0 & 0 & 0 & 0 & 0.707 & 0 \\
0 & 0 & 0 & 0 & 0 & 1 & 0 & 0 & 0 & 0 & 0.781 & 0 & 0 & 0.243 \\
0 & 0 & 0 & 0 & 0 & 0 & 0 & 0 & 0 & 0 & 0.625 & 0 & 0 & 0.971 \\
0 & 0 & 1 & -1 & 0 & 0 & 0 & 0 & 0 & 0.781 & -0.781 & 0 & 0 & 0 \\
1 & -1 & 0 & 0 & 0 & 0 & 0 & 0 & 0 & 0.625 & -0.625 & 0 & 0 & 0
\end{bmatrix}$$
$$(4.39)$$

whereby the boundary nodes 1, 5, and 9 and their degrees of freedom are disregarded.

A number of $\bar{n}_E = n_E - n + 1 = 3$ more or less arbitrary member forces are prescribed and Eq. (4.37) remains with $n = 12$ equations for the remaining 11 member forces plus

the loading factor λ. This is principally solvable for a well-behaved structural system. The members 1, 7, 11, see Fig. 4.7b, are chosen for prescription by chance. This leads to the following steps to estimate an admissible loading factor:

– They are prescribed with their bearing capacities $s_1 = 0.05\,\text{MN}$, $s_7 = 0.1\,\text{MN}$, $s_{11} = -0.8\,\text{MN}$. The solution of the modified system (Eq. (4.37)) leads to $s_2 = 0$, $s_3 = 0.1$, $s_4 = -0.375$, $s_5 = 0.6372$, $s_6 = 0.6372$, $s_8 = 0$, $s_9 = -0.05$, $s_{10} = -0.88$, $s_{12} = -0.0707$, $s_{13} = 0$, $s_{14} = 0.0515$ and a loading factor $\lambda = 0.5498$.

– The computed member forces lead to stresses $\sigma_5 = 637\,\text{MN/m}^2$, $\sigma_6 = 637$, $\sigma_{10} = -44$ for the members 5, 6, and 10. This is not admissible, as the stresses exceed the material strength and the limit state condition (Eq. (4.22)) is violated for these members. All other computed member stresses are below material strength.

– All member forces are reduced by the smaller of the factors $500/637 = 0.785$ and $-40/-44 = 0.909$ which is 0.785 and leaves members 5 and 6 in a yielding state.

– To maintain equilibrium according to Eq. (4.37), the loading factor also has to be reduced by the same factor leading to a final loading factor of $\lambda = 0.785 \cdot 0.5498 = 0.43$. This is a *lower bound* for the real loading factor. The admissible loading is not less but may be larger.

– Deformations can be determined as described in Section 4.4. With two yielding members $n_Y = 2$ and $n_E - n = 2$. Thus, the matrix $\mathbf{Q}'$ has 2×2 dimension and Eq. (4.36) can only be fulfilled with zero deformations. This solution does not fulfill Eq. (4.23) and the solution of the rigid-plastic problem is not yet found.

Another choice by chance with the members 9, 11, 13 leads to the lower bound of $\lambda = 0.081$ and leaves only member 1 in a yielding state. No nonzero deformation can be found fulfilling the kinematic compatibility conditions.

Using the binomial coefficient there are

$$\binom{n_E}{\bar{n}_E} = \frac{n_E!}{\bar{n}_E!(n_E - \bar{n}_E)!} = 364 \tag{4.40}$$

possibilities for a choice of $\bar{n}_E = 3$ out of $n_E = 12$. This trial and error method to determine the largest value λ and therewith a solution of the rigid-plastic problem is obviously cumbersome.

The *simplex method* can be applied to determine the exact solution. The method yields the following results:

– The member stresses are shown in Fig. 4.8a with the five yielding members 1, 3, 5, 6, and 7. The corresponding loading factor is $\lambda = 0.44$. The horizontal tie in half-height is fully utilized which leads to some increase of the limit load.

– The results of Fig. 4.8a have to be compared the results of the elastoplastic calculation, see Fig. 4.7b. Both approaches basically lead to the same ultimate limit load and a similar stress distribution.
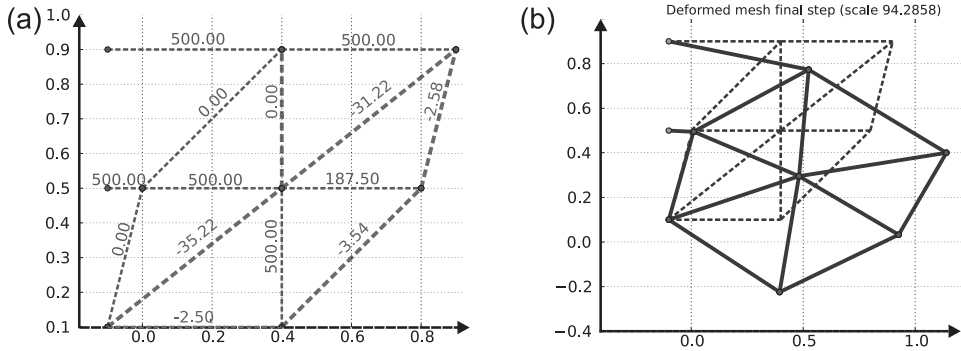
Figure 4.8: Example 4.3 (a) Member stresses. (b) Displacement mode.

- Displacements can be determined as is described in Section 4.4. With the five yielding members 1, 3, 5, 6, and 7 is $n_Y = 5 > n_E - n = 2$, i.e., three member strains may be chosen arbitrarily while the remaining two are determined with by Eq. (4.36). A choice $\varsigma_1 = 0.1, \varsigma_3 = 0.03, \varsigma_5 = 0.1$ leads to

$$\mathbf{e} = \begin{pmatrix} 0.1 & 0 & .03 & 0 & 0.1 & 0.1225 & 0.03125 & 0 & 0 & 0 & 0 & 0 & 0 & 0 \end{pmatrix}^T \quad (4.41)$$

With Eq. (4.28) the energy is $\bar{\mathbf{s}}_u \cdot \bar{\mathbf{e}} = 0.122375$

- The displacements can be determined by Eq. (4.35)$_1$. Results are shown in Fig. 4.8b. The vertical displacement of the loaded node 7 is computed with -0.278125.

- A displacement scaling factor of $1/0.278125 = 3.5955$ has to be chosen to fulfill Eq. (4.29) with $\mathbf{p}_0$ from Eq. (4.38). This leads to an energy $\bar{\mathbf{s}}_u \cdot \bar{\mathbf{e}} = 0.44$ and corresponds to the maximum loading factor as is stated by the limit theorem of plasticity.

End Example 4.3

In contrast to the elastoplastic model of Example 4.2 the determination of absolute deformations is not possible with the rigid-plastic approach due to arbitrary choice of some member strains. A deformation mode can be determined to some extent.

4.5 More Application Aspects

The focus of strut-and-tie models is on ultimate limit loads of reinforced concrete structures. This primarily depends on the strength of the ties and struts. Furthermore, strength of members depends on cross-sectional areas and material strength of materials. While both data can be reliably – within usual scatter – determined for the reinforcement uncertainties remain for concrete struts.

A conservative rule to determine the width of struts can be derived from the inspection of nodes connecting struts and ties. Some hints will be given in the following paragraph. The estimation of the concrete compressive strength of struts is insofar difficult as pure uniaxial
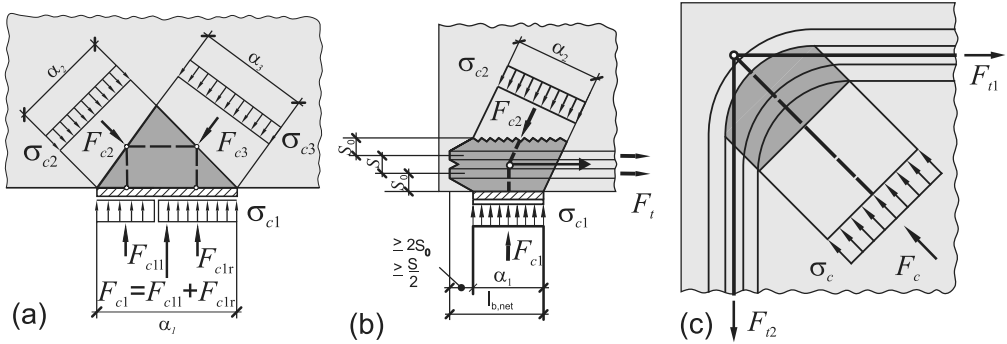
Figure 4.9: (a) Compression node. (b) Compression–tension node. (c) Reinforcement redirection node.

compression states are generally not given in plates. A principal compression in many cases is combined with a more or less pronounced lateral principal tension. An example can be seen with the introductory example and Fig. 4.1b where the diagonal compression fields with their major principal compression have a minor principal tension. Such a lateral tension reduces the compressive strength. Thus, the strength for struts should be reduced compared to uniaxial compressive strength. Recommendations are given in [26, 6.5.2], [18, 7.3.6.2].

An essential part of strut-and-tie models are nodes. This term gets a specific meaning in this context different from a node in a finite element discretization. Nodes connect struts and ties and permit an exchange of forces. The most important types are given by:

– Compression node without ties, see Fig. 4.9a

– Compression tension node with one tie, see Fig. 4.9b

– Compression tension node with two ties, see Fig. 4.9c

A characteristic length is given for each of the three types, e.g., the length of a bearing or the length of a diagonal connecting the radius of curvature of a rebar. This length determines the initial width of struts. The width may increase due to a fan out of a compression field, see Fig. 4.2b, but this may be neglected for a conservative estimation of a strut width.

The mentioned characteristic length also defines a space for the node itself. Complex multiaxial stress states are given within this space to reach a balance of forces from struts and ties. A failure of concrete may occur due to this stress states and a check has to be performed. The uniaxial compressive strength f_c serves as basic value. A reference value for the strength of nodes is derived from

$$\sigma_R = k_c \, \nu f_c \tag{4.42}$$

with a general reduction factor ν ruled by material ductility, which is different for different concrete grades, and a factor k_c regarding the type of node. Recommendations for the choice of ν, k_c are given in [26, 6.5.4], [18, 7.3.6.4]. Nominal uniaxial stresses $\sigma_{c,i}$ derived from given strut forces $F_{c,i}$, see Fig. 4.9 for the current setup, should fulfill $|\sigma_{c,i}| < \sigma_R$ whereby some safety margin has to be regarded in practice.

Deformations of strut-and-tie models have been a minor aspect up to now as determination of ultimate limit loads was the major issue. It has been shown for rigid- or elastoplastic analyses that the ultimate limit load is reached in a process whereby certain members reach their yielding strength in a sequence. Yielding of subsequent members in this sequence requires sufficient plastic deformations of prior members. Thus, sufficient plastic deformations without failure in the sense of collapse are required to reach the ultimate limit load. The whole structure will become unstable or not reach the potential ultimate limit load in the case of premature failure of a single member.

- In other words, a justified application of the strut-and-tie model to a real structure requires a sufficient *ductility* for the respective structure.

Ductility in this context means that all rebars and compression fields and the areas where they exchange forces ($\rightarrow$ nodes) may have large enough strains with a nearly constant level of stresses. While this is generally fulfilled for the reinforcement the required ductility is not necessarily given for concrete. Thus, a minimum orthogonal reinforcement net is required for plates irrespective of stresses determined with models.

Chapter 5

Multiaxial Concrete Material Behavior

5.1 Basics

5.1.1 Continua and Scales

Continuum mechanics provides a framework to describe the behavior of solids. A basic assumption within this framework is *homogeneity*, i.e., material parameters are constant or continuous in space. Two scales are considered to describe structural concrete with continuum mechanics: mesoscale and macroscale.

- The *mesoscale* distinguishes the cement matrix, aggregates, and the interfacial transition zone (ITZ). Each of these material phases is regarded as a homogeneous solid with its own material law and its own material parameters.

The ITZ generally forms the weakest link. For its characterization, see [61]. Spatial dimensions of the mesoscale have to be chosen in the scale of [mm] to resolve the phases spatially. A continuous displacement is assumed along contact surfaces of different phases in the case of deformations. This leads to discontinuities of strains along contact surfaces due to different stiffness of phases.

Regarding a concrete specimen composed of phases its internal geometric characteristics are random as a matter of principle, e.g., size, shape, position, and orientation of aggregates are random. Thus, two samples chosen out of a collection of specimens of same geometry and with the same material parameters of phases will show different reactions under the same imposed action. The variation of reactions depends on the size of the specimen relative to the size of the largest aggregates and the type of the action. The variations of reactions tend to become smaller for larger specimen sizes. If they are considered to be negligible for the relevant types of action the specimen size constitutes a *representative volume element* (RVE).

Regarding concrete the spatial dimensions of an RVE are in a scale of a few times of the largest dimension of the aggregates or in a scale of [cm], respectively. This corresponds to the macroscale, see also Section 2.1.

- Concrete, cement matrix, aggregates, and interfacial transition zone are homogenized within the *macroscale* with a single type of material law and a corresponding set of material parameters.

The material parameters of the homogenized continuum may be determined analytically from the material parameters of the phases by mixture theories, see e.g., [69], [95]. But such approaches are limited regarding the mesoscale randomness of concrete. As an alternative, numerical multiscale methods may provide macroscale parameters derived from numerical mesoscale calculations considering particular actions and phase properties. Finally, parameters of macroscale material laws may directly be chosen according to the experimental behavior of specimens with at least RVE size using parameter identification and calibration methods.

An initiation and propagation of cracks may occur in a continuum with limited tensile strength. Thus, a continuum may become a *discontinuum* along curves or surfaces indicating a crack geometry. Cracks are macrocracks, see Section 2.1, within the framework of continuum mechanics with a defined boundary. Microcracks, on the other hand, are modeled inherently through material laws. The phase between micro- and macrocracking, see Fig. 2.2a, is covered with the *cohesive crack model*, see Section 5.7. This model assigns surface tractions along *fictitious crack* boundaries to model crack branching and bridging within the framework of continuum mechanics under the assumption of homogeneous materials.

Considering methods with a discretization of space like finite element methods a single element should not be exposed to larger gradients of reactions within itself. This leads to upper bounds for element sizes or fineness of discretization.

- Due to local inhomogeneities, a discretization of a given structure requires an order of 10 times more elements for each spatial dimension within the mesoscale compared to discretizations within the macroscale.

Thus, numerical calculations of larger structures are performed in a macroscale using homogenized material laws derived within continuum mechanics.

5.1.2 Characteristics of Concrete Behavior

The macroscale will be used in the following to describe the stress–strain behavior of concrete. Due to current state of knowledge the only reliable way to access the characteristics of concrete behavior is given through observation in general and experiments performed under controlled conditions in particular. Sizes of specimen at least have to correspond to an RVE to yield reproducible results. The following major characteristics of concrete behavior – within the short term time scale, see Section 2.1 – are experimentally derived under this premise:

– The tensile strength is low compared to the compressive strength.

  Uniaxial concrete strength has already been discussed in Section 2.1, see Figs. 2.1, 2.2b. Uniaxial compressive strength f_c is roughly 10–15 times higher as the uniaxial tensile strength f_{ct} for normal-graded concrete, see [26, Table 3.1]. Such a relation is still valid for multiaxial tensile states compared to multiaxial compressive states, see Section 5.4.3.

– The compressive strength increases with multiaxial stress states.

Specimen exposed to large (hydrostatic) pressures sustain a compaction but will not fail under ideal conditions. A lower subordinated lateral confining compression supports a material's compressive bearing capacity in a principal orientation. Furthermore, strains corresponding to states of multiaxial strength increase compared to the uniaxial case. Modeling of multiaxial strength is also described in Section 5.4.3. Comprehensive experimental data are available, see e.g., [57], [51], [38].

– A reduced stiffness and permanent strains occur with unloading.

The microstructure of a solid material is changed with the application of loads. Two major effects can be distinguished: slidings within crystalline structures and formation of microcracks. These effects lead to a different response with the removal of loads. Slidings lead to permanent strains which can be modeled with *plasticity*, see Section 5.5. Microcracking leads to a reduced material stiffness compared to the virgin unloaded state and can be modeled with *damage*, see Section 5.6.

– A softening behavior develops in the postpeak regime.

The postpeak regime comprises material behavior after material strength has been utilized. Uniaxial softening behavior has also already been discussed in Section 2.1, see Figs. 2.1 and 2.2b. Due to ongoing microcracking stresses decrease while strains increase whereby the solid material's coherence is still preserved.

This effect can be seen for exposures including shear and/or tension. Nevertheless, in the end every solid material will loose its coherence and will ultimately fail for such exposures. Ductile materials will fail with relatively large strains, brittle with relatively small strains. Concrete is classified in between as quasi-brittle. Experimental investigations are given with, e.g., [90], [91].

– A volume dilatation occurs under compression in the postpeak regime.

The magnitude of stress is generally different in different orientations. Regarding high compressive stress levels or their postpeak regimes this must lead to a disaggregation of inhomogeneous materials like concrete, see Fig. 5.1. Hard aggregates dislocate in
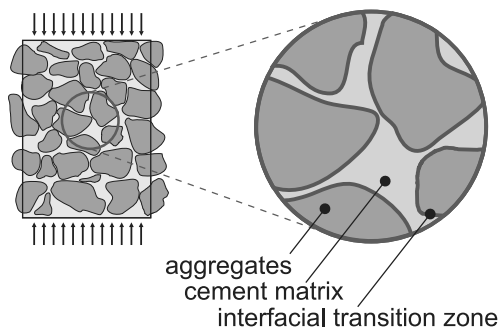

Figure 5.1: Concrete in mesoscale.

the relatively soft cement matrix. This is observed as dilatation on the macroscale. Experimental data are given in [57].

– Anisotropy is induced through loading.

The effect of load-induced anisotropy becomes particularly evident with the formation of cracking, see Fig. 2.2a. Less or no stresses can be transmitted across a developing crack, but at least compressive stresses can still be transmitted in the direction of cracks. Thus, macroscopic relations between stresses and strains depend on the orientation within a material whereby the evolution of material orientations depend on the loading history.

– The activation of crack energy, see Section 2.1, leads to *size effects*.

Crack bands basically have the same width in small concrete structures and large concrete structures for the same concrete. Thus, for the same crack pattern crack bands occupy relatively more volume in small structures and crack energy or energy dissipation, respectively, is relatively larger in small structures. As a consequence, small concrete structures behave more ductile regarding their load–displacement relations compared to large concrete structures. This issue is strongly related to fracture mechanics and cohesive cracks, see Section 5.7.

These observations indicate the complexity of the mechanical behavior of concrete compared to other common building materials like metals, wood, glass, and plastics. Further characteristic effects of concrete behavior arise with the long-term time scale on one hand and the highly dynamical time scale on the other hand.

5.2   Continuum Mechanics

5.2.1   Displacements and Strains

Items of continuum mechanics are introduced in the following as they are necessary for the formulation of material laws for solids like concrete. A comprehensive description of continuum mechanics is given in, e.g., [64], [97].

We consider a solid body in space. Space is measured in a 3D Cartesian coordinate system in the following if not otherwise stated. A *space point* $\mathbf{x}$ has a vector of coordinates $(\ x_1\quad x_2\quad x_3\ )^T$. Indication of coordinate directions is changed compared to Section 1.3 and performed with integer numbers to facilitate the notation.

A *body* occupies an area of space in a *configuration*, see Fig. 5.2a. This configuration changes with time t due to a loading history. A *material point* is identified by the space point $\mathbf{X}$ it occupies in a *reference configuration* at a time t_0 and $\mathbf{X} = \mathbf{x}$ for $t = t_0$.

Displacements are defined with $\mathbf{u} = \mathbf{x} - \mathbf{X}$ and have a vector of components $\mathbf{u} = (\ u_1\quad u_3\quad u_3\ )^T$. They become zero in the reference configuration per definition. Displacements are considered to be small in the following if not otherwise stated. A notion of small is that they have a magnitude of millimeters while the body has dimensions in the magnitude of meters.

Strain is derived from displacements with small strain components

$$\epsilon_{ij} = \frac{1}{2}\left(\frac{\partial u_i}{\partial x_j} + \frac{\partial u_j}{\partial x_i}\right) = \epsilon_{ji}, \qquad i, j = 1, \ldots, 3 \tag{5.1}$$

Strain components involve two directions: a displacement direction u_i, u_j and a reference direction x_i, x_j. Thus, small strain components form a symmetric tensor of the second order. The components are arranged in a matrix

$$\boldsymbol{\epsilon}_M = \begin{bmatrix} \epsilon_{11} & \epsilon_{12} & \epsilon_{13} \\ \epsilon_{12} & \epsilon_{22} & \epsilon_{23} \\ \epsilon_{13} & \epsilon_{23} & \epsilon_{33} \end{bmatrix} \tag{5.2}$$

or in a vector in the *Voigt notation*

$$\boldsymbol{\epsilon} = \begin{pmatrix} \epsilon_{11} \\ \epsilon_{22} \\ \epsilon_{33} \\ \gamma_{23} \\ \gamma_{13} \\ \gamma_{12} \end{pmatrix} = \begin{pmatrix} \epsilon_{11} \\ \epsilon_{22} \\ \epsilon_{33} \\ 2\epsilon_{23} \\ 2\epsilon_{13} \\ 2\epsilon_{12} \end{pmatrix} \tag{5.3}$$

utilizing symmetry of shear-strain components. The Voigt notation also introduces the engineering notation for shear-strain components $\gamma_{ij} = 2\epsilon_{ij}$, $i \neq j$ which simplifies the writing of material laws. The components of a second-order tensor obey particular transformation laws based upon transformation laws for vectors ($\rightarrow$ first-order tensors) in the case of a transformation of the underlying coordinate system, see Appendix C.

5.2.2 Stresses and Material Laws

Strain leads to *stress*. It is at first defined through *Cauchy stress* $\boldsymbol{\sigma}$ with reference to an infinitesimal tetrahedron at a position $\mathbf{x}$ with a tetrahedron base area dA, base normal $\mathbf{n} = (\begin{array}{ccc} n_1 & n_2 & n_3 \end{array})^T$ exposing a force vector $d\mathbf{f}$ and a traction vector $\mathbf{t} = d\mathbf{f}/dA$. The force $d\mathbf{f}$ is equilibrated by three force vectors $d\mathbf{f}_i$ on each coordinate plane i, see Fig. 5.2b. Each of these forces corresponds to a traction vector $\mathbf{t}_i$ and each traction has three Cauchy stress components σ_{ij}. Thus, nine stress components are given with $i, j = 1, \ldots, 3$. The first index denotes the coordinate plane's normal and the second index the global direction. Thus, stress components form a tensor of the second order. The components are arranged with a matrix

$$\boldsymbol{\sigma}_M = \begin{bmatrix} \sigma_{11} & \sigma_{12} & \sigma_{13} \\ \sigma_{21} & \sigma_{22} & \sigma_{23} \\ \sigma_{31} & \sigma_{32} & \sigma_{33} \end{bmatrix} \tag{5.4}$$

In order to have equilibrium a relation

$$\mathbf{t} = \boldsymbol{\sigma}_M \cdot \mathbf{n} \tag{5.5}$$

must hold with the traction vector $\mathbf{t}$ on the tetrahedron base and the product of the matrix $\boldsymbol{\sigma}_M$ and the tetrahedron base normal $\mathbf{n}$. Considering equilibrium of an infinitesimal cube it can be shown that

$$\sigma_{ij} = \sigma_{ji} \tag{5.6}$$
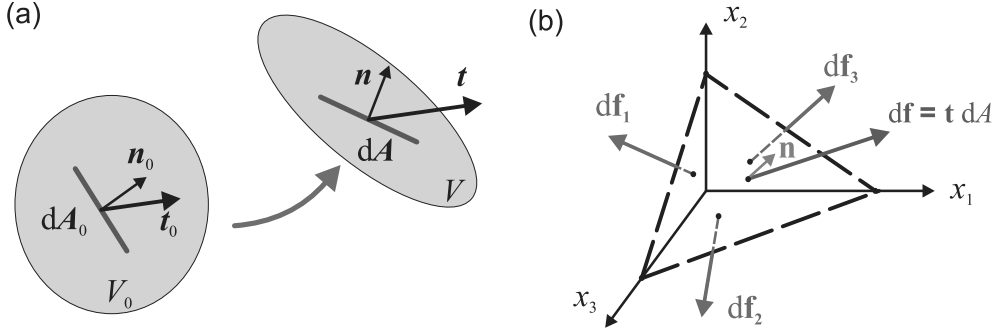
Figure 5.2: (a) Body in reference and deformed configuration. (b) Infinitesimal stress tetrahedron.

and stress components also form a symmetric tensor of second order. In a similar way as strain components Cauchy stress components can be arranged in a vector with the Voigt notation

$$\boldsymbol{\sigma} = \begin{pmatrix} \sigma_{11} \\ \sigma_{22} \\ \sigma_{33} \\ \sigma_{23} \\ \sigma_{13} \\ \sigma_{12} \end{pmatrix} \tag{5.7}$$

utilizing symmetry of Cauchy stress. *Pressure* is derived from stress components as

$$p = -\frac{1}{3}\left(\sigma_{11} + \sigma_{22} + \sigma_{33}\right) \tag{5.8}$$

and the *deviatoric stress* $\boldsymbol{\sigma}'$ as

$$\boldsymbol{\sigma}' = \begin{pmatrix} \sigma'_{11} \\ \sigma'_{22} \\ \sigma'_{33} \\ \sigma'_{23} \\ \sigma'_{13} \\ \sigma'_{12} \end{pmatrix} = \begin{pmatrix} \sigma_{11} + p \\ \sigma_{22} + p \\ \sigma_{33} + p \\ \sigma_{23} \\ \sigma_{13} \\ \sigma_{12} \end{pmatrix} = \begin{pmatrix} \frac{2}{3}\sigma_{11} - \frac{1}{3}\sigma_{22} - \frac{1}{3}\sigma_{33} \\ \frac{2}{3}\sigma_{22} - \frac{1}{3}\sigma_{11} - \frac{1}{3}\sigma_{33} \\ \frac{2}{3}\sigma_{33} - \frac{1}{3}\sigma_{11} - \frac{1}{3}\sigma_{22} \\ \sigma_{23} \\ \sigma_{13} \\ \sigma_{12} \end{pmatrix} \tag{5.9}$$

This may also be written as

$$\boldsymbol{\sigma}' = \mathbf{I}_{\text{dev}} \cdot \boldsymbol{\sigma}, \qquad \mathbf{I}_{\text{dev}} = \begin{bmatrix} \frac{2}{3} & -\frac{1}{3} & -\frac{1}{3} & 0 & 0 & 0 \\ -\frac{1}{3} & \frac{2}{3} & -\frac{1}{3} & 0 & 0 & 0 \\ -\frac{1}{3} & -\frac{1}{3} & \frac{2}{3} & 0 & 0 & 0 \\ 0 & 0 & 0 & 1 & 0 & 0 \\ 0 & 0 & 0 & 0 & 1 & 0 \\ 0 & 0 & 0 & 0 & 0 & 1 \end{bmatrix} \tag{5.10}$$

with the deviatoric unit matrix $\mathbf{I}_{\text{dev}}$. Similar relations may be derived for strain.

Incremental changes of strain and stress with progressing time t are defined with *strain* and *stress rate*

$$\dot{\boldsymbol{\epsilon}} = \frac{\partial \boldsymbol{\epsilon}}{\partial t} = \lim_{\Delta t \to 0} \frac{\Delta \boldsymbol{\epsilon}}{\Delta t}, \qquad \dot{\boldsymbol{\sigma}} = \frac{\partial \boldsymbol{\sigma}}{\partial t} = \lim_{\Delta t \to 0} \frac{\Delta \boldsymbol{\sigma}}{\Delta t} \qquad (5.11)$$

Cauchy stress and small strain are conjugate with respect to energy as

$$\dot{u} = \boldsymbol{\sigma} \cdot \dot{\boldsymbol{\epsilon}} \qquad (5.12)$$

denotes the rate of *internal energy* per volume for material points within a continuous body or rate of specific internal energy. This may contain both recoverable and dissipated parts, see Section 5.10. Other measures for stresses and conjugated strains, which are relevant in the case of larger displacements, are discussed in, e.g., [9], [64].

The stress–strain relation of a specific material may generally be described through an incremental material law

$$\dot{\boldsymbol{\sigma}} = \mathbf{C}_T \cdot \dot{\boldsymbol{\epsilon}} \qquad (5.13)$$

whereby a material specific *tangential material stiffness* $\mathbf{C}_T$ depends on the loading history. As stress and strain each are a tensor of second order the material stiffness has to be a tensor of fourth order. The Voigt notation of stresses and strains allows to arrange the components of $\mathbf{C}_T$ in a matrix.

If the components of $\mathbf{C}_T$ are constant with $\mathbf{C}_T = \mathbf{C}$, Eq. (5.13) may be integrated in time t to give

$$\boldsymbol{\sigma} = \mathbf{C} \cdot \boldsymbol{\epsilon} \qquad (5.14)$$

i.e., a linear material law.

5.2.3 Coordinate Transformations and Principal States

Transformations of coordinate systems clarify characteristics of material states and material behavior. A further Cartesian coordinate system is regarded beneath the basic global system with the same origin but different orientation or different directions of axes, respectively. The relation between these systems is ruled by three rotation angles, see Fig. 5.3a, and a
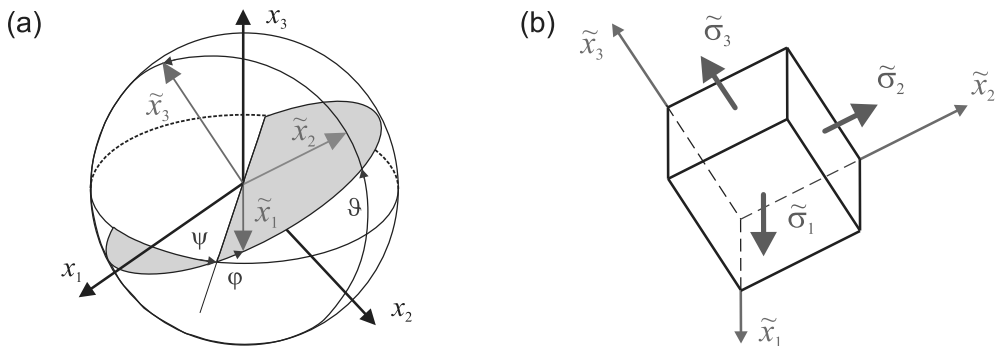

Figure 5.3: (a) Rotation of coordinate system. (b) Principal stress space.

transformation matrix $\mathbf{Q}$ depending on the rotation angles. The matrix $\mathbf{Q}$ is orthogonal, i.e., $\mathbf{Q}^{-1} = \mathbf{Q}^T$. Values of the components of stress and strain differ in the two systems. A strain

$$\tilde{\boldsymbol{\epsilon}} = \mathbf{Q} \cdot \boldsymbol{\epsilon} \tag{5.15}$$

is given in the transformed system corresponding to the strain $\boldsymbol{\epsilon}$ in the initial system. A stress $\boldsymbol{\sigma}$ in the initial system is related by

$$\boldsymbol{\sigma} = \mathbf{Q}^T \cdot \tilde{\boldsymbol{\sigma}} \tag{5.16}$$

to the stress $\tilde{\boldsymbol{\sigma}}$ in the transformed system. With $\tilde{\boldsymbol{\sigma}} = \tilde{\mathbf{C}} \cdot \tilde{\boldsymbol{\epsilon}}$ the material stiffness transforms according to

$$\tilde{\mathbf{C}} = \mathbf{Q} \cdot \mathbf{C} \cdot \mathbf{Q}^T, \quad \mathbf{C} = \mathbf{Q}^T \cdot \tilde{\mathbf{C}} \cdot \mathbf{Q} \tag{5.17}$$

The rotation matrix $\mathbf{Q}$ is a function of the rotation angles only. In the case of 2D states with one rotation angle the exact form of $\mathbf{Q}$ is given in Appendix C.

On basis of Eq. (5.5) a matrix eigenvalue problem

$$\boldsymbol{\sigma}_M \cdot \mathbf{m} = \sigma \; \mathbf{m} \tag{5.18}$$

may be stated for a state of stress with given components σ_{ij}. Due to the symmetry of $\boldsymbol{\sigma}_M$ this problem is solved through real eigenpairs $\mathbf{n}_i, \sigma_i$ with $i = 1, \ldots, 3$. The three orthogonal unit vectors $\mathbf{m}_i$ form *principal directions* and a distinguished Cartesian coordinate system or *principal system*, respectively. A transformation matrix $\mathbf{Q}$ relating the initial system and the principal system is constructed from the direction cosines of the principal directions and the initial coordinate axes. The transformed stress state has *principal stresses* $\tilde{\sigma}_{11} = \sigma_1, \tilde{\sigma}_{22} = \sigma_2, \tilde{\sigma}_{33} = \sigma_3$ and vanishing shear-stress components $\tilde{\sigma}_{12} = \tilde{\sigma}_{13} = \tilde{\sigma}_{23} = 0$.

- Principal compression is signed as negative and principal tension as positive in the following.

Principal stresses and principal directions form the *principal stress state* which is still described by six values: the three principal stress values and three values for, e.g., the angles specifying the principal directions. In the case of 2D states with only one rotation angle φ the angle determining principal directions is given by Eq. (6.5) with $\sigma_x = \sigma_{11}$, $\sigma_y = \sigma_{22}$, $\sigma_{xy} = \sigma_{12}$ and the principal stress values are given by Eq. (6.4).

The same approach as for stresses is valid for strains with

$$\boldsymbol{\epsilon}_M \cdot \mathbf{n} = \epsilon \; \mathbf{n} \tag{5.19}$$

leading to a *principal strain state* with principal strains ϵ_1, ϵ_2, ϵ_3 and own corresponding principal directions $\mathbf{n}_1$, $\mathbf{n}_2$, $\mathbf{n}_3$. Tensorial shear-strain components ϵ_{13}, ϵ_{23}, ϵ_{12} must be used for $\boldsymbol{\epsilon}_M$ in Eq. (5.19). The principal directions of strain must not necessarily coincide with the principal directions of stress. This depends on the type of the material law which connects strain and stress and is discussed in Section 5.3.

Principal states furthermore are distinguished as all strains $\tilde{\boldsymbol{\epsilon}}$ transformed according to Eq. (5.15) have the same principal values and principal directions for arbitrary rotations $\mathbf{Q}$. The same holds for all stresses $\tilde{\boldsymbol{\sigma}}$ transformed according to Eq. (5.16).

- Principal states are independent from the choice of coordinate systems. Thus, principal states indicate a physical point of view of stress and strain.

Regarding a material point its state of stress and strain is preferably characterized by the corresponding principal values and directions.

Invariants are often used as alternative formulation for principal values. In the same way as principal values they do not change with a change of coordinate systems. In the case of stress its first invariant I_1 and the second and third invariant of its deviator are predominantly used. They are defined as

$$
\begin{aligned}
I_1 &= \sigma_{11} + \sigma_{22} + \sigma_{33} \\
&= \sigma_1 + \sigma_2 + \sigma_3 \\
J_2 &= \tfrac{1}{2}\left[(\sigma_{11} - \sigma_m)^2 + (\sigma_{22} - \sigma_m)^2 + (\sigma_{33} - \sigma_m)^2\right] \\
&\qquad\qquad + \sigma_{23}\sigma_{32} + \sigma_{13}\sigma_{31} + \sigma_{12}\sigma_{21} \\
&= \tfrac{1}{6}\left[(\sigma_1 - \sigma_2)^2 + (\sigma_2 - \sigma_3)^2 + (\sigma_3 - \sigma_1)^2\right] \\
J_3 &= (\sigma_1 - \sigma_m)(\sigma_2 - \sigma_m)(\sigma_3 - \sigma_m)
\end{aligned}
\tag{5.20}
$$

with $\sigma_m = (\sigma_1 + \sigma_2 + \sigma_3)/3$. The first invariant corresponds to pressure, see Eq. (5.8), with $p = -I_1/3$. An interpretation of J_2, J_3 is demonstrated in Section 5.4.2 with Eqs. (5.45, 5.47). A detailed description of stress and strain invariants is given in [64, 3.3].

5.3 Isotropy, Linearity, and Orthotropy

5.3.1 Isotropy and Linear Elasticity

Isotropy is strongly connected with various aspects of directions. The following types of directions have to be distinguished:

– Action directions: principal directions of given strains.

– Reaction directions: principal directions of response stresses.

– Material directions: a coordinate system spanned by four material points in the reference configuration.

An isotropic material behaves in the similar way in every action direction. This can be stated more precisely as follows:

– The reaction directions coincide with the action directions.

– Principal stress values are independent from action directions, i.e., principal stress values do not change with a change of action directions relative to material directions but unchanging principal strain values.

This descriptive definition of isotropy also has to be formulated mathematically. We consider a given strain or action $\boldsymbol{\epsilon}$ with an associated response $\boldsymbol{\sigma} = \mathbf{C} \cdot \boldsymbol{\epsilon}$. The loading directions are rotated into other arbitrary directions $\tilde{\boldsymbol{\epsilon}}$ with $\tilde{\boldsymbol{\epsilon}} = \mathbf{Q} \cdot \boldsymbol{\epsilon}$ according to Eq. (5.15).

Isotropy requires, that the rotated associated response $\tilde{\boldsymbol{\sigma}}$ has the the same material law, i.e., $\tilde{\boldsymbol{\sigma}} = \mathbf{C} \cdot \tilde{\boldsymbol{\epsilon}}$, while rotating $\boldsymbol{\sigma}$ according to Eq. (5.16). With $\boldsymbol{\sigma} = \mathbf{Q}^T \cdot \tilde{\boldsymbol{\sigma}} = \mathbf{Q}^T \cdot \mathbf{C} \cdot \tilde{\boldsymbol{\epsilon}} = \mathbf{Q}^T \cdot \mathbf{C} \cdot \mathbf{Q} \cdot \boldsymbol{\epsilon}$ a requirement

$$
\mathbf{C} = \mathbf{Q}^T \cdot \mathbf{C} \cdot \mathbf{Q}
\tag{5.21}
$$

follows for arbitrary rotations $\mathbf{Q}$. This imposes restrictions for $\mathbf{C}$. A general form

$$
\mathbf{C} = \begin{bmatrix}
C_{11} & C_{12} & C_{13} & C_{14} & C_{15} & C_{16} \\
C_{21} & C_{22} & C_{23} & C_{24} & C_{25} & C_{26} \\
C_{31} & C_{32} & C_{33} & C_{34} & C_{35} & C_{36} \\
C_{41} & C_{42} & C_{43} & C_{44} & C_{45} & C_{46} \\
C_{51} & C_{52} & C_{53} & C_{54} & C_{55} & C_{56} \\
C_{61} & C_{62} & C_{63} & C_{64} & C_{65} & C_{66}
\end{bmatrix}
\tag{5.22}
$$

is assumed. It can be shown that for *arbitrary* rotations $\mathbf{Q}$ the isotropy requirement (Eq. (5.21)) can only be fulfilled with a form

$$
\mathbf{C} = \begin{bmatrix}
C_1 & C_2 & C_2 & 0 & 0 & 0 \\
C_2 & C_1 & C_2 & 0 & 0 & 0 \\
C_2 & C_2 & C_1 & 0 & 0 & 0 \\
0 & 0 & 0 & \frac{1}{2}(C_1 - C_2) & 0 & 0 \\
0 & 0 & 0 & 0 & \frac{1}{2}(C_1 - C_2) & 0 \\
0 & 0 & 0 & 0 & 0 & \frac{1}{2}(C_1 - C_2)
\end{bmatrix}
\tag{5.23}
$$

A significant question concerns the principal directions of stress and strain.

- Stresses and strains will have the same principal directions if they are related by an isotropic material matrix $\mathbf{C}$ like Eq. (5.23).

Assuming constant values for C_1, C_2, Eq. (5.23) corresponds to the triaxal *isotropic linear elastic* material law

$$
\mathbf{E} = \begin{bmatrix}
\frac{E(1-\nu)}{(1+\nu)(1-2\nu)} & \frac{E\nu}{(1+\nu)(1-2\nu)} & \frac{E\nu}{(1+\nu)(1-2\nu)} & 0 & 0 & 0 \\
\frac{E\nu}{(1+\nu)(1-2\nu)} & \frac{E(1-\nu)}{(1+\nu)(1-2\nu)} & \frac{E\nu}{(1+\nu)(1-2\nu)} & 0 & 0 & 0 \\
\frac{E\nu}{(1+\nu)(1-2\nu)} & \frac{E\nu}{(1+\nu)(1-2\nu)} & \frac{E(1-\nu)}{(1+\nu)(1-2\nu)} & 0 & 0 & 0 \\
0 & 0 & 0 & \frac{E}{2(1+\nu)} & 0 & 0 \\
0 & 0 & 0 & 0 & \frac{E}{2(1+\nu)} & 0 \\
0 & 0 & 0 & 0 & 0 & \frac{E}{2(1+\nu)}
\end{bmatrix}
\tag{5.24}
$$

with Young's modulus E and Poisson's ratio ν.

5.3.2 Orthotropy

Different restrictions of the arbitrary choice of $\mathbf{Q}$ in Eq. (5.21) applied to Eq. (5.22) lead to different types of *anisotropy*. An *orthotropic* material is given if Eq. (5.21) is fulfilled for three rotations $\mathbf{Q}$ each with an angle 180° around each coordinate axis. This can be fulfilled with a form

$$
\mathbf{C} = \begin{bmatrix}
C_{11} & C_{12} & C_{13} & 0 & 0 & 0 \\
C_{21} & C_{22} & C_{23} & 0 & 0 & 0 \\
C_{31} & C_{32} & C_{33} & 0 & 0 & 0 \\
0 & 0 & 0 & C_{44} & 0 & 0 \\
0 & 0 & 0 & 0 & C_{55} & 0 \\
0 & 0 & 0 & 0 & 0 & C_{66}
\end{bmatrix}
\tag{5.25}
$$

with 12 nonzero components [64, (6.2.24)]. This result implies the coincidence of coordinate axes and the *material symmetry directions*. The material symmetry directions are given through material directions forming a Cartesian coordinate system in the case of an orthotropic material.

The same material may be rigidly rotated in space leading to a deviation of the material symmetry directions from the spatial coordinate directions. The application of Eq. (5.21) on Eq. (5.22) then leads to a fully occupied matrix $\mathbf{C}$ under the assumption of orthotropy. Formal differences arise compared to Eq. (5.25) but 12 independent material parameters remain.

- Stresses and strains will have the same principal directions if they coincide with the material symmetry directions, otherwise not.

Thermodynamic postulates about a nonnegative product $\boldsymbol{\epsilon} \cdot \boldsymbol{\sigma} = \boldsymbol{\epsilon} \cdot \mathbf{C} \cdot \boldsymbol{\epsilon}$ or a positive definite matrix $\mathbf{C}$, see Section 5.10, require the symmetry of the material stiffness matrix. In the case of orthotropy with material symmetry directions aligned to coordinate axes this leads to

$$
\mathbf{C} =
\begin{bmatrix}
C_{11} & C_{12} & C_{13} & 0 & 0 & 0 \\
C_{12} & C_{22} & C_{23} & 0 & 0 & 0 \\
C_{13} & C_{23} & C_{33} & 0 & 0 & 0 \\
0 & 0 & 0 & C_{44} & 0 & 0 \\
0 & 0 & 0 & 0 & C_{55} & 0 \\
0 & 0 & 0 & 0 & 0 & C_{66}
\end{bmatrix}
\tag{5.26}
$$

with nine nonzero components. A compliance form, see Eq. (1.51), with some physical evidence – material coefficients are directly taken from experimental results – is given by

$$
\mathbf{D} =
\begin{bmatrix}
\frac{1}{E_1} & -\frac{\nu_{12}}{E_1} & -\frac{\nu_{13}}{E_1} & 0 & 0 & 0 \\
-\frac{\nu_{21}}{E_2} & \frac{1}{E_2} & -\frac{\nu_{23}}{E_2} & 0 & 0 & 0 \\
-\frac{\nu_{31}}{E_3} & -\frac{\nu_{32}}{E_3} & \frac{1}{E_3} & 0 & 0 & 0 \\
0 & 0 & 0 & \frac{1}{G_4} & 0 & 0 \\
0 & 0 & 0 & 0 & \frac{1}{G_5} & 0 \\
0 & 0 & 0 & 0 & 0 & \frac{1}{G_6}
\end{bmatrix}
\tag{5.27}
$$

where ν_{ij} is a measure for the deformation in the i-direction caused by a stress in the j-direction. Relations $\nu_{12}/E_1 = \nu_{21}/E_2, \dots$ and so on must hold to preserve symmetry.

5.3.3 Plane Stress and Strain

Regarding again the isotropic case simplified forms can be derived from Eq. (5.24) for plane strain or plane stress. In both cases $\gamma_{23} = \gamma_{13} = 0$. *Plane strain* is determined with $\epsilon_{33} = 0$ and a direct subset of Eq. (5.24) may be used for

$$
\begin{pmatrix} \sigma_{11} \\ \sigma_{22} \\ \sigma_{12} \end{pmatrix}
= \frac{E}{1+\nu}
\begin{bmatrix}
\frac{1-\nu}{1-2\nu} & \frac{\nu}{1-2\nu} & 0 \\
\frac{\nu}{1-2\nu} & \frac{1-\nu}{1-2\nu} & 0 \\
0 & 0 & \frac{1}{2}
\end{bmatrix}
\cdot
\begin{pmatrix} \epsilon_{11} \\ \epsilon_{22} \\ \gamma_{12} \end{pmatrix}
\tag{5.28}
$$

The lateral stress is given by $\sigma_{33} = \frac{E\nu}{(1+\nu)(1-2\nu)}(\epsilon_{11} + \epsilon_{22})$. *Plane stress* is determined with $\sigma_{33} = 0$. Using this condition with Eqs. (5.14, 5.24) leads to

$$\begin{pmatrix} \sigma_{11} \\ \sigma_{22} \\ \sigma_{12} \end{pmatrix} = \frac{E}{1-\nu^2} \begin{bmatrix} 1 & \nu & 0 \\ \nu & 1 & 0 \\ 0 & 0 & \frac{1-\nu}{2} \end{bmatrix} \cdot \begin{pmatrix} \epsilon_{11} \\ \epsilon_{22} \\ \gamma_{12} \end{pmatrix} \tag{5.29}$$

The lateral strain is given by $\epsilon_{33} = -\frac{\nu}{E}(\sigma_{11} + \sigma_{22})$.

Plane stress shall also be treated for the symmetric orthotropic case whereby material symmetry directions coincide with the coordinate directions. With $\sigma_{33} = 0$ and $\gamma_{23} = \gamma_{13} = 0$ the flexibility form (Eq. (5.27)) leads to

$$\begin{pmatrix} \epsilon_{11} \\ \epsilon_{22} \\ \gamma_{12} \end{pmatrix} = \begin{bmatrix} \frac{1}{E_1} & -\frac{\nu_{12}}{E_1} & 0 \\ -\frac{\nu_{21}}{E_2} & \frac{1}{E_2} & 0 \\ 0 & 0 & \frac{1}{G_6} \end{bmatrix} \cdot \begin{pmatrix} \sigma_{11} \\ \sigma_{22} \\ \sigma_{12} \end{pmatrix} \tag{5.30}$$

The inversion yields the stiffness form

$$\begin{pmatrix} \sigma_{11} \\ \sigma_{22} \\ \sigma_{12} \end{pmatrix} = \frac{1}{1-\nu_{12}\nu_{21}} \begin{bmatrix} E_1 & \nu_{12}E_2 & 0 \\ \nu_{21}E_1 & E_2 & 0 \\ 0 & 0 & (1-\nu_{12}\nu_{21})G \end{bmatrix} \cdot \begin{pmatrix} \epsilon_{11} \\ \epsilon_{22} \\ \gamma_{12} \end{pmatrix} \tag{5.31}$$

with $G = G_6$, see also [21, (6.110)]. A notation $\nu_1 = \nu_{12}$ ($\to$ deformation in 1-direction caused by a lateral stress in 2-direction) and $\nu_2 = \nu_{21}$ ($\to$ deformation in 2-direction caused by a lateral stress in 1-direction) is used in the following. Requiring symmetry $\nu_1 E_2 = \nu_2 E_1$ and using a modified Poisson's ratio

$$\bar{\nu} = \frac{\nu_2 E_1}{\sqrt{E_1 E_2}} = \frac{\nu_1 E_2}{\sqrt{E_1 E_2}} \to \nu_2 = \frac{\bar{\nu}\sqrt{E_1 E_2}}{E_1}, \ \nu_1 = \frac{\bar{\nu}\sqrt{E_1 E_2}}{E_2}, \ \nu_1\nu_2 = \bar{\nu}^2 \tag{5.32}$$

finally leads to

$$\begin{pmatrix} \sigma_{11} \\ \sigma_{22} \\ \sigma_{12} \end{pmatrix} = \begin{bmatrix} \frac{E_1}{1-\bar{\nu}^2} & \frac{\bar{\nu}\sqrt{E_1 E_2}}{1-\bar{\nu}^2} & 0 \\ \frac{\bar{\nu}\sqrt{E_1 E_2}}{1-\bar{\nu}^2} & \frac{E_2}{1-\bar{\nu}^2} & 0 \\ 0 & 0 & G \end{bmatrix} \cdot \begin{pmatrix} \epsilon_{11} \\ \epsilon_{22} \\ \gamma_{12} \end{pmatrix} \tag{5.33}$$

whereby $E_1, E_2 \geq 0$ is assumed.

The material coefficients E_1, E_2, $\bar{\nu}$ may be relatively easily approximated from experiments with two sets of uniaxial stress–strain data determined from orthogonal directions. A problem might remain with the experimental determination of the shear modulus G. The invariance of shear flexibility is postulated to circumvent experimental inconvenience. Regarding Eq. (5.21) it is assumed that the shear coefficient G in Eq. (5.33) does not change for all plane transformations. A plane transformation has a rotation angle φ and the rotation matrix is defined by

$$\mathbf{Q} = \begin{bmatrix} \cos^2\varphi & \sin^2\varphi & -\cos\varphi\sin\varphi \\ \sin^2\varphi & \cos^2\varphi & \cos\varphi\sin\varphi \\ 2\cos\varphi\sin\varphi & -2\cos\varphi\sin\varphi & \cos^2\varphi - \sin^2\varphi \end{bmatrix} \tag{5.34}$$

leading to a rotation of stresses and strains around the plane's normal with an arbitrary angle φ, see Appendix C. The requirement of shear invariance can be fulfilled with a form

$$\mathbf{C} = \begin{bmatrix} \frac{E_1}{1-\bar{\nu}^2} & \frac{\bar{\nu}\sqrt{E_1 E_2}}{1-\bar{\nu}^2} & 0 \\ \frac{\bar{\nu}\sqrt{E_1 E_2}}{1-\bar{\nu}^2} & \frac{E_2}{1-\bar{\nu}^2} & 0 \\ 0 & 0 & \frac{E_1+E_2-2\bar{\nu}\sqrt{E_1 E_2}}{4(1-\bar{\nu}^2)} \end{bmatrix} \tag{5.35}$$

The other coefficients corresponding to C_{11}, C_{12}, C_{22} are not necessarily invariant with respect to coordinate transformations. This matrix includes Eq. (5.29) for the isotropic plane stress state as special case with $E = E_1 = E_2$, $\nu = \bar{\nu}$.

The uniaxial stress–strain relations in the two material symmetry directions shall be exposed finally. The 1-direction has $\sigma_{22} = 0$ leading to

$$\sigma_{11} = E_1\,\epsilon_{11}, \quad \epsilon_{22} = -\frac{\bar{\nu}}{\sqrt{E_1 E_2}}\,\sigma_{11} \tag{5.36}$$

With given values for σ_{11}, ϵ_{11}, ϵ_{22} from a test 1 two equations are given for three unknowns E_1, E_2, $\bar{\nu}$. The 2-direction has $\sigma_{11} = 0$ leading

$$\sigma_{22} = E_2\,\epsilon_{22}, \quad \epsilon_{11} = -\frac{\bar{\nu}}{\sqrt{E_1 E_2}}\,\sigma_{22} \tag{5.37}$$

With given values for σ_{22}, ϵ_{22}, ϵ_{11} from a test 2 – strains from test 1 and test 2 are not the same – two further equations are given for one remaining material parameter. Thus, the set of four equations (5.36, 5.37) is overdetermined for the unknowns E_1, E_2, $\bar{\mu}$. A best fit may to be found with a least square approach, see Appendix D.

5.4 Nonlinear Material Behavior

5.4.1 Tangential Stiffness

Regarding the uniaxial case nonlinear material behavior of concrete is characterized by a decreasing tangential material stiffness, see Fig. 2.1. This basic idea is transferred to the multiaxial case. A general formulation of nonlinear material behavior has been given in Eq. (5.13):

$$\dot{\boldsymbol{\sigma}} = \mathbf{C}_T \cdot \dot{\boldsymbol{\epsilon}} \tag{5.38}$$

Regarding initial behavior of previously unloaded, virgin concrete it can be assumed that it behaves initially as a linear elastic isotropic material. The initial tangential material stiffness $\mathbf{C}_T$ is given according to Eq. (5.24). Values for the initial Young's modulus E and the initial Poisson's ratio depending on concrete grade are given by, e.g., [26, 3.1.3], [18, 5.1.7].

But tangential stiffness $\mathbf{C}_T$ is subject to change beyond the initial state and may depend on stress $\boldsymbol{\sigma}$, strain $\boldsymbol{\epsilon}$ and internal state variables $\boldsymbol{\kappa}$

$$\mathbf{C}_T = \mathbf{C}_T(\boldsymbol{\sigma}, \boldsymbol{\epsilon}, \boldsymbol{\kappa}) \tag{5.39}$$

Internal state variables $\boldsymbol{\kappa}$ comprise a loading history. They are necessary as an actual state $\boldsymbol{\sigma}, \boldsymbol{\epsilon}$ for a given $\dot{\boldsymbol{\epsilon}}$ may lead to different responses $\dot{\boldsymbol{\sigma}}$ for different loading histories. Internal state variables require *evolution laws*

$$\dot{\boldsymbol{\kappa}} = \boldsymbol{\mathcal{F}}(\boldsymbol{\sigma}, \boldsymbol{\epsilon}, \boldsymbol{\kappa}) \tag{5.40}$$

describing their rates depending on stress and strain and absolute values of internal state variables.

Aspects of isotropy and anisotropy as have been discussed in Section 5.3 are also an issue for nonlinear behavior. Isotropic nonlinear behavior is characterized in the same way as has been formulated in Section 5.3.1. The previous reasoning regarding $\boldsymbol{\sigma}, \boldsymbol{\epsilon}$ in the same way applies to rates $\dot{\boldsymbol{\sigma}}, \dot{\boldsymbol{\epsilon}}$ leading the same conclusion about the principal directions of the stress and strain rates and to the same restrictions for the coefficients of an isotropic tangential material stiffness $\mathbf{C}_T$

- A *nonlinear isotropic* material behaves in the same way in every action direction. Principal directions of stress *increments* coincide with principal directions of strain *increments* for a given material state.

  The values of principal stress *increments* are independent from the directions of principal strain and principal strain increments.

Thus, an isotropic tangential material stiffness in analogy to Eq. (5.21) obeys a relation

$$\mathbf{C}_T = \mathbf{Q}^T \cdot \mathbf{C}_T \cdot \mathbf{Q} \tag{5.41}$$

for arbitrary rotations $\mathbf{Q}$. As a consequence the tangential material stiffness $\mathbf{C}_T$ has to follow a form like Eq. (5.23) which allows only for two independent coefficients.

But initially isotropic materials may become anisotropic in higher loading regimes. In the case of concrete a load-induced anisotropy especially arises with cracking whereby the direction normal to a crack has a strongly reduced capacity to transmit tensile stresses while stiffness and strength remain unaffected in the direction of a crack, see Fig. 2.2a.

- Orthotropy may be used to model load-induced anisotropy due to cracking.

The tangential material stiffness $\mathbf{C}_T$ then has to obey to a form like Eq. (5.26) or to Eq. (5.35) in the case of plane stress and shear isotropy whereby the matrix coefficients may depend on stress, strain and loading history according to Eq. (5.39). The orthotropic tangential material flexibility $\mathbf{D}_T$ for 3D states gets a form according to Eq. (5.27) with varying coefficients. The corresponding forms are derived in Section 5.7.2 within the framework of smeared crack models.

5.4.2 Principal Stress Space and Isotropic Strength

Stress limit states mark the other end compared to initial states. They describe *strength* of materials. For initially isotropic materials like concrete such *stress limit states* may generally be described by an isotropic *strength condition*

$$f(\sigma_1, \sigma_2, \sigma_3) = 0 \tag{5.42}$$

using principal stress values $\sigma_1, \sigma_2, \sigma_3$. Stress states with $f(\sigma_1, \sigma_2, \sigma_3) \leq 0$ are admissible, states $f(\sigma_1, \sigma_2, \sigma_3) > 0$ cannot be sustained. Orientation of principal stress directions has no influence in the case of isotropic materials.

- In more general cases the strength condition may be a function of principal stress values and principal stress directions relative to the material directions.

Stress–strain behavior described by Eq. (5.38) is often separated from strength limit states described by Eq. (5.42) and formally both are treated independently. To have a consistent material description the integration of stresses $\dot{\boldsymbol{\sigma}}$ from Eq. (5.38) over the loading history driven by a time t should not lead to stress states violating the strength condition (Eq. (5.42)). Elastoplastic materials described in Section 5.5 or damaged materials described in Section 5.6 link stress–strain relations and strength in such a way that the consistency of the material description is assured.

Regarding concrete a *load-induced anisotropy* – e.g., tensile strength is reached in one direction while a compressive strength is utilized in orthogonal directions – may be combined with an isotropic strength condition.

- An *iso*tropic strength condition basically allows for *aniso*tropic stress–strain relations.

Such isotropic conditions are used for concrete and will be considered in the following. In doing so it is appropriate to have equivalent measures for the principal stress values. Principal stress values span a triaxial Cartesian coordinate system ($\rightarrow$ principal stress space) and the corresponding stress state may be described by a vector. The following significant elements of the stress space have to be pointed out:

- *Hydrostatic axis*: a space diagonal with a direction $\mathbf{n}_\xi = (\begin{array}{ccc} 1 & 1 & 1 \end{array})^T/\sqrt{3}$. A direction is a vector of length 1 by definition.

- The projection of a stress vector $\boldsymbol{\sigma} = (\begin{array}{ccc} \sigma_1 & \sigma_2 & \sigma_3 \end{array})^T$ on the hydrostatic axis: $\boldsymbol{\xi} = \xi(\begin{array}{ccc} 1 & 1 & 1 \end{array})^T/\sqrt{3}$ with length $\xi = (\sigma_1 + \sigma_2 + \sigma_3)/\sqrt{3}$. This is different compared to the mean stress $(\sigma_1 + \sigma_2 + \sigma_3)/3$ or the hydrostatic pressure $-(\sigma_1 + \sigma_2 + \sigma_3)/3$.

- With $\boldsymbol{\xi}$ given, its corresponding *deviatoric plane*: this plane has $\boldsymbol{\xi}$ as normal, i.e., $(\boldsymbol{\sigma} - \boldsymbol{\xi}) \cdot \boldsymbol{\xi} = 0$ or $\sigma_1 + \sigma_2 + \sigma_3 = \sqrt{3}\xi$.

- The projection of a stress vector $\boldsymbol{\sigma} = (\begin{array}{ccc} \sigma_1 & \sigma_2 & \sigma_3 \end{array})^T$ on its deviatoric plane

$$\boldsymbol{\rho} = \boldsymbol{\sigma} - \boldsymbol{\xi} = \frac{1}{3} \begin{pmatrix} 2\sigma_1 - \sigma_2 - \sigma_3 \\ -\sigma_1 + 2\sigma_2 - \sigma_3 \\ -\sigma_1 - \sigma_2 + 2\sigma_3 \end{pmatrix} \tag{5.43}$$

- The projection of the particular stress vector $\boldsymbol{\sigma} = (\begin{array}{ccc} 1 & 0 & 0 \end{array})^T$ on the deviatoric plane: $\boldsymbol{\rho}_1 = 2/3(\begin{array}{ccc} 1 & -\frac{1}{2} & -\frac{1}{2} \end{array})^T$. It has a direction $\bar{\boldsymbol{\rho}}_1 = \sqrt{2/3}(\begin{array}{ccc} 1 & -\frac{1}{2} & -\frac{1}{2} \end{array})^T$ called the *Rendulic direction* in the following.

An isotropic strength condition like Eq. (5.42) forms a *strength surface* in the principal stress space and defines *triaxial strength*. A stress vector – and in particular a point on this surface – can be described by *Haigh–Westergaard coordinates* with the following components:

– The *hydrostatic length* ξ has already been introduced as length of the stress vector on the hydrostatic axis:

$$\xi = \frac{1}{\sqrt{3}}\left(\sigma_1 + \sigma_2 + \sigma_3\right) = \frac{I_1}{\sqrt{3}} \quad \rightarrow \quad I_1 = \sqrt{3}\,\xi \tag{5.44}$$

– The *deviatoric length* ρ results from the length of the vector $\boldsymbol{\rho}$ from Eq. (5.43). The evaluation of the expression leads to the second invariant of the stress deviator, see Eq. (5.20), and

$$\rho = |\boldsymbol{\rho}| = \sqrt{2J_2} \quad \rightarrow \quad J_2 = \frac{\rho^2}{2} \tag{5.45}$$

– The *deviatoric angle* θ spans between the Rendulic direction and deviatoric direction

$$\cos\theta = \frac{1}{\rho}\,\boldsymbol{\rho} \cdot \bar{\boldsymbol{\rho}}_1 \tag{5.46}$$

A commonly used alternative of this formulation is given by

$$\cos 3\theta = 4\cos^3\theta - 3\cos\theta = \frac{3\sqrt{3}}{2}\,\frac{J_3}{\sqrt{J_2^3}} \tag{5.47}$$

with the second and third invariant J_2, J_3 of the stress deviator, see Eq. (5.20). Equation (5.47) yields one solution in the range $0° \leq \theta \leq 60°$. But any interchanging of $\sigma_1, \sigma_2, \sigma_3$ in invariants leads to the same solution θ (Fig. 5.4).

A *Rendulic plane* is spanned by all stress vectors with a deviatoric angle $\theta = 0$ with arbitrary values for the hydrostatic length ξ and deviatoric length ρ.

Regarding an isotropic strength surface the principal stress values may interchange their position in Eq. (5.42) as the orientation of principal stress directions is not relevant with respect to material directions, i.e., $f(\sigma_1, \sigma_2, \sigma_3) = f(\sigma_1, \sigma_3, \sigma_2) = f(\sigma_2, \sigma_3, \sigma_1) = f(\sigma_2, \sigma_1, \sigma_3) = f(\sigma_3, \sigma_1, \sigma_2) = f(\sigma_3, \sigma_2, \sigma_1)$. Thus,

$$\sigma_1 \geq \sigma_2 \geq \sigma_3 \tag{5.48}$$

(signed!) may be set without loss of generality. From this point of view, a state of stress is uniquely determined by ξ, ρ and θ in the range $0 \leq \theta \leq 60°$ as determined by Eq. (5.47).
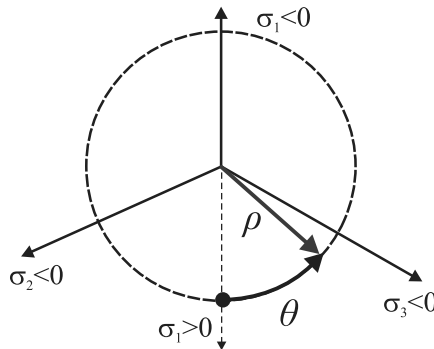

Figure 5.4: Deviatoric length and angle in the deviatoric plane.

5.4.3 Strength of Concrete

Strength of solid materials is determined experimentally with specimen of at least a size of an RVE, see Section 5.1.1. Cylindrical specimen are often used for concrete. A typical experimental setup is shown in Fig. 5.5 with the *triaxial cell*. It allows applying longitudinal and radial pressure independently from another. The radial pressure is connected with a circumferential pressure of the same value to establish equilibrium. Both form the confining pressure. A first principal stress directly corresponds to the longitudinal pressure, the confining pressure leads to the identical second- and third-principal stress. A test is started with identical longitudinal and confining pressures. Then the longitudinal pressure is changed until it reaches an extremal value corresponding to strength. Such a setup has the following locations in the principal stress space:

– The *compressive meridian* with $\sigma_1 = \sigma_2 > \sigma_3$ (signed): a cylindrical specimen with compression $\sigma_3 < 0$ in the longitudinal direction and circumferential confining pressure $\sigma_1 = \sigma_2 < 0$, $|\sigma_1| < |\sigma_3|$. From Eq. (5.20), we get $J_2 = (\sigma_1 - \sigma_3)^2/3$ and $J_3 = -2(\sigma_1 - \sigma_3)^3/27$ and from Eq. (5.47) $\cos 3\theta = -1$ or $\theta = 60°$.

– The *tensile meridian* with $\sigma_1 > \sigma_2 = \sigma_3$ (signed): a cylindrical specimen with circumferential confining pressure $\sigma_2 = \sigma_3 < 0$ and a longitudinal compression $\sigma_1 < 0$, $|\sigma_1| < |\sigma_3|$. From Eq. (5.20), we get $J_2 = (\sigma_1 - \sigma_3)^2/3$ and $J_3 = 2(\sigma_1 - \sigma_3)^3/27$ and from Eq. (5.47) $\cos 3\theta = 1$ or $\theta = 0°$.

The compressive and tensile meridian form distinguished curves within the strength surface as is shown in Fig. 5.6. They are determined as the intersection of the strength surface with the Rendulic planes with $\theta = 60°$ and $\theta = 0°$.

Strength surfaces of *concrete* themselves form a smoothed, curved tetrahedron, see Fig. 5.6. Its tip is located in the positive octant ($\sigma_1 > 0, \sigma_2 > 0, \sigma_3 > 0$) near to the origin. The origin indicates the triaxial tensile strength. The strength surface opens in the negative octant($\sigma_1 < 0, \sigma_2 < 0, \sigma_3 < 0$) and strength "increases" under pressure.

– More precisely, the admissible deviatoric length increases with increasing pressure for a certain range of pressures. This also depends on the deviatoric angle.
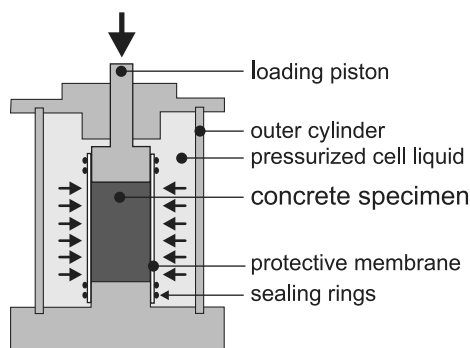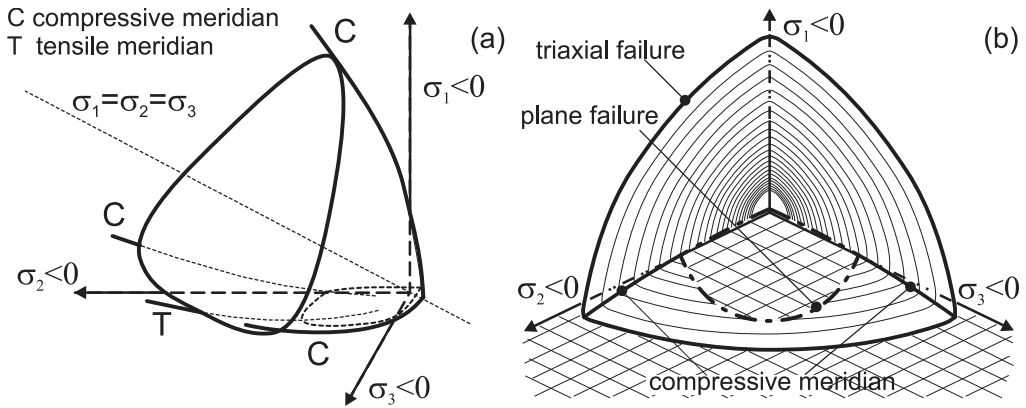

Figure 5.5: Triaxial cell.

Figure 5.6: Strength surfaces: (a) general view direction; (b) pressure axis view direction.

– Deviatoric concrete strength under very high pressures is not yet really known. From a theoretical point of view there is no strength limit for a pure pressure. Practically, pure pressure is not reachable in experimental setups. Small deviatoric parts cannot be avoided.

– Many experimental data exist for the compressive and the tensile meridian due to the relatively simple triaxial cell setup, see Fig. 5.5. Both meridians are slightly curved. The tensile meridian falls below the compressive meridian if both are sketched in a plane.

– The range between compressive and tensile meridian with a deviatoric angle $0° < \theta < 60°$ completes the whole strength surface due to its isotropy. But this range has three different principal stresses which cannot not be realized with the conventional triaxial cell according to Fig. 5.5. *True* triaxial cells are required with a much higher experimental effort and experimental data are rare in this range [38].

– The tensile strength in multiaxial tension does not significantly differ from uniaxial tensile strength. Thus, it should be possible to reach the uniaxial tensile strength in three directions simultaneously. But this has not been proved experimentally up to now.

A stress–strain relation has to be defined for all states within the strength surface. They may be assumed as isotropic linear elastic initially and become increasingly nonlinear when approaching the strength surface itself. Basic approaches to describe nonlinear material behavior are given with elastoplasticity described in Section 5.5 or damage described in Section 5.6. A selection of widely referenced formulations for the strength surface of concrete is given in the following:

– The strength surface of *Ottosen* [73]

$$f = a\,\frac{J_2}{f_c^2} + \lambda\,\frac{\sqrt{J_2}}{f_c} + b\,\frac{I_1}{f_c} - 1 = 0 \qquad (5.49)$$

with the uniaxial compression strength f_c (unsigned), a, b are constants, and λ is a function of 3θ

$$\begin{aligned}
\lambda &= k_1 \, \cos \left[\tfrac{1}{3} \arccos(k_2 \cos 3\theta) \right], && \text{for } \cos 3\theta \geq 0 \\
\lambda &= k_1 \, \cos \left[\tfrac{\pi}{3} - \tfrac{1}{3} \arccos(-k_2 \cos 3\theta) \right], && \text{for } \cos 3\theta \leq 0
\end{aligned} \tag{5.50}$$

in which k_1, k_2 are constants. The four material constants a, b, k_1, k_2 are determined from tensile strength f_{ct}, biaxial strength, and points on the compressive meridian.

– The strength surface of *Hsieh–Ting–Chen* [45]

$$f = a \, \frac{J_2}{f_c^2} + b \, \frac{\sqrt{J_2}}{f_c} + c \, \frac{\sigma_1}{f_c} + d \, \frac{I_1}{f_c} - 1 = 0 \tag{5.51}$$

with constants a, b, c, d and the largest principal stress σ_1. This may be written as

$$f = \bar{a} \left(\frac{\rho}{f_c} \right)^2 + \left(\bar{b} \cos\theta + \bar{c} \right) \frac{\rho}{f_c} + \bar{d} \, \frac{\xi}{f_c} - 1 = 0 \tag{5.52}$$

with the hydrostatic length ξ, see Eq. (5.44), deviatoric length ρ, see Eq. (5.45) and deviatoric angle θ, see Eq. (5.47).

– The strength surface of *Willam/Warnke* [94], [21, Section 5.5].

$$\bar{\rho} = \frac{2\rho_c(\rho_c^2 - \rho_t^2)\cos\theta + \rho_c(2\rho_t - \rho_c)\sqrt{4(\rho_c^2 - \rho_t^2)\cos^2\theta + 5\rho_t^2 - 4\rho_t\rho_c}}{4(\rho_c^2 - \rho_t^2)\cos^2\theta + (\rho_c - 2\rho_t)^2} \tag{5.53}$$

with

$$\bar{\xi} = a_0 + a_1 \, \rho_t + a_2 \, \rho_t^2, \qquad \bar{\xi} = b_0 + b_1 \, \rho_c + b_2 \, \rho_c^2 \tag{5.54}$$

and $\bar{\xi} = \xi/f_c$, $\bar{\rho} = \rho/f_c$. The parameters ρ_t describe the normalized tensile meridian, i.e., $\theta = 0°$ and ρ_c the normalized compressive meridian, i.e., $\theta = 60°$. The parameters $a_0, a_1, a_2, b_0, b_1, b_2$ are material constants. As compressive and tensile meridian should meet at the same point on the ξ-axis it is $a_0 = b_0$.

With the hydrostatic length ξ given the values of ρ_t, ρ_c are determined from Eq. (5.54). This may be used to determine the deviatoric length ρ with Eq. (5.53) depending on θ.

These approaches in a first view provide the same shapes of strength surfaces, see Fig. 5.6. Differences are given with details, e.g., the simplicity of formulation, the number of material constants, the exact course of compressive and tensile meridian, the occurrence of sharp edges. Sharp edges are curves on the strength surface with nonunique normal. The formulation of *Hsieh/Ting/Chen*, e.g., has a sharp compressive meridian while the formulation of *Willam/Warnke* has no sharp edges.

Triaxial strength includes *biaxial strength* as a special case with one zero principal stress or a plane stress state, respectively. Biaxial strength is determined through the intersection of the triaxial strength surface with any of the planes $\sigma_1 = 0$ or $\sigma_2 = 0$ or $\sigma_3 = 0$. We assume $\sigma_3 = 0$ irrespective to the convention equation (5.48). This leads to a closed curve in the $\sigma_1 - \sigma_2$ stress plane instead of a surface in the stress space. A curve with biaxial strength related to uniaxial strength is shown in Fig. 5.7a which is valid for normal-graded concrete [57]. It has the following characteristics:
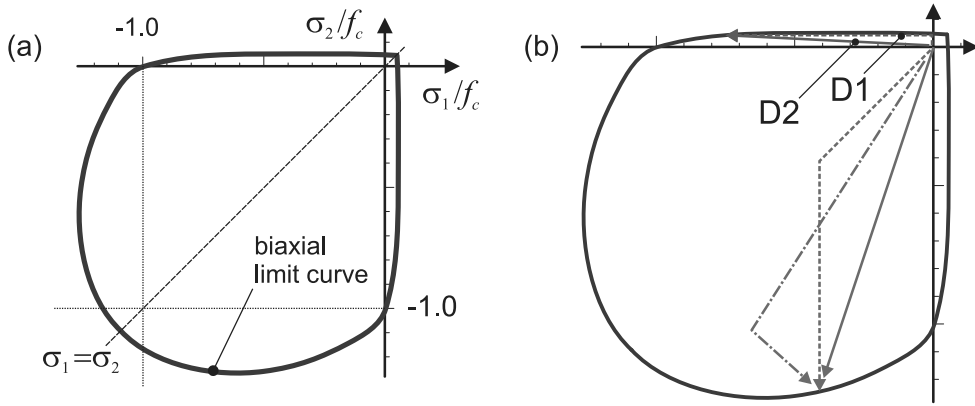
Figure 5.7: (a) Biaxial strength. (b) Stress paths.

– A lateral compression leads to an increased compressive strength in the higher loaded direction. The highest strength is roughly given for $\sigma_2 \approx 0.5\,\sigma_3$ with $|\sigma_3| > |\sigma_2|$ or vice versa.

– The tensile strength of a direction is only influenced to a minor extent by lateral compression or tension.

Biaxial strength includes *uniaxial strength* as a further special case with two zero principal stresses. The uniaxial strength is determined through the intersection of the biaxial limit curve with a stress coordinate axis cutting the uniaxial compressive and tensile strength.

It is generally assumed that multiaxial strength is independent from the stress path, i.e., different loading histories with different paths aiming at the same point of the strength surface or strength curve actually have the same ultimate point or strength, respectively. But the stress–strain behavior may be different. Regarding, e.g., the stress paths D1 and D2 of Fig. 5.7b, the path D1 will lead to a *load-induced anisotropy* due to approaching the tensile strength and cracking while a major amount of compressive strength and stiffness remains in the orthogonal direction. On the other hand the path D2 will have a more or less isotropic stress–strain behavior. A simple formulation for load-induced anisotropy under plane stress conditions will be given in Section 5.4.4. A comprehensive description of the influence of cracking is given in Section 5.7.

5.4.4   Phenomenological Approach for the Biaxial Anisotropic Stress–Strain Behavior

Load-induced anisotropy, which is characteristic for concrete, shall be treated for the plane stress case in a pragmatic direct way discussed in [21]. We consider a material point during its loading history and assume that its strains are known. Thus, also its principal strain values and principal strain directions are known. These principal strain directions span a local Cartesian coordinate system which will be used in the following. The local system may be different for every material point but this is not relevant for the basic approach. Stresses

and tangential material matrix which are at first determined in the local system have to be transformed into the global system in a final step.

A uniaxial behavior is assumed in each local coordinate direction. The uniaxial behavior is described by a generalized form of Eq. (2.1), see [21, 6.8.2]

$$\sigma = \frac{a\,\epsilon}{1 + \left(\dfrac{a\,\epsilon_p}{\sigma_p} - 2\right)\dfrac{\epsilon}{\epsilon_p} + \left(\dfrac{\epsilon}{\epsilon_p}\right)^2} \tag{5.55}$$

whereby σ, ϵ are stress and strain in a principal strain direction and σ_p, ϵ_p are experimentally determined values of maximum stress and the corresponding strain in this principal direction under biaxial conditions. The value a represents the initial Young's modulus. It is assumed as

$$a = \frac{E_c}{1 - \nu\alpha} \tag{5.56}$$

with the initial Young's modulus E_c under uniaxial loading, the corresponding initial Poisson's ratio ν and the ratio α of the principal stress in the orthogonal direction to the principal stress in the direction considered. This approach makes a material stiffer under biaxial compression. The parameter α is not known a priori. It also influences the values of σ_p, ϵ_p. Its value has to be estimated and to be corrected if necessary. The tangential material stiffness derived from Eq. (5.55) is given by

$$E_T = \frac{a\left[1 - \left(\dfrac{\epsilon}{\epsilon_p}\right)^2\right]}{\left[\left(1 - \dfrac{\epsilon}{\epsilon_p}\right)^2 + \dfrac{a\,\epsilon}{\sigma_p}\right]^2} \tag{5.57}$$

whereby the parameters a, ϵ_p, σ_p are assumed as constant. The tangential material stiffness in a principal direction depends on the strain in that direction. A value $\epsilon = 0$ yields $E_T = a$ and $\epsilon = \epsilon_p$ yields $E_T = 0$.

A combination of Eqs. (5.35), (5.38), and (5.57) is proposed for anisotropic stress–strain behavior of concrete under plane stress conditions, see [21, 6.8.2], [67, 3.4.2.3], and the coefficients of Eq. (5.35) are replaced by values according to Eq. (5.57). This approach intrinsically considers a biaxial strength condition of any choice. The approach considers a variable tangential modulus but loading and unloading are not distinguished. Thus, it is classified as *hypoelastic*. The application is demonstrated with the following Example 5.1.

Example 5.1 Modeling of biaxial stress–strain behavior with orthotropic hypoelasticity
A stress ratio value
$$\alpha = \frac{\sigma_2}{\sigma_1} = 0.5 \tag{5.58}$$

is assumed, which rules the nonlinear material behavior. The corresponding experimental results of [57] provide $\sigma_{p1} = -36\,\mathrm{MN/m^2}, \epsilon_{p1} = -0.003$ and $\sigma_{p2} = -18\,\mathrm{MN/m^2}, \epsilon_{p2} = -0.001$. Furthermore, $E_c = 30\,000\,\mathrm{MN/m^2}, \nu = 0.2$ are assumed. Firstly, this leads to $a = 30\,000/(1 - 0.2 \cdot 0.5) = 33\,333\,\mathrm{MN/m^2}$ with Eq. (5.56).
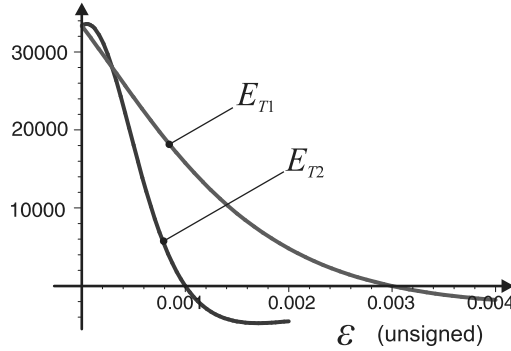
Figure 5.8: Example 5.1: Tangential material stiffness.

These values yield for the compressive range (Eq. (5.57))

$$E_{T1} = \frac{33\,333 \left[1 - \left(\frac{\epsilon_1}{-0.003}\right)^2\right]}{\left[\left(1 - \frac{\epsilon_1}{-0.003}\right)^2 - \frac{33\,333}{36}\epsilon_1\right]^2}, \quad E_{T2} = \frac{33\,333 \left[1 - \left(\frac{\epsilon_2}{-0.001}\right)^2\right]}{\left[\left(1 - \frac{\epsilon_2}{-0.001}\right)^2 - \frac{33\,333}{18}\epsilon_2\right]^2} \tag{5.59}$$

whereby strains ϵ_1, ϵ_2 have to be considered with their signs. The computed values are shown in Fig. 5.8a depending on the absolute value of ϵ_1, ϵ_2.

The tangential moduli E_{T1}, E_{T2} are used in Eq. (5.35) instead of E_1, E_2 to derive a tangential material stiffness $\mathbf{C}_T$ of a hypoelastic type. Regarding the values of the equivalent Poisson's ratio $\bar{\nu}$, see Eq. (5.32), $\nu_1 = \nu$ is assumed leading to

$$\nu_2 = \nu \frac{E_{T2}}{E_{T1}} \tag{5.60}$$

This may yield special effects in the case of, e.g., $E_{T1} \leq 0$, but shall not be examined with further details.

End Example 5.1

The approach has some limitations:

– The stress ratio parameter α, which has been assumed as constant in deriving the coefficients of the tangential material stiffness, generally is not constant in applications. Thus, the values a, ϵ_p, σ_p will change during a load history.

– Principal directions of stress and strain will not coincide due to variations in α. Thus, shear stresses will arise in the principal directions of strains, which are assmued as natural coordinate system for load-induced anisotropy.

It has to be concluded that the extension of phenomenological approaches, which work well for uniaxial behavior, may become awkward for biaxial and especially triaxial behavior. This motivates for the application of frameworks like damage and plasticity, which generalize important aspects of mechanical behavior of solids.

5.5   Isotropic Plasticity

5.5.1   A Framework for Multiaxial Elastoplasticity

Basic properties of plasticity have already been described in Section 2.3. They become evident with the unloading of a material: the same stiffness occurs for unloading as the initial stiffness for loading and permanent strains remain for a stress free state. In the case of an isotropic material the general triaxial stress–strain relation for such a behavior is given by

$$\boldsymbol{\sigma} = \mathbf{E} \cdot (\boldsymbol{\epsilon} - \boldsymbol{\epsilon}_p) \tag{5.61}$$

with the isotropic linear elastic material matrix $\mathbf{E}$ according to Eq.(5.24), total strains $\boldsymbol{\epsilon}$ and permanent strains $\boldsymbol{\epsilon}_p$. This leads to zero stresses $\boldsymbol{\sigma} = \mathbf{0}$ in the case of total strains equal to permanent plastic strains $\boldsymbol{\epsilon} = \boldsymbol{\epsilon}_p$. The rate form

$$\dot{\boldsymbol{\sigma}} = \mathbf{E} \cdot (\dot{\boldsymbol{\epsilon}} - \dot{\boldsymbol{\epsilon}}_p) \tag{5.62}$$

has to be used for general purposes. Plastic strains are variable. In the case of a *stress-based* plasticity they are derived with a *flow rule*

$$\dot{\boldsymbol{\epsilon}}_p = \dot{\lambda} \frac{\partial G}{\partial \boldsymbol{\sigma}} \tag{5.63}$$

using a flow potential $G(\boldsymbol{\sigma}, \kappa_p)$, a plastic multiplier λ, and an internal state variable κ_p comprising the load history. Equation (5.63) may lead to shear components $\epsilon_{23}, \epsilon_{13}, \epsilon_{12}$ instead of $\gamma_{23}, \gamma_{13}, \gamma_{12}$, see Eq. (5.3), depending on the formulation of G.

A change of plastic strains or plastic flow occurs in the case of yielding. Yielding is ruled by a *yield function*

$$F(\boldsymbol{\sigma}, \kappa_p) = 0 \tag{5.64}$$

Yielding may only occur for states of loading. Loading is distinguished from unloading by *Kuhn–Tucker conditions*

$$F \le 0, \quad \dot{\lambda} \ge 0, \quad F\,\dot{\lambda} = 0 \tag{5.65}$$

– In case $F < 0$ is $\dot{\lambda} = 0$, i.e., elastic loading/reloading or unloading occurs and permanent strains will not change.

– In case $F = 0$ is $\dot{\lambda} \ge 0$, i.e., plastic loading may occur and permanent strains may chance. This implies a consistency condition

$$\dot{F} = \frac{\partial F}{\partial \boldsymbol{\sigma}} \cdot \dot{\boldsymbol{\sigma}} + \frac{\partial F}{\partial \kappa_p}\,\dot{\kappa}_p = 0 \tag{5.66}$$

Finally, the formalism has to be completed with an evolution law for the internal state variable. This is assumed with

$$\dot{\kappa}_p = \dot{\lambda}\, H(\boldsymbol{\sigma}, \kappa_p) \tag{5.67}$$

The functions $F(\boldsymbol{\sigma}, \kappa_p)$, $G(\boldsymbol{\sigma}, \kappa_p)$, $H(\boldsymbol{\sigma}, \kappa_p)$ are material functions specific for a particular material. They have to be known and to be defined in advance.

- To cover initially elastic behavior the state variable κ_p generally has an initial value $\kappa_{p0} > 0$ for the unloaded virgin material.

The actual state of the material is described by a given stress $\boldsymbol{\sigma}$ and a given state variable κ_p. Thus, the conditions for loading and unloading may be evaluated as follows.

In the case of *unloading* $F < 0$ the stress increment is given by

$$\dot{\boldsymbol{\sigma}} = \mathbf{E} \cdot \dot{\boldsymbol{\epsilon}} \tag{5.68}$$

according to Eq. (5.62).

In the case of *loading*, i.e., $F = 0$, Eq. (5.66) is combined with Eqs. (5.62) and (5.67) to yield

$$\frac{\partial F}{\partial \boldsymbol{\sigma}} \cdot [\mathbf{E} \cdot (\dot{\boldsymbol{\epsilon}} - \dot{\boldsymbol{\epsilon}}_p)] + \frac{\partial F}{\partial \kappa_p} \dot{\lambda} H = 0 \tag{5.69}$$

Using Eq. (5.63) this can be solved for $\dot{\lambda}$ leading to

$$\dot{\lambda} = \frac{1}{A} \frac{\partial F}{\partial \boldsymbol{\sigma}} \cdot \mathbf{E} \cdot \dot{\boldsymbol{\epsilon}}, \qquad A = -\frac{\partial F}{\partial \kappa_p} H + \frac{\partial F}{\partial \boldsymbol{\sigma}} \cdot \mathbf{E} \cdot \frac{\partial G}{\partial \boldsymbol{\sigma}} \tag{5.70}$$

Combining Eqs. (5.70), (5.63), and (5.62) leads to the incremental material law

$$\dot{\boldsymbol{\sigma}} = \mathbf{C}_T \cdot \dot{\boldsymbol{\epsilon}} \tag{5.71}$$

with a tangential material stiffness

$$\mathbf{C}_T = \mathbf{E} - \frac{1}{A} \mathbf{E} \cdot \frac{\partial G}{\partial \boldsymbol{\sigma}} \frac{\partial F}{\partial \boldsymbol{\sigma}} \cdot \mathbf{E} \tag{5.72}$$

with $\mathbf{E}$ according to Eq. (5.24). The form $\frac{\partial G}{\partial \boldsymbol{\sigma}} \frac{\partial F}{\partial \boldsymbol{\sigma}}$ is an *outer* or *dyadic product* of two vectors. An outer or dyadic product $\mathbf{a}\,\mathbf{b}$ yields a matrix $\mathbf{c}$ with components $c_{ij} = a_i b_j$. This is not necessarily symmetric. A correct evaluation of the tangential material stiffness is essential for the solution of nonlinear equations, see Section 1.6 and Eq. (1.65). Regarding incremental approaches or discretization in time such algorithms like radial return and algorithmic material modulus are appropriate [9, 5.9].

An *associated plasticity* with identity $G = F$ of flow potential and yield condition simplifies the whole formalism.

Example 5.2 Mises elastoplasticity with special consideration of uniaxial behavior
Mises elastoplasticity is a relatively simple approach and is used to demonstrate the general procedures of elastoplasticity in this example. It is practically applied to metals and has an associated flow rule with a yield function limiting the deviatoric length, see Eq. (5.45). The *Mises yield function* and the identical flow rule are given by

$$F = G = \sqrt{\frac{3}{2}}\, \rho_\sigma - \kappa_p = \sqrt{3J_2} - \kappa_p \tag{5.73}$$

with the second invariant J_2 of the stress deviator, see Eq. $(5.20)_2$. This leads to partial derivatives

$$\frac{\partial F}{\partial \boldsymbol{\sigma}} = \frac{\partial G}{\partial \boldsymbol{\sigma}} = \frac{1}{2}\sqrt{\frac{3}{J_2}}\,\boldsymbol{\sigma}', \qquad \frac{\partial F}{\partial \kappa_p} = -1 \tag{5.74}$$

with the stress deviator $\boldsymbol{\sigma}'$, see Eq. (5.9). The tensor components $\sigma_{23}, \sigma_{32}\ldots$ have to be distinguished while computing $\partial F/\partial \boldsymbol{\sigma}$. Regarding the tangential stiffness according to Eq. (5.72) it can be shown that

$$\frac{\partial F}{\partial \boldsymbol{\sigma}} \cdot \mathbf{E} = G\sqrt{\frac{3}{J_2}}\,\boldsymbol{\sigma}', \quad G = \frac{E}{2(1+\nu)} \tag{5.75}$$

with the meaning of G as shear modulus for the current example. Regarding Eq. (5.70)

$$A = H + 3G \tag{5.76}$$

finally leads to

$$\mathbf{C}_T = \mathbf{E} - \frac{G}{1+\frac{H}{3G}}\frac{1}{J_2}\,\boldsymbol{\sigma}'\,\boldsymbol{\sigma}' \tag{5.77}$$

Full tensor notations are required in this context to derive Eq. (5.76). The product $\boldsymbol{\sigma}'\,\boldsymbol{\sigma}'$ is an outer or dyadic product of second-order tensors leading to a fourth-order tensor.

In the case of *uniaxial stress* with $\sigma_{22} = \sigma_{33} = \sigma_{23} = \sigma_{13} = \sigma_{12} = 0$ is

$$J_2 = \frac{1}{3}\sigma_{11}^2, \quad F = \sigma_{11} - \kappa_p \tag{5.78}$$

with the initial Young's modulus E and Poisson's ratio ν. The full tangential material stiffness under uniaxial stress conditions after some rearrangements is evaluated as

$$\mathbf{C}_T = \frac{E}{1+\nu}\begin{bmatrix} \frac{1}{3}\frac{(3\alpha+1-3\nu\alpha+\nu)}{(1-2\nu)(1+\alpha)} & \frac{1}{3}\frac{(3\nu\alpha+\nu+1)}{(1-2\nu)(1+\alpha)} & \frac{1}{3}\frac{(3\nu\alpha+\nu+1)}{(1-2\nu)(1+\alpha)} & 0 & 0 & 0 \\[2mm] \frac{1}{3}\frac{(3\nu\alpha+\nu+1)}{(1-2\nu)(1+\alpha)} & \frac{1}{6}\frac{(6\alpha+5-6\nu\alpha-4\nu)}{(1-2\nu)(1+\alpha)} & \frac{1}{6}\frac{(6\nu\alpha+8\nu-1)}{(1-2\nu)(1+\alpha)} & 0 & 0 & 0 \\[2mm] \frac{1}{3}\frac{(3\nu\alpha+\nu+1)}{(1-2\nu)(1+\alpha)} & \frac{1}{6}\left(\frac{6\nu\alpha+8\nu-1}{(1-2\nu)(1+\alpha)}\right) & \frac{1}{6}\frac{(6\alpha+5-6\nu\alpha-4\nu)}{(1-2\nu)(1+\alpha)} & 0 & 0 & 0 \\[2mm] 0 & 0 & 0 & \frac{1}{2} & 0 & 0 \\[1mm] 0 & 0 & 0 & 0 & \frac{1}{2} & 0 \\[1mm] 0 & 0 & 0 & 0 & 0 & \frac{1}{2} \end{bmatrix} \tag{5.79}$$

with $\alpha = (1+\nu)\frac{2}{3}\frac{H}{E}$. In the case of uniaxial stress also is $\dot{\sigma}_{22} = \dot{\sigma}_{33} = \dot{\sigma}_{23} = \dot{\sigma}_{13} = \dot{\sigma}_{12} = 0$. Thus, regarding Eqs. (5.71, 5.79) with the Voigt notation (Eqs. (5.3, 5.7)) leads to $\gamma_{23} = \gamma_{13} = \gamma_{12} = 0$ and

$$\dot{\epsilon}_{22} = \dot{\epsilon}_{33} = -\frac{3\nu\alpha+1+\nu}{3\alpha+2+2\nu}\,\dot{\epsilon}_{11} \tag{5.80}$$

This, in turn, may be used to determine

$$\dot{\sigma}_{11} = C_{T,11}\,\dot{\epsilon}_{11} + C_{T,12}\,\dot{\epsilon}_{22} + C_{T,13}\,\dot{\epsilon}_{33} = \frac{\alpha\,E}{\alpha+\frac{2}{3}(1+\nu)}\,\dot{\epsilon}_{11} = \frac{H}{1+\frac{H}{E}}\,\dot{\epsilon}_{11} \tag{5.81}$$

in the case of loading. The elastic part of longitudinal strain may be determined with $\dot{\epsilon}_{el,11} = \dot{\sigma}_{11}/E$ yielding a plastic strain

$$\dot{\epsilon}_{p,11} = \dot{\epsilon}_{11} - \dot{\epsilon}_{el,11} = \frac{1}{H}\dot{\sigma}_{11} \quad \rightarrow \quad \dot{\sigma}_{11} = H\dot{\epsilon}_{p,11} \tag{5.82}$$

The material function H is assumed as constant for Mises plasticity and corresponds to the *hardening modulus.* Regarding Eq. (5.78)$_2$ with $F = 0$ in the case of loading leads to $\sigma_{11} = \kappa_p$. But the longitudinal stress σ_{11} also corresponds to a current uniaxial yield stress f_y. Thus $\kappa_p = f_y$ and f_y replaces κ_p for Mises plasticity.

Pure shear with $\sigma_{11} = \sigma_{22} = \sigma_{33} = \sigma_{23} = \sigma_{13} = 0$ and $\sigma_{12} \neq 0$ may be treated in an analogous way leading to

$$\dot{\sigma}_{12} = \frac{H}{3 + \frac{H}{G}}\dot{\gamma}_{12}, \quad \dot{\gamma}_{p,12} = \dot{\gamma}_{12} - \dot{\gamma}_{el,12} = \frac{3}{H}\dot{\sigma}_{12} \tag{5.83}$$

This employs the engineering notation for shear strains, see Eq. (5.3), as the inverse of Eq. (5.77) is used instead of Eq. (5.63) to derive the relation for the plastic shear strain increment.

Mises plasticity is characterized by four material constants: initial Young's modulus E, Poisson's ratio ν, hardening modulus H, and initial uniaxial yield stress f_{yk}. The value of f_{yk} may be directly taken from a given uniaxial bilinear stress–strain relation, see Fig. 2.10a. The value of H is indirectly determined from such a relation by transforming Eq. (5.81) into

$$H = \frac{\frac{\Delta\sigma_{11}}{\Delta\epsilon_{11}}}{1 - \frac{1}{E}\frac{\Delta\sigma_{11}}{\Delta\epsilon_{11}}} \tag{5.84}$$

The current yield stress f_y starts with the initial value f_{yk} and changes in the case of plastic loading as is ruled by the hardening modulus. This applies in the same way to tension and compression. The values for H, f_{yk} derived from a uniaxial bilinear stress–strain relation may also be used for the general triaxial case whereby f_y corresponds to κ_p and f_{yk} to the initial κ_{p0}. *Ideal Mises elastoplasticity* is given by $H = 0$ and $f_y = f_{yk} = const.$ as a special case.

<div style="text-align:right">*End Example 5.2*</div>

The initial isotropy of the material behavior due to the isotropy of **E** is retained during a loading history under the condition of Eq. (5.41). This will be the case if the functions F, G, H depend on stress through principal stress values

$$F = F(\sigma_1, \sigma_2, \sigma_3, \kappa_p), \quad G = G(\sigma_1, \sigma_2, \sigma_3, \kappa_p), \quad H = H(\sigma_1, \sigma_2, \sigma_3, \kappa_p) \tag{5.85}$$

or through stress invariants

$$F = F(I_1, J_2, J_3, \kappa_p), \quad G = G(I_1, J_2, J_3, \kappa_p), \quad H = H(I_1, J_2, J_3, \kappa_p) \tag{5.86}$$

with I_1, J_2, J_3 according to Eq. (5.20).

The orientation of principal stress directions relative to material directions has no influence for isotropic materials. This allows the representation of yield functions as surfaces in principal stress space. Yield functions F are related to multiaxial strength, see Eq. (5.42), as the latter forms a boundary for yield criteria, i.e., $F \leq f$. Multiaxial strength is fixed and does not depend on state variables in contrast to yield functions. Finally it has to be noted that isotropic elastoplasticity does not allow to model load-induced anisotropy.

5.5.2 Pressure-Dependent Yield Functions

Mises elastoplasticity is characterized through its limitation of the deviatoric length of the stress state. This is independent from pressure and treats compression and tension in the same way. Thus, Mises elastoplasticity is not adequate to describe multiaxial concrete behavior. As an alternative the yield function of *Drucker–Prager* introduces pressure through the first stress invariant I_1

$$F = \kappa_p a \, I_1 + \sqrt{3 J_2} - \kappa_p \tag{5.87}$$

with stress invariants I_1, J_2 according to Eq. (5.20) and the internal state variable κ_p. Using Haigh–Westergaard coordinates (Eqs. (5.44–5.47)) Eq. (5.87) may be reformulated as

$$F = \kappa_p a \sqrt{3} \, \xi + \sqrt{3/2} \, \rho - \kappa_p \tag{5.88}$$

With $F = 0$ this forms a circular cone in principal stress space with a radius $\rho = \sqrt{2/3} \, \kappa_p$ in the deviatoric plane $\xi = 0$ and an apex ($\to \rho = 0$) located at $\xi_0 = 1/(\sqrt{3} \, a)$, see Fig. 5.9. The cone opens in the compressive octant with $a > 0$. Material parameters are given with the value of a and the initial value κ_{p0} of the internal state variable.

An *angle of internal friction* ϑ is defined through the ratio of deviatoric length to total hydrostatic length measured from the cone's apex. It is given by

$$\tan \vartheta = \frac{\rho}{\xi_0 - \xi} \tag{5.89}$$

This can be written as

$$\tan \vartheta = \sqrt{2} \, a \, \kappa_p \tag{5.90}$$

using $F = 0$ from Eq. (5.87) or $\xi = 1/(a\sqrt{3}) - \rho/(\kappa_p a \sqrt{2})$, respectively. Starting from a value $\tan \vartheta_0 = \sqrt{2} \, a \, \kappa_{p0}$ the angle of internal friction changes with the internal state parameter κ_p.

The *Mohr–Coulomb* yield function based on Coulomb friction makes the bearable shear stress τ in a plane dependent on the plane's normal stress σ

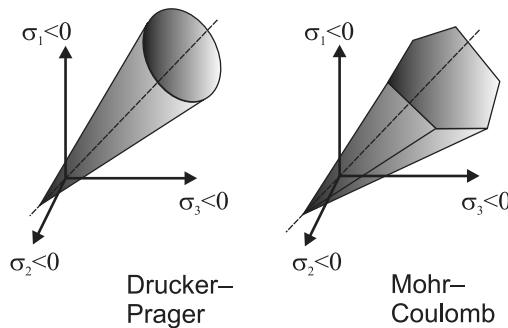$$\tau = c - \sigma \, \tan \phi \tag{5.91}$$

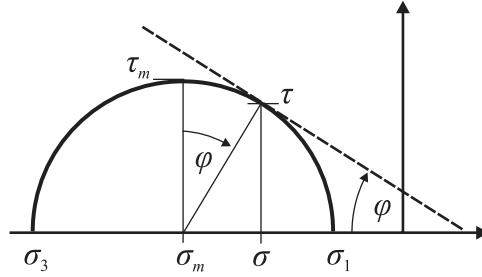Figure 5.9: Surfaces of Mohr–Coulomb and Drucker–Prager yield functions in principal stress space.

Figure 5.10: Mohr circle for Mohr–Coulomb yield type.

with a cohesion c and an *angle of external friction* ϕ. Regarding triaxial stress states the maximum shear stress is given by $\tau_m = (\sigma_1 - \sigma_3)/2$ under the condition of Eq. (5.48) and its attached normal stress by $\sigma_m = (\sigma_1 + \sigma_3)/2$ [64, 3.4]. They are related to a pair τ, σ with the largest ratio $|\tau/\sigma|$, see Fig. 5.10, by $\sigma = \sigma_m + \tau_m \sin\phi$, $\tau = \tau_m \cos\phi$. This leads Eq. (5.91) to

$$
\begin{aligned}
F &= \cos\phi\,(\tau + \sigma\tan\phi - c) \\
&= \tau_m + \sin\phi\,\sigma_m - c\,\cos\phi \\
&= \frac{1}{2}(\sigma_1 - \sigma_3) + \frac{\sin\phi}{2}(\sigma_1 + \sigma_3) - c\,\cos\phi
\end{aligned}
\tag{5.92}
$$

The condition $F = 0$ spans a plane between the compressive meridian $\sigma_2 = \sigma_1 > \sigma_3$ (signed!) and the tensile meridian $\sigma_2 = \sigma_3 < \sigma_1$. For compressive and tensile meridians see Section 5.4.3. An alternative formulation deriving hydrostatic length ξ from deviatoric length ρ is given for the *compressive meridian* with

$$
\xi = \frac{\sqrt{3}}{12}\frac{12c\cos\phi - \sqrt{6}\rho_{\mathrm{comp}}(3 - \sin\phi)}{\sin\phi}
\tag{5.93}
$$

and for the *tensile meridian* with

$$
\xi = \frac{\sqrt{3}}{12}\frac{12c\cos\phi - \sqrt{6}\rho_{\mathrm{tens}}(3 + \sin\phi)}{\sin\phi}
\tag{5.94}
$$

This leads to a relation

$$
\frac{\rho_{\mathrm{comp}}}{\rho_{\mathrm{tens}}} = \frac{3 + \sin\phi}{3 - \sin\phi}
\tag{5.95}
$$

indicating the different slope of compressive and tensile meridian with respect to the hydrostatic axis. A value of, e.g., $\phi = 30°$ leads to $\rho_{\mathrm{comp}} = 7/5\,\rho_{\mathrm{tens}}$. This factor becomes larger for increasing values of ϕ.

A cyclic interchanging of principal stresses leads to totally six planes forming the hexagonal cone with an apex at $\sigma_1 = \sigma_2 = \sigma_3 = c\cot\phi$ and $\xi_0 = \sqrt{3}c\cot\phi$, see Fig. 5.9. Angles of internal friction ϑ are derived according to Eq. (5.89). Regarding the Mohr–Coulomb compressive meridian the value is given with

$$
\tan\vartheta = \frac{\rho_{\mathrm{comp}}}{\xi_0 - \xi} = 2\sqrt{2}\,\frac{\sin\phi}{3 - \sin\phi}
\tag{5.96}
$$

As an example, an angle of external friction $\phi = 30°$ leads to an angle of internal friction $\vartheta = 54.7°$ on the compressive meridian. The external angle of friction may be subject to change due to the loading history. Thus, it is determined with

$$\phi = \kappa_{mc}\,\phi_0 \tag{5.97}$$

with the internal state variable κ_{mc} and an initial angle of internal friction ϕ_0. An initial value $\kappa_{mc,0} = 1$ is appropriate for the internal state variable. With a fixed apex position $\sigma_1 = \sigma_2 = \sigma_3 = f_t = c\cot\phi$ the cohesion is determined by

$$c = f_t\,\tan\phi \tag{5.98}$$

see also Eq. (5.92). The parameters ϕ_0, f_t serve as material constants for the Mohr–Coulomb yield function whereby f_t corresponds to a tensile strength. The yield function has the *Rankine limit function* as a special case with $\tan\phi = 1$. This restricts sustainable tensile stresses but allows unbounded compressive stresses.

The actual size of the yield functions of Drucker–Prager and Mohr–Coulomb in the principal stress space is ruled by the value of the respective internal state variables κ_p, κ_{mc}. An evolution law has to be defined for each according to Eqs. (5.67, 5.85). The limits are defined by initial values $\kappa_{p,0}, \kappa_{mc,0}$ which mark the elastic range and final values $\kappa_{p,\max}, \kappa_{mc,\max}$ when the surface of a yield function reaches a strength surface. This may be followed by a decrease of κ_p, κ_{mc} leading to a softening behavior. The parameters $\kappa_{p0}, \kappa_{p,\max}$ or $\kappa_{mc0}, \kappa_{mc,\max}$ have to be defined as further material parameters for the respective case.

The question of *flow rules* remains to be treated. In the case of Drucker–Prager a variation of the yield function (5.87)

$$G = \kappa_{pg}\,a\,I_1 + \sqrt{3J_2} \tag{5.99}$$

is often used as flow rule with an own internal state parameter κ_{pg} leading to *nonassociated plasticity* with $G \neq F$. In order to derive plastic strain increments according to Eq. (5.63)

$$\dot{\boldsymbol{\epsilon}}_p = \dot{\lambda}\,\frac{\partial G}{\partial\boldsymbol{\sigma}} \tag{5.100}$$

the derivative with respect to stress is required. The tensor notation is used for stresses and strains in the following. Regarding Eqs. (5.20, 5.74) the derivatives of the flow function are given by

$$\frac{\partial G}{\partial\boldsymbol{\sigma}} = \kappa_{pg}\,a\,\mathbf{I} + \frac{1}{2}\sqrt{\frac{3}{J_2}}\,\boldsymbol{\sigma}' \tag{5.101}$$

with the unit matrix $\mathbf{I}$. Volume change is of special interest in the following. It is defined with the *volumetric strain* ϵ_V as

$$\epsilon_V = \epsilon_{11} + \epsilon_{22} + \epsilon_{33} \tag{5.102}$$

With Eqs. (5.100, 5.101) the rate of plastic volume change is determined as

$$\dot{\epsilon}_{pV} = \dot{\epsilon}_{p11} + \dot{\epsilon}_{p22} + \dot{\epsilon}_{p33} = 3\dot{\lambda}\kappa_{pg}\,a \tag{5.103}$$

as $\sigma'_{11} + \sigma'_{22} + \sigma'_{33} = 0$ for deviatoric stresses by definition, see Eq. (5.9). As the material parameter has a condition $a > 0$ and $\dot{\lambda} \geq 0$ due to the Kuhn–Tucker conditions Eq. (5.65) a

value $\kappa_{pg} > 0$ indicates a dilation of volume or *dilatancy* while $\kappa_{pg} < 0$ indicates a compaction of volume. In analogy to Eq. (5.90) an *angle of dilantancy* is defined as

$$\tan \vartheta' = \sqrt{2}\, a\, \kappa_{pg} \tag{5.104}$$

For concrete it has to be considered that its most relevant states lie in the compressive octant of the principal stress state.

- Regarding experimental data a compaction is seen for concrete for moderate compressive stress levels. This turns into dilation for larger ratios of deviatoric length ρ to hydrostatic length ξ while approaching the strength surface, see [21, 6.2.2].

The evolution law for the internal state parameter κ_{pg} for plastic flow has to be formulated in analogy to Eq. (5.67). A similar approach for nonassociated plasticity may be followed regarding the Mohr–Coulomb type of plasticity. More details are given, e.g., in [21, 6.4.4].

The *deviatoric projections*, i.e., the intersections of yield or strength surfaces of Drucker–Prager and Mohr–Coulomb with the deviatoric plane, are shown in Fig. 5.11. The values of ϑ for Drucker–Prager and ϕ for Mohr–Coulomb are chosen such that the compressive meridian of Mohr–Coulomb coincides with the surface of Drucker–Prager. Both strength surfaces form limiting cases for the observed behavior of concrete.

A sketch of the deviatoric projection of the Willam–Warnke strength surface Eq. (5.53) is also given in Fig. 5.11. It shows the drawbacks of Drucker–Prager and Mohr–Coulomb. Drucker–Prager has identical compressive and tensile meridians, Mohr–Coulomb has sharp edges along the meridians with undefined yield surface gradients. Other projections show straight compressive and tensile meridians for both in contrast to experimental data. The more realistic Willam–Warnke surface in turn may be used a base for a yield function whereby the material parameters of the strength surface are formulated as functions of internal state parameters.

The *tangential material stiffness* according to Eq.(5.71) for both Drucker–Prager and Mohr–Coulomb in the case of loading is given by Eq. (5.72). This incorporates the elasticity
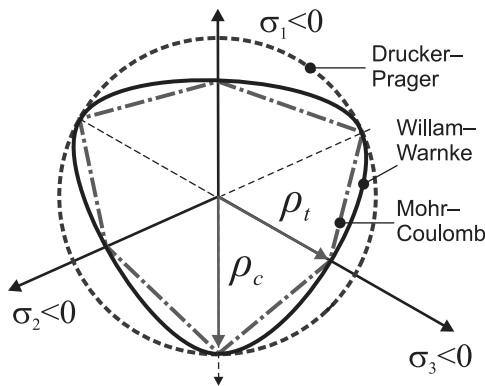

Figure 5.11: Intersections of Mohr–Coulomb and Drucker–Prager yield surfaces with the deviatoric plane.

matrix $\mathbf{E}$ and the derivatives of yield function $\frac{\partial F}{\partial \boldsymbol{\sigma}}$ and flow function $\frac{\partial G}{\partial \boldsymbol{\sigma}}$, respectively. The scalar parameter A, see Eq. $(5.70)_2$, includes the evolution law H, see Eq. (5.67), for the internal state variables κ_p and κ_{mc} used in the flow functions.

Flow functions like Mises, Drucker–Prager, or Mohr–Coulomb cover plasticity due to increasing deviatoric parts of the stress state. No plasticity will arise due to increasing hydrostatic compression with these types of predominantly *deviatoric plasticity*. But experimental data indicate a plastic compaction of a concrete's grain structure under increasing hydrostatic compression. This effect may also be treated with the formalism of plasticity or predominantly *volumetric plasticity*, respectively.

A flow function may be given by a sphere section in the principal stress state for this purpose. Volumetric and deviatoric plasticity may be combined with an extension of Eq. (5.62)

$$\dot{\boldsymbol{\sigma}} = \mathbf{E} \cdot (\dot{\boldsymbol{\epsilon}} - \dot{\boldsymbol{\epsilon}}_d - \dot{\boldsymbol{\epsilon}}_v) \tag{5.105}$$

Each plastic part has its own yield function F, flow function G, Kuhn–Tucker conditions, see Eq. (5.65), and evolution laws for internal state variables. This leads to the following cases:

- Loading in the elastic range without yielding.

- Loading in the elastoplastic range with predominantly deviatoric yielding.

- Loading in the elastoplastic range with predominantly volumetric yielding.

- Loading in the elastoplastic range with both deviatoric and volumetric yielding.

- Unloading in the elastic range without yielding.

The occurrence of cases is ruled by the particular Kuhn–Tucker conditions. In the case of both deviatoric and volumetric yielding the tangential material stiffness $\mathbf{C}_T$ is determined with an extended set of equations based on Eqs. (5.69–5.72). Implementations of the foregoing concepts are given in, e.g., [28], [32], [39].

5.6 Isotropic Damage

Elastoplasticity is characterized through the evolution of permanent strains with a constant nominal material stiffness. In contrast, damage assumes a degrading material stiffness without permanent strains upon unloading. The basic approach for *isotropic damage* is

$$\boldsymbol{\sigma} = (1 - D) \, \mathbf{E} \cdot \boldsymbol{\epsilon} \tag{5.106}$$

with the isotropic linear elastic material stiffness $\mathbf{E}$ according to Eq. (5.24). This is applicable for the triaxial behavior and includes biaxial and uniaxial behavior as special cases. Equation (5.106) introduces a state variable D. This *scalar damage variable* by definition has a range

$$0 \leq D \leq 1 \tag{5.107}$$

whereby $D = 0$ denotes a fully undamaged material and $D = 1$ a fully damaged material leading to $\boldsymbol{\sigma} = \mathbf{0}$ for every $\boldsymbol{\epsilon}$. The value of D is not allowed to decrease. It may retain its value or increase during a loading process, i.e., $\dot{D} \geq 0$. The damage variable D needs a law
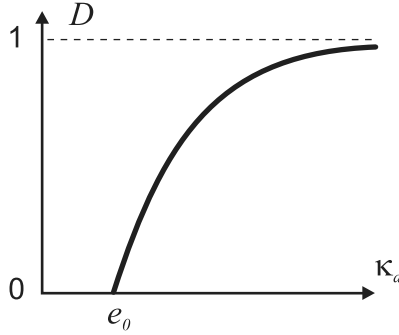
Figure 5.12: Damage variable D depending on equivalent strain κ_d.

describing its development from 0 to 1. It is generally coupled to an *internal state variable* κ_d which comprises the load history but has *not* necessarily conditions like $0 \leq \kappa_d \leq 1$, $\dot{\kappa}_d \geq 0$. Stress-based damage uses the stress history to drive κ_d while strain-based damage uses the strain history. In the following relatively simple forms of evolution laws are given for κ_d. The conventions $\sigma_1 \geq \sigma_2 \geq \sigma_3$ or $\epsilon_1 \geq \epsilon_2 \geq \epsilon_3$ with signed values have to be followed.

The approach for *strain-based damage* starts with the following relation between damage variable D and the state variable κ_d

$$D(\kappa_d) = \begin{cases} 0 & \kappa_d \leq e_0 \\ 1 - \mathrm{e}^{-\left(\frac{\kappa_d - e_0}{e_d}\right)^{g_d}} & \kappa_d > e_0 \end{cases} \tag{5.108}$$

see Fig. 5.12, with constant material parameters e_0, e_d, g_d. This form guarantees the condition $0 \leq D \leq 1$ for arbitrary values $\kappa_d \geq 0$. The internal state variable κ_d is considered as *equivalent strain* for strain-based damage. The equivalent strain is related to the strain $\boldsymbol{\epsilon}$ with a *damage function*. The formulation of such a relation has a range of alternatives. An exemplary selection is given in the following:

– The *Rankine* damage function

$$F = \begin{cases} \alpha \epsilon_1 - \kappa_d & \epsilon_1 > 0 \\ 0 & \text{else} \end{cases} \tag{5.109}$$

with the largest principal strain ϵ_1 and a material constant α. This models tensile failure in the direction of the largest principal strain or stress, respectively.

– The *Hsieh–Ting–Chen* damage function

$$F = c_1 J_{2,\epsilon} + \kappa_d \left(c_2 \sqrt{J_{2,\epsilon}} + c_3 \epsilon_1 + c_4 I_{1,\epsilon} \right) - \kappa_d^2 \tag{5.110}$$

with the largest principal strain ϵ_1, the first strain invariant $I_{1,\epsilon}$ of $\boldsymbol{\epsilon}$ and the second invariant $J_{2,\epsilon}$ of the deviator of $\boldsymbol{\epsilon}$, see Eq. (5.20) for the definition of invariants. Strain tensor components are used instead of stress tensor components. The coefficients $c_1, \ldots, c_4$ are further constant material parameters.

This damage function includes *uniaxial tension* with $\epsilon_2 = \epsilon_3 = -\nu\,\epsilon_1$ as special case leading to

$$J_{2,\epsilon} = \tfrac{1}{3}(1+\nu)^2\,\epsilon_1^2, \qquad I_{1,\epsilon} = (1-2\nu)\,\epsilon_1$$
$$F = c_1\,\frac{(1+\nu)^2}{3}\,\epsilon_1^2 + \kappa_d\left(c_2\,\frac{1+\nu}{\sqrt{3}} + c_3 + c_4\,(1-2\nu)\right)\epsilon_1 - \kappa_d^2 \tag{5.111}$$

The special case of *uniaxial compression* is $\epsilon_1 = \epsilon_2 = -\nu\,\epsilon_3$ leads to

$$J_{2,\epsilon} = \tfrac{1}{3}(1+\nu)^2\,\epsilon_3^2, \qquad I_{1,\epsilon} = (1-2\nu)\,\epsilon_3$$
$$F = c_1\,\frac{(1+\nu)^2\,\epsilon_3^2}{3} + \kappa_d\left(-c_2\,\frac{1+\nu}{\sqrt{3}} - c_3\,\nu + c_4\,(1-2\nu)\right)\epsilon_3 - \kappa_d^2 \tag{5.112}$$

Equation (5.110) has a formal similarity to Eq. (5.51) of the *Hsieh–Ting–Chen* strength surface. Actually the damage function (5.110) in the end leads to a multiaxial strength condition as formulated with Eq. (5.51).

– More alternatives are described in, e.g., [16, 6.2.3].

– A general form is given by $F = F(\epsilon_1, \epsilon_2, \epsilon_3, \kappa_d)$ or $F = F(I_1, J_2, J_3, \kappa_d)$. The dependency on principal strain values or principal strain invariants ensures the isotropy of the stress–strain relations according to Eq. (5.21).

We briefly consider the case that this isotropic dependency is not given using, e.g., $F = \alpha\epsilon_{11} - \kappa_d$ similar to Eq. (5.109) but with the principal value replaced by ϵ_{11}. A Poisson's ratio $\nu = 0$ is assumed. Thus, a uniaxial state in the 1-direction leads to an equivalent damage strain and a damage. A rotation $\mathbf{Q}$ of the coordinate system by 90° will transform the nonzero strain ϵ_{11} into a nonzero strain ϵ_{22} and the zero strain ϵ_{22} into a zero strain ϵ_{11}. Damage will vanish due to this transformation. The isotropy condition (Eq. (5.21)) obviously cannot be fulfilled with the material law Eq. (5.106).

The equivalent strain κ_d may be connected to damage D by Eq. (5.108) for both damage functions. Other formulations for the relation between D and κ_d are possible but should have the characteristics shown in Fig. 5.12.

Similar to elastoplasticity loading states have to be distinguished from unloading states for damage. This is again done with *Kuhn–Tucker conditions*

$$F \le 0, \quad \dot{D} \ge 0, \quad F\dot{D} = 0 \tag{5.113}$$

similar to Eq. (5.65).

– In case $F < 0$ is $\dot{D} = 0$, i.e., unloading occurs and damage will not change.

– In case $F = 0$ is $\dot{D} \ge 0$, i.e., loading occurs and damage may increase. This implies a consistency condition similar to Eq. (5.66)

$$\dot{F} = \frac{\partial F}{\partial \boldsymbol{\epsilon}} \cdot \dot{\boldsymbol{\epsilon}} + \frac{\partial F}{\partial \kappa_d}\,\dot{\kappa}_d = 0 \quad \rightarrow \quad \dot{\kappa}_d = -\frac{1}{\frac{\partial F}{\partial \kappa_d}}\,\frac{\partial F}{\partial \boldsymbol{\epsilon}} \cdot \dot{\boldsymbol{\epsilon}} \tag{5.114}$$

leading to the evolution law for the equivalent strain.

Finally it has to be noted that scalar damage D and equivalent strain κ_d are not strictly coupled by Eq. (5.108) but through the interaction of Eqs. (5.108, 5.113, 5.114), i.e., D and κ_d are decoupled in case of $\dot{\kappa}_d < 0$.

Stress-based damage shall only briefly be mentioned. The internal state variable κ_d becomes an equivalent stress in the case of stress-based damage. Again a damage function may be used to connect the equivalent stress to the stress state $\boldsymbol{\sigma}$. Yield functions as have been previously derived for elastoplasticity – Drucker–Prager, Mohr–Coulomb or more complex types to cover characteristics of concrete behavior – may basically be used for this purpose whereby the internal state parameter of elastoplasticity κ_p is replaced by an equivalent stress measure.

The relation between the damage variable D and the equivalent stress has to have another characteristic as is shown in Fig. 5.12 for strain-based damage as measures of stress in general and equivalent stress in particular have upper limits due to limited strength. The relations are not straightforward anymore and have to be formulated implicitly. Finally, the stress-based damage has to be completed by Kuhn–Tucker conditions in the same way as Eq. (5.113) to distinguish loading from unloading.

We will refer to strain-based damage in the following and demonstrate aspects of its application with the following example.

Example 5.3 Uniaxial stress–strain relations with *Hsieh–Ting–Chen* damage
We assume strain-based damage with damage variable according to Eq. (5.108) and the damage function according to *Hsieh–Ting–Chen* equation (5.110). The material parameters are given in Table 5.1 including the Poissons's ratio ν and a nominal value E_0 of Young's modulus. Principal signed strains and stresses are used as stress and strain measure in the following. A uniaxial stress state is assumed with $\sigma_1 \neq 0$, $\sigma_2 = \sigma_3 = 0$.

$E_0\,(\mathrm{MN/m^2})$	30 0000	$e_0\,(-)$	2.836×10^{-4}	$c_1\,(-)$	1.738
$\nu\,(-)$	0.2	$e_d\,(-)$	1.910×10^{-3}	$c_2\,(-)$	0.608
		$g_d\,(-)$	2	$c_3\,(-)$	7.700
				$c_4\,(-)$	2.993

Table 5.1: Material parameters of Example 5.3.

Considering continuously increasing *compression* with $\dot{\epsilon}_3 < 0$, $\dot{D} > 0$ and applying Kuhn–Tucker conditions (5.112) yields $F = -\epsilon_3 - \kappa_d = 0$ and $\kappa_d = -\epsilon_3$. Equations (5.106, 5.108) lead to

$$\sigma_3 = (1 - D)\, E_0\, \epsilon_3 = \mathrm{e}^{-\left(\frac{-\epsilon_3 - e_0}{e_d}\right)^{g_d}} E_0\, \epsilon_3 \tag{5.115}$$

in case $\epsilon_3 \leq -e_0$.

Considering continuously increasing *tension* with $\dot{\epsilon}_1 > 0$, $\dot{D} > 0$, Eq. (5.111) yields $F = \alpha\, \epsilon_1 - \kappa_d = 0$ and $\kappa_d = \alpha\, \epsilon_1$ with α depending on $\nu, c_1, \ldots, c_4$. The values given in Table 5.1 result in $\alpha = 10$. Equations (5.106, 5.108) lead to

$$\sigma_1 = (1 - D)\, E_0\, \epsilon_1 = \mathrm{e}^{-\left(\frac{\alpha\, \epsilon_1 - e_0}{e_d}\right)^{g_d}} E_0\, \epsilon_1 \tag{5.116}$$

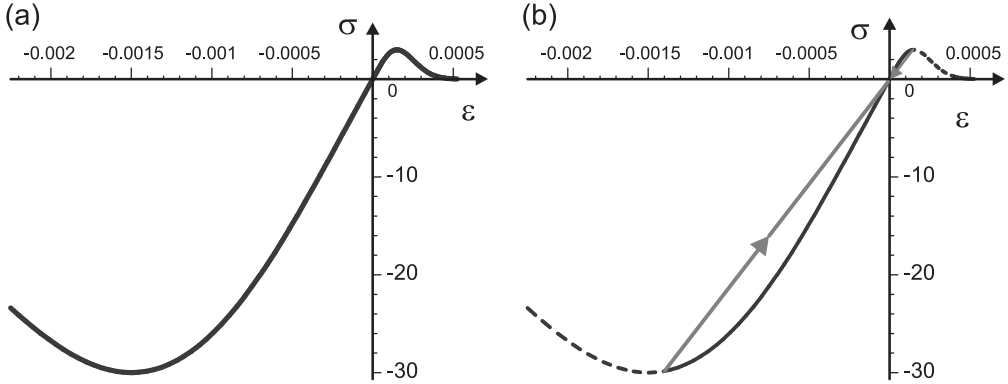in case $\epsilon_1 \geq e_0/\alpha$.

Figure 5.13: Example 5.3 (a) Uniaxial stress–strain relation. (b) Loading, unloading, and reloading.

The stress–strain relation evaluated from Eqs. (5.115, 5.116) is shown in Fig. 5.13a. It has the following properties:

– The stress–strain curve reproduces the empirical curves Fig. 2.1 for compression and Fig. 2.2b for tension.

– The computed initial value of Young's modulus – ratio of stress and strain in the uniaxial case – corresponds to the prescribed value E_0 of Table 5.1.

– The uniaxial compressive strength is determined with $f_c = 30\,\mathrm{MN/m^2}$ at a strain $\epsilon_{c1} = -0.0015 = -1.5‰$, and the uniaxial tensile strength with $f_{ct} = 3\,\mathrm{MN/m^2}$.

The values of E_0, f_c, ϵ_{c1} are provided as basic parameters of concrete properties. While E_0 can directly adopted for the material law the values f_c, ϵ_{c1} are input for a calibration procedure. A general choice $g_d = 2$ proves to be appropriate. Thus, two unknowns e_0, e_d remain in Eq. (5.115) to reproduce $\sigma_3 = -f_c$ for $\epsilon_3 = \epsilon_{c1}$. This constitutes a small nonlinear problem which may be solved, e.g., iteratively with the Newton–Raphson method in analogy to Eq. (1.72).

The corresponding tensile strength is determined by the combination of parameters $c_1, \ldots, c_4$ leading to an equivalent strain scaling factor α. A target value f_{ct} is reached with an appropriate choice of $c_1, \ldots, c_4$. The corresponding strain comes as a result.

Materials with damage considerably differ from elastoplastic materials in the case of unloading. This is demonstrated with the following loading history:

– Compression loading in a range $-1.4 \times 10^{-3} \le \epsilon_3 \le 0$ with $\dot{\epsilon}_3 < 0$, $\dot{D} > 0$, $F = 0$.

– Unloading in a range $-1.4 \times 10^{-3} \le \epsilon_3 \le 0$ with $\dot{\epsilon}_3 > 0$, $\dot{D} = 0$, $F = -\epsilon_3 - \kappa'_d < 0$, i.e., $\epsilon_3 > -\kappa'_d$ with $\kappa'_d = 1.4 \cdot 10^{-3}$.

– Change of index in stress and strain from 3 to 1 due to change from compressive into tensile regime. The physical direction actually is not changed.

– Elastic reloading ranging from $0 \leq \epsilon_1 \leq \kappa_d'/\alpha$ with $\dot{\epsilon}_1 > 0, \dot{D} = 0, F = \epsilon_1 \alpha - \kappa_d' < 0$.

– Resumed loading ranging from $\kappa_d'/\alpha \leq \epsilon_1 \leq 0.5 \cdot 10^{-3}$ with $\dot{\epsilon}_1 > 0, \dot{D} > 0, F = 0$.

The resulting stress–strain curve in shown in Fig. 5.13b. In contrast to elastoplasticity there are no permanent strains after unloading to zero stress. But the unloading stiffness – actually a secant stiffness – is reduced in contrast to the unloading stiffness of elastoplasticity.

———————————————————————————————— End Example 5.3

The incremental form of the material law for damage (Eq. (5.106)) remains to be added. The derivative with respect to time t is given by

$$\begin{aligned}
\dot{\boldsymbol{\sigma}} &= (1-D)\,\mathbf{E} \cdot \dot{\boldsymbol{\epsilon}} - \mathbf{E} \cdot \boldsymbol{\epsilon}\,\dot{D} \\
&= (1-D)\,\mathbf{E} \cdot \dot{\boldsymbol{\epsilon}} - \boldsymbol{\sigma}_0\,\dot{D}
\end{aligned} \tag{5.117}$$

To derive the rate of $\dot{D}$ we consider D as the function of equivalent strain κ_d, see Eq. (5.108). A general form is determined by

$$\dot{D} = \frac{\mathrm{d}D}{\mathrm{d}\kappa_d}\,\dot{\kappa}_d = -\frac{\frac{\mathrm{d}D}{\mathrm{d}\kappa_d}}{\frac{\partial F}{\partial \kappa_d}}\,\frac{\partial F}{\partial \boldsymbol{\epsilon}} \cdot \dot{\boldsymbol{\epsilon}} \tag{5.118}$$

using Eq. (5.114) for $\dot{\kappa}_d$. Thus, Eq. (5.117) can be written as

$$\dot{\boldsymbol{\sigma}} = \mathbf{C}_T \cdot \dot{\boldsymbol{\epsilon}} \tag{5.119}$$

with

$$\mathbf{C}_T = \begin{cases} (1-D)\,\mathbf{E} + \dfrac{\frac{\mathrm{d}D}{\mathrm{d}\kappa_d}}{\frac{\partial F}{\partial \kappa_d}}\,\boldsymbol{\sigma}_0\,\dfrac{\partial F}{\partial \boldsymbol{\epsilon}} & \text{for loading} \\ (1-D)\,\mathbf{E} & \text{unloading} \end{cases} \tag{5.120}$$

The form $\boldsymbol{\sigma}_0 \frac{\partial F}{\partial \boldsymbol{\epsilon}}$ is again an outer or dyadic product of two vectors. The quantities $\frac{\partial F}{\partial \boldsymbol{\epsilon}}, \frac{\partial F}{\partial \kappa_d}$, $\frac{\mathrm{d}D}{\mathrm{d}\kappa_d}$ have to be computed from the forms for F, D.

The foregoing description covers very basic ideas of damage. A comprehensive treatment is given in [59]. Several refinements have been developed regarding the characteristics of concrete behavior:

– Tensile states are distinguished from compressive states using positive and negative projections of, e.g., strain. Such projections are determined using the spectral decomposition of the strain tensor. A tensile and compressive damage is assigned to each projection and each damage type acts independently. This covers the effect that concrete retains its compressive stiffness and strength after a tensile loading.

– Isotropic damage assigns the same stiffness degradation in every material orientation. Such an approach cannot capture a load-induced anisotropy, see Section 5.1.2. *Anisotropic damage* introduces a stiffness degradation which depends on the orientation within a material.

A special but relatively convenient form of anisotropic damage is given by *orthotropic damage*. This may be realized with the degradation of Young's moduli of the orthotropic compliance (Eq. (5.27)).

– Isotropic damage and elastoplasticity can be coupled with the combination of Eqs. (5.61, 5.106) leading to

$$\boldsymbol{\sigma} = (1 - D)\, \mathbf{E} \cdot (\boldsymbol{\epsilon} - \boldsymbol{\epsilon}_p) \tag{5.121}$$

comprising damage function, yield function, flow rule, Kuhn–Tucker conditions, internal state variables and their evolution laws for damage and plasticity.

A combination of all these concepts is basically possible. Implementations are given in, e.g., [15], [23], [33], [41], [52].

5.7 Multiaxial Crack Modeling

5.7.1 Basic Concepts of Crack Modeling

Crack formation is a characteristic property of plain and reinforced concrete structures. Cracks are unavoidable due to the relatively low tensile strength of concrete. Crack formation changes the relations of stiffness. Thus, it allows for a redistribution of stresses and internal forces within a structure on one hand, on the other hand crack width has to be limited to ensure durability and visual integrity of a structure.

The topics of crack formation are part of fracture mechanics. Linear elastic fracture mechanics (LEFM) forms the core. LEFM analyses given cracks in homogeneous elastic bodies whereby cracks are surfaces or planes, respectively, within 3D bodies or curves or lines within 2D bodies defining internal boundaries allowing for discontinuities of displacements.

LEFM distinguishes three basic *fracture modes* which are amenable for the analytical treatment within the framework of elasticity:

– Mode-I: Opening arising from a tensile stress normal to the crack plane,

– Mode-II: Sliding from a shear stress parallel to the crack plane but normal to the front of the crack plane,

– Mode-III: Tearing from a shear stress parallel to the crack plane and parallel to the front of the crack plane.

see Fig. 5.14. *Fracture types* are are another category beneath fracture modes. We distinguish: brittle fracture, quasi-brittle fracture and ductile fracture. These types are connected to the material behavior in the case of failure. We consider the uniaxial stress–strain relations to simplify the discussion, see Fig. 5.14b. The behavior before reaching the strength is assumed as elastic.

– *Brittle fracture* is connected with a sudden drop of stress after reaching strength. The internal elastic energy is transformed into the energy to form new surfaces. This type of failure is typical for glass.

– *Quasi-brittle fracture* is connected with decreasing stress after reaching strength. The internal energies are transformed into process zone creation, see Section 2.1 and Fig. 2.2a. This type of failure is typical for concrete and many geomaterials.
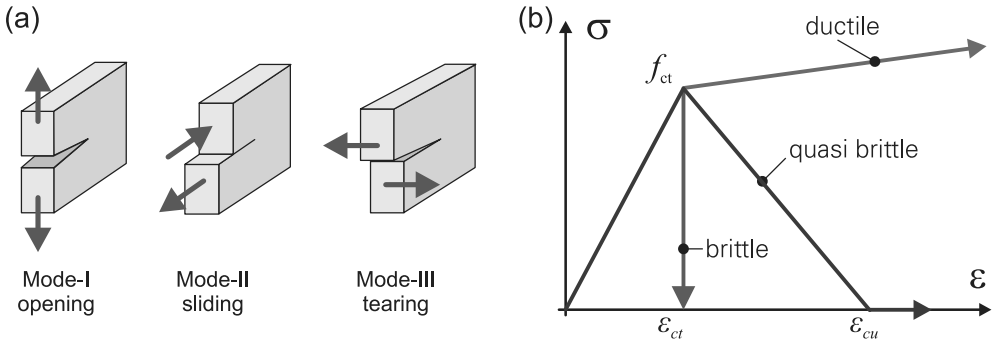
Figure 5.14: (a) Fracture modes. (b) Material failure types.

– *Ductile fracture* is connected with yielding and hardening, i.e., with a slightly increasing stress after the strain passes the point of yielding. Yielding and hardening go on for a relatively long range of strain before localization starts ending with rupture. The internal energies are predominantly transformed into crystalline sliding. This is typical for metals.

The application of LEFM is restricted to cases with brittle failure. Quasi-brittle failure will be considered in the following and LEFM is not directly applicable anymore. The formation of a process zone or crack band ending up in macrocracking has already been discussed in Section 2.1. Continuum mechanics is not appropriate for a detailed microscopic or even mesoscopic description of the complex mechanisms during crack-band formation. Furthermore, the macroscale viewpoint, see Section 5.1.1, requires the homogenization of the crack band. The transmission of forces via crack bridges and crack branches, see Fig. 2.2a, is represented with the cohesive crack model.

• The *cohesive crack model* assigns surface tractions along *fictitious crack* boundaries. A cohesive crack law relates surface tractions and fictitious crack widths.

The fictitious crack width is conjugate to crack tractions with respect to energy. Both can be considered as generalized stresses or strains, respectively. The cohesive crack model is illustrated with Fig. 5.15 for mode-I. The fictitious crack width w insofar has a physical meaning as the traction corresponds to strength for $w = 0$ and the traction becomes zero for $w = w_{cr}$ whereby the critical crack width w_{cr} corresponds to the beginning macrocrack width. Such a value can be estimated from experimental data. Furthermore, some physical interpretation is given in Eqs. (2.4, 2.5).

The fictitious crack implies two crack surfaces as opposite boundaries. These crack surfaces change their relative position during cracking and the relative position change is used as fictitious crack width. One of these surfaces is chosen as reference. Each position on the reference surface has a *tangential cracking plane* supporting a local Cartesian coordinate system with a normal **n**.

The distance between the crack surfaces is measured by a fictitious crack width *normal component* w_1 and two fictitious crack width *sliding components* w_2, w_3 in the local coordinate
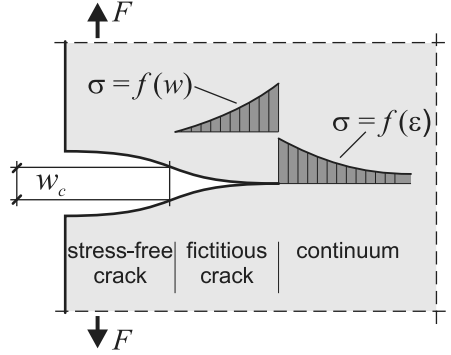
Figure 5.15: Cohesive crack model.

system. They form a fictitious crack width vector

$$\mathbf{w}_c = \left(\begin{array}{c} w_1 \\ w_2 \\ w_3 \end{array} \right) \tag{5.122}$$

The cohesive crack model assumes a crack traction vector $\mathbf{t}_c$. Due to equilibrium reasons its components are connected to the *local* Cauchy stress, see Eqs. (5.5, 5.16), by

$$\mathbf{t}_c = \left(\begin{array}{c} t_1 \\ t_2 \\ t_3 \end{array} \right) = \left(\begin{array}{c} \tilde{\sigma}_{11} \\ \tilde{\sigma}_{12} \\ \tilde{\sigma}_{13} \end{array} \right) \tag{5.123}$$

in the tangential cracking plane. A material law relates stresses and strains in a continuum. In the same way a material law relates crack traction and crack width in a crack. A general approach is formulated as

$$t_1 = f_n(w_1), \quad t_2 = f_s(w_2), \quad t_3 = f_s(w_3) \tag{5.124}$$

with different laws f_n for the *normal* component and f_s for the *sliding* component. The relation f_n for the normal component corresponds to mode-I or uniaxial cracking in the softening range, see Section 2.1 and Fig. 2.2b. A separation of the horizontal axis in a strain section up to tensile strength and a following crack width section leads to a form as shown in Fig. 5.16. The w-section of the horizontal axis has to be scaled according to Eq. (2.5) in order to reproduce the crack energy equations (2.6) and (2.7). An approach for the sliding is given with shear retention within the context of the smeared crack model, see Section 5.7.2.

Basically all material frameworks like plasticity or damage may be used to formulate relations connecting the generalized strain $\mathbf{w}_c$ with the generalized stress $\mathbf{t}_c$. They are written in a general form as

$$\dot{\mathbf{t}}_c = \mathbf{C}_{cLT} \cdot \dot{\mathbf{w}}_c, \qquad \dot{\mathbf{w}}_c = \mathbf{D}_{cLT} \cdot \dot{\mathbf{t}}_c \tag{5.125}$$

with a local tangential crack stiffness $\mathbf{C}_{cLT}$ and a local tangential crack compliance $\mathbf{D}_{cLT}$, compare Eqs. (1.50, 1.51).
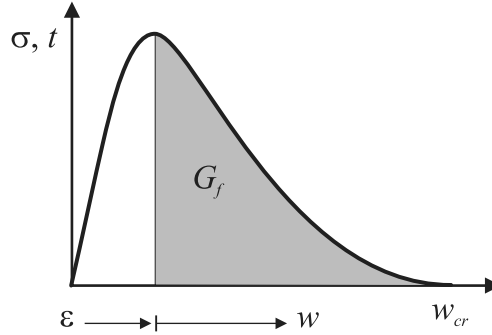
Figure 5.16: Material law for cohesive crack model/normal components.

The fictitious crack concept allows one to model crack propagation for quasi-brittle materials based on continuum mechanics and within the macroscale. It is still connected with a discontinuity of displacements along crack surfaces or crack curves. The explicit modeling of such displacement discontinuities requires special methods like the *extended finite-element-method* (XFEM) [50], [89] or the *element free Galerkin* (EFG) method [8], [58]. These methods describe displacement discontinuities explicitly on the system level with an explicit description of crack geometry.

- Methods like XFEM and EFG perform a *discrete crack modeling.*

Alternatives are given with local approaches which model such discontinuities on the element level with *embedded discontinuity* formulations [70], [72]. For a comprehensive treatment of fracture mechanics, cohesive cracks, size effects and other related topics see [6], [49].

5.7.2 Multiaxial Smeared Crack Model

A widely used approach for crack modeling is given by the *smeared crack model*. It has already been discussed in Section 2.5 for the uniaxial case. A first question concerns onset of cracking. Cracking starts in the uniaxial case when the uniaxial stress reaches the uniaxial tensile strength f_{ct}.

This is extended to the multiaxial case with the *Rankine criterion*. We consider a material point with a given multiaxial stress state. Cracking starts when the largest principal stress, see Section 5.2.3, reaches the uniaxial tensile strength f_{ct}. Using the uniaxial strength as a criterion for a multiaxial case is justified by experimental data indicating that for concrete the values of multiaxial tensile strength do not significantly differ from the uniaxial value f_{ct}, see Section 5.4.3 and Figs. 5.6 and 5.7. The crack direction is assumed as normal to the direction of the principal stress inducing the crack. Thus, principal direction and the normal **n** of the local tangential cracking plane, see Section 5.7.1, coincide.

The local cracking plane provides a coordinate system for components of the fictitious crack width vector $\mathbf{w}_c$, see Eq. (5.122). In analogy to Eq. (2.5) a *crack strain* for the multiaxial case is defined as

$$\dot{\boldsymbol{\epsilon}}_c = \frac{1}{b_w} \mathbf{L} \cdot \dot{\mathbf{w}}_c \tag{5.126}$$

with the crack-band width b_w, see Section 2.1, and an incidence matrix $\mathbf{L}$

$$\mathbf{L} = \begin{bmatrix} 1 & 0 & 0 \\ 0 & 0 & 0 \\ 0 & 0 & 0 \\ 0 & 0 & 0 \\ 0 & 0 & 1 \\ 0 & 1 & 0 \end{bmatrix} \tag{5.127}$$

assigning differences of displacements to strains in Voigt notation, see Eq. (5.3). The crack width is connected to crack tractions by Eq. (5.125). Furthermore, in order to keep local equilibrium crack tractions are related to the *local* Cauchy stress by Eq. (5.123) which may be reformulated as

$$\dot{\mathbf{t}}_c = \mathbf{L}^T \cdot \dot{\boldsymbol{\sigma}} \tag{5.128}$$

assigning crack tractions to the Cauchy stress in Voigt notation, see Eq. (5.7). This is still measured in the local coordinate system tangential to the crack surface. As its orientation in the global coordinate system should be known a coordinate transformation matrix $\mathbf{Q}'$ can be determined and local crack strains and local Cauchy stresses can be transformed into the global system according to Eqs. (5.15, 5.16).

Thus, in analogy to Eq. (2.45), we set for the multiaxial case

$$\dot{\boldsymbol{\epsilon}} = (1 - \xi)\,\dot{\boldsymbol{\epsilon}}_u + \xi\,\mathbf{Q}' \cdot \dot{\boldsymbol{\epsilon}}_c, \qquad \xi = \frac{b_w}{L} \tag{5.129}$$

with the total strain $\boldsymbol{\epsilon}$, the strain $\boldsymbol{\epsilon}_u$ of the uncracked material and a characteristic length L of the respective element. The combination of Eqs. (5.125$_2$, 5.126, 5.128, 5.129) yields

$$\dot{\boldsymbol{\epsilon}} = (1 - \xi)\,\dot{\boldsymbol{\epsilon}}_u + \mathbf{D}_{cT} \cdot \dot{\boldsymbol{\sigma}} \tag{5.130}$$

with

$$\mathbf{D}_{cT} = \frac{1}{L}\,[\mathbf{Q}' \cdot \mathbf{L}] \cdot \mathbf{D}_{cLT} \cdot [\mathbf{Q}' \cdot \mathbf{L}]^T \tag{5.131}$$

For 1D states this simplifies to

$$D_{cT} = \frac{1}{L_e}\,D_{cLT} \tag{5.132}$$

with the element length L_e, the uniaxial tangential compliance D_{cT} relating stress and strain and the uniaxial tangential compliance D_{cLT} with respect to crack width and crack traction.

The material behavior of the uncracked material has to be considered in the next step. We use the general formulations (Eqs. (1.50, 1.51)) for tangential material stiffness and compliance

$$\dot{\boldsymbol{\sigma}} = \mathbf{C}_T \cdot \dot{\boldsymbol{\epsilon}}_u, \qquad \dot{\boldsymbol{\epsilon}}_u = \mathbf{D}_T \cdot \dot{\boldsymbol{\sigma}} \tag{5.133}$$

The combination with Eq. (5.130) leads to

$$\dot{\boldsymbol{\epsilon}} = [(1 - \xi)\,\mathbf{D}_T + \mathbf{D}_{cT}] \cdot \dot{\boldsymbol{\sigma}} \tag{5.134}$$

which can be transformed into

$$\dot{\boldsymbol{\sigma}} = [(1 - \xi)\,\mathbf{I} + \mathbf{C}_T \cdot \mathbf{D}_{cT}]^{-1} \cdot \mathbf{C}_T \cdot \dot{\boldsymbol{\epsilon}} \tag{5.135}$$

using $\mathbf{C}_T \cdot \mathbf{D}_T = \mathbf{I}$. This is a generalization of the uniaxial case (Eqs. (2.51, 2.52)). Equation (5.135) resembles the incremental material law $\dot{\boldsymbol{\sigma}} = \mathbf{C}_T \cdot \dot{\boldsymbol{\epsilon}}$ for zero crack-band width $\xi = 0$ and a rigid crack band $\mathbf{D}_{cT} = \mathbf{0}$. It leads to $\dot{\boldsymbol{\sigma}} = \frac{1}{1-\xi} \mathbf{C}_T \cdot \dot{\boldsymbol{\epsilon}}$ for $\mathbf{D}_{cT} = \mathbf{0}$ only.

Basically any type of material law – elasticity, elastoplasticity, damage – may be used for the material description of the uncracked material or the formulation of the tangential material stiffness $\mathbf{C}_T$, respectively. An example for biaxial elasticity with limited tensile strength will be given in Section 6.2. A combination of smeared cracking and triaxial elastoplasticity is described in [20].

The comprehension of crack formation introduces anisotropy in combination with isotropic material laws for uncracked materials. This is valid both for explicit discrete crack modeling and for the smeared crack model. The latter performs a superposition – smearing – of cracks and uncracked material covering some area of material represented by a single material point, i.e., an integration point regarding finite elements. This approach does not require an explicit modeling of displacement discontinuities.

- The multiaxial smeared crack approach can be used as a model for load-induced anisotropy which is compatible with the standard displacement-based FEM.

Due to smearing a crack geometry cannot be precisely determined unlike to discrete crack modeling, only some area of cracking.

Multiple cracking can be treated with an extension of Eq. (5.129)

$$\dot{\boldsymbol{\epsilon}} = (1 - \xi)\, \dot{\boldsymbol{\epsilon}}_u + \xi \left(\mathbf{Q}'_1 \cdot \dot{\tilde{\boldsymbol{\epsilon}}}_{c,1} + \mathbf{Q}'_2 \cdot \dot{\tilde{\boldsymbol{\epsilon}}}_{c,2} + \cdots \right) \tag{5.136}$$

whereby $\mathbf{Q}'_i$ denotes the orientation of a crack i. This leads to an extended form of Eq. (5.135). A final question concerns the evolution of crack orientations within the smeared crack model. This question arises with the usage of the Rankine criterion. Principal stress orientations may change regarding a load history. This leads to two alternative concepts regarding stress orientations:

- *Fixed crack*: The crack orientation is fixed with the position occurring for the onset of cracking. This corresponds to clearly separated opposite crack surfaces or macrocracks, see Fig. 2.2a.

- *Rotating crack*: The crack orientation follows the direction of principal stresses, i.e., it may change during a load history. This corresponds to crack bands and microcracking, where the orientation of a bunch of microcracks may change upon a changing of a principal tensile stress direction. Cracking is limited to mode-I cracking, see Fig. 5.14a, with rotating cracks.

Although the fixed crack concept seems to be more realistic from a phenomenological point of view some complications are involved. In many practical applications it yields too a stiff behavior of the cracked material. Furthermore, it introduces a relative sliding of crack surfaces with sliding components w_2, w_3, see Eq. (5.122), leading to in-plane crack tractions t_2, t_3, see Eq. (5.123). A sliding law f_s, see Eq.(5.124), has to be formulated. Sliding includes two major components:

- *Dowel action*: Rebars crossing a crack have to sheared and bended.

 – *Aggregate interlock*: Crack surfaces are rough especially due to preferable failure of the interfacial transition zone (ITZ), see Section 5.1.1. This leads especially to friction between aggregates.

A reliable formulation of a sliding law is difficult due to rare multiaxial experimental data including rebars in contrast to data for the tensile softening law f_n derived from uniaxial experimental setups with plain concrete. The concept of shear retention is used as a very approximate approach. It uses the isotropic elastic shear stiffness, see Eq. (5.24), reduced by a *shear retention factor* β

$$f_s = \beta \, \frac{E}{2(1+\nu)}, \quad 0 \leq \beta \leq 1 \tag{5.137}$$

with an often chosen value $\beta = 0.5$. An approach to adopt this factor to increasing crack width is given in [19] which avoids artificial locking risks. Concepts of cracks may be combined starting with a rotating crack and switching over to a fixed crack in case some threshold crack width value is exceeded. But this introduces one more estimate coefficient.

Finally, the effect of *crack closure* has to be considered: a cracked material more or less regains stiffness after a reduction of crack width to zero or a relatively small value. An example is given in Section 6.2.

5.8 The Microplane Model

A deeper inspection of mesoscales or microscales of materials, see Sections 2.1 and 5.1.1, reveals that stiff parts embedded in a matrix interact in microscopic boundary layers, see Fig. 5.17a. The microplace concept represents these layers by a variety of microscopic planes. Stress and strain vectors are defined with respect to these planes and material laws are formulated to relate them. A superposition of microplanes finally yields homogenized relations between strains and stresses. In another view microplanes may be imagined as the tangent planes of a sphere surrounding every continuum point, see Fig. 5.17b.
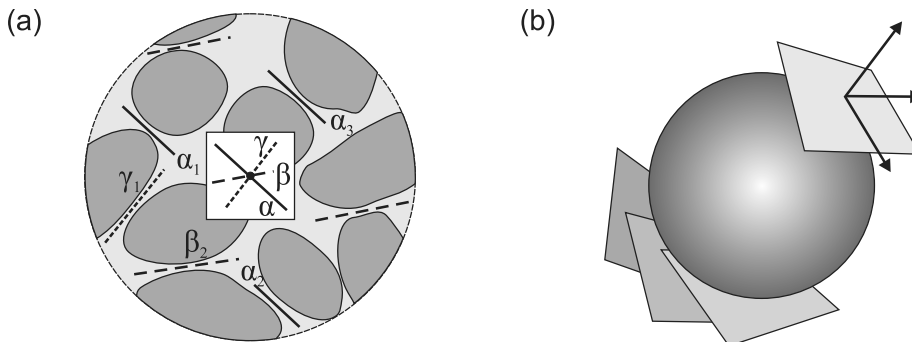

Figure 5.17: Microplane (a) Interaction layers [5]. (b) Microplanes in unit sphere [56]).

A basic question of the microplane concept concerns how stress and strain tensors are related to stress and strain vectors. A local approach for stresses is given by Eq. (5.5)

$$\mathbf{t} = \boldsymbol{\sigma}_M \cdot \mathbf{n} \tag{5.138}$$

called *static constraint* with the microplane normal $\mathbf{n}$. The same approach can be used for strains leading to a *strain vector*

$$\mathbf{e} = \boldsymbol{\epsilon}_M \cdot \mathbf{n} \tag{5.139}$$

called *kinematic constraint* with the strain tensor $\boldsymbol{\epsilon}_M$ according to Eq. (5.2). As local behavior is generally driven by prescribed strains derived from a global FEM calculation the kinematic constraint is chosen as a base.

Thus, we assume a given strain vector $\mathbf{e}$ on a particular microplane. The microplane has a local Cartesian coordinate system with a normal $\mathbf{n}$ and two orthogonal in-plane vectors $\mathbf{m}$, $\mathbf{l}$. The orientation of $\mathbf{m}$, $\mathbf{l}$ is arbitrary within the plane. The scalar projections of the strain vector are given by

$$
\begin{array}{ccccc}
\epsilon_N & = & \mathbf{n}^T \cdot \mathbf{e} & = & \mathbf{n}^T \cdot \boldsymbol{\epsilon}_M \cdot \mathbf{n} \\
\epsilon_M & = & \mathbf{m}^T \cdot \mathbf{e} & = & \mathbf{m}^T \cdot \boldsymbol{\epsilon}_M \cdot \mathbf{n} \\
\epsilon_L & = & \mathbf{l}^T \cdot \mathbf{e} & = & \mathbf{l}^T \cdot \boldsymbol{\epsilon}_M \cdot \mathbf{n}
\end{array} \tag{5.140}
$$

with the scalar normal strain ϵ_N and the scalar in-plane strains ϵ_M, ϵ_L. This may be written as

$$\epsilon_N = \mathbf{N}^T \cdot \boldsymbol{\epsilon}, \quad \epsilon_M = \mathbf{M}^T \cdot \boldsymbol{\epsilon}, \quad \epsilon_L = \mathbf{L}^T \cdot \boldsymbol{\epsilon} \tag{5.141}$$

called *normal-tangential* (N-T) split with vectors $\mathbf{N}$, $\mathbf{M}$, $\mathbf{L}$ containing rearranged components of $\mathbf{n}$, $\mathbf{m}$, $\mathbf{l}$ and a strain $\boldsymbol{\epsilon}$ arranged according to the Voigt notation (5.3).

These measures of strain have to be connected to scalar measures of stress σ_N, σ_M, σ_L through a material law. We anticipate that the values of σ_N, σ_M, σ_L have been determined. An statically equivalent Cauchy stress $\boldsymbol{\sigma}$, see Section 5.2.2, has to be found. Statical equivalence can be formulated with the principle of virtual work, see Eq. (1.5). This is reformulated regarding a unit sphere [5]

$$\frac{2\pi}{3}\, \delta\boldsymbol{\epsilon}^T \cdot \boldsymbol{\sigma} = \int_A \left(\delta\epsilon_N \sigma_N + \delta\epsilon_M \sigma_M + \delta\epsilon_L \sigma_L \right)\, \mathrm{d}A \tag{5.142}$$

with the unit sphere surface A and virtual strains $\delta\boldsymbol{\epsilon}$ and $\delta\epsilon_N$, $\delta\epsilon_M$, $\delta\epsilon_L$. This can be rewritten as

$$\frac{2\pi}{3}\, \delta\boldsymbol{\epsilon}^T \cdot \boldsymbol{\sigma} = \delta\boldsymbol{\epsilon}^T \cdot \int_A \left(\sigma_N\, \mathbf{N} + \sigma_M\, \mathbf{M} + \sigma_L\, \mathbf{L} \right)\, \mathrm{d}A \tag{5.143}$$

and is fulfilled by

$$\boldsymbol{\sigma} = \frac{3}{2\pi} \int_A \left(\sigma_N\, \mathbf{N} + \sigma_M\, \mathbf{M} + \sigma_L\, \mathbf{L} \right)\, \mathrm{d}A \tag{5.144}$$

for arbitrary virtual strains $\delta\boldsymbol{\epsilon}$. The evaluation of the integral is performed numerically whereby the unit sphere surface is approximated by plane facets. Each facet corresponds to a microplane with its own orientation $\mathbf{n}$, $\mathbf{m}$, $\mathbf{l}$ and for a given strain $\boldsymbol{\epsilon}$ each has to be evaluated with a split according to Eq. (5.140) and related to values for σ_N, σ_M, σ_L. The

number of facets and the type of numerical integration has a major influence on the final relations between $\boldsymbol{\epsilon}$ and $\boldsymbol{\sigma}$ for given material laws connecting $\sigma_N, \sigma_M, \sigma_L$ and $\epsilon_N, \epsilon_M, \epsilon_L$

A scalar volumetric strain is defined as

$$\epsilon_V = \frac{\epsilon_{11} + \epsilon_{22} + \epsilon_{33}}{3} \tag{5.145}$$

and a scalar deviatoric strain as

$$\epsilon_D = \epsilon_N - \epsilon_V = \boldsymbol{\epsilon}^T \cdot \mathbf{N}_D \tag{5.146}$$

called *volumetric-deviatoric* (V-D) split. The corresponding scalar measures of stress are σ_V, σ_D with

$$\sigma_V = \frac{\sigma_{11} + \sigma_{22} + \sigma_{33}}{3}, \qquad \sigma_D = \sigma_N - \sigma_V \tag{5.147}$$

The scalar volumetric stress σ_V corresponds to pressure p, see Eq. (5.8). The deviatoric part $\boldsymbol{\sigma}'$ of Cauchy stress remains to be evaluated to determine total Cauchy stress, see Eq. (5.9). Subtracting $\delta\epsilon_V \, \sigma_V$ from both sides of Eq. (5.142) and using $\sigma_N = \sigma_V + \sigma_D$, $\delta\epsilon_N = \delta\epsilon_V + \delta\epsilon_D$ and $\delta\epsilon_V \sigma_D = 0$ leaves after some rearrangements

$$\frac{2\pi}{3} \delta\boldsymbol{\epsilon}^T \cdot \boldsymbol{\sigma}' = \int_A \left(\delta\epsilon_D \sigma_D + \delta\epsilon_M \sigma_M + \delta\epsilon_L \sigma_L \right) \, \mathrm{d}A \tag{5.148}$$

and finally [5]

$$\boldsymbol{\sigma}' = \frac{3}{2\pi} \int_A \left(\sigma_D \, \mathbf{N}_D + \sigma_M \, \mathbf{M} + \sigma_L \, \mathbf{L} \right) \, \mathrm{d}A \tag{5.149}$$

A *volumetric-deviatoric-tangential* (V-D-T) split combines both forgoing splits and uses scalar strain measures $\epsilon_V, \epsilon_D, \epsilon_M, \epsilon_L$ and scalar stress measures $\sigma_V, \sigma_D, \sigma_M, \sigma_L$.

A key issue is the formulation of the respective material laws, i.e., the relations between scalar measures of strain and stress. We mention the V-D-T split in the following as the other splits may be treated in the same way. The most general form of a material law is given by

$$\begin{array}{rcl} \sigma_V(t) & = & \mathcal{V}_{\tau=0}^t \left[\epsilon_V(\tau), \epsilon_D(\tau), \epsilon_M(\tau), \epsilon_L(\tau) \right] \\ \sigma_D(t) & = & \mathcal{D}_{\tau=0}^t \left[\epsilon_V(\tau), \epsilon_D(\tau), \epsilon_M(\tau), \epsilon_L(\tau) \right] \\ \sigma_M(t) & = & \mathcal{M}_{\tau=0}^t \left[\epsilon_V(\tau), \epsilon_D(\tau), \epsilon_M(\tau), \epsilon_L(\tau) \right] \\ \sigma_L(t) & = & \mathcal{L}_{\tau=0}^t \left[\epsilon_V(\tau), \epsilon_D(\tau), \epsilon_M(\tau), \epsilon_L(\tau) \right] \end{array} \tag{5.150}$$

whereby $\mathcal{F}, \mathcal{G}, \mathcal{H}, \mathcal{L}$ are functionals of the history of the scalar strains in time t. The formats of linear elasticity, nonlinear elasticity or hypoelasticity, plasticity, damage and combinations thereof may be used to formulate specific laws. The popular microplane model M4 [5] uses hypoelastic relations

$$\dot{\sigma}_V = E_V \; \dot{\epsilon}_V, \quad \dot{\sigma}_D = E_D \; \dot{\epsilon}_D, \quad \dot{\sigma}_M = E_T \; \dot{\epsilon}_M, \quad \dot{\sigma}_L = E_T \; \dot{\epsilon}_L \tag{5.151}$$

whereby scalar tangential material stiffness values E_V, E_D, E_T each may depend on all scalar strains. This is combined with strength conditions for each scalar stress. Provisions have to be taken in order that stress values determined from hypoelasticity do not violate such strength conditions. A damage approach for the microplane model is given in [55], [60], an elastoplastic approach in [56].

The microplane model shows similarities to the smeared crack model. Both work with scalar measures of stress and strain. While the smeared crack model considers at most a very few planes to apply scalar relations the microplane model basically uses all orientations. Thus, it does not need tensorial relations as the smeared crack model does to have an embedding frame. The microplane model has as major advantageous feature that it models initial or load-induced anisotropy in a natural and relatively simple way.

5.9 Localization and Regularization

5.9.1 Mesh Dependency

A basic property of the stress–strain behavior of concrete in its limit state is given by *strain softening*: stress decreases while strain increases, see Fig. 2.1. The effects of strain softening on structural behavior have been demonstrated for a tension bar with Example 2.1. A zone of localization develops in a relatively small area of a structure leading to a snap-back behavior in the load–displacement relation.

This type of behavior shall again be discussed for a simplified configuration. We consider a bar model according to Fig. 5.18a. The bar consists of three sections. A linear elastic behavior $\sigma = E\,\epsilon$ is considered for the first and third section. The center section has a linear elastic behavior initially up to a maximum stress value or strength followed by a linear stress decrease, see Figs. 2.2b and 5.18b. This softening material behavior is described by

$$\sigma = \begin{cases} E\,\epsilon & \epsilon \le \epsilon_{ct} \\ f_{ct}\dfrac{\epsilon_{cu} - \epsilon}{\epsilon_{cu} - \epsilon_{ct}} & \epsilon_{ct} < \epsilon \le \epsilon_{cu} \\ 0 & \epsilon_{cu} < \epsilon \end{cases} \tag{5.152}$$

with $f_{ct} = E\,\epsilon_{ct}$. Softening is characteristic for *quasi-brittle failure*. The total internal energy of the softening part in a loading state $\epsilon \ge \epsilon_{cu}$ is given by $G = \frac{1}{2}A\,L_e\,f_{ct}\,\epsilon_{cu}$ with a bar cross-sectional area A. A part of this energy related to the cracked area

$$G_f = \frac{1}{2}\,L_e\,f_{ct}\,(\epsilon_{cu} - \epsilon_{ct}), \quad L_e = \alpha\,L \tag{5.153}$$
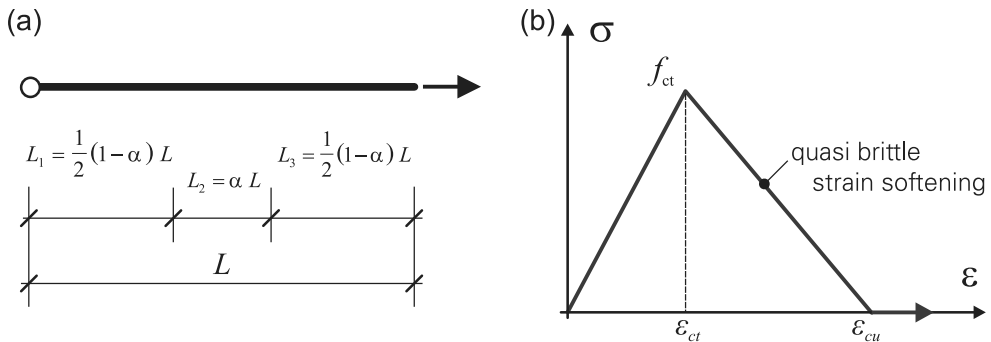
(a)

(b)

Figure 5.18: (a) Model for softening bar. (b) Material model for softening bar.

is dissipated as crack energy G_f, see Eqs. (2.6, 2.7), as a state $\epsilon \geq \epsilon_{cu}$ corresponds to a crack and the initial uncracked state cannot be recovered. The case $\epsilon_{ct} = \epsilon_{cu}$ with a sudden stress drop to zero corresponds to a perfectly *brittle failure*. The internal energy difference $(G - A\,G_f)$ is theoretically regained within the softening material.

The bar is loaded with a stress σ at the right end and fixed at the left end. All bar sections have the stress σ due to equilibrium. The displacement of the right end is given by

$$u = \epsilon_1 L_1 + \epsilon L_e + \epsilon_2 L_2 \tag{5.154}$$

with the strains ϵ_1, ϵ_2 for the lateral sections and the strain ϵ for the center section. This leads at first to a right-end displacement

$$u = \frac{\sigma}{E}\,L, \quad \epsilon \leq \epsilon_{ct} \tag{5.155}$$

Furthermore, we consider the softening of the center section and use Eq. (5.152) for $\epsilon_{ct} \leq \epsilon \leq \epsilon_{cu}$. Lateral strains are $\epsilon_1 = \epsilon_2 = \sigma/E$ in this strain range. With $L_e = \alpha L$ and $L_1 + L_2 = (1 - \alpha)\,L$ and regarding Eqs. (5.152, 5.154) the stress σ or loading, respectively, can be determined depending on the displacement. This yields

$$\frac{\sigma}{f_{ct}} = \frac{\alpha\,\epsilon_{cu} - \frac{u}{L}}{\alpha\,\epsilon_{cu} - \epsilon_{ct}} \tag{5.156}$$

We assume $\epsilon_{c1} = 0.01$, $\epsilon_{cu1} = 0.03$ for an example. Results for the related loading σ/f_{ct} depending on related displacement u/L are shown in Fig. 5.19 for different values of the softening length ratio α. The bar behavior after reaching the strength f_{ct} strongly depends on the softening length. A decreasing loading occurs with an increasing strain in the center softening section while strains decrease elastically in the remaining parts. A relatively small softening length leads to a *snack-back* behavior: decreasing elastic strains overcompensate increasing softening strains leading to a decreasing displacement.

We transfer this setup to a bar discretized with a number n_E of two-node bar elements along a line, see Section 1.3. All elements are chosen with the same length and a material law according to Eq. (5.152). But we assume one element with a slightly reduced strength f_{ct}
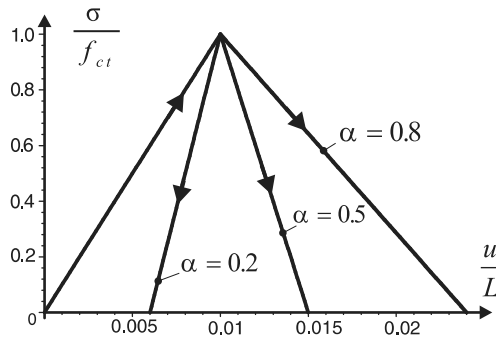

Figure 5.19: Load–displacement relations for a softening bar.

or slightly reduced cross section compared to all other $n_E - 1$ elements. Thus, the softening length ratio is given by $\alpha = 1/(n_E - 1)$ and the snap-back behavior will be more pronounced for a finer discretization. The same effect will occur with a homogeneous system, i.e., the same strength and cross section for all elements, but a nonhomogeneous stress state, e.g., due to a distributed loading along the bar.

Basically the same phenomenon can be seen for 2D states along curves which connect 2D elements and for 3D states along surfaces which connect 3D elements. The spatial thickness of the softening band will spread over one element – maybe two or three in cases when the softening band does not align to single element boundaries – and will reduce with finer discretizations.

- A discretization may have a considerable influence on the numerical results for structures with softening materials in the case of nonhomogeneous structural properties or nonhomogenous stress states. Results are mesh dependent. A convergence cannot be reached with finer discretizations in postpeak regimes.

In the same way the dissipated energy, see Eq. (5.153) for 1D elements, approaches to zero for an increasing number of elements or decreasing value α. This contradicts to experimental data of real systems with softening materials which show considerable energy dissipation while passing the softening process up to an ultimate failure.

5.9.2 Regularization

Strain softening is connected with some amount of dissipation of internal energy in zones of localization and in particular within crack bands of concrete structures. On the other hand, a mesh dependency of discretized systems with softening materials becomes evident – using standard material and element formulations as have been described up to now – with a dissipated energy converging to zero upon the refinement of the discretization. Thus, energy dissipation in localization zones or crack energy of concrete models can be used as an indicator for mesh dependency.

We consider the crack energy of mode-I cracking due to principal tension failure according to the Rankine criterion, see Section 5.7.2. A setup of mode-I cracking has already been discussed in Section 2.1, see Fig. 2.2b. The corresponding crack energy G_f has been defined in Eqs. (2.6, 2.7). Its value is assumed as a constant material parameter due to current state of knowledge.

- The crack energy should be reproduced for systems with softening materials independent from discretization. The corresponding provisions are regarded as *regularization*.

We consider again the simple three-section bar shown in Fig. 5.18 and the stress–strain relations (5.152). The center section is modified with the application range of the softening stress–strain relation

$$\sigma = f_{ct} \frac{\epsilon_{cu} - \epsilon}{\epsilon_{cu} - \epsilon_{ct}}, \qquad \epsilon_{ct} < \epsilon \le \frac{b_w}{L_e} \left(\epsilon_{cu} - \epsilon_{ct} \right) \qquad (5.157)$$

with the concrete tensile strength f_{ct}, the crack-band width b_w, see Section 2.1, and the section or element length L_e, respectively. After this modification of stress–strain relations

the crack energy, see Eq. (5.153), is given by

$$G_f = \frac{1}{2} \, b_w \, f_{ct} \, (\epsilon_{cu} - \epsilon_{ct}) \tag{5.158}$$

This yields the correct crack energy independent from the element length L_e. The range of strain has been scaled in the softening range according to the ratio of crack-band width to element length. This compensates the influence of element dimensions on the integration of stress–strain relations to determine the energy: small elements gain a large integration range of strains, large elements a low integration range. This approach may also be applied to multiaxial cases as will be demonstrated indirectly.

- A regularization can be reached with a scaling of strains in the softening range of stress–strain relations. This scaling depends on the ratio of the crack-band width to a characteristic element length and leads to the *crack-band method*.

But the stress–strain relations will become dependent on a characteristic element length.

There are strong relations between the crack-band method and the smeared crack method. This will again be demonstrated for the simple case. Equations (5.157, 5.158) lead to a tangential material stiffness

$$C_T = \frac{L_e}{b_w} \frac{f_{ct}}{\epsilon_{cu} - \epsilon_{ct}} = L_e \frac{f_{ct}^2}{2G_f} \tag{5.159}$$

and a compliance

$$D_T = \frac{1}{C_T} = \frac{1}{L_e} \frac{2G_f}{f_{ct}^2} \tag{5.160}$$

We compare this to the compliance D_{cT} of the normal components of the cohesive crack model according to Eq. (5.125). The linear approximation of the relation between t_1 and w_1 in the range $w \leq w_{cr}$, see Fig. 5.16, leads to a crack energy $G_f = \frac{1}{2} f_{ct} w_{cr}$. Thus

$$D_{cLT} = \frac{w_{cr}}{f_{ct}} = \frac{2G_f}{f_{ct}^2} \tag{5.161}$$

and regarding Eq. (5.160) the crack band compliance is given with

$$D_T = \frac{D_{cLT}}{L_e} \tag{5.162}$$

This corresponds to Eq. (5.132) or $D_T = D_{cT}$, respectively, with the compliance D_{cT} of the smeared crack model. In the same way as for the smeared crack model, the compliance D_T of strains and stresses in a crack band is related through the element length to the compliance D_{cLT} of crack widths and crack tractions. This may be generalized for multiaxial states.

- The crack-band method and the smeared crack model are basically equivalent. The smeared crack model leads to a regularization in the same way as the crack-band method.

The reproduction of crack energy has been defined as major criterion for regularization. The crack energy contributes to the ductile behavior of whole structures or structural elements. Ductile behavior concerns the relations between loads and displacements or over-all behavior. Insofar regularization first of all ensures the correct modeling of the over-all behavior of structures with softening materials.

The crack-band model reproduces crack energy and over-all behavior of structures but will not reproduce local behavior. The spatial thickness of the softening band will still spread over one element and will still reduce with finer discretizations, see Section 5.9.1. What changes is strain within softening elements which is scaled according to element size in order to retain the crack energy. The real behavior within crack bands is different and has already been discussed for the uniaxial or mode-I case, see Fig. 2.3 and Example 2.1.

Nonlocal methods can resolve the local crack-band behavior additionally to regularization. We consider again the simple three section bar shown in Fig. 5.18 with the stress–strain relations (5.152). The center section is modified regarding its variable strain argument ϵ

$$\sigma = f_{ct} \frac{\epsilon_{cu} - \bar{\epsilon}}{\epsilon_{cu} - \epsilon_{ct}}, \quad \epsilon_{ct} < \epsilon \le (\epsilon_{cu} - \epsilon_{ct}) \tag{5.163}$$

with the *integral form* of nonlocal strain $\bar{\epsilon}$

$$\bar{\epsilon}(x) = \frac{1}{S} \int_L g(s)\, \epsilon(x + s)\, \mathrm{d}s \tag{5.164}$$

with a fixed coordinate x, a variable coordinate s, a bar length L and a weighting function

$$g(s) = \mathrm{e}^{-\frac{s^2}{2R^2}}, \qquad S = \int_L g(s)\, \mathrm{d}s \tag{5.165}$$

The weighting function $g(s)$ corresponds to a bell-shaped curve with maximum 1 for $s = 0$. The parameter R determines the lateral decline of g. Small values cause a steep decline with a small range while large values cause a flat decline with a large range. The nonlocal approach according to Eq. (5.164) decreases the local extremal value of ϵ and broadens the base depending on the parameter R, see Fig. 5.20. Spatially constant strains would remain constant in contrast.

The length R is assumed as constant and independent from a discretization. Thus, the approach Eq. (5.164) spans over a number of neighbored elements depending on the ratio of R to single element length. This enforces a smoothing of strain peak values independent from a discretization, see Fig. 5.20, and leads to a crack-band width b_w which also does not depend on the discretization. Furthermore, the value of R and the resulting value of b_w are approximately proportional and have the same magnitude. This corresponds to the physical significance of the crack-band width, which primarily depends on the concrete aggregate size, see Section 2.1.

- Nonlocal methods introduce a characteristic length R as a material parameter. This characteristic length is a measure for the heterogeneity of the material as it is observed in the mesoscale, see Fig. 5.1, and compensates a "loss" of information due to homogenization.

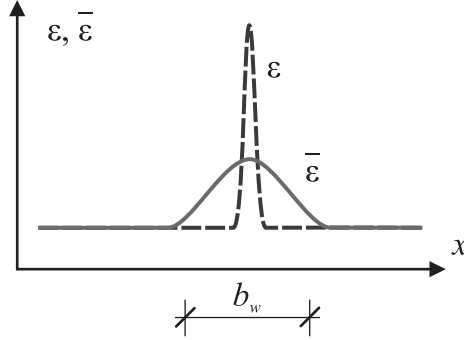For a comprehensive treatment of nonlocal methods see [47], [6], [77].

Figure 5.20: Nonlocal uniaxial strain.

An alternative for the integral nonlocal formulation equation (5.164) shall be derived in the following [75]. A second-order Taylor expansion of $\epsilon(x + s)$ leads to

$$\epsilon(x + s) \approx \epsilon(x) + \frac{\partial \epsilon}{\partial x}\, s + \frac{1}{2}\, \frac{\partial^2 \epsilon}{\partial x^2}\, s^2 \tag{5.166}$$

Insertion into Eq. (5.164) yields a differential nonlocal formulation

$$\begin{aligned}
\bar{\epsilon} &\approx \frac{1}{S}\int_{-\infty}^{\infty} g(s)\,\mathrm{d}s\ \epsilon + \frac{1}{2S}\int_{-\infty}^{\infty} g(s)\,s^2\,\mathrm{d}s\ \frac{\partial^2 \epsilon}{\partial x^2} \\
&= \epsilon + \frac{R^2}{2}\ \frac{\partial^2 \epsilon}{\partial x^2}
\end{aligned} \tag{5.167}$$

under the simplifying assumption of an infinite bar length L and regarding the antisymmetry of the linear s-term. This form is not yet appropriate for common finite element formulations due to the second derivative $\partial^2 \epsilon / \partial x^2$. Thus, the second derivative of Eq. (5.167) is formed

$$\frac{\partial^2 \bar{\epsilon}}{\partial x^2} = \frac{\partial^2 \epsilon}{\partial x^2} + \frac{R^2}{2}\ \frac{\partial^4 \epsilon}{\partial x^4} \tag{5.168}$$

multiplied by $R^2/2$ and subtracted from Eq. (5.167). This yields

$$\bar{\epsilon} - \frac{R^2}{2}\ \frac{\partial^2 \bar{\epsilon}}{\partial x^2} = \epsilon - \frac{R^4}{4}\ \frac{\partial^4 \epsilon}{\partial x^4} \tag{5.169}$$

Neglecting the last term on the basis of the assumption $R < 1$, $R^4 \ll R^2$ leads to the final *differential form* of nonlocal strain

$$\bar{\epsilon}(x) - \frac{R^2}{2}\ \frac{\partial^2 \bar{\epsilon}(x)}{\partial x^2} = \epsilon(x) \tag{5.170}$$

This differential equation is driven by a given strain strain function $\epsilon(x)$ determined in a superordinated calculation. Its solution $\bar{\epsilon}(x)$ is used as strain to determine the stress according to, e.g., Eq. (5.163).

Integral or differential nonlocal forms like Eq. (5.164) or Eq. (5.170) may be generalized for multiaxial cases and may also be applied to internal state variables connected to strain states, e.g., the equivalent damage strain of the damage material model, see Section 5.6. Both forms retain their capabilities regarding regularization and the resolution of crack bands with such applications. But the objective requires a discretization of crack bands itself with a sufficient number of elements. Thus, common crack-band widths in the dimension of 10^{-2} m lead to fine discretizations and large discretized systems.

5.9.3 Gradient Damage

The uniaxial differential form Eq. (5.170) of nonlocal strain in the following is generalized to multiaxial damage using an equivalent strain measure. The approach is known as *gradient damage*. The damage material model described in Section 5.6 is used as frame of application. The generalized gradient damage form is given by

$$\bar{\kappa}(\mathbf{x}) - c\,\Delta\bar{\kappa}(\mathbf{x}) = \kappa(\mathbf{x}), \qquad c = \frac{R^2}{2} \tag{5.171}$$

with the spatial coordinate $\mathbf{x}$, the nonlocal equivalent damage strain $\bar{\kappa}(\mathbf{x})$, the Laplace differential operator Δ, the local equivalent damage strain $\kappa(\mathbf{x})$ and a characteristic material length R. We replace κ_d from Section 5.6 with κ to simplify the notation.

The gradient damage approach shall be incorporated in the finite element method. To begin with, Eq. (5.171) has to be transformed into a *weak integral formulation*. Such a procedure has already been demonstrated for beams in Section 3.2 whereby outlining a standard way. In the case of Eq. (5.171) the standard way starts with

$$\int_V \delta\bar{\kappa} \left[\kappa - \bar{\kappa} + c\,\Delta\bar{\kappa}\right] \mathrm{d}V = \int_V \delta\bar{\kappa}\,\kappa\,\mathrm{d}V - \int_V \delta\bar{\kappa}\,\bar{\kappa}\,\mathrm{d}V + \int_V c\,\delta\bar{\kappa}\,\Delta\bar{\kappa}\,\mathrm{d}V = 0 \tag{5.172}$$

with the volume V of the body under consideration and a test function $\delta\bar{\kappa}$. The product rule of differentiation leads to

$$\delta\bar{\kappa}\,\Delta\bar{\kappa} = \operatorname{div}\left(\delta\bar{\kappa}\,\nabla\bar{\kappa}\right) - \nabla\delta\bar{\kappa}\cdot\nabla\bar{\kappa} \tag{5.173}$$

with the scalar product $\cdot$, the divergence operator div, and the nabla operator ∇. Application of the Gauss divergence theorem [54] leads to

$$\int_V \operatorname{div}\left(\delta\bar{\kappa}\,\nabla\bar{\kappa}\right)\,\mathrm{d}V = \int_A \delta\bar{\kappa}\,\mathbf{n}\cdot\nabla\bar{\kappa}\,\mathrm{d}A \tag{5.174}$$

with the surface A of the body and the outer surface normals $\mathbf{n}$. Thus, Eq. (5.172) can be written in a form

$$\int_V \delta\bar{\kappa}\,\bar{\kappa}\,\mathrm{d}V + \int_V c\,\nabla\delta\bar{\kappa}\cdot\nabla\bar{\kappa}\,\mathrm{d}V = \int_V \delta\bar{\kappa}\,\kappa\,\mathrm{d}V + \int_A c\,\delta\bar{\kappa}\,\mathbf{n}\cdot\nabla\bar{\kappa}\,\mathrm{d}A \tag{5.175}$$

This form is suited for a discretization with respect to the nonlocal equivalent damage strain $\bar{\kappa}$ while the local value κ is given as driving part.

The surface integral part remains to be discussed. Additional boundary conditions for the nonlocal equivalent damage strain are required, i.e., either $\bar{\kappa}$ or the normal derivative $\mathbf{n} \cdot \nabla \bar{\kappa}$ have to be specified in every point of the surface A. We assume that $\bar{\kappa}$ can be prescribed along a part A_κ of the whole surface A and that $\delta \bar{\kappa} = 0$ can be set along A_κ. Furthermore, we consider cases with strains localizing in narrow bands with approximately perpendicular orientations to the boundary. As any major damage gradients $\nabla \bar{\kappa}$ arise perpendicularly to the band of localization, i.e., in boundary direction, the condition $\mathbf{n} \cdot \nabla \bar{\kappa} = 0$ can be set along the that part of A where $\bar{\kappa}$ is not prescribed [75]. Thus, Eq. (5.175) is simplified as

$$\int_V \delta \bar{\kappa}\, \bar{\kappa}\, \mathrm{d}V + \int_V c\, \nabla \delta \bar{\kappa} \cdot \nabla \bar{\kappa}\, \mathrm{d}V = \int_V \delta \bar{\kappa}\, \kappa\, \mathrm{d}V \tag{5.176}$$

This weak integral formulation of Eq. (5.171) will be used in the following and has to be combined with the material law.

First of all, the local κ in Eq. (5.108) is replaced by the nonlocal $\bar{\kappa}$

$$D(\bar{\kappa}) = 1 - \mathrm{e}^{-\left(\frac{\bar{\kappa} - e_0}{e_d}\right)^{g_d}}, \quad \bar{\kappa} \geq e_0 \tag{5.177}$$

and we obtain the increment of damage $\mathrm{d}D$ depending on the increment $\mathrm{d}\bar{\kappa}$ of the nonlocal equivalent damage

$$\mathrm{d}D = \frac{\mathrm{d}D}{\mathrm{d}\bar{\kappa}}\, \mathrm{d}\bar{\kappa} = \frac{1}{h}\, \mathrm{d}\bar{\kappa}, \qquad \frac{1}{h} = \frac{g_d \left(\frac{\bar{\kappa} - e_0}{e_d}\right)^{g_d}}{\bar{\kappa} - e_0}\, \mathrm{e}^{-\left(\frac{\bar{\kappa} - e_0}{e_d}\right)^{g_d}} \tag{5.178}$$

Using Eq. (5.117) the stress increment is given by

$$\begin{aligned} \mathrm{d}\boldsymbol{\sigma} &= (1 - D)\, \mathbf{E} \cdot \mathrm{d}\boldsymbol{\epsilon} - \mathbf{E} \cdot \boldsymbol{\epsilon}\, \mathrm{d}D \\ &= (1 - D)\, \mathbf{E} \cdot \mathrm{d}\boldsymbol{\epsilon} - \frac{1}{h}\, \boldsymbol{\sigma}_0\, \mathrm{d}\bar{\kappa}, \quad \boldsymbol{\sigma}_0 = \mathbf{E} \cdot \boldsymbol{\epsilon} \end{aligned} \tag{5.179}$$

This completes the material and gradient damage parts. The *equilibrium of forces* has the condition

$$\int_V \delta \boldsymbol{\epsilon}^T \cdot \boldsymbol{\sigma}\, \mathrm{d}V = \int_V \delta \mathbf{u}^T \cdot \bar{\mathbf{p}}\, \mathrm{d}V + \int_{A_t} \delta \mathbf{u}^T \cdot \bar{\mathbf{t}}\, \mathrm{d}A \tag{5.180}$$

according to Eq. (1.52). The weak forms (Eqs. (5.176, 5.180)) are discretized by

$$\mathbf{u} = \mathbf{N}_u \cdot \boldsymbol{v}, \quad \bar{\kappa} = \mathbf{N}_\kappa \cdot \bar{\boldsymbol{\kappa}} \tag{5.181}$$

with the matrices $\mathbf{N}_u$, $\mathbf{N}_\kappa$ of form functions and the vectors $\boldsymbol{v}$, $\bar{\boldsymbol{\kappa}}$ of nodal values of displacement and nonlocal equivalent damage strain as global unknowns. The global unknowns and their increments are given by

$$\begin{aligned} \boldsymbol{\epsilon} &= \mathbf{B}_u \cdot \boldsymbol{v}, \quad \mathrm{d}\boldsymbol{\epsilon} = \mathbf{B}_u \cdot \mathrm{d}\boldsymbol{v} \\ \nabla \bar{\kappa} &= \mathbf{B}_\kappa \cdot \bar{\boldsymbol{\kappa}}, \quad \mathrm{d}\nabla \bar{\kappa} = \mathbf{B}_\kappa \cdot \mathrm{d}\bar{\boldsymbol{\kappa}} \end{aligned} \tag{5.182}$$

The test functions $\delta \mathbf{u}$, $\delta \bar{\kappa}$ are discretized in the same way. Using Eqs. (5.181, 5.182) together with the weak forms (Eqs. (5.176, 5.180)) leads to

$$\mathbf{r} = \mathbf{p} - \mathbf{f}(\mathbf{a}) = 0 \tag{5.183}$$

with

$$\mathbf{p} = \left(\begin{array}{c} \mathbf{p}_u \\ 0 \end{array} \right), \quad \mathbf{f} = \left(\begin{array}{c} \mathbf{f}_u \\ \mathbf{f}_\kappa \end{array} \right), \quad \mathbf{a} = \left(\begin{array}{c} \boldsymbol{\upsilon} \\ \bar{\boldsymbol{\kappa}} \end{array} \right) \tag{5.184}$$

and *external nodal forces*

$$\mathbf{p}_u = \int_V \mathbf{N}_u^T \cdot \bar{\mathbf{p}} \, \mathrm{d}V + \int_{A_t} \mathbf{N}_u^T \cdot \bar{\mathbf{t}} \, \mathrm{d}A \tag{5.185}$$

and *extended internal nodal forces*

$$\mathbf{f}_u = \int_V \mathbf{B}_u^T \cdot \boldsymbol{\sigma} \, \mathrm{d}V, \quad \mathbf{f}_\kappa = \int_V \left[\mathbf{N}_\kappa^T \left(\bar{\kappa} - \kappa \right) + c \, \mathbf{B}_\kappa^T \cdot \nabla \bar{\kappa} \right] \mathrm{d}V \tag{5.186}$$

with $\mathbf{f}_u$ depending on $\boldsymbol{\sigma} \leftarrow \boldsymbol{\epsilon} \leftarrow \boldsymbol{\upsilon}$ and $\boldsymbol{\sigma} \leftarrow D \leftarrow \bar{\boldsymbol{\kappa}}$ and $\mathbf{f}_\kappa$ depending on $\bar{\boldsymbol{\kappa}}$ and on the local $\kappa \leftarrow \boldsymbol{\epsilon} \leftarrow \boldsymbol{\upsilon}$. Thus, $\mathbf{f}_u$ and $\mathbf{f}_\kappa$ are coupled and Eq. (5.183) forms a system of nonlinear algebraic equations.

The solution of the nonlinear algebraic system requires a tangential stiffness matrix

$$\mathbf{K}_T = \frac{\partial \mathbf{f}}{\partial \mathbf{a}} = \left[\begin{array}{cc} \frac{\partial \mathbf{f}_u}{\partial \boldsymbol{\upsilon}} & \frac{\partial \mathbf{f}_u}{\partial \bar{\boldsymbol{\kappa}}} \\ \frac{\partial \mathbf{f}_\kappa}{\partial \boldsymbol{\upsilon}} & \frac{\partial \mathbf{f}_\kappa}{\partial \bar{\boldsymbol{\kappa}}} \end{array} \right] = \left[\begin{array}{cc} \mathbf{K}_{uu} & \mathbf{K}_{u\kappa} \\ \mathbf{K}_{\kappa u} & \mathbf{K}_{\kappa\kappa} \end{array} \right] \tag{5.187}$$

Equations $(5.186)_1$ and (5.179) yield

$$\mathbf{K}_{uu} = \int_V (1 - D) \, \mathbf{B}_u^T \cdot \mathbf{E} \cdot \mathbf{B}_u \, \mathrm{d}V, \qquad \mathbf{K}_{u\kappa} = - \int_V \frac{1}{h} \mathbf{B}_u^T \cdot \boldsymbol{\sigma}_0 \cdot \mathbf{N}_\kappa \, \mathrm{d}V \tag{5.188}$$

and Eqs. (5.114) and $(5.186)_2$ for the loading case lead to

$$\mathbf{K}_{\kappa u} = - \int_V \frac{1}{H} \mathbf{N}_\kappa^T \cdot \mathbf{n}^T \cdot \mathbf{B}_u \, \mathrm{d}V, \qquad \mathbf{K}_{\kappa\kappa} = \int_V \left(\mathbf{N}_\kappa^T \cdot \mathbf{N}_\kappa + c \, \mathbf{B}_\kappa^T \cdot \mathbf{B}_\kappa \right) \mathrm{d}V \tag{5.189}$$

with $\mathrm{d}\kappa = \frac{1}{H} \mathbf{n}$ and $H = \frac{\partial F}{\partial \kappa}$, $\mathbf{n} = \frac{\partial F}{\partial \boldsymbol{\epsilon}}$ and the damage function F, see Section 5.6. In the case of unloading is $\mathbf{K}_{u\kappa} = 0$. The tangential system stiffness matrix $\mathbf{K}_T$ is unsymmetrical, but this occurs generally for damage formulations not derived from potentials with the principle of maximum dissipation.

The iteration rule is

$$\begin{array}{rcl} \delta \mathbf{a} & = & \left[\mathbf{K}_T^{(\nu)} \right]^{-1} \cdot \mathbf{r}(\mathbf{a}^{(\nu)}) \\ \mathbf{a}^{(\nu+1)} & = & \mathbf{a}^{(\nu)} + \delta \mathbf{a} \end{array} \tag{5.190}$$

according the the Newton–Raphson method, see Eq. (1.72). This is generally embedded in an incremental load application, see Section 1.6.

Example 5.4 Gradient damage formulation for the uniaxial two-node bar
The gradient damage formulation is illustrated with the simple uniaxial tensile case in connection with the uniaxial two-node bar element, see Section 1.3. The same interpolation is chosen for displacements and nonlocal damage strain $\mathbf{N}_u = \mathbf{N}_\kappa = \mathbf{N}$ with $\mathbf{N}$ from Eq. (1.22). As elements are assembled according to Section 1.5, it is sufficient to consider a single element.

The following relations are given for the element level, see Eqs. (1.43, 5.111, 5.179)

$$
\begin{aligned}
\mathbf{E} &= & \left[\, E \,\right] \\
\boldsymbol{\sigma}_0 &= & \left(\, E\,\epsilon \,\right) \\
F &= & c_1 \frac{(1+\nu)^2}{3}\,\epsilon^2 + \kappa\left(c_2 \frac{1+\nu}{\sqrt{3}} + c_3 + c_4\left(1-2\nu\right)\right)\epsilon - \kappa^2 \\
\mathbf{n} = \frac{\partial F}{\partial \epsilon} &= & 2c_1 \frac{(1+\nu)^2}{3}\,\epsilon + \kappa\left(c_2 \frac{1+\nu}{\sqrt{3}} + c_3 + c_4\left(1-2\nu\right)\right)
\end{aligned}
\tag{5.191}
$$

The uniaxial two-node element has as nodal degrees of freedom

$$
\mathbf{a}_e = \left(\, u_I \quad \bar{\kappa}_I \quad u_J \quad \bar{\kappa}_J \,\right)^T
\tag{5.192}
$$

A first lattice for the internal nodal forces and tangential element stiffness matrix is prepared as

$$
\boldsymbol{\mathcal{B}} = \left[\begin{array}{cccc} B_I & 0 & B_J & 0 \\ 0 & B_I & 0 & B_J \end{array}\right], \quad B_I = \tfrac{2}{L_e}\left(-\tfrac{1}{2}\right),\ B_J = \tfrac{2}{L_e}\left(\tfrac{1}{2}\right), \quad \boldsymbol{\mathcal{C}} = \left[\begin{array}{cc} (1-D)\,E & 0 \\ 0 & c \end{array}\right]
\tag{5.193}
$$

leading to a base $\boldsymbol{\mathcal{B}}^T \cdot \boldsymbol{\mathcal{C}} \cdot \boldsymbol{\mathcal{B}}$ of the stiffness matrix covering the parts $\mathbf{K}_{uu}$ and the second part of $\mathbf{K}_{\kappa\kappa}$, see Eqs. (5.188, 5.189). The matrix $\boldsymbol{\mathcal{C}}$ is variable due to a variable damage D. Nonlocal damage strains and nodal displacements are still uncoupled with this approach. Coupling is performed using

$$
\boldsymbol{\mathcal{N}} = \left[\begin{array}{cccc} B_I & 0 & B_J & 0 \\ 0 & N_I & 0 & N_J \end{array}\right], \quad N_I = \tfrac{1}{2}(1-r),\ N_J = \tfrac{1}{2}(1+r), \quad \boldsymbol{\mathcal{C}}' = \left[\begin{array}{cc} 0 & -\frac{E\,\epsilon}{h} \\ -\frac{1}{H}\frac{\partial F}{\partial \epsilon} & 1 \end{array}\right]
\tag{5.194}
$$

with B_I, B_J as in Eq. (5.193). The numerical integration is performed with one point integration leading to an tangential element stiffness matrix

$$
\mathbf{K}_{Te} = \frac{L_e}{2}\left[\boldsymbol{\mathcal{B}}^T \cdot \boldsymbol{\mathcal{C}} \cdot \boldsymbol{\mathcal{B}} + \boldsymbol{\mathcal{N}}^T \cdot \boldsymbol{\mathcal{C}}' \cdot \boldsymbol{\mathcal{N}}\right]
\tag{5.195}
$$

To derive the extended internal nodal forces a generalized strain is defined with

$$
\boldsymbol{\mathcal{E}} = \left(\begin{array}{c} \epsilon \\ \nabla\bar{\kappa} \end{array}\right) = \boldsymbol{\mathcal{B}} \cdot \mathbf{a}_e
\tag{5.196}
$$

leading to a general stress

$$
\boldsymbol{\mathcal{S}} = \boldsymbol{\mathcal{C}} \cdot \boldsymbol{\mathcal{E}}
\tag{5.197}
$$

and to a base $\boldsymbol{\mathcal{B}}^T \cdot \boldsymbol{\mathcal{S}}$ of the extended internal nodal forces, see Eq. (5.186). The coupling part $\mathbf{N}^T\left(\bar{\kappa} - \kappa\right)$ is still missing. Another general stress like parameter is introduced as

$$
\boldsymbol{\mathcal{S}}' = \left(\begin{array}{c} 0 \\ \bar{\kappa} - \kappa \end{array}\right)
\tag{5.198}
$$

finally leading to

$$
\mathbf{f}_e = \frac{L_e}{2}\left(\boldsymbol{\mathcal{B}}^T \cdot \boldsymbol{\mathcal{S}} + \boldsymbol{\mathcal{N}}^T \cdot \boldsymbol{\mathcal{S}}'\right)
\tag{5.199}
$$

A scaling of the components of the components $\mathbf{K}_{\kappa u}, \mathbf{K}_{\kappa\kappa}$ of $\mathbf{K}_T$, see Eq. (5.187), or of the second rows in $\boldsymbol{\mathcal{C}}, \boldsymbol{\mathcal{C}}'$ may be necessary to avoid large differences of values in $\mathbf{K}_T$ and a bad numerical condition. Young's modulus E is appropriate as scaling factor.

End Example 5.4

The way demonstrated in Example 5.4 may be applied to other element types in an analogous way. The assemblage of element contributions to the global system is performed in the same way as for all other element types. The particular implementation example is practiced with Example 2.1. More aspects concerning gradient damage are given in, e.g., [55], [74], [30], [76].

5.10 General Requirements for Material Laws

General requirements for material laws fall under the two categories *objectivity* and *thermodynamic restrictions*. Regarding solids the basics of thermodynamics are given in the following postulates whereby neglecting temperature aspects:

1. The change of internal energy $\dot{U}$ of a solid body should be equal to the power $\dot{P}$ applied by external forces plus the change in kinetic energy $\dot{K}$

$$\dot{U} = \dot{P} + \dot{K} \tag{5.200}$$

   This is stated for a whole body and may be transformed into a local formulation using the Gauss divergence theorem [54, 10.7], [64, 5.4]

$$\dot{u} = \boldsymbol{\sigma}^T \cdot \dot{\boldsymbol{\epsilon}} \tag{5.201}$$

   with the specific internal energy rate $\dot{u}$, the Cauchy stress $\boldsymbol{\sigma}$ and the strain rate $\dot{\boldsymbol{\epsilon}}$. The first postulate provides a definition for the specific internal energy.

2. A diversity of formulations exists for the second postulate. Regarding solid materials the specific internal energy is split into a *recoverable energy* $\psi(\boldsymbol{\epsilon})$ depending on the strain $\boldsymbol{\epsilon}$ only and into a dissipated energy d with

$$\dot{u} = \dot{\psi} + \dot{d} \tag{5.202}$$

   The *Clausius–Duhem* formulation postulates

$$\dot{d} = \dot{u} - \dot{\psi} \geq 0 \tag{5.203}$$

   i.e., energy dissipated in materials should not be negative. In contrast to the first postulate the second postulate might impose restrictions for the formulation of stress–strain relations.

A stress–strain relation not fulfilling the Clausius–Duhem inequality is not regarded as suitable to describe local material behavior. The fulfillment can generally be proven for simple nonlinear stress–strain relations. This is shown for isotropic damage, see Section 5.6. The key is the formulation of the specific recoverable energy ψ. In the case of isotropic damage with a stress–strain relation according to Eq. (5.106) it is given by

$$\psi = \frac{1}{2} \left(1 - D\right) \boldsymbol{\epsilon}^T \cdot \mathbf{E} \cdot \boldsymbol{\epsilon} \tag{5.204}$$

with the scalar damage parameter D and the linear elastic material stiffness according to Eq. (5.24). In the case of vanishing damage $D = 0$ this yields the strain energy of isotropic linear elastic materials. The rate is given by

$$
\begin{aligned}
\dot{\psi} &= -\frac{\dot{D}}{2}\,\boldsymbol{\epsilon}^T \cdot \mathbf{E} \cdot \boldsymbol{\epsilon} + (1 - D)\,\boldsymbol{\epsilon}^T \cdot \mathbf{E} \cdot \dot{\boldsymbol{\epsilon}} \\
&= -\frac{\dot{D}}{2}\,\boldsymbol{\epsilon}^T \cdot \mathbf{E} \cdot \boldsymbol{\epsilon} + \boldsymbol{\sigma}^T \cdot \dot{\boldsymbol{\epsilon}}
\end{aligned}
\tag{5.205}
$$

Equations (5.201, 5.202) lead to a dissipation rate

$$
\dot{d} = \frac{\dot{D}}{2}\,\boldsymbol{\epsilon}^T \cdot \mathbf{E} \cdot \boldsymbol{\epsilon}
\tag{5.206}
$$

Thus, $\dot{d} \geq 0$ as $\dot{D} \geq 0$ by definition, see Eq. (5.113), and $\boldsymbol{\epsilon}^T \cdot \mathbf{E} \cdot \boldsymbol{\epsilon} \geq 0$ as the matrix $\mathbf{E}$ is positive definite.

A further restriction may be formulated with the *Drucker stability postulate* [13, 3.1], [64, 6.6 Part 2]. It states that

$$
\dot{\boldsymbol{\sigma}}^T \cdot \dot{\boldsymbol{\epsilon}} \geq 0
\tag{5.207}
$$

This can obviously not be fulfilled for softening materials of, e.g., a damage type, see Fig. 5.13a. Regarding the Example 5.3 with uniaxial compressive concrete behavior it is $\dot{\sigma} > 0$ and $\dot{\epsilon} < 0$ and Drucker's postulate is violated. This corresponds to the fact that softening materials need a regularization to reach discretization objectivity when used in numerical methods, see Section 5.9. A regularization is not required for materials fulfilling the Drucker stability postulate.

Objectivity or material frame indifference of stress–strain relations must be given with respect to rotating and translating coordinate systems [64, 6.7]. We consider a solid body with boundary conditions preventing rigid body motions and with some loading applied in a quasistatic state. This leads to strains $\boldsymbol{\epsilon}$ and stresses $\boldsymbol{\sigma}$. The stress–strain relations are denoted with $\boldsymbol{\sigma} = \mathbf{f}(\boldsymbol{\epsilon})$.

An arbitrary rotation is applied to this setup. Depending on the reference configuration – Lagrangian or Eulerian [64, 4.5] – such rotations may be considered as equivalent with particular types of coordinate transformations and require a transformation of the position of the body, of the applied forces and of strains and stresses.

Transformation rules for, e.g., plane states are given in Appendix C. The transformation of strains is denoted with $\boldsymbol{\epsilon} \to \tilde{\boldsymbol{\epsilon}}$ and the transformation of stresses with $\boldsymbol{\sigma} \to \tilde{\boldsymbol{\sigma}}$. Objectivity requires that $\mathbf{f}(\tilde{\boldsymbol{\epsilon}})$ yields $\tilde{\boldsymbol{\sigma}}$ with unchanged function $\mathbf{f}$. This issue is relevant for Eulerian reference configurations with incremental material laws according to Eq. (5.13) and large displacements leading to the formulation of corotational or objective stress rates [9, 3.7]. This issue is of minor relevance within the context of reinforced concrete structures.

Chapter 6

Plates

6.1 Lower Bound Limit Analysis

6.1.1 The General Approach

Plates are plane surface structures in contrast to bars and beams which are line structures. They are characterized by in-plane loading. *Length* and *height* are significant as geometrical properties. Regarding a plate position the state of stress and strain is assumed as constant throughout the *thickness*. A corresponding kinematic assumption has been given in Section 1.3.

Plates have already been treated in Section 4.1 in the context of strut-and-tie models. Strut-and-tie models regard uniaxial stress–strain relations. This is a simple but crude model to describe the material behavior of concrete. Actually biaxial states are the characteristic for plates, see e.g., Fig. 4.1. Thus, design and simulation methods for plates of reinforced concrete regarding biaxial states are described in the following. The limited tensile strength of concrete still plays a dominant role.

We start with a design method considering local equilibrium on one hand and the limited strength of concrete and reinforcement on the other hand. This leads to a *lower bound limit analysis* performed on plates. An analysis of a similar type has already been described in Section 4.4 for rigid plastic systems. Plane stress conditions, see Eq. (1.45), are assumed in the following, but the approach in the same way may be applied to plane strain conditions (1.44).

A plate is given with geometry, boundary conditions, properties, and loading. Loading is prescribed as *unit loading* – load or largest load in a combination has a value 1 – multiplied by a loading factor. It is sufficient to describe the material properties by the concrete's initial Young's modulus E_c and its Poisson's ratio ν and, most important, by the strength of concrete and reinforcement. Local equilibrium, which is the first condition of a limit analysis, can be determined with a linear elastic analysis with the unit loading applied.

- Stresses resulting from a linear analysis due to a unit loading can be linearly scaled with the loading factor.

As a further condition, the loading factor is determined such that the stresses do not exceed the strength of the materials at any point of the plate. In other words:

- The loading factor is scaled such that stresses reach the strength of the materials exactly in at least one point of the plate. This includes strength of concrete as well as strength of reinforcement.

The two conditions – equilibrium and strength – correspond to Eq. (4.27) of the rigid plastic analysis for truss systems. Their limit theorems of plasticity, see Section 4.4, also apply to the limit analysis of a plate.

- The loading factor of a limit analysis corresponds to a lower bound of the admissible load of the plate with respect to setup of the unit loading.

The analysis conforms to a *proof of the admissible load for a given system*. The crucial point is to combine strength of concrete and reinforcement in an appropriate way while regarding the restricted tensile strength of concrete.

A variant is given by the *design procedure for a given load*, i.e., compressive strength of concrete or the amount of the reinforcement are adjusted such that the strength condition is not violated. The shape and dimension of the concrete body are assumed as prescribed in this context.

The described procedures base upon a linear elastic analysis. Analytical solutions for plates are available for simple cases, see e.g., [31]. Finite element solutions are appropriate for more complex situations, an example has been demonstrated in Section 4.1. A suitable element type is given by the quad element, see Section 1.3. Young's modulus and Poisson's ratio, see Eq. (1.45), can be chosen according to the initial values of concrete.

The calculation with finite elements yields a strain state $\epsilon_x, \epsilon_y, \gamma_{xy}$ for every integration point of every finite element. These integration point strain values may be extrapolated to every desired point using Eq. (1.40). But these strains are generally discontinuous along element boundaries compared to the strains of neighbor elements as only the continuity of displacements is required. As a consequence, stresses derived from strains will also be discontinuous. This might lead to ambiguities for, e.g., a design based on a limit analysis. Continuous stress fields can be derived with so-called mixed formulations. An example is given in the following.

Example 6.1 Continuous interpolation of stress fields with the quad element
Stress fields in a whole body are generally discontinuous along element boundaries. A method to derive a continuous field from a discontinuous field is derived in the following [98, 12.6].

We consider a given stress field $\boldsymbol{\sigma}$ determined from a computation with quad elements, see Section 1.3, which generally leads to stress jumps along the element edges. Another stress field $\bar{\boldsymbol{\sigma}}$ is constructed according to the interpolation of a displacement field, see Eq. (1.18), leading to

$$\bar{\boldsymbol{\sigma}} = \mathbf{N}(\mathbf{r}) \cdot \bar{\boldsymbol{\sigma}}_e \tag{6.1}$$

whereby the vector $\bar{\boldsymbol{\sigma}}_e$ collects the stresses of all nodes belonging to an element e.

- Stress fields interpolated in the same way as displacement fields are continuous throughout a whole body for an interpolation with quad elements.

The continuous interpolation arises from the compatibility requirement, see Section 1.7. The question remains how to determine the nodal stress values $\bar{\boldsymbol{\sigma}}_e$. An obvious approach is to minimize the difference between $\boldsymbol{\sigma}$ and $\bar{\boldsymbol{\sigma}}$ in an integral sense. This leads to

$$\int_V \delta\bar{\boldsymbol{\sigma}}^T \ (\bar{\boldsymbol{\sigma}} - \boldsymbol{\sigma}) \ \mathrm{d}V = 0 \tag{6.2}$$

with the test functions $\delta\bar{\boldsymbol{\sigma}} = \mathbf{N} \cdot \delta\bar{\boldsymbol{\sigma}}_e$, compare Eqs. (1.57). As with finite element computations, see Section 1.5, the integration is performed element by element and using Eq. (6.1) results in

$$\int_{V_e} \mathbf{N}^T \cdot \mathbf{N} \, \mathrm{d}V \cdot \bar{\boldsymbol{\sigma}}_e = \int_{V_e} \mathbf{N}^T \cdot \boldsymbol{\sigma} \, \mathrm{d}V \tag{6.3}$$

as $\delta\bar{\boldsymbol{\sigma}}_e$ is arbitrary. The left-hand integral corresponds to a unit mass matrix, see Eq. $(1.58)_2$. The left-hand and right-hand integrals may be evaluated with a numerical integration procedure, see Section 1.6. Furthermore, element contributions are assembled into a whole system as is done with finite elements computations. This yields a system of linear algebraic equations for the unknown nodal values $\bar{\boldsymbol{\sigma}}_e$. The solution costs for this system may be minimized with a lumped unit mass matrix [98, (12.69)].

Finally the continuous stress field may be computed using Eq. (6.1). Actually the continuous field is more accurate than the original stress field with respect to an exact solution.

— End Example 6.1

6.1.2 Reinforced Concrete Contributions

The key item of the general setup outlined in the previous section is to find an appropriate combination of concrete and reinforcement strength as reference values for the calculated stress state. The following procedure orients at the *modified compression field theory* [92]. The determination of principal stresses, see also Section 5.2.3, is needed as prerequisite. A given plane stress state $\sigma_x, \sigma_y, \sigma_{xy}$ has principal stresses σ_1, σ_2

$$\sigma_1 = \frac{\sigma_x + \sigma_y}{2} + \sqrt{\left(\frac{\sigma_x - \sigma_y}{2}\right)^2 + \sigma_{xy}^2}, \quad \sigma_2 = \frac{\sigma_x + \sigma_y}{2} - \sqrt{\left(\frac{\sigma_x - \sigma_y}{2}\right)^2 + \sigma_{xy}^2} \tag{6.4}$$

with an angle of orientation φ

$$\cos 2\varphi = \frac{\dfrac{\sigma_x - \sigma_y}{2}}{\sqrt{\left(\dfrac{\sigma_x - \sigma_y}{2}\right)^2 + \sigma_{xy}^2}} \tag{6.5}$$

which is positive from the x-axis in the counterclockwise direction. Equation (6.5) has one solution for φ in the range $0 \ldots \pi/2$. The value of φ multiplied by the sign of σ_{xy} indicates the direction of σ_1 and the direction of σ_2 is perpendicular. The relations have a well-known representation with the Mohr circle, see Fig. 6.1.

An alternative and more general representation of stresses is given by

$$\begin{aligned} \sigma_1 &= \sigma_x \cos^2 \varphi + \sigma_y \sin^2 \varphi + \sigma_{xy} \, 2 \cos \varphi \sin \varphi \\ \sigma_2 &= \sigma_x \sin^2 \varphi + \sigma_y \cos^2 \varphi - \sigma_{xy} \, 2 \cos \varphi \sin \varphi \end{aligned} \tag{6.6}$$
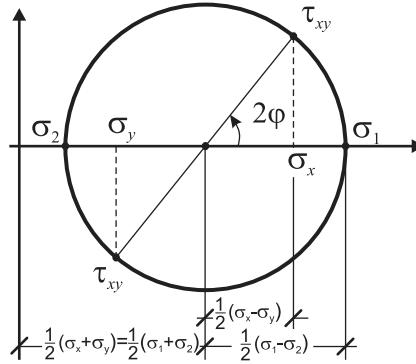
Figure 6.1: Mohr circle.

whereby φ indicates the direction of σ_1 and $\varphi + \pi/2$ the direction of σ_2. This form is derived from the rules for plane coordinate transformations, see Appendix C, Eq. (C.11), and allows one to control the stress values depending on the orientation angle φ. These transformation rules also require $(\sigma_y - \sigma_x)\cos\varphi\sin\varphi + \sigma_{xy}(\cos^2\varphi - \sin^2\varphi) = 0$ for vanishing shear stresses under the orientation φ. Combining this requirement with Eqs. (6.6) leads to a solution for $\sigma_x, \sigma_y, \sigma_{xy}$ depending on $\sigma_1, \sigma_2, \varphi$

$$
\begin{aligned}
\sigma_x &= \sigma_1 \cos^2\varphi + \sigma_2 \sin^2\varphi \\
\sigma_y &= \sigma_1 \sin^2\varphi + \sigma_2 \cos^2\varphi \\
\sigma_{xy} &= \sin\varphi\cos\varphi\,(\sigma_1 - \sigma_2)
\end{aligned}
\tag{6.7}
$$

Equations in the set Eqs. (6.5, 6.4) cannot be mixed with or complemented to equations in the set Eqs. (6.7). Finally, the relation $\sigma_1 \geq \sigma_2$ resulting from Eqs. (6.4) should be regarded for the following. The following cases have to considered from now on:

– *Pure compression* with the principal stresses $\sigma_1 \leq 0$, $\sigma_2 \leq 0$.

– *Mixed tension–compression* with the principal stresses $\sigma_1 > 0$, $\sigma_2 \leq 0$.

– *Pure tension* with the principal stresses $\sigma_1 > 0$, $\sigma_2 > 0$.

We assume that pure compression does not require contributions from a reinforcement. A reinforcement is required for mixed tension–compression and pure tension. The contributions of reinforcement and concrete are separated in the following.

Concrete has its own principal stress state with values σ_{c1}, σ_{c2} with an orientation φ of σ_{c1} and $\sigma_{c1} > \sigma_{c2}$ (signed!). It is assumed that it can sustain a compression in an orientation $\varphi + \pi/2$, but no stresses are transferred in the orientation φ. This implies cracking in the orientation $\varphi + \pi/2$ and principal stresses $\sigma_{c1} = 0$, $\sigma_{c2} < 0$. A notation $\sigma_{c2} = \sigma_c$ and $\varphi_c = \varphi + \pi/2$ is used from now on.

- The orientation φ_c of concrete principal compression and the corresponding compressive concrete stress σ_c serve as variables for the limit analysis.

Using Eqs. (6.7) and regarding $\sin\varphi = -\cos\varphi_c$, $\cos\varphi = \sin\varphi_c$ the concrete contribution in the global directions is given by

$$
\begin{array}{rcl}
\sigma_{c,x} & = & \sigma_c \cos^2\varphi_c \\
\sigma_{c,y} & = & \sigma_c \sin^2\varphi_c \\
\sigma_{c,xy} & = & \sigma_c \sin\varphi_c \cos\varphi_c
\end{array}
\tag{6.8}
$$

Further contributions come from the reinforcement. The content of reinforcement can be measured by the ratio ρ_s of reinforcement cross area A_s related to the cross-sectional area A. Regarding plates more than one major reinforcement orientation appears. Every orientation i is directed with an angle φ_{si}. Corresponding rebars form a *reinforcement group* with a reinforcement ratio ρ_{si}. Reinforcement stress is uniaxial by definition. The principal stress state of a reinforcement group i is determined through a single nonzero value, that is $\sigma_{si1} \neq 0$, while the other principal stress component vanishes, i.e., $\sigma_{si,2} = 0$. A notation $\sigma_{si} = \sigma_{si,1}$ is used in the following.

- Reinforcement group orientation φ_{si} and group stress σ_{si} serve as further variables for the limit analysis.

Although the approach allows for an arbitrary number of reinforcement orientations their number is restricted to two, $i = 1, 2$, in the following to simplify the notation. Thus, Eq. (6.7) also yields reinforcement contributions in the global directions with

$$
\begin{array}{rcl}
\sigma_{s1,x} & = & \sigma_{s1} \cos^2\varphi_{s1} \\
\sigma_{s1,y} & = & \sigma_{s1} \sin^2\varphi_{s1} \\
\sigma_{s1,xy} & = & \sigma_{s1} \sin\varphi_{s1} \cos\varphi_{s1}
\end{array}
\tag{6.9}
$$

and

$$
\begin{array}{rcl}
\sigma_{s2,x} & = & \sigma_{s2} \cos^2\varphi_{s2} \\
\sigma_{s2,y} & = & \sigma_{s2} \sin^2\varphi_{s2} \\
\sigma_{s2,xy} & = & \sigma_{s2} \sin\varphi_{s2} \cos\varphi_{s2}
\end{array}
\tag{6.10}
$$

Summed contributions from concrete and reinforcement groups are assumed to be in equilibrium with the given stress state $\sigma_x, \sigma_y, \sigma_{xy}$ determined from a superordinated analysis. Thus, regarding also the reinforcement ratios ρ_{s1}, ρ_{s2} the conditions

$$
\begin{array}{rcl}
\rho_{s1}\ \sigma_{s1,x} + \rho_{s2}\ \sigma_{s2,x} + \sigma_{c,x} & = & \sigma_x \\
\rho_{s1}\ \sigma_{s1,y} + \rho_{s2}\ \sigma_{s2,y} + \sigma_{c,y} & = & \sigma_y \\
\rho_{s1}\ \sigma_{s1,xy} + \rho_{s2}\ \sigma_{s2,xy} + \sigma_{c,xy} & = & \sigma_{xy}
\end{array}
\tag{6.11}
$$

must hold in every position of the plate.

- The reinforcement ratios ρ_{si} of every reinforcement group are used as final variables for the limit analysis.

Inserting Eqs. (6.8)–(6.10) into Eq. (6.11) yields three equations for eight variables φ_c, σ_c, $\varphi_{s1}, \sigma_{s1}, \varphi_{s2}, \sigma_{s2}$, and ρ_{s1}, ρ_{s2}. The values of the reinforcement orientations $\varphi_{s1}, \varphi_{s2}$ may be prescribed without loss of generality as they are ruled by practical considerations or construction site constraints, respectively. As a consequence six variables finally remain with three equilibrium equations with a prescribed local "loading" $\sigma_x, \sigma_y, \sigma_{xy}$.

Thus, problems cannot yet be solved with the current formulation. The conditions of kinematic compatibility introducing measures of strain and material laws relating stresses with strains are still missing. Approaches to consider them are discussed in [46, Chapters 6,7], [92] introducing strains $\epsilon_x, \epsilon_y, \gamma_{xy}$ and principal strains ϵ_1, ϵ_2 as further variables together with relations between strains and principal strains and uniaxial material laws for reinforcement and concrete. This yields an extended but complete set of equations. The computed values $\epsilon_x, \epsilon_y, \gamma_{xy}$ will more or less deviate from those directly determined in the initial finite element computation. Thus, kinematic compatibility would be limited within the current setup.

But such an approach will not be pursued in the following. A limit analysis – supported by the first limit theorem of plasticity, see Section 4.4 – does not regard kinematic compatibility and replaces stress–strain relations with material strength conditions leading to a lower bound for an admissible loading.

We consider a special but very common case. It is assumed that reinforcement directions are aligned to global coordinate axes leading to $\varphi_{s1} = 0$, $\varphi_{s2} = \pi/2$. Equations (6.9, 6.10) yield

$$
\begin{aligned}
\sigma_{s1,x} &= \sigma_{s1} \\
\sigma_{s2,y} &= \sigma_{s2} \\
\sigma_{s1,y} = \sigma_{s1,xy} = \sigma_{s2,x} &= \sigma_{s2,xy} = 0
\end{aligned}
\tag{6.12}
$$

Combining Eqs. $(6.8)_3$, $(6.11)_3$, and (6.12) leads to

$$
\sin \varphi_c \cos \varphi_c = \frac{\sigma_{xy}}{\sigma_c}
\tag{6.13}
$$

where $\sigma_c < 0$ by definition and σ_{xy} has to be taken with the correct sign. With a prescribed value of σ_{xy} and an assumed value of σ_c Eq. (6.13) has two solutions for φ_c in the range $-\pi/2 \leq \varphi_c \leq \pi/2$ under the condition $|\sigma_{xy}/\sigma_c| \leq 0.5$, see Fig. 6.2. Using a notation $\sigma_{s1,x} = \sigma_{sx}$, $\sigma_{s2,y} = \sigma_{sy}$ and $\rho_{s1} = \rho_x, \rho_{s2} = \rho_y$, Eqs. $(6.11)_{1,2}$ and Eqs. $(6.8)_{1,2}$ finally result in

$$
\begin{aligned}
\rho_x\,\sigma_{sx} &= \sigma_x - \sigma_c \cos^2 \varphi_c \\
\rho_y\,\sigma_{sy} &= \sigma_y - \sigma_c \sin^2 \varphi_c
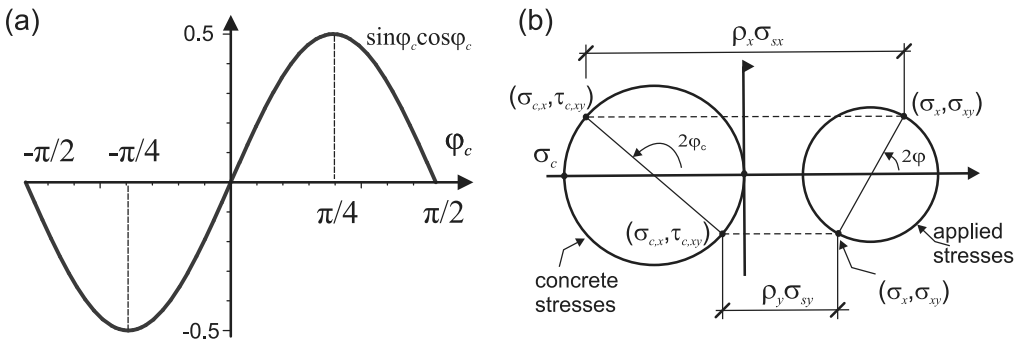\end{aligned}
\tag{6.14}
$$

Figure 6.2: (a) $\sin \varphi_c \cos \varphi_c$ and solution range of Eq. (6.13). (b) Mohr circles collecting contributions.

with concrete stress σ_c, concrete stress orientation φ_c, reinforcement stresses σ_{sx}, σ_{sy}, and reinforcement ratios ρ_{sx}, ρ_{sy} in the global x- and y-orientation. Their relations can again be illustrated with Mohr circles, see Fig. 6.1b. Equations (6.13, 6.14) involving prescribed values $\sigma_x, \sigma_y, \sigma_{xy}$ and variables $\rho_x, \rho_y, \sigma_{sx}, \sigma_{sy}$, and σ_c, φ_c are used for design considerations in the following. Similar approaches are described in [16, Section 2.2], [46, Chapter 4].

A further special case shall be added for completion. We consider again the general formulation with Eqs. (6.8–6.11) applied to the cross section of a *web of a beam* with a height z between chords as a limiting case of a plate. The conditions $\sigma_y = 0$ (no vertical "loading"), $\rho_{s2} = 0$ and variable parameters $\varphi_{s1}, \rho_{s1}, \sigma_c, \varphi_c$ are assumed. Equations (6.11, 6.8, 6.9) yield

$$
\begin{aligned}
\rho_s \cos^2 \varphi_s\, \sigma_s + \sigma_c \cos^2 \varphi_c &= \sigma_x \\
\rho_s \sin^2 \varphi_s\, \sigma_s + \sigma_c \sin^2 \varphi_c &= 0 \\
\rho_s \sin \varphi_s \cos \varphi_s\, \sigma_s + \sigma_c \sin \varphi_c \cos \varphi_c &= \sigma_{xy}
\end{aligned}
\tag{6.15}
$$

with the index omitted for the reinforcement group. Furthermore, we use a shear force $V = -z\,b\,\sigma_{xy}$ with a cross section width b, a difference of normal force $\Delta N = z\,b\,\sigma_x$ along the web height and an admissible reinforcement stress $\sigma_s = f_y$ with a yield stress f_y. Thus, Eqs. (6.15) lead to

$$
\begin{aligned}
\sigma_c &= -\frac{V}{z\,b\,(\sin \varphi_c \cos \varphi_c - \cot \varphi_s \sin^2 \varphi_c)} \\
\rho_s &= \frac{V}{f_y\, z\, b\,(\sin^2 \varphi_s \cot \varphi_c - \sin \varphi_s \cos \varphi_s)} \\
\Delta N &= -V\,(\cot \varphi_c + \cot \varphi_s)
\end{aligned}
\tag{6.16}
$$

whereby the concrete stress orientation is generally allowed with a range $0 < \varphi_c < \pi/2$ and the reinforcement orientation in a range $\pi/2 \le \varphi_s \le \pi$ for $V > 0$. In the case of stirrups with $\varphi_s = \pi/2$ this simplifies to

$$
\rho_s = \frac{V}{f_y\, z \cot \varphi_c}, \quad \sigma_c = -\frac{V}{z}\,(\cot \varphi_c + \tan \varphi_c), \quad \Delta N = -V \cot \varphi_c
\tag{6.17}
$$

and in the optimal case of diagonal concrete compression $\varphi_c = \pi/4$ and shear reinforcement $\varphi_s = 3\pi/4$ to

$$
\sigma_c = -\frac{V}{z}, \quad \rho_s = \frac{V}{f_y\, z}, \quad \Delta N = 0
\tag{6.18}
$$

These relations are identical to well-known design rules for the shear reinforcement of beams, see [26, 6.2.3]. A shifting distance a for the bending reinforcement in the upper and lower chord is defined with $a\,V = z\,\Delta N/2$. This leads to the well-known equation

$$
a = \frac{z}{2}\,(\cot \varphi_c + \cot \varphi_s) = \frac{z}{2}\,(\cot \varphi_c - \cot \alpha)
\tag{6.19}
$$

with $\alpha = 2\pi - \varphi_s$, see [26, 9.2.1.3].

The previous case assumes a constant stress state along a cross section of a web and concentrated forces in the upper and lower chords. Let us consider a setup with four of such webs in a spatial configuration forming a quadrangular cross section connected with four

chords. This leads to a hollow box girder. A loading is given by prescribed resulting internal forces – two bending moments, a torsional moment, a normal force and two shear forces – derived from external actions. The loading has to be in equilibrium with chord forces and web stresses. But equilibrium conditions will not suffice to determine them from the internal forces. Compatible web strains and relations connecting strains with stresses, as have been mentioned in Section 6.1.2, have to be introduced. Such an approach was elaborated in [78], [79]. With the finite element method at hand shell elements allowing for membrane forces in space combined with local bending, see Chapter 8, involving stress–strain relations for reinforced concrete, see Section 8.7, are another option.

6.1.3   A Design Approach

An arbitrary point is regarded within a plate with a local load given as stress state $\sigma_x, \sigma_y, \sigma_{xy}$ determined from a superordinated analysis. Corresponding principal stresses are given by σ_1, σ_2. A design approach shall be derived for this setup.

Concrete is assumed as isotropic, see Section 5.4.2. Its biaxial strength is shown in Fig. 5.7a. A lower strength bound for all compressive states is given by the uniaxial compressive strength f_c, i.e., $|\sigma_{c2}| < f_c$, see Fig. 6.3. Tensile stress states with $\sigma_{c1} > 0$ are excluded for concrete within the current scope. Regarding the pure *compression state*, see Section 6.1.2, given principal stresses should fulfill the conditions $\sigma_1 \leq f_c$ and $\sigma_2 \leq f_c$. In case they do not, the loading has to be scaled down, see Section 6.1.1, or plate dimensions have to be changed to fulfill the strength conditions. A compressive reinforcement might be another option. This alternative can be treated as an extension of the tension–compression case.

Mixed tension–compression and *pure tension* which require a reinforcement remain to be described. A special but common case is given with the orientations of the reinforcement aligned to the x- and y-axis of the global coordinate system. It is ruled by Eqs. (6.13, 6.14). The amount of reinforcement has to be determined for both orientations while concrete strength should not be exceeded. As concrete is not allowed to have a tensile stress Eq. (6.13)
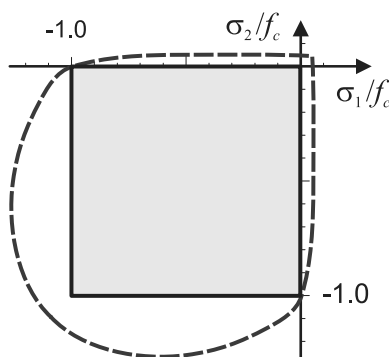

Figure 6.3: Strength square for biaxial concrete strength.

leads to a constraint

$$\varphi_c \leq 0 \ \text{for} \ \sigma_{xy} \geq 0 \qquad \text{or} \qquad \varphi_c > 0 \ \text{for} \ \sigma_{xy} < 0 \tag{6.20}$$

and regarding the compressive limit to a constraint

$$|\sigma_c| = \left| \frac{\sigma_{xy}}{\sin \varphi_c \cos \varphi_c} \right| \leq f_c \tag{6.21}$$

with the concrete compressive orientation φ_c. The "best" case or largest admissible shear stress $|\sigma_{xy}| = 0.5 \, f_c$ is connected with $|\varphi_c| = \pi/4$, see Fig. 6.2a. The given shear stress component σ_{xy} may not exceed this value. In case it does the loading again has to be scaled down or plate dimensions have to be changed to fulfill the constraint. We assume that some margin is possible for φ_c.

- According to a general design practice for reinforced concrete the concrete compressive orientation φ_c is prescribed as a basic design parameter.

This approach deserves a remark: Reality has a unique "solution" for φ_c. We might miss this solution in the current approach as the deformation behavior is not taken into account. An estimation of φ_c value should not be too far away from a comprehensive solution or sound empirical values. Under this premise, we expect to reach a reliable design.

To begin with, φ_c may freely be chosen within the range not violating the constraint Eq. (6.21). Thus, Eqs. (6.14) may be used to determine values $\rho_x \sigma_{sx}$ and $\rho_y \sigma_{sy}$ for given values of σ_x, σ_y. The uniaxial yield stress f_{yk}, see Fig. 2.10a, is used as a strength for the reinforcement leading to $\sigma_{sx} = \sigma_{sy} = f_{yk}$ and

$$\rho_x = \frac{1}{f_{yk}} \left(\sigma_x - \sigma_c \cos^2 \varphi_c \right), \qquad \rho_y = \frac{1}{f_{yk}} \left(\sigma_y - \sigma_c \sin^2 \varphi_c \right) \tag{6.22}$$

This is the required result of reinforcement design in the case of computed values $\rho_x > 0$ and $\rho_y > 0$. The total amount of reinforcement is given by

$$\begin{aligned} \rho_{tot} &= \rho_x + \rho_y = \frac{1}{f_{yk}} \left(\sigma_x - \sigma_c \cos^2 \varphi_c + \sigma_y - \sigma_c \sin^2 \varphi_c \right) \\ &= \frac{1}{f_{yk}} \left(\sigma_x + \sigma_y - \sigma_c \right) \end{aligned} \tag{6.23}$$

The contribution $-\sigma_c$ is positive due to the constraint (6.20). Thus, for a given value σ_{xy} concrete stress $|\sigma_c| = |\sigma_{xy}/\sin \varphi_c \cos \varphi_c|$ has to be minimized to minimize the total amount of reinforcement. This is reached with $\varphi_c = \pm \pi/4$, see Fig. 6.2a, depending on the sign of σ_{xy}.

- A concrete compressive orientation $\varphi_c = \pm \pi/4$ leads to optimal results for the utilization of concrete strength and the value of required reinforcement.

The minimum reinforcement amount is determined by

$$\rho_{\text{tot,min}} = \frac{1}{f_{yk}} \left(\sigma_x + \sigma_y + 2|\sigma_{xy}| \right) \tag{6.24}$$

These relations are valid only for orthogonal reinforcement meshes with coordinate directions aligned to reinforcement directions.

The cases with values $\rho_x < 0$ or $\rho_y < 0$ computed from Eq. (6.22) are still open. Such values may be interpreted as required compression reinforcement with a reinforcement stress $\sigma_{sx} = -f_{yk}$ and/or $\sigma_{sy} = -f_{yk}$, see Eqs. (6.14). A compression reinforcement can be avoided in a mixed case, i.e., $\rho_x < 0$, $\rho_y > 0$, or vice versa.

The case $\rho_x < 0$, $\rho_y > 0$ is treated exemplary. The basic idea is to prescribe the value of $\rho_x \sigma_{sx}$ instead of φ_c. Prescribing $\rho_x \sigma_{sx} = 0$ leaves $\rho_y \sigma_{sy}$, σ_c and φ_c as unknowns to be determined from three Eqs. (6.13, 6.14). This set of equations is nonlinear and cannot be solved directly. A numerical method like the Newton–Raphson method may be used instead, see Eq. (1.72). Collecting Eqs. (6.14, 6.13) by

$$\mathbf{u} = \begin{pmatrix} \sigma_c \\ \rho_y\, \sigma_{sy} \\ \varphi_c \end{pmatrix}, \qquad \mathbf{f}(\mathbf{u}) = \begin{pmatrix} \sigma_x - \sigma_c \cos^2 \varphi_c \\ \sigma_y - \sigma_c \sin^2 \varphi_c - \rho_y\, \sigma_{sy} \\ \dfrac{\sigma_{xy}}{\sigma_c} - \sin \varphi_c \cos \varphi_c \end{pmatrix} = 0 \qquad (6.25)$$

leads to the iteration rule

$$\mathbf{u}^{(\nu+1)} = \mathbf{u}^{(\nu)} - \begin{bmatrix} \dfrac{\partial f_1}{\partial u_1} & \dfrac{\partial f_1}{\partial u_2} & \dfrac{\partial f_1}{\partial u_3} \\ \dfrac{\partial f_2}{\partial u_1} & \dfrac{\partial f_2}{\partial u_2} & \dfrac{\partial f_2}{\partial u_3} \\ \dfrac{\partial f_3}{\partial u_1} & \dfrac{\partial f_3}{\partial u_2} & \dfrac{\partial f_3}{\partial u_3} \end{bmatrix}^{-1}_{\mathbf{u}=\mathbf{u}^{(\nu)}} \cdot \mathbf{f}(\mathbf{u}^{(\nu)}) \qquad (6.26)$$

This generally converges with an appropriate start value $\mathbf{u}^{(0)}$ and leads to the required solution for $\sigma_c, \rho_y \sigma_{sy}, \varphi_c$. The analogous method can be used in case with prescribed $\rho_y \sigma_{sy} = 0$ and unknown values for $\rho_x\, \sigma_{sx}, \sigma_c, \varphi_c$.

The design procedure has to be performed at representative positions of the plate under consideration. Every position will have its particular result for the required reinforcement. This is demonstrated with the following example of a deep beam.

Example 6.2 Reinforcement design for a deep beam with linear elastic internal forces
We refer to the example of Fig. 4.1 with the same system and loading. Young's modulus and Poisson's ratio are chosen with $E = 31\,900\,\mathrm{MN/m^2}$, $\nu = 0.2$ for a linear elastic calculation. The reinforcement yield strength is assumed with $f_{yk} = 500\,\mathrm{MN/m^2}$. The width of the deep beam is $b = 0.6\,\mathrm{m}$. Safety factors are not regarded. All units are based on [MN] and [m]. Plane stress conditions are assumed.

A state of stress with components $\sigma_x, \sigma_y, \sigma_{xy}$ is calculated for each integration point of each element and the design procedure is performed for all these points. This gives a representative overall picture of the whole deep beam. Four characteristic points with different types of a stress state are considered.

– Biaxial principal compression:

Element 61 is considered, see Fig. 6.4a, with the lower right integration point. Computed stresses are $\sigma_x = -0.86, \sigma_y = -3.66, \sigma_{xy} = -0.87$. This leads to principal compressive stresses with values $-3.91, -0.61$. A reinforcement is not necessary from a structural point of view.
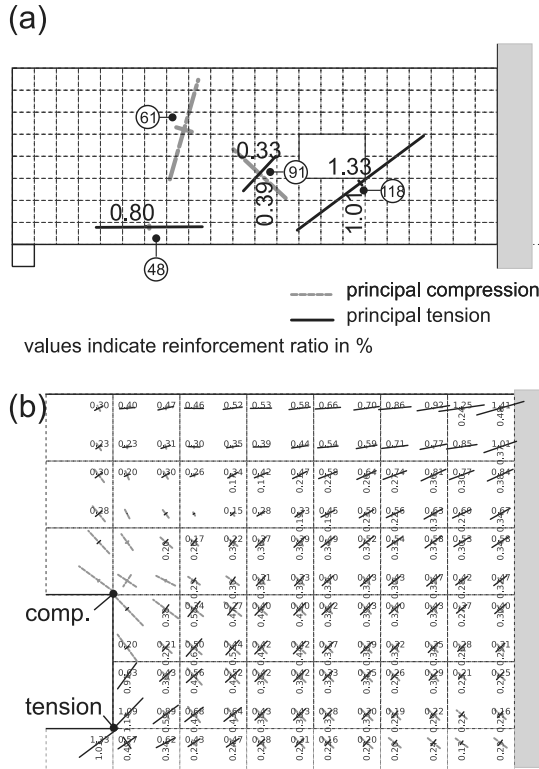
(a)

(b)

Figure 6.4: Example 6.2 (a) Characteristic stress points with required reinforcement. (b) Reinforcement of the upper right part.

– Biaxial principal tension:

Element 118 is considered with the upper right integration point with $\sigma_x = 3.90, \sigma_y = 2.27, \sigma_{xy} = 2.76$ with principal tensile stresses $5.96, 0.21$. The direction of concrete compressive stress is chosen with $\varphi_c = -\pi/4$. Using Eq. (6.13) leads to $\sigma_c = -2\sigma_{xy} = -5.52 \,\mathrm{MN/m^2}$ and Eq. (6.22) yields

$$
\begin{aligned}
\rho_x &= \frac{1}{f_{yk}} \left(\sigma_x - \sigma_c \cos^2 \varphi_c\right) &= 0.0133 \\
\rho_y &= \frac{1}{f_{yk}} \left(\sigma_y - \sigma_c \sin^2 \varphi_c\right) &= 0.0101
\end{aligned}
\tag{6.27}
$$

This leads to reinforcement cross sections $a_{sx} = t\,\rho_x = 0.00798 \,\mathrm{m^2/m}$ ($\rightarrow 79.8\,\mathrm{cm^2/m}$) and $a_{sy} = t\,\rho_y = 0.00604\,\mathrm{cm^2/m}$ ($\rightarrow 60.4\,\mathrm{cm^2/m}$). These related values are required locally only, not over the whole of a cross-sectional width of 1 m.

A concrete compression part is obviously necessary even in the case of biaxial principal tension to ensure equilibrium. To reach the state with reinforcement yielding in the global x- and y-directions and a concrete diagonal under compression some amount of

redistribution of internal forces might be necessary. This is generally connected with some amount of cracking with crack directions more or less aligned to the concrete diagonal.

– Mixed principal stresses:

Element 91 is considered with the upper left integration point with $\sigma_x = -0.61, \sigma_y = -0.30, \sigma_{xy} = 2.24$, and principal stresses $-2.70, 1.78$. Concrete compressive direction is again chosen with $\varphi_c = -\pi/4$ leading to $\sigma_c = -4.48\,\text{MN/m}^2$. This yields $\rho_x = 0.0033$, $\rho_y = 0.0039$ in the same way like Eq. (6.27).

– Mixed principal stresses with initially negative reinforcement ratio

Element 48 is considered with the upper left integration point with $\sigma_x = 4.01, \sigma_y = -0.11, \sigma_{xy} = 0.02$ and principal stress values $4.01, -0.12$. A concrete compressive direction $\varphi_c = -\pi/4$ leads to $\rho_y\,\sigma_{sy} < 0$. Thus, $\rho_y\,\sigma_{sy} = 0$ is prescribed and an iteration is performed according to Eq. (6.26). This yields $\sigma_c = -0.10\,\text{MN/m}^2, \varphi_c = -0.43\pi$, and $\rho_x = 0.0080$ with $\sigma_{sx} = f_{yk}$.

Local results for the required reinforcement have to be transformed into a general reinforcement layout. A minimum reinforcement ratio is necessary to compensate for effects which have are not explicitly regarded like temperature and shrinkage gradients and to control the width of cracks. The minimum ratio is chosen with $\rho_{x,\min} = \rho_{y,\min} = \rho_{\min} = 0.0015 = 0.15\,\%$ supported by [26, 9.7]. This minimum ratio serves as a base for supplementary reinforcement.

Figure 6.4b shows the computed principal stresses for the upper right portion of the deep beam and the corresponding values for the required reinforcement – horizontal %-ratios for the x-reinforcement and vertical %-ratios for the y-reinforcement – in case they exceed $\rho_{\min}$. The final reinforcement layout will use characteristic maximum values to cover larger areas with the same reinforcement. Single rebars of larger diameter may also be used to treat smaller areas with higher reinforcement demand. Their contribution may also be calculated as reinforcement ratio within some near surrounding.

End Example 6.2

The basic procedure – perform a linear elastic calculation for internal forces followed by a reinforcement design and concrete proof with methods of limit analysis – shows analogies to the common practice for design and proof of reinforced concrete beams considering bending, shear, and torsion.

Furthermore, analogies are given to strut-and-tie models, see Section 4.1, as a local system of reinforcement ties and a concrete strut is regarded in the plate's position under consideration. Thus, similar remarks as are appropriate for strut-and-tie models have to be added:

– Concrete compressive strength:

The concrete contribution within this scope is basically uniaxial for principal stress states with tensile components. But lateral tension may actually lead to a decrease in the compressive concrete strength. This is regarded by reduction factors applied on f_c in the same way as for strut-and-tie models, see Section 4.5. Consider also [16, Section 2.2.7].

– Ductility requirements:

In order to reach stress limit states a larger redistribution of internal forces may be necessary. This may require larger deformations or a sufficient ductility of the whole system, respectively.

– Serviceability:

The current analysis does not consider deformations. But each local tie may be regarded as a small uniaxial tension bar. Thus, a crack width may be estimated according to Appendix B. The reinforcement stresses σ_{sx}, σ_{sy} required for such an estimation are determined using Eqs. (6.13, 6.14) with given reinforcement ratios ρ_x, ρ_y and given stresses $\sigma_x, \sigma_y, \sigma_{xy}$.

In the case of a local diagonal concrete strut $\varphi_c = \pi/2$, see Example 6.2 with the cases "biaxial principal tension" and "mixed principal stresses," the crack direction theoretically deviates from the reinforcement directions by a larger value. This may be considered for crack width estimation, see Appendix B.

The concept of added contributions of concrete and reinforcement – each with its own principal orientation – to reach equilibrium with a local stress state given from a superordinated calculation may be transferred from biaxial states to triaxial states [29], [71], [93]. This corresponds to spatial strut-and-tie models with a spatial system of reinforcement ties and a spatial reinforcement strut leading to design rules as an spatial extension of Eqs. (6.22).

Limit analysis bases upon stresses derived with linear elastic stress–strain relations. Such linear elastic relations may lead to stress concentrations with small areas of high stresses characterized by distinct peak values. Such high values may be crucial for the reinforcement design of plates.

On the other hand, nonlinear stress–strain relations may result in smoothed stress states, i.e., stress peaks are smoothed while stresses moderately increase in the surrounding. But such stress–strain relations must be explicitly considered in the model. This is demonstrated with the following sections. Cracking of concrete again plays a major role.

6.2 Crack Modeling

A major cause of nonlinear behavior of reinforced concrete is given with cracking. Cracking in uniaxial stress states has already been described in Section 2.1. Its consequences for the behavior of reinforced tension bars were demonstrated in Example 2.4. The reinforced tension bar basically also covers the behavior of the cracked tension zone of reinforced cross sections of a beam, see Section 3.1.3. Finally, cracking in multiaxial stress states has been treated in Section 5.7. These concepts are adapted for biaxial cracking and combined with a reinforcement in the following.

Crack initiation is determined with the Rankine criterion, see Section 5.7.1. A crack starts when the largest principal stress σ_1 reaches the tensile strength f_{ct}. The *crack direction* is given with the direction perpendicular to the direction φ, see Eq. (6.5), of σ_1. The determination of *crack length* depends on a scan method. A *scan method* first of all defines how points for testing the cracking criterion are selected.
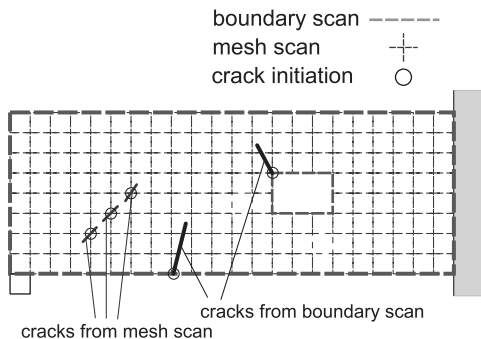
Figure 6.5: Scan methods for cracks.

A mesh-based scan method scans a whole domain in discrete points constituting a regular or irregular mesh, see Fig. 6.5. Regarding finite elements, such a testing mesh is naturally given by the element integration points. If the testing mesh is sufficiently dense, *crack propagation* is described by an increasing number of cracked points, e.g., points with a stress state fulfilling the Rankine criterion. As a consequence, the crack length question is not explicitly addressed in the mesh-based scan method.

A boundary-based scan method distinguishes crack initiation and crack propagation. A crack in most cases initiates from a boundary. Thus, boundary points are scanned for testing the cracking criterion like the Rankine criterion. If a scanned point fulfills the criterion for crack initiation, it becomes a *crack tip*. A crack may propagate with the movement of its crack tip. Regarding existing crack tips the following items have to be addressed:

– A criterion whether *propagation* of a crack tip will take place at all for a given state of strain and stress. This is not necessarily identical with the crack initiation criterion.

– A rule for the *direction* of a crack tip movement in the case of crack propagation.

– A further rule for the *length* of the crack tip movement.

The Rankine criterion obviously does not allow for a complete treatment. Energy criteria, e.g., are proposed as a base for a simultaneous resolution of this set [85]. Taking altogether, quite sophisticated models are required to describe crack propagation with the boundary-based scan method.

The *mesh-based method* will be used in the following. This method has proven its practicability and avoids dealing with the crack length problem. A drawback may be considered insofar as a crack geometry is not precisely captured but cracking of concrete is a diffuse matter anyway. Nevertheless, a number of items arise with this approach, which have already been touched in Section 5.7, but are rephrased and specified regarding 2D states:

– Rotating crack versus fixed crack:

   Testing of a particular point with a known stress state is performed with, e.g., the Rankine criterion. This decides whether this point has to be regarded as cracked, and

if so, to determine its orientation. Cracking requires a reformulation of the material stiffness which depends on the crack orientation.

Regarding a load history, principal stress orientations may change. This leads to two alternative concepts regarding crack orientations, *fixed* crack and *rotating* crack, see Section 5.7.2. The crack orientation is fixed for the fixed crack with that value occurring in crack initiation, while crack orientation follows the direction of principal stresses for the rotating crack, i.e., it may change during a load history.

The fixed crack concept seems to be more realistic from a phenomenological point of view but in practical applications it yields a behavior of the cracked material which is generally to stiff. Thus, the rotating crack concept will be used in the following.

– Cohesive crack:

A set of representative points of a plate are controlled for crack initiation with the mesh-based scan method. A local coordinate system is chosen in every point aligned to principal stress directions with the x-axis in the principal tensile direction. A crack initiates if the largest principal tensile stress exceeds the tensile strength. This principal tensile stress is orthogonal to crack surfaces by definition in the rotating crack concept. Therefore, the immediate cracking situation can be regarded as uniaxial. A process zone or crack band, respectively, arises with the crack initiation, see Section 2.1. It is characterized by high strains within a crack band width b_w, see Fig. 2.3. The distance b_w accounts roughly to a small multiple of the largest aggregate diameter and is kept constant. A crack width w is defined as the distance change between left and right border of the process zone. This distance starts with a value b_w. The crack width is determined by

$$w_1 = b_w\,\epsilon_{c1} \tag{6.28}$$

with the mean crack band strain ϵ_c, compare also Eq. (2.5). The index 1 is used in the following to indicate the affiliation with the largest principal stress σ_1.

Uniaxial cracking behavior of concrete is characterized by the cohesive crack model with crack traction depending on crack width, see Section 5.7.1 and Fig. 5.15. A typical crack traction–crack width relation characterized by softening is shown in Fig. 5.16. This is simplified as linear in the following, see Fig. 6.6, and leads to a relation

$$t_1 = \begin{cases} f_{ct}\left(1 - \dfrac{w_1 - b_w\epsilon_{ct}}{w_{cr}}\right) & b_w\epsilon_{ct} < w_1 \leq w_{cr} \\ 0 & w_1 > w_{cr} \end{cases} \tag{6.29}$$

with the concrete strain $\epsilon_{ct} = f_{ct}/E_c$ at crack initiation, the crack traction t_1 and the crack width w_1. The gray shaded area corresponds to the crack energy G_f, see Eq. (2.7), which is assumed as material constant. The smallest crack width with vanishing crack tractions, the *critical crack width* w_{cr} is determined by

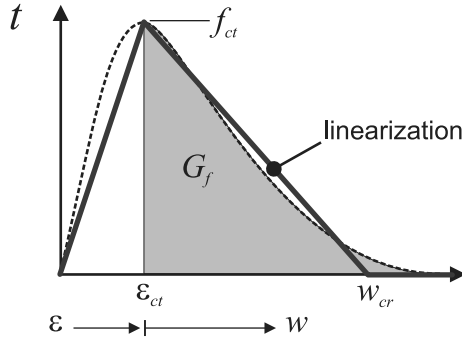$$w_{cr} = \frac{2G_f}{f_{ct}} + b_w\,\epsilon_{ct} \tag{6.30}$$

as a material constant.

Figure 6.6: Linearized cohesive crack model.

– Smeared crack:

We introduced the notion of a black box embracing of piece of cracked material with an orientation in the crack normal direction or smeared crack model, see Section 2.5 with Fig. 2.13, and Section 5.7.2. The box is chosen such that one crack or one crack band, respectively, arises in it. The crack band is within the box but the exact position is not localized.

Assuming a box with a length $L_c \geq b_w$ leads to a box strain in the crack normal direction

$$\epsilon_1 = \frac{1}{L_c} \left[(L_c - b_w)\,\epsilon_{u1} + b_w\,\epsilon_{c1} \right] = (1 - \xi)\,\epsilon_{u1} + \xi\,\epsilon_{c1}, \quad \xi = \frac{b_w}{L_c} \qquad (6.31)$$

see Eqs. (2.45, 5.129), with the strain ϵ_{u1} of the uncracked bulk material and the mean strain ϵ_{c1} of the crack band. The length L_c denotes a *characteristic length* of the quad element. Square formatted elements are preferable. A characteristic element length

$$L_c = \sqrt{\frac{A}{(n_i + 1)^2}} \qquad (6.32)$$

is appropriate with the element area A and integration order n_i. Gauss integration order $n_i = 1$, e.g., has 2×2 integration points for a quad-element, see Table 1.1. A combination of Eqs. (6.28–6.31) has already been demonstrated in Example 2.3. This will be extended to biaxial states of stress in the following section.

The smeared crack approach allows one to model cracks, which are more or less discontinuous in reality, using the quad element with a continuous displacement interpolation as described in Section 1.3.

The concepts of the rotating, cohesive, smeared crack will be used for 2D crack modeling. This is a relatively simple and convenient approach. Furthermore, it includes a regularization regarding the softening behavior of concrete in the tension regime, see Section 5.9.2.

6.3 Linear Stress–Strain Relations with Cracking

Load-induced anisotropy has been described as one of the characteristics of concrete behavior, see Section 5.1.2. Corresponding stress–strain relations for 2D states will be derived in this section with the following assumptions:

- Linear elastic, biaxial material behavior with a plane stress state according to Eq. (1.45).

- A limited tensile strength with crack initiation according to the Rankine criterion, see Section 5.7.1 and a strength value f_{ct} as for the uniaxial tensile strength.

- A cohesive crack behavior according to Eq. (6.29).

- Element strains for cracks are determined with the smeared crack model, see Eq. (6.31).

Each component represents a simplified model within its scope. On the other hand, the simplifications allow deriving relatively compact stress–strain relations. More realistic models – for, e.g., nonlinear behavior of concrete in the compressive range or bilinear or nonlinear relations for the crack-traction depending on the crack width – essentially follow the same procedure.

We consider a 2D state of strain with given components $\epsilon_x, \epsilon_y, \gamma_{xy}$, see Eq. (5.3), determined from a superordinated calculation. The notation of indices is adapted for the current context. Principal strains can be derived in analogy to principal stresses with Eqs. (6.4, 6.5), whereby $\epsilon_{xy} = \gamma_{xy}/2$ has to be used as shear component. This leads to principal strains ϵ_1, ϵ_2 with $\epsilon_1 \geq \epsilon_2$ and the orientation angle φ of ϵ_1. The following states have to be considered, see Figures 5.16 and 6.7:

1. Initial loading in the tensile range up to crack initiation followed by softening.

2. Unloading until a stress free state is reached.

3. Crack closure with loading in the compressive range.

4. Reloading into the tensile range.

We start with the *initial loading* in the tensile range. Due to the isotropy properties, see Section 5.3.1, the linear elastic law (Eq. (1.45)) is also valid in the principal system and yields relations

$$\epsilon_1 = \frac{1}{E}\left(\sigma_1 - \nu\,\sigma_2\right), \quad \epsilon_2 = \frac{1}{E}\left(\sigma_2 - \nu\,\sigma_1\right). \tag{6.33}$$

with principal stresses σ_1, σ_2, a Young's modulus E_c for concrete and its Poisson's ratio ν. A first crack occurs in the case of a computed $\sigma_1 \geq f_{ct}$.

- The principal stress σ_1 in the uncracked material and the crack traction t_1, see Eqs. (5.123, 6.29), are identical for rotating cracks combined with the Rankine cracking criterion due to equilibrium reasons.

The smeared strain in the normal crack direction is given according to Eq. (6.31). The set of Eqs. (6.28, 6.29, 6.31, 6.33) comprises the material or system parameters E, ν, b_w, L_c, f_{ct} and w_{cr}. The strain

$$\epsilon_{ct} = \frac{f_{ct}}{E_c} \tag{6.34}$$

will be used instead of f_{ct} if appropriate. Principal strain values ϵ_1, ϵ_2 are prescribed. Thus, there remain five unknowns σ_1, σ_2, w_1, ϵ_1, ϵ_{c1} with the aforementioned five equations. Two further assumptions are made:

– $b_w \ll L_c$ or $\xi \ll 1$, i.e., the element size is large compared to crack band width. This is insofar justified as plates, which are currently under consideration, have dimensions in the range of 10^1 m while b_w is in the range of 10^{-2} m.

– $\epsilon_{ct} b_w \ll w_{cr}$, i.e., elastic energy until cracking is small compared to crack energy.

These assumptions are not mandatory but simplify the stress–strain relations. Regarding a range $\epsilon_1 > \epsilon_{ct}$, $w_1 < w_{cr}$ a solution for the stresses is given with

$$
\begin{aligned}
\sigma_1 &= f_{ct} \frac{1 - \alpha\epsilon_1 - \alpha\nu\epsilon_2}{1 - \alpha\epsilon_{ct}(1 - \nu^2)} \\
\sigma_2 &= E_c \frac{(1 - \alpha\epsilon_{ct})\epsilon_2 - \alpha\epsilon_{ct}\nu\,\epsilon_1 + \epsilon_{ct}\nu}{1 - \alpha\epsilon_{ct}(1 - \nu^2)}
\end{aligned}
\tag{6.35}
$$

with $\alpha = L_c/w_{cr}$ and for the crack width with

$$w_1 = \frac{\epsilon_1 + \nu\,\epsilon_2 - \epsilon_{ct}(1 - \nu^2)}{1 - \alpha\epsilon_{ct}(1 - \nu^2)} L_c \tag{6.36}$$

Equation (6.35) leads to a tangential material stiffness

$$\mathbf{C}_T = \frac{E}{1 - \alpha\epsilon_{ct}(1 - \nu^2)} \begin{bmatrix} -\alpha\epsilon_{ct} & -\alpha\epsilon_{ct}\nu \\ -\alpha\epsilon_{ct}\nu & 1 - \alpha\epsilon_{ct} \end{bmatrix} \tag{6.37}$$

The parameter $\alpha\epsilon_{ct}$ should fulfill a condition $\alpha\epsilon_{ct} < 1$ which leads to restrictions for the characteristic element length L_c of an element for a given material.

Unloading until a stress-free state is assumed to have a damage characteristic, compare Section 5.6. Unloading starts from a state $w_1 = \bar{w}_1$, $\sigma_1 = \bar{\sigma}_1$ in the softening range of the crack traction–crack width relation, see Fig. 6.7, and follows the "damage" path until a zero-state with zero strains, no deformations and initiated crack closure. Relation (6.29) for the crack traction depending on the crack width is replaced by

$$\sigma_1 = t_1 = \bar{\sigma}_1 \frac{w_1}{\bar{w}_1} \tag{6.38}$$

and the largest crack width $\bar{w}_1$ becomes a state variable. The corresponding stress $\bar{\sigma}_1$ may be derived from $\bar{w}_1$. Principal strains ϵ_1, ϵ_2 are again prescribed from a superordinated
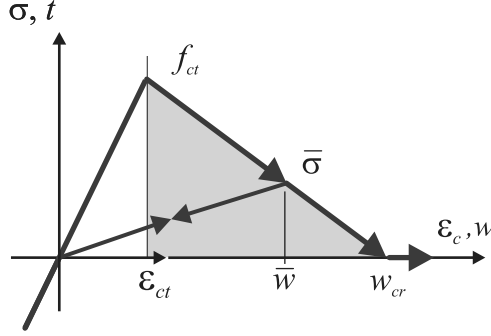
Figure 6.7: Cohesive crack model with unloading and reloading.

calculation. The unknowns σ_1, σ_2, w_1, ϵ_1, ϵ_{c1} are determined with Eqs. (6.28, 6.31, 6.33, 6.38) leading to

$$\sigma_1 = \frac{\epsilon_1 + \nu\epsilon_2}{1 + \frac{\beta}{E}(1 - \nu^2)}\,\beta$$

$$\sigma_2 = \frac{[E + \beta]\,\epsilon_2 + \nu\beta\,\epsilon_1}{1 + \frac{\beta}{E}(1 - \nu^2)}$$

$$w_1 = \frac{\epsilon_1 + \nu\epsilon_2}{1 + \frac{\beta}{E}(1 - \nu^2)}\,L \tag{6.39}$$

$$\mathbf{C}_{tan} = \frac{1}{1 + \frac{\beta}{E}(1 - \nu^2)}\begin{bmatrix} E + \beta & \nu\beta \\ \nu\beta & \beta \end{bmatrix}$$

with $\beta = \bar{\sigma}_1\,L/\bar{w}_1$ and the same simplifying assumptions as for the loading case.

Crack closure followed by *compressive loading* is treated as isotropic linear elastic with stress–strain relations according to Eq. (6.33) or Eq. (1.45), respectively. *Unloading* in the compressive range follows the same relations until the zero-state with $\epsilon_1 = 0$.

The principal strain ϵ_1 alters into w_1 with the transition into *tensile reloading*. The "damage" path is followed again with stress–strain relations and crack width according to Eqs. (6.39) until the crack width w_1 reaches the value of the state variable $\bar{w}_1$. A state of loading follows with ongoing softening ruled by Eqs. (6.35–6.37) with increasing values of $\bar{w}_1$ and decreasing values of $\bar{\sigma}_1$.

Finally, the state of *macrocracking* is reached with $w_1 = w_{cr}$. Crack tractions become zero. A further unloading will occur with zero crack tractions until the zero-state is reached again with a crack closure. Compression states are again ruled by the linear elastic isotropic law. A further reloading follows the previous path in the opposite direction.

Regarding a point with a crack in the principal 1-direction a further crack may arise in the principal 2-direction in the case of biaxial principal tension leading to a *multiple cracking*. This is covered by Eq. (5.136) for general cases but is reformulated in the current context. Multiple cracks are dual cracks in 2D states. *Dual cracks* are orthogonal in the case of rotating cracks with the Rankine cracking criterion. The states as have been listed

in Section 6.2 also apply to the second crack and the relations derived subsequently are the same for both directions. A further assumption is made.

- In the case of dual cracking a decoupling of principal directions with neglecting Poisson's ratio $\nu = 0$ considerably simplifies the relations for stresses, crack widths and tangential stiffness.

As a consequence, the basic equations (6.33) are modified as

$$\epsilon_i = \frac{1}{E} \sigma_i \tag{6.40}$$

with $i = 1, 2$. Thus, the state of *loading* is described by

$$
\begin{aligned}
\sigma_i &= f_{ct} \frac{1 - \alpha \epsilon_i}{1 - \alpha \epsilon_{ct}} \\
w_i &= \frac{\epsilon_i - \epsilon_{ct}}{1 - \alpha \epsilon_{ct}} L_c \\
\mathbf{C}_T &= \frac{E}{1 - \alpha \epsilon_{ct}} \begin{bmatrix} -\alpha \epsilon_{ct} & 0 \\ 0 & -\alpha \epsilon_{ct} \end{bmatrix}
\end{aligned}
\tag{6.41}
$$

with $\alpha = L_c / w_{cr}$ and $E \epsilon_{ct} = f_{ct}$. The state of *unloading* before crack closure is described by

$$
\begin{aligned}
\sigma_i &= \frac{\epsilon_i}{1 + \frac{\beta}{E}} \beta \\
w_i &= \frac{\epsilon_i}{1 + \frac{\beta}{E}} L \\
\mathbf{C}_{\tan} &= \frac{1}{1 + \frac{\beta}{E}} \begin{bmatrix} E + \beta & 0 \\ 0 & \beta \end{bmatrix}
\end{aligned}
\tag{6.42}
$$

and finally *crack closure* and compression again with Eq. (6.40). This approach also covers a mixture of states, e.g., one direction in the loading softening state and the other direction in the unloading state or crack closure state. Such mixtures will occur in plates due to a considerable redistribution of stresses during the formation of cracks.

All these relations are derived in a local coordinate system aligned to the principal axes of strain. Principal stresses are determined in the same system by definition. This is admissible due to the Rankine crack criterion and the rotating crack approach. Stresses and tangential material stiffness have to be transformed to the global system for usage with Eqs. $(1.58)_1$ and (1.65). The transformation is performed using Eqs. (5.16, 5.17) with the transformation matrix $\mathbf{Q}$ for 2D states according to Appendix C, Eq. (C.11) with the orientation angle φ of the principal strain state.

All derived relations include a characteristic length L_c according to Eq. (6.32) of the particular quad element under consideration. This ensures the recovery of crack energy and accomplishes the regularization, see Section 5.9.2, of the softening with model crack-traction–crack-width relations Eq. (6.29).

6.4 2D Modeling of Reinforcement and Bond

To start with a single reinforcement bar may be modeled with 2D bar elements, see Section 1.3. The material behavior of rebars is uniaxial and may be described by the uniaxial elastoplastic law, see Section 2.3. Thus, modeling of rebars may be considered as a special case of a elastoplastic truss, which has already been discussed in Section 4.3. But this truss is embedded in concrete and interacts with it via bond.

Basic mechanisms of *bond* have already been discussed in Section 2.4. Two approaches have to be distinguished with respect to modeling with finite elements:

- Rigid bond:

  It is assumed that slip between concrete and reinforcement can be disregarded. As a consequence, finite elements for reinforcement on one hand and concrete on the other hand share the same nodes, see Fig. 6.8a. This enforces the same displacements of concrete and reinforcement in nodes. There might be minor displacement differences along a rebar axis between nodes, but this is not significant if the mesh is not too coarse.

- Flexible bond:

  Slip between concrete and reinforcement in the longitudinal direction is regarded while both have the same displacement in the lateral direction. As a consequence finite elements for reinforcement on one hand and concrete on the other hand have to have their own nodes, see Fig. 6.8b. Concrete nodes and reinforcement nodes have to be connected by a special type of spring elements, see Section 1.3. This type of element is a so-called *bond element*, which is constrained or very stiff in the lateral rebar direction and has a bond law, see Fig. 2.11b, in the longitudinal direction.

For the sake of brevity and simplicity a rigid bond will be assumed in the following, if not otherwise stated.

Reinforcement meshes are predominantly used for plates beneath single rebars or groups of a few rebars. A reinforcement mesh consists of two orthogonal reinforcement groups, see Section 6.1.2. The rebars of a group have a relatively small diameter and a narrow spacing.
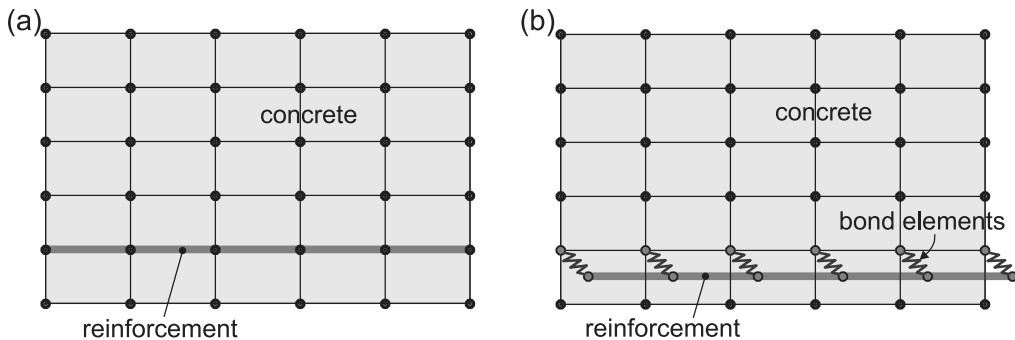

Figure 6.8: Bond (a) Rigid. (b) Flexible.

To model each bar of a reinforcement group with a number of finite element bars is very elaborate.

A smeared model is used instead, i.e., reinforcement bars of a group are modeled as a *reinforcement sheet*. The cross section of a reinforcement mesh is given by the cross section A_s of a single bar and the bar spacing s. This leads to a sheet thickness

$$b_s = \frac{A_s}{s} \tag{6.43}$$

and a reinforcement ratio

$$\rho = \frac{b_s}{b} \tag{6.44}$$

with a thickness b of the plate. A more common notation is used with a_s which denotes the total reinforcement cross section in cm^2 related to a width of 1 m, i.e., $a_s = 100\, b$ if b is measured in m. Anyway, the sheet has to be implemented into the model.

- A reinforcement sheet is regarded as a plate. The numerical model may be established with quad elements. This has to be combined with uniaxial behavior as a special case of anisotropy.

It is assumed that a reinforcement sheet has an orientation φ_s given by the direction of its bars. This is measured positive counterclockwise starting from the global x-direction. A rotated Cartesian coordinate system is assigned with the $\tilde{x}$-axis in the bar direction.

A given global strain state $\boldsymbol{\epsilon} = \begin{pmatrix} \epsilon_x & \epsilon_y & \gamma_{xy} \end{pmatrix}^T$ can be transformed to the rotated system using Eq. (5.15)

$$\tilde{\boldsymbol{\epsilon}} = \mathbf{Q} \cdot \boldsymbol{\epsilon} \tag{6.45}$$

with

$$\mathbf{Q} = \begin{bmatrix} \cos^2 \varphi_s & \sin^2 \varphi_s & \cos \varphi_s \sin \varphi_s \\ \sin^2 \varphi_s & \cos^2 \varphi_s & -\cos \varphi_s \sin \varphi_s \\ -2\cos \varphi_s \sin \varphi_s & 2\cos \varphi_s \sin \varphi_s & \cos^2 \varphi_s - \sin^2 \varphi_s \end{bmatrix} \tag{6.46}$$

see Appendix C, Eq. (C.13). This leads to a strain $\tilde{\epsilon}_x$ which can be used to determine a stress $\tilde{\sigma}_x$ according to the uniaxial material law (Eqs. (2.39, 2.40)) appropriate for the reinforcement. The rotated stress state is given by $\tilde{\boldsymbol{\sigma}} = \begin{pmatrix} \tilde{\sigma}_x & 0 & 0 \end{pmatrix}^T$. This is transformed back to the global system with Eq. (5.16)

$$\boldsymbol{\sigma} = \mathbf{Q}^T \cdot \tilde{\boldsymbol{\sigma}} \tag{6.47}$$

The tangential material stiffness in the rotated system is given by

$$\tilde{\mathbf{C}}_T = \begin{bmatrix} C_T & 0 & 0 \\ 0 & 0 & 0 \\ 0 & 0 & 0 \end{bmatrix} \tag{6.48}$$

with $C_T = E_s$ in the case of loading below the yield limit and unloading and $C_T = E_T$ at the yield limit, see Fig. 2.10. This is transformed to the global system with Eq. (5.17)

$$\mathbf{C}_T = \mathbf{Q}^T \cdot \tilde{\mathbf{C}}_T \cdot \mathbf{Q} = C_T \begin{bmatrix} \cos^4 \varphi_s & \cos^2 \varphi_s \sin^2 \varphi_s & \cos^3 \varphi_s \sin \varphi_s \\ \cos^2 \varphi_s \sin^2 \varphi_s & \sin^4 \varphi_s & \sin^3 \varphi_s \cos \varphi_s \\ \cos^3 \varphi_s \sin \varphi_s & \sin^3 \varphi_s \cos \varphi_s & \cos^2 \varphi_s \sin^2 \varphi_s \end{bmatrix} \tag{6.49}$$
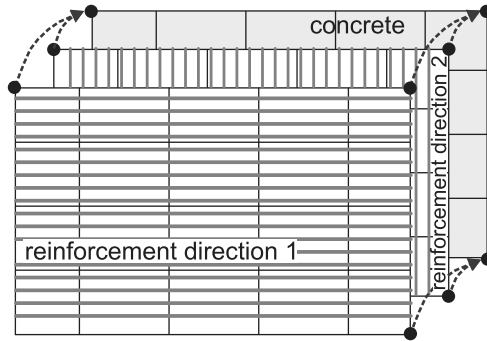
Figure 6.9: Overlay of elements.

leading to a symmetric but fully occupied matrix $\mathbf{C}_T$. With Eqs. (6.45)–(6.49) the required components are given for modeling a reinforcement sheet using quad elements or other element types for 2D states.

The procedure for a reinforcement sheet covers a particular reinforcement group out of the two groups of a reinforcement mesh. The two reinforcement sheets and the model for concrete with stress–strain relations as have been described, e.g., in the previous Section 6.3 have to be combined to complete the model for a reinforced concrete plate.

This is performed with an *overlay* of elements, see Fig. 6.9. Each part is modeled separately with its own finite element mesh as has been described before. These parts share the same geometry and – assuming a rigid bond – the same nodes. They are simply added in the assembling process, see Section 1.5. Finally, bar elements for single reinforcement bars may be superposed.

Cracking of the concrete part may be considered with the smeared crack model also in the case of overlays with reinforcement sheets and single rebars. Increased smeared strains due to concrete cracking are coupled to the reinforcement strains. Concrete and reinforcement parts influence each other whereby deformation modeling is integral due to smearing of crack strains.

The application of the basic set of constituents – limit tensile strength of concrete, load-induced anisotropy, smeared crack model, reinforcement sheets with rigid bond – is demonstrated with the following example.

Example 6.3 Simulation of cracked reinforced deep beam
We refer to the deep beam example given in Fig. 4.1 and already treated in Example 6.2 with a limit analysis. In contrast to Example 6.2, the nonlinear stress–strain behavior of concrete and reinforcement will be considered to some extent. System and loading are shown in Fig.4.1a. The thickness of deep beam is $b = 0.6\,\text{m}$. The following *material properties* are assumed:

- The concrete material model is chosen according to Section 6.3. The following material parameters are used: Young's modulus $E_c = 31\,900\,\text{MN/m}^2$, Poisson's ratio $\nu = 0.2$, and tensile strength $f_{ct} = 1.0\,\text{MN/m}^2$.

– Crack energy has a magnitude of roughly $100\,\mathrm{Nm/m^2}$, see [18, 5.1.5.2]. A value of $G_f = 50\,\mathrm{Nm/m^2}$ is chosen for the following. Furthermore, a crack band width $b_w = 0.02\,\mathrm{m}$ is chosen. This leads to a critical crack width $w_{cr} = 0.1\,\mathrm{mm}$ according to Eq. (6.30).

– The reinforcement material model is chosen according to Section 2.3. As parameters are used: Young's modulus $E_s = 200\,000\,\mathrm{MN/m^2}$, initial yield limit $f_{yk} = 500\,\mathrm{MN/m^2}$, ultimate strength $f_t = 550\,\mathrm{MN/m^2}$, strain at ultimate strength $\epsilon_u = 0.05$. The latter values lead to a hardening modulus $E_T = 1053\,\mathrm{MN/m^2}$.

The *reinforcement* is modeled with two orthogonal reinforcement sheets with indices $i = 1, 2$. The parameters are chosen with $\varphi_{s1} = 0$, $b_{s1} = 0.006$ m and $\varphi_{s2} = \pi/2$, $b_{s2} = 0.006$ m which corresponds to reinforcement ratios of $\rho_{s1} = \rho_{s2} = 1\%$. Plane stress conditions are assumed for the concrete part.

The *loading* is applied by displacement control of a node, where a concentrated load acts upon, see Fig. 4.1a. Distributed loads are neglected. The actual loading is given by the reaction force of the displaced node. In contrast to load control the control of displacements allows to model limit states of a structure, i.e., limited loading with increasing displacements. The term loading is also maintained for control of displacements. The target displacement of the loaded node is prescribed with 0.04 m.

The *discretization* is shown in Fig. 6.10a. It consists of 209 nodes and $3 \times 176 + 1$ quad elements, see Section 1.3, of uniform size and quadratic shape. Thereof, 176 elements are used for the concrete layer and 176 elements each for the two reinforcement directions. The integration order, see Eq. (1.68), is generally chosen with $n_i = 1$ leading to 2×2 integration within a particular element. The characteristic element length is determined with $L_c = 0.25$ m following Eq. (6.32). Special care has to be given for the lower left-hand support. A *nodal* support of the reinforced concrete deep beam itself is not appropriate as this leads to concentrated high tensile stresses. A more realistic approach is given with a support by an extra element, whereby this element is assumed as linear elastic with $E_c = 31\,900\,\mathrm{M/m^2}$, $\nu = 0.2$ and with a vertical nodal support of its lower two nodes. This support may move freely in the horizontal direction.

The *solution procedure* deserves remarks. The problem is physically nonlinear due to concrete cracking and elastoplastic reinforcement behavior and requires and incrementally
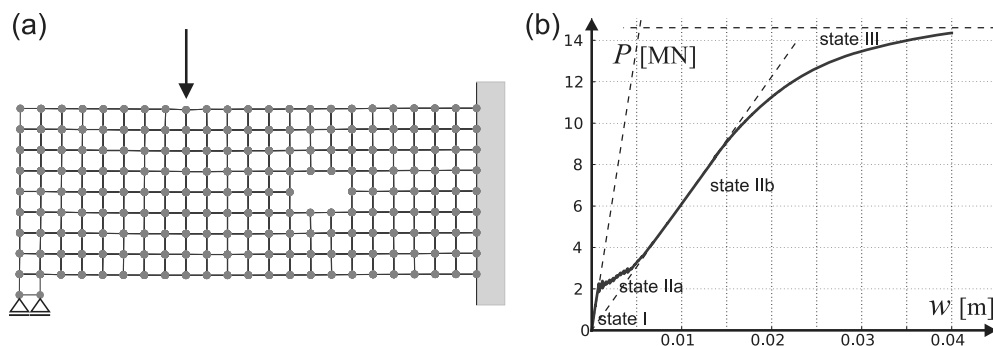

Figure 6.10: Example 6.3 (a) Discretization. (b) Load–displacement relation.

iterative approach, see Section 1.6. Cracking will start in an early stage of loading. In the case of a detection of a new crack an equilibrium iteration sequence is performed without applying a load increase. A new loading increment is only applied on a cracked system in equilibrium. This procedure is separately performed for each new crack.

- A new crack generally leads to state changes, see Section 6.2, in previously existing cracks, e.g., a loading state of a previously existing crack changes into unloading or crack closure with the initiation of a new crack.

This leads to a nonsmooth, rough load–displacement behavior leading to derivatives with jumps. Thus, special care has to be given to the iteration matrix in the incrementally iterative solution method. The BFGS method, see Appendix A, is used instead of the Newton–Raphson method, as the latter often will not lead to convergence during the equilibrium iterations.

A proper selection of load or pseudo time *step increments* is a matter of experience and sometimes intuition is required in such problems. A value $\Delta t = 0.01$ is chosen here with a target value $t = 1.0$ and 100 iteration sequences arise caused by load increments. But there are roughly 500 more iteration sequences caused by cracking. Each iteration sequence may have a large number of single iterations before it reaches convergence or equilibrium, respectively. Taking all together the computation time is large compared to all other examples.

Computational results are described in the following. The computed curve for the load depending on the displacement of the loaded node is shown in Fig. 6.10b. Four stages can be seen as is typical for reinforced concrete:

- Uncracked state I.

- Crack formation state IIa with elastic reinforcement behavior.

- Stabilized cracking state IIb with elastic reinforcement behavior.

- Stabilized cracking state III with yielding reinforcement.

This is basically the same behavior as for the reinforced concrete tension bar, see Example 2.4. But the transitions are gradual in the current example, as a larger number of elements are included in a state change, each with a differentiated behavior. The loading for a displacement of 4 cm is computed with $P = 14.3\,\mathrm{MN}$. This should be near to the ultimate limit load of this model due to the horizontal characteristic of the load–displacement curve.

Computed *concrete stresses* of the last computed step are shown in Fig. 6.11a. Low tensile stresses remain according to the prescribed tensile strength. The minimum concrete stress ($\to$ maximum compression) is computed with $-96\,\mathrm{MN/m^2}$ near the load application point. This computed value is beyond the compressive strength of normal graded concrete, but a linear elastic behavior is assumed for compressive concrete in the current model. On the other hand, a concentrated point load as assumed does not occur in reality. Furthermore, a biaxial compressive state is given which leads to some amount of strength increase of concrete, see Fig. 5.7a.

The computed *reinforcement stresses* in the last computed step are shown in Fig. 6.11b. Horizontal lines belong to the stresses of the horizontal reinforcement direction, vertical lines to the stresses of the vertical stress direction. Horizontal stresses reach the yield strength in the lower midspan area and the upper right side support area. Small reinforcement areas have compression due to bond with concrete.
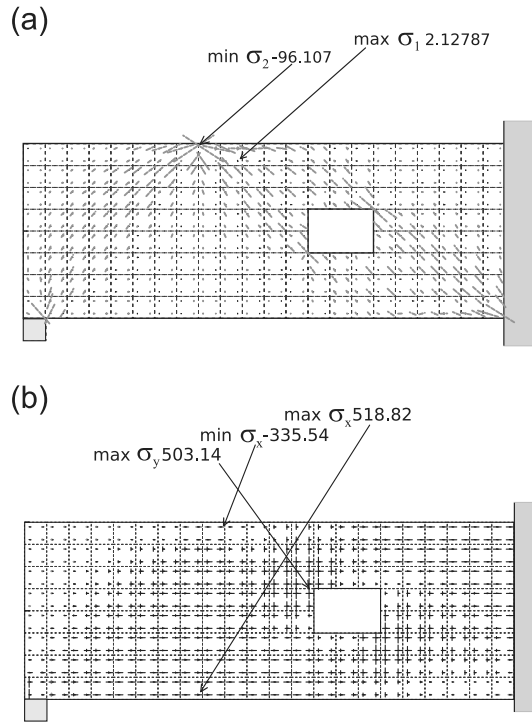
(a)

(b)

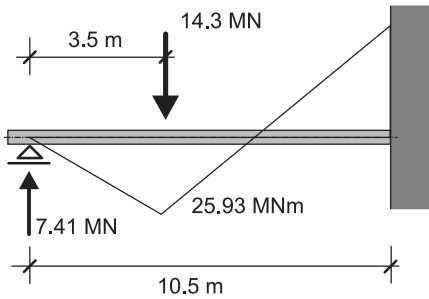Figure 6.11: Example 6.3 principal stresses. (a) Concrete. (b) Reinforcement.

Figure 6.12: Example 6.3 beam model.

Some simple manual *comparative calculations* are recommended for nonlinear numerical calculations if possible. The external loading connected with the prescribed displacement of 4 cm is determined with $P = 14.3\,\text{MN}$ at the point of application in the last computed step and the vertical support reaction on the left-hand lower support with $A = 7.46\,\text{MN}$.

A manual calculation with a simple beam model – span $L = 10.5$ m measured from inner support edges, loaded at $L_p = 3.5$ m, hinge support at the lower left side, fully restrained on right side, see Fig. 6.12 – leads to a left-hand support reaction of $A = 7.41$ MN and a mid-span moment $M_f = 25.9$ MNm. An internal lever arm of $d = 3$ m between resulting compression and tension forces is assumed regarding the cross section below the loaded node. This leads to a reinforcement force of $F_s = 25.9/3 = 8.6$ MN and a reinforcement of $A_s \approx 170 \, \text{cm}^2$ assuming a reinforcement stress of $500 \, \text{MN/m}^2$. With a reinforcement ratio $\rho = 1\,\%$ and a deep beam thickness $b = 0.6$ m this requires a reinforcement area of $170/0.6 \approx 2.8$ m in the vertical direction beginning from the bottom. This roughly matches to the area of computed reinforcement yielding, see Fig. 6.11b.

End Example 6.3

The model of Example 6.3 combines equilibrium, nonlinear material behavior with limited material strength and – in contrast to the companion Example 6.2 – kinematic compatibility. An issue remains with the actually limited compressive strength of concrete, which has not been considered.

6.5 Embedded Reinforcement

The combination of concrete and reinforcement for the case of rigid bond has been demonstrated with the overlay approach, see Fig. 6.9. This can be applied for reinforcement sheets as well as for bar elements representing single rebars. An alternative for rigid bond is given by the *embedding of reinforcement.*. This is again demonstrated with the quad element, see Section 1.3. Such an element has a part of a rebar embedded whose position is given as a line with an arbitrary orientation.

The overlay approach introduces position constraints insofar as nodes of the concrete part and the reinforcement part coincide. An embedded reinforcement may have an arbitrary position, see Fig. 6.13a. A unique element without overlays is used for the interpolation of displacements according to Eqs. (1.18, 1.35). This leads to continuous strains according to
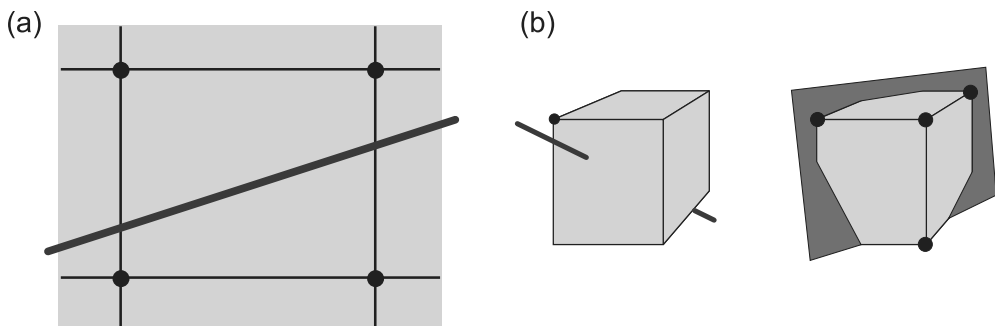

Figure 6.13: Reinforcement embeddings. (a) 2D. (b) 3D.

Eq. (1.40). Strains lead to stresses and stresses have to be transformed into internal nodal forces by integration, see Eq. (1.9).

Standard numerical integration, with, e.g., Gauss integration, see Eq. (1.68), relies on smooth stress fields to yield reliable integration results. This is generally the case for homogeneous materials but not for materials with reinforcing embeddings.

- Stress discontinuities arise within elements with an embedded reinforcement.

Such stress continuities are given with the stress along the rebar line. We assume the position of the rebar line in global coordinates x, y with

$$y = a\,x + b \tag{6.50}$$

with constant coefficients a, b. This can be transformed into a rebar line position described with local coordinates r, s

$$s = \tilde{a}\,r + \tilde{b}, \quad -1 \le r \le 1 \tag{6.51}$$

using Eq. (1.36). Strains along the rebar line can be determined by Eq. (1.40) using these local coordinates. As rebar stress are uniaxial the global strains ϵ_x, ϵ_y, γ_{xy} have to be transformed into the direction φ_s of the rebar according to Eq. (6.45). The resulting strains $\tilde{\epsilon}_x$, $\tilde{\epsilon}_y$, $\tilde{\gamma}_{xy}$ are not principal strains ($\tilde{\gamma}_{xy} \ne 0$), but only the component $\tilde{\epsilon}_x$ is relevant for a rebar stress state $\tilde{\sigma}_x \ne 0$ and $\tilde{\sigma}_y = \tilde{\sigma}_{xy} = 0$. The stress component $\tilde{\sigma}_x$ is derived from the material law for the reinforcement, see Section 2.3. Finally, the the stress discontinuity along the rebar line is determined transforming the stress state $\tilde{\boldsymbol{\sigma}}$ back to the global system using Eq. (6.47) leading to a rebar stress $\boldsymbol{\sigma}_s$.

As the position of the rebar line is arbitrary its contribution to internal forces, see Eq. (1.9), is generally not captured, with, e.g., Gauss integration according to Eq. (1.68) which covers the concrete part only.

- The contribution of rebar stresses to the internal nodal forces have to be superposed to the contribution of concrete stresses with their own integration procedure.

An additional Gauss integration along a line in analogy to Eq. (1.68)

$$\int_{-1}^{+1} \boldsymbol{\sigma}_s(r)\,J(r)\,A_s\,\mathrm{d}r = A_s \sum_{i=0}^{n_i} \eta_i\,\boldsymbol{\sigma}_s(\xi_i)\,J(\xi_i) \tag{6.52}$$

may be used for this purpose. This uses the rebar cross-sectional area A_s, sampling points ξ_i and sampling weights η_i according to Table 1.1 and a Jacobian $J(r)$, see Eqs. (1.20,1.23), relating the local coordinate r to the global coordinate x. An integration order $n_i = 1$ with two integration points should be adequate for embedded rebars in quad elements also with integration order 1 and 2×2 integration points.

Contributions of rebar lines to tangential stiffness matrices, see Eq. (1.65), can be considered in an analogous way. In contrast to reinforcement overlays which allow for a flexible bond, see Fig. 6.8, an embedded reinforcement is restricted to rigid bond only. On the other hand, an overlay of rebars with rigid bond may be considered as a special case of an embedded reinforcement where the rebar line coincides with element boundaries. The embedding approach may be generalized for 3D states, see Fig. 6.13b.

Chapter 7

Slabs

7.1 A Placement

Elementary structural types treated up to now have been bars, beams, and plates. First of all these types are characterized by their geometric properties. Two geometric dimensions of bars and beams – height and width – are small compared to the length. One geometric dimension of plates – width – is small compared to height and length or span, respectively.

Slabs, as a further structural type has the height as small geometric dimension compared to width and span. The placement in a common geometric frame is shown in Fig. 7.1a. The name width is not really appropriate to denote the second long dimension. Actually it becomes another span in an area. Due to their geometric properties plates and slabs may be classified as *plane surface structures* while bars and beams are *line structures*. The difference between plates and slabs is given through the way a loading is applied: the loading direction for a plate is in-plane while the loading direction of a slab is normal to the slab's plane.

A position on the surface area of a slab is determined through coordinates x, y, see Fig. 7.1b. A position has cross sections with a z-direction and a corresponding coordinate. These coordinates form a Cartesian system. In contrast to beams an indefinite number of
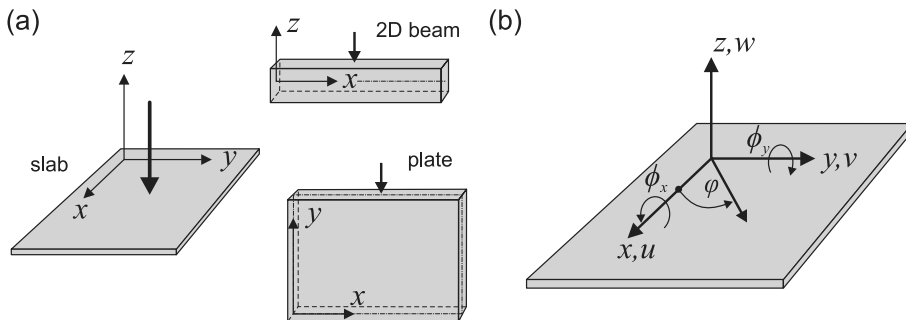
Figure 7.1: (a) Structural types. (b) Coordinate system for slabs.

cross sections exists in a position x, y which are characterized by an in-plane direction angle φ, see Fig. 7.1. Two cross sections are regarded as representative: the first with $\varphi = 0$ and a normal in the x-direction and the second with $\varphi = \pi/2$ and normal in the y-direction.

7.2   Cross-Sectional Behavior

7.2.1   Kinematic and Kinetic Basics

Each structural type is characterized by a kinematic assumption restraining the mathematical description of its displacements. The *kinematic assumption* for slabs is basically the same as for beams, see Section 3.1.1.

- The *Bernoulli–Navier hypothesis* states that undeformed plane cross sections of a slab remain plane during a deformation.

A reference axis has been chosen for beams as a reference to describe the displacement of plane cross sections. A plane surface area or *reference plane* is used for the same purpose regarding slabs. A coordinate system has already been defined in the previous section. The reference plane is placed in the midst of a slab. Bottom and top coordinates are given by $z_1 = -h/2$, $z_2 = h/2$ with the slab height h. A synonym for the height of slabs is *thickness*.

The displacements of every material point of a slab with the coordinates x, y, z are given with the horizontal displacements $u(x, y, z)$ in the x-direction and $v(x, y, z)$ in the y-direction and furthermore with the lateral displacement or deflections $w(x, y, z)$ in the z-direction. The Bernoulli hypothesis for slabs is included in the following formulation:

$$
\begin{aligned}
w(x, y, z) &= w(x, y, 0) \\
&= \bar{w}(x, y) \\
u(x, y, z) &= \bar{u}(x, y) - z\, \phi_y \\
&= \bar{u}(x, y) - z \left[\frac{\partial \bar{w}(x, y)}{\partial x} - \gamma_x(x, y) \right] \\
v(x, y, z) &= \bar{v}(x, y) - z\, \phi_x \\
&= \bar{v}(x, y) - z \left[\frac{\partial \bar{w}(x, y)}{\partial y} - \gamma_y(x, y) \right]
\end{aligned}
\tag{7.1}
$$

with *cross-section rotation angles* $\phi_x(x, y)$, $\phi_y(x, y)$, *shear angles* $\gamma_x(x, y)$, $\gamma_y(x, y)$ and displacements $\bar{u}(x, y)$, $\bar{v}(x, y)$, $\bar{w}(x, y)$ of the reference plane.

- Equation $(7.1)_1$ states that every material point in a cross section has the same deflection but it may change with the reference plane coordinates.

- Equation $(7.1)_3$ states that the cross section with x-normal rotates by an angle ϕ_y during a deformation.

- Equation $(7.1)_5$ states that the cross section with y-normal rotates by an angle ϕ_x during a deformation.

– Equations $(7.1)_{4,6}$ decouple the rotations of the cross sections ϕ_y, ϕ_x and the slopes of the reference plane $\partial \bar{w}/\partial x, \partial \bar{w}/\partial y$ by the angles γ_x, γ_y. The relations are

$$\phi_y = \frac{\partial \bar{w}}{\partial x} - \gamma_x, \quad \phi_x = \frac{\partial \bar{w}}{\partial y} - \gamma_y \tag{7.2}$$

compare Eq. (3.2). The connection of γ with shear becomes evident with its relation to the shear strain, see Eqs. $(7.3)_{4,5}$.

– The case $\gamma_x \ll \phi_y,\, \gamma_y \ll \phi_x$ with the assumption $\gamma_x, \gamma_y = 0$ leads to the *Kirchhoff slab* where cross sections remain rectangular to the reference plane after deformation. The inclusion of shear deformation leads to the *Reissner–Mindlin slab*. Cross sections remain plane after deformation but are not rectangular to the reference plane after deformation for the Reissner–Mindlin slab.

Slab kinematics may be considered as extension of beam kinematics, see Eq. (3.3), in two directions. Thus, slab strains are defined as

$$
\begin{aligned}
\epsilon_x &= \frac{\partial u}{\partial x} & &= \frac{\partial \bar{u}}{\partial x} - z\left[\frac{\partial^2 \bar{w}}{\partial x^2} - \frac{\partial \gamma_x}{\partial x}\right] \\
\epsilon_y &= \frac{\partial v}{\partial y} & &= \frac{\partial \bar{v}}{\partial y} - z\left[\frac{\partial^2 \bar{w}}{\partial y^2} - \frac{\partial \gamma_y}{\partial y}\right] \\
\gamma_{xy} &= \frac{\partial u}{\partial y} + \frac{\partial v}{\partial x} & &= \frac{\partial \bar{u}}{\partial y} + \frac{\partial \bar{v}}{\partial x} - z\left[2\frac{\partial^2 \bar{w}}{\partial x \partial y} - \frac{\partial \gamma_x}{\partial y} - \frac{\partial \gamma_y}{\partial x}\right] \\
\gamma_{xz} &= \frac{\partial u}{\partial z} + \frac{\partial w}{\partial x} & &= -\frac{\partial \bar{w}}{\partial x} + \gamma_x + \frac{\partial w}{\partial x} = \gamma_x \\
\gamma_{yz} &= \frac{\partial v}{\partial z} + \frac{\partial w}{\partial y} & &= -\frac{\partial \bar{w}}{\partial y} + \gamma_y + \frac{\partial w}{\partial y} = \gamma_y
\end{aligned}
\tag{7.3}
$$

The strains of the reference plane are given by

$$\bar{\epsilon}_x = \frac{\partial \bar{u}}{\partial x}, \quad \bar{\epsilon}_y = \frac{\partial \bar{v}}{\partial y}, \quad \bar{\gamma}_{xy} = \frac{\partial \bar{u}}{\partial y} + \frac{\partial \bar{v}}{\partial x} \tag{7.4}$$

With the inclusion of shear deformations curvature is advantageously defined as

$$
\begin{aligned}
\kappa_x &= \frac{\partial^2 w}{\partial x^2} - \frac{\partial \gamma_x}{\partial x} \\
\kappa_y &= \frac{\partial^2 w}{\partial y^2} - \frac{\partial \gamma_y}{\partial y} \\
\kappa_{xy} &= 2\frac{\partial^2 w}{\partial x \partial y} - \frac{\partial \gamma_x}{\partial y} - \frac{\partial \gamma_y}{\partial x}
\end{aligned}
\tag{7.5}
$$

The quantities $\bar{\epsilon}_x, \bar{\epsilon}_x, \bar{\epsilon}_{xy}$ and $\kappa_x, \kappa_y, \kappa_{xy}$ each form the components of a symmetric second-order tensor defined by a displacement direction and the direction of a reference plane.

• The variables $\bar{\epsilon}_x, \bar{\epsilon}_x, \bar{\epsilon}_{xy},\ \kappa_x, \kappa_y, \kappa_{xy},\ \gamma_x, \gamma_y$ which depend on x, y only are chosen as *generalized strains* for slabs whereby $\bar{\epsilon}_x, \bar{\epsilon}_x, \bar{\epsilon}_{xy}$ indicate the strain of the reference plane, $\kappa_x, \kappa_y, \kappa_{xy}$ the curvatures of deformed cross sections and γ_x, γ_y the shearing angles of deformed cross sections relative to the reference plane.

Combining Eqs. (7.3, 7.5) leads to strain formulations

$$\epsilon_x = \bar{\epsilon}_x - z\,\kappa_x, \quad \epsilon_y = \bar{\epsilon}_y - z\,\kappa_y, \quad \gamma_{xy} = \bar{\gamma}_{xy} - z\,\kappa_{xy} \tag{7.6}$$

with $\epsilon_x, \epsilon_y, \gamma_{xy}$ linearly varying along the beam height with extremal values at the top and bottom of the cross section and constant $\gamma_{xz} = \gamma_x, \gamma_{yz} = \gamma_y$ along the beam height. Nevertheless, all these strains are varying with the reference plane coordinates x, y.

At a given location x, y these strains may be transformed to other directions leading to values $\epsilon'_x, \epsilon'_y, \gamma'_{xy}$. The orientation is measured by the angle φ counterclockwise against the x-axis. The transformation rule is given by

$$\begin{pmatrix} \tilde{\epsilon}_x \\ \tilde{\epsilon}'_y \\ \tilde{\gamma}_{xy} \end{pmatrix} = \begin{bmatrix} \cos^2\varphi & \sin^2\varphi & \cos\varphi\sin\varphi \\ \sin^2\varphi & \cos^2\varphi & -\cos\varphi\sin\varphi \\ -2\cos\varphi\sin\varphi & 2\cos\varphi\sin\varphi & \cos^2\varphi - \sin^2\varphi \end{bmatrix} \cdot \begin{pmatrix} \epsilon_x \\ \epsilon_y \\ \gamma_{xy} \end{pmatrix} \tag{7.7}$$

see Appendix C, Eq. (C.13). This transformation is connected with a principal direction φ_ϵ with $\tilde{\gamma}_{xy} = 0$ and principal strains ϵ_1, ϵ_2. For a given x, y the principal values $\epsilon_1, \epsilon_2, \varphi_\epsilon$ may vary along the height z.

Regarding the *reference plane* strains $\bar{\epsilon}_x, \bar{\epsilon}_y, \bar{\gamma}_{xy}$ and curvatures $\kappa_x, \kappa_y, \kappa_{xy}$ they have the same transformation rule (Eq. (7.7)). Thus, they also have principal values and directions $\bar{\epsilon}_1, \bar{\epsilon}_2, \varphi_{\bar{\epsilon}}$ and $\kappa_1, \kappa_2, \varphi_\kappa$, respectively. But the orientation of the principal systems must not be the same, i.e., $\varphi_\epsilon, \varphi_{\bar{\epsilon}}$ and φ_κ may have different values. But $\varphi_\epsilon = \varphi_{\bar{\epsilon}}$ in the case of $\kappa_x = \kappa_y = \kappa_{xy} = 0$ and $\varphi_\epsilon = \varphi_\kappa$ in the case of $\bar{\epsilon}_x = \bar{\epsilon}_y = \bar{\epsilon}_{xy} = 0$ due to Eq. (7.6).

Generalized slab strains have to be connected to *generalized slab stresses* or internal forces, respectively, to describe the material behavior. At a slab position x, y such internal forces are defined as

$$n_x = \int_{-h/2}^{h/2} \sigma_x\,\mathrm{d}z, \quad n_y = \int_{-h/2}^{h/2} \sigma_y\,\mathrm{d}z, \quad n_{xy} = \int_{-h/2}^{h/2} \sigma_{xy}\,\mathrm{d}z$$

$$m_x = -\int_{-h/2}^{h/2} \sigma_x\,z\,\mathrm{d}z, \quad m_y = -\int_{-h/2}^{h/2} \sigma_y\,z\,\mathrm{d}z, \quad m_{xy} = -\int_{-h/2}^{h/2} \sigma_{xy}\,z\,\mathrm{d}z \tag{7.8}$$

$$v_x = \int_{-h/2}^{h/2} \sigma_{xz}\,\mathrm{d}z, \quad v_y = \int_{-h/2}^{h/2} \sigma_{yz}\,\mathrm{d}z$$

see Figs. 7.2 and 7.4. In analogy to generalized strains the quantities n_x, n_y, n_{xy} and m_x, m_y, m_{xy} each form a symmetric second-order tensor defined by a force direction and the direction of a reference plane.

Cauchy stresses $\sigma_x, \sigma_y, \sigma_{xy}, \sigma_{xz}, \sigma_{yz}$ depend on $\epsilon_x, \epsilon_y, \gamma_{xy}, \gamma_{xz}, \gamma_{yz}$ through a material law. Biaxial stress–strain relations are at least required in contrast to bars and beams. Such laws may be derived as special cases of multiaxial stress–strain relations, see Chapter 5. The corresponding relations between internal forces and generalized slab strains are derived through integration along slab thickness. This is exemplary demonstrated for linear elastic behavior in the following Section 7.2.2.

Equation (7.8) is a generalization of the corresponding relations for beams, see Eq. (3.9), and generalized pairs $(n_x, \bar{\epsilon}_x), \ldots, (m_x, \kappa_x), \ldots$ and $(v_x, \gamma_x), \ldots$ are conjugate with respect to internal energy.
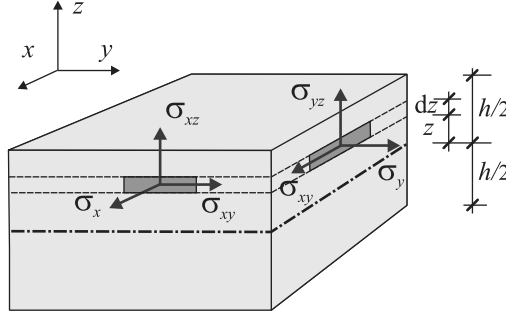
Figure 7.2: Stresses on slab element.

7.2.2 Linear Elastic Behavior

We consider linear isotropic elasticity under plane stress conditions, see Eq. (1.45). The combination with Eq. (7.6) yields normal stresses

$$
\begin{aligned}
\sigma_x &= \frac{E}{1-\nu^2}\left(\epsilon_x + \nu\,\epsilon_y\right) \\
&= \frac{E}{1-\nu^2}\left[(\bar{\epsilon}_x + \nu\bar{\epsilon}_y) - z\left(\kappa_x + \nu\,\kappa_y\right)\right] \\
\sigma_y &= \frac{E}{1-\nu^2}\left[(\bar{\epsilon}_y + \nu\bar{\epsilon}_x) - z\left(\kappa_y + \nu\,\kappa_x\right)\right]
\end{aligned}
\tag{7.9}
$$

and as a shear stress in planes parallel to the reference plane

$$
\sigma_{xy} = G\,\gamma_{xy} = G\left(\bar{\gamma}_{xy} - z\,\kappa_{xy}\right)
\tag{7.10}
$$

with $G = E/2(1+\nu)$. The both remaining out-of-plane shear stress components are derived from Eq. (5.24) as

$$
\sigma_{xz} = G\,\gamma_{xz} = G\,\gamma_x, \quad \sigma_{yz} = G\,\gamma_{yz} = G\,\gamma_y
\tag{7.11}
$$

Stresses from Eqs. (7.9–7.11) are used to determine internal forces from Eq. (7.8) leading to

$$
\begin{aligned}
n_x &= \frac{E}{1-\nu^2}\left(\bar{\epsilon}_x + \nu\,\bar{\epsilon}_y\right)\int_{-h/2}^{h/2}\mathrm{d}z = K_n\left(\bar{\epsilon}_x + \nu\,\bar{\epsilon}_y\right) \\
n_y &= K_n\left(\bar{\epsilon}_y + \nu\,\bar{\epsilon}_x\right) \\
n_{xy} &= \frac{E}{2(1+\nu)}\,\bar{\epsilon}_{xy}\int_{-h/2}^{h/2}\mathrm{d}z = (1-\nu)\,K_n\,\frac{\bar{\epsilon}_{xy}}{2} \\
m_x &= \frac{E}{1-\nu^2}\left(\kappa_x + \nu\,\kappa_y\right)\int_{-h/2}^{h/2}z^2\,\mathrm{d}z = K\left(\kappa_x + \nu\,\kappa_y\right) \\
m_y &= K\left(\kappa_y + \nu\,\kappa_x\right) \\
m_{xy} &= \frac{E}{2(1+\nu)}\,\kappa_{xy}\int_{-h/2}^{h/2}z^2\,\mathrm{d}z = (1-\nu)\,K\,\frac{\kappa_{xy}}{2} = (1-\nu)\,K\,\frac{\partial^2 w}{\partial x \partial y}
\end{aligned}
\tag{7.12}
$$

$$v_x = \alpha G \gamma_x \int_{-h/2}^{h/2} \mathrm{d}z = \alpha\, Gh\, \gamma_x$$

$$v_y = \alpha\, Gh\, \gamma_y$$

regarding $\int_{-h/2}^{h/2} z\mathrm{d}z = 0$ and with the slab stiffness

$$K_n = \frac{E\,h}{1-\nu^2}, \quad K = \frac{E\,h^3}{12(1-\nu^2)} \tag{7.13}$$

see also [31, Section 189], Young's modulus E, Poisson's ratio ν, and the shear reduction factor α, see Section 3.1.2. This is again an extension of the corresponding beam relations, see Eqs. (3.9–3.13). In order to determine solutions, we regard a balance of variables and equations:

– Variables: Three displacement variables $\bar{u}, \bar{v}, w$, eight deformation variables $\bar{\epsilon}_x, \bar{\epsilon}_y, \bar{\gamma}_{xy}$, $\kappa_x, \kappa_y, \kappa_{xy}, \gamma_x, \gamma_y$, 8 force variables $n_x, n_y, n_{xy}, m_x, m_y, m_{xy}, v_x, v_y$, which makes together 19 variables.

– Equations: Eight force–displacement relations (7.12), six kinematic relations (7.4), (7.5), which makes together 14 equations. This is complemented with five equilibrium conditions, see Eqs. (7.16)–(7.18).

The slopes $\partial w/\partial x$, $\partial w/\partial y$ need not to be addressed in this particular balance. In case the enumerated variables are directly determined from the enumerated equations, the slopes result from the derivatives of the deflection surface $w(x,y)$.

Plates are included as a special case with $\kappa_x = \kappa_y = \kappa_{xy} = 0$ and $\gamma_x = \gamma_y = 0$ leading to $m_x = m_y = m_{xy} = 0$ and $v_x = v_y = 0$.

7.2.3 Reinforced Cracked Sections

The limited strength of concrete and in particular its limited tensile strength has again to be regarded. The uniaxial case has already been treated in Section 3.1.3. An outline for a biaxial generalization is described in the following. We regard an arbitrary slab position x, y.

A *layer model* is applied in this position with respect to cross sections. The slab thickness is subdivided into layers, see Fig. 7.3. The strain of each layer is determined by the kinematic relations Eqs. (7.3). Furthermore, the stress of each layer is computed from strains with an appropriate material law. This has the following aspects:

– The in-plane reaction – stresses from $\epsilon_x, \epsilon_y, \gamma_{xy}$ – is decoupled from vertical shear reaction – stresses from γ_{xz}, γ_{yz}. This corresponds to the approach for beams, see Sections 3.1.3.1 and 3.5.4.

– The in-plane reaction is biaxial. Each layer is regarded as a plate. Thus, a biaxial material law can be used.

– Each layer may have its own material law which allows one to distinguish between concrete layers and reinforcement layers. This implies rigid bond due to the Bernoulli–Navier hypothesis for slab cross sections, see Eqs. (7.1).
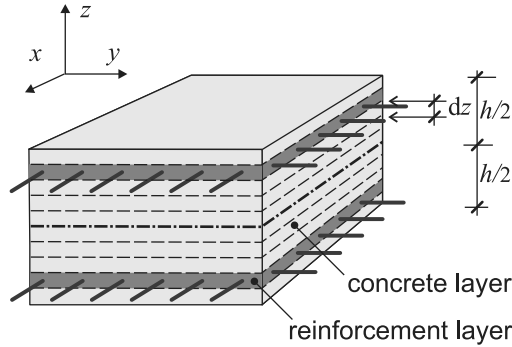
Figure 7.3: Layer model.

– Regarding concrete, a first approach to model cracks in a biaxial setting has been described in Section 6.2. This includes limited tensile strength, the Rankine crack criterion, smeared cracks, crack orientation, crack width, crack tractions, and softening.

In difference to plates cracking states will generally vary for different layers along the slab thickness in a slab position. This concerns the event of cracking itself, but furthermore actual values for crack orientation and crack width.

– Regarding the reinforcement, smeared layers or reinforcement sheets are appropriate as have been described in Section 6.4.

This approach yields stresses $\sigma_x, \sigma_y, \sigma_{xy}$ for every layer in a slab position x, y. Internal forces n_x, n_y, n_{xy} and m_x, m_y, m_{xy} are determined according to Eqs. (7.8). An integration of stresses is performed along thickness to determine resulting internal forces according to Eq. (7.8). The integrations along the thickness coordinate z has to be performed numerically. One-dimensional integration with the schemes of Gauss, Simpson, Newton–Cotes, or Labatto may be used.

Internal shear forces v_x, v_y remain to be treated. A layer is not capable to cover transverse shear with stress components σ_{xz}, σ_{yz}. Transverse shear for reinforced concrete has already been discussed in Section 3.5.4 in the context of structural beams. Structural beams and slabs both rely on the assumption of plane deformed cross sections. Regarding transverse shear behavior of slabs a substantially better approach as the strut-and-tie model for beam shear is not yet available. This leads to a proposal adopted from Eq. (7.12) with

$$v_x = \alpha\, Gh\, \gamma_x, \quad v_y = \alpha\, Gh\, \gamma_y, \quad G = \frac{E_c}{2(1+\nu)} \tag{7.14}$$

with a shear modulus G, a reduction factor α, and the initial values of Young's modulus E_c and Poisson's ratio ν of the respective concrete. The reduction factor may be chosen with $\alpha = 0.5$ according to Section 3.5.4.

A tangential material stiffness can be derived in analogy or extension, respectively, of the tangential material stiffness for reinforced concrete beams, see Eqs. (3.53–3.56). The general

form for an incremental internal forces–generalized strain relation is given by

$$
\begin{Bmatrix}
n_x \\
n_y \\
n_{xy} \\
m_x \\
m_y \\
m_{xy} \\
v_x \\
v_y
\end{Bmatrix}
=
\begin{bmatrix}
C_{T11} & C_{T12} & C_{T13} & C_{T14} & C_{T15} & C_{T16} & 0 & 0 \\
C_{T21} & C_{T22} & C_{T23} & C_{T24} & C_{T25} & C_{T26} & 0 & 0 \\
C_{T31} & C_{T32} & C_{T33} & C_{T34} & C_{T35} & C_{T36} & 0 & 0 \\
C_{T41} & C_{T42} & C_{T43} & C_{T44} & C_{T45} & C_{T46} & 0 & 0 \\
C_{T51} & C_{T52} & C_{T53} & C_{T54} & C_{T55} & C_{T56} & 0 & 0 \\
C_{T61} & C_{T62} & C_{T63} & C_{T64} & C_{T65} & C_{T66} & 0 & 0 \\
0 & 0 & 0 & 0 & 0 & 0 & C_{T77} & 0 \\
0 & 0 & 0 & 0 & 0 & 0 & 0 & C_{T88}
\end{bmatrix}
\cdot
\begin{Bmatrix}
\bar{\epsilon}_x \\
\bar{\epsilon}_y \\
\bar{\gamma}_{xy} \\
\kappa_x \\
\kappa_y \\
\kappa_{xy} \\
\gamma_x \\
\gamma_y
\end{Bmatrix}
\tag{7.15}
$$

within the actually given framework. This includes a coupling between internal normal forces and internal moments which is characteristic for cracked reinforced concrete cross sections, see Section 3.1.3.2.

The coefficients C_{Tij} of the tangential material stiffness matrix to a large extent have to be derived each with its particular numerical integration. Thus, the layer model is computationally expensive.

A partially decoupled model may be derived as follows. This is based on principal values for strains $\bar{\epsilon}_x, \bar{\epsilon}_y, \bar{\gamma}_{xy}$ and curvatures $\kappa_x, \kappa_y, \kappa_{xy}$ of the reference plane. *It is assumed that the principal directions of strains and curvature are at least approximately the same.* Thus, a transformation to a common principal system is possible. Furthermore, each principal direction is treated like a beam cross section with unit width, see Section 3.1.3. Thus, lateral expansion or Poisson's effects are disregarded. The stresses along the cross section in each principal direction are determined as for cracked reinforced concrete beams. The integration of stresses over slab thickness leads to principal moments m_1, m_2 and principal normal forces n_1, n_2. Finally, the principal values are transformed back to the global system to yield internal moments m_x, m_y, m_{xy} and internal normal forces n_x, n_y, n_{xy}.

7.3   Equilibrium of Slabs

7.3.1   Strong Equilibrium

Equilibrium has to be regarded as the third item beneath kinematic compatibility and material laws. The symbols u, v will be used for the displacements of the reference plane instead of $\bar{u}, \bar{v}$ in the following to simplify the notation. We regard a position x, y of the reference plane with a distributed loading p_x, p_y, p_z. Other descriptions use an opposite sign convention for z-coordinate and the corresponding displacement w. This reverses the sign in the moment–curvature relations.

The *strong differential formulation* of *static equilibrium* for an infinitesimal section of a slab is at first considered. The internal forces are shown in Fig. 7.4. Equilibrium of normal forces in the x- and y-directions is given by

$$
\frac{\partial n_x}{\partial x} + \frac{\partial n_{xy}}{\partial y} + p_x = 0, \quad \frac{\partial n_y}{\partial y} + \frac{\partial n_{xy}}{\partial x} + p_y = 0 \tag{7.16}
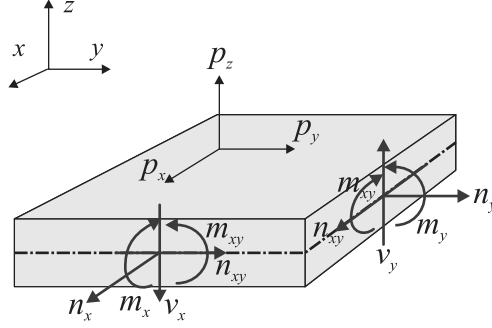$$

Figure 7.4: Slab equilibrium.

equilibrium of shear forces in the z-direction with

$$\frac{\partial v_x}{\partial x} + \frac{\partial v_y}{\partial y} + p_z = 0 \tag{7.17}$$

and equilibrium of moments with

$$\frac{\partial m_x}{\partial x} + \frac{\partial m_{xy}}{\partial y} + v_x = 0, \quad \frac{\partial m_y}{\partial y} + \frac{\partial m_{xy}}{\partial x} + v_y = 0 \tag{7.18}$$

These equilibrium conditions are independent from kinematic assumptions and material laws. The case of plates is included as a special case with $p_z = 0$. This leaves Eqs. (7.16) only.

We regard the linear elastic *Kirchhoff slab* as a commonly used but another special case. The combination of Eqs. (7.18, 7.17) yields

$$\frac{\partial^2 m_x}{\partial x^2} + 2\frac{\partial^2 m_{xy}}{\partial x \partial y} + \frac{\partial^2 m_y}{\partial y^2} = p_z \tag{7.19}$$

Shear deformations are neglected. Thus, Eq. (7.5) leads to

$$\kappa_x = \frac{\partial^2 w}{\partial x^2}, \quad \kappa_y = \frac{\partial^2 w}{\partial y^2}, \quad \kappa_{xy} = 2\frac{\partial^2 w}{\partial x \partial y} \tag{7.20}$$

Using this for Eqs. $(7.12)_{4-6}$ leads to

$$\begin{aligned}
\frac{\partial^2 m_x}{\partial x^2} &= K\left(\frac{\partial^2 \kappa_x}{\partial x^2} + \nu\frac{\partial^2 \kappa_y}{\partial x^2}\right) &= K\left(\frac{\partial^4 w}{\partial x^4} + \nu\frac{\partial^4 w}{\partial x^2 \partial y^2}\right) \\
\frac{\partial^2 m_y}{\partial y^2} &= K\left(\frac{\partial^2 \kappa_y}{\partial y^2} + \nu\frac{\partial^2 \kappa_x}{\partial y^2}\right) &= K\left(\frac{\partial^4 w}{\partial y^4} + \nu\frac{\partial^4 w}{\partial y^2 \partial x^2}\right) \\
\frac{\partial^2 m_{xy}}{\partial x \partial y} &= (1-\nu)\frac{K}{2}\frac{\partial^2 \kappa_{xy}}{\partial x \partial y} &= (1-\nu)\,K\,\frac{\partial^4 w}{\partial x^2 \partial y^2}
\end{aligned} \tag{7.21}$$

The combination of Eqs. (7.19) and (7.21) finally gives

$$\frac{\partial^4 w}{\partial x^4} + \nu\frac{\partial^4 w}{\partial x^2 \partial y^2} + 2(1-\nu)\frac{\partial^4 w}{\partial x^2 \partial y^2} + \frac{\partial^4 w}{\partial y^4} + \nu\frac{\partial^4 w}{\partial y^2 \partial x^2} = \frac{p_z}{K} \tag{7.22}$$

or the well-known relation

$$\frac{\partial^4 w}{\partial x^4} + 2\frac{\partial^4 w}{\partial x^2 \partial y^2} + \frac{\partial^4 w}{\partial y^4} = \frac{p_z}{K} \tag{7.23}$$

with the stiffness K from Eq. (7.13). Boundary conditions are given with appropriate combinations of w, $\frac{\partial w}{\partial x}$, $\frac{\partial^2 w}{\partial x^2}$, $\frac{\partial^3 w}{\partial x^3}$. The physical meaning of the latter comes from the relations like

$$m_x = K\left(\frac{\partial^2 w}{\partial x^2} + \nu\frac{\partial^2 w}{\partial y^2}\right), \qquad v_x = -\left(\frac{\partial m_x}{\partial x} + \frac{\partial m_{xy}}{\partial y}\right) \tag{7.24}$$

and similar relations for the other internal forces, see Eqs. (7.12). The determination of analytical solutions for the partial differential equation of fourth-order Eq. (7.23) is challenging from a mathematical point of view. A comprehensive discussion is given in [31].

7.3.2   Weak Equilibrium

Equilibrium again has to be reformulated as *weak integral equilibrium*. To start with, we reconsider the kinematic relations (7.2, 7.5) as

$$
\begin{aligned}
\phi_y &= \frac{\partial w}{\partial x} - \gamma_x \quad \rightarrow \quad \gamma_x = \frac{\partial w}{\partial x} - \phi_y \\
\phi_x &= \frac{\partial w}{\partial y} - \gamma_y \quad \rightarrow \quad \gamma_y = \frac{\partial w}{\partial y} - \phi_x \\
\kappa_x &= \frac{\partial^2 w}{\partial x^2} - \frac{\partial \gamma_x}{\partial x} = \frac{\partial \phi_y}{\partial x} \\
\kappa_y &= \frac{\partial^2 w}{\partial y^2} - \frac{\partial \gamma_y}{\partial y} = \frac{\partial \phi_x}{\partial y} \\
\kappa_{xy} &= \frac{\partial \phi_y}{\partial y} + \frac{\partial \phi_x}{\partial x}
\end{aligned}
\tag{7.25}
$$

An equivalent to the strong differential equilibrium formulation (Eqs. (7.16–7.18)) is given by the *weak integral equilibrium* formulation for a slab of area A with a *potential coupling* of normal forces and moments

$$
\begin{aligned}
&\int_A \delta u\left(\frac{\partial n_x}{\partial x} + \frac{\partial n_{xy}}{\partial y} + p_x\right)\mathrm{d}A \\
&\quad + \int_A \delta v\left(\frac{\partial n_y}{\partial y} + \frac{\partial n_{xy}}{\partial x} + p_y\right)\mathrm{d}A + \int_A \delta w\left(\frac{\partial v_x}{\partial x} + \frac{\partial v_y}{\partial y} + p_z\right)\mathrm{d}A \\
&\quad\quad + \int_A \delta\phi_y\left(\frac{\partial m_x}{\partial x} + \frac{\partial m_{xy}}{\partial y} + v_x\right)\mathrm{d}A + \int_A \delta\phi_x\left(\frac{\partial m_y}{\partial y} + \frac{\partial m_{xy}}{\partial x} + v_y\right)\mathrm{d}A \\
&= 0
\end{aligned}
\tag{7.26}
$$

with test functions $\delta u, \delta v, \delta w, \delta\phi_y, \delta\phi_x$. This is a generalization of the approach for beams, see Section 3.2. Those terms with derivatives of internal forces are partially integrated leading to

$$\int_A \delta u \left(\frac{\partial n_x}{\partial x} + \frac{\partial n_{xy}}{\partial y} \right) \mathrm{d}A = -\int_A \left(\frac{\partial \delta u}{\partial x} n_x + \frac{\partial \delta u}{\partial y} n_{xy} \right) \mathrm{d}A + \oint_S \delta u(n_x e_x + n_{xy} e_y)\mathrm{d}S$$

$$\int_A \delta v \left(\frac{\partial n_y}{\partial y} + \frac{\partial n_{xy}}{\partial x} \right) \mathrm{d}A = -\int_A \left(\frac{\partial \delta v}{\partial y} n_y + \frac{\partial \delta v}{\partial x} n_{xy} \right) \mathrm{d}A + \oint_S \delta v(n_{xy} e_x + n_y e_y)\mathrm{d}S$$

$$\int_A \delta w \left(\frac{\partial v_x}{\partial x} + \frac{\partial v_y}{\partial y} \right) \mathrm{d}A = -\int_A \left(\frac{\partial \delta w}{\partial x} v_x + \frac{\partial \delta w}{\partial y} v_y \right) \mathrm{d}A + \oint_S \delta w(v_x e_x + v_y e_y)\mathrm{d}S$$

$$\int_A \delta\phi_y \left(\frac{\partial m_x}{\partial x} + \frac{\partial m_{xy}}{\partial y} + v_x \right) \mathrm{d}A = -\int_A \left(\frac{\partial \delta\phi_y}{\partial x} m_x + \frac{\partial \delta\phi_y}{\partial y} m_{xy} - \delta\phi_y v_x \right) \mathrm{d}A$$

$$+ \oint_S \delta\phi_y(m_x e_x + m_{xy} e_y)\mathrm{d}S$$

$$\int_A \delta\phi_x \left(\frac{\partial m_y}{\partial y} + \frac{\partial m_{xy}}{\partial x} + v_y \right) \mathrm{d}A = -\int_A \left(\frac{\partial \delta\phi_x}{\partial y} m_y + \frac{\partial \delta\phi_x}{\partial x} m_{xy} - \delta\phi_x v_y \right) \mathrm{d}A$$

$$+ \oint_S \delta\phi_x(m_{xy} e_x + m_y e_y)\mathrm{d}S$$

$$(7.27)$$

with line integrals $\oint_S$ along the slab's boundary S and a unit normal vector $\mathbf{e}$ with components e_x, e_y along the boundary. Combining Eqs. (7.26, 7.27) yields

$$\int_A (\delta\epsilon_x n_x + \delta\epsilon_y n_y + \delta\gamma_{xy} n_{xy} + \delta\kappa_x m_x + \delta\kappa_y m_y + \delta\kappa_{xy} m_{xy} + \delta\gamma_x v_x + \delta\gamma_y v_y)\,\mathrm{d}A$$

$$= \int_A (\delta u\, p_x + \delta v\, p_y + \delta w\, p_z)\,\mathrm{d}A$$

$$+ \oint_S \Big[\delta u(n_x e_x + n_{xy} e_y) + \delta v(n_{xy} e_x + n_y e_y) + \delta w(v_x e_x + v_y e_y) \qquad (7.28)$$

$$+ \delta\phi_y(m_x e_x + m_{xy} e_y) + \delta\phi_x(m_{xy} e_x + m_y e_y) \Big]\mathrm{d}S$$

with virtual strains

$$\delta\epsilon_x = \frac{\partial \delta u}{\partial x}, \quad \delta\epsilon_y = \frac{\partial \delta v}{\partial y}, \quad \delta\gamma_{xy} = \frac{\partial \delta u}{\partial y} + \frac{\partial \delta v}{\partial x} \qquad (7.29)$$

and virtual curvatures

$$\delta\kappa_x = \frac{\partial \delta\phi_y}{\partial x}, \quad \delta\kappa_y = \frac{\partial \delta\phi_x}{\partial y}, \quad \delta\kappa_{xy} = \frac{\partial \delta\phi_y}{\partial y} + \frac{\partial \delta\phi_x}{\partial x} \qquad (7.30)$$

and virtual shear deformations

$$\delta\gamma_x = \frac{\partial \delta w}{\partial x} - \delta\phi_y, \quad \delta\gamma_y = \frac{\partial \delta w}{\partial y} - \delta\phi_x \qquad (7.31)$$

A generalizing matrix notation of Eq. (7.28) is given by

$$\int_A \delta\boldsymbol{\epsilon}^T \cdot \boldsymbol{\sigma}\,\mathrm{d}A = \int_A \delta\mathbf{u}^T \cdot \mathbf{p}\,\mathrm{d}A + \oint_S \delta\mathbf{U}^T \cdot \mathbf{t}\,\mathrm{d}S \qquad (7.32)$$

with

$$
\begin{aligned}
\boldsymbol{\epsilon} &= \begin{pmatrix} \epsilon_x & \epsilon_y & \gamma_{xy} & \kappa_x & \kappa_y & \kappa_{xy} & \gamma_x & \gamma_y \end{pmatrix}^T \\
\boldsymbol{\sigma} &= \begin{pmatrix} n_x & n_y & n_{xy} & m_x & m_y & m_{xy} & v_x & v_y \end{pmatrix}^T \\
\mathbf{u} &= \begin{pmatrix} u & v & w & \phi_y & \phi_x \end{pmatrix}^T \\
\mathbf{p} &= \begin{pmatrix} p_x & p_y & p_z & 0 & 0 \end{pmatrix}^T \\
\mathbf{U} &= \begin{pmatrix} u_s & v_s & w_s & \phi_{sy} & \phi_{sx} \end{pmatrix}^T \\
\mathbf{t} &= \begin{pmatrix} n_{sx} & n_{sy} & v_s & m_{sx} & m_{sy} \end{pmatrix}^T
\end{aligned}
\tag{7.33}
$$

with the displacement boundary values $u_s, v_s, w_s, \phi_{sy}, \phi_{sx}$ and forces at boundaries

$$
\begin{aligned}
n_{sx} &= n_x e_x + n_{xy} e_y \\
n_{sy} &= n_{xy} e_x + n_y e_y \\
v_s &= v_x e_x + v_y e_y \\
m_{sx} &= m_x e_x + m_{xy} e_y \\
m_{sy} &= m_{xy} e_x + m_y e_y
\end{aligned}
\tag{7.34}
$$

A coupling of normal forces and moments – as arises with reinforced cracked concrete, see Section 3.1.3.2 – occurs with a dependence of normal forces on strains and additionally curvatures and also of moments on curvature and strains.

7.3.3 Decoupling

A decoupling is generally practiced for plane surface structures. In case normal forces do not depend on curvature and moments do not depend on strains – e.g., for a linear elastic material behavior – weak equilibrium can be formulated independently for Eq. (7.16) and for Eqs. (7.17, 7.18). Regarding normal forces this leads to

$$
\begin{aligned}
\boldsymbol{\epsilon} &= \begin{pmatrix} \epsilon_x & \epsilon_y & \gamma_{xy} \end{pmatrix}^T \\
\boldsymbol{\sigma} &= \begin{pmatrix} n_x & n_y & n_{xy} \end{pmatrix}^T \\
\mathbf{u} &= \begin{pmatrix} u & v \end{pmatrix}^T \\
\mathbf{p} &= \begin{pmatrix} p_x & p_y \end{pmatrix}^T \\
\mathbf{U} &= \begin{pmatrix} u_s & v_s \end{pmatrix}^T \\
\mathbf{t} &= \begin{pmatrix} n_{sx} & n_{sy} \end{pmatrix}^T
\end{aligned}
\tag{7.35}
$$

to be used for Eq. (7.32). This describes *plates* with biaxial plane strain or plane stress. Regarding bending only leads to

$$
\begin{aligned}
\boldsymbol{\epsilon} &= \begin{pmatrix} \kappa_x & \kappa_y & \kappa_{xy} & \gamma_x & \gamma_y \end{pmatrix}^T \\
\boldsymbol{\sigma} &= \begin{pmatrix} m_x & m_y & m_{xy} & v_x & v_y \end{pmatrix}^T \\
\mathbf{u} &= \begin{pmatrix} w & \phi_y & \phi_x \end{pmatrix} \\
\mathbf{p} &= \begin{pmatrix} p_z & 0 & 0 \end{pmatrix} \\
\mathbf{U} &= \begin{pmatrix} w_s & \phi_{sy} & \phi_{sx} \end{pmatrix}^T \\
\mathbf{t} &= \begin{pmatrix} v_s & m_{sx} & m_{sy} \end{pmatrix}^T
\end{aligned}
\tag{7.36}
$$

to be used for Eq. (7.32). These relations correspond to the *Reissner–Mindlin slab*. It is characterized by decoupling the deflection w from the slopes ϕ_y, ϕ_x by the shear deformation γ_x, γ_y, see Eq. (7.25). Thus, w, ϕ_y, ϕ_x may be interpolated as independent displacement

variables within the finite element approach. As a further consequence, C^0-continuity is sufficient for the interpolation of w, ϕ_y, ϕ_x, see also Section 1.7.

The common approach is given with the *Kirchhoff slab* which disregards shear deformations. It has the assumptions $\frac{\partial w}{\partial x} = \phi_y \rightarrow \gamma_x = 0$, $\frac{\partial w}{\partial y} = \phi_x \rightarrow \gamma_y = 0$ and is a special case of the Reissner–Mindlin slab from a purely mechanical point of view. Thus, Eq. (7.36) is modified as

$$
\begin{aligned}
\boldsymbol{\epsilon} &= \begin{pmatrix} \kappa_x & \kappa_y & \kappa_{xy} \end{pmatrix}^T \\
\boldsymbol{\sigma} &= \begin{pmatrix} m_x & m_y & m_{xy} \end{pmatrix}^T \\
\mathbf{u} &= \begin{pmatrix} w & \phi_y & \phi_x \end{pmatrix} \\
\mathbf{p} &= \begin{pmatrix} p_z & 0 & 0 \end{pmatrix} \\
\mathbf{U} &= \begin{pmatrix} w_s & \phi_{sy} & \phi_{sx} \end{pmatrix}^T \\
\mathbf{t} &= \begin{pmatrix} v_s & m_{sx} & m_{sy} \end{pmatrix}^T
\end{aligned}
\tag{7.37}
$$

to be used for Eq. (7.32). The relations between curvatures and deflections are given by

$$
\kappa_x = \frac{\partial^2 w}{\partial x^2}, \quad \kappa_y = \frac{\partial^2 w}{\partial y^2}, \quad \kappa_{xy} = 2\frac{\partial^2 w}{\partial x \partial y}
\tag{7.38}
$$

according to Eq. (7.5). We close this classification assuming a linear elastic material behavior according to Eqs. $(7.12)_{4-6}$. The relation between generalized stresses and generalized stresses for the Kirchhoff slab can be formulated as

$$
\boldsymbol{\sigma} = \mathbf{C} \cdot \boldsymbol{\epsilon}, \quad \mathbf{C} = K \begin{bmatrix} 1 & \nu & 0 \\ \nu & 1 & 0 \\ 0 & 0 & \frac{1-\nu}{2} \end{bmatrix}, \quad K = \frac{E\,h^3}{12(1-\nu^2)}
\tag{7.39}
$$

with Young's modulus E, Poisson's ratio ν, and the slab height h. The set of Eqs. (7.32, 7.37, 7.39) in the framework of weak equilibrium is equivalent to the classical partial differential equation for Kirchhoff slab Eq. (7.23). But the former allows for arbitrary geometries and boundary conditions in combination with numerical methods while the latter is restricted to relatively simple cases in spite of the mathematical challenge it involves.

The Kirchhoff slab described by Eqs. (7.32, 7.37) will be treated in the following of this chapter because of its current practical importance. This must ignore the coupling of bending moments and normal. This coupling is expressed, e.g., by the occupation of the tangential material stiffness (Eq. (7.15)). The effects of this characteristic of cracked reinforced concrete sections has been demonstrated for beams with Example 3.2. In this example it is shown that the activation of normal forces in the case of lateral loading depends on the displacement boundary conditions.

- Restrained horizontal displacements in most case lead to a slight normal compression of cracked reinforced cross sections.

Thus, the coupling effect is generally ignored for beams and slabs. The Kirchhoff approach for slabs is appropriate under this condition. The special case derived from Eq. (7.15)

$$
\begin{pmatrix} m_x \\ m_y \\ m_{xy} \end{pmatrix} = \begin{bmatrix} C_{T11} & C_{T12} & C_{T13} \\ C_{T21} & C_{T22} & C_{T23} \\ C_{T31} & C_{T32} & C_{T33} \end{bmatrix} \cdot \begin{pmatrix} \kappa_x \\ \kappa_y \\ \kappa_{xy} \end{pmatrix}
\tag{7.40}
$$

is used with adapted notations for the coefficients C_{Tij}. This is a generalization of Eq. (7.39). The coupling effect will be again considered in the context of shells, see Section 8.

7.4 Structural Slab Elements

7.4.1 Area Coordinates

Equations (7.37, 7.38) define the variables of the Kirchhoff slab. The definition of generalized strains (Eq. (7.38)) requires a C^1-continuity of the interpolation functions for w to ensure compatibility and integrability of Eq. (7.32), see also Section 1.7. This corresponds to the continuity of slopes ϕ_y, ϕ_x and some more constraints along inter element boundaries. This requirement is not trivial to fulfill within the two-dimensional setting [99, 1.1,1.2]. Thus, the continuity requirement has to be relaxed leading to *nonconforming* element formulations.

Three independent interpolation variables are given by w, ϕ_y, ϕ_x, see Eq. (7.37)$_3$. Triangular areas or elements are a first choice in order to approach continuity requirements. Furthermore, usage of *area coordinates* $L_i, i = 1, \ldots, 3$ instead of length coordinates is appropriate to indicate a position within triangle. They are defined with

$$
\begin{aligned}
x &= L_1 x_1 + L_2 x_2 + L_3 x_3 \\
y &= L_1 y_1 + L_2 y_2 + L_3 y_3 \\
L_1 + L_2 + L_3 &= 1
\end{aligned}
\tag{7.41}
$$

with the coordinates x_I, y_I of a node $I = 1, \ldots, 3$. The values of L_i denote relative areas, see Fig. 7.5. The definition leads to

$$
L_1 = a_1 + b_1 x + c_1 y, \quad L_2 = a_2 + b_2 x + c_2 y, \quad L_3 = a_3 + b_3 x + c_3 y
\tag{7.42}
$$

with

$$
\begin{aligned}
a_1 &= \frac{y_3 x_2 - y_2 x_3}{2\Delta}, & b_1 &= \frac{y_2 - y_3}{2\Delta}, & c_1 &= \frac{x_3 - x_2}{2\Delta} \\
a_2 &= \frac{y_1 x_3 - y_3 x_1}{2\Delta}, & b_2 &= \frac{y_3 - y_1}{2\Delta}, & c_2 &= \frac{x_1 - x_3}{2\Delta} \\
a_3 &= \frac{y_2 x_1 - y_1 x_2}{2\Delta}, & b_3 &= \frac{y_1 - y_2}{2\Delta}, & c_3 &= \frac{x_2 - x_1}{2\Delta}
\end{aligned}
\tag{7.43}
$$
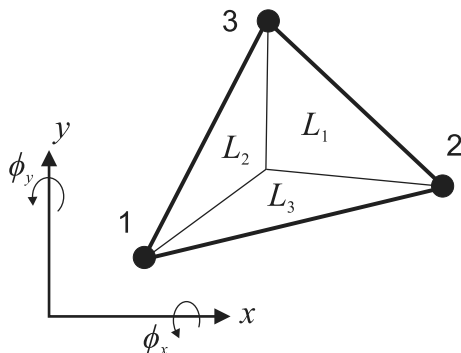
Figure 7.5: Triangular element and area coordinates.

and

$$
\begin{aligned}
\Delta &= \frac{1}{2}\det \begin{vmatrix} 1 & x_1 & y_1 \\ 1 & x_2 & y_3 \\ 1 & x_2 & y_3 \end{vmatrix} \\
&= \text{area123} \\
&= \frac{1}{2}\left(y_1 x_3 + y_3 x_2 + y_2 x_1 - y_2 x_3 - y_3 x_1 - y_1 x_2\right)
\end{aligned} \tag{7.44}
$$

Area coordinates of nodes are given by

$$
\begin{aligned}
x = x_1, y = y_1 &\quad\rightarrow\quad L_1 = 1, L_2 = 0, L_3 = 0 \\
x = x_2, y = y_2 &\quad\rightarrow\quad L_1 = 0, L_2 = 1, L_3 = 0 \\
x = x_3, y = y_3 &\quad\rightarrow\quad L_1 = 0, L_2 = 0, L_3 = 1
\end{aligned} \tag{7.45}
$$

and derivatives of area coordinates with respect to length coordinates

$$
\frac{\partial L_i}{\partial x} = b_i, \qquad \frac{\partial L_i}{\partial y} = c_i \tag{7.46}
$$

with b_i, c_i according to Eq. (7.43)

7.4.2   A Triangular Kirchhoff Slab Element

We consider a triangular element with three corner nodes and nine nodal degrees of freedom. Thus, an interpolation approach for the deflections w on area coordinates is given by, e.g.,

$$
\begin{aligned}
w ={}& \alpha_1 L_1 + \alpha_2 L_2 + \alpha_3 L_3 + \alpha_4 L_1 L_2 + \alpha_5 L_2 L_3 + \alpha_6 L_3 L_1 \\
&+ \alpha_7 L_1^2 L_2 + \alpha_8 L_2^2 L_3 + \alpha_9 L_3^2 L_1 \\
\phi_y = \frac{\partial w}{\partial x} ={}& \frac{\partial w}{\partial L_1}\frac{\partial L_1}{\partial x} + \frac{\partial w}{\partial L_2}\frac{\partial L_2}{\partial x} + \frac{\partial w}{\partial L_3}\frac{\partial L_3}{\partial x} \\
={}& \left(\alpha_1 + \alpha_4 L_2 + \alpha_6 L_3 + 2\alpha_7 L_1 L_2 + \alpha_9 L_3^2\right) b_1 \\
&+ \left(\alpha_2 + \alpha_4 L_1 + \alpha_5 L_3 + \alpha_7 L_1^2 + 2\alpha_8 L_2 L_3\right) b_2 \\
&+ \left(\alpha_3 + \alpha_5 L_2 + \alpha_6 L_1 + \alpha_8 L_2^2 + 2\alpha_9 L_1 L_3\right) b_3 \\
\phi_x = \frac{\partial w}{\partial y} ={}& \frac{\partial w}{\partial L_1}\frac{\partial L_1}{\partial y} + \frac{\partial w}{\partial L_2}\frac{\partial L_2}{\partial y} + \frac{\partial w}{\partial L_3}\frac{\partial L_3}{\partial y} \\
={}& \left(\alpha_1 + \alpha_4 L_2 + \alpha_6 L_3 + 2\alpha_7 L_1 L_2 + \alpha_9 L_3^2\right) c_1 \\
&+ \left(\alpha_2 + \alpha_4 L_1 + \alpha_5 L_3 + \alpha_7 L_1^2 + 2\alpha_8 L_2 L_3\right) c_2 \\
&+ \left(\alpha_3 + \alpha_5 L_2 + \alpha_6 L_1 + \alpha_8 L_2^2 + 2\alpha_9 L_1 L_3\right) c_3
\end{aligned} \tag{7.47}
$$

This yields for node 1 with $L_1 = 1, L_2 = L_3 = 0$

$$
\begin{aligned}
w_1 &= \alpha_1 \\
\phi_{1y} &= \alpha_1 b_1 + (\alpha_2 + \alpha_4 + \alpha_7)\, b_2 + (\alpha_3 + \alpha_6)\, b_3 \\
\phi_{1x} &= \alpha_1 c_1 + (\alpha_2 + \alpha_4 + \alpha_7)\, c_2 + (\alpha_3 + \alpha_6)\, c_3
\end{aligned} \tag{7.48}
$$

see Fig. 7.5, and for node 2 with $L_2 = 1, L_2 = L_3 = 0$

$$
\begin{aligned}
w_2 &= \alpha_2 \\
\phi_{2y} &= (\alpha_1 + \alpha_4)\,b_1 + \alpha_2 b_2 + (\alpha_3 + \alpha_5 + \alpha_8)\,b_3 \\
\phi_{2x} &= (\alpha_1 + \alpha_4)\,c_1 + \alpha_2 c_2 + (\alpha_3 + \alpha_5 + \alpha_8)\,c_3
\end{aligned}
\tag{7.49}
$$

and finally for node 3 with $L_3 = 1, L_1 = L_2 = 0$

$$
\begin{aligned}
w_3 &= \alpha_3 \\
\phi_{3y} &= (\alpha_1 + \alpha_6 + \alpha_9)\,b_1 + (\alpha_2 + \alpha_5)\,b_2 + \alpha_3 b_3 \\
\phi_{3x} &= (\alpha_1 + \alpha_6 + \alpha_9)\,c_1 + (\alpha_2 + \alpha_5)\,c_2 + \alpha_3 c_3
\end{aligned}
\tag{7.50}
$$

The solution for the coefficients of the interpolation approach is

$$
\begin{aligned}
\alpha_1 &= w_1 \\
\alpha_2 &= w_2 \\
\alpha_3 &= w_3 \\
\alpha_4 &= -c_3\phi_{2y} + w_2 - w_1 + b_3\phi_{2x} \\
\alpha_5 &= -\phi_{3y}c_1 - w_2 + w_3 + b_1\phi_{3x} \\
\alpha_6 &= -c_2\phi_{1y} + w_1 - w_3 + b_2\phi_{1x} \\
\alpha_7 &= -b_3\phi_{2x} + c_3\phi_{2y} - b_3\phi_{1x} + c_3\phi_{1y} - 2w_2 + 2w_1 \\
\alpha_8 &= -b_1\phi_{2x} + c_1\phi_{2y} - b_1\phi_{3x} + \phi_{3y}c_1 + 2w_2 - 2w_3 \\
\alpha_9 &= -b_2\phi_{1x} + c_2\phi_{1y} - b_2\phi_{3x} + c_2\phi_{3y} - 2w_1 + 2w_3
\end{aligned}
\tag{7.51}
$$

leading to

$$
\begin{aligned}
w = &- L_1(-1 + L_2 - 2L_1 L_2 - L_3 + 2L_3^2)w_1 + L_1(c_3 L_1 L_2 + L_3^2 c_2 - L_3 c_2)\phi_{1y} + \\
&- L_1(b_2 L_3^2 + b_3 L_1 L_2 - b_2 L_3)\phi_{1x} + L_2(-2L_1^2 - L_3 + L_1 + 1 + 2L_2 L_3)w_2 + \\
&L_2(-c_3 L_1 + c_3 L_1^2 + c_1 L_2 L_3)\phi_{2y} + -L_2(-b_3 L_1 + b_3 L_1^2 + b_1 L_2 L_3)\phi_{2x} + \\
&L_3(L_2 + 2L_3 L_1 - 2L_2^2 + 1 - L_1)w_3 + L_3(c_1 L_2^2 + c_2 L_3 L_1 - c_1 L_2)\phi_{3y} + \\
&- L_3(b_1 L_2^2 + b_2 L_3 L_1 - b_1 L_2)\phi_{3x}
\end{aligned}
\tag{7.52}
$$

Generalized strains or curvatures, see Eq. (7.38), are derived with

$$
\begin{aligned}
\frac{\partial^2 w}{\partial x^2} &= \frac{\partial^2 w}{\partial x \partial L_1}\frac{\partial L_1}{\partial x} + \frac{\partial^2 w}{\partial x \partial L_2}\frac{\partial L_2}{\partial x} + \frac{\partial w^2}{\partial x \partial L_3}\frac{\partial L_3}{\partial x} = \kappa_x \\
\frac{\partial^2 w}{\partial y^2} &= \frac{\partial^2 w}{\partial y \partial L_1}\frac{\partial L_1}{\partial y} + \frac{\partial^2 w}{\partial y \partial L_2}\frac{\partial L_2}{\partial y} + \frac{\partial w^2}{\partial y \partial L_3}\frac{\partial L_3}{\partial y} = \kappa_y \\
\frac{\partial^2 w}{\partial x \partial y} &= \frac{\partial^2 w}{\partial x \partial L_1}\frac{\partial L_1}{\partial y} + \frac{\partial^2 w}{\partial x \partial L_2}\frac{\partial L_2}{\partial y} + \frac{\partial w^2}{\partial x \partial L_3}\frac{\partial L_3}{\partial y} = \frac{\kappa_{xy}}{2} \\
\frac{\partial^2 w}{\partial y \partial x} &= \frac{\partial^2 w}{\partial x \partial y}
\end{aligned}
\tag{7.53}
$$

or

$$
\begin{aligned}
\kappa_x &= B_{11}w_1 + B_{12}\phi_{1y} + B_{13}\phi_{1x} + B_{14}w_2 + B_{15}\phi_{2y} + B_{16}\phi_{2x} + B_{17}w_3 + B_{18}\phi_{3y} + B_{19}\phi_{3x} \\
\kappa_y &= B_{21}w_1 + B_{22}\phi_{1y} + B_{23}\phi_{1x} + B_{24}w_2 + B_{25}\phi_{2y} + B_{26}\phi_{2x} + B_{27}w_3 + B_{28}\phi_{3y} + B_{29}\phi_{3x} \\
\frac{\kappa_{xy}}{2} &= B_{31}w_1 + B_{32}\phi_{1y} + B_{33}\phi_{1x} + B_{34}w_2 + B_{35}\phi_{2y} + B_{36}\phi_{2x} + B_{37}w_3 + B_{38}\phi_{3y} + B_{39}\phi_{3x}
\end{aligned}
\tag{7.54}
$$

with

$$B_{11} = -8b_3b_1L_3 + 4b_1^2L_2 + 2(4b_2b_1 - 2b_3^2)L_1 + 2(-b_2b_1 + b_3b_1)$$
$$B_{12} = 4b_1c_2b_3L_3 + 2c_3b_1^2L_2 + 2(2c_3b_1b_2 + c_2b_3^2)L_1 - 2b_1c_2b_3 \qquad (7.55)$$
$$\cdots$$

These derivations demonstrate the basic procedure. Obviously the issue becomes elaborate. The selection of higher order polynomial terms becomes a delicate question with several options [99, 1.5].

The particular approach (Eq. (7.47)) belongs to the class of nonconforming elements, i.e., C^1-continuity is not strictly given. This must not be a criterion for exclusion. A severe drawback is that the patch test, see Section 1.7, is not fulfilled for arbitrary element shapes. Improved forms with efficient performance are proposed by [87] using fourth-order terms instead of cubic terms in Eq. $(7.47)_1$.

7.5 System Building and Solution Methods

System building for system with structural elements like beams and slabs has some specialties. General aspects have already been treated in Section 1.6, particular items regarding beams have been discussed in Section 3.4. They are shortly rephrased and specified with respect to slabs.

Generalized strains are approximated with finite element approximations

$$\boldsymbol{\epsilon} = \mathbf{B} \cdot \boldsymbol{v}_e \qquad (7.56)$$

see Eq. (1.21), with $\boldsymbol{v}_e$ according to Eq. $(7.33)_3$, $(7.36)_3$, or $(7.37)_3$ applied to all nodes of an element and $\boldsymbol{\epsilon}$ according to Eq. $(7.33)_1$, $(7.36)_1$ or $(7.37)_1$ for the coupled problem, the Reissner–Mindlin slab or the Kirchhoff slab, respectively. In the case of a Kirchhoff slab, the matrix $\mathbf{B}$ is determined, e.g., by Eq. (7.54).

Numerical integration of triangular elements has to be treated differently compared to four-sided elements. Area coordinates, see Section 7.4.1, are used to mark a position within an triangular element. Sampling points and weights, compare Section 1.6, are used for the numerical integration of internal nodal forces, external loads, and stiffness matrices. Regarding area coordinates they are given in Table 7.1 up to integration order 2, compare also Table 1.1.

n_i	L_1	L_2	L_3	η_i
0	1/3	1/3	1/3	1
1	1/2	1/2	0	1/3
	0	1/2	1/2	1/3
	1/2	0	1/2	1/3
2	1/3	1/3	1/3	$-27/48$
	0.6	0.2	0.2	25/48
	0.2	0.6	0.2	25/48
	0.2	0.2	0.6	25/48

Table 7.1: Sampling points and weights for triangular numerical integration.

The integration of the weak equilibrium condition (Eq. (7.32)) has to be performed element by element. *Assembling* of element contributions, see Section 1.5, leads to

$$\mathbf{r}(\boldsymbol{v}) = \mathbf{f}(\boldsymbol{v}) - \mathbf{p} = \mathbf{0} \tag{7.57}$$

with nodal internal forces $\mathbf{f}$, nodal displacements $\boldsymbol{v}$ of all elements and external nodal loads $\mathbf{p}$, compare Eq. (1.69). In the case of *linear material behavior* internal nodal forces may be written as

$$\mathbf{f}(\boldsymbol{v}) = \mathbf{K} \cdot \boldsymbol{v} \quad \rightarrow \quad \mathbf{K} \cdot \boldsymbol{v} = \mathbf{p} \tag{7.58}$$

with a constant stiffness matrix $\mathbf{K}$ assembled from element stiffness matrices

$$\mathbf{K}_I = \int_{V_I} \mathbf{B}^T \cdot \mathbf{C} \cdot \mathbf{B} \, \mathrm{d}V \tag{7.59}$$

compare Eqs. (1.61, 1.62), with $\mathbf{C}$ according to Eq. (7.39) in the case of a Kirchhoff slab. This yields an immediate solution for the displacement with a given load $\mathbf{p}$

$$\boldsymbol{v} = \mathbf{K}^{-1} \cdot \mathbf{p} \tag{7.60}$$

whereby an inversion is not explicitly performed but a Gauss triangularization and backsubstitution.

Kinematic boundary conditions have to provide a stable support and to prevent rigid body motions. Boundary forces are given by Eq. (7.34) with a unit normal vector $\mathbf{e}$ with components e_x, e_y along the boundary. To simplify the formulations a boundary edge parallel to the global y-axis with $x = const., e_x = 1, e_y = 0$ is considered exemplary, i.e.,

$$v_s = v_x, \quad m_{sx} = m_x, \quad m_{sy} = m_{xy} \tag{7.61}$$

along the boundary edge. The following cases are considered:

– Free edge:

  Values v_s, m_{sx}, m_{sy} are prescribed – in most cases with 0 – and go directly into the boundary force vector $\mathbf{t}$, see Eqs. (7.36)$_6$ and (7.37)$_6$. Their mutual dependency given by Eq. (7.18) must be regarded if necessary in cases they are not zero. This corresponds to the notion of compensatory shear forces within the theory of Kirchhoff slabs.

– Simply supported edge:

  Regarding Eqs. (7.36)$_5$ and (7.37)$_5$ kinematic boundary conditions $w = w_s = 0$ and $\varphi_y = \phi_{sx} = 0$ characterize the simply supported edge. On the other hand, φ_x is not prescribed and the corresponding force $m_{sx} = m_x$ has to be prescribed, generally with a value 0.

  But as ϕ_x is prescribed the corresponding boundary force $m_{sy} = m_{xy}$ has to result from the computation and is transmitted to the slab's support. It is connected to a compensatory shear force which is combined with the internal shear force v_x.

– Clamped edge:

  Regarding Eqs. (7.36)$_5$, (7.37)$_5$ kinematic boundary conditions $w = w_s = 0$ and $\varphi_x = \phi_{sy} = 0, \varphi_y = \phi_{sx} = 0$ are given. All the corresponding boundary forces are determined from the computation, whereby $m_{sy} = m_{xy} = 0$ as $\partial \phi_y / \partial y = 0$.

A boundary edge parallel to the global x-axis with $y = const.$ is treated in the same way with indices exchanged. A straight skew or curved boundary edge with, e.g., simply support leads to a prescribed coupling of ϕ_y, ϕ_x and m_x, m_y, m_{xy} along the boundary. These may be regarded as additional constraint conditions.

Kinematic boundary conditions are applied to nodes and directly implemented upon assembling the system by the modification of the system's stiffness matrix and load vector, see Section 3.4.3 for the basic approach. Boundary forces or reactions, respectively, are automatically computed as internal nodal forces for those boundary degrees of freedom which have kinematic boundary conditions prescribed. These particular internal nodal forces are not equilibrated by external nodal loads.

The computation of slabs arises as an everyday task. Linear elastic behavior is generally assumed in practical problems. Nevertheless geometric properties and boundary conditions prevent an analytical treatment and only numerical methods may provide useful solutions. This is demonstrated with the following example.

Example 7.1 Linear elastic rectangular slab with opening and free edges
The slab's geometry with opening and boundary conditions is shown in Fig. 7.6a. A single support is given in the lower left corner. The left and the lower edges are not supported. The upper and right edges are simply supported (hinged). The material properties are assumed with a Young's modulus $E = 31\,900\,\text{MN/m}^2$ and a Poisson's ratio $\nu = 0.2$. The slab thickness is $h = 0.3\,\text{m}$. A uniform loading is given by $p = 10\,\text{kN/m}^2$ which does not act in the opening area.

Kirchhoff slab theory is assumed and only moments will be directly considered as internal forces, see Eq. (7.37). A triangular slab element is chosen according to Section 7.4.2 in the variant proposed by [87]. The discretization is given by 132 elements which are shown in Fig. 7.6b. The computation leads to the following results:

– Principal moments – derived from m_x, m_y, m_{xy} in analogy to principal stresses, see Eqs. (6.4, 6.5) and Eq. (7.66) – give instructive information about the load-bearing behavior. The computed values are shown in Fig. 7.6b whereby the arrow direction
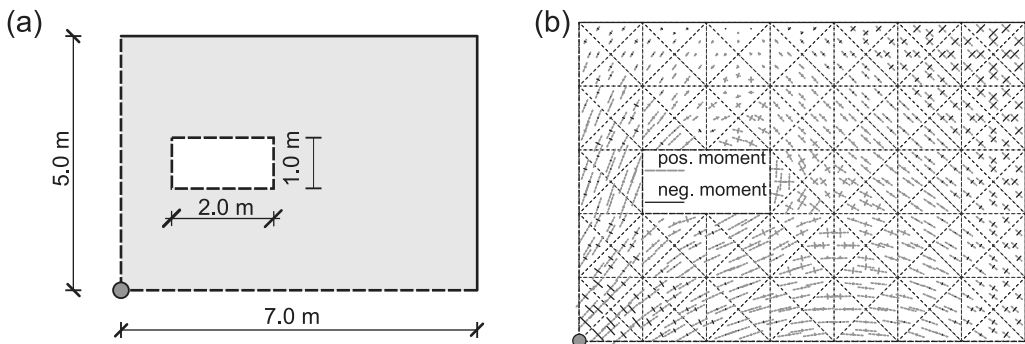
Figure 7.6: Example 7.1 (a) System. (b) Discretization and principal moments.

(a)

(b)
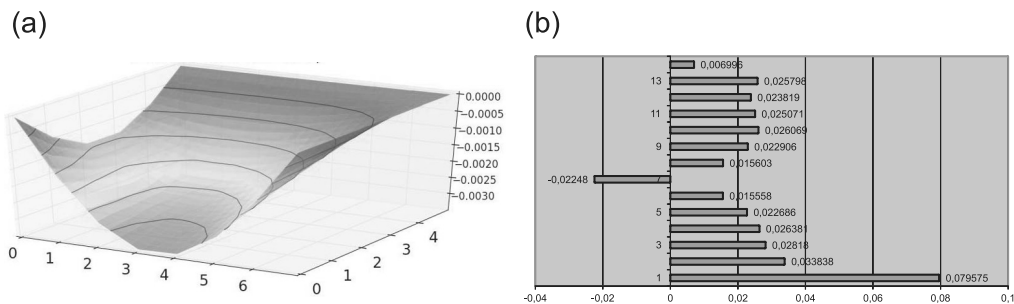
Figure 7.7: Example 7.1 (a) Deflections (opening not shown). (b) Boundary support reactions.

indicates the stress direction caused by the respective moment. Positive values have compressive stresses on the upper side and tensile stresses on the lower side, negative values the opposite. Principal moments are basically aligned to the free edges and are connected with a uniaxial behavior along the free edges.

A skew orientation of principal moments with opposite sign and approximately the same absolute value arises in the upper right corner and reversed near the lower left single support. This indicates the effect of *twisting*.

– The computed deflections are shown in Fig. 7.7a. They obviously conform to prescribed boundary conditions. The maximum deflection is in the range of 3 cm, i.e., $w_{max}/L \approx 1/230$. Thus, thickness and stiffness are too low for serviceability.

– The computed reaction forces in the boundary nodes are listed in Fig. 7.7b. Number 1 belongs to the lower left single support, the numbers 2–6 to the right edge, the number 7 to the right upper corner and the numbers 8–14 to the upper edge.

The sum of all reaction forces equals 330 kN and thus equals the total loading. The by far largest reaction force is given the simple support. The upper right reaction force corresponds to uplift. This conforms to the theory of slabs with twisting stiffness.

End Example 7.1

A redistribution of moments generally occurs with nonlinear material behavior. An approach for nonlinear behavior for slabs is described in Section 7.7.

7.6 Lower Bound Limit Analysis

7.6.1 General Approach and Principal Moments

Principles of a *lower bound limit analysis* have already been described in Section 6.1.1 regarding plates. Internal forces are determined with a linear elastic computation with a unit load applied. Internal forces can be scaled with a loading factor. The loading factor is adapted such that the cross-sectional resistance resulting from thickness, concrete strength, and the

strength of reinforcement – basically by its amount – is not exceeded in every position of the slab reference plane ($\rightarrow$ admissible load proof) or the design of thickness, concrete strength and amount of reinforcement is adapted to a given loading factor ($\rightarrow$ design procedure).

The key item is again to find an appropriate combination of concrete and reinforcement strength as reference values for the calculated state of internal forces. This needs the determination of *principal moments* as prerequisites. The task has basically been treated in Section 6.1.2.

Moments m_x, m_y, m_{xy} as they are defined by Eq. (7.8) and Fig. 7.4 behave as components of a second-order tensor in the same way as the components of a plane stress tensor do as they are directly derived from stress components. This has some side effects: the transformation of a second-order moment tensor or its corresponding principal values into a moment vector similar to Eq. (5.5) does not directly lead to a rotating moment vector in the classical sense. In addition a rotation with $\pi/2$ has to be performed due to the lever arm z.

The transformation of tensorial moments into a coordinate system rotated by an angle φ (positive counterclockwise, see Eq. (C.11)) is given by

$$\widetilde{\mathbf{m}} = \mathbf{T} \cdot \mathbf{m} \tag{7.62}$$

in the same way as for stresses with

$$\widetilde{\mathbf{m}} = \begin{pmatrix} \tilde{m}_x \\ \tilde{m}_y \\ \tilde{m}_{xy} \end{pmatrix}, \quad \mathbf{T} = \begin{bmatrix} \cos^2 \varphi & \sin^2 \varphi & 2 \cos \varphi \sin \varphi \\ \sin^2 \varphi & \cos^2 \varphi & -2 \cos \varphi \sin \varphi \\ -\cos \varphi \sin \varphi & \cos \varphi \sin \varphi & \cos^2 \varphi - \sin^2 \varphi \end{bmatrix}, \quad \mathbf{m} = \begin{pmatrix} m_x \\ m_y \\ m_{xy} \end{pmatrix} \tag{7.63}$$

The *principal direction* is defined with the condition of vanishing shear components

$$\sqrt{1 - \cos^2 2\varphi} \cdot \frac{m_y - m_x}{2} + \cos 2\varphi \cdot m_{xy} = 0 \tag{7.64}$$

Within a range $0 \leq \varphi \leq \pi/2$ a unique solution φ is determined by

$$\cos 2\varphi = \frac{\dfrac{m_x - m_y}{2}}{\sqrt{(\dfrac{m_x - m_y}{2})^2 + m_{xy}^2}} \tag{7.65}$$

for $m_{xy} \neq 0$. Principal moments are already given by m_x, m_y for $m_{xy} = 0$. A solution φ multiplied by the sign of m_{xy} indicates the direction of a principal moment m_1. A second principal moment m_2 is perpendicular. They have the values

$$m_1 = \frac{m_x + m_y}{2} + \sqrt{\left(\frac{m_x - m_y}{2}\right)^2 + m_{xy}^2}, \quad m_2 = \frac{m_x + m_y}{2} - \sqrt{\left(\frac{m_x - m_y}{2}\right)^2 + m_{xy}^2} \tag{7.66}$$

According to the definition of Eq. (7.8) and Fig. 7.4 a moment m_x leads to stresses σ_x, m_y to σ_y and m_{xy} to σ_{xy}. Assigning an internal lever arm z yields the corresponding *couple force resultants*

$$t_x = \pm\frac{m_x}{z}, \quad t_y = \pm\frac{m_y}{z}, \quad t_{xy} = \pm\frac{m_{xy}}{z} \tag{7.67}$$

Each of the two components may be attached to a lower and upper layer of the slab.

- All considerations regarding reinforcement design of plates, see Section 6.1, may be applied to the *layer forces* and the required upper or lower reinforcement, respectively.

This is summarized in the following, which has to be applied to the upper and lower layer in the same way.

7.6.2 Design Approach for Bending

An approach combining an admissible *load proof* regarding *concrete* together with a *design* procedure regarding the *reinforcement* is developed in the following. Upper and lower reinforcements have to be distinguished whereby each of them is connected with layer forces for a given position of the reference plane. The procedure is the same for both.

Layer forces have principal values as the moments have they are derived from. The values t_x, t_y, t_{xy} are connected to the principal values t_1, t_2 by

$$
\begin{aligned}
t_x &= t_1 \cos^2 \varphi + t_2 \sin^2 \varphi \\
t_y &= t_1 \sin^2 \varphi + t_2 \cos^2 \varphi \\
t_{xy} &= (t_1 - t_2) \sin \varphi \cos \varphi
\end{aligned}
\tag{7.68}
$$

according to Eq. (6.7) with the angle φ measured from the x-axis to the 1-axis (counterclockwise positive, see Eq. (C.12)). This form may also be derived in analogy to Eq. (7.63) with a sign reversal of φ and a zero mixed component.

Two reinforcement directions $\varphi_{s1}, \varphi_{s2}$ and a concrete direction φ_c are considered. These directions describe the principal 1-directions for each part. The corresponding principal stress values are transformed to the global directions applying Eq. (7.68) to each part, whereby the stresses in the principal 2-directions vanish due to the uniaxial behavior of each part. This leads to

$$
\begin{aligned}
t_{c,x} &= t_{c,1} \cos^2 \varphi_c, & t_{c,y} &= t_{c,1} \sin^2 \varphi_c, & t_{c,xy} &= t_{c,1} \sin \varphi_c \cos \varphi_c \\
t_{s1,x} &= t_{s1,1} \cos^2 \varphi_{s1}, & t_{s1,y} &= t_{s1,1} \sin^2 \varphi_{s1}, & t_{s1,xy} &= t_{s1,1} \sin \varphi_{s1} \cos \varphi_{s1} \\
t_{s2,x} &= t_{s2,1} \cos^2 \varphi_{s2}, & t_{s2,y} &= t_{s2,1} \sin^2 \varphi_{s2}, & t_{s2,xy} &= t_{s2,1} \sin \varphi_{s2} \cos \varphi_{s2}
\end{aligned}
\tag{7.69}
$$

see also Eqs. (6.8, 6.9). A notation $t_c = t_{c,1}$, $t_{s1} = t_{s1,1}$, $t_{s2} = t_{s2,1}$ will be used in the following. Reinforcement forces are connected to reinforcement stresses through reinforcement cross sections a_{s1}, a_{s2} per unit width with

$$
t_{s1} = a_{s1}\, \sigma_{s1}, \qquad t_{s2} = a_{s2}\, \sigma_{s2}
\tag{7.70}
$$

The parts contribute to total forces in analogy to Eq. (6.11)

$$
\begin{aligned}
t_{c,x} + t_{s1,x} + t_{s2,x} &= t_x \\
t_{c,y} + t_{s1,y} + t_{s2,y} &= t_y \\
t_{c,xy} + t_{s1,xy} + t_{s2,xy} &= t_{xy}
\end{aligned}
\tag{7.71}
$$

The usage of Eqs. (7.69, 7.70) in Eq. (7.71) first of all yields three equations for the variables $t_c, \varphi_c, \sigma_{s1}, a_{s1}, \varphi_{s1}, \sigma_{s2}, a_{s2}, \varphi_{s2}$ and the lever arm z. Three further Eqs. (7.67) connect

t_x, t_y, t_{xy} to moments m_x, m_y, m_{xy} by the internal lever arm z. Thereby m_x, m_y, m_{xy} are given, e.g., from a linear elastic FE-calculation which has been performed in advance. It is reasonable to prescribe the four values $\sigma_{s1}, \varphi_{s1}, \sigma_{s2}, \varphi_{s2}$. Thus, the parameters $t_c, \varphi_c, a_{s1}, a_{s2}$ and z remain open for design purposes.

Again a special but *common case* is considered. It is assumed that the reinforcement directions are aligned to global coordinate axes, i.e., $\varphi_{s1} = 0$, $\varphi_{s2} = \pi/2$ and therefore $\sin \varphi_{s1} = 0, \cos \varphi_{s1} = 1, \sin \varphi_{s2} = 1, \cos \varphi_{s2} = 0$. This leads to

$$
\begin{array}{llll}
t_{s1,x} = t_{sx} = a_{sx}\,\sigma_{sx}, & t_{s1,y} = 0, & t_{s1,xy} = 0 \\
t_{s2,y} = t_{sy} = a_{sy}\,\sigma_{sy}, & t_{s2,x} = 0, & t_{s2,xy} = 0
\end{array}
\tag{7.72}
$$

with $\sigma_{sx} = \sigma_{s1}$, $a_{sx} = a_{s1}$, $\sigma_{sy} = \sigma_{sy}$, $a_{sy} = a_{sy}$. Insertion into Eq. (7.71) together with Eq. $(7.69)_1$ yields

$$
\begin{array}{rcl}
t_c \cos^2 \varphi_c + a_{sx}\,\sigma_{sx} & = & t_x \\
t_c \sin^2 \varphi_c + a_{sy}\,\sigma_{sy} & = & t_y \\
t_c \sin \varphi_c \cos \varphi_c & = & t_{xy}
\end{array}
\tag{7.73}
$$

To exploit the reinforcement's load carrying capacity stresses $\sigma_{s1} = \sigma_{s2} = f_{yk}$ are used with the reinforcement yield limit f_{yk}.

The concrete force – negative by definition with an appropriate choice of φ_c for a given t_{xy} – is determined by

$$
t_c = \frac{t_{xy}}{\sin \varphi_c \cos \varphi_c}
\tag{7.74}
$$

according to Eq. $(7.73)_3$. The bearing capacity of the compression zone can be estimated with some assumptions about the values and the distribution of concrete stresses. A constant concrete stress distribution is assumed with a value $\sigma_c = -\chi\, f_c$, a zero line of bending x measured from the compressed side and the compression stress zone height $k\,x$, see Fig. 7.8. Values $\chi = 0.95$, $k = 0.8$ can be used supported by [26, 3.1.7]. This leads to $t_c = -\chi f_c k\,x$. Furthermore, $z = d - k\,x/2$ with the structural height d. Finally, a concrete moment $m_c =$
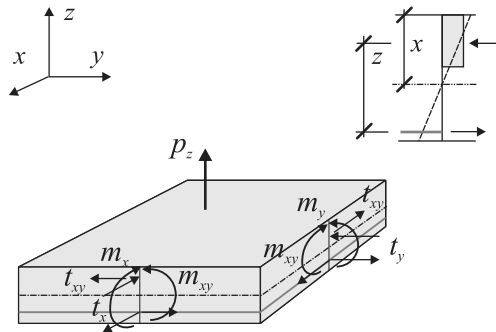
Figure 7.8: Slab reinforcement.

$t_c z = -\chi f_c k \, xz$ is introduced. The last two equations yield

$$x = \frac{d}{k}\left(1 - \sqrt{1 + \frac{2m_c k}{\bar{f}_c d^2}}\right), \quad z = \frac{d}{2}\left(1 + \sqrt{1 + \frac{2m_c k}{\bar{f}_c d^2}}\right) \tag{7.75}$$

with $\bar{f}_c = \chi f_c k$ and $m_c < 0$ by definition.

The amount of required reinforcement can be determined using Eq. (7.73)

$$\begin{aligned}
a_{sx} &= \frac{t_x - t_c \cos^2 \varphi_c}{f_y} = \frac{\pm m_x - m_c \cos^2 \varphi_c}{z\, f_y} \\
a_{sy} &= \frac{t_y - t_c \sin^2 \varphi_c}{f_y} = \frac{\pm m_y - m_c \sin^2 \varphi_c}{z\, f_y}
\end{aligned} \tag{7.76}$$

whereby the positive sign is used for the lower slab side and the negative sign for the upper side, see Fig. 7.4, with

$$m_c \sin \varphi_c \cos \varphi_c = \pm m_{xy} \tag{7.77}$$

derived from Eqs. (7.74, 7.67) and $t_c = m_c/z$. Setting $z = 1, m = \sigma$ recovers the approach for the reinforcement design of plates, see Section 6.1.2.

Summarizing, four equations given by Eqs. (7.75)$_2$ and (7.77, 7.76) are available the five remaining variables $a_{sx}, a_{sy}, m_c, z, \varphi_c$. Regarding φ_c a first choice

$$\varphi_c = \begin{cases} -\dfrac{\pi}{4} & \text{for } m_{xy} \geq 0 \\[2mm] \dfrac{\pi}{4} & m_{xy} < 0 \end{cases} \tag{7.78}$$

is appropriate as has been shown in Section 6.1.2. This leads to $t_c = -2|t_{xy}|$ and $m_c = -2|m_{xy}|$. The internal lever arm z can be determined with Eq. (7.75)$_2$ and finally the required reinforcement with $a_{sx} = \pm m_x + |m_{xy}|/(z\, f_y)$ and $a_{sy} = \pm m_y + |m_{xy}|/(z\, f_y)$ with Eqs. (7.76).

A computed value $a_{si} < 0, i = x, y$ indicates that the concrete stress direction should be changed, the angle φ_c has to be modified to reach $a_{si} = 0$. This case is covered by the nonlinear system of four equations (7.75)$_2$, (7.76) with $a_{si} = 0$ and (7.77) for four unknowns φ_c, m_c, z and a_{sj} with $i \neq j$. This system has to be solved iteratively in a similar way as has been demonstrated for plates, see Section 6.1.3.

The concrete compression height has to be restricted to assure a sufficient rotation capacity. The zero line x of bending measured should not exceed $\approx d/2$ supported by [26, 5.6.3]. A condition $x \leq d/2$ leads to

$$|m_c| \leq \frac{1 - \left(1 - \frac{k}{2}\right)^2}{2} \bar{f}_c d^2 = 0.32\, \bar{f}_c d^2 \tag{7.79}$$

with $k = 0.8$. A sufficient rotation capacity enables deformations that are necessary for a redistribution of internal forces to adjust to the conditions caused by a prescribed value of φ_c. The design approach is demonstrated with the following example.

Example 7.2 Reinforcement design for a slab with linear elastic internal forces
We refer to Example 7.1 with the same system and loading. Moments have been calculated for each element integration point with a linear elastic calculation. The reinforcement strength is assumed with $f_{yk} = 435 \, \text{MN/m}^2$ and the uniaxial concrete compressive strength (unsigned) with $f_c = 17.0 \, \text{MN/m}^2$ leading to $\bar{f}_{cd} = 12.92$. The structural height of the slab is $d = 0.25 \, \text{m}$. Safety factors are not explicitly regarded for the loading.

Computed principal moments and the required *lower* side reinforcement for a section left to the opening are shown in Fig. 7.9a. The vertical number indicates the required amount of reinforcement in cm^2/m in the y-direction, the horizontal number in x-direction. The relatively rough discretization with four integration points per element is also indicated. Lower reinforcement (first number in a pair) and upper reinforcement (second number in a pair) are shown in Fig. 7.9b for selected points. Their different characteristics of bending are described in the following.
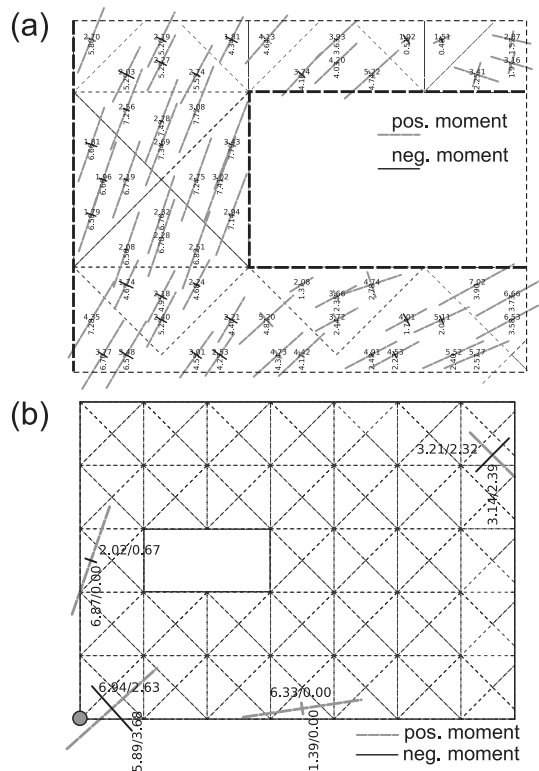
Figure 7.9: Example 7.2 (a) Required lower reinforcement of the left section. (b) Required reinforcement of selected points.

– Position $x = 0.17, y = 2.5$ near midspan left free edge.

Computed moments are $m_x = 0.001 \, \text{MNm/m}, m_y = 0.051, m_{xy} = 0.020$ leading to principal moments $m_1 = 0.058, m_2 = -0.006$ with a direction $\varphi = 71°$.
Lower reinforcement: Assuming $\varphi = -45°$ yields $a_{sx} = 2.02 \, \text{cm}^2/\text{m}, a_{sy} = 6.87$ with $z/d = 0.95$ and $x/d = 0.10$.
Upper reinforcement: $\varphi_c = 45°$ leads to $a_{sy} < 0$. Thus, an iteration has to be performed leading to $a_{sx} = 0.67 \, \text{cm}^2/\text{m}, a_{sy} = 0$ with $z/d = 0.92$, $x/d = 0.16$ and $\varphi_c = 69°$ computed.

– Position $x = 6.5, y = 4.17$ near upper right corner of simple line support.

Computed moments are $m_x = 0.004 \, \text{MNm/m}, m_y = 0.004, m_{xy} = -0.028$ leading to $m_1 = 0.032, m_2 = -0.024$ with $\varphi_1 = -45°$. The curvature is negative in the corner's diagonal direction and positive lateral to it. This indicates a load transfer "over edge" supporting a load transfer in the corner's diagonal and corresponds to a twisting effect.
Lower reinforcement: $\varphi = 45°$ yields $a_{sx} = 3.21 \, \text{cm}^2/\text{m}, a_{sy} = 3.14$ with $z/d = 0.0.93$, $x/d = 0.14$.
Upper reinforcement: $\varphi = -45°$ yields $a_{sx} = 2.32 \, \text{cm}^2/\text{m}, a_{sy} = 2.39$ with $z/d = 0.93$, $x/d = 0.14$ (must here be the same as the upper values).

– Position $x = 3.5, y = 0.17$ near midspan lower free edge.

Computed moments are $m_x = 0.060 \, \text{MNm/m}, m_y = 0.007, m_{xy} = 0.008$ leading to $m_1 = 0.061, m_2 = 0.006$ with $\varphi_1 = 8°$. *Lower* reinforcement: $\varphi = 45°$ yields $a_{sx} = 6.33 \, \text{cm}^2/\text{m}, a_{sy} = 1.39$ with $z/d = 0.98$, $x/d = 0.04$.
An *upper* reinforcement is not necessary as both principal stresses are positive and lead to a upper biaxial compressive stress state.

– Position $x = 0.5, y = 0.17$ near lower left single support.

Computed moments are $m_x = 0.02 \, \text{MNm/m}, my = 0.011, m_{xy} = 0.046$ leading to $m_1 = 0.061, m_2 = -0.030$ with $\varphi_1 = 42°$. The curvature is positive in the corner's diagonal direction and negative lateral to it. This corresponds to the major load transfer along the free edges compared to the diagonal.
Lower reinforcement: $\varphi_c = -45°$ yields $a_{sx} = 6.94 \, \text{cm}^2/\text{m}, a_{sy} = 5.89$ with $z/d = 0.88$, $x/d = 0.24$.
Upper reinforcement: $\varphi_c = 45°$ yields $a_{sx} = 2.63 \, \text{cm}^2/\text{m}, a_{sy} = 3.68$ with $z/d = 0.88$, $x/d = 0.24$ (must here be the same as the upper values).

As compressive heights are computed with $x/d < 0.5$ for all points the required load bearing capacity of concrete, see Eq. (7.79), is provided.

End Example 7.2

The same comments as for plates regarding concrete strength, ductility requirements, and crack width estimation, see Section 6.1.3, are also valid for slabs.

7.6.3   Design Approach for Shear

Shear has to be considered as further action beneath bending. In the case of Kirchhoff slabs, shear forces have to be calculated as derivatives of bending moments

$$v_x = -\frac{\partial m_x}{\partial x} - \frac{\partial m_{xy}}{\partial y}, \quad v_y = -\frac{\partial m_y}{\partial y} - \frac{\partial m_{xy}}{\partial x} \tag{7.80}$$

see Eq. (7.18). Bending moments itself are determined from curvature using Eq. (7.39) in the case of linear elastic material behavior. Furthermore, curvature is determined from finite element interpolation with Eq. (7.56). Summarized, another derivative has to be determined from $\mathbf{B} \cdot \boldsymbol{v}_e$. This might be elaborate regarding, e.g., relations like Eqs. (7.54, 7.55). In addition the accuracy decreases with computation of higher displacement derivatives.

A separate interpolation or approximation of moments within elements should be less expansive and yield sufficiently reliable shear force values. This may base on a linear approach

$$m = a\,x + b\,y + c \tag{7.81}$$

and

$$\frac{\partial m}{\partial x} = a, \quad \frac{\partial m}{\partial y} = b \tag{7.82}$$

where m stands for m_x, m_y, m_{xy}. The coefficients a, b, c need at least three computed values, e.g., from three integration points within triangular elements and the integration order $n_i = 1$, see Table 7.1. In the case of more integration points a linear regression analysis may be used to determine the three coefficients, see Appendix D. These coefficients immediately lead to shear force values v_x, v_y regarding Eqs. (7.80, 7.82) which are constant within the interpolation area.

Similar to the transformation rules for moments (Eq. (7.63)) a transformation rule for shear forces is required in the following. A cross section with normal vector $\mathbf{e} = (\ \cos\varphi \quad \sin\varphi\ )^T$ is regarded, whereby φ denotes the angle with the global x-axis. The shear force in this cross section is calculated from v_x, v_y, see Fig. 7.4, by

$$v_\varphi = v_x \cos\varphi + v_y \sin\varphi \tag{7.83}$$

This corresponds to Eq. (7.34)$_3$.

Shear forces become relevant near supported edges or supported points. Shear arises from change of longitudinal forces resulting from change of moments. This change of forces in adjacent positions leads to forces in horizontal cross sections and adjoined shear forces in vertical cross sections, see Fig. 7.10. In the case of reinforced concrete these forces are realized by concrete struts and reinforcement ties. The mechanisms are basically the same for beams and slabs.

Principal longitudinal forces t_1, t_2 computed from t_x, t_y, t_{xy} are used in the case of slabs. The force t_1 acts at a cross section with a normal directed with an angle φ_t against the x-axis, the force t_2 at a cross section perpendicular to it. Each of these has an opposite longitudinal force – both forming a couple for moments m_1, m_2 – and a shear force v_φ computed with Eq. (7.83). This completes a principal cross section of a slab from an internal force point of view.
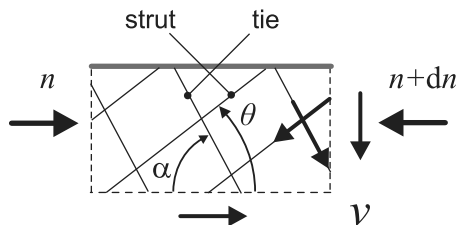
Figure 7.10: Shear mechanism.

- Regarding shear design a principal cross section of a slab is treated like a beam cross section of unit width.

Thus, the strut and tie approach for beam shear should also be applicable for principal cross sections of slabs. The value of v_φ is used for an appropriate procedure. Following [26, 6.2.1] shear reinforcement is not necessary for slabs in case v_φ does not exceed a threshold value $v_{Rd,c}$. Due to current state of knowledge this threshold depends on concrete strength, slab thickness and the amount of longitudinal reinforcement.

The amount of longitudinal reinforcement needs some specification in the context of principal cross sections. Reinforcement relations are determined by $t_{sx} = a_{sx}f_y$, $t_{sx} = a_{sx}f_y$, see Eq. (7.72). The transformation of reinforcement forces to the principal system is performed according to Eq. (7.63) and leads to

$$t_{s\varphi} = t_{sx} \cos^2 \varphi_t + t_{sy} \sin^2 \varphi_t \tag{7.84}$$

This transformation differs from Eq. (7.83), as t_{sx}, t_{sy} are in plane and subject to a transformation of both direction and reference length, while v_x, v_y are orthogonal to plane and subject to transformation of reference length only. A principal reinforcement amount is defined in analogy to Eq. (7.84) as

$$a_{s\varphi} = a_{sx} \cos^2 \varphi_t + a_{sy} \sin^2 \varphi_t \tag{7.85}$$

The value can be used to determine the threshold value for $v_{Rd,c}$ according to, e.g., [26, 6.2.2]. Larger values $a_{s\varphi}$ lead to larger threshold values $v_{Rd,c}$. An abundant value $a_{s\varphi}$ might be useful to avoid a slab shear reinforcement which generally is considered as inconvenient on construction sites.

In case shear reinforcement is unavoidable its amount within this setting may be determined in a similar way as for beam cross sections. The relations for the web of a beam which have been derived in Section 6.1.2 – see Eqs. (6.16) applied to unit width – may be used for this purpose whereby V is replaced by v_φ. Shear proof and design has to be performed for both principal directions. The shear reinforcement, if necessary, has to be superposed.

Example 7.3 Computation of shear forces and shear proof
We refer to Examples 7.1 and 7.2 with the same system and loading. With four integration points for a triangular element, see Table 7.1 and Fig. 7.9a, four sets of m_x, m_y, m_{xy} are computed for each element.
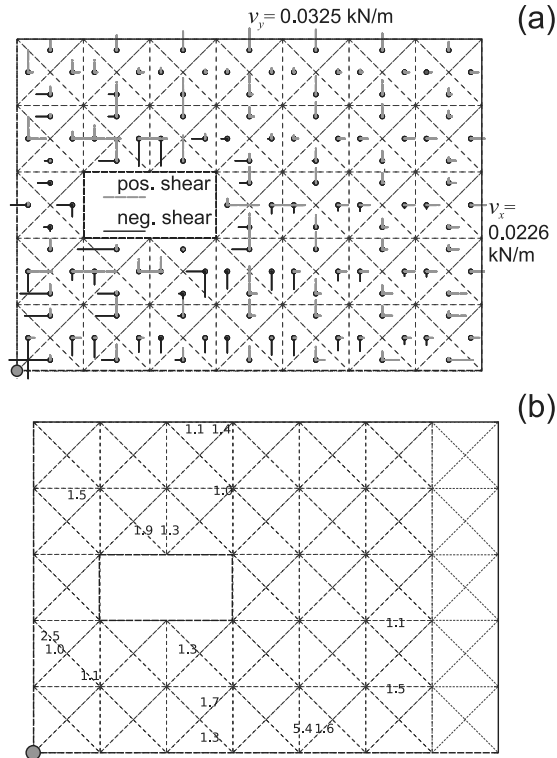
Figure 7.11: Example 7.3 (a) Computed shear forces. (b) Critical shear points.

A linear approximation of moments is performed within each element according to Eq. (7.81) with details given in Appendix D. Derivatives of moments are determined according to Eqs. (D.17,D.18), which are constant within an element. Thus, shear forces v_x, v_y computed with Eq. (7.80) are also constant within an element but may differ from element to element. The results are shown in Fig. 7.11a.

Shear forces within elements adjacent to the right and upper boundary edge correspond to support reactions. Regarding an element base length of 1 m these values match to support reactions from nodal forces, see Fig. 7.7b. The positive sign of shear forces, see Fig. 7.4 for sign conventions, corresponds to the negative (downward) external loading. Larger negative shear forces prevail around the left lower single support. This also corresponds to the negative external loading. Shear forces distribution looks somehow confuse around the central opening. A finer discretization may presumably help to have more evidence regarding this area.

A shear proof can be performed according to the outline given before. A basic proof value is determined with the shear force admitted in case without shear reinforcement, see [26, 6.2.2]

$$v_{Rd,c} = 0.10 \cdot \kappa \cdot (100\rho_s \cdot f_{ck})^{1/3} \cdot d \qquad (7.86)$$

with $f_{ck} = 30\,\text{MN/m}^2, d = 0.25\,\text{m}$ and $\kappa = 1.89$ for the current example. The prefactor is chosen according to [24, 6.2.2]. The parameter ρ_s denotes the reinforcement ratio, that is $\rho_s = a_{s\varphi}/d$ in the current context. A typical value is given by $a_s = 5\,\text{cm}^2/\text{m}$ and $\rho_s = 5 \cdot 10^{-4}/0.25 = 0.002$. This leads to $v_{Rd,c} = 0.086\,\text{MN/m}^2$. A value v_φ is computed throughout the slab with Eq. (7.83) and compared to the admissible shear force according to Eq. (7.86) with the reinforcement from Eq. (7.85).

The points computed with $|v_\varphi| > v_{Rd,c}$ are shown in Fig. 7.11b whereby the values indicate the ratio $|v_\varphi|/v_{Rd,c}$. Most of them are insofar not critical as the computed necessary bending reinforcement is low, i.e., the necessary shear bearing capacity may be reached with larger bending reinforcement, which is built in anyway to have a minimum uniform bending reinforcement.

End Example 7.3

A particular occurrence of shear is given with *punching*, i.e., shear forces are regarded with respect to single supports. A design value for punching results from a computed support reaction force. Design of slabs regarding punching obeys the common methods of reinforced concrete [26, 6.4].

7.7 Kirchhoff Slabs with Nonlinear Material Behavior

Analysis of Kirchhoff slabs is based on Eqs. (7.32, 7.37). A linear elastic material behavior according to Eq. (7.39) has been used in the preceding examples of this chapter. A simplified approach to describe nonlinear moment–curvature behavior will be described in the following. Nonlinear behavior in a general form is covered by the tangential material stiffness (Eq. (7.40)) . An incremental simplified approach formally following Eq. (7.39) with $\nu = 0$ is chosen as

$$\dot{\boldsymbol{\sigma}} = \mathbf{C}_T \cdot \dot{\boldsymbol{\epsilon}}, \quad \mathbf{C}_T = \begin{bmatrix} K_{Tx} & 0 & 0 \\ 0 & K_{Ty} & 0 \\ 0 & 0 & K_{Txy} \end{bmatrix} \tag{7.87}$$

with the bending stiffness K_{Tx}, K_{Ty} derived from uniaxial beam behavior. This corresponds to an orthotropic behavior. An approach for the twisting stiffness $C_{T33} = K_{Txy}$ may be based on the theory of orthotropic slabs [31, 119.] leading to

$$K_{Txy} = \frac{1}{2}\sqrt{K_{Tx}\,K_{Ty}} \tag{7.88}$$

The slab's cross sections with normals in the x- and y-directions, see Fig. 7.1b, are treated separately to derive K_{Tx}, K_{Ty} and each is derived as for a beam cross section of unit width.

An elastoplastic moment–curvature relation is assumed for the following, see Fig. 2.10 and Fig. 3.3 with $N = 0$. Material behavior in each direction is described by

- initial bending stiffness K_s,

- initial yielding moment m_{yk},

- hardening bending stiffness K_T,

- current plastic curvature κ_p as state parameter

in analogy to uniaxial elastoplastic behavior, see Section 2.3. These values are related in analogy to Eqs. (2.39, 2.40). Regarding reinforced concrete these values may be determined with an analysis of moment–curvature relations as was demonstrated with Example 3.1.

An alternative approach is based upon the setup shown in Fig. 7.8 of Section 7.6. To simplify the description a reinforcement is assumed on the tension side only, a reinforcement on the compression side may be included as an extension. Basic relations for the simplified case have already been discussed in Section 7.6.2. A yield moment m_{yk} is given by

$$m_{yk} = t_r\, z, \qquad t_c = -t_r \tag{7.89}$$

with the reinforcement tension force t_r, the concrete compression force t_c and the internal lever arm z. Assuming a constant concrete stress distribution these forces are

$$t_r = a_s\, f_{yk}, \qquad t_c = -\bar{f}_c\, x, \qquad \bar{f}_c = \chi f_c k \tag{7.90}$$

with the reinforcement cross-sectional area per unit width a_s, the strength of the reinforcement f_{yk}, the concrete strength f_c, the compression zone height x and coefficients χ, k, see Section 7.6.2. These equations are solved for

$$x = a_s\, \frac{f_{yk}}{\bar{f}_c} \tag{7.91}$$

The internal lever arm is given by

$$z = d - \frac{k\, x}{2} \tag{7.92}$$

with the constructive height d and the yield moment by

$$m_{yk} = a_s f_{yk}\, z = a_s f_{yk} \left(d - \frac{k}{2} \frac{a_s f_{yk}}{\bar{f}_c} \right) \tag{7.93}$$

and finally the initial yield curvature by

$$\kappa_{yk} = \frac{\epsilon_{yk}}{d - x} = \frac{\frac{f_{yk}}{E_s}}{d - \frac{a_s f_{yk}}{\bar{f}_c}} \tag{7.94}$$

see Eq. (3.18), with Young's modulus E_s of the reinforcement. It has to be considered that a_s is the cross-sectional area of reinforcement per unit slab width.

The initial bending stiffness is further determined by

$$K_s = \frac{m_{yk}}{\kappa_{yk}} \tag{7.95}$$

A hardening can be considered with a hardening of the reinforcement stress up to reaching its strength f_t. This leads to m_t, κ_t using Eqs. (7.93, 7.94) and to a hardening bending stiffness

$$K_T = \frac{m_t - m_{yk}}{\kappa_t - \kappa_{yk}} \tag{7.96}$$

These equations can be applied to each cross-section direction with its own a_s and d. The initial stiffness K_s as well as the hardening stiffness K_T are used for K_{Tx}, K_{Ty} in their appropriate range. The application is demonstrated with the following example.

Example 7.4 Elastoplastic rectangular slab with opening and free edges
We refer to Example 7.1 with the same geometry, boundary conditions and loading. The
height of the slab is $h = 0.3$ m.

Furthermore, a reinforced concrete is assumed with the following parameters:

$$f_c = 17\,\text{MN/m}^2, \quad \chi = 0.95, \quad k = 0.8 \quad \rightarrow \quad \bar{f}_c = 12.92\,\text{MN/m}^2 \tag{7.97}$$

for the concrete and

$$E_s = 200\,000\,\text{MN/m}^2, \quad f_{yk} = 435\,\text{MN/m}^2, \quad f_t = 480\,\text{MN/m}^2 \tag{7.98}$$

and

$$a_{sx} = a_{sy} = 5.13\,\text{cm}^2/\text{m}, \quad d_x = d_y = 0.25\,\text{m} \tag{7.99}$$

for the reinforcement. With Eq. (7.91) this leads to a compression zone height

$$x_i = 5.13 \cdot 10^{-4} \cdot \frac{435}{12.92} = 0.0173\,\text{m}, \qquad i = x, y \tag{7.100}$$

with Eq. (7.93) to a yield moment

$$m_{yk,i} = 5.13 \cdot 10^{-4} \cdot 435 \left(0.25 - \frac{0.8}{2} \frac{5.13 \cdot 10^{-4} \cdot 435}{12.92} \right) = 0.054\,\text{MNm/m} \tag{7.101}$$

and with Eq. (7.94) to yield a curvature

$$\kappa_{yk,i} = \frac{\frac{435}{200\,000}}{0.25 - 0.0173} = 0.935 \cdot 10^{-2}\,\text{m}^{-1} \tag{7.102}$$

The initial bending stiffness is given with

$$K_{s,i} = \frac{0.054}{0.935 \cdot 10^{-2}} = 5.80\,\text{MNm}^2/\text{m} \tag{7.103}$$

according to Eq. (7.95) and in a similar way the hardening bending stiffness with $K_{T,i} = 0.12\,\text{MNm}^2/\text{m}, \; i = x, y$ similar to Eq. (7.96). Actually the initial bending stiffness should be larger due to tension stiffening effects, see Sections 2.7 and 3.5.3. But this effect should loose its influence in the range of yielding.

The same discretization is used as in Example 7.1. An incrementally iterative scheme with Newton–Raphson iteration within each loading increment, see Section 1.6, is used as the solution method. The load increment size is controlled with the arc length method, see Appendix A.

The computed principal moments for the final loading are shown in Fig. 7.12a and the deflection in Fig. 7.12b. The maximum displacements increase by a factor of approximately 12 compared to the linear elastic case of Example 7.1. This corresponds to bending stiffness relations which are $72.5\,\text{MNm}^2/\text{m}$, see Eq. (7.13), for the linear elastic case and $5.8\,\text{MNm}^2/\text{m}$ for the current example. Slight redistributions of moments can be observed, compare Fig. 7.6b for the linear elastic case with Fig. 7.12a. But moments m_x, m_y do not exceed the prescribed

(a)

(b)
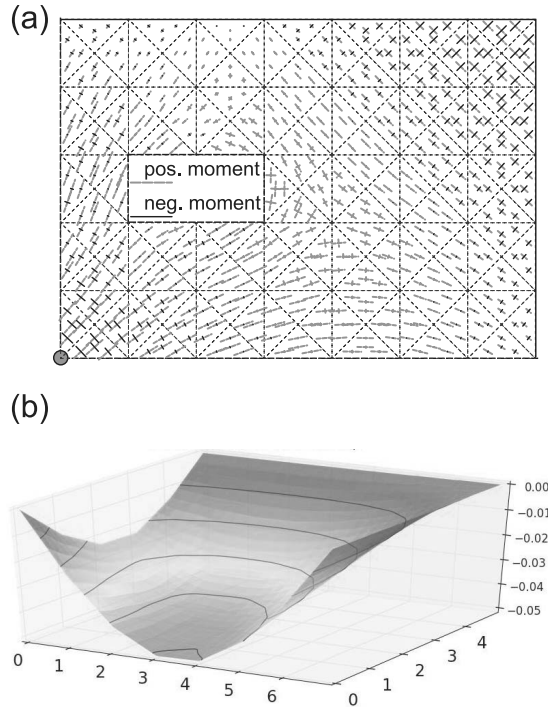
Figure 7.12: Example 7.4 (a) Discretization and principal moments. (b) Deflections (opening not shown).

yield limit of $m_{y,i} = 0.054\,\mathrm{MNm/m}$ while maximum values are in range of $0.06\,\mathrm{MNm/m}$ in the case of the linear elastic calculations.

The potential for moment redistribution compared to the linear elastic case is limited in this particular example due to the boundary conditions with free edges and a single support. Furthermore, the results are quite sensitive with respect to the twisting stiffness K_{xy} in this example.

End Example 7.4

Proof and design regarding shear can be performed according to Section 7.6.3 whereby elastic moments in Eq. (7.80) have to be replaced by elastoplastic moments.

The approach for moments depending on curvature according to Eq. (7.87) is *not* isotropic according to Section 5.3.1. A transformation of, e.g., the data of Example 7.4 in a rotated coordinate system, then applying Eq. (7.87) in the diagonal form followed the the back transformation of results in analogy to Eqs. (7.62, C.12) will lead to different moments compared to Example 7.4.

Equation (7.87) is related to a coordinate system which is aligned to orthogonal reinforcement directions. Such a coordinate system may be considered as local and corotational allowing for a variation of reinforcement directions. Thus, the material behavior in a slab

position is described in a local system and the relation to the global system is ruled in analogy to Eqs. (5.15, 5.16, 5.41) with generalized strains and stresses and transformation matrices according to Eqs. (C.13, C.12). Nonorthogonal reinforcement directions in a slab position may be treated with different local coordinate systems in the same slab position.

Elastoplasticity of moments may also be covered within the framework for multiaxial elastoplasticity as has been described in Section 5.5.1 with $\boldsymbol{\sigma}$, $\boldsymbol{\epsilon}$ according to Eq. (7.37), $\mathbf{C}$ from Eq. (7.39) replacing $\mathbf{E}$ and appropriate formulations [1] for the yield function F and the flow potential G.

---

[1] The plastic state parameter κ_p should be distinguished from plastic curvature if necessary.

Chapter 8

Shells

8.1 Approximation of Geometry and Displacements

Finally, thin shells are treated as further structural element type. Shell kinematics is quite complex [34]. Thus, deviating from the standard way for structural elements up to now – kinematics, generalized material behavior, equilibrium formulated in generalized forces, appropriate element types – a short track coupled to a simple standard finite shell element is described in the following. We use the continuum-based four-node shell element as is discussed in [25], [2, 5.4.2].

Shells include plates and slabs as special cases. In particular, they can model slabs exposed to the combined action of lateral and in-plane actions. This effect has already been discussed for cracked reinforced concrete beams in a simpler setup, see Examples 3.2 and 3.4, and will be extended to cracked reinforced surface structures.

Shells in a first approach can be considered as an extension of slabs whereby the reference plane becomes a simply or doubly curved *reference surface*. The geometry of a surface in space is described by coordinates

$$x_1 = x_1(r, s), \quad x_2 = x_2(r, s), \quad x_3 = x_3(r, s) \tag{8.1}$$

in a global Cartesian system with base vectors $\mathbf{e}_1, \mathbf{e}_2, \mathbf{e}_3$. The indication of the global coordinate directions is changed compared to previous sections to facilitate the notation. Isoparametric coordinates r, s serve as independent variables. Thus, a pair r, s identifies a point of the reference surface or a *shell position*. Every shell position has a thickness h. Reference surface and thickness occupy a *shell body*.

Furthermore, every shell position has a *shell director*. This is a unit vector $\mathbf{V}_n$ describing a direction of a cross section.

- The validity of the *Bernoulli–Navier hypothesis* – stating that undeformed plane cross sections remain plane during a deformation – in the case of thin shells is assumed for cross sections defined by shell directors.

A shell director may be chosen independently from the geometry definition given by Eq. (8.1). But generally it coincides more or less with the normal of the reference surface in the case of smooth geometries.

A *local Cartesian coordinate system* is defined for a shell position using, e.g., the unit vector $\mathbf{e}_2$ of the global coordinate system with the vector cross product $\times$ leading to a unit vector $\mathbf{V}_\alpha$

$$\mathbf{V}_\alpha = \frac{\mathbf{e}_2 \times \mathbf{V}_n}{|\mathbf{e}_2 \times \mathbf{V}_n|}, \qquad \mathbf{e}_2 \times \mathbf{V}_n = \begin{pmatrix} V_{n3} \\ 0 \\ -V_{n1} \end{pmatrix} \tag{8.2}$$

see Fig. 8.1, and another unit vector $\mathbf{V}_\beta$

$$\mathbf{V}_\beta = \mathbf{V}_n \times \mathbf{V}_\alpha = \begin{pmatrix} V_{\alpha 3} V_{n2} \\ V_{\alpha 1} V_{nz} - V_{\alpha 3} V_{n1} \\ -V_{\alpha 1} V_{n2} \end{pmatrix} \tag{8.3}$$

Vectors $\mathbf{V}_\alpha, \mathbf{V}_\beta, \mathbf{V}_n$ in this sequence form an orthogonal, normalized, right-handed coordinate system which more or less leans against the reference surface.

A *shell geometry* is approximated by an isoparametric finite element interpolation. Nodes are placed in the reference surface spanning a mesh of quadrilateral elements whereby each element has four nodes. The reference surface of a quadrilateral element must not be plane in space. The geometry of the *undeformed* shell is interpolated by

$$x_i(r,s,t) = \sum_{K=1}^{4} N_K(r,s)\, x_{iK} + \frac{t}{2} \sum_{K=1}^{4} h_K N_K(r,s)\, V_{niK}, \quad i = 1,\ldots,3 \tag{8.4}$$

see Fig. 8.1a, with

x_i	*i*th coordinate of shell body
r, s	*local* isoparametric coordinates within the reference surface
t	*local* isoparametric coordinate lateral to the reference surface
$N_K(r,s)$	$= \frac{1}{4}(1 + r_K r)(1 + s_K s)$ according to Eq. (1.19)
r_K, s_K	local isoparametric coordinates of node K
x_{iK}	*i*th coordinate of node K
h_K	shell thickness at node K
V_{niK}	*i*th component of director at node K
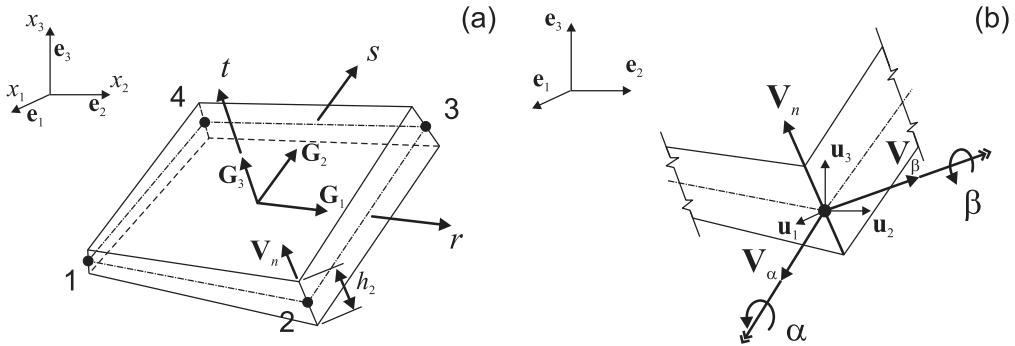
Figure 8.1: Shell element [25] (a) Element geometry. (b) Local coordinate system.

The quantities x_i, x_{iK}, h_K have dimensions of [length] while $-1 \leq r, s, t \leq 1$ and $r_K, s_K = \pm 1$ are dimensionless. Equation (8.4) leads to the Jacobian similar to Eq. (1.37)

$$\mathbf{J} = \left[\begin{array}{ccc} J_{11} & J_{12} & J_{13} \\ J_{21} & J_{22} & J_{23} \\ J_{31} & J_{32} & J_{33} \end{array} \right] = \left[\begin{array}{ccc} \frac{\partial x_1}{\partial r} & \frac{\partial x_1}{\partial s} & \frac{\partial x_1}{\partial t} \\ \frac{\partial x_2}{\partial r} & \frac{\partial x_2}{\partial s} & \frac{\partial x_2}{\partial t} \\ \frac{\partial x_3}{\partial r} & \frac{\partial x_3}{\partial s} & \frac{\partial x_3}{\partial t} \end{array} \right] \tag{8.5}$$

connecting global coordinates with local isoparametric coordinates. Its components are given by

$$\frac{\partial x_i}{\partial r} = \sum_{K=1}^{4} b_{rK} x_{iK} + \frac{t}{2} \sum_{K=1}^{4} b_{rK} h_K V_{niK}$$
$$\frac{\partial x_i}{\partial s} = \sum_{K=1}^{4} b_{sK} x_{iK} + \frac{t}{2} \sum_{K=1}^{4} b_{sK} h_K V_{niK} \quad i = 1, \ldots, 3 \tag{8.6}$$
$$\frac{\partial x_i}{\partial t} = \frac{1}{2} \sum_{k=1}^{4} N_K h_K V_{niK}$$

with

$$b_{rK} = \frac{\partial N_K}{\partial r} = \frac{1}{4} r_K (1 + s_K s), \quad b_{sK} = \frac{\partial N_K}{\partial s} = \frac{1}{4} s_K (1 + r_K r) \tag{8.7}$$

Shell displacements have to be approximated in the next step. For this purpose, we introduce a *small* rotation α around the vector $\mathbf{V}_\alpha$, see Eq. (8.2), and a small rotation β around the vector $\mathbf{V}_\beta$, see Eq. (8.3). This leads to a vector $\mathbf{v}$

$$\mathbf{v} = -\alpha \, \mathbf{V}_\beta + \beta \, \mathbf{V}_\alpha \tag{8.8}$$

lying in the plane spanned by $\mathbf{V}_\alpha, \mathbf{V}_\beta$, see Fig. 8.1b. The vector $\mathbf{v}$ is in particular given at nodes with $\mathbf{v}_K = -\alpha \, \mathbf{V}_{\beta K} + \beta \, \mathbf{V}_{\alpha K}$ and $\mathbf{V}_{\beta K}, \mathbf{V}_{\alpha K}$ determined from Eqs. (8.2, 8.3) using the particular director $\mathbf{V}_{nK}$. A vector $\mathbf{v}_K$ with components v_{iK} is used to displace a director $\mathbf{V}_{nK}$ leading to an interpolation of displacements

$$u_i(r, s, t) = \sum_{K=1}^{4} N_K(r, s) \, u_{iK} + \frac{t}{2} \sum_{K=1}^{4} h_K N_K(r, s) \, v_{iK}, \quad i = 1, \ldots, 3 \tag{8.9}$$

in the same way as coordinates whereby

u_i *i*th component of displacement
u_{iK} *i*th component of displacement of node K
v_{iK} $= -\alpha_K V_{\beta iK} + \beta_K V_{\alpha iK}$ *i*th component of director change at node K

This approach realizes the Bernoulli–Navier hypothesis with respect to cross sections defined by shell directors.

8.2 Approximation of Deformations

Shell deformations are derived from shell displacements by their derivatives with respect to spatial coordinates. We start regarding the local isoparametric coordinates

$$
\begin{pmatrix} \dfrac{\partial u_i}{\partial r} \\[2mm] \dfrac{\partial u_i}{\partial s} \\[2mm] \dfrac{\partial u_i}{\partial t} \end{pmatrix} = \sum_{K=1}^{4} \begin{bmatrix} b_{rK} & t\,g_{\alpha iK} b_{rK} & t\,g_{\beta iK} b_{rK} \\ b_{sK} & t\,g_{\alpha iK} b_{sK} & t\,g_{\beta iK} b_{sK} \\ 0 & g_{\alpha iK} N_K & g_{\beta iK} N_K \end{bmatrix} \cdot \begin{pmatrix} u_{iK} \\ \alpha_K \\ \beta_K \end{pmatrix}, \quad i = 1,\ldots,3 \qquad (8.10)
$$

with scaled rotation axes

$$
\begin{aligned}
\mathbf{g}_{\alpha K} &= -\frac{1}{2} h_K\, \mathbf{V}_{\beta K}\,, & \begin{pmatrix} g_{\alpha 1 K} \\ g_{\alpha 2 K} \\ g_{\alpha 3 K} \end{pmatrix} &= -\frac{1}{2} h_K \begin{pmatrix} V_{\beta 1 K} \\ V_{\beta 2 K} \\ V_{\beta 3 K} \end{pmatrix} \\[3mm]
\mathbf{g}_{\beta K} &= \frac{1}{2} h_K\, \mathbf{V}_{\alpha K}\,, & \begin{pmatrix} g_{\beta 1 K} \\ g_{\beta 2 K} \\ g_{\beta 3 K} \end{pmatrix} &= \frac{1}{2} h_K \begin{pmatrix} V_{\alpha 1 K} \\ V_{\alpha 2 K} \\ V_{\alpha 3 K} \end{pmatrix}
\end{aligned}
\qquad (8.11)
$$

Equation (8.10) is transformed into derivatives with respect to global coordinates with the inverse of the Jacobian

$$
\begin{pmatrix} \dfrac{\partial u_i}{\partial x_1} \\[2mm] \dfrac{\partial u_i}{\partial x_2} \\[2mm] \dfrac{\partial u_i}{\partial x_3} \end{pmatrix} = \mathbf{J}^{-1} \cdot \begin{pmatrix} \dfrac{\partial u_i}{\partial r} \\[2mm] \dfrac{\partial u_i}{\partial s} \\[2mm] \dfrac{\partial u_i}{\partial t} \end{pmatrix} \quad i = 1,\ldots,3 \qquad (8.12)
$$

with

$$
\mathbf{J}^{-1} = \begin{bmatrix} J_{11}^{-1} & J_{12}^{-1} & J_{13}^{-1} \\ J_{21}^{-1} & J_{22}^{-1} & J_{23}^{-1} \\ J_{31}^{-1} & J_{32}^{-1} & J_{33}^{-1} \end{bmatrix} = \begin{bmatrix} \dfrac{\partial r}{\partial x_1} & \dfrac{\partial r}{\partial x_2} & \dfrac{\partial r}{\partial x_3} \\[2mm] \dfrac{\partial s}{\partial x_1} & \dfrac{\partial s}{\partial x_2} & \dfrac{\partial s}{\partial x_3} \\[2mm] \dfrac{\partial t}{\partial x_1} & \dfrac{\partial t}{\partial x_2} & \dfrac{\partial t}{\partial x_3} \end{bmatrix} \qquad (8.13)
$$

Equations (8.10, 8.12, 8.13) may be used to obtain the interpolation of the small strain tensor components

$$
\epsilon_{ij} = \frac{1}{2} \left(\frac{\partial u_i}{\partial x_j} + \frac{\partial u_j}{\partial x_i} \right), \quad i,j = 1,\ldots,3 \qquad (8.14)
$$

This is identical to the strains of a three-dimensional body. The difference arises from the constrained freedom to deform according to Eq. (8.9) including the Bernoulli–Navier hypothesis. The second-order strain tensor as a whole is given by

$$
\mathbf{E} = \sum_{i=1}^{3} \sum_{j=1}^{3} \epsilon_{ij}\, \mathbf{e}_i \mathbf{e}_j \qquad (8.15)
$$

whereby $\mathbf{e}_i \mathbf{e}_j$ is the tensor product of the global system unit vectors $\mathbf{e}_i$ and $\mathbf{e}_j$. Deformations according to Eq. (8.14) are measured in the global Cartesian system and are inconvenient for

thin curved shell bodies. A *covariant* or so-called *natural* coordinate system is more suitable [2, p. 425]. Its base vectors are formed by the Jacobian $\mathbf{J}$ as

$$\mathbf{G}_1 = \begin{pmatrix} \mathcal{G}_{11} \\ \mathcal{G}_{12} \\ \mathcal{G}_{13} \end{pmatrix} = \begin{pmatrix} J_{11} \\ J_{21} \\ J_{31} \end{pmatrix}, \mathbf{G}_2 = \begin{pmatrix} \mathcal{G}_{21} \\ \mathcal{G}_{22} \\ \mathcal{G}_{23} \end{pmatrix} = \begin{pmatrix} J_{12} \\ J_{22} \\ J_{32} \end{pmatrix}, \mathbf{G}_3 = \begin{pmatrix} \mathcal{G}_{31} \\ \mathcal{G}_{32} \\ \mathcal{G}_{33} \end{pmatrix} = \begin{pmatrix} J_{13} \\ J_{23} \\ J_{33} \end{pmatrix}$$

(8.16)

with jth component $\mathcal{G}_{ij}$ of base vector i measured in the absolute Cartesian system.

- $\mathbf{G}_1$ is the tangential vector along the space curve given with varying r while s, t are hold constant, $\mathbf{G}_2$ the tangential vector along the curve with varying s and r, t constant and $\mathbf{G}_3$ with varying t and r, s constant.

The covariant system generally is skew and not normalized, i.e., $\mathbf{G}_i \cdot \mathbf{G}_j \neq 0$ for $i \neq j$ and $\mathbf{G}_i \cdot \mathbf{G}_j \neq 1$ for $i = j$.

Thus, a *contravariant* coordinate system is introduced with base vectors

$$\mathbf{G}^1 = \begin{pmatrix} \mathcal{G}^{11} \\ \mathcal{G}^{12} \\ \mathcal{G}^{13} \end{pmatrix} = \begin{pmatrix} J_{11}^{-1} \\ J_{12}^{-1} \\ J_{13}^{-1} \end{pmatrix}, \mathbf{G}^2 = \begin{pmatrix} \mathcal{G}^{21} \\ \mathcal{G}^{22} \\ \mathcal{G}^{23} \end{pmatrix} = \begin{pmatrix} J_{21}^{-1} \\ J_{22}^{-1} \\ J_{23}^{-1} \end{pmatrix}, \mathbf{G}^3 = \begin{pmatrix} \mathcal{G}^{31} \\ \mathcal{G}^{32} \\ \mathcal{G}^{33} \end{pmatrix} = \begin{pmatrix} J_{31}^{-1} \\ J_{32}^{-1} \\ J_{33}^{-1} \end{pmatrix}$$

(8.17)

utilizing the inverse $\mathbf{J}^{-1}$ of the Jacobian. Due to the definitions of $\mathbf{G}_i, \mathbf{G}^j$ the properties $\mathbf{G}_i \cdot \mathbf{G}^j = 0$ hold for $i \neq j$ and $\mathbf{G}_i \cdot \mathbf{G}^j = 1$ for $i = j$. The components $\mathcal{G}_{ij}$ of the covariant base form a second-order tensor. But it is not symmetric, i.e., $\mathcal{G}_{ij} \neq \mathcal{G}_{ji}$. The same holds for the contravariant base: $\mathcal{G}^{ij} \neq \mathcal{G}^{ji}$. Contravariant and covariant systems may also formally be derived for Cartesian coordinate systems, but then they coincide due to normalization and orthogonality.

Following the approach in [2, 2.4, 6.5.2], [25] the strain as a whole is described as

$$\mathbf{E} = \sum_{i=1}^{3} \sum_{j=1}^{3} \tilde{\epsilon}_{ij} \, \mathbf{G}^i \mathbf{G}^j$$

(8.18)

with so-called *covariant strain components* $\tilde{\epsilon}_{ij}$ or *natural strains*. Writing indices of $\tilde{\epsilon}_{ij}$ as subscripts and thus making these quantities "contravariant" is pure convention but quite convenient in the context of tensor calculus. Another view on strains is

$$\epsilon_{ij} = \sum_{i=1}^{3} \sum_{j=1}^{3} \mathbf{e}_i \cdot \mathbf{E} \cdot \mathbf{e}_j, \qquad \tilde{\epsilon}_{ij} = \sum_{i=1}^{3} \sum_{j=1}^{3} \mathbf{G}_i \cdot \mathbf{E} \cdot \mathbf{G}_j$$

(8.19)

Natural strain components have a dimension of [length^2] as $\mathbf{G}^i, \mathbf{G}^j$ each have a dimension of [length^{-1}]. Identity of Eqs. (8.15, 8.18) together with Eq. (8.14) leads to

$$\tilde{\epsilon}_{ij} = \sum_{r=1}^{3} \sum_{s=1}^{3} \mathcal{G}_{ir} \mathcal{G}_{js} \, \epsilon_{rs} = \frac{1}{2} \sum_{k=1}^{3} \left(\mathcal{G}_{ik} \frac{\partial u_k}{\partial \xi_j} + \mathcal{G}_{jk} \frac{\partial u_k}{\partial \xi_i} \right), \quad i,j = 1, \dots, 3$$

(8.20)

with $\xi_1 = r, \xi_2 = s, \xi_3 = t$. This may be shown using (1) $\mathbf{G}_i \cdot \mathbf{G}^j = 0$ for $i \neq j$, (2) $\mathbf{e}_j \cdot \mathbf{G}_i = \mathbf{G}_i \cdot \mathbf{e}_j = \mathcal{G}_{ij}$ and (3) $\mathcal{G}_{ij} = J_{ji} = \partial x_j / \partial \xi_i$.

Combining Eqs. (8.10, 8.20) the interpolation of contravariant strain components is given by

$$\tilde{\boldsymbol{\epsilon}} = \sum_{K=1}^{4} \mathbf{B}_K \cdot \mathbf{u}_K \tag{8.21}$$

with

$$
\begin{aligned}
\tilde{\boldsymbol{\epsilon}} &= \begin{pmatrix} \tilde{\epsilon}_{11} & \tilde{\epsilon}_{22} & \tilde{\epsilon}_{33} & 2\tilde{\epsilon}_{23} & 2\tilde{\epsilon}_{13} & 2\tilde{\epsilon}_{12} \end{pmatrix}^T \\
\mathbf{B}_K &= \begin{bmatrix} \mathcal{G}_{11}b_{rK} & \mathcal{G}_{12}b_{rK} & \mathcal{G}_{13}b_{rK} & t\,b_{rK}\mathcal{H}_{11K} & t\,b_{rK}\mathcal{H}_{12K} \\ \mathcal{G}_{21}b_{sK} & \mathcal{G}_{22}b_{sK} & \mathcal{G}_{23}b_{sK} & t\,b_{sK}\mathcal{H}_{21K} & t\,b_{sK}\mathcal{H}_{22K} \\ \vdots & \vdots & \vdots & \vdots & \vdots \end{bmatrix} \\
\mathbf{u}_K &= \begin{pmatrix} u_{1K} & u_{2K} & u_{3K} & \alpha_K & \beta_K \end{pmatrix}^T
\end{aligned}
\tag{8.22}
$$

and

$$
\begin{aligned}
\mathcal{H}_{11K} &= \mathcal{G}_{11}\,g_{\alpha 1K} + \mathcal{G}_{12}\,g_{\alpha 2K} + \mathcal{G}_{13}\,g_{\alpha 3K}, & \mathcal{H}_{12K} &= \mathcal{G}_{11}\,g_{\beta 1K} + \mathcal{G}_{12}\,g_{\beta 2K} + \mathcal{G}_{13}\,g_{\beta 3K} \\
\mathcal{H}_{21K} &= \mathcal{G}_{21}\,g_{\alpha 1K} + \mathcal{G}_{22}\,g_{\alpha 2K} + \mathcal{G}_{23}\,g_{\alpha 3K}, & \mathcal{H}_{22K} &= \mathcal{G}_{21}\,g_{\beta 1K} + \mathcal{G}_{22}\,g_{\beta 2K} + \mathcal{G}_{23}\,g_{\beta 3K} \\
\vdots & & \vdots &
\end{aligned}
\tag{8.23}
$$

with $\mathcal{G}_{ij}$ according to Eqs. (8.5, 8.16), b_{rK}, b_{sK} according to Eq. (8.7), both depending on r, s, and g_{ixK}, g_{iyK} according to Eq. (8.11) whereby K indicates the element's nodes. The approach (Eq. (8.22)) still includes a nonzero strain component $\tilde{\epsilon}_{33}$ normal to the shell's reference surface. This results from the continuum-based approach. Its absolute value should be considerably smaller compared to the other components in practical applications.

Regarding Eq. (8.22), the discretized strain state of every position in the shell body is ruled by five degrees of freedom per node. A so-called *five-parameter shell model* is given corresponding to the *Reissner–Mindlin* shell kinematics.

8.3 Shell Stresses and Material Laws

Strains have to be related to stresses to derive a structural resistance. The concept of Cauchy stresses, see Section 5.2.2, is used for continuum-based shell formulations in contrast to beams and slabs. Stress components have been introduced with respect to the global Cartesian system. The stress tensor as whole is given by

$$\mathbf{S} = \sum_{i=1}^{3} \sum_{j=1}^{3} \sigma_{ij}\, \mathbf{e}_i \mathbf{e}_j \tag{8.24}$$

in analogy to Eq. (8.15). Within the context of shells it is appropriate to use the covariant system (Eq. (8.16)) as a base for stress components

$$\mathbf{S} = \sum_{i=1}^{3} \sum_{j=1}^{3} \tilde{\sigma}^{ij}\, \mathbf{G}_i \mathbf{G}_j \tag{8.25}$$

with so-called contravariant stress components $\tilde{\sigma}^{ij}$. The identity of Eqs. (8.24, 8.25) leads to

$$\tilde{\sigma}^{ij} = \sum_{r=1}^{3}\sum_{s=1}^{3} \mathcal{G}^{ir}\mathcal{G}^{js}\,\sigma_{rs} \tag{8.26}$$

This may be shown using (1) $\mathbf{G}_i \cdot \mathbf{G}^j = 0$ for $i \neq j$, (2) $\mathbf{e}_j \cdot \mathbf{G}^i = \mathbf{G}^i \cdot \mathbf{e}_j = \mathcal{G}^{ij}$.

The motivation of introducing contravariant stress components is given by formulating the rate of internal specific strain energy. It is defined as

$$\dot{u} = \sum_{i=1}^{3}\sum_{j=1}^{3} \sigma_{ij}\,\dot{\epsilon}_{ij} \tag{8.27}$$

in the global Cartesian system, see Section 5.10. This particular formulation of the strain energy establishes the formulation of the principle of virtual displacements, see Eq. (1.52), which on the other hand is a basis for the finite element method.

Using the transformation rules (Eqs. (8.20, 8.26)) and regarding $\mathbf{G}_i \cdot \mathbf{G}^j = 0$ for $i \neq j$ and $\mathbf{G}_i \cdot \mathbf{G}^j = 1$ for $i = j$ it can be shown that

$$\sum_{i=1}^{3}\sum_{j=1}^{3} \sigma_{ij}\,\dot{\epsilon}_{ij} = \sum_{i=1}^{3}\sum_{j=1}^{3} \tilde{\sigma}^{ij}\,\dot{\tilde{\epsilon}}_{ij} \tag{8.28}$$

i.e., contravariant stress components are complementary to covariant strain components from an energetic point of view.

- When using covariant or natural strain components to describe shell deformations it is mandatory to use contravariant stress components for weak equilibrium conditions like the principle of virtual displacements.

To enable a comprehensible description of the material behavior of shells it is appropriate to use the local system $\mathbf{V}_\alpha, \mathbf{V}_\beta, \mathbf{V}_n$ as has been introduced with the shell director $\mathbf{V}_n$ and Eqs. (8.2, 8.3). The local system is an orthogonal, normalized, and right handed or Cartesian coordinate system, respectively. On one hand it leans against the shell's reference surface, thus it may change with every point of the reference surface and in this way forms a *local corotational* coordinate system. On the other hand, it is appropriate for the description of material behavior due to its normalization and orthogonality.

To facilitate the notation $\mathbf{V}_1 = \mathbf{V}_\alpha$, $\mathbf{V}_2 = \mathbf{V}_\beta$, $\mathbf{V}_3 = \mathbf{V}_n$ is used in the following for the local Cartesian coordinate system.

- *Local stress* components $\bar{\sigma}_{ij}$ and *local strain* components $\bar{\epsilon}_{ij}$ related to the local corotational Cartesian system are appropriate to formulate the stress–strain relations for thin shells.

In analogy to Eqs. (8.15, 8.24) these stress and strain components are given by

$$\mathbf{S} = \sum_{i=1}^{3}\sum_{j=1}^{3} \bar{\sigma}_{ij}\,\mathbf{V}_i\mathbf{V}_j, \qquad \mathbf{E} = \sum_{i=1}^{3}\sum_{j=1}^{3} \bar{\epsilon}_{ij}\,\mathbf{V}_i\mathbf{V}_j \tag{8.29}$$

As they are referenced in a Cartesian system no distinction between contravariant and co-variant components is necessary.

To determine local material behavior the natural strains $\tilde{\epsilon}$ as they are derived from nodal displacements using Eq. (8.21) have to be transformed into local strains $\bar{\epsilon}$. The identity of Eq. $(8.29)_1$ and Eq. (8.18) leads to

$$\bar{\epsilon}_{ij} = \sum_{r=1}^{3} \sum_{s=1}^{3} \mathcal{T}_{ir} \mathcal{T}_{sj} \tilde{\epsilon}_{rs} \tag{8.30}$$

with

$$\mathcal{T}_{ij} = \mathbf{V}_i \cdot \mathbf{G}^j, \quad \mathcal{T}_{ij} \neq \mathcal{T}_{ji} \tag{8.31}$$

This may be written as a matrix operation

$$\bar{\epsilon} = \mathbf{T} \cdot \tilde{\epsilon} \tag{8.32}$$

with $\bar{\epsilon}, \tilde{\epsilon}$ ordered according to Eq. (5.3) and the components of $\mathbf{T}$ derived from Eq. (8.31).

To begin with a linear elastic material behavior is considered. The shell body differs from the three-dimensional continuum ruled by the linear elastic law (Eq. (5.24)) insofar as its normal stress in a plane normal to the reference surface should be negligible compared to all other stress components. Thus, we use

$$\bar{\sigma} = \bar{\mathbf{C}} \cdot \bar{\epsilon} \tag{8.33}$$

with $\bar{\sigma}$ ordered as in Eq. (5.7) and

$$\bar{\mathbf{C}} = \begin{bmatrix} \frac{E(1-\nu)}{(1+\nu)(1-2\nu)} & \frac{E\nu}{(1+\nu)(1-2\nu)} & 0 & 0 & 0 & 0 \\ \frac{E\nu}{(1+\nu)(1-2\nu)} & \frac{E(1-\nu)}{(1+\nu)(1-2\nu)} & 0 & 0 & 0 & 0 \\ 0 & 0 & 0 & 0 & 0 & 0 \\ 0 & 0 & 0 & \frac{E}{2(1+\nu)} & 0 & 0 \\ 0 & 0 & 0 & 0 & \frac{E}{2(1+\nu)} & 0 \\ 0 & 0 & 0 & 0 & 0 & \frac{E}{2(1+\nu)} \end{bmatrix} \tag{8.34}$$

according to Eq. (5.24) whereby the influence of the collateral components $\bar{\epsilon}_{33}$, $\bar{\sigma}_{33}$ has been neglected due to the assumption of thin shells. Relation (8.33) may be generalized in the incremental form as

$$\dot{\bar{\sigma}} = \bar{\mathbf{C}}_T \cdot \dot{\bar{\epsilon}} \tag{8.35}$$

see also Eq. (5.13), with the tangential material stiffness $\bar{\mathbf{C}}_T$ covering nonlinear behavior as desired. Local stress components $\bar{\sigma}_{ij}$ have to be transformed into contravariant components $\tilde{\sigma}_{ij}$, see Section 8.4. It can be shown that

$$\tilde{\sigma} = \mathbf{T}^T \cdot \bar{\sigma} \tag{8.36}$$

with $\tilde{\sigma}$ ordered as in Eq. (5.7) and the transposed of the transformation matrix $\mathbf{T}$ from Eq. (8.32). This bases on the identity of Eqs. $(8.29)_2$ and (8.26). Finally, the combination

of Eqs. (8.36, 8.33, 8.32) leads to

$$\tilde{\boldsymbol{\sigma}} = \mathbf{T}^T \cdot \bar{\mathbf{C}} \cdot \mathbf{T} \cdot \tilde{\boldsymbol{\epsilon}} = \widetilde{\mathbf{C}} \cdot \tilde{\boldsymbol{\epsilon}} \tag{8.37}$$

which yields a transformation law

$$\widetilde{\mathbf{C}} = \mathbf{T}^T \cdot \bar{\mathbf{C}} \cdot \mathbf{T} \tag{8.38}$$

for the material matrix. This transformation law is also valid for a tangential and nonlinear material matrix. Material matrices are required to determine the tangential stiffness of discretized systems, see Section 1.5.

8.4 System Building

The current theory treats the shell body as a continuum with constraints regarding deformations. Thus, in a first approach the general form (Eq. (1.52)) is used to describe weak equilibrium

$$\int_V \delta\tilde{\boldsymbol{\epsilon}}^T \cdot \tilde{\boldsymbol{\sigma}} \, \mathrm{d}V + \int_V \delta\mathbf{u}^T \cdot \ddot{\mathbf{u}} \, \varrho \mathrm{d}V = \int_V \delta\mathbf{u}^T \cdot \bar{\mathbf{p}} \, \mathrm{d}V + \int_{A_t} \delta\mathbf{u}^T \cdot \bar{\mathbf{t}} \, \mathrm{d}A \tag{8.39}$$

whereby the product $\delta\tilde{\boldsymbol{\epsilon}}^T \cdot \tilde{\boldsymbol{\sigma}}$ replaces $\delta\boldsymbol{\epsilon}^T \cdot \boldsymbol{\sigma}$ with $\tilde{\boldsymbol{\epsilon}}$ according to Eq. (8.21) and $\tilde{\boldsymbol{\sigma}}$ according to Eq. (8.36).

For the evaluation of integrals, see Eqs. (1.58–1.60). Integration is performed by numerical methods, the basic approach has been described in Section 1.6. It will be extended to the case of continuum-based shells. The integration of internal nodal forces is performed with

$$\mathbf{f}_I = \int_{V_I} \mathbf{B}^T(r,s,t) \cdot \tilde{\boldsymbol{\sigma}}(r,s,t) \, \mathrm{d}V = \int_{-1}^{+1}\int_{-1}^{+1}\int_{-1}^{+1} \mathbf{B}^T(r,s,t) \cdot \tilde{\boldsymbol{\sigma}}(r,s,t) \, J(r,s,t) \, \mathrm{d}t\mathrm{d}r\mathrm{d}s \tag{8.40}$$

see Eq. (1.58), with $\mathbf{B}$ assembled with the $\mathbf{B}_K$'s from Eq.(8.22) and $\tilde{\boldsymbol{\sigma}}$ from Eq. (8.36). The local isoparametric coordinates are given by r, s, t and the determinant $J = \det\mathbf{J}$ of the Jacobian is given by Eq. (8.5). Internal nodal forces are determined numerically by

$$\mathbf{f}_I = \sum_{i=0}^{n_u} \sum_{j=0}^{n_u} \sum_{k=0}^{n_v} \eta_i\eta_j\eta_k \, \mathbf{B}^T(r_i,s_j,t_k) \cdot \tilde{\boldsymbol{\sigma}}(r_i,s_j,t_k) \, J(r_i,s_j,t_k) \tag{8.41}$$

with integration orders n_u, n_v, sampling points r_i, s_j, t_k and weighting factors $\eta_{i,j,k}$. Let us assume that a Gaussian integration is used. Then it may be appropriate to use different integration orders n_u along the reference surface with local coordinates r, s and n_v along the collateral direction with the local coordinate t.

- The collateral direction of thin shells needs a different treatment compared to the in-surface directions due to shell bending with transverse linear strains.

In the case of linear elastic material behavior integration orders $n_u = n_v = 1$ with two sampling points in each direction, see Table 1.1, are appropriate as stresses appear linearly. In the case of nonlinear material behavior stresses may vary nonlinearly with kinks and jumps. This occurs in particular for the cross sections of cracked reinforced concrete and requires a higher integration order for the collateral direction, e.g., $n_v = 4$ with 5 sampling points while the in-surface directions may remain with $n_u = 1$ and 2 sampling points in each direction. It may also be appropriate to choose a different integration scheme for the collateral directions, e.g., a Lobatto scheme which yields a higher accuracy in cases with extreme integrand values on the boundary.

As every node has five kinematic degrees of freedom the Equation (8.40) leads to five components for internal forces $\mathbf{f}_I$ at every node I. That are three force components with respect to the global coordinate system and two bending moment components with respect to the local directions $\mathbf{V}_\alpha, \mathbf{V}_\beta$, see Eqs. (8.2, 8.3).

Prescribed distributed loads $\bar{\mathbf{p}}$, see Eq. (1.52), are given as forces per volume and pre-scribed surface tractions $\bar{\mathbf{t}}$ are given as forces per area, each with directions related to the global coordinate system. The corresponding nodal forces, see Eq. (1.58), again have five components for each node. Element stiffness and mass matrices have 20×20 entries with the four node element. Assembling of element contributions is performed in the standard way, see Section 1.5.

Due to the continuum-based approach structural response is described by strains and stresses varying with the position in the reference surface and the collateral direction distance. Regarding shells and slabs a more familiar approach is given with internal forces such as normal forces, moments, and shear forces. It is appropriate to refer them to the local corotational system, see Section 8.3. In an analogous way as for slabs, see Eq. (7.8), resulting local internal forces are derived from local stresses $\bar{\boldsymbol{\sigma}}$, see Eq. (8.33), by

$$\bar{n}_1 = \frac{h}{2} \int_{-1}^{1} \bar{\sigma}_{11} \, \mathrm{d}t, \quad \bar{n}_2 = \frac{h}{2} \int_{-1}^{1} \bar{\sigma}_{22} \, \mathrm{d}t, \quad \bar{n}_{12} = \frac{h}{2} \int_{-1}^{1} \bar{\sigma}_{12} \, \mathrm{d}t$$

$$\bar{m}_1 = -\frac{h^2}{4} \int_{-1}^{1} \bar{\sigma}_{11} \, t \mathrm{d}t, \quad \bar{m}_2 = -\frac{h^2}{4} \int_{-1}^{1} \bar{\sigma}_{22} \, t \mathrm{d}t, \quad \bar{m}_{12} = -\frac{h^2}{4} \int_{-1}^{1} \bar{\sigma}_{12} \, t \mathrm{d}t \qquad (8.42)$$

$$\bar{v}_1 = \frac{h}{2} \int_{-1}^{1} \bar{\sigma}_{13} \, \mathrm{d}t, \quad \bar{v}_2 = \frac{h}{2} \int_{-1}^{1} \bar{\sigma}_{23} \, \mathrm{d}t$$

with the local shell thickness h and the isoparametric local coordinate $-1 \le t \le 1$. In practice, the integration is again performed numerically. Thus, nonlinear materials are automatically covered. For integration method and order see the remarks above concerning integration of system integrals.

8.5 Slabs and Beams as a Special Case

A rectangular *slab element* of constant thickness h is considered as a special case of the general shell element, see Fig. 8.2. The director indicating cross-sectional directions is given by $\mathbf{V}_N = \mathbf{V}_3 = \begin{pmatrix} 0 & 0 & 1 \end{pmatrix}^T$ and completed to a local coordinate system by $\mathbf{V}_\alpha = \mathbf{V}_1 = \begin{pmatrix} 1 & 0 & 0 \end{pmatrix}^T$, $\mathbf{V}_\beta = \mathbf{V}_2 = \begin{pmatrix} 0 & 1 & 0 \end{pmatrix}^T$. The local system coincides with the global coordinate system. Thus, after some calculations the matrix $\mathbf{B}$ of interpolation functions
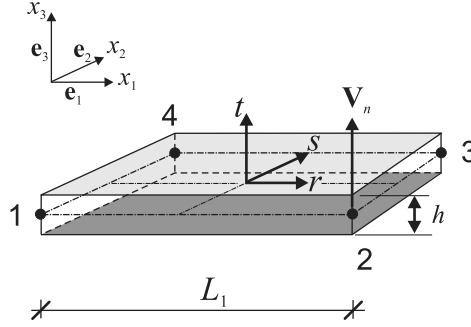
Figure 8.2: Slab element as a special case of a shell element.

(Eq. (8.22)) is written as

$$
\mathbf{B}_K =
\begin{bmatrix}
J_{11}b_{rK} & 0 & 0 & 0 & t\dfrac{h}{2}J_{11}b_{rK} \\[2ex]
0 & J_{22}b_{sK} & 0 & -t\dfrac{h}{2}J_{22}b_{sK} & 0 \\[2ex]
0 & 0 & 0 & 0 & 0 \\[2ex]
0 & 0 & J_{33}b_{sK} & -\dfrac{h}{2}J_{22}N_K & 0 \\[2ex]
0 & 0 & J_{33}b_{rK} & 0 & \dfrac{h}{2}J_{11}N_K \\[2ex]
J_{11}b_{sK} & J_{22}b_{rK} & 0 & -t\dfrac{h}{2}J_{22}b_{rK} & t\dfrac{h}{2}J_{11}b_{sK}
\end{bmatrix}
\tag{8.43}
$$

with the components J_{ij} of the Jacobian according to Eq. (8.5), b_{sK}, b_{rK} according to Eq. (8.7) and N_K according to Eq. (8.4). This element formulation is suitable to treat coupled normal forces and bending moments for slabs.

A plane *beam element* is derived as a special case assuming that a displacement in the $x_1 - x_3$-plane is applied with $\mathbf{u}_1 = \mathbf{u}_4 = \begin{pmatrix} u_1 & 0 & w_1 & 0 & \beta_1 \end{pmatrix}^T$, $\mathbf{u}_2 = \mathbf{u}_3 = \begin{pmatrix} u_2 & 0 & w_2 & 0 & \beta_2 \end{pmatrix}^T$ leading to

$$
\begin{pmatrix}
\tilde{\epsilon}_{11} \\
\tilde{\epsilon}_{22} \\
\tilde{\epsilon}_{33} \\
2\tilde{\epsilon}_{23} \\
2\tilde{\epsilon}_{13} \\
2\tilde{\epsilon}_{12}
\end{pmatrix}
=
\begin{pmatrix}
-\frac{1}{2}J_{11}u_1 - t\dfrac{h}{4}J_{11}\beta_1 + \dfrac{1}{2}J_{11}u_2 + t\dfrac{h}{4}J_{11}\beta_2 \\
0 \\
0 \\
0 \\
-\frac{1}{2}J_{33}w_1 + \dfrac{h}{4}J_{11}(1-r)\beta_1 + \dfrac{1}{2}J_{33}w_2 + \dfrac{h}{4}J_{11}(1+r)\beta_2 \\
0
\end{pmatrix}
\tag{8.44}
$$

see Eqs. (8.4–8.7, 8.21). Furthermore, we have $J_{11} = L_1/2$, $J_{33} = h/2$, see Eq. (8.5), with the element length L_1, see Fig. 8.2.

It is convenient to transform natural strain components $\tilde{\epsilon}_{ij}$ back into the global Cartesian coordinate system for the cases under consideration. Transformation rules are again derived by the identity of Eqs. (8.15, 8.18). Thus, the transformation is given by

$$\epsilon_{11} = \left(\mathcal{G}^{11}\right)^2 \tilde{\epsilon}_{11} = \frac{4}{L_1^2}\,\tilde{\epsilon}_{11}, \quad \epsilon_{13} = \mathcal{G}^{11}\,\mathcal{G}^{33}\,\tilde{\epsilon}_{13} = \frac{4}{L_1 h}\,\tilde{\epsilon}_{13} \tag{8.45}$$

This finally leads to

$$\begin{pmatrix} \epsilon_{11} \\ 2\epsilon_{13} \end{pmatrix} = \frac{1}{L_1} \begin{bmatrix} -1 & 0 & -t\,\dfrac{h}{2} & 1 & 0 & t\,\dfrac{h}{2} \\ 0 & -1 & \dfrac{L_1}{2}(1-r) & 0 & 1 & \dfrac{L_1}{2}(1+r) \end{bmatrix} \cdot \begin{pmatrix} u_1 \\ w_1 \\ \beta_1 \\ u_2 \\ w_2 \\ \beta_2 \end{pmatrix} \tag{8.46}$$

This interpolation of strains corresponds to the interpolation of strains of the 2D Timoshenko beam element, see Eq. (3.97). It becomes obvious with (1) setting $2\epsilon_{13} = \gamma$, (2) regarding the reversed orientation of rotations, see Eq. (8.8), and (3) adopting Eq. (3.5) ruling beam kinematics to the current case with $\epsilon_{11} = \epsilon + t\,\frac{h}{2}\,\kappa$, $-1 \le t \le 1$.

8.6 Locking

Problems of artificial stiffening or *locking* have already been mentioned for the Timoshenko beam element, see Section 3.3.3. They will be demonstrated within the context of the thin shell element whereby using the aforementioned simplified cases to make the locking problem comprehensible within a limited frame.

A state of uniform bending in the longitudinal x_1-direction is applied to Eq. (8.46) with $\beta_2 = -\beta_1 = \beta/2$ and $u_1 = w_1 = u_2 = w_2 = 0$. Equation (8.46) yields

$$\epsilon_{11} = t\,\frac{h}{2}\,\frac{\beta}{L_1}, \qquad \gamma_{13} = \frac{1}{2}\,\beta\,r, \qquad -1 \le r, t \le 1 \tag{8.47}$$

with a longitudinal local coordinate r and a collateral local coordinate t. The term $z = t\,\frac{h}{2}$ with the thickness h describes the distance from the reference plane and $\frac{\beta}{L_1}$ corresponds to a curvature. A linear elastic behavior is assumed with $\nu = 0$ to simplify the discussion leading to

$$\sigma_{11} = E\,\epsilon_{11} = E\,t\,\frac{h}{2}\,\frac{\beta}{L_1} = E\,z\,\frac{\beta}{L_1}, \qquad \sigma_{13} = G\,\gamma_{13} = \frac{1}{2}\,G\,\beta\,r \tag{8.48}$$

with a normal stress σ_{11} in the longitudinal x_1-direction, a shear stress σ_{13} in the vertical x_3-direction, Young's modulus E and $G = \frac{E}{2}$, see Eqs. (5.3, 5.7, 5.14, 5.24). This corresponds to stresses in beams with $\kappa = \frac{\beta}{L_1}$, see Eqs. (3.7, 3.8) and leads to a resulting moment and shear force per unit width

$$m = E\,\frac{h^3}{12}\,\frac{\beta}{L_1}, \qquad v = \frac{1}{2}\,G\,h\,\beta r \tag{8.49}$$

Thus, the applied deformation results in a constant bending moment and a linearly varying shear force along the element. This obviously violates equilibrium conditions locally, as a zero shear force is required throughout the element in the case of constant bending moment. A *spurious transverse shear force* arises with this type of element. The *local* error shall be measured by

$$\frac{v}{m} = 3\frac{L_1}{h^2}\,r, \quad -1 \le r \le 1 \tag{8.50}$$

It becomes larger with more slender elements, i.e., with decreasing thickness or increasing element length.

Local or strong equilibrium is not enforced within the finite element method, but weak or integral equilibrium, see Section 1.5. As a consequence, nodal forces resulting from integration of internal forces have to be in equilibrium. For the case under consideration nodal forces according to Eq. (8.40) are given by

$$\mathbf{r} = \int_{-1}^{1}\int_{-1}^{1} \frac{1}{L_1} \begin{bmatrix} -1 & 0 \\ 0 & -1 \\ -t\frac{h}{2} & \frac{L_1}{2}(1-r) \\ 1 & 0 \\ 0 & 1 \\ t\frac{h}{2} & \frac{L_1}{2}(1+r) \end{bmatrix} \cdot \begin{pmatrix} E\,t\,\frac{h}{2}\frac{\beta}{L_1} \\ \frac{1}{4}\,E\,\beta\,r \end{pmatrix} \frac{h}{2}\,\mathrm{d}t\,\frac{L_1}{2}\,\mathrm{d}r = E \begin{pmatrix} 0 \\ 0 \\ -\frac{h^3}{12}\frac{\beta}{L_1} - \frac{h}{24}\,L_1\beta \\ 0 \\ 0 \\ \frac{h^3}{12}\frac{\beta}{L_1} + \frac{h}{24}\,L_1\beta \end{pmatrix} \tag{8.51}$$

The nonzero nodal forces are conjugate to the applied rotation angle $-\beta/2$ on the left-hand side $r = -1$ and $\beta/2$ on the right-hand side $r = 1$. Insofar moments are justified from a mechanical point of view whereby forming an equilibrated system. As has been mentioned β/L_1 is a curvature. Furthermore, $Eh^3/12$ is the bending stiffness per unit width. Thus, the first term in each entry corresponds to a reasonable mechanical behavior.

The second part $\pm EhL_1\beta/24$ leads to an additional spurious moment resulting from the spurious shear force. This moment corresponds to an additional *spurious stiffness* of this element. The influence of these effects increase with decreasing thickness h and a constant element length L_1, i.e., with increasing element slenderness. The spurious effects reduce with finer discretizations, i.e., decreasing L_1 for a constant h. A convergence is basically given, but it is reached very slowly with a large parameter c, see Section 1.7, Eq. (1.118).

- The thin continuum-based shell element as has been defined in Section 8.1 yields much too stiff models in practical applications due to spurious transverse shear forces. A *transverse shear locking* occurs.

A number of locking phenomena are known, e.g.,

- transverse shear locking, i.e., spurious transverse shear forces in the case of transverse bending,

- in-plane shear locking, i.e., spurious in-plane shear forces in the case of in-plane bending,

- membrane locking, i.e., spurious membrane forces in the case of transverse bending,

and others [11, 6.4].

Transverse shear locking is a major cause for deficiencies of slab and shell elements. But nevertheless, it has the property that spurious shear stresses disappear in distinguished points of an element, e.g in the point $r = 0$ for the case under consideration in Section 8.5. On the other hand, such shear forces that are reasonable from a mechanical point of view yield a value in these distinguished points. This motivates established approaches to avoid locking.

– Reduced integration of system integrals, see Eqs. (1.58, 1.65, 1.68).

   This corresponds to an integration at $r = 0$, $s = 0$ for the current element. Reduced integration does not affect integration order along the local t-axis. Albeit, a numerical instability of results, so-called *hour glassing*, may occur with reduced integration. The occurrence of hour glassing depends on the discretized geometry and applied boundary and loading conditions

– Transverse *shear strains* are approximated with their own fields applying a mixed interpolation.

   These fields are connected to the fields given by Eq. (8.21) through the values of $\tilde\epsilon_{13}, \tilde\epsilon_{23}$ in those distinguished points with vanishing spurious transverse shear forces. These points are given by the coordinates $A : r = 0, s = 1$, $B : r = -1, s = 0$, $C : r = 0, s = -1$ and $D : r = 1, s = 0$ for the element under consideration. The particular strains determined by Eq. (8.21) are given by $\tilde\epsilon_{13}^A, \tilde\epsilon_{13}^B, \tilde\epsilon_{13}^C, \tilde\epsilon_{13}^D$ and regarding $\tilde\epsilon_{23}$ in a corresponding way. Anchored by these values the fields for transverse shear strains are assumed with

$$\tilde\epsilon_{13}(r,s) = \frac{1}{2}\,(1+s)\,\tilde\epsilon_{13}^A + \frac{1}{2}\,(1-s)\,\tilde\epsilon_{13}^C$$
$$\tilde\epsilon_{23}(r,s) = \frac{1}{2}\,(1+r)\,\tilde\epsilon_{23}^D + \frac{1}{2}\,(1-r)\,\tilde\epsilon_{23}^B \qquad (8.52)$$

   The approach is called *assumed natural strain* (ANS) method [25] and leads to a modification of the rows 4 and 5 of the matrix $\mathbf{B}_K$, see Eq. (8.22). This modification is straightforward with evaluating Eq. (8.21) in points A, B, C, D and combining it with Eq. (8.52).

Assuming strains partially independent from displacements or applying mixed interpolations in a first instance is not covered by the principle of virtual displacements Eqs. (1.52, 1.53). Thus, an extended weak form like the principle of Hu-Washizu [2, 4.4.2] might be required, see also Section 1.7. This involves fields for stresses and strains as independent solution variables.

The application of assumed strains requires an additive split of the matrix $\mathbf{B}$ from Eq. (8.22). The current approach of Eq. (8.52) leading to an extension of Eq. (8.22) as indicated above allows such a split. Independent parts of the stress field are eliminated in advance applying reasonable assumptions. Thus, the mixed interpolation may finally be applied in the framework of the principle of virtual displacements.

The effects of shear locking and the cure with ANS is demonstrated with the following example.

Example 8.1 Convergence study for linear simple slab

We consider a quadratic linear elastic slab with a span $L = L_1 = L_2 = 8.0\,\mathrm{m}$, a thickness $h = 0.25\,\mathrm{m}$ and material parameters $E = 33\,000\,\mathrm{MN/m^2}, \nu = 0.2$ in accordance with common concrete grades. The slab is simply supported along its edges, i.e., hinged with zero vertical displacements. A constant vertical loading is assumed with $q = 16\,\mathrm{kN/m^2}$ downward.

Assuming the Kirchhoff theory, see Section 7.3.3, an exact solution for this problem is described in [31, 78.b)] whereby neglecting shear deformations. The maximum deflection in the center point is given by an infinite double sum

$$w_{\mathrm{max}}^e = \frac{16q\,L^4}{K\,\pi^6}, \sum_m \sum_n \frac{\sin\frac{n\pi}{2}\sin\frac{m\pi}{2}}{mn(m^2+n^2)^2}, \quad K = \frac{1}{1-\nu^2}\frac{E\,h^3}{12} \tag{8.53}$$

This yields a converged value $w_{\mathrm{max}}^e = 5.95 \cdot 10^{-3}\,\mathrm{m}$. A small convergence study is performed with meshes of 1 element up to 16 elements whereby quarter symmetry is used. Figure 8.3 shows the meshes. Boundary conditions of nodes along symmetry axes are given by prescribing appropriate zero rotations. The maximum deflection w_{max} arises at right lower corner node. Computed values are
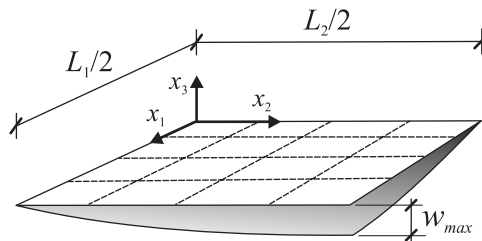
Figure 8.3: Example 8.1 discretizations.

Discretization	1×1	2×2	3×3	4×4
$w_{\mathrm{max}}\,[\mathrm{m}]$	$5.39 \cdot 10^{-3}$	$5.87 \cdot 10^{-3}$	$5.95 \cdot 10^{-3}$	$5.98 \cdot 10^{-3}$

whereby the ANS method, see Eq. (8.52), has been applied to avoid transverse shear locking. If it is not applied, i.e., Eq. (8.22) is used as is without modifications regarding the entries for $\tilde{\epsilon}_{23}, \tilde{\epsilon}_{13}$, the computed maximum deflection would be $w_{\mathrm{max}} = 1.44 \cdot 10^{-3}\,\mathrm{m}$ for the 4×4-discretization. That is an error of roughly 80%. Inclusion of shear deformations leads to slightly larger converged displacement compared to Kirchhoff theory.

End Example 8.1

8.7   Reinforced Concrete Shells

8.7.1   The Layer Model

Aspects of local behavior of cracked reinforced concrete have been described from several points of view up to now:

- Cross-sectional behavior of tension bars in Section 2.6.

- Cross-sectional behavior of beams in Section 3.1.3.

- Biaxial behavior of plates in Sections 6.3 and 6.4.

- Elastoplastic behavior of Kirchhoff slabs in Section 7.7.

- An outline of cross sectional behavior of slabs based on the layer model was given in Section 7.2.3.

The layer model is also suitable for continuum-based thin shells. In contrast to slabs aspects of reference or coordinate systems have to be regarded. A local corotational system, see Section 8.3, is appropriate implying local stress components $\bar{\sigma}_{ij}$ and local strain components $\bar{\epsilon}_{ij}$.

Basically the approach Eq. (8.33)

$$\bar{\boldsymbol{\sigma}}(r,s,t) = \bar{\mathbf{C}} \cdot \bar{\boldsymbol{\epsilon}}(r,s,t) \tag{8.54}$$

with local isoparametric coordinates r,s,t or its incremental form

$$\dot{\bar{\boldsymbol{\sigma}}}(r,s,t) = \bar{\mathbf{C}}_T \cdot \dot{\bar{\boldsymbol{\epsilon}}}(r,s,t) \tag{8.55}$$

allow for an arbitrary material behavior with variable material stiffness $\bar{\mathbf{C}}$ or tangential material stiffness $\bar{\mathbf{C}}_T$ within the context of continuum mechanics, see Eq. (5.13). Local isoparametric coordinates translate into global coordinates with Eq. (8.4). Regarding a shell position r,s in the reference surface it is suitable to use the concept of layers.

- A layer is a plane through the point r,s,t with the shell director $\mathbf{V}_n(r,s)$ as normal. Every thickness coordinate t has its own layer whereby it shares the normal with all layers of the same shell position r,s.

A layer is comparable to a slab sector as indicated in Figs. 7.2 and 7.3, whereby stress and strain component indices are replaced with $x \to 1$, $y \to 2$, $z \to 3$. Material behavior with respect to a layer is based on stress components $\bar{\sigma}_{11}, \bar{\sigma}_{22}, \bar{\sigma}_{12}$ and strain components $\bar{\epsilon}_{11}, \bar{\epsilon}_{22}, \bar{\gamma}_{12}$. Furthermore, for reinforced cracked concrete it is appropriate to decouple transverse shear characterized by $\bar{\sigma}_{13}, \bar{\sigma}_{23}, \bar{\gamma}_{13}, \bar{\gamma}_{23}$ from layer behavior. These assumptions motivate a generalization

$$\bar{\mathbf{C}} = \begin{bmatrix} C_{11} & C_{12} & 0 & 0 & 0 & C_{16} \\ C_{21} & C_{22} & 0 & 0 & 0 & C_{26} \\ 0 & 0 & 0 & 0 & 0 & 0 \\ 0 & 0 & 0 & c_{44} & 0 & 0 \\ 0 & 0 & 0 & 0 & c_{55} & 0 \\ C_{61} & C_{62} & 0 & 0 & 0 & C_{66} \end{bmatrix} \tag{8.56}$$

of Eq. (8.34) with component ordering according to Eqs. (5.3, 5.7). Uppercase coefficients mark layer behavior while lowercase coefficients mark transverse shear behavior.

The *transverse* shear stiffness has already been discussed in Section 3.5.4 in the context of structural beams. This was rephrased in the context of slabs in Section 7.2.3. The approach for slabs (Eq. (7.14)) is also used for the layers of shells leading to

$$c_{44} = c_{55} = \alpha\,G, \quad G = \frac{E_c}{2(1+\nu)} \tag{8.57}$$

with a reduction factor α and the initial values of Young's modulus E_c of concrete, its Poisson's ratio ν and the resulting shear modulus G. According to Section 3.5.4, the reduction factor may be chosen with $\alpha = 0.5$.

The *in-plane* stress–strain relations in a general form are given by

$$\begin{pmatrix} \bar{\sigma}_{11} \\ \bar{\sigma}_{22} \\ \bar{\sigma}_{12} \end{pmatrix} = \begin{bmatrix} C_{11} & C_{12} & C_{16} \\ C_{21} & C_{22} & C_{26} \\ C_{61} & C_{62} & C_{66} \end{bmatrix} \cdot \begin{pmatrix} \bar{\epsilon}_{11} \\ \bar{\epsilon}_{22} \\ \bar{\gamma}_{12} \end{pmatrix} \tag{8.58}$$

or the corresponding incremental form. This corresponds to a biaxial plane stress state and has been discussed for plates, see Chapter 6. The thickness of a counterpart plate corresponds to the "thickness" of a layer. Such a thickness is a matter of t-integration of stresses into nodal forces, see Eq. (8.40), or resulting internal forces, see Eq. (8.42). The thickness is implicitly included in a numerical integration process.

Taking this into account the following procedure is appropriate for reinforced concrete shell layers:

– Modeling of cracks due to limited tensile strength of concrete is treated in Section 6.2. This leads to a stress–strain relation in a principal local coordinate system, see Eqs. (6.35–6.37). This material relation is based on principal strains ϵ_1, ϵ_2 derived from $\bar{\epsilon}_{11}, \bar{\epsilon}_{22}, \bar{\gamma}_{12}$. Principal strain directions also rule crack directions.

  The application of such relations requires the coordinate system transformations "natural system" → "local system" → "principal system" and backward. This looks elaborate but is justifiable to cover geometrical and physical complexity. The back transformation to the local system leads to a form conforming to Eq. (8.58). This may be transferred to the form Eq. (8.56) and finally be used in Eq. (8.33).

  Such calculations are performed for each concrete layer t. A principal strain direction may change with t for a given shell point r, s, i.e., crack faces may become curved surfaces in space.

– Reinforcement and bond are treated in Section 6.4. Rigid bond is assumed in the following. Regarding thin reinforcement meshes the same procedure as described for plates, see Section 6.4, may be applied for reinforced shell layers.

  A difference is given as shell reinforcement layers are not implemented as separate elements but subject to integration along the collateral t-direction within the frame given by Eqs. (8.40, 8.42). A reinforcement layer of sheet thickness h_R, see Eq. (6.43),

is regarded with a collateral coordinate t_R. The contribution of this layer to internal forces, see Eq. (8.42), is given by

$$\bar{n}_{R1} = h_R \, \bar{\sigma}_{R11}, \quad \bar{n}_{R2} = h_R \, \bar{\sigma}_{R22}, \quad \bar{n}_{R12} = h_R \, \bar{\sigma}_{R12}$$
$$\bar{m}_{R1} = -\frac{h_R^2}{2} \, t_R \, \bar{\sigma}_{R11}, \quad \bar{m}_{R2} = -\frac{h_R^2}{2} \, t_R \, \bar{\sigma}_{R22}, \quad \bar{m}_{R12} = -\frac{h_R^2}{2} \, t_R \, \bar{\sigma}_{R12} \tag{8.59}$$

with local reinforcement stresses $\bar{\sigma}_{R11}, \bar{\sigma}_{R22}, \bar{\sigma}_{R12}$ determined in analogy to Eq. (6.47) and its related equations. Thin reinforcement layers do not contribute to transverse shear forces. The described approach may be applied to multiple reinforcement layers while adding up their contributions. It corresponds to the concept of embedded reinforcement, see Section 6.5.

Reinforcement strains and stresses are subject to the same transformations as for concrete layers.

Larger reinforced concrete shells were built in a large number for a wide span of applications during the twenties up to the sixties of the 20th century [48]. Due to expensive formwork and other upcoming restrictions their application mainly reduced to cooling towers of large power plants nowadays. A future perspective may arise with, e.g., upwind solar chimneys.

8.7.2 Slabs as Special Case

The relevance of the shell approach for reinforced concrete arises with the combination of bending with normal or membrane forces, respectively. This has to be regarded for folded plates or plates with an orientation in 3D space. A special case of these setups is given with widely used T-beams. Plates act simultaneously as slabs in these cases and combined actions will arise anyway.

Regarding the structural behavior of simple slabs bending and membrane forces may interact in the case of cracked reinforced concrete sections. This has already been shown for plane beams in Example 3.2 and will be demonstrated for slabs with the following example.

Example 8.2 Nonlinear calculation for a simple slab
We consider the system of Example 8.1 with the same dimensions. Material properties, reinforcement and loading are chosen as follows:

- A concrete grade C30/37 according to EC2 [26, 3.1] with Young's modulus $E_c = 33\,000 \, \text{MN/m}^2$ and a characteristic concrete strength of $f_{ck} = 30 \, \text{MN/m}^2$.

- Reinforcing steel properties from EC2 [26, 3.2] with Young's modulus $E_s = 200\,000 \, \text{MN/m}^2$, yield strength $f_{yk} = 500 \, \text{MN/m}^2$ and tensile strength $f_t = 525 \, \text{MN/m}^2$ at a strain of $\epsilon_{uk} = 25 \cdot 10^{-3}$. Reinforcement cover with $c = 0.02 \, \text{m}$ and the effective depth of cross section with $d \approx 0.22 \, \text{m}$.

- Self-weight is given by $g = 0.25 \cdot 25 = 6.25 \, \text{kN/m}^2$ and a variable service load of $q = 5.0 \, \text{kN/m}^2$ is assumed. These are characteristic values, see Section 9.3, and are multiplied by safety factors for a design load of, e.g., $p = 1.35 \cdot 6.25 + 1.50 \cdot 5.0 = 16 \, \text{kN/m}^2$.

A reinforcement has to be determined in advance. This is performed according to [26, 6.1]. Internal forces for a predesign are computed based on Eqs. $(7.12)_{4-6}$ whereby deflections and curvatures are determined with an extension of Eq. (8.53) taking variable coordinates into account. Standard tables for slabs may be used instead. The decisive values of bending moments and twisting moment are given by

$$m_x = m_y = 45.3 \,\text{kNm/m}, \quad m_{xy} = 38.0 \,\text{kNm/m} \tag{8.60}$$

Reinforcement forces are determined with $f_s = m/z$ with the internal lever arm z. A good estimation is given by $z = 0.8\,d$. The design value for the reinforcement strength is chosen with $f_{yd} = 500/1.15 = 435 \,\text{MN/m}^2$. Finally, the required reinforcement cross section area a_s is ruled by $f_{yd}\,a_s = m/(0.8\,d)$. This yields

$$\begin{aligned}
a_{sx} = a_{sy} &= \frac{1}{435}\,\frac{45.3 \cdot 10^{-3}}{0.8 \cdot 0.22} \rightarrow 5.9 \,\text{cm}^2/\text{m} \\
a_{sxy} &= \frac{1}{435}\,\frac{38.0 \cdot 10^{-3}}{0.8 \cdot 0.22} \rightarrow 5.0 \,\text{cm}^2/\text{m}
\end{aligned} \tag{8.61}$$

Twisting moments may be seen as skew principal moments which are directed along the diagonals of the slab's corners. This leads to, e.g., upper diagonal tension which is hold by reinforcement in the x- and y-direction. Transformation of stresses and of their reference length leads to the relation for a_{sxy}.

Bending moments m_x, m_y occur in the slab midpoint while the twisting moments occur in the corner points. The bending moments require a bottom reinforcement while the twisting moment also requires an upper reinforcement. A bottom reinforcement of $a_{sx,\text{lower}} = a_{sy,\text{lower}} = 6.0 \,\text{cm}^2/\text{m}$ and an upper reinforcement $a_{sx,\text{upper}} = a_{sy,\text{upper}} = 5.0 \,\text{cm}^2/\text{m}$ are chosen for the whole slab in the following.

A closer look shows that the failure of this slab occurs due reinforcement failure while concrete compression remains approximately in the elastic regime. But the concrete will crack due to tensile stresses. This activates the reinforcement and leads to a different behavior compared to the elastic case. The approach of Section 8.7.1 with cracked concrete behavior as described in Section 6.2 will be used in the following. The tension stress of concrete is restricted to a value of $f_{ct} = 1 \,\text{MN/m}^2$. Reinforcement is regarded as has been determined before. This leads to the following model parameters:

– The reinforcement layers are chosen with

	sheet thickness a_R (m)	sheet height coordinate t_R (m)
lower x-direction	$0.6 \cdot 10^{-3}$	-0.10
lower y-direction	$0.5 \cdot 10^{-3}$	-0.10
upper x-direction	$0.5 \cdot 10^{-3}$	0.10
upper y-direction	$0.5 \cdot 10^{-3}$	0.10

Sheet height coordinates t_R are assumed to be the same in the x- and y-directions to preserve symmetry. The tension stiffening effect, see Section 2.7, is regarded.

– A quarter slab is discretized with 4×4 elements. Due to the physical nonlinearities the loading is applied in 10 steps. An equilibrium iteration has to be performed within each loading step leading to an incrementally iterative scheme, see Section 1.6.

– A Gaussian quadrature is used for integration of system matrices and vectors. Integration orders, see Section 8.4, Eq. (8.40), are chosen with an order $n_u = 1$ in the reference surface directions and with $n_v = 4$ in the collateral direction. Collateral integration of reinforcement contributions is performed separately while considering their discrete positions t_R.

The results of the numerical computation are described in the following.

– The *load factor* depending on *midpoint deflection* is shown in Fig. 8.4a. The staggered course is caused by the prescription of the load factor. Every load factor increment requires an adaption of cracking leading to a jump in deflection. Again three stages can be seen: Stage I with basically linear behavior and only sporadic cracking.

Stage IIa with crack formation leading to a *nearly* final state of cracking. The load level is hold constant during this stage. Deflections increase to a multiple of the value at the end of stage I, which may happen rapidly due to constant loading.

Stage IIb of a nearly final cracking state with a much lower stiffness compared to stage I. A few more cracks arise connected with the staggered course.
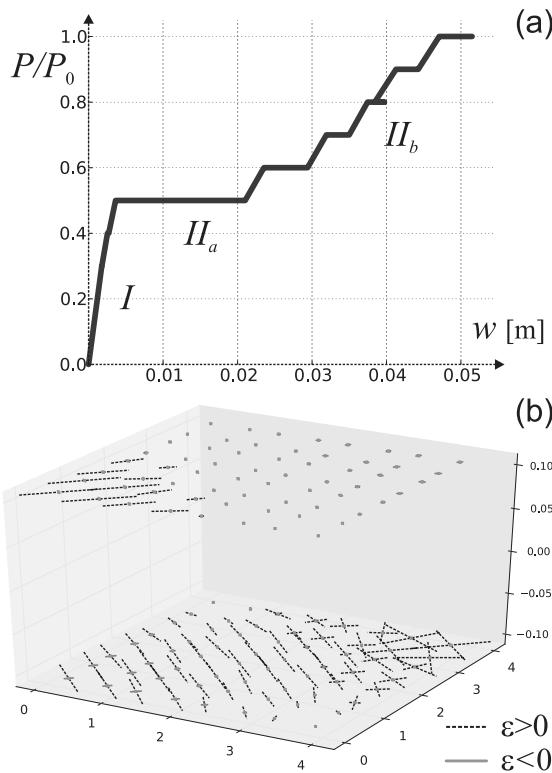
Figure 8.4: Example 8.2 (a) Load factor–deflection relation. (b) Principal strains in upper and lower concrete layer.

The final deflection of $w_\mathrm{max} = 5.15 \cdot 10^{-2}$ m is roughly 8 times higher compared to the linear elastic case of Example 8.1 and leads to deflection-span ratio of $\approx 1/150$. This looks not admissible according to [26, 7.4.1(4)] which prescribes a ratio of $1/250$ for ordinary cases. But such a value has to be reached with a load safety factor 1.

– *Cracking* is modeled as smeared, see Section 6.2. It is extended as biaxial cracking with two cracking directions. Smeared strains in cracked integration points are shown in Fig. 8.4b. The top and bottom layers are chosen out of the five concrete layers. The lateral thickness direction has a different scale as the ground directions.

Length and orientation of spatial crosses indicate size and orientation of principal values of smeared strains. Cracks are not shown explicitly but arise orthogonal to the strain directions. Top and bottom show a different behavior due to bending.

The bottom layer has two orthogonal cracks in the central region from bending moments and single cracks in diagonal direction in corner regions from twisting moments. The corresponding principal strains are across the diagonal direction for the latter.

The top layer has no cracks in the central region as it is under compression. But it has single cracks across the corner's diagonal direction from twisting moments. The corresponding principal strains are in diagonal direction.

– The *principal moments* are shown in Fig. 8.5a. Bar directions indicate the directions of the corresponding stresses. A positive moment has tension on the lower surface and compression on the upper surface.

Skew principal moment directions with opposite signs in the corner region correspond to twisting moments. The *negative* moment *in* the diagonal direction has diagonal tension on the upper side which is compensated by *upper x-* and *y-*reinforcement. The *positive* moment *across* the diagonal direction has the corresponding tension on the lower side. It is compensated by *lower x-* and *y-*reinforcement.

Central areas also have skew principal moments but with the same sign and nearly same size. Thus, there will be only minor twisting moments. Lower surface tension is compensated by *lower x-* and *y-*reinforcement.

– A new phenomenon compared to Example 8.1 is given with membrane forces, which are determined in analogy to the internal forces $\bar{n}_1, \bar{n}_2, \bar{n}_{12}$ of Eq. $(8.42)_{1-3}$. They are caused by the elongation effect of cracked reinforced cross sections which has already been discussed for beams in Example 3.2, Section 3.4.3. In contrast to beams an elongation may have a different direction for every point of the slab's reference surface as the crack directions may be different.

This leads to *eigenstresses*, i.e., self-equilibrating internal forces without reaction forces on supports. Thus, kinematic compatibility is preserved even in case local elongations or contractions. The corresponding principal membrane forces are shown in Fig. 8.5b. In case that horizontal movements of the slab are prevented on the supporting edges horizontal reaction forces will arise and the whole slab will come under compression.
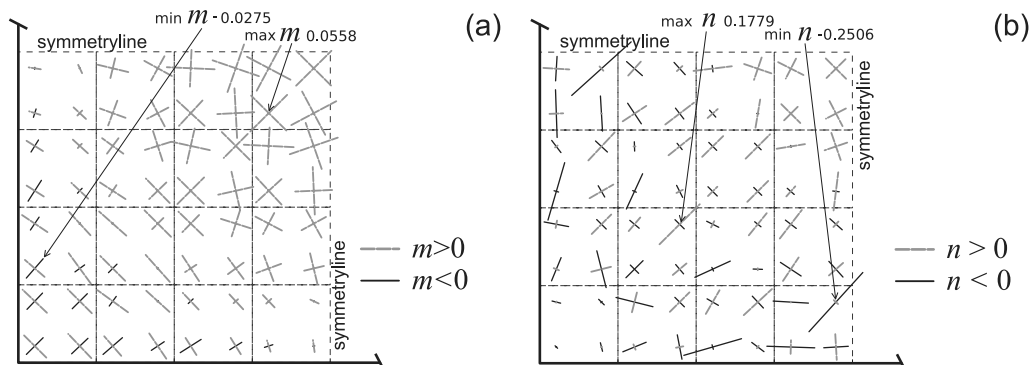
Figure 8.5: Example 8.2 with quarter of slab. (a) Principal moments. (b) Principal membrane forces.

End Example 8.2

8.7.3   The Plastic Approach

Nonlinear calculations for cracked reinforced concrete slabs as a special case of shells may become complex even for simple geometries. This has been demonstrated with Examples 7.4 and 8.2. A plastic analysis is also permitted by current codes [26, 5.6]. It bases upon the limit theorems of plasticity, see Section 4.4. The application has been demonstrated with

– rigid plastic strut-and-tie models, see Section 4.4 with Example 4.3,

– lower bound limit analysis for plates, see Section 6.1 with Example 6.2,

– lower bound limit analysis for slabs, see Section 7.6 with Examples 7.2 and 7.3.

Another application is given with the *yield line method*. This method divides a slab into rigid parts connected by lines where moments have their ultimate limit value when exposed to an external loading. The choice of such lines is basically arbitrary. The external loading is given by $p = \lambda p_0$ with a distributed reference loading p_0 and a scalar loading factor λ.

The corresponding system of external loading and internal forces generally cannot be assumed to be in equilibrium. It is difficult to find an equilibrating system for slabs as they are highly statically indeterminate. Thus, the *lower bound* theorem 1, see Section 4.4, cannot be applied. On the other hand, the lines of yielding act as plastic hinges and the kinematic compatibility is preserved. This makes the *upper bound* theorem 2, see again Section 4.4, applicable. Regarding slabs with yield lines the procedure can be outlined as follows:

– With thickness, concrete cover, reinforcement and concrete grade given the ultimate limit values of moments m_u can be determined.

– A yield line geometry is assumed parametrized by shape parameters which serve as minimization variables. The path along the yield lines is measured with a variable s. With shape parameters given the deflection is ruled by the deflection $w^\star$ of one distinct point in the slab's reference plane.

– Under the assumption of small displacements the rotations θ along the yield lines depend on $w^\star$ in a linear way. Furthermore, the integration of $\int m_u\theta\,\mathrm{d}s$ leads to an *internal work* W_I.

– The deflections w of all rigid parts of the slab also linearly depend on $w^\star$. Furthermore, integration $\int p_0 w\,\mathrm{d}a$ with a indicating area leads to an *external work* W_E.

– In analogy to Eq. (4.32) an *upper limit* of the admissible loading factor λ is given by

$$\text{upper limit of } \lambda = \frac{W_I}{W_E} = \frac{\int m_u\theta\,\mathrm{d}s}{\int p_0 w\,\mathrm{d}a} \tag{8.62}$$

The upper limit has to be minimized with respect to the shape parameters to gain a reliable estimation of the loading factor λ.

Single items will be explained with a simple setup in the following. This starts with the limit moment m_u. The corresponding relations have been already been described in Section 7.7 with Eqs. (7.89–7.93). This leads to

$$m_{u,i} = a_{si}f_y\,z, \quad z = d_i - \frac{x}{2}, \quad x = a_{si}\,\frac{f_y}{\chi k\,f_c}, \qquad i = x,y \tag{8.63}$$

with m_y replaced by the limit moment in each direction $m_{u,i}$. The quantities have the following meaning whereby the index i indicates the direction: a_{si} is the cross-sectional area of reinforcement per unit slab width, f_y the yield strength of the reinforcement, z the internal lever arm, d_i the structural height, x the height of the compressive zone, f_c the concrete compressive strength, and χ, k are accounting for the assumed rectangular stress distribution [26, 3.1.7(3)].

We regard a rectangular slab as shown in Fig. 8.6, see also [65, 24.5.3]. It is simply supported along its edges, i.e., hinged without vertical displacements. A constant distributed reference loading q_0 is used. Figure 8.6 also shows a sketch of assumed yield lines which are determined to a large extent by symmetry in this simple case. A single shape parameter
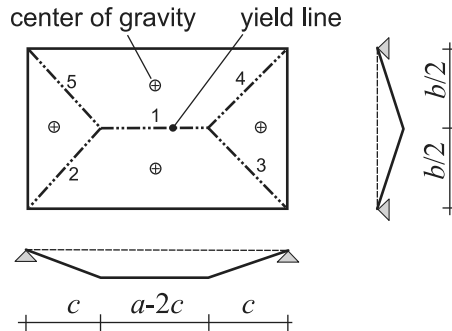
Figure 8.6: Simple slab with yield lines.

is given with the distance c. The deflection $w^\star$ is determined with the displacement of the center line. It is connected with rotations

$$\phi_1 = 2\frac{2w^\star}{b}, \quad \phi_{2-5} = \frac{2w^\star}{b}\frac{1}{\cos\varphi}, \quad \varphi = \arctan\frac{b}{2c} \tag{8.64}$$

along the yield lines. The lengths of the yield lines are given by

$$s_1 = a - 2c, \quad s_{2-5} = c\frac{1}{\cos\varphi} \tag{8.65}$$

and finally, the directions of the yield lines by

$$\varphi_1 = 0, \quad \varphi_2 = \varphi_4 = \varphi, \quad \varphi_3 = \varphi_5 = \frac{\pi}{2} + \varphi \tag{8.66}$$

The ultimate limit moments of the x- and y-directions have to be transformed into a moment with stress components normal to the cross section inclined with an angle φ against the x-axis. Thus, they have to be transformed with a rotation $\varphi - \pi/2$. The transformation rules are given by Eq. (7.63) with $m_{u,xy} = 0$. For the case under consideration this yields

$$
\begin{aligned}
m_{u,i} &= \cos^2\left(\varphi_i - \frac{\pi}{2}\right)m_{u,x} + \sin^2\left(\varphi_i - \frac{\pi}{2}\right)m_{u,y} \quad i = 1,\dots,5 \text{ for yield lines} \\
&= \sin^2\varphi_i\, m_{u,x} + \cos^2\varphi_i\, m_{u,y}
\end{aligned} \tag{8.67}
$$

see also [65, Fig. 24.27, 24.5.2.1]. This leads to

$$
\begin{aligned}
m_{u,1} &= m_{u,y} \\
m_{u,2-5} &= \sin^2\varphi\, m_{u,x} + \cos^2\varphi\, m_{u,y}
\end{aligned} \tag{8.68}
$$

With the foregoing results the *internal work* is given by

$$W_I = \sum_{i=1}^{5} m_{u,i}\phi_i s_i = \left(\frac{4a}{b}m_{u,y} + \frac{2b}{c}m_{u,x}\right)w^\star \tag{8.69}$$

The external work remains to be determined. This requires at first the ground areas of the four rigid parts

$$a_{1,3} = \frac{1}{2}(a - c)\,b, \quad a_{2,4} = \frac{1}{2}bc \tag{8.70}$$

The loading assigned to each part has a resultant in its respective gravity center. They are also shown in Fig. 8.6. The deflections of these centers are given by

$$w_{1,3} = \frac{1}{6}\frac{3a - 4c}{(a - c)}w^\star, \quad w_{2,4} = \frac{1}{3}w^\star \tag{8.71}$$

With the foregoing results the *external work* is determined by

$$W_E = p_0 \sum_{i=1}^{4} a_i w_i = p_0 b\left(\frac{a}{2} - \frac{c}{3}\right)w^\star \tag{8.72}$$

Equation (8.62) finally yields the *upper limit* of the loading, see also [65, 24.5.3]

$$\text{upper limit of } p = \text{upper limit of } \lambda p_0 = \frac{\dfrac{4a}{b} m_{u,y} + \dfrac{2b}{c} m_{u,x}}{b\left(\dfrac{a}{2} - \dfrac{c}{3}\right)} \tag{8.73}$$

The *minimum* of the upper limit has to be determined to derive an approximation for the admissible loading. The minimum value of Eq. (8.73) is derived by differentiation with respect to the shape parameter and equating the result to zero. This leads to

$$c = \frac{b}{2} \frac{\sqrt{m_{ux}^2 \beta^2 + 3 m_{uy} m_{ux}} - m_{ux}\beta}{m_{uy}}, \quad \beta = \frac{b}{a} \tag{8.74}$$

This value has to inserted into Eq. (8.73) to gain the minimum of the upper value. The application is demonstrated with the following example.

Example 8.3 Simple slab with yield line method
We consider the system of Example 8.2 with the same dimensions, concrete grade and reinforcement. The following parameters are used

$$a = b = 8.0\,\text{m}, \quad d_x = d_y = 0.225, \quad a_{sx} = a_{sy} = 6.0\,\text{cm}^2/\text{m} \tag{8.75}$$

and

$$f_{yk} = 500\,\text{MN/m}^2, \quad f_c = 30\,\text{MN/m}^2 \tag{8.76}$$

Safety factors are not explicitly taken into consideration. The ultimate limit moments are determined by Eq. (8.63) and $\bar{f}_c = \chi f_c k$, $\chi = 0.95$, $k = 0.8$ leading to

$$x = a_s \frac{f_y}{\bar{f}_c} = 0.013\,\text{m}, \quad z = d - \frac{x}{2} = 0.218\,\text{m} \tag{8.77}$$

and

$$m_u = a_s f_y\, z = 0.065\,\text{MNm/m} \tag{8.78}$$

The shape parameter c is determined by Eq. (8.74) and $m_{ux} = m_{uy} = m_u$ and $\beta = 1$ leading to $c = b/2 = 4.0\,\text{m}$. Finally, the admissible loading is given with the insertion of c into Eq. (8.73)

$$p = \left(\frac{\dfrac{4a}{b} + \dfrac{2b}{c}}{b\left(\dfrac{a}{2} - \dfrac{c}{3}\right)}\right) m_u = 0.0246\,\text{MN/m}^2 \quad \rightarrow \quad 24.6\,\text{kN/m}^2 \tag{8.79}$$

This value has to be compared to the design loading of $16\,\text{kN/m}^2$, see Example 8.2.

End Example 8.3

A hand calculation of the yield line method has to be performed with some care. An assumed yield line scheme may severely deviate from the real failure mechanism of that case. Problems are generally not so simple as with Fig. 8.6. Thus, even large variations of shape parameters do not allow modeling the real mechanism. This will lead to an overestimation

of the admissible loading even in the case of correct determination of the minimum of an optimization.

A systematic approach for slabs is described in [22] fulfilling both the upper bound theorem and the lower bound theorem. Thus, rigid plastic solutions are derived which fulfill equilibrium, kinematic compatibility, and material limit states, compare Section 4.4 regarding rigid plastic solutions for strut-and-tie models.

In case the method leads to a correct estimation of the admissible loading a sufficient ductility has to be provided by reinforcement design to allow for the rotations ϕ which are necessary to yield the ultimate limit moments according to Eq. (8.63). This issue has already been addressed for strut-and-tie models in Section 4.5 and for plates and slabs in Section 6.1.3. The yield line method is basically applicable regarding ultimate limit loads of structures. Aspects of serviceability are not covered. A comprehensive presentation of yield line methods is given in [71].

Chapter 9

Randomness and Reliability

9.1 Basics of Uncertainty and Randomness

We rely on models relating properties, see Section 1.1. A property is either an input parameter or a response variable. A variable is derived with the solution for the mathematical model whereby parameters determine the model's coefficients. It is assumed that the mathematical model can be solved with a desired degree of accuracy. Thus, the solution is solely depending on the parameters.

We use parameters like material properties, geometric dimensions, loadings, and constraints and up to now assumed determined parameter values to make *deterministic* predictions for variables. But this assumption does not care for uncertainty.

- Predictions will be uncertain due to deviations of real parameter values from assumed parameter values.

A parameter may be identified as variable in another context. Material stiffness and strength, e.g., may be solutions in a microscopic material model. On the other hand, we do not have models in the sense of Section 1.1 for, e.g., construction site processes leading to deviations of real geometric dimensions from dimensions in design documents. Thus, uncertainty is classified as epistemic or aleatoric [82].

- *Aleatoric* uncertainty comes from fundamental unpredictability of single phenomena or events, respectively.

- *Epistemic* uncertainty comes from insufficient knowledge.

Both types more or less mixed in real phenomena. Aleatoric uncertainty is also regarded as *randomness* which is strongly connected to the *probability* of events.

The distinction between input parameters and response variables will not be pursued in the following, both are subsumed as random variables. To start with, we regard a *population* of, e.g., cantilever columns exposed to a concentrated top load due to supporting weights of other parts. The loading in a first approach has two parameters, the magnitude of the load and the magnitude e of the eccentricity with respect to the center of the cross-sectional area.

Both are regarded as random. We consider the population E of eccentricities as *univariate random variable*. Its probability is described by a *distribution function*

$$F_E(e) = P(E \leq e) \tag{9.1}$$

whereby $0 \leq P(E \leq e) \leq 1$ denotes the portion of events from E with eccentricities smaller than e. The distribution function is the integral of the *probability density function $f_E(e)$*

$$F_E(e) = \int_{-\infty}^{e} f_E(e)\,\mathrm{d}e, \qquad f_E(e) = \frac{\mathrm{d}f_E(e)}{\mathrm{d}e} \tag{9.2}$$

The probability density function is determined from measurements on real *samples* out of the population. Such samples should yield a sound assessment of the distribution type and its parameters like mean μ_E and standard deviation σ_E. A prominent type is given with the normal distribution, see Fig. 9.1a. Samples also mark the range of feasible *realizations*.
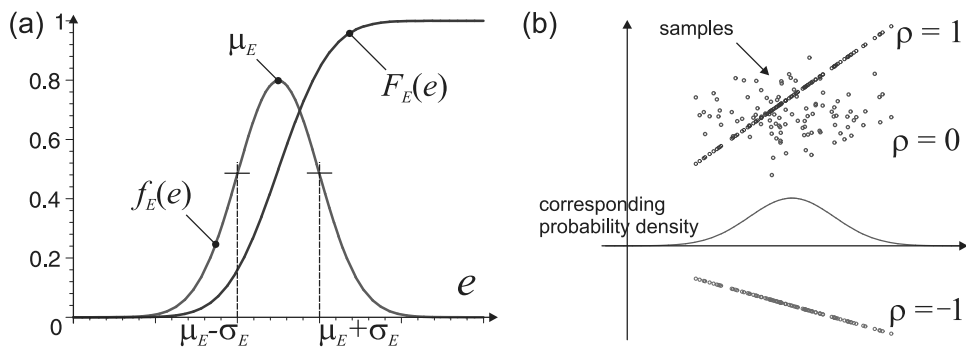
Figure 9.1: (a) Normal distribution. (b) Correlation.

Regarding randomness for structures generally *multivariate random variables* or random vectors have to be considered. A simple one is given by a *bivariate random variable* with random components, lets say R and E. The concepts of distribution functions and probability density functions are generalized with joint functions having vector arguments. The components of a random vector may exhibit a *correlation*. This is measured by a scalar $-1 \leq \rho \leq 1$ for bivariate random variables and indicates a degree of dependence. A value $\rho = -1$ is for full reverse correlation, $\rho = 0$ for independent or uncorrelated variables and $\rho = 1$ for full concordant correlation, see Fig. 9.1b.

An extension of random variables is given by *random fields* whereby randomness of a property extends over space, i.e., along a line, a plane or over a volume of a structure [86]. An example is shown for the tensile strength of samples of concrete bars in Fig. 9.2. Strength is a one-dimensional random field within a single bar. The correlation of the strength of neighbor points is described by the *correlation length*. Samples of two populations with different correlations lengths are shown in Fig. 9.2. Furthermore, randomness extends over the population of bars with five samples in Fig. 9.2 for each case. A random field may be seen as a high-dimensional random vector in the case of spatially discretized systems whereby correlation between spatially neighbored property values is described by the correlation length.

low correlation
length

high correlation
length
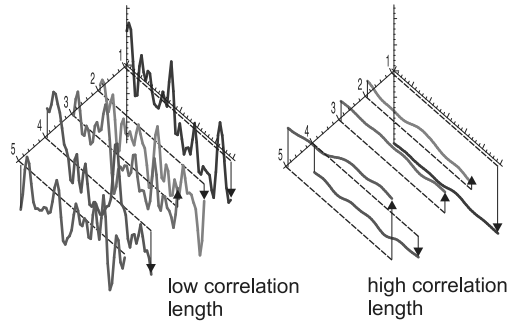
Figure 9.2: Uniaxial random fields.

Randomness is qualitatively treated with *stochastics* which embraces probabilistics and statistics [54, G]. Randomness of model input parameters will lead to randomness of response variables or model solutions. The model may be regarded as filter transforming distributions of parameters into distributions of responses. Regarding structural analysis the filter may become complex in the form of finite element methods. The process of filtering is performed with *stochastic finite element methods* [88]. General aspects of stochastics are discussed in [1], issues of building structures and concrete are treated in [18, Chapter 4], [35]. A particular aspect – failure probability – will be described in the following [14, Chapter 6].

9.2 Failure Probability

We consider a population of systems with random variables for the action and for the resistance. A normal distribution is assumed for the resistance R with realizations r, a mean μ_R and a standard deviation σ_R.

$$f_R(r) = \frac{1}{\sigma_R \sqrt{2\pi}} \ e^{-\frac{1}{2}\left(\frac{r-\mu_R}{\sigma_R}\right)^2} \tag{9.3}$$

It is standardized with a transformation

$$\bar{R} = \frac{R - \mu_R}{\sigma_R}, \tag{9.4}$$

leading to a transformed mean $\mu_{\bar{R}} = 0$, a transformed standard deviation $\sigma_{\bar{R}} = 1$ and a probability density function

$$f_{\bar{R}}(\bar{r}) = \frac{1}{\sqrt{2\pi}} \ e^{-\frac{\bar{r}^2}{2}}, \tag{9.5}$$

Furthermore, a *reference period* T_E is considered. Each sample of the population is exposed to the random action during the reference period. This yields a extreme maximum action E during the reference period, see Fig. 9.3, which is a random variable as its base action is. We also assume a normal distribution for the extreme action E with realizations e, a mean value μ_E and a standard deviation σ_E.
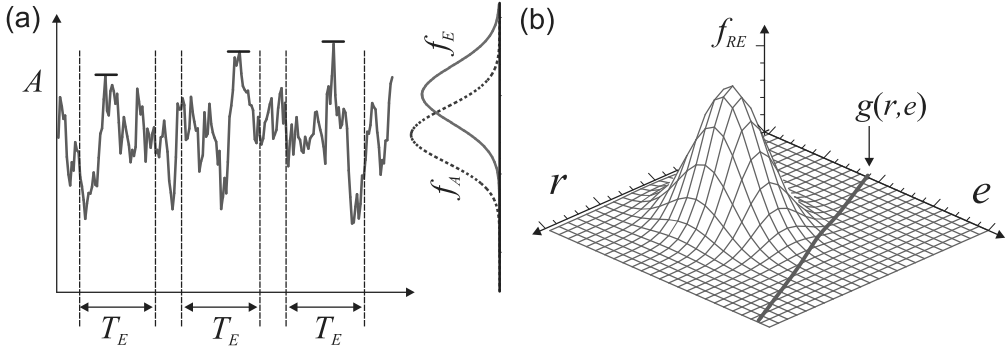
Figure 9.3: (a) Actions and their extreme values. (b) Joint probability density of resistance and extreme actions.

- The mean and the standard deviation of the extreme action may depend upon the value of the reference period T_E for a given distribution type.

Larger values lead to larger means and larger standard deviations of the extreme action. It is again standardized with a transformation

$$\bar{E} = \frac{E - \mu_E}{\sigma_E} \tag{9.6}$$

leading to $\mu_{\bar{E}} = 0, \sigma_{\bar{E}} = 1$ and a probability density

$$f_{\bar{E}}(\bar{e}) = \frac{1}{\sqrt{2\pi}} \ \mathrm{e}^{-\frac{\bar{e}^2}{2}} \tag{9.7}$$

Regarding structural systems it may be assumed that R and E are statistically independent. This yields a *joint probability density function* as a product of the single probability densities

$$f_{RE}(R, E) = f_R(R) \, f_E(E) = \frac{1}{2\pi} \ \mathrm{e}^{-\frac{1}{2}\left(\frac{r-\mu_R}{\sigma_R}\right)^2} \ \mathrm{e}^{-\frac{1}{2}\left(\frac{e-\mu_E}{\sigma_E}\right)^2} \tag{9.8}$$

or

$$f_{\bar{R}\bar{E}}(\bar{r}, \bar{e}) = f_{\bar{R}}(\bar{r}) \, f_{\bar{E}}(\bar{e}) = \frac{1}{2\pi} \ \mathrm{e}^{-\frac{\bar{r}^2}{2}} \ \mathrm{e}^{-\frac{\bar{e}^2}{2}} \tag{9.9}$$

see Fig. 9.3, with a rotational symmetry with respect to the origin $\bar{r} = 0, \bar{e} = 0$.

A *limit-state condition* is described with the *limit-state function* $g(R, E)$ and a curve

$$g(R, E) = R - a\,E - b = 0 \tag{9.10}$$

separating the failure domain $g \leq 0$ in the R, E-plane from the domain of nonfailure. The limit-state condition may also be standardized with Eqs. (9.4, 9.6) leading to

$$\beta + \alpha_R \, \bar{r} + \alpha_E \, \bar{e} = 0 \tag{9.11}$$

in the $\bar{r}, \bar{e}$-plane with the *reliability index*

$$\beta = \frac{\mu_R - a\mu_E - b}{\sqrt{\sigma_R^2 + a^2\sigma_E^2}} \tag{9.12}$$

and the *sensitivity parameters*

$$\alpha_R = \frac{\sigma_R}{\sqrt{\sigma_R^2 + a^2\sigma_E^2}}, \quad \alpha_E = \frac{-a\sigma_E}{\sqrt{\sigma_R^2 + a^2\sigma_E^2}} \tag{9.13}$$

with

$$\alpha_E^2 + \alpha_R^2 = 1 \tag{9.14}$$

The sensitivity parameters α_R, α_E indicate the influence of R and E on the system's randomness. In case $\sigma_R \gg \sigma_E$ is $\alpha_R \to 1, \alpha_E \to 0$ and the randomness depends on R only. In case $\sigma_R \ll \sigma_E$ is $\alpha_R \to 0, \alpha_E \to -1$ and the randomness depends on E only. The sensitivity parameters correspond to an angle φ with $\cos\varphi = \alpha_R, \quad \sin\varphi = \alpha_E$, whereby φ indicates the inclination of the linear standardized limit-state condition (Eq. (9.11)) against the $\bar{e}$-axis. A further simplification is reached with a transformation to variables $\tilde{r}, \tilde{e}$

$$\bar{r} = \tilde{r}\,\alpha_R - \tilde{e}\,\alpha_E, \quad \bar{e} = \tilde{r}\,\alpha_E + \tilde{e}\,\alpha_R \tag{9.15}$$

corresponding a rotation of the $\bar{r}, \bar{e}$-coordinate system with the angle φ. The limit-state condition (Eq. (9.11)) can be written as

$$\tilde{r} + \beta = 0 \tag{9.16}$$

in the $\tilde{r}, \tilde{e}$-coordinate system whereby the failure domain is given by

$$\tilde{r} \le -\beta \tag{9.17}$$

The *failure probability* for the population of systems with respect to the reference period is derived from the integration of the joint probability density $f_{\tilde{R}\tilde{E}}$ in the range defined by Eq. (9.17). The functions $f_{\bar{R}\bar{E}}$, see Eq. (9.9) and $f_{\tilde{R}\tilde{E}}$ are basically the same due to their rotational symmetry. Therefore, the failure probability is given by

$$p_F = \int_{-\infty}^{\infty} \int_{-\infty}^{-\beta} f_{\tilde{R}\tilde{E}}\ \mathrm{d}\tilde{r}\,\mathrm{d}\tilde{e} = \int_{-\infty}^{-\beta} f_{\bar{R}}\,\mathrm{d}\bar{r} \tag{9.18}$$

with $f_{\bar{R}}$ according to Eq. (9.5) leading to

$$p_F = \Phi(-\beta) \tag{9.19}$$

with the probability function Φ of the standardized normal distribution.

- The failure probability depends only on the the reliability index β for normal distributions of the extreme action E and the resistance R. Larger values of β lead to a smaller failure probability.

The reliability index increases with increasing distance between mean values of resistance and extreme actions and decreases with increasing standard deviations of resistance and extreme actions.

Finally, we consider a distinguished realization:

- The *design point* (r_d, e_d) is the realization of random variables with the highest probability or the highest value of the joint probability density function whereby fulfilling the limit-state condition $g(r_d, e_d) = 0$.

For the current setup, the design point may be located in the $\tilde{r}, \tilde{e}$-coordinate system with the condition

$$\tilde{r}_d = -\beta, \qquad \tilde{e}_d = 0 \tag{9.20}$$

It is transformed into the plane of standardized $\bar{r}, \bar{e}$-variables using the transformation equation (9.15)

$$\begin{aligned} \bar{r}_d &= -\beta\,\alpha_R \\ \bar{e}_d &= -\beta\,\alpha_E \end{aligned} \tag{9.21}$$

Finally, using Eqs. (9.4, 9.6) the design point for the origin variables is given by

$$\begin{aligned} r_d &= \mu_R + \sigma_R\,\bar{r}_d &= \mu_R - \beta\alpha_R\,\sigma_R \\ e_d &= \mu_E + \sigma_E\,\bar{e}_d &= \mu_E - \beta\alpha_E\,\sigma_E \end{aligned} \tag{9.22}$$

This realization of the random variables fulfills the limit-state condition (Eq. (9.10)) with $g(r_d, e_d) = 0$ as is required. The determination of the design point is not so straightforward for more general cases.

- Basically an optimization for the joint probability density function of the random variables has to be performed to determine the design point whereby the optimization has the constraint of the limit-state function.

Standard optimization techniques may be used for this purpose.

Regarding the current setup the determination of failure probability is demonstrated with the following simple example.

Example 9.1 Analytical failure probability of cantilever column
We consider a population of reinforced concrete cantilever columns with a height of $L = 5\,\mathrm{m}$ and a constant cross section. The dimensions of the cross section and the material properties chosen as in Example 3.1. The corresponding moment–curvature relation is shown in Fig. 3.3. The maximum moment M which can be sustained by this particular cross section is assumed as random variable.

A concentrated permanent downward loading of $P = 2\,\mathrm{MN}$ is given on top the cantilever beam. It has some eccentricity e regarding the centered reference axis whereby e is oriented along the larger cross-sectional dimension of $h = 0.4\,\mathrm{m}$. This eccentricity is assumed as random variable for the action. This leads to a realized random moment $P\,e$. Second order effects are not regarded in a first approach. The limit-state condition is given by

$$g = M - |P|\,e = 0 \tag{9.23}$$

		M	e
Mean μ	(MNm)/(m)	0.27	0.1
Standard deviation σ	(MNm)	0.015	0.02
Sensitivity parameter α	–	0.351	−0.936
10%-Quantile	(MNm)	0.251	
90%-Quantile	(MNm)		0.126
Design point	(MNm)/(m)	0.261	0.131

Table 9.1: Parameters of Example 9.1.

A normal distribution is assumed for resistance ($\to M$) and action ($\to e$) with parameters given in Table 9.1. The quantile value $S_{k,x\%}$ of a random variable S has the following meaning: x percent of all samples of S have a value below $S_{k,x\%}$. On the other hand, $100 - x\%$ of all samples of S have a value above $S_{k,x\%}$. Quantile values are derived from the inverse of the probability function of S qith $S_{k,x\%} = F_S^{-1}(x)$.

The reliability index is determined from Eq. (9.12) with $\beta = 1.6386$ leading to a design point also given in Table 9.1 and a failure probability of

$$p_F = 0.0506 \tag{9.24}$$

using Eq. (9.19). A portion of $5\,\%$ of the population of cantilever columns under consideration will fail according to this model. In this special case the failure probability is independent from the reference period T_E, see Section 9.2, as the action is assumed as permanent and is constant during any reference period.

— End Example 9.1

The evaluation of the failure probability may be generalized regarding multivariate random variables, see Appendix E.

Furthermore, nonnormal distributions and nonlinear limit-state functions have to be considered. A linear or nonlinear limit-state function yields a scalar value $z = g(r, e)$ which may be seen as *safety margin*. The relation between z and r, e may be approximated with a Taylor expansion with an expansion point $z_0 = g(r_0, e_0)$

$$z = z_0 + \left.\frac{\partial g}{\partial r}\right|_{r_0,e_0} (r - r_0) + \left.\frac{\partial g}{\partial e}\right|_{r_0,e_0} (e - e_0) + \cdots \tag{9.25}$$

The safety margin corresponds to a dependent random variable Z. Its mean μ_Z and standard deviation σ_Z may be approximated from the means μ_R, μ_E and standard deviations σ_R, σ_E based on the Taylor expansion. A normal distribution is assumed for the safety margin in a further step. Thus, the failure probability is determined as

$$p_F = \int_{-\infty}^{0} \frac{1}{\sqrt{2}\sigma_Z} \mathrm{e}^{-\frac{1}{2}\left(\frac{z-\mu_Z}{\sigma_Z}\right)^2} \,\mathrm{d}z = \Phi\left(-\frac{\mu_Z}{\sigma_Z}\right) \tag{9.26}$$

with the probability function Φ of the standardized normal distribution. Equation (9.26) is also used as an approximation for failure probabilities in case that basic variables R, E do not follow a normal distribution and are more or less correlated.

A specification is given with the *first-order reliability method (FORM)*. Distributions for the basic random variables are transformed into standardized uncorrelated normal distributions whereby the limit-state function or safety margin is transformed accordingly. Regarding all points fulfilling the limit-state condition the design point, see Section 9.2, has the shortest distance β to the origin in the transformed system. It is chosen as expansion point for a linear Taylor expansion. This finally yields a failure probability

$$p_F = \int_{-\infty}^{-\beta} \frac{1}{\sqrt{2}}\, \mathrm{e}^{-\frac{\tilde{z}^2}{2}}\, \mathrm{d}\tilde{z} = \Phi\left(-\beta\right) \tag{9.27}$$

similar to Eq. (9.18). The approach may be extended to multivariate random variables. The major problem concerns the determination of the design point in the case of nonlinear limit-state functions.

The methods based on expansions of the limit-state function require its differentiability. This might be a limitation, e.g., when a distinction of cases has to be done. An alternative formulation for the limit-state condition

$$I_g(r, e) = \left\{ \begin{array}{ll} 1 & \text{if } g(r,e) \leq 0 \\ 0 & \text{else} \end{array} \right. \tag{9.28}$$

avoids the differentiation of g and allows for general formulations of the limit-state function. The failure probability is determined as

$$p_F = \int_{-\infty}^{\infty} \int_{-\infty}^{\infty} f_{RE}(r, e)\, I_g(r, e)\, \mathrm{d}r\mathrm{d}e \tag{9.29}$$

with the joint probability density function f_{RE} of the basic random variables. This is approximately evaluated with

$$p_F \approx \frac{1}{m} \sum_{i=1}^{m} I_g(r_i, e_i) \tag{9.30}$$

using m sample pairs (r_i, e_i) according to a joint distribution probability f_{RE}. This type of numerical evaluation of the failure probability belongs to *Monte Carlo simulations*. A variant is given by *importance sampling*

$$p_F = \int_{-\infty}^{\infty} \int_{-\infty}^{\infty} \frac{f_{RE}(r, e)}{h_{RE}(r, e)}\, h_{RE}(r, e)\, I_g(r, e)\, \mathrm{d}r\mathrm{d}e \tag{9.31}$$

extending Eq. (9.29) with another arbitrary joint distribution probability function h_{RE} leading to

$$p_F \approx \frac{1}{m} \sum_{i=1}^{m} \frac{f_{RE}(r_i, e_i)}{h_{RE}(r_i, e_i)}\, I_g(r_i, e_i) \tag{9.32}$$

whereby samples are determined according to the distribution probability h_{RE}. It should be chosen such that most samples are taken in the area with the largest probability of failure, i.e., around the design point. The application is demonstrated with the following example.

Example 9.2 Approximate failure probability of cantilever column with a Monte Carlo simulation.

We refer to Example 9.1 and treat the same problem. The limit-state function from Eq. (9.23) is not changed at first. The samples are generated on the basis of a random number generator $G[0, 1]$ which provides real equally distributed random numbers in the interval $[0, 1]$. Random numbers of a normal distribution with mean μ and standard deviation σ are determined with

$$\mu + \sigma \, \Phi^{-1}(G[0, 1]) \quad \rightarrow \quad \text{sample} \tag{9.33}$$

with the inverse distribution function Φ^{-1} of the standardized normal distribution. This is applied with two independent generators G to each of M and e with the parameters of Table 9.1. An example of a set with $m = 100$ samples is shown in Fig. 9.4 together with the linear limit-state function g. The evaluation of Eq. (9.30) leads to $p_f = 0.03$, i.e., 3 samples out of $m = 100$ are detected in the failure domain.
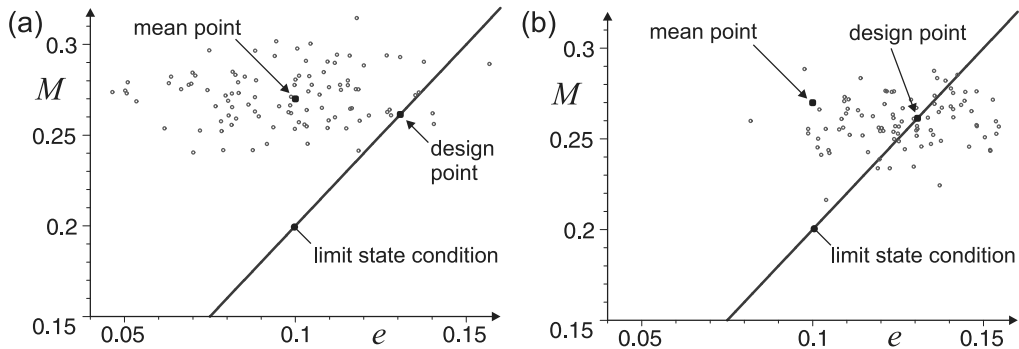
Figure 9.4: Example 9.2 (a) Sampling around mean. (b) Importance sampling.

This indicates a weakness of the method. The event of failure has a small probability and only a relatively few numbers of samples determine the approximate value of the failure probability. This leads to relatively large errors. Importance sampling may be used to shift the area of sampling which is at first centered around the mean (μ_e, μ_M). A shift to the design point, see Section 9.2, should lead to a relatively large number of samples from the failure domain. This is reached based on the joint probability density function f_{Me} whereby the design values e_d and M_d replace the mean values μ_e and μ_M to derive the joint probability density h_{Me}, see Eq. (9.32). An example with $m = 100$ samples is shown in Fig. 9.4b whereby the evaluation of Eq. (9.32) leads to $p_f = 0.055$. Importance sampling generally leads to a significant improvement of the failure probability estimation for a given number m.

Second-order effects basically have to be regarded for a cantilever column, see Section 3.7 with Example 3.8. We assume a simplified quadratic limit-state condition

$$g(M, e) = M - |P| \, e_1 \left(\frac{e}{e_1} - \frac{e^2}{e_1^2} \right) - M_1 \frac{e^2}{e_1^2} \tag{9.34}$$

which resembles the linear limit-state condition for $e = 0$ with the same tangent but otherwise approximately covers second-order effects with a representative limit state $e = e_1$, $M = M_1$

for the behavior of the cantilever column model. In contrast to Example 3.8, where the structural limit load is reached before a local-bearing capacity of cross sections is exhausted, the quantity M_1 shall correspond to cross-sectional failure. The values are assumed with $e_1 = \mu_e$, $M_1 = 0.23$, i.e., a 15% increase of moment at the mean eccentricity due to second-order effects. The nonlinear limit-state condition is shown in Fig. 9.5.
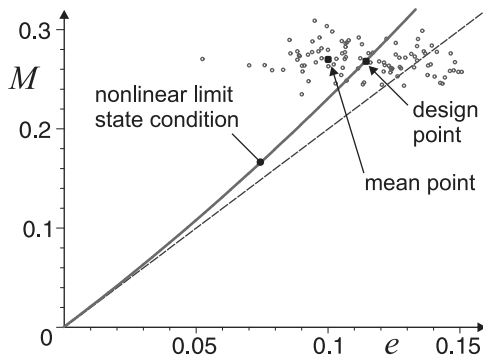
Figure 9.5: Example 9.2 with nonlinear limit-state condition.

The corresponding design point can determined with an optimization of the joint probability density function f_{Me} under the constraint of the limit-state function (Eq. (9.34)) whereby f_{Me} is given according to Eq. (9.8) with the parameters from Table 9.1. An approximate solution is $e_d = 0.114$, $M_d = 0.268$ which is used for importance sampling. The results for an example set with $m = 100$ samples are shown in Fig. 9.5. The probability failure is determined with $p_f = 0.20$ according to Eq. (9.32). Thus, a second-order analysis leads to a considerably higher failure risk for the current setup.

We considered sets with m samples. Actually the chosen number $m = 100$ is too low to reproduce the results for the failure probability, especially with ordinary sampling according to Eq. (9.30). A convergence study is necessary to determine a magnitude of m which yields the same failure probability for each set of samples within a given tolerance. This exceeds the scope of the current example.

End Example 9.2

Monte Carlo methods have the following properties regarding the evaluation of failure probabilities:

- Model behavior is ruled through a limit-state condition which relates the models properties and variables and leads to the result 1/0 or failure/nonfailure, respectively.

- Multivariate random variables are allowed composed of model parameters.

- Any type of joint probability density function is possible. Random variables may be correlated.

On the other hand, the demand for computational resources may become very high due to the required large number of evaluations of the limit-state function: each evaluation may

become very elaborate for complex nonlinear models. This might be prohibitive for a Monte Carlo analysis. Response surface methods may be a workaround.

Another issue concerns the availability of distribution data or samples of involved random variables in the case of building structures. Often the number of available samples is not large enough to gain reliable results. Concepts of confidence have to be incorporated and statements about a failure probability are supplied with a probability. Randomness, which is quantified with statistical methods by definition, expands into a wider scope of uncertainty. Concepts of fuzziness may be used to quantify this [68].

9.3 Design and Safety Factors

Up to now we described the *analysis* of the failure probability for a population of structures with the same model and with given properties for the involved random variables. On the other hand, a *design* has to adjust properties such that a target failure probability is not exceeded. This may be reached with a trial and error approach. But such a way is generally not reasonable. Concepts based on safety factors are used for practical design which are intuitive and practiced in building design based on long time experience. But safety factors should be related to failure probability in a quantitative manner.

To begin with, we have to consider different aspects of the action E. Loading and internal forces have to be distinguished. A loading is transformed into internal forces with a structural analysis. Deformation parameters, e.g., edge strains, may replace internal forces as a measure. Anyway, a linear relation is assumed.

- All structural analysis for the present is linear.

Furthermore, it is deterministic: a deterministic loading leads to a deterministic internal force or deformation e in some critical position of a structure. This position has a deterministic resistance r – with the same measure as e – and a limit-state function

$$g(r, e) = r - e \tag{9.35}$$

whereby failure shall again be given for $g(r, e) \leq 0$.

- A *deterministic design* has to fulfill the condition

$$r > e \tag{9.36}$$

The corresponding methods are straightforward with e resulting from a structural analysis and r from mechanics of materials.

But we should consider the bivariate random variable (R, E) instead with a limit-state function $g(r, e)$ for the realizations. The safety margin, see Section 9.2, is derived with

$$Z = R - E \tag{9.37}$$

and the failure domain is given with realizations $z \leq 0$. In the case of uncorrelated normal distributions for R and E the random variable Z follows also a normal distribution and has as mean and standard deviation

$$\mu_Z = \mu_R - \mu_E, \quad \sigma_Z = \sqrt{\sigma_R^2 + \sigma_E^2} \tag{9.38}$$

The failure probability of the position under consideration is given according to Eq. (9.26)

$$p_F = \Phi\left(-\frac{\mu_Z}{\sigma_Z}\right) = \Phi(-\beta) \tag{9.39}$$

with the reliability index β from Eq. (9.12) and leads to the same result as Eq. (9.19).

- A *probabilistic design* states a target failure probability and determines the parameters of the involved random variables such that the corresponding failure probability does not exceed the target value.

The failure probability p_F is often replaced with the reliability index β within this context using Eq. (9.39). Action parameters μ_E, σ_E are practically prescribed and a designing engineer has only small influence on σ_R. Thus, a probabilistic design practically determines μ_R.

A probabilistic design is generally considered as inconvenient with the background of traditional design practice. A link to safety factors has to be derived. We consider an example of probability density functions of R and E as shown in Fig. 9.6. The overlap of these functions corresponds to the failure probability. On the other hand, the overlap is related to the "distance" between f_R and f_E.

- A *semiprobabilistic design* adjusts the "distance" between the probability densities of resistance and action such that a target failure probability is not exceeded.

The "distance" or *global safety factor* is measured by the ratio

$$\gamma = \frac{r_k}{e_k} > 1 \tag{9.40}$$

of *characteristic values* for resistance r_k and action e_k. Quantile values, see Section 9.2, are used as characteristic values. Common choices are the 5% quantile for R (5% of the population of resistances fall below this value) and the 95% quantile for E (95% of the population of the actions fall below this value). In the case of normal distributions they are given by

$$r_k = \mu_R - \delta_{5\%}\,\sigma_R, \qquad e_k = \mu_E + \delta_{95\%}\,\sigma_E \tag{9.41}$$
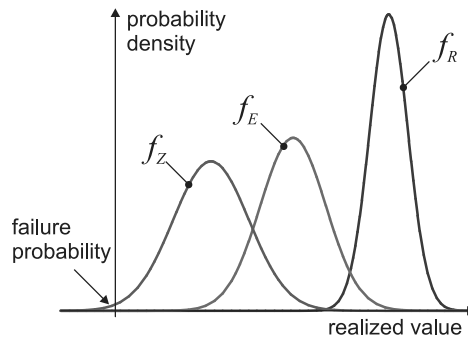
Figure 9.6: Safety margin.

The quantile coefficients $\delta_{5\%} = -(r_{k,5\%} - \mu_R)/\sigma_R$ and $\delta_{95\%} = (e_{k,95\%} - \mu_E)/\sigma_E$ correspond to standardized distances similar to the reliability index β. They are determined from the inverse Φ^{-1} of the standardized normal distribution with $\Phi(-\delta_{5\%}) = 0.05$ and $\Phi(\delta_{95\%}) = 0.95$ leading to $\delta_{95\%} = \delta_{5\%} = \delta = 1.65$.

It is appropriate to relate characteristic values to design values, see Section 9.2, and the global safety factor is reformulated as

$$\gamma = \gamma_R \, \gamma_E \tag{9.42}$$

with *partial safety factors*

$$\gamma_R = \frac{r_k}{r_d} > 1, \quad \gamma_E = \frac{e_d}{e_k} > 1 \tag{9.43}$$

whereby using the limit-state condition $g(r_d, e_d) = r_d - e_d = 0$. The partial safety factor for the resistance is given by

$$\gamma_R = \frac{\mu_R - \delta \, \sigma_R}{\mu_R - \beta \alpha_R \, \sigma_R} = \frac{1 - \delta \, \nu_R}{1 - \beta \, \nu_R \alpha_R} \tag{9.44}$$

and for the action by

$$\gamma_E = \frac{\mu_E - \beta \alpha_E \, \sigma_E}{\mu_E + \delta \, \sigma_E} = \frac{1 - \beta \, \nu_E \alpha_E}{1 + \delta \, \nu_E} \tag{9.45}$$

see Eqs. (9.22), with the coefficients of variation

$$\nu_R = \frac{\sigma_R}{\mu_R}, \quad \nu_E = \frac{\sigma_E}{\mu_E} \tag{9.46}$$

Some care has to be taken for γ_R according to Eq. (9.44) with large values ν_R and/or small values α_R which might lead to values $\gamma_R < 1$. This is not reasonable. There is no similar risk regarding γ_E as $\alpha_E < 0$ by definition, see Eq. (9.13).

In the end, the safety factors depend on the reliability index β or the failure probability, the coefficients of variation ν_R, ν_E, the sensitivity parameters α_R, α_E and the parameter δ for quantile values. Within limits the choice for δ is a matter of convention only. The choice for the failure probability reflects a desired overall safety standard. Unique values of the coefficients of variation and sensitivity should be valid for the populations of the involved resistances and actions in an ideal scenario.

- A semiprobabilistic design with *constant*, *predefined* safety factors yields a failure probability not exceeding the target in an ideal scenario.

Thus, a semiprobabilistic design is performed such that required characteristic values for the resistance are derived from prescribed characteristic values of actions through safety factors. The attribute "semi" reflects deviations between the ideal scenario and the reality. Anyway, a *design procedure* is summarized as follows whereby an alternative has to be chosen, e.g., from the following a), b) or c):

1. Determination of characteristic values for the loading

    a) Compute design values for the loading with partial safety factor γ_E.

    b) Do nothing.

    c) Compute nominal value for the loading with safety factor γ.

2. Computation of internal forces with a structural analysis

    a) Design values of internal forces e_d are already there.

    b) Internal forces are characteristic values e_k and have to be modified with partial safety factors γ_E for design values e_d.

    a/b) Design values for the resistance according to $r_d > e_d$ used for characteristic values r_k with partial safety factors γ_R.

    c) Characteristic values of internal forces r_k are already there.

3. Construction detailing according to mechanics of materials to reach a required value r_k

All three alternatives should be equivalent in the case of a linear model with a linear structural analysis but this will change for a nonlinear case, see later remarks. Partial safety factors are useful regarding different models for the resistance while retaining one model for the action. Aspects of safety factors will be demonstrated with the following example.

Example 9.3 Bounds for safety factors for single span beam with distributed loading
We consider the population of single span beams with distributed vertical loading. Loading is random due to its magnitude and leads to a random mid-span moment. The resistance is given by the moment bearing capacity.

    The target is that no more than 1 beam out of 10^6 should fail within a year. A service life or reference period of $T_E = 50$ years is assumed. This leads to a target failure probability of $p_F = 50 \cdot 10^{-6}$ or a safety index $\beta = 3.9$. The value for δ is chosen with 1.65, see Eq. (9.41).

    We consider the probability of realizations of a normal distributed random variable in a bandwidth of, e.g., $\pm 10\,\%$ around its mean. The probability is given by

$$P = \Phi\left(\frac{(\mu + 0.1\mu) - \mu}{\sigma}\right) - \Phi\left(\frac{(\mu - 0.1\mu) - \mu}{\sigma}\right) = \Phi\left(\frac{0.1}{\nu}\right) - \Phi\left(-\frac{0.1}{\nu}\right) \tag{9.47}$$

with the coefficient of variation $\nu = \sigma/\mu$ and the standardized normal distribution function Φ. The function $P(\nu)$ is shown in Fig. 9.7. It allows making estimations for ν. We assume
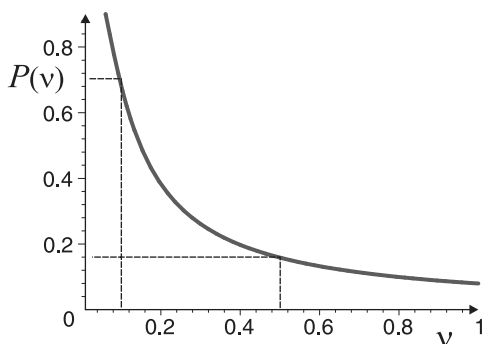
Figure 9.7: Example 9.3 function $P(\nu)$.
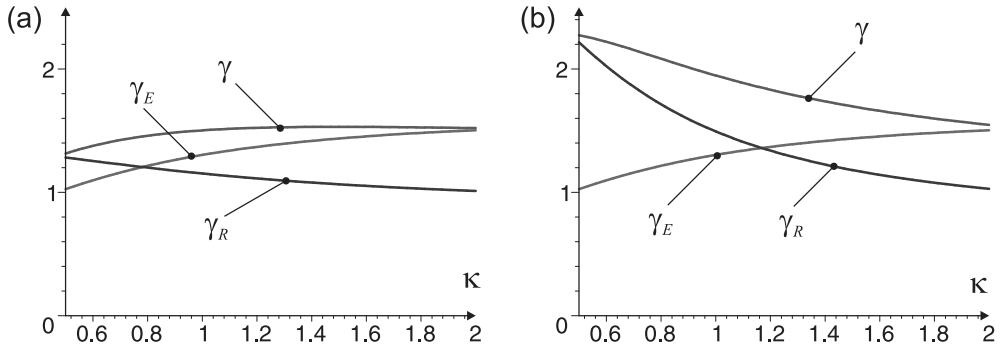
Figure 9.8: Example 9.3 safety factors (a) $\nu_R = 0.1$. (b) $\nu_R = 0.2$.

that 70% of the resistance are within the bandwidth and 15% of the action leading to $\nu_R = 0.1$, $\nu_E = 0.5$. The sensitivity coefficients (Eqs. (9.13, 9.14)) remain to be determined with $a = 1$, $b = 0$. They are reformulated as

$$\alpha_R = \frac{1}{\sqrt{1+\kappa^2}}, \quad \alpha_E = -\sqrt{1 - \alpha_R^2}, \quad \kappa = \frac{\sigma_E}{\sigma_R} \tag{9.48}$$

The ratio κ of standard deviations is still not determined and kept open. Partial safety factors are given by

$$\gamma_R = \frac{0.835}{1 - \frac{0.39}{\sqrt{(1+\kappa^2)}}}, \quad \gamma_E = 0.55 + 1.07\sqrt{1 - \frac{1}{1+\kappa^2}} \tag{9.49}$$

according to Eqs. (9.44, 9.45). The partial safety factors and the global safety factor $\gamma = \gamma_R\,\gamma_E$ are shown in Fig. 9.8 depending on the ratio κ of standard deviations. One might argue over the chosen lower limit $\kappa \geq 0.5$. On the other hand, the assumed standard deviations are $\sigma_R = 0.1\,\mu_R$, $\sigma_E = 0.5\,\mu_E$. This requires $\mu_E \geq 0.1\,\mu_R$ which is reasonable as the required safety distance obviously is not endangered. The choice of maximum values with $\gamma_R = 1.3$ and $\gamma_E = 1.5$ is on the safe side.

Another construction type shall be considered with a coefficient of variation $\nu_R = 0.2$. The corresponding safety factors are shown in Fig. 9.8b. The required relation $\mu_E \geq 0.2\,\mu_R$ still seems to be reasonable. The partial safety factor γ_E for the action is influenced to a minor extent but γ_R for the resistance increases considerably together with γ. The safe side choice is $\gamma_R = 2.2$ and $\gamma_E = 1.5$.

End Example 9.3

"Safe" assumptions regarding α_E, α_R whereby violating Eq. (9.14) are generally used for the determination of partial safety factors, see Appendix E, instead of treating σ_E/σ_R as unknown variable as in Example 9.3.

A linear structural behavior or linear structural analysis, respectively, was assumed for the design procedure with safety factors as has been summarized before. Lower bound limit

analysis for plates, see Section 6.1, and slabs, see Section 7.6, are based on a linear structural analysis. But this is a special case in the context of nonlinear models for reinforced concrete structures.

Regarding nonlinear structural analysis the different aspects of action – loading and internal forces or deformations – become an issue. The coefficients of variation of a loading type may undergo modifications due to the "filter" of nonlinear structural analysis leading to different coefficients of variation on the level of internal forces or deformations. Thus, the alternatives a) and b) from the design procedure described before – applying the partial safety factor γ_E on the load level or on the level of internal forces – might lead to different failure probabilities using the same partial safety factors γ_E, γ_R. Furthermore, usage of forces or deformations as measure in the limit-state function g, see Eq. (9.35), may lead to significant differences.

Partial safety factors γ_E are generally applied on the load level which corresponds to alternative a) of the design procedure. But a recalibration of safety factors might be necessary to compensate the nonlinear relations between loading and internal forces. This should advantageously be performed with modifications of the partial safety factors γ_R on the resistance side maintaining the same safety factors on the action side for linear and nonlinear analysis of different construction types. Regarding reinforced concrete structures rules for the determination of partial safety factors on the resistance side in the case of nonlinear computations are given in [16, 3.6], [18, 7.11.3], [24, 5.7]. These rules are based on mean values of the material strength of concrete and reinforcement whereby the resulting integrated resistance is divided by one partial safety factor γ_R covering both components.

Up to now safety has been regarded as a matter of local behavior, i.e., failure of a whole structure is defined to occur with a failure – $r = e$ – in the most critical part of a structure. But a structure as a whole may still maintain some integrity in the case of ductile statically indeterminate systems. This may lead to safety margins which are generally not explicitly taken into account for the design of structures.

Appendix A

Solution of Nonlinear Algebraic Equation Systems

The majority of the example problems are nonlinear due to nonlinear material behavior. Nonlinear material behavior is not only characteristic for cracked reinforced concrete but also occurs with all other solid materials at the latest with approaching strength. Discretization of nonlinear problems in space and time leads to a form

$$\mathbf{r}(\boldsymbol{v}) = \mathbf{p} - \mathbf{f}(\boldsymbol{v}) = \mathbf{0}, \qquad \mathbf{r}, \mathbf{p}, \mathbf{f}, \boldsymbol{v}, \mathbf{0} \in \mathbb{R}^n \tag{A.1}$$

with a prescribed $\mathbf{p}$ an unknown $\boldsymbol{v}$, see Eq. (1.69) for quasistatic problems, Eq. (1.80) for transient problems, and Eq. (1.95) for dynamic problems. Nonlinear problems also arise with the deformation state of cracked reinforced cross sections, see Section 3.1.3.3, or the determination of an equilibrium system for local strut-and-tie models, see Section 6.1.3.

We assume that Eq. (A.1) has a solution for $\boldsymbol{v}$, e.g., the underlying structural system has to be supported such that rigid body motions are prevented in the case of quasistatic or transient problems and the loading of a system should not exceed its load-bearing capacity.

A solution method has already been mentioned with the Newton–Raphson method, see Eqs. (1.70–1.72). We will illustrate this method in the following and describe some variations. This is based on the scalar form $n = 1$ of Eq. (A.1)

$$r(v) = p - f(v) = 0 \tag{A.2}$$

A first guess of the unknown is on hand with $v^{(0)}$ with a residual $r(v^{(0)})$. Equation (A.2) is expanded with a linear Taylor row

$$r(v^{(\nu)} + \delta v) = r(v^{(\nu)}) + \left.\frac{\mathrm{d}r(v)}{\mathrm{d}v}\right|_{v=v^{(\nu)}} \delta v, \tag{A.3}$$

to determine a correcting change δv. The condition $r(v^{(\nu)} + \delta v) = 0$ leads to

$$
\begin{aligned}
\delta v &= -\left.\frac{\mathrm{d}r(v)}{\mathrm{d}v}\right|_{v=v^{(\nu)}}^{-1} r(v^{(\nu)}) \\
&= \left[K_T^{(\nu)}\right]^{-1} r(v^{(\nu)}), \qquad K_T^{(\nu)} = \left.\frac{\mathrm{d}f(v)}{\mathrm{d}v}\right|_{v=v^{(\nu)}}
\end{aligned}
\tag{A.4}
$$
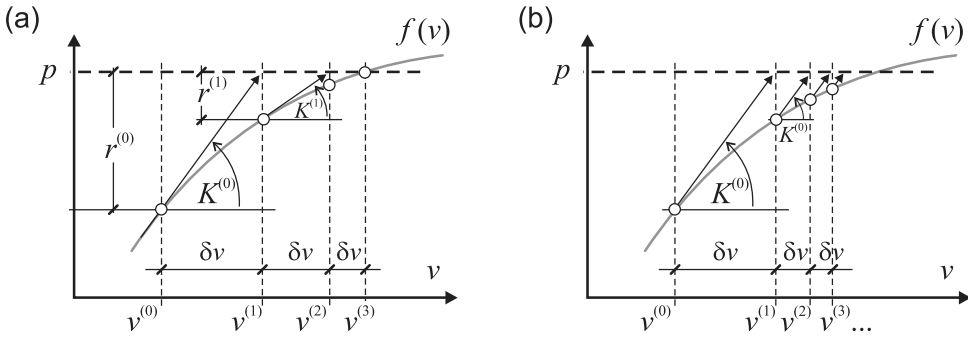
Figure A.1: (a) Newton–Raphson method. (b) Modified Newton–Raphson method.

with $[x]^{-1} = 1/x$ and an improved solution should be given by

$$v^{(\nu+1)} = v^{(\nu)} + \delta v \tag{A.5}$$

Equations (A.4, A.5) define an iteration sequence with an index (i) starting with $i = 0$. This is illustrated in Fig. A.1. The iteration stops if the iterated residual is small compared to, e.g., the initial residual $r^{(0)}$.

Equations (A.3–A.5) correspond to Eqs. (1.70-1.72) which are for $n > 1$. The reciprocal of the scalar stiffness $\mathrm{d}f/\mathrm{d}v$ becomes the inverse $\mathbf{K}_T^{-1}$ of the tangential stiffness matrix $\mathbf{K}_T$, see Eq. (1.71). The tangential stiffness matrix has a dimension $n \times n$. The solution correction is determined with

$$\delta \boldsymbol{v} = \mathbf{K}_T^{-1} \cdot \mathbf{r}, \qquad \delta \boldsymbol{v} \in \mathbb{R}^n, \quad \mathbf{K}_T, \, \mathbf{K}_T^{-1} \in \mathbb{R}^{n \times n} \tag{A.6}$$

in the i-iteration as a generalization of Eq. (A.4). But the inversion is quite expensive from a computational point of view for large values of n.

A *LU decomposition* is performed instead using a *Gaussian elimination* which requires considerably less operation compared to an inversion. The matrix $\mathbf{K}_T$ is decomposed into

$$\mathbf{K}_T = \mathbf{L} \cdot \mathbf{U}, \qquad \mathbf{L}, \, \mathbf{U} \in \mathbb{R}^{n \times n} \tag{A.7}$$

with a lower triangular matrix $\mathbf{L}$ with components $L_{ij} = 0$, $j > i$ and $L_{ii} = 1$ and an upper triangular matrix $\mathbf{U}$ with components $U_{ij} = 0$, $j < i$. Thus, the task of a particular iteration is reformulated as

$$\mathbf{L} \cdot \boldsymbol{\omega} = \mathbf{r}, \qquad \mathbf{U} \cdot \delta \boldsymbol{v} = \boldsymbol{\omega}, \qquad \boldsymbol{\omega} \in \mathbb{R}^n \tag{A.8}$$

or a sequence of *forward* and *backward* substitutions which for given $\mathbf{L}$, $\mathbf{U}$, $\mathbf{r}$ is computationally relatively inexpensive due to the triangular structure of $\mathbf{L}$, $\mathbf{U}$. The computational costs can be further reduced with the *modified Newton–Raphson method*. The LU decomposition is performed only once for a iteration sequence. The scalar version derived from Eq. (A.4) is given by

$$\delta v = \left[K_T^{(0)} \right]^{-1} r(v^{(\nu)}) \tag{A.9}$$
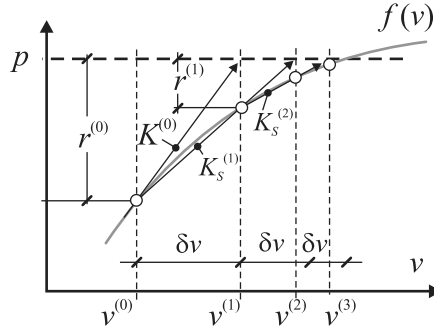
Figure A.2: Secant method.

and illustrated in Fig. A.2. On the other hand, the modified Newton–Raphson method requires more iterations than the Newton–Raphson method to reach convergence $\mathbf{r} \to \mathbf{0}$. But the convergence of the iterative approach to solve linear equations cannot be guaranteed.

- The Newton–Raphson method generally converges for a predominant smooth dependence of $\mathbf{f}$ on $\boldsymbol{v}$.

This is the case with Example 2.2, see Fig. 2.9, or Example 4.2, see Fig. 4.7a. But convergence will not be reached for "rough" dependence of $\mathbf{f}$ on $\boldsymbol{v}$. This is the case with Example 2.4, see Fig. 2.14b, or Example 6.3, see Fig. 6.10b, in the states of crack formation.

- In the cases of rough $\mathbf{f} - \boldsymbol{v}$-behavior, i.e., the tangential stiffness does not approximately indicate the actual $\mathbf{f} - \boldsymbol{v}$-path, the Newton–Raphson method generally will not converge to a solution $\boldsymbol{v}$ with a residual $\mathbf{r} \to \mathbf{0}$.

A further variation is given with *secant methods*. We consider again the scalar forms Eqs. (A.2–A.5) which are condensed as

$$
\begin{aligned}
\delta v &= \left[K_S^{(\nu)} \right]^{-1} r(v^{(\nu)}) \\
v^{(\nu+1)} &= v^{(\nu)} + \delta v
\end{aligned}
\tag{A.10}
$$

with K_S replacing K_T. The choice of K_S is basically arbitrary as long as it leads to a convergence of the sequence $v^{(\nu+1)}$ to the solution of $r(v) = p - f(v) = 0$. A secant method defines a sequence of secant stiffnesses K_S with

$$
K_S^{(\nu+1)} \, \delta v = \delta r, \qquad \delta v = v^{(\nu+1)} - v^{(\nu)}, \ \ \delta r = r(v^{(\nu)}) - r(v^{(\nu+1)})
\tag{A.11}
$$

see Fig. A.2. The secant stiffness $K_S^{(\nu+1)}$ is used for the *following* iteration according to Eq. (A.10):

$$
v^{(\nu+2)} = v^{(\nu+1)} + \left[K_S^{(\nu+1)} \right]^{-1} r(v^{(\nu+1)})
\tag{A.12}
$$

The generalization of the condition Eq. (A.11) for $n > 1$ is given by

$$
\mathbf{K}_S^{(\nu+1)} \, \delta \mathbf{v} = \delta \mathbf{r}, \qquad \delta \boldsymbol{v} = \boldsymbol{v}^{(\nu+1)} - \boldsymbol{v}^{(\nu)}, \qquad \delta \mathbf{r} = \mathbf{r}(v^{(\nu)}) - \mathbf{r}(v^{(\nu+1)})
\tag{A.13}
$$

but in contrast to the scalar case $n = 1$ this has not a unique solution for $\mathbf{K}_S^{(\nu+1)}$ anymore. This is already easily demonstrated for $n = 2$. Assuming a symmetric but otherwise unknown secant stiffness matrix and known vectors $\delta \boldsymbol{v}$, $\delta \mathbf{r}$ there are two equations for three unknown components of the secant stiffness.

This gives room for alternatives. A popular approach is given with the *BFGS method* which defines the secant stiffness matrix by

$$\mathbf{K}_S^{(\nu+1)} = \mathbf{K}_S^{(\nu)} + \frac{\delta \mathbf{r} \cdot \delta \mathbf{r}^T}{\delta \mathbf{r}^T \cdot \delta \boldsymbol{v}} - \frac{\mathbf{K}_S^{(\nu)} \cdot \delta \boldsymbol{v} \cdot \delta \boldsymbol{v}^T \cdot \mathbf{K}_S^{(\nu)}}{\delta \boldsymbol{v}^T \cdot \mathbf{K}_S^{(\nu)} \cdot \delta \boldsymbol{v}} \tag{A.14}$$

whereby the secant stiffness fulfills Eq. $(A.13)_1$. Furthermore, the inverse is given with the so-called *BFGS normal form*

$$\left[\mathbf{K}_S^{(\nu+1)} \right]^{-1} = \left(\mathbf{I} - \frac{\delta \boldsymbol{v} \cdot \delta \mathbf{r}^T}{\delta \mathbf{r}^T \cdot \delta \boldsymbol{v}} \right) \cdot \left[\mathbf{K}_S^{(\nu)} \right]^{-1} \cdot \left(\mathbf{I} - \frac{\delta \mathbf{r} \cdot \delta \boldsymbol{v}^T}{\delta \mathbf{r}^T \cdot \delta \boldsymbol{v}} \right) + \frac{\delta \boldsymbol{v} \cdot \delta \boldsymbol{v}^T}{\delta \mathbf{r}^T \cdot \delta \boldsymbol{v}} \tag{A.15}$$

with the unit matrix $\mathbf{I}$. This is used with the iteration rule

$$\boldsymbol{v}^{(\nu+2)} = \boldsymbol{v}^{(\nu+1)} + \left[\mathbf{K}_S^{(\nu+1)} \right]^{-1} \cdot \mathbf{r}(\boldsymbol{v}^{(\nu+1)}) \tag{A.16}$$

as the generalization of Eq. (A.12). The computation of the sequence of the BFGS normal forms may be efficiently implemented on the basis of the LU decomposition of a given $\mathbf{K}_S^{(0)}$ – the initial tangential stiffness is appropriate – with a recursion on vector products like $\delta \boldsymbol{v} \cdot \delta \mathbf{r}^T$ [63, S.269], [66, (5)]. A description of details exceeds the current scope.

- The BFGS method – with the option to combine it with a so-called line search – might converge to a solution $\boldsymbol{v}$ with a residual $\mathbf{r} \to \mathbf{0}$ in cases of rough $\mathbf{f} - \boldsymbol{v}$-behavior where the Newton–Raphson method fails.

It has been successfully used for, e.g., Examples 2.4, 6.3, each with pronounced crack formation.

All described iteration methods are generally embedded in an incrementally iterative approach, see Section 1.6, whereby the "load" terms $\mathbf{p}$ or p are prescribed with increments to reach a target value. The size of increments is fixed starting from zero and uniformly approaching a target value. Such a type of incrementing will not work with, e.g., snap-back behavior of structures, see Example 2.1 with Fig. 2.5a. The size of loading increments has to be reduced after reaching the peak in order to follow the load–displacement behavior.

The *arc length method* can be used to reach variable loading increments. We consider the general form Eq. (A.1) slightly modified as

$$\mathbf{r}(\lambda, \boldsymbol{v}) = \lambda \, \mathbf{p}_0 - \mathbf{f}(\boldsymbol{v}) = 0 \tag{A.17}$$

with a target load $\mathbf{p}_0$ and a loading factor λ. The loading history is discretized with

$$\lambda_{i+1} = \lambda_i + \Delta\lambda, \quad i = 0, 1, 2, \ldots \tag{A.18}$$

with $\lambda_0 = 0$ and variable $\lambda_{i+1}, \Delta\lambda_i$. In the same way $\boldsymbol{v}$ is discretized with respect to loading history

$$\boldsymbol{v}_{i+1} = \boldsymbol{v}_i + \Delta\boldsymbol{v} \tag{A.19}$$

with $\boldsymbol{v}_0 = \mathbf{0}$ and variable $\boldsymbol{v}_{i+1}, \Delta\boldsymbol{v}$.

- The vector increment $\Delta \boldsymbol{v}$ related to an increment of loading indicates an *arc* in the vector space $\mathbb{R}^n$.

Starting from a known state i the application of Eq. (A.17) on the following unknown state $i+1$ yields

$$\mathbf{r}(\lambda_{i+1},\, \boldsymbol{v}_{i+1}) = \lambda_{i+1}\, \mathbf{p}_0 - \mathbf{f}(\boldsymbol{v}_{i+1}) = 0 \tag{A.20}$$

This generally nonlinear equation is solved with iteration sequences $\boldsymbol{v}_{i+1}^{(0)}, \boldsymbol{v}_{i+1}^{(1)}, \dots$ and $\lambda_{i+1}^{(0)}, \lambda_{i+1}^{(1)}, \dots$ whereby

$$\begin{aligned}
\delta \boldsymbol{v} &= \boldsymbol{v}_{i+1}^{(\nu+1)} - \boldsymbol{v}_{i+1}^{(\nu)} \\
\Delta \boldsymbol{v}^{(\nu+1)} &= \boldsymbol{v}_{i+1}^{(\nu+1)} - \boldsymbol{v}_i = \Delta \boldsymbol{v}^{(\nu)} + \delta \boldsymbol{v}
\end{aligned} \tag{A.21}$$

and

$$\begin{aligned}
\delta \lambda &= \lambda_{i+1}^{(\nu+1)} - \lambda_{i+1}^{(\nu)} \\
\Delta \lambda^{(\nu+1)} &= \lambda_{i+1}^{(\nu+1)} - \lambda_i
\end{aligned} \tag{A.22}$$

The iteration rule is given in analogy to Eq. (A.6) with

$$\begin{aligned}
\delta \boldsymbol{v} &= [\mathbf{K}]^{-1} \cdot \mathbf{r}(\lambda_{i+1}^{(\nu+1)}, \boldsymbol{v}_{i+1}^{(\nu)}) \\
&= \lambda_{i+1}^{(\nu+1)}\, [\mathbf{K}]^{-1} \cdot \mathbf{p}_0 - [\mathbf{K}]^{-1}\, \mathbf{f}(\boldsymbol{v}_{i+1}^{(\nu)}) \\
&= \delta \lambda\, [\mathbf{K}]^{-1} \cdot \mathbf{p}_0 + [\mathbf{K}]^{-1} \cdot \mathbf{r}(\lambda_{i+1}^{(\nu)}, \boldsymbol{v}_{i+1}^{(\nu)})
\end{aligned} \tag{A.23}$$

with some kind of stiffness $\mathbf{K}$ according to the Newton–Raphson method, the modified Newton–Raphson method or a secant method. The inversion is not explicitly performed but a LU decomposition is used instead. The iteration starts with $\boldsymbol{v}_{i+1}^{(0)} = \boldsymbol{v}_i$, $\Delta \boldsymbol{v}^{(0)} = \mathbf{0}$, $\lambda_{i+1}^{(0)} = \lambda_i$.

The iteration rule may be rewritten as

$$\delta \boldsymbol{v} = \delta \lambda\ \boldsymbol{v}_0 + \delta \boldsymbol{v}^{(\nu)} \tag{A.24}$$

with

$$\begin{aligned}
\boldsymbol{v}_0 &= [\mathbf{K}]^{-1} \cdot \mathbf{p}_0 \\
\delta \boldsymbol{v}^{(\nu)} &= [\mathbf{K}]^{-1} \cdot \mathbf{r}(\lambda_{i+1}^{(\nu)}, \boldsymbol{v}_{i+1}^{(\nu)})
\end{aligned} \tag{A.25}$$

A further condition is needed to determine the variable λ_{i+1}. It is derived from

$$\Delta \boldsymbol{v}^{(\nu+1)^T} \cdot \Delta \boldsymbol{v}^{(\nu+1)} = \gamma^2 \tag{A.26}$$

with $\Delta \boldsymbol{v}^{(\nu+1)}$ according to Eq. (A.21) and a scalar γ controlling the *arc length size*. The evaluation yields a quadratic equation for the correction $\delta \lambda$ of the loading factor

$$a\, \delta \lambda^2 + b\, \delta \lambda + c + d = \gamma^2 \tag{A.27}$$

with

$$\begin{aligned}
a &= \boldsymbol{v}_0^T \cdot \boldsymbol{v}_0 \\
b &= \Delta \boldsymbol{v}^{(\nu)^T} \cdot \boldsymbol{v}_0 + \delta \boldsymbol{v}^{(\nu)^T} \cdot \boldsymbol{v}_0 \\
c &= 2 \Delta \boldsymbol{v}^{(\nu)^T} \cdot \delta \boldsymbol{v}^{(\nu)} + \delta \boldsymbol{v}^{(\nu)^T} \cdot \delta \boldsymbol{v}^{(\nu)} \\
d &= \Delta \boldsymbol{v}^{(\nu)^T} \cdot \Delta \boldsymbol{v}^{(\nu)}
\end{aligned} \tag{A.28}$$

These coefficients are determined with the results of the ν-iteration whereby $b = c = d = 0$ and $a > 0$ for $\nu = 0$. Furthermore, $\mathbf{r}(\lambda_{i+1}^{(0)}, \boldsymbol{v}_{i+1}^{(0)}) = \mathbf{r}(\lambda_i, \boldsymbol{v}_i) \approx \mathbf{0}$ is reasonable. Equation (A.27) can be further simplified with $d = \gamma^2$ for $\nu > 0$ as the prescribed arc length size should not change during the iteration. Two real solutions are given with

$$\delta\lambda = \frac{-b \pm \sqrt{b^2 - ac'}}{a} \tag{A.29}$$

in case $b^2 - ac' > 0$ with $c' = c + d - \gamma^2$. The scalar product

$$g = \Delta\boldsymbol{v}^{(\nu)T} \cdot \Delta\boldsymbol{v}^{(\nu+1)} = \Delta\boldsymbol{v}^{(\nu)T} \cdot \left(\Delta\boldsymbol{v}^{(\nu)} + \delta\lambda\,\boldsymbol{v}_0 + \delta\boldsymbol{v}^{(\nu)} \right) \tag{A.30}$$

may be used to determine the solution to choose. That with a larger value g makes the actual arc $\Delta\boldsymbol{v}^{(\nu+1)}$ more similar to the previous arc $\Delta\boldsymbol{v}^{(\nu)}$ and is generally the choice. It is finally used in Eq. (A.24) to determine the correction $\delta\boldsymbol{v}$. In case $\nu = 0$ with $\Delta\boldsymbol{v}^{(0)} = \mathbf{0}$ the $\Delta\boldsymbol{v}$ of the previous loading increment may be used. In case $i = 0, \nu = 0$ the choice $\delta\lambda = +\gamma/\sqrt{a}$ is appropriate.

The case $b^2 - ac' < 0$ remains to be treated. The prescribed arc length γ cannot be reached with any length of $\delta\lambda$ for given directions $\boldsymbol{v}_0$ and $\delta\boldsymbol{v}^{(\nu)}$. In most cases it may be reached with an increased γ. An alternative approach is to minimize the left-hand side of Eq. (A.27). This yields the smallest value γ which can be reached.

For more details about the arc length method see [9, 6.5.3], [3, 8.4.3]. It has been used for Examples 2.1 and 4.2.

Appendix B

Crack Width Estimation

Formation of cracks is a characteristic property of structural reinforced concrete. It influences the local stiffness of structures. The stiffness is reduced in areas with high tension leading to a redistribution of stresses within statically indeterminate structures: softer areas are relieved while stiffer areas gain stresses compared to a linear elastic calculation. Furthermore, stresses from constraints like settlements or temperatures are reduced. Insofar crack formation leads to favorable effects. On the other hand, the overall deformation of cracked structures increases, the corrosion risk of steel reinforcement grows in cracked areas and the visual impression suffers with larger cracks. Thus, crack width has to be controlled and methods to predict crack width are required.

The direct computation of crack width has been demonstrated with Example 2.4 with a fine discretization using an element length in the order of 1 cm. Such a fine discretization practically leads to a discrete modeling of cracks, see Section 5.7.1. But such fine discretizations are not appropriate for the modeling or structures like plates, slabs, and shells. Crack modeling is generally performed with the smeared crack model for such structures, see Sections 5.7.2, 6.2, and 6.3, with characteristic elements lengths considerably larger than 1 cm. Therefore, an alternative model for crack width estimation is required. This will be described in the following.

This model is based on the uniaxial tension bar whereby analytical crack width relations are derived with some simplifying assumptions. This leads to crack width estimations which primarily depend on the reinforcement stress. On the other hand, crack situations in, e.g., plates may be considered as uniaxial in the context of the Rankine criterion, see Section 5.7.1.

- Crack width estimations for uniaxial tension bars may also be applied to cracked plates locally with rebar stresses and reinforcement parameters given.

Furthermore, such estimations may also be transferred to slabs and shells in the context of layer models, see Sections 7.2.3 and 8.7.1. The simplified model for crack width estimations is also suitable for reinforced concrete beams when applied to the tension zone or the immediate surrounding of rebars in cracked cross sections.

Details of the uniaxial tension bar have been described in Section 2.6. The current setup refers to Fig. 2.17a with a cracked reinforced cross section and is shown in Fig. B.1a.
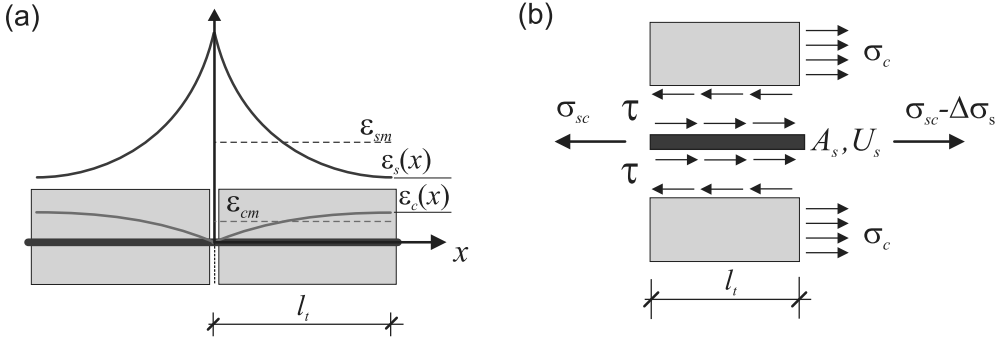
Figure B.1: (a) Strains at cracked cross section. (b) Equilibrium with bond stresses.

Assuming a centered symmetry the width w of the crack can be determined as

$$w = 2 \int_0^{l_t} \left(\epsilon_s(x) - \epsilon_c(x) \right) \, \mathrm{d}x \tag{B.1}$$

with the *force transfer length* l_t, the rebar strain $\epsilon_s(x)$, and the concrete strain $\epsilon_c(x)$ which are variable in the longitudinal direction. The transfer length corresponds to the length from the crack to the position with constant strains or local extrema of strains. Mean strains within the transfer length are given by

$$\epsilon_{sm} = \frac{1}{l_t} \int_0^{l_t} \epsilon_s(x) \, \mathrm{d}x, \qquad \epsilon_{cm} = \frac{1}{l_t} \int_0^{l_t} \epsilon_c(x) \, \mathrm{d}x \tag{B.2}$$

and crack width may be rewritten as

$$w = 2l_t \left(\epsilon_{sm} - \epsilon_{cm} \right) \tag{B.3}$$

Strains $\epsilon_s(x)$, $\epsilon_c(x)$ are related to rebar stresses $\sigma_s(x)$ and concrete stresses $\sigma_c(x)$. The following stress–strain relations are assumed

$$\sigma_s = E_s \, \epsilon_s, \qquad \sigma_c = \begin{cases} E_c \, \epsilon_c & \epsilon_c \leq f_{ct}/E_c \\ 0 & \text{else} \end{cases} \tag{B.4}$$

Regarding the crack position $x = 0$ the concrete stress is zero and the rebar stress has its maximum value $\sigma_s(0) = \sigma_{sc}$. The rebar stress decreases with x and reaches its minimum value with $x = l_t$. We use a rebar stress difference

$$\Delta \sigma_s = \sigma_{sc} - \sigma_s(l_t) \tag{B.5}$$

and determine the mean rebar stress along l_t with

$$\sigma_{sm} = \sigma_{sc} - \beta_t \, \Delta \sigma_s \tag{B.6}$$

compare also Fig. 2.17a. The parameter β_t has already been used in Section 2.7. It encompasses the extent of load transfer between rebar and concrete or bond quality, respectively. A value $\beta_t = 0$ denotes no stress transfer and no effective bond, a value $\beta_t = 1$ immediate stress transfer and perfect bond. The values are generally assumed in the range $0.4 \leq \beta_t \leq 0.6$ [26, 7.3.4], [18, 7.6.4.4].

For reasons of equilibrium, see Fig. B.1b, the concrete stress along the longitudinal direction is given by

$$\sigma_c(x) = \rho_{\text{eff}} \left[\sigma_{sc} - \sigma_s(x) \right] \tag{B.7}$$

whereby $\rho_{\text{eff}} = A_s / A_{c,\text{eff}}$ is the effective reinforcement ratio with the cross section area A_s of the rebar and the effective cross section area $A_{c,\text{eff}}$ of the concrete. The cross section area $A_{c,\text{eff}}$ has already been discussed in Section 2.7. The concrete stress has its maximum at $x = l_t$ with a value

$$\sigma_{c,\max} = \rho_{\text{eff}} \, \Delta\sigma_s \tag{B.8}$$

Using Eqs. (B.6,B.7) the mean concrete stress results to

$$\sigma_{cm} = \frac{1}{l_t} \int_0^{l_t} \sigma_c(x) \, \mathrm{d}x = \rho_{\text{eff}} \, \beta_t \, \Delta\sigma_s \tag{B.9}$$

The load transfer between concrete and reinforcement is connected with bond stresses $\tau(x)$. For reasons of equilibriums, see Fig. B.1b, it is related to the rebar stress difference $\Delta\sigma_s$ through

$$A_s \, \Delta\sigma_s = C_s \int_0^{l_t} \tau(x) \, \mathrm{d}x \tag{B.10}$$

with the reinforcement circumference C_s. Using the mean bond stress τ_m this can be written as

$$\Delta\sigma_s = \frac{C_s}{A_s} \, l_t \, \tau_m = \frac{4l_t}{d_s} \, \tau_m \tag{B.11}$$

with the reinforcement diameter d_s and $C_s / A_s = 4/d_s$. The mean bond stress τ_m is assumed to be proportional to the concrete tensile strength f_{ct} according to [26, 8.4.2]

$$\tau_m = \eta \, f_{ct} \tag{B.12}$$

with η in the range of 2. More data about bond are given in [18, 6.1.1]. Equation (B.11) leads to a relation for the stress transfer length

$$l_t = \frac{d_s}{4\tau_m} \, \Delta\sigma_s \tag{B.13}$$

This yields the first part of Eq. (B.3) determining the crack width. The mean reinforcement strain

$$\epsilon_{sm} = \frac{\sigma_{sm}}{E_s} = \frac{1}{E_s} \, (\sigma_{sc} - \beta_t \, \Delta\sigma_s) \tag{B.14}$$

using Eq. (B.6) and the mean concrete strain

$$\epsilon_{cm} = \frac{\sigma_{cm}}{E_c} = \frac{1}{E_c} \rho_{\text{eff}} \, \beta_t \, \Delta\sigma_s \tag{B.15}$$

using Eq. (B.9) complete the second part. This finally yields

$$w = \frac{d_s}{2\tau_m} \frac{\Delta\sigma_s}{E_s} \left[\sigma_{sc} - \beta_t \left(1 + \alpha_e \rho_{\text{eff}} \right) \Delta\sigma_s \right] \tag{B.16}$$

with a priori known or assumed parameters $d_s, \rho_{\text{eff}}, \tau_m$ and the stiffness ratio $\alpha_e = E_s/E_c$. The rebar stress σ_{sc} in the crack's cross section is determined through the external loading. The rebar stress difference $\Delta\sigma_s$ remains to be determined. Thus, two limiting cases are regarded which are the state with single cracks and the state with stabilized cracking.

A tension bar is in the uncracked state at load initiation whereby concrete properties are subject to scatter. A first single crack will arise in the cross section with the smallest overall tensile strength due to increasing loading starting from zero. The softening behavior, see Fig. 5.16, is neglected for crack width estimation as the critical crack width w_{cr} generally does not exceed 0.1 mm while the relevant crack width is in the range considerably above 0.1 mm within this context. Perfect brittle tensile behavior of concrete behavior, see Fig. 5.14b, is assumed for the following.

A *single crack* is characterized by

$$\epsilon_s(l_t) = \epsilon_c(l_t) \tag{B.17}$$

whereby strains of concrete and reinforcement match beyond the stress transfer length. Replacing strains with stresses whereby using Eqs. (B.5, B.7) leads to

$$\frac{1}{E_s}(\sigma_{sc} - \Delta\sigma_s) = \frac{1}{E_c}\rho_{\text{eff}}\,\Delta\sigma_s \tag{B.18}$$

and

$$\Delta\sigma_s = \frac{\sigma_{sc}}{1 + \alpha_e\rho_{\text{eff}}} \tag{B.19}$$

and the crack width of the first single crack can finally be determined with Eq. (B.16).

Further cracks develop with slightly increasing loading in the cross sections with the currently smallest tensile strength. With a rising number of cracks we have to introduce crack spacing s_c. Crack spacing on one hand has the condition

$$s_c \geq l_t \tag{B.20}$$

as a crack is not possible within l_t because of the decreasing concrete stresses towards the crack. On the other hand, crack spacing reduces with an increasing number of cracks. Cracking will occur as long as $s_c \geq 2l_t$ with slightly increasing loading whereby reducing crack spacing and will finally reach a stabilized state with $s_c < 2l_t$. The concrete stress will not reach the tensile strength anymore under this condition. The process has been demonstrated with all its stages in Example 2.4.

The state of *stabilized cracking* is characterized by

$$l_t \leq s_c < 2l_t \tag{B.21}$$

Loading may further considerably increase but the maximum concrete stress, see Eq. (B.8), will not exceed f_{ct}. This leads to a condition $\Delta\sigma_s \leq f_{ct}/\rho_{\text{eff}}$ for stabilized cracking. We assume the equality

$$\Delta\sigma_s = \frac{f_{ct}}{\rho_{\text{eff}}} \tag{B.22}$$

for usage with the crack width relation (B.16). This finally yields the crack width estimation for stabilized cracking

$$w = \frac{d_s}{2\tau_m}\frac{f_{ct}}{\rho_{\text{eff}}}\frac{1}{E_s}\left[\sigma_{sc} - \beta_t\left(1 + \alpha_e\rho_{\text{eff}}\right)\frac{f_{ct}}{\rho_{\text{eff}}}\right] \tag{B.23}$$
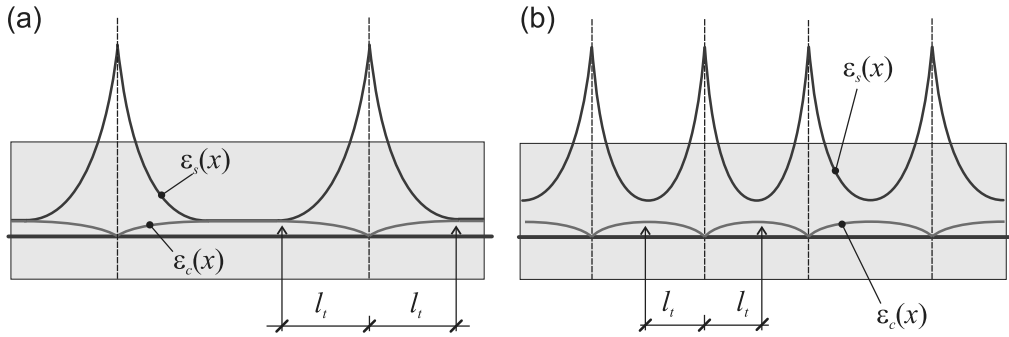
Figure B.2: Crack states. (a) Single cracks. (b) Stabilized cracks.

Stabilized cracking is characterized by the following properties:

– Increased loading is completely carried by the reinforcement until its load-bearing capacity is reached.

– Between two cracks, a position exists where the slip between concrete and reinforcement is equal to zero. This position margins the force transfer lengths of the cracks to the left and to the right, see Fig. 2.16b for an example.

– At this position the reinforcement stress has a minimum while the concrete stress has a maximum, which does not reach the concrete tensile strength, see Fig. 2.15a for an example.

– The reinforcement strain increases compared to the concrete strain, which retains its course. This distinguishes the state of stabilized cracking from the state of single cracks, see Fig. B.2.

The crack width of stabilized cracking has to be considered as relevant. Thus, variations of Eq. (B.23) are used in codes for crack width estimation [26, 7.3.4], [18, 7.6.4.4]. For a discussion of the influence of imposed strains from temperature and shrinkage on the crack width estimation see [42].

The application of all these rules is generally stipulated for reinforced concrete beams. The predominant variable is given with the rebar stress σ_{sc} in the cracked cross section, compare also Fig. 3.2, while the parameters d_s, τ_m, f_{ct}, ρ_{eff}, E_s, β_t, α_e are assumed to be known within this simplified setup.

The estimation may also be directly applied for cracked positions in plates or layers of slabs or shells when the reinforcement direction is orthogonal to the crack direction. This should the case for the positions with the largest stresses. In case that principal tension or crack normals deviates by more than 15° from reinforcement directions rules for crack width estimations are given in [26, 7.3.4(4)] or [18, 7.6.4.4.3].

Appendix C

Transformations of Coordinate Systems

Cartesian coordinate systems are used throughout this textbook to describe space if not otherwise stated. Coordinates x_i are measured with respect to three (3D space) or two (2D plane) orthogonal base vectors $\mathbf{e}_i$ of unit length. Orthogonality of unit vectors leads to

$$\mathbf{e}_i \cdot \mathbf{e}_j = \mathbf{e}_j \cdot \mathbf{e}_i = \begin{cases} 1 & i = j \\ 0 & i \neq j \end{cases} \tag{C.1}$$

with the vector product $\cdot$. The sequence of base vectors has a right-hand orientation.

We restrict to the 2D plane in the following. A vector $\mathbf{x}$ describing a position is written as

$$\overrightarrow{\mathbf{r}} = x_1\,\mathbf{e}_1 + x_2\,\mathbf{e}_2 \tag{C.2}$$

or alternatively in another Cartesian system rotated by an angle φ

$$\overrightarrow{\mathbf{r}} = \tilde{x}_1\,\tilde{\mathbf{e}}_1 + \tilde{x}_2\,\tilde{\mathbf{e}}_2 \tag{C.3}$$

positive in the counterclockwise direction, see Fig. C.1. The base vectors $\tilde{\mathbf{e}}_1, \tilde{\mathbf{e}}_2$ are still orthogonal according to Eq. (C.1). The rotated coordinates are given by

$$\begin{aligned} \tilde{x}_1 &= & x_1\,\mathbf{e}_1 \cdot \tilde{\mathbf{e}}_1 + x_2\,\mathbf{e}_2 \cdot \tilde{\mathbf{e}}_1 \\ &= & x_1\,\cos\varphi + x_2\,\cos(\pi/2 - \varphi) \\ &= & x_1\,\cos\varphi + x_2\,\sin\varphi \\ \tilde{x}_2 &= & x_1\,\mathbf{e}_1 \cdot \tilde{\mathbf{e}}_2 + x_2\,\mathbf{e}_2 \cdot \tilde{\mathbf{e}}_2 \\ &= & x_1\,\cos(\pi/2 + \varphi) + x_2\,\cos\varphi \\ &= & -x_1\,\sin\varphi + x_2\,\cos\varphi \end{aligned} \tag{C.4}$$

after applying Eq. (C.1). This may be written as

$$\tilde{\mathbf{x}} = \mathbf{Q} \cdot \mathbf{x} \tag{C.5}$$

with

$$\tilde{\mathbf{x}} = \begin{pmatrix} \tilde{x}_1 \\ \tilde{x}_1 \end{pmatrix}, \quad \mathbf{Q} = \begin{bmatrix} \cos\alpha & \sin\alpha \\ -\sin\alpha & \cos\alpha \end{bmatrix}, \quad \mathbf{x} = \begin{pmatrix} x_1 \\ x_1 \end{pmatrix} \tag{C.6}$$
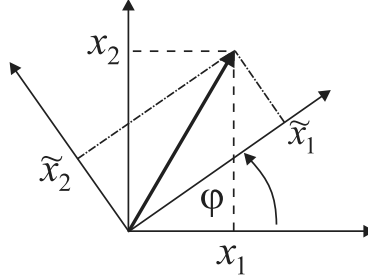
Figure C.1: Plane coordinate transformation.

collecting the coordinate components in a vector notation. The back transformation is given as

$$\mathbf{x} = \mathbf{Q}^T \cdot \tilde{\mathbf{x}} \tag{C.7}$$

as $\mathbf{Q}^{-1} = \mathbf{Q}^T$. Any other vector – e.g., displacement, velocity, force – of a form corresponding to Eq. (C.2) has as transformation rules for its components

$$\tilde{\mathbf{a}} = \mathbf{Q} \cdot \mathbf{a}, \quad \mathbf{a} = \mathbf{Q}^T \cdot \tilde{\mathbf{a}}, \tag{C.8}$$

with $\tilde{\mathbf{a}} = \begin{pmatrix} \tilde{a}_x & \tilde{a}_y \end{pmatrix}^T$ and $\mathbf{a} = \begin{pmatrix} a_x & a_y \end{pmatrix}^T$.

We have to consider second-order tensors beneath vector or first-order tensors. A second-order tensor is given with the Cauchy stress $\boldsymbol{\sigma}$, see Section 5.2.2. Regarding plane states the stress tensor is written as

$$\mathbf{S} = \sigma_{11}\,\mathbf{e}_1\mathbf{e}_1 + \sigma_{12}\,\mathbf{e}_1\mathbf{e}_2 + \sigma_{21}\,\mathbf{e}_2\mathbf{e}_1 + \sigma_{22}\,\mathbf{e}_2\mathbf{e}_2 \tag{C.9}$$

with an outer or dyadic base $\mathbf{e}_1\mathbf{e}_1, \mathbf{e}_1\mathbf{e}_2, \mathbf{e}_2\mathbf{e}_1, \mathbf{e}_2\mathbf{e}_2$, compare also Eq. (8.24). The dyadic base emerges from force direction and direction of the normal of the reference plane, see Eq. (5.5). The second-order tensor is described alternatively in another Cartesian system rotated by an angle φ

$$\mathbf{S} = \tilde{\sigma}_{11}\,\tilde{\mathbf{e}}_1\tilde{\mathbf{e}}_1 + \tilde{\sigma}_{12}\,\tilde{\mathbf{e}}_1\tilde{\mathbf{e}}_2 + \tilde{\sigma}_{21}\,\tilde{\mathbf{e}}_2\tilde{\mathbf{e}}_1 + \tilde{\sigma}_{22}\,\tilde{\mathbf{e}}_2\tilde{\mathbf{e}}_2 \tag{C.10}$$

The identity of these formulations may be used to expose the values of the tensor components in the rotated system. Applying vector products with $\tilde{\mathbf{e}}_1$, $\tilde{\mathbf{e}}_1$ whereby exploiting their orthogonality and the symmetry of tensor components $\sigma_{12} = \sigma_{21}$ leads to

$$\begin{pmatrix} \tilde{\sigma}_{11} \\ \tilde{\sigma}_{22} \\ \tilde{\sigma}_{12} \end{pmatrix} = \begin{bmatrix} \cos^2\varphi & \sin^2\varphi & 2\cos\varphi\sin\varphi \\ \sin^2\varphi & \cos^2\varphi & -2\cos\varphi\sin\varphi \\ -\cos\varphi\sin\varphi & \cos\varphi\sin\varphi & \cos^2\varphi - \sin^2\varphi \end{bmatrix} \cdot \begin{pmatrix} \sigma_{11} \\ \sigma_{22} \\ \sigma_{12} \end{pmatrix} \tag{C.11}$$

in analogy to Eq. (C.4). The inversion is derived in the analogous way and yields

$$\begin{pmatrix} \sigma_{11} \\ \sigma_{22} \\ \sigma_{12} \end{pmatrix} = \begin{bmatrix} \cos^2\varphi & \sin^2\varphi & -2\cos\varphi\sin\varphi \\ \sin^2\varphi & \cos^2\varphi & 2\cos\varphi\sin\varphi \\ \cos\varphi\sin\varphi & -\cos\varphi\sin\varphi & \cos^2\varphi - \sin^2\varphi \end{bmatrix} \cdot \begin{pmatrix} \tilde{\sigma}_{11} \\ \tilde{\sigma}_{22} \\ \tilde{\sigma}_{12} \end{pmatrix} \tag{C.12}$$

Strain tensor components $\epsilon_{11}, \epsilon_{12} = \epsilon_{21}, \epsilon_{22}$ as a subset of Eq. (5.2) are transformed in the same way. This leads to

$$
\begin{pmatrix} \tilde{\epsilon}_{11} \\ \tilde{\epsilon}_{22} \\ \tilde{\gamma}_{12} \end{pmatrix} = \begin{bmatrix} \cos^2\varphi & \sin^2\varphi & \cos\varphi\sin\varphi \\ \sin^2\varphi & \cos^2\varphi & -\cos\varphi\sin\varphi \\ -2\cos\varphi\sin\varphi & 2\cos\varphi\sin\varphi & \cos^2\varphi - \sin^2\varphi \end{bmatrix} \cdot \begin{pmatrix} \epsilon_{11} \\ \epsilon_{22} \\ \gamma_{12} \end{pmatrix} \tag{C.13}
$$

regarding the definition $\gamma_{ij} = 2\epsilon_{ij}$, $i \neq j$ for strain components in engineering notation. This transformation matrix is transposed to the back-transformation matrix of stresses (Eq. (C.12)). The inversion is again derived in the analogous way and yields

$$
\begin{Bmatrix} \epsilon_{11} \\ \epsilon_{22} \\ \gamma_{12} \end{Bmatrix} = \begin{bmatrix} \cos^2\varphi & \sin^2\varphi & -\cos\varphi\sin\varphi \\ \sin^2\varphi & \cos^2\varphi & \cos\varphi\sin\varphi \\ 2\cos\varphi\sin\varphi & -2\cos\varphi\sin\varphi & \cos^2\varphi - \sin^2\varphi \end{bmatrix} \cdot \begin{Bmatrix} \tilde{\epsilon}_{11} \\ \tilde{\epsilon}_{22} \\ \tilde{\gamma}_{12} \end{Bmatrix} \tag{C.14}
$$

This back-transformation matrix is transposed to the transformation matrix of stresses (Eq. (C.11)).

Cartesian transformations of vectors and second-order tensors in 3D space are derived in a similar way based on extended formulations of Eqs. (C.2,C.3) and (C.9,C.10) whereby involving three rotation angles and again exploiting orthogonality of base vectors.

Appendix D

Regression Analysis

Regression analysis leads to an *approximation* of multiple given data by combining functions with a few degrees of freedom. We consider n discrete data f_i determined from a survey over a plane in positions x_i, y_i. A linear approximation leads to errors

$$r_i = a\,x_i + b\,y_i + c - f_i, \quad i = 1, \ldots, n \tag{D.1}$$

We search for the optimal coefficients a, b, c. The problem may be also written as

$$\mathbf{r(a)} = \mathbf{X} \cdot \mathbf{a} - \mathbf{f} \tag{D.2}$$

with

$$\mathbf{X} = \begin{bmatrix} x_1 & y_1 & 1 \\ x_2 & y_2 & 1 \\ \vdots & \vdots & \vdots \\ x_n & y_n & 1 \end{bmatrix}, \quad \mathbf{a} = \begin{pmatrix} a \\ b \\ c \end{pmatrix}, \quad \mathbf{f} = \begin{pmatrix} f_1 \\ f_2 \\ \vdots \\ f_n \end{pmatrix} \tag{D.3}$$

The error shall be zero $\mathbf{r(a)} = \mathbf{0}$, i.e.,

$$\mathbf{X} \cdot \mathbf{a} = \mathbf{f} \tag{D.4}$$

This is an overdetermined set of linear equations for $n > 3$ and will not have a solution for $\mathbf{a}$. Thus, we will minimize the error with minimizing the error length $e(\mathbf{a}) = \mathbf{r}^T \cdot \mathbf{r}$. The error length is given by

$$\begin{aligned} e &= (\mathbf{X} \cdot \mathbf{a} - \mathbf{f})^T \cdot (\mathbf{X} \cdot \mathbf{a} - \mathbf{f}) \\ &= \mathbf{a}^T \cdot \mathbf{X}^T \cdot \mathbf{X} \cdot \mathbf{a} - 2\mathbf{a}^T \cdot \mathbf{X}^T \cdot \mathbf{f} + \mathbf{f}^T \cdot \mathbf{f} \end{aligned} \tag{D.5}$$

The error length is minimized under the condition

$$\frac{\partial e}{\partial \mathbf{a}} = 0 \tag{D.6}$$

leading to

$$\mathbf{X}^T \cdot \mathbf{X} \cdot \mathbf{a} = \mathbf{X}^T \cdot \mathbf{f} \tag{D.7}$$

This corresponds to the well-known method of the least squares.

The basic approach allows for many specifications. We consider n discrete data f_i along a line in positions x_i. A quadratic approximation leads to errors

$$r_i = a\,x_i^2 + b\,x_i + c - f_i, \quad i = 1, \ldots, n \tag{D.8}$$

This may be written in the same way as Eq. (D.2) with

$$\mathbf{X} = \begin{bmatrix} x_1^2 & x_1 & 1 \\ x_2^2 & x_2 & 1 \\ \vdots & \vdots & \vdots \\ x_n^2 & x_n & 1 \end{bmatrix} \tag{D.9}$$

and may be solved for the optimal coefficients a, b, c with Eq. (D.2).

The dimension of the underlying space is arbitrary. We use area coordinates L_1, L_2, L_3, see Section 7.4.1 with Eq. (7.42), for a linear approximation of a given field m

$$r = a\,L_1 + b\,L_2 + c\,L_3 - m \tag{D.10}$$

defined over a triangle, see Fig. 7.5. Four survey points are used due to four sampling points $\mathbf{L}_i$ of a numerical integration. The sampling points have the coordinates

$$\mathbf{L}_1 = \begin{pmatrix} 1/3 \\ 1/3 \\ 1/3 \end{pmatrix}, \quad \mathbf{L}_2 = \begin{pmatrix} 0.6 \\ 0.2 \\ 0.2 \end{pmatrix}, \quad \mathbf{L}_3 = \begin{pmatrix} 0.2 \\ 0.6 \\ 0.2 \end{pmatrix}, \quad \mathbf{L}_4 = \begin{pmatrix} 0.2 \\ 0.2 \\ 0.6 \end{pmatrix} \tag{D.11}$$

This may be written as

$$\mathbf{r(a)} = \mathbf{X} \cdot \mathbf{a} - \mathbf{m} \tag{D.12}$$

with

$$\mathbf{X} = \begin{bmatrix} 1/3 & 1/3 & 1/3 \\ 0.6 & 0.2 & 0.2 \\ 0.2 & 0.6 & 0.2 \\ 0.2 & 0.2 & 0.6 \end{bmatrix}, \quad \mathbf{a} = \begin{pmatrix} a \\ b \\ c \end{pmatrix}, \quad \mathbf{m} = \begin{pmatrix} m_1 \\ m_2 \\ m_3 \\ m_4 \end{pmatrix} \tag{D.13}$$

and Eq. (D.7) yields

$$\mathbf{A} \cdot \mathbf{a} = \mathbf{X}^T \cdot \mathbf{m} \tag{D.14}$$

with

$$\mathbf{A} = \mathbf{X}^T \cdot \mathbf{X} = \frac{1}{225} \begin{bmatrix} 124 & 88 & 88 \\ 88 & 124 & 88 \\ 88 & 88 & 124 \end{bmatrix}, \quad \mathbf{A}^{-1} = \frac{1}{6} \begin{bmatrix} \frac{53}{2} & -11 & -11 \\ -11 & \frac{53}{2} & -11 \\ -11 & -11 & \frac{53}{2} \end{bmatrix} \tag{D.15}$$

and finally

$$\mathbf{a} = \frac{1}{4} \begin{bmatrix} 1 & \frac{23}{3} & -\frac{7}{3} & -\frac{7}{3} \\ 1 & -\frac{7}{3} & \frac{23}{3} & -\frac{7}{3} \\ 1 & -\frac{7}{3} & -\frac{7}{3} & \frac{23}{3} \end{bmatrix} \cdot \mathbf{m} \tag{D.16}$$

whereby **m** is given from the field m evaluated in the sampling points. The three rows of the matrix each add up to 1 with the prefactor. With known coefficients **a**, the derivatives of the field m with respect to global coordinate axes x, are determined by

$$
\begin{aligned}
\frac{\partial m}{\partial x} &= \frac{\partial m}{\partial L_1}\frac{\partial L_1}{\partial x} + \frac{\partial m}{\partial L_2}\frac{\partial L_2}{\partial x} + \frac{\partial m}{\partial L_3}\frac{\partial L_3}{\partial x} \\
&= a\,b_1 + b\,b_2 + c\,b_3
\end{aligned}
\tag{D.17}
$$

and

$$
\frac{\partial m}{\partial x} = a\,c_1 + b\,c_2 + c\,c_3
\tag{D.18}
$$

with b_i, c_i according to Eq. (7.46).

Appendix E

Reliability with Multivariate Random Variables

We consider a structure with n random properties or variables $X_1, X_2, \ldots, X_n$ with a joint probability density function

$$f_X(x_1, x_2, \ldots, x_n) \tag{E.1}$$

Nonnormal distributions may be transformed into normal distributions using the model of NATAF [62]. Furthermore, correlated multivariate normal distributions may be transformed into uncorrelated normal distributions based on the spectral decomposition of the covariance matrix. Thus, we assume the following form for the joint probability function:

$$f_X(x_1, y_2, \ldots, x_n) = \frac{1}{\sigma_1\sqrt{2\pi}}\,\mathrm{e}^{-\frac{1}{2}\left(\frac{x_1-\mu_1}{\sigma_i}\right)^2}\frac{1}{\sigma_2\sqrt{2\pi}}\,\mathrm{e}^{-\frac{1}{2}\left(\frac{x_2-\mu_2}{\sigma_i}\right)^2}\cdots\frac{1}{\sigma_n\sqrt{2\pi}}\,\mathrm{e}^{-\frac{1}{2}\left(\frac{x_n-\mu_n}{\sigma_i}\right)^2} \tag{E.2}$$

for uncorrelated random variables $X_1, X_2, \ldots, X_n$ of normal distribution each with a mean μ_i and a standard deviation σ_i. The failure behavior of a structure is ruled through a limit-state function

$$g(x_1, x_2, \ldots, x_n) = a_0 + a_1\,x_1 + a_2\,x_2 + \cdots + a_n\,x_n \tag{E.3}$$

with

$$g \leq 0 \tag{E.4}$$

indicating failure. The function g may have undergone transformations due to the aforementioned transformations of random variables.

The random variables are standardized with

$$Y_i = \frac{X_i - \mu_i}{\sigma_i}, \quad i = 1, \ldots, n \tag{E.5}$$

leading to a joint probability density function

$$f_Y(y_1, y_2, \ldots, y_n) = \frac{1}{(2\pi)^{\frac{n}{2}}}\,\mathrm{e}^{-\frac{1}{2}\left(y_1^2 + y_2^2 + \cdots + y_n^2\right)} \tag{E.6}$$

This function is characterized by radial symmetry, i.e., all arguments with the same distance $r = \sqrt{y_1^2 + y_2^2 + \cdots + y_n^2}$ to the origin have the same function value. This corresponds to hyperspheres in the n-dimensional space of the random variables.

The standardization (Eq. (E.5)) leads to a standardized limit-state function

$$h(y_1, y_1, \ldots, y_n) = \beta + \alpha_1 y_1 + \alpha_2 y_2 + \cdots + \alpha_n y_n \tag{E.7}$$

with a reliability index

$$\beta = \frac{a_0 + a_1 \mu_1 + a_2 \mu_2 + \cdots + a_n \mu_n}{\sqrt{a_1^2 \sigma_1^2 + a_2^2 \sigma_2^2 + \cdots + a_n^2 \sigma_n^2}} \tag{E.8}$$

and sensitivity parameters

$$\alpha_i = \frac{a_i \sigma_i}{\sqrt{a_1^2 \sigma_1^2 + a_2^2 \sigma_2^2 + \cdots + a_n^2 \sigma_n^2}} \tag{E.9}$$

with

$$\alpha_1^2 + \alpha_2^2 + \cdots \alpha_n^2 = 1 \tag{E.10}$$

and $h \leq 0$ again indicating failure. The limit-state function may also be written as

$$h = \beta + \boldsymbol{\alpha}^T \cdot \mathbf{y} \tag{E.11}$$

with

$$\boldsymbol{\alpha} = \begin{pmatrix} \alpha_1 \\ \alpha_2 \\ \vdots \\ \alpha_n \end{pmatrix}, \quad \mathbf{y} = \begin{pmatrix} y_1 \\ y_2 \\ \vdots \\ y_n \end{pmatrix} \tag{E.12}$$

The condition $h = 0$ defines a limit-state hyperplane with the unit normal $\boldsymbol{\alpha}$. We define another coordinate transformation, i.e., a hyperrotation with

$$y_1 \mathbf{e}_1 + y_2 \mathbf{e}_2 + \cdots + y_n \mathbf{e}_n = \tilde{y}_1 \tilde{\mathbf{e}}_1 + \tilde{y}_2 \tilde{\mathbf{e}}_2 + \cdots + \tilde{y}_n \tilde{\mathbf{e}}_n \tag{E.13}$$

with unit vectors $\mathbf{e}_i, \tilde{\mathbf{e}}_i$ of Cartesian coordinate systems, see also Section C, and choose $\tilde{\mathbf{e}}_1 = \boldsymbol{\alpha}$. The application of the orthogonality condition, see Eq. (C.1), leads to

$$\mathbf{y} = \mathbf{A} \cdot \tilde{\mathbf{y}} \tag{E.14}$$

with

$$\mathbf{A} = \begin{bmatrix} \alpha_1 & \gamma_{12} & \cdots & \gamma_{1n} \\ \alpha_2 & \gamma_{22} & \cdots & \gamma_{2n} \\ \vdots & \vdots & \ddots & \vdots \\ \alpha_n & \gamma_{n2} & \cdots & \gamma_{nn} \end{bmatrix}, \quad \tilde{\mathbf{y}} = \begin{pmatrix} y_1 \\ y_2 \\ \vdots \\ y_n \end{pmatrix} \tag{E.15}$$

The $(n-1)\,n$ unknown coefficients γ_{ij} are determined with the $2(n-1)$ orthogonality conditions $\boldsymbol{\alpha} \cdot \tilde{\mathbf{e}}_i = 0$, $\tilde{\mathbf{e}}_i \cdot \tilde{\mathbf{e}}_i = 1$, $i = 2, \ldots, n$ with coefficients of $\tilde{\mathbf{e}}_i$ measured in the original system with base vectors $\mathbf{e}_i$. This is under determined with a degree $n^2 - 3n + 2$ and leaves free choices. The limit-state hyperplane is given by

$$\beta + \boldsymbol{\alpha}^T \cdot \mathbf{A} \cdot \tilde{\mathbf{y}} = \beta + \tilde{y}_1 = 0 \tag{E.16}$$

regarding orthogonality of rotated base vectors and Eq. (E.10).

The *failure probability* is given by

$$p_F = \int \cdots \int_{h \leq 0} \int f_Y(y_1, y_2, \ldots, y_n)\, \mathrm{d}y_1 \mathrm{d}y_2 \cdots \mathrm{d}y_n \tag{E.17}$$

This may also be written as

$$p_F = \int_{-\infty}^{\infty} \cdots \int_{-\infty}^{\infty} \int_{-\infty}^{-\beta} f_Y(\tilde{y}_1, \tilde{y}_2, \ldots, \tilde{y}_n)\, \mathrm{d}\tilde{y}_1 \mathrm{d}\tilde{y}_2 \cdots \mathrm{d}\tilde{y}_n \tag{E.18}$$

due to the radial symmetry of f_Y and finally leads to

$$p_F = \int_{-\infty}^{-\beta} \frac{1}{\sqrt{2\pi}}\, \mathrm{e}^{-\frac{\tilde{y}_1^2}{2}}\, \mathrm{d}\tilde{y}_1 = \Phi(-\beta) \tag{E.19}$$

with the probability function Φ of the standardized normal distribution.

The *design values* – the realization of random variables fulfilling the limit-state condition $h = 0$ with the highest failure probability – are given by

$$\tilde{y}_{1d} = -\beta, \quad \tilde{y}_{2d} = 0, \ldots, \tilde{y}_{nd} = 0 \tag{E.20}$$

in the transformed system. This is the point with the smallest hyperdistance to the origin. Back transformation using Eq. (E.14) leads to

$$y_{id} = -\beta\, \alpha_i \tag{E.21}$$

The design values in the original system are finally determined as

$$x_{id} = \mu_i - \beta\alpha_i\, \sigma_i, \quad i = 1, \ldots, n \tag{E.22}$$

using Eq. (E.5). The value of a sensitivity parameter α_i is in the range

$$-1 \leq \alpha_i \leq 1 \tag{E.23}$$

A value $|\alpha_i| \ll 1$ indicates that the random variable X_i has only a small contribution to the randomness of the structure; a value approaching ± 1 indicates a predominant contribution compared to all other random variables. The influence of X_i may be classified as favorable in case $\alpha_i > 0$ and unfavorable in case $\alpha_i < 0$. Random variables for material strength are generally favorable. Random variables for actions may be unfavorable or favorable. An increasing loading in certain cases may lead to decreasing internal forces at critical points of statically indeterminate systems. Nevertheless, such a loading is classified as unfavorable to preserve consistency.

Characteristic values are defined as quantile values

$$x_{ik} = \mu_i + \delta_i\, \sigma_i \tag{E.24}$$

with quantile coefficients δ_i. They are determined as

$$\delta_i = \Phi^{-1}(P_i) \tag{E.25}$$

with the inverse of the probability function Φ and the quantile probability P_i. A common choice is $P_i = 0.05$ – 5% of all samples of X_i are below x_{ik} – in the case of a favorable X_i leading to $\delta_i = -1.65$ and furthermore $P_i = 0.95$ – 95% of all samples of X_i are below x_{ik} – in the case of an unfavorable X_i leading to $\delta_i = 1.65$.

A *partial safety factor* for a favorable random variable is defined as

$$\gamma_i = \frac{x_{ik}}{x_{id}} = \frac{\mu_i - |\delta_i|\,\sigma_i}{\mu_i - \beta\alpha_i\,\sigma_i} = \frac{1 - |\delta_i|\,\nu_i}{1 - \beta\alpha_i\,\nu_i} > 1 \tag{E.26}$$

and for an unfavorable random variable as

$$\gamma_i = \frac{x_{id}}{x_{ik}} = \frac{1 - \beta\alpha_i\,\nu_i}{1 + \delta_i\,\nu_i} > 1 \tag{E.27}$$

with the coefficient of variation

$$\nu_i = \frac{\sigma_i}{\mu_i} \tag{E.28}$$

Such an approach may result in different partial safety factors for the same action in cases when the action is favorable in one position of the structure and unfavorable in another position. A *global safety factor*

$$\gamma = \frac{x_{1k}}{x_{2k}} = \frac{x_{1k}}{x_{1d}}\frac{x_{2d}}{x_{2k}} = \gamma_1\,\gamma_2 \tag{E.29}$$

can be derived in the very special case of $n = 2$ with a favorable resistance random variable X_1 and another unfavorable action random variable X_2 and $a_0 = 0$, $a_2 = -a_1$ regarding the limit-state function (Eq. (E.3)).

Two significant aspects have to be regarded while deriving partial safety factors. The failure probability or reliability index β, respectively, and the quantile coefficients δ_i are generally prescribed. More or less reliable estimations can be made for coefficients of variation ν_i based on statistical data. A first aspect is that the sensitivity parameters α_i are often afflicted with a major uncertainty.

A second aspect concerns the dependences between sensitivity parameters, see Eq. (E.9). Such dependences are inconvenient properties regarding partial safety factors for resistances and actions. The latter ones should be chosen independent from the construction type. But this is not possible for a given target reliability index due to the dependences between sensitivity parameters. Thus, sensitivity parameters are assumed on the "safe" with relatively large absolute values concerning Eq. (E.26) and relatively small absolute values concerning Eq. (E.27) while not fulfilling Eq. (E.10) [35, B.5]. On the other hand, additional safety is created with this approach as the reliability index β increases as a side effect.

A final issue concerns the combination of different random variables into one in order to facilitate practical design. So-called combination coefficients are used to combine actions like live load with, e.g., wind load using the respective characteristic values instead of using own partial safety factors [35, B.8].

Appendix F

Programs and Example Data

A computational model, see Fig. 1.1, should be available under the website

- `http://www.concrete-fem.com`.

It is written as PYTHON 2.7 source code

- ($\to$ `http://www.python.org`)

whereby using parts of

- NUMPY ($\to$ `http://www.numpy.org`),

- SCIPY ($\to$ `http://www.scipy.org`),

- MATPLOTLIB ($\to$ `http://matplotlib.org`).

It is provided as a number of modules. The modules all have a prefix `X`. This is a placeholder and might be subject to change. The following modules are currently used:

`X-Fem`	Main module inluding all described analysis types with finite elements
`X-SimFem`	Simplified main module with reduced analysis possibilities
`X-FemBasics`	Basic finite element procedures
`X-FemInOut`	Input, output and plotting of data
`X-FemMat`	Procedures related to material types
`X-FemElem`	Procedures related to element types
`X-FemSteps`	Procedures related to loadings and boundary conditions
`X-PlaD`	Reinforcement design for plates and slabs based on linear elastic analysis
`X-Simplex`	Ideal plastic analysis for 2D trusses with the Simplex method
`X-ExpliFem`	Main module for explicit dynamic analysis
`X-PostPlot`	Plot of given results only

These modules altogether form the `X`-package. Modules may be edited and executed using an integrated development environment (IDE) like

- IDLE

Idle is part of the basic python package. An alternative IDE is given as

- ECLIPSE

which has to be installed separately with Python support as plug-in.

Most of the examples of this textbook are computed executing one of the above listed modules. Corresponding data are also available under `http://www.concrete-fem.com` and are organized with a leading name according to a scheme

- `<name> := E<chapter>-<example>`

whereby `<chapter>` and `<example>` have to be replaced with their actual numbers and `<name>` is a prefix for files belonging to a particular example problem.

Some examples are not connected with computations. A rest of examples is treated with the computer algebra system (CAS) MAPLE 7. The corresponding sheets should also be available under `http://www.concrete-fem.com`.

A list of all examples follows ordered with `<Chapter>.<Example>` with a notation of a used module or other program:

2.1	Concrete tensile bar with localization	`X-Fem`
2.2	Concrete tensile bar with creep and imposed strains	`X-Fem`
2.3	Simple uniaxial smeared crack model	-
2.4	Reinforced concrete tension bar	`X-Fem`
3.1	Computation of moment-curvature relations for given normal forces	`X-FemMat`
3.2	Simple reinforced concrete beam	`X-Fem`
3.3	Creep deformations of reinforced concrete beam	`X-Fem`
3.4	Effect of temperature actions on a reinforced concrete beam	`X-Fem`
3.5	Effect of tension stiffening on a reinforced concrete beam with external and temperature loading	`X-Fem`
3.6	Prestressed reinforced concrete beam	`X-Fem`
3.7	Stability limit of cantilever column	MAPLE
3.8	Ultimate limit for reinforced concrete cantilever column	`X-Fem`
3.9	Beam under impact load	`X-Fem`
4.1	Deep beam with strut-and-tie model	`X-Fem`
4.2	Corbel with an elastoplastic strut-and-tie model	`X-Fem`
4.3	Corbel with rigid-plastic strut-and-tie model	`X-Simplex`
5.1	Modeling of biaxial stress–strain behavior with orthotropic hypoelasticity	-
5.2	Mises elastoplasticity with special consideration of uniaxial behavior	-
5.3	Uniaxial stress–strain relations with *Hsieh–Ting–Chen* damage	MAPLE
5.4	Gradient damage formulation for the uniaxial two-node bar	–

The data of a particular problem treated by the X-package are given with plain ASCII files with a naming scheme

- `<name>.<type>.txt`

They should be editable with basic editors on all systems, but should remain as plain ASCII files after editing. The types for the problem data are as follows:

`<type>`		user defined	written by a module
`input`	Model data	mandatory	–
`opt`	Options for written files	optional	–
`plt`	Scaling factors for plots	optional	–
`protocol`	Protocol of computation	–	always
`elemout`	Results for element integration points	–	always
`nodeout`	Results for nodes	–	always
`timeout`	Results for every time increment for selected nodes	–	if `opt` exists

An optional file `<name>.pkl` contains restart data.

Files of type `input` are organized through *sections*. Every section starts with a key word which may be followed by options. The following *section keywords* are currently used:

	followed by
`*NODE`	Nodal data
`*SOLID SECTION`	Definitions for bars, trusses, plates with reference to material types and element types
`*BEAM SECTION`	Definitions for beam structures with reference to material types and element types
`*SHELL SECTION`	Definitions for slab and shell structures with reference

*MATERIAL	Material types and their parameters
*ELEMENT	Elements with their nodes
*STEP	Definitions for type of simulation, the incrementally iterative procedure to be used, boundary conditions, loading and output intervals

Simulation steps have to be distinguished from time or load factor increments.

- A step defined by a section keyword *STEP comprises a period with a application of a particular simulation type on the model defined by the other section keywords. It contains a sequence of time or load factor increments as defined within a step.

A whole simulation must have at least one step but may consist of a sequence of steps, e.g., a step with a dynamic simulation may follow a quasistatic simulation whereby the final state of the former define the initial state of the latter.

Each section in files of type `input` may be followed by further *keywords* each beginning with a *. Further documentation about keywords should be available under `http://www.concrete-fem.com`. A line with leading ** may be used as comment line and is ignored. Leading blanks and blank lines are generally ignored.

Files for results are organized as follows.

Files with a type `nodeout` have superordinated output sections for every point in time or load history defined for output in the *STEP-section of `input`-files. Every node has a line within every output section with data for coordinates, values for nodal degrees of freedom and internal nodal forces. Types of nodal degrees of freedom and nodal forces depend on the element type, i.e., are different for, e.g., beam elements and plate elements.

Files with a type `elemout` also have superordinated output sections for every point in time or load history defined for output in the *STEP-section of `input`-files. Subsections correspond to every element. Every element integration point has a line within every element subsection with data for coordinates and further values like, e.g., generalized strains and stresses and further values depending on the element and material type.

Files with a type `timeout` have a line for all computed time increment with values of every nodal degree of freedom as is defined in a file of type `opt`.

Further documentation about contents of the file types `elemout` and `timeout` and about the syntax of files of type `opt` should be available under `http://www.concrete-fem.com`.

Bibliography

[1] B. Ayyub and R. McCuen. *Probability, statistics and reliability for engineers and scientists.* Chapman & Hall/CRC, Boca Raton, FL, 2nd edition, 2003.

[2] K. Bathe. *Finite Element Procedures.* Prentice-Hall, Englewood Cliffs, NJ, 1996.

[3] K. Bathe. The inf-sup condition and its evaluation for mixed finite element methods. *Computers and Structures*, 79:243–252, 2001.

[4] Z. P. Bažant and S. Baweja. Creep and shrinkage prediction model for analysis and design of concrete structures – model b3. *Materials and Structures*, 28(6):357–365, 1995.

[5] Z. P. Bažant, F. Caner, I. Carol, M. D. Adley, and S. A. Akers. Microplane model m4 for concrete. i. formulation with work conjugate deviatoric stress, ii: Algorithm and calibration. *Journal of Engineering Mechanics*, 126:944–980, 2000.

[6] Z. P. Bažant and J. Planas. *Fracture and Size Effect in Concrete and Other Quasibrittle Materials.* CRC Press, Boca Raton, FL, 1998.

[7] A. Belarbi and T. Hsu. Constitutive laws of concrete in tension and reinforcing bars stiffened by concrete. *ACI Structural Journal*, 91(4), 1994.

[8] T. Belytschko, Y. Krongauz, D. Organ, M. Fleming, and P. Krysl. Meshless methods: an overview and recent developments. *Comput. Methods Appl. Mech. Eng.*, 139:3–46, 1996.

[9] T. Belytschko, W. Liu, and B. Moran. *Nonlinear Finite Elements for Continua and Structures.* John Wiley & Sons, Chichester, 2000.

[10] J. M. Biggs. *Introduction to Structural Dynamics.* McGraw-Hill, New York, 1964.

[11] M. Bischoff. *Theorie und Numerik einer dreidimensionalen Schalenformulierung.* Institut für Baustatik, Bericht Nr.30, Universität Stuttgart, 1999.

[12] P. Bischoff. Effects of shrinkage on tension stiffening and cracking in reinforced concrete. *Can. J. Civ. Eng.*, 28:363–374, 2001.

[13] A. Bower. *Applied mechanics of solids.* CRC Press, Boca Raton, FL, 2010.

[14] C. Bucher. *Computational Analysis of Randomness in Structural Mechanics*. CRC Press, 2009.

[15] I. Carol, E. Rizzi, and K. Willam. On the formulation of anisotropic elastic degradation. I. Theory based on ap seudo-logarithmic damage tensor rate.II.Generalized pseudo-Rankine model for tensile damage. *International Journal of Solids and Structures*, 38:491 – 546, 2001.

[16] CEB-FIP. *Practitioners' guide to finite element modelling of reinforced concretestructures*. Bulletin Nr. 45. International Federation for Structural Concrete FIB, Lausanne, 2008.

[17] CEB-FIP. *Design examples for strut-and-tie-models*. Bulletin Nr. 61. International Federation for Structural Concrete FIB, Lausanne, 2011.

[18] CEB-FIP. *Model Code for Concrete Structures 2010*. International Federation for Structural Concrete (FIB), Lausanne, Switzerland, 2012.

[19] L. Cedolin and S. D. Poli. Finite element studies of shear-critical r/c beams. *Journal of Engineering Mechanics*, 103:395–410, 1977.

[20] J. Cervenka and V. K. Papanikolaou. Three dimensional combined fracture-plastic material model for concrete. *International Journal of Plasticity*, 24(12):2192 – 2220, 2008.

[21] W. Chen and A. Saleeb. *Constitutive Equations for Engineering Materials, Volume 1: Elasticity and Modeling*. Elsevier Science B.V., Amsterdam, 2nd edition, 1994.

[22] L. Damkilde and S. Krenk. Limits – a system for limit state analysis and optimal material layout. *Computers & Structures*, 64(1-4):709 – 718, 1997.

[23] R. Desmorat, F. Gatuingt, and F. Ragueneau. Nonlocal anisotropic damage model and related computational aspects for quasi-brittle materials. *Engineering Fracture Mechanics*, 74:1539–1560, 2007.

[24] DIN EN 1992-1-1. *Bemessung und Konstruktion von Stahlbeton- und Spannbetontragwerken - Teil 1-1: Allgemeine Bemessungsregeln und Regeln für den Hochbau*, Januar 2011.

[25] E. Dvorkin and K. Bathe. A continuum mechanics based four-node shell element for general nonlinear analysis. *Eng. Comput.*, 1:77–88, 1984.

[26] EN 1992-1-1. *Eurocode 2: Design of concrete structures – Part 1-1: General rules andrules for buildings*, December 2004.

[27] K. Fields and P. Bischoff. Tension stiffening and cracking of high-strength reinforced concrete tension members. *ACI Structural Journal*, 101(4), 2004.

[28] P. Folino and G. Etse. Performance dependent model for normal and high strength concretes. *International Journal of Solids and Structures*, 49:701–719, 2012.

[29] S. Foster, P. Marti, and N. Mojsilovic. Design of reinforced concrete solids using stress analysis. *ACI Structural Journal*, 100:758–764, 2003.

[30] M. Geers, R. de Borst, W. Brekelmans, and R. Peerlings. Strain-based transient-gradient damage model for failure analyses. *Comput. Methods Appl. Mech. Eng.*, 160:133–153, 1998.

[31] K. Girkmann. *Flächentragwerke*. Springer-Verlag, Wien, 6th edition, 1974.

[32] P. Grassl, K. Lundgren, and K. Gylltoft. Concrete in compression: a plasticity theory with a novel hardening law. *International Journal of Solids and Structures*, 39:5205–5223, 2002.

[33] P. Grassl, D. Xenos, U. Nystrom, R. Rempling, and K. Gylltoft. Cdpm2: A damage-plasticity approach to modelling the failure of concrete. *International Journal of Solids and Structures*, 50:3805–3816, 2013.

[34] A. E. Green and W. Zerna. *Theoretical Elasticity*. Clarendon Press, Oxford, 1954.

[35] J. Grünberg. *Grundlagen der Tragwerksplanung - Sicherheitskonzept und Bemessungsregeln für den konstruktiven Ingenieurbau / Erläuterungen zu DIN 1055-100*. Beuth Verlag, Berlin, 1st edition, 2004.

[36] F. Gruttmann and W. Wagner. Shear correction factors in timoshenko's beam theory for arbitrary shaped cross-sections. *Computational Mechanics*, 27(3):199–207, 2001.

[37] H. Bachmann et.al. *Vibration Problems in Structures – Practical Guidelines*. Birkhäuser Verlag, Basel, Boston, Berlin, 1995.

[38] T. Hampel, K. Speck, S. Scheerer, R. Ritter, and M. Curbach. High-performance concrete under biaxial and triaxial loads. *J. Eng. Mech.*, 135(11):1274–1280., 2009.

[39] D. Han and W. Chen. A non uniform hardening plasticity model for concrete materials. *Mechanics of Materials*, 4:283–302, 1985.

[40] J. Hartig, U. Häussler-Combe, and K. Schicktanz. Influence of bond properties on the tensile behaviour of textile reinforced concrete. *Cement and Concrete Composites*, 30(10):898 – 906, 2008.

[41] U. Häussler-Combe and J. Hartig. Formulation and numerical implementation of a constitutive law for concrete with strain-based damage and plasticity. *International Journal of Non-Linear Mechanics*, 43(5):399–415, 2008.

[42] U. Häussler-Combe and J. Hartig. Evaluation of concrete cracking due to restrained thermal loading and shrinkage. *ACI Structural Journal*, 109(1), 2012.

[43] J. He and Z. Fu. *Modal Analysis*. Elsevier B.V., Amsterdam, 2001.

[44] G. Hofstetter and H. A. Mang. *Computational Mechanics of Reinforced Concrete Structures*. Vieweg, Braunschweig; Wiesbaden, 1995.

[45] S. Hsieh, E. Ting, and W. Chen. A plasticity fracture-model for concrete. *Int. J. Solids Structures*, 18:181–197, 1982.

[46] T. Hsu. *Unified Theory of Reinforced Concrete*. CRC Press, Boca Raton, FL, 1993.

[47] M. Jirasek. Nonlocal models for damage and fracture: comparison of approaches. *International Journal of Solids and Structures*, 35:4133–4155, 1998.

[48] J. Joedicke. *Schalenbau*. Dokumente der Modernen Architektur 2. Karl Krämer Verlag, Stuttgart, 1962.

[49] B. L. Karihaloo. *Fracture Mechanics and Structural Concrete*. Longman Scientific & Technical Harlow, Essex, England, 1st edition, 1995.

[50] B. L. Karihaloo and Q. Z. Xiao. Accurate simulation of frictionless and frictional cohesive crack growth in quasi-brittle materials using xfem. In A. Carpinteri, P. Gambarova, G. Ferro, and G. Plizzari, editors, *Fracture Mechanics of Concrete and Concrete Structures – New Trends in FractureMechanicsofConcrete*, pages 99–110, London, 2007. Taylor & Francis Group.

[51] K.B. Gerstle et.al. Behavior of concrete under multiaxial stress states. *Journal of the Engineering Mechanics Division*, 106(6):1383–1403, 1980.

[52] M. Kitzig and U. Häußler-Combe. Modeling of plain concrete structures based on an anisotropic damage formulation. *Materials and Structures*, 44:1837–1853, 2011.

[53] W. B. Krätzig and H. J. Niemann. *Dynamics of Civil Engineering Structures*. A.A. Balkema, Rotterdam, 1996.

[54] E. Kreyszig. *Advanced Engineering Mathematics*. John Wiley & Sons, 9th edition edition, 2006.

[55] E. Kuhl, E. Ramm, and R. de Borst. An isotropic gradient damage model for quasi-brittle materials. *Comput. Methods Appl. Mech. Eng.*, 183:87–103, 2000.

[56] E. Kuhl, E. Ramm, and K. Willam. Failure analysis of elasto-plastic material models on different levels of observation. *International Journal of Solids and Structures*, 37:7259–7280, 2000.

[57] H. Kupfer, H. Hilsdorf, and H. Rüsch. Behavior of concrete under biaxial stresses. *ACI Journal*, 66:656–666, 1969.

[58] G. Lee, H. Chung, and C. Choi. Adaptive crack propagation analysis with the element-free galerkin method. *Int. J. Numer. Meth. Eng.*, 56:331–350, 2003.

[59] J. Lemaitre and R. Desmorat. *Engineering Damage Mechanics*. Springer-Verlag, Berlin, 2005.

[60] M. Leukart and E. Ramm. Identification and interpretation of microplane material laws. *Journal of Engineering Mechanics*, 132:295–305, 2006.

[61] K. Liao, P. Chang, Y. Peng, and C. Yang. A study on characteristics of interfacial transition zone in concrete. *Cement and Concrete Research*, 34:977–989, 2004.

[62] P. Liu and A. Kiureghian. Multivariate distribution models with prescribed marginals and covariances. *Probabilistic Engineering Mechanics*, 1:105–112, 1986.

[63] D. G. Luenberger. *Linear and Nonlinear Programming*. Addison-Wesley, Reading, MA, 2. Auflage edition, 1984.

[64] L. E. Malvern. *Introduction to the Mechanics of a Continuous Medium*. Prentice-Hall, Englewood Cliffs, NJ, 1st edition, 1969.

[65] P. Marti. *Theory of Structures – Fundamentals, Framed Structures, Plates and Shells*. Ernst & Sohn, Berlin, 2013.

[66] H. Matthies and G. Strang. The solution on nonlinear finite element equations. *International Journal for Numerical Methods in Engineering*, 14:1613–1626, 1979.

[67] G. Mehlhorn and J. Kollegger. Anwendung der Finite Elemente Methode im Stahlbetonbau. In G. Mehlhorn, editor, *Der Ingenieurbau - Rechnerorientierte Baumechanik*, pages 293–425. Ernst & Sohn, 1996.

[68] B. Möller and M. Beer. *Fuzzy randomness / uncertainty in civil engineering and computational mechanics*. Springer, Berlin; Heidelberg [u.a.], 2004.

[69] T. Mori and K. Tanaka. Average stress in matrix and average elastic energy of materials with misfitting inclusions. *Acta Metallurgica*, 21:571–574, 1973.

[70] J. Mosler and G. Meschke. Embedded crack vs. smeared crack models: a comparison of elementwise discontinuous crack path approaches with emphasis on mesh bias. *Comput. Methods Appl. Mech. Eng.*, 193:3351–3375, 2004.

[71] M. P. Nielsen and L. C. Hoang. *Limit Analysis and Concrete Plasticity*. Taylor & Francis, Boca Raton, FL, 3rd edition, 2010.

[72] J. Olivier, A. Huespe, M. Pulido, and E. Chavez. From continuum mechanics to fracture mechanics: the strong discontinuity approach. *Engineering Fracture Mechanics*, 69:113–136, 2002.

[73] N. Ottosen. A failure criterion for concrete. *Journal of Engineering Mechanics*, 103:527–535, 1977.

[74] J. Pamin. Gradient plasticity and damage models: a short comparison. *Computational Materials Science*, 32:472–479, 2005.

[75] R. Peerlings, R. de Borst, W. Brekelmans, and J. de Vree. Gradient enhanced damage for quasi-brittle materials. *Int. J. Numer. Meth. Eng.*, 39:3391–3403, 1996.

[76] R. Peerlings, M. Geers, R. de Borst, and W. Brekelmans. A critical comparsion of nonlocal and gradient-enhanced softening continua. *International Journal of Solids and Structures*, 38:7723–7746, 2001.

[77] S. Pijaudier-Cabot and Z. P. Bažant. Nonlocal damage theory. *Journal of Engineering Mechanics*, 113:1512–1533, 1987.

[78] K. Rahal and M. Collins. Analysis of sections subjected to combined shear and torsion – a theoreticalmodel. *ACI Structural Journal*, pages 459–469, 1995.

[79] K. Rahal and M. Collins. Combined torsion and bending in reinforced concrete beams. *ACI Structural Journal*, March-April:157–165, 2003.

[80] J. Reddy. On locking-free shear deformable beam finite elements. *Comp. Meth. Applied Mech. Eng.*, 149:113–132, 1997.

[81] G. Rombach. *Anwendung der Finite-Elemente-Methode im Betonbau.* Ernst & Sohn, Berlin, 2nd edition, 2006.

[82] C. J. Roy and W. L. Oberkampf. A comprehensive framework for verification, validation, and uncertainty quantification in scientific computing. *Comput. Methods Appl. Mech. Eng.*, 200:2131–2144, 2011.

[83] L. E. Schwer. An overview of the ptc 60/v&v 10: guide for verification and validation in computational solid mechanics. *Engineering with Computers*, 23(4):245–252, 2007.

[84] M. J. sek and Z. P. Bažant. *Inelastic Analysis of Structures.* John Wiley & Sons, New York, 1st edition, 2001.

[85] G. Sih. *Mechanics of Fracture Initiation and Propagation*, volume 11 of *Engineering Applications of Fracture Mechanics.* Springer, Netherlands, Amsterdam, 1991.

[86] P. Spanos and B. Zeldin. Monte carlo treatment of random fields: a broad perspective. *Appl. Mech. Rev.*, 51:219–237, 1998.

[87] B. Specht. Modified shape functions for the three-node plate bending element passing the patch test. *Int. J. Num. Meth. Eng.*, 26:705–715, 1988.

[88] G. Stefanou. The stochastic finite element method: Past, present and future. *Comput. Methods Appl. Mech. Eng.*, 198:1031–1051, 2009.

[89] M. Stolarska, D. L. Chopp, N. Moes, and T. Belytschko. Modelling crack growth by level sets in the extended finite element method. *Int. J. Numer. Meth. Eng.*, 51:943–960, 2001.

[90] J. van Mier. Multiaxial strain-softening of concrete. *Materials and Structures*, 19(3):190–200, 1986.

[91] J. van Mier et. al. Strain-softening of concrete in uniaxial compression. *Materials and Structures*, 30(3):195–209, 1997.

[92] F. Vecchio and M. Collins. The modified compression-field theory for reinforced concrete elements subjected to shear. *ACI Journal*, 83-22:219–231, 1986.

[93] F. Vecchio and R. Selby. Toward compression-field analysis of reinforced concrete solids. *Journal of Structural Engineering*, 117(6):1740–1758, 1991.

[94] K. Willam and E. Warnke. Constitutive model for the triaxial behavior of concrete. In *IABSE Proceedings Vol. 19*. International Association for Bridge and Structural Engineering, 1975.

[95] P. Wriggers. and S. Moftah. Mesoscale models for concrete: Homogenisation and damage behaviour. *Finite Elements in Analysis and Design*, 42:623–636, 2006.

[96] W. Wunderlich and W. Pilkey. *Mechanics of Structures – Variational and Computational Methods*. CRC Press, Boca Raton, FL, 2nd edition, 2003.

[97] H. Ziegler. *An Introduction to Thermomechanics*. North-Holland, Amsterdam, 1st edition, 1977.

[98] O. C. Zienkiewicz and R. L. Taylor. *The Finite Element Method, Volume 1*. McGraw-Hill, London, 4th edition, 1989.

[99] O. C. Zienkiewicz and R. L. Taylor. *The Finite Element Method, Volume 2*. McGraw-Hill, London, 4th edition, 1991.

Index